REPORT DOCUMENTATION PAGE		AFRL-SR-AR-TR-02- 0192
1. AGENCY USE ONLY (*leave Blank*)	2. REPORT DATE March 11, 2002	

4. TITLE AND SUBTITLE

Origin and Control of Unsteady Loading of Aerodynamic Surfaces Due to Vortex Breakdown and Stall

5. FUNDING NUMBERS

F49620-00-1-0009

6. AUTHOR(S)

Donald Rockwell

7. PERFORMING ORGANIZATION NAME(S) AND ADDRESS(ES)

Department of Mechanical Engineering and Mechanics
Lehigh University
354 Packard Laboratory, 19 Memorial Drive West
Bethlehem, PA 18015

8. PERFORMING ORGANIZATION REPORT NUMBER

9. SPONSORING/MONITORING AGENCY NAME(S) AND ADDRESS(ES)

Dr. John D. Schmisseur, Program Manager
Unsteady Aerodynamics and Hypersonics
AFOSR/NA, Room 732
801 North Randolph Street
Arlington VA 22203-1977

10. SPONSORING/MONITORING AGENCY REPORT NUMBER

20020617 036

11. SUPPLEMENTARY NOTES

The views, opinions and/or findings contained in this report are those of the author(s) and should not be construed as an official Air Force Office of Scientific Research position, policy or decision, unless so designated by other documentation.

12a. DISTRIBUTION/AVAILABILITLY STATEMENT

Approved for public release;
distribution unlimited.

12b. DISTRIBUTION CODE

13. ABSTRACT (*Maximum 200 words*)

The occurrence of vortex breakdown on a swept wing at high angle-of-attack is a well-known phenomenon. It has important consequences for the unsteady loading of the wing surface, as well as the surface of an aerodynamic appendage, the most prevalent form being the tail of an aircraft. These types of vortex-surface interactions can be manipulated using simple control techniques. The first involves small-amplitude perturbations of either the wing or the aerodynamic surface. Another effective approach involves insertion of a wire in the vortex, whereby the wire is either transverse to, or in-line with, the axis of the vortex. All of the foregoing control techniques can significantly alter both the onset and structure of vortex breakdown. As a consequence, the unsteady loading that the vortex breakdown imposes upon the aerodynamic surface is altered as well. The major thrust of this research program has been determination of the source of the unsteadiness by use of cinema versions of high-image-density particle image velocimetry (PIV), which generates space-time representations of the flow patterns. With this approach, it is possible to determine the underlying physics of the forcing functions for the unsteady loading. Furthermore, using this same experimental approach, it has been possible to determine the origin of loading in other configurations, which have links to aerodynamics.

14. SUBJECT TERMS			15. NUMBER OF PAGES
Vortex, vibration, vortex-tail Interaction			16. Price Code
17. SECURITY CLASSIFICATION OF REPORT	18. SECURITY CLASSIFICATION OF THIS PAGE	19. SECURITY CLASSIFICATION OF ABSTRACT	20. LIMITATION OF ABSTRACT
Unclassified	Unclassified	Unclassified	

ORIGIN AND CONTROL OF UNSTEADY LOADING OF AERODYNAMIC SURFACES DUE TO VORTEX BREAKDOWN AND STALL

AFOSR GRANT #F49620-00-1-0009
1 October 1999 to 30 September 2001

Donald Rockwell
Department of Mechanical Engineering and Mechanics
354 Packard Laboratory, 19 Memorial Drive West
Lehigh University
Bethlehem, PA 18015

SUMMARY

The occurrence of vortex breakdown on a swept wing at high angle-of-attack is a well-known phenomenon. It has important consequences for the unsteady loading of the wing surface, as well as the surface of an aerodynamic appendage, the most prevalent form being the tail of an aircraft. These types of vortex-surface interactions can be manipulated using simple control techniques. The first involves small-amplitude perturbations of either the wing or the aerodynamic surface. Another effective approach involves insertion of a wire in the vortex, whereby the wire is either transverse to, or in-line with, the axis of the vortex. All of the foregoing control techniques can significantly alter both the onset and structure of vortex breakdown. As a consequence, the unsteady loading that the vortex breakdown imposes upon the aerodynamic surface is altered as well. The major thrust of this research program has been determination of the source of the unsteadiness by use of cinema versions of high-image-density particle image velocimetry (PIV), which generates space-time representations of the flow patterns. With this approach, it is possible to determine the underlying physics of the forcing functions for the unsteady loading. Furthermore, using this same experimental approach, it has been possible to determine the origin of loading in other configurations, which have links to aerodynamics.

A full description and illustration of the experimental equipment set-up and procedures, as well as all acquired images and data, are included in the publications given in this report.

The personnel supported under this research grant includes Professor D. Rockwell, Director of the project, Professor B. Sahin, Ph.D. candidate Y. Kim (dissertation still in progress), and Research Scientists Dr. H. Akilli, Dr. J.-C. Lin and Dr. M. Özgören.

RESULTS

The overall emphasis of this research program has been on detailed characterization of the flow physics associated with unsteady loading of aerodynamic surfaces. In the journal publications cited in the following, details of the experimental approaches and techniques, experimental configurations, and images and graphs that describe these basic phenomena are given in detail. A common feature in all investigations has been use of the technique of high-image-density particle image velocimetry to determine instantaneous patterns of velocity, vorticity and streamline topology, in addition to averaged representations of these images, which also include global patterns of Reynolds stress and velocity fluctuations.

"Vortex Structure on a Delta Wing at High Angle-of-Attack", *AIAA Journal*, Vol. 40, No. 2, February, pp. 285-292, 2002 (with M. Özgören and B. Sahin).

The structure of the leading-edge vortex from a delta wing at high angle-of-attack is addressed using a scanning laser version of high-image-density particle image velocimetry. Emphasis is on the global patterns of instantaneous vorticity. These patterns are related to distributions of averaged and fluctuating velocity and vorticity. At low angle-of-attack, in absence of vortex breakdown, it is possible to detect a total of five distinct layers of vorticity; they all exhibit small-scale concentrations of azimuthal vorticity. Immediately downstream of the trailing-edge of the wing, larger-scale vorticity concentrations appear in the outermost vorticity layers. At sufficiently high angle-of-attack, vortex breakdown evolves from the innermost two vorticity layers. For all of these classes of vortical structures, the values of dimensionless wavelength and circulation are assessed. Moreover, the onset of vortex breakdown is interpreted in terms of both instantaneous and averaged patterns of velocity and vorticity. These considerations lead to a direct comparison of vorticity-based and stagnation criteria for breakdown. In turn, these criteria are linked to the onset of regions of fluctuating vorticity in the initial region of breakdown. *This investigation is described in Appendix A.*

"Perturbations of a Delta Wing: Control of Vortex Breakdown and Buffeting", AIAA *Journal of Aircraft*, Vol. 38, No. 6, November-December, pp. 1040-1050, 2001 (with M. Özgören and B. Sahin).

A delta wing is subjected to small-amplitude perturbations over a range of periods, in order to simulate leading-edge control concepts. Substantial modifications of the instantaneous and averaged structure of the leading-edge vortex are attainable, both with and without a downstream impingement plate. The features of the vortex response are characterized using a technique of high-image-density particle image velocimetry. The location of the onset of vortex breakdown can either be advanced or retarded, and the attendant changes in vortex structure are interpreted in the context of buffeting of the impingement plate. Comparison of the vortex structure with and without deployment of the plate shows a dramatic influence of the plate. *The results of this study are summarized in Appendix B.*

"Vortex Breakdown-Edge Interaction: Consequence of Edge Oscillations", *AIAA Journal*, Vol. 39, No. 5, pp. 865-876, 2001 (with B. Sahin, H. Akilli and J.-C. Lin).

A technique of high-image-density particle image velocimetry is employed to determine the instantaneous and averaged features of distortion of vortex breakdown incident upon a stationary and an oscillating leading-edge. It is demonstrated that the onset of vortex breakdown can be advanced or retarded substantially, depending upon the period of the edge oscillation relative to the inherent frequency of vortex breakdown. These features are interpreted with the aid of global representations of averaged and rms distributions of velocity, vorticity and Reynolds stress, as well as a cinema sequence of instantaneous patterns of velocity and vorticity. Moreover, instantaneous, wholefield images in a cinema sequence allow evaluation of global representations of spectra and cross-spectra, providing further insight into the central mechanisms that dictate the surface loading of the edge. *This investigation is described in Appendix C.*

"Control of Vortex Breakdown by a Transversely-Oriented Wire", *Physics of Fluids*, Vol. 13, No. 2, pp. 452-463, 2001 (with H. Akilli and B. Sahin).

A small wire oriented orthogonally to the axis of the leading-edge vortex on a delta wing at high angle-of-attack generates substantial changes in the vortex structure, which is characterized using a technique of high-image-density particle image velocimetry. A wire having a diameter two orders of magnitude smaller than the diameter of the leading-edge vortex prior to the onset of vortex breakdown can substantially advance the onset of breakdown by as much as fifteen vortex diameters. Depending upon the dimensionless diameter of the wire and wire location along the axis of the vortex, the onset of vortex breakdown can occur either upstream or downstream of the wire. Contours of constant velocity indicate that the rate of decrease of streamwise velocity along the centerline of the vortex is substantially enhanced, even for locations well upstream of the wire, relative to the case of vortex breakdown in absence of a wire. *This program is summarized in Appendix D.*

"Vortex Breakdown from a Pitching Delta Wing Incident Upon a Plate: Flow Structure as the Origin of Buffet Loading", *Journal of Fluids and Structures* (with M. Özgören and B. Sahin).

A delta wing is subjected to both static and dynamic variations of angle-of-attack; the vortices from the wing impinge upon a stationary plate. A technique of high-image-density particle image velocimetry is employed to compare the patterns of vortex development with and without the impingement plate. For the limiting case of static variations of angle-of-attack, the presence of the plate exerts a large influence on the onset of vortex breakdown. In contrast, dynamic (unsteady) variation of angle-of-attack yields changes of breakdown location that are generally similar for cases with and without the impingement plate. The detailed structure of the vortex breakdown-plate interaction is represented by patterns of instantaneous velocity and vorticity, which serve as the origin of buffet-induced loading of the surface of the plate. *This investigation is described in Appendix E.*

"Control of Vortex Breakdown by a Coaxial Wire", *Physics of Fluids* (with H. Akilli and B. Sahin).

A very small diameter wire is tethered from the apex of a delta wing and nominally aligned with the centerline of the leading-edge vortex. The wire can alter both the onset and structure of vortex breakdown. A technique of high-image-density particle image velocimetry allows acquisition of patterns of instantaneous and averaged vorticity and velocity, which reveal the relationship between: advancement of vortex breakdown towards the apex of the wing; and corresponding changes of patterns of vorticity and velocity contours. The diameter of the wire is one percent of the core diameter of the pre-breakdown vortex. It is possible to alter the onset of vortex breakdown by as much as approximately one chord length of the wing. A critical parameter is the length of the wire, which is normalized by: the chord of the wing; or the distance to onset of vortex breakdown in absence of the wire. Once a critical length of the wire is attained, further increases in length have no effect on the onset of breakdown. This effect is interpreted in terms of abrupt changes in patterns of vorticity and streamwise gradients of velocity along the central region of the vortex. It is possible to attain a switch in sign of azimuthal vorticity and a wakelike region of the vortex, in absence of a stagnation point. *These results are given in Appendix F*

"Imaging of Unsteady Separated Flows: Global Approaches to New Insight", *Experiments in Fluids*, Vol. 29, No. 7, pp. S255-S273, 2000.

Quantitative characterization of unsteady, separated flows is central to understanding the physics of flow-structure interactions, which can give rise to vibration and noise generation. Global, instantaneous representations, obtained form high-image-density particle image velocimetry, can provide a basis for identification and classification of flow patterns. Moreover, these representations allow direct links to established theoretical concepts, which can be expressed in terms of vorticity. Case studies of vortex-dominated flows are addressed using these approaches, with the aim of defining challenges and future prospects. *This overview is given in Appendix G.*

"Oscillations of a Turbulent Jet Incident Upon an Edge", *Journal of Fluids and Structures*, Vol. 15, No. 6, August, pp. 791-829, 2001 (with J.-C. Lin)

For the case of a jet originating from a fully turbulent channel flow and impinging upon a sharp edge, the possible onset and nature of coherent oscillations has remained unexplored. In this investigation, high-image-density particle image velocimetry and surface pressure measurements are employed to determine the instantaneous, whole-field characteristics of the turbulent jet-edge interaction in relation to the loading of the edge. It is demonstrated that even in absence of acoustic resonant or fluid-elastic effects, highly coherent, self-sustained oscillations rapidly emerge above the turbulent background. Two clearly identifiable modes of instability are evident. These modes involve large-scale vortices that are phase-locked to the gross undulations of the jet and its interaction with the edge, and small-scale vortices, which are not phase-locked. Time-resolved imaging of instantaneous vorticity and velocity reveals the form, orientation, and strength of the large-scale concentrations of vorticity approaching the edge in relation to rapid agglomeration of small-scale vorticity concentrations. Such vorticity field-edge interactions exhibit rich complexity, relative to the simplified pattern of vortex-edge

interaction traditionally employed for the quasi-laminar edgetone. Furthermore, these interactions yield highly nonlinear surface pressure signatures. The origin of this nonlinearity, involving coexistence of multiple frequency components, is interpreted in terms of large- and small-scale vortices embedded in distributed vorticity layers at the edge. Eruption of the surface boundary layer on the edge due to passage of the large-scale vortex does not occur; rather apparent secondary vorticity concentrations are simply due to distension of the oppositely-signed vorticity layer at the tip of the edge. The ensemble-averaged turbulent statistics of the jet quickly take on an identity that is distinct from the statistics of the turbulent boundary layer in the channel. Large increases in Reynolds stress occur due to onset of the small-scale concentrations of vorticity immediately downstream of separation; substantial increases at locations further downstream arise from development of the large-scale vorticity concentrations. *This investigation is described in Appendix H.*

"Organized Oscillations of an Initially-Turbulent Flow Past a Cavity", *AIAA Journal*, Vol. 39, No. 6, pp. 1139-1151, 2001 (with J.-C. Lin)

The unsteady flow structure due to a turbulent boundary layer past a rectangular, open cavity is characterized using a cinematographic technique of high-image-density particle image velocimetry. Organized small- and large-scale vortical structures emerge above the turbulent background in absence of mechanisms that typically enhance the organized nature of such shear flows: acoustic resonance; Mach wave reflections; and elastic effects of the cavity boundary. The large-scale vortical structures induce ordered pressure fluctuations at the impingement corner of the cavity; their magnitude and phase shift are characterized using simultaneous imaging and pressure measurements. Within the cavity, a jet-like flow occurs along the cavity walls, and it eventually modulates the separating shear layer at the leading-corner of the cavity. The nature of this wall jet flow is a function of the impingement process at the trailing corner of the cavity. Calculation of the turbulence statistics based on flow images reveals that the turbulence in the separated shear layer along the mouth of the cavity and in the jet-like flow within the cavity rapidly dominates the turbulent structure of the inflow. *This work is summarized in Appendix I.*

"Flow Past Two Cylinders in Tandem: Instantaneous and Averaged Flow Structure", *Journal of Fluids and Structures*, in press (with J.-C. Lin and Y. Yang).

A technique of high-image-density particle image velocimetry is employed to characterize the instantaneous and averaged patterns of velocity, vorticity and Reynolds stress due to flow past two cylinders in tandem. These features of the flow patterns are characterized in the gap region as a function of the distance between the cylinders. In turn, they are related to the patterns in the near-wake of the two-cylinder system.

Along the gap between the cylinders, small-scale concentrations of vorticity are formed in the separated shear layers. These concentrations buffet the surface boundary layer on the downstream cylinder, and thereby influence the eventual shedding of large-scale vortices. Within the gap, the instantaneous structure of the recirculation zones can exhibit both symmetrical and asymmetrical patterns.

In the near-wake of the downstream cylinder, the form of the vortex shedding, as well as the averaged patterns of the flow structure, are substantially altered, relative to the case of a single cylinder. The width of the near-wake, as represented by averaged patterns of vorticity, is substantially narrower and the magnitudes of the peak Reynolds stress are significantly attenuated. On the other hand, if the gap region is sufficiently large such that Kármán-like vortices form between the cylinders, the near-wake of the downstream cylinder shows distinctive patterns, and both the wake width and the magnitude of the Reynolds stresses become larger, relative to those at smaller gap width. *This study is described in Appendix J.*

APPENDIX A

Ozgoren-2 FIN 060701

Vortex Structure on a Delta Wing at High Angle-of-Attack*

by

M. Özgören* and B. Sahin*
Department of Mechanical Engineering
Cukurova University
Balcali 01330 Adana
Turkey
* On leave at Lehigh University

D. Rockwell
Department of Mechanical Engineering
and Mechanics
354 Packard Laboratory
19 Memorial Drive West
Lehigh University, Bethlehem, PA 18015

Abstract

The structure of the leading-edge vortex from a delta wing at high angle-of-attack is addressed using a scanning laser version of high-image-density particle image velocimetry. Emphasis is on the global patterns of instantaneous vorticity. These patterns are related to distributions of averaged and fluctuating velocity and vorticity. At low angle-of-attack, in absence of vortex breakdown, it is possible to detect a total of five distinct layers of vorticity; they all exhibit small-scale concentrations of azimuthal vorticity. Immediately downstream of the trailing-edge of the wing, larger-scale vorticity concentrations appear in the outermost vorticity layers. At sufficiently high angle-of-attack, vortex breakdown evolves from the innermost two vorticity layers. For all of these classes of vortical structures, the values of dimensionless wavelength and circulation are assessed. Moreover, the onset of vortex breakdown is interpreted in terms of both instantaneous and averaged patterns of velocity and vorticity. These considerations lead to a direct comparison of vorticity-based and stagnation

***Akilli, H, Sahin, B. and Rockwell, D. 2002 "Vortex Structure on a Delta Wing at High Angle-of-Attack", *AIAA Journal*, Vol. 40, No. 2, February, pp. 285-292.**

criteria for breakdown. In turn, these criteria are linked to the onset of regions of fluctuating vorticity in the initial region of breakdown.

Nomenclature

C = Chord of delta wing

D_{PR} = Diameter of vortex measured at interface of vorticity layers P and R at a location prior to the onset of breakdown, i.e. a distance 0.375 C upstream of trailing-edge of wing

D_v = Characteristic vortex diameter of vortex prior to onset of breakdown at location a distance 0.6 C upstream of trailing-edge of wing

D_v^* = Characteristic diameter of vortex prior to onset of breakdown at location a distance 0.375 C upstream of trailing-edge of wing

M = Magnification

Re = Reynolds number, $Re = U_\infty C/\nu$

U_{ref} = Reference velocity

U_∞ = Freestream velocity

V = Total velocity

$\langle V \rangle$ = Averaged velocity

w = Axial velocity of vortex

z = Axial coordinate along centerline of vortex

α = Angle-of-Attack of delta wing

Γ^* = Dimensionless circulation, $\Gamma^* = \Gamma/\pi\, U_{ref} D_v$

λ = Wavelength

Λ = Sweep angle of delta wing

ν = Kinematic viscosity

σ = Radial coordinate from centerline of vortex

ω = Vorticity

$<\omega>$ = Averaged vorticity

ω_{rms} = Root-mean-square of vorticity fluctuation

Introduction

Buffeting of Aerodynamic Surfaces due to Unsteadiness of Vortices

The unsteady structure of the vortex from a swept leading-edge has important consequences for the time-dependent loading, i.e. buffeting, of both the wing and the tail of an aircraft. Such loading is due to the convection of patterns of vorticity past the wing or tail. The best known vorticity pattern arises from vortex breakdown; it often takes the form of a helical spiral. The relationship between the qualitative pattern(s) of vorticity due to vortex breakdown and the surface buffeting has been addressed by Gursul and Xie[1]; this work was preceded by a wide variety of investigations, originating with the works of Earnshaw and Lawford[2] and Mabey[3]. In addition to vortex breakdown, other origins of steady and unsteady vorticity concentrations can occur on a leading-edge vortex, as assessed by Riley and Lawson[4]. Furthermore, a rotating vortex in absence of a leading-edge can give rise to patterns of three-dimensional vorticity, as described by Sreedhar and Ragab[5]. Irrespective of the physical origin of a vorticity pattern, it can potentially contribute to the buffeting of an adjacent aerodynamic surface, as long as it exhibits unsteadiness. In the sections that follow, the possible origins of vorticity patterns are described in further detail, in order to provide a basis for defining the unresolved issues and the objectives of the present investigations.

Vortex Breakdown on a Delta Wing

The theoretical framework, as well as experimental investigations of vortex breakdown are addressed in the reviews and investigations of Sarpkaya[6,7,8], Hall[9], Liebovich[10,11], Escudier[12], Brown and Lopez[13], Lopez and Perry[14], Delery[15], Visbal[16] and Rusak, Wang and Whiting[17]. An interesting observation, as demonstrated by qualitative flow visualization is the existence of the same general form of instability of the breakdown region over a very wide range of Reynolds number. For example, the dye visualization of vortex breakdown on a delta wing at low Reynolds number $Re = 0.65 \times 10^4$ by Wérle[18] exhibits the same general form as smoke visualization at $Re = 5.8 \times 10^5$ [5] by Pagan and Solignac[19]. That is, the occurrence of a spiral-like instability, apparently arising from a predominantly inviscid instability mechanism, is clearly evident in both cases. This observation suggests that numerical and experimental investigations at varying values of Re should reveal certain common mechanisms of unsteadiness in the breakdown region.

In recent years, global experimental approaches to characterizing vortex breakdown on a delta wing have involved the investigations of Towfighi and Rockwell[20] and Lin and Rockwell[21]. These investigations characterized instantaneous patterns of vorticity and streamline topology associated with breakdown. They were guided by the theoretical work of Brown and Lopez[13], who formulated a relationship between alteration of the vorticity field in the vicinity of vortex breakdown and occurrence of a stagnation condition along the axis of the vortex. As addressed in Towfighi and Rockwell[20], the appropriate equation of Brown and Lopez[13] is:

$$w(o,z) = \frac{1}{2}\int_{-\infty}^{\infty}\int_{0}^{\infty}\frac{\sigma^2\omega(\sigma,z')}{[\sigma^2+(z-z')^2]^{3/2}}d\sigma\,dz' \qquad (1)$$

In this equation, the axial velocity along the centerline of the vortex is designated as w(o,z), the coordinate z is along the axis of the vortex, the radial coordinate σ is measured from the centerline of the vortex, and ω is the azimuthal vorticity at location (σ,z). The important feature of this equation is, according to Brown and Lopez[13], that only when the azimuthal vorticity becomes negative can a zero or negative velocity occur on the axis of the vortex. This concept is suggested in the experiments Towfighi and Rockwell[20] and in the numerical simulation of Visbal[20]. However, the nature of rapid distortion of the velocity field and the alteration of patterns of azimuthal vorticity in both instantaneous and averaged forms, as well as root-mean-square vorticity fluctuations in the region of vortex breakdown have not been established.

Instabilities in the Vortex from a Delta Wing

Although vortex breakdown is generally attributed to be the primary source of generation of vorticity concentrations, two alternate, and apparently unrelated, mechanisms occur on the outer periphery of the vortex, leading to generation of streamwise vorticity concentrations in the shear layer formed from the leading-edge. Riley and Lowson[4] provide an assessment of these instabilities.

The first type is a time-varying instability, which is analogous to the classical Kelvin-Helmholtz instability of the corresponding two-dimensional separated shear layer. This instability, which gives rise to apparent concentrations of vorticity in the separating shear layer from the windward side of the wing, has been characterized using qualitative visualization by Gad-el-Hak and Blackwelder[23,24] and Lowson[25]. The generation of small-scale structures due to separation of the vorticity layer from the leeward side of the wing is demonstrated in the numerical simulations of Gordnier and Visbal[26] and Visbal and Gordnier[27]. In the event that a delta wing is subjected to unsteady rolling motion, vorticity concentrations formed in the shear

layers emanating from both the leeward and windward sides of the wing are evident, giving rise to coexisting patterns of counterrotating vortices, as shown by Cipolla and Rockwell[28].

The second type of shear layer instability has a steady form. It can give rise to identifiable, small-scale vortices about the primary vortex formed from the leading-edge, as addressed by Payne[29], Payne, Ng, Nelson and Schiff[30], Lowson[25] and Reynolds and Abtahi[31]. These small-scale vortices apparently take the form of steady longitudinal structures. Laser Doppler anemometry measurements in the cross-flow plane on a delta wing by Riley and Lowson[4] define quantitatively the series of vorticity concentrations about the primary vortex due to these longitudinal structures.

Issues and Objectives

To date, the instantaneous, quantitative structure of the aforementioned classes of vorticity concentrations has not been addressed in relation to those due to vortex breakdown. . To be sure, the first type of vorticity concentrations can occur even when the second type is not present; this is expected to be the case at low angle-of-attack of the wing, when vortex breakdown does not occur. At high angle-of-attack, not only vortex breakdown occurs within the interior of the vortex, but also three-dimensional flow separation, and perhaps associated vorticity concentrations, arise from the leeward side of the wing in the vicinity of the trailing-edge (Su, Liu and Lui[32]). The end result of all of these possible origins of vorticity concentrations would be a complex pattern of concentrations that mutually influence each other.

The objective of the present investigation is to identify, then to evaluate quantitatively, coexisting concentrations of azimuthal vorticity, which can arise from several possible origins. Determination of the dimensionless wavelengths and values of circulation of each of these classes of vorticity concentration yields information directly related to the buffet loading of an

of the laser beam was 125 Hz. To implement the technique of high-image-density PIV, it is necessary to seed the flow with small particles. In the present experiment, hollow plastic spheres, which were metallic-coated and had a diameter of fourteen μm, were employed as scattering particles. They were essentially neutrally buoyant; moreover, calculations showed that the particle slip was insignificant in the regions of small streamline curvature at the center of the vortex.

A Canon EOS-1-35mm camera was employed for capturing the multiply-exposed particle images generated by successive scans of the laser beam. The shutter speed of the camera was 1/25 sec, and the f-stop was f = 5. In order to capture the critical field of view, the camera lens had a value of magnification M = 1:4.3. An oscillating bias mirror was deployed immediately in front of the camera lens, in order to avoid issues associated with directional ambiguity. The framing rate of the motor-driven camera was 5.55 frames/sec.

Patterns of particle images were recorded on high-resolution 35 mm film (300 lines/mm). These negatives were digitized with a resolution of 125 pixels/mm. The velocity field was obtained by applying a single-frame, cross-correlation technique to the patterns of particle images. The size of the interrogation window was 90 × 90 pixels, with 50% overlap. The criterion of high-image-density was well exceeded by ensuring that about 40 to 60 particle images were located within the interrogation window. The total number of velocity vectors was 5,734 per frame. During post-processing, a Gaussian filter with a factor of p = 1.3 was applied to the velocity field. No additional filtering of the data was carried out. The effective grid size in the physical plane of the laser sheet was 1.53 mm × 1.53 mm. The field of view in the images shown herein varies from 62 mm × 144 mm to 104 mm × 144 mm, depending upon the region of interest. The estimated uncertainty of velocity and vorticity is less than 1% and 6% respectively.

adjacent aerodynamic surface. It is particularly insightful to employ a technique that provides global, instantaneous patterns of vorticity. A method of high-image-density particle image velocimetry yields these types of representations. In turn, the instantaneous patterns of vorticity can be related to averaged patterns of both vorticity and velocity, in order to provide insight into criteria that dictate the onset of unsteadiness.

Experimental System and Techniques

A delta wing is located in a water channel having a water height of 559 mm. It was mounted at mid-depth at its midchord on a vertical, streamlined sting, with a width of 3 mm and a length of 38 mm. The fact that the sting did not influence the physics of the phenomena addressed herein was verified by: extensive dye injection at various locations on the leeward surface of the wing; and comparison of the onset of vortex breakdown with established values. The cross-sectional dimensions of the channel were 610 mm × 927 mm. Figure 1 provides plan and side views of the delta wing, which have a sweep angle of $\Lambda = 75°$, a thickness of 3.2 mm and a chord C = 222 mm. The bevel angle of the wing was 34°; it was beveled only on the windward side. Over the course of the experiment, values of angle-of-attack $\alpha = 24°$, 30°, 32° and 35° were employed. For all cases, the value of freestream velocity was maintained constant at 48 mm/s, corresponding to a Reynolds number based on C of $Re = 1.07 \times 10^4$.

A laser-scanning technique of high-image-density particle image velocimetry (Rockwell et al.[32]) allowed characterization of instantaneous patterns of flow quantities over a plane passing through the centerline of the vortex. The orientation and extent of the scanning laser beam (20 W) that defines the laser sheet of observation is given in Figure 1. This beam was generated, first of all, by transmitting it through a series of steering and focusing optics. The beam then impinged upon a rotating polygonal mirror with eight facets. The effective scanning frequency

With sequences of PIV images at hand, it is possible to evaluate averages of velocity V and vorticity ω. The following definitions were employed for these averages.

$$< V > = \frac{1}{N} \sum_{n=1}^{N} V_n(x,y) \tag{2a}$$

$$< \omega > = \frac{1}{N} \sum_{n=1}^{N} \omega_n(x,y) \tag{2b}$$

$$\omega_{rms} = \left\{ \frac{1}{N} \sum_{n=1}^{N} [\omega_n(x,y) - < \omega(x,y) >]^2 \right\}^{1/2}, \tag{2c}$$

in which N is the total number of PIV images. Averaged representations were constructed from averaging a total of thirty-six images.

In this investigation, values of dimensionless circulation and wavelength are calculated. The velocity and length scales used for normalization are as follows. A reference velocity, defined as U_{ref}, corresponds to the velocity in the undisturbed region of the free-stream, at a horizontal distance of 3.6C and a vertical distance of 4.1C from the midchord of the wing. The reference diameter D_v of the leading-edge vortex is defined as the distance between maximum-positive and maximum-negative values of vorticity across the leading-edge vortex; it is evaluated at a distance 0.6 C upstream of the trailing-edge of the wing at α = 24°, in which C is the wing chord. Further definitions of characteristic vortex diameter, based on the same concept as for D_v, are defined in subsequent sections of the text. The maximum values of uncertainty of the dimensionless wavelength λ/D_v and circulation $\Gamma^* = \Gamma/\pi\, U_{ref}\, D_v$ are estimated to be 4% and 7% respectively.

Structure of Leading-Edge Vortex

Overview of Instantaneous and Averaged Patterns of Vorticity and Velocity

The structure of the leading-edge vortex upstream of the trailing-edge of the wing is shown in Figure 2. Patterns of instantaneous vorticity ω, averaged vorticity $<\omega>$, root-mean-square vorticity fluctuation ω_{rms} and averaged velocity $<V>$ are directly compared for the same instant of time. Referring, first of all, to the pattern of averaged vorticity $<\omega>$, a total of five distinct layers are detectable. They are designated as P^+, P^-, R^+, R^- and S^+ respectively. Layers P^+, R^+, and S^+ are all positive (thick white lines), while layers P^- and R^- are negative (thin white lines). Layers P^- and P^+ correspond to the innermost portion of the vortex and, at sufficiently high angle-of-attack, appear to be associated with vortex breakdown. Layers R^+ and R^- bound the innermost layers P^- and P^+. Finally, layer S^+ is immediately adjacent to the surface of the wing. The patterns of instantaneous vorticity ω corresponding to these averaged layers are shown in the top image of Figure 2. Detectable, small-scale concentrations of azimuthal vorticity are discernible. Referring to the image of averaged fluctuating vorticity, represented by ω_{rms}, it is evident that relatively high vorticity fluctuations occur in the region defined by averaged vorticity layers P^- and R^+, and discernible fluctuations are evident at the junction of layers P^+ and R^-, as well as at the wall layer S^+. The pattern of averaged velocity $<V>$ indicates a continuous decrease of velocity along the centerline of the vortex, but does not show existence of a wake-like region, which would be characteristic of vortex breakdown.

The patterns shown in Figure 2 evolve to the forms exhibited in Figure 3a at locations downstream of the trailing-edge of the wing. Most notably, the averaged layers P^- and R^+ eventually exhibit distinct concentrations of vorticity, designated as A^+, A^- through D^+, D^-. It should be emphasized that these concentrations occur in absence of vortex breakdown. That is,

the pattern of instantaneous vorticity ω does not indicate the onset of pronounced, alternating patterns of vorticity within the central region of the vortex. The pattern of averaged (rms) vorticity fluctuations ω_{rms} shows relatively high levels of fluctuating vorticity corresponding to the generation of the vorticity concentrations A through D, as designated in the pattern of instantaneous vorticity ω.

The consequences of increase in angle-of-attack are exhibited in Figure 3b. In this case, $\alpha = 30°$. The pattern of instantaneous vorticity shows even more pronounced concentrations in the outer region of the vortex, again designated as A^+, A^- through D^+. At this higher angle-of-attack, pronounced vortex breakdown is clearly evident. The vortical structures arising from the onset of vortex breakdown are designated as Q^+ and Q^-. They appear to evolve from the centermost vorticity layers P^+ and P^-. Note that the switch in sign of azimuthal vorticity at the onset of vortex breakdown is in accord with that defined previously by Towfighi and Rockwell[20] and is compatible with the theoretical prediction of Brown and Lopez[11]. The pattern of averaged vorticity $<\omega>$ clearly shows the aforementioned switch in azimuthal vorticity as the onset of vortex breakdown occurs from layers P^+ and P^-. Examination of the averaged vorticity fluctuations ω_{rms} show relatively high levels, both in the region corresponding to vortex breakdown, as well as in the region associated with the onset and development of the counter-rotating vortex pairs.

The corresponding patterns at still higher value of angle-of-attack $\alpha = 32°$ are exhibited in Figure 3c. The vorticity concentrations A^+ through C^- are indeed pronounced and, in this case, occur near the onset of vortex breakdown, as for Figure 3b. In Figure 3c, where the angle-of-attack α is only 2° larger than for Figure 2b, the onset of breakdown has moved upstream of the trailing-edge of the wing. The pattern of averaged vorticity $<\omega>$ shows that the switch in sign

of the azimuthal vorticity occurs sharply at a well-defined location, in contrast to the more gradual transformation at the lower angle-of-attack in Figure 3b. The pattern of averaged (rms) vorticity fluctuations ω_{rms} exhibits relatively high vorticity levels at the onset of vortex breakdown and at the edges of the breakdown bubble. In addition, a layer of relatively high fluctuating vorticity occurs in the region between the breakdown bubble and the free-stream; it is, of course, associated with the array of vorticity concentrations in the outer layer of the vortex. Finally, all of these phenomena associated with the patterns of vorticity involve an abrupt transformation of the averaged velocity field $< V >$ from a jet-like flow to a wake-like flow involving a region of negative velocity immediately after the onset of vortex breakdown.

Wavelengths and Circulation of Characteristic Vorticity Concentrations

Figure 3d directly compares representative images of instantaneous vorticity from the lowest to the highest angle-of-attack. Of particular interest for buffeting of aerodynamic surfaces are the streamwise wavelength λ between adjacent vortical structures of like sign, and the dimensionless circulation Γ^* of these vortical structures. In all images shown in Figure 3d, it is evident that small-scale, lower-level concentrations of vorticity are typically detectable in the vorticity layers upstream of vortex breakdown. In previous figures, these layers of vorticity were designated as P^+, P^-, R^+, R^- and S^+. At each angle-of-attack, a total of three consecutive images of instantaneous vorticity were considered, and the averaged value of wavelength λ between adjacent concentrations was evaluated. These values of λ are normalized by the characteristic vortex diameter D_v, evaluated as the distance between the extrema of averaged positive and negative vorticity layers P^+ and P^- prior to the onset of vortex breakdown, as defined in Section 2. Over the range of angle-of-attack $24° \leq \alpha \leq 32°$, representative values of λ for the small-scale, low-level concentrations are in the range $1.0 \lesssim \lambda/D_v \lesssim 1.6$. These values of dimensionless

wavelength are smaller than those associated with the abrupt onset of vorticity concentrations in the vortex breakdown region, designated as Q^+ and Q^- in previous figures. A region of Q^+ contains, for example, a sequence of positive vorticity concentrations having a characteristic streamwise wavelength λ. Considering the range of angle-of-attack in Figure 3d, the representative values of wavelength between Q^+ (or Q^-) concentrations of like sign lie in the range $1.7 \lesssim \lambda/D_v \lesssim 2.0$. Finally, the wavelength between the vorticity concentrations of like sign in the array A^+, A^- through D^+, D^- is also of interest. Over the range of angle-of-attack considered, this wavelength lies in the range $2.0 \lesssim \lambda/D_v \lesssim 3.0$. It should be emphasized that the same reference length scale D_v is used for all of the foregoing comparisons.

Consider the smallest-scale concentrations in the top image of Figure 3d, also shown in Figure 2. These concentrations are related to the layers P^+, P^-, R^+, R^- in the averaged image of Figure 2. It is instructive to consider dimensionless length scales at a location where the concentrations in layers P and R are well developed. Choosing a distance 0.375 C upstream of the trailing-edge of the wing, the representative wavelength is $\lambda/D_v^* = 0.76$, in which D_v^* is the local diameter of the vortex. An alternate length scale for normalizing λ between these small-scale concentrations is D_{PR}, defined as the distance across the vortex, measured from the interface between P^+ and R^- to the interface between P^- and R^+, as defined in the averaged image of Figure 2. Values of λ/D_{PR} are approximately $\lambda/D_{PR} = 0.48$, where D_{PR} is also evaluated at 0.375 C upstream of the trailing-edge of the wing. The physical basis for this normalization is that the small-scale concentrations of opposite sign in layers P^+ and R^- appear to form a counterrotating system; likewise for the concentrations P^- and R^+. In fact, inspection of the locations of the peaks of the concentrations in layer R^+ in Figure 2, for example, shows that they tend to occur at

the valleys between the peaks of layer P^-. For the case of a free rotating vortex, the numerical simulation of Sreedhar and Ragab[5] shows generation of counterrotating vortex pairs about the periphery of the vortex, apparently due to a centrifugal instability similar to the structures observed in a Taylor-Couette flow between rotating cylinders. Using the same definitions as in the foregoing, the wavelengths of these counterrotating vorticity concentrations are in the range $0.46 \lesssim \lambda/D_{PR} \lesssim 1.0$.

The dimensionless circulation Γ^* of the concentrations of azimuthal vorticity is defined as $\Gamma/\pi U_{ref} D_v$, in which D_v is the pre-breakdown diameter of the vortex and U_{ref} is a reference velocity; both of these parameters are defined in Section 2. It is evident from observing the instantaneous images in Figure 3d that the largest values of circulation correspond to the concentrations of vorticity in the regions Q^+ and Q^-. At angle-of-attack $\alpha = 30°$, the values of dimensionless circulation are in the range $0.4 \lesssim \Gamma^* \lesssim 0.5$, while at the high angle-of-attack $\alpha = 32°$, they lie in the range $1.1 \lesssim \Gamma^* \lesssim 1.2$. These values compare with those of the individual concentrations of vorticity in the array A^+, A^- through D^+, D^-. For this array, the values of dimensionless circulation are in the range $0.1 \lesssim \Gamma^* \lesssim 0.4$ over the range of angle-of-attack considered. It is therefore evident that the higher values of circulation of the concentrations in the vortex array on the exterior of the vortex approach the lower values of those associated with vortex breakdown. Finally, the small-scale concentrations of vorticity in the vorticity layers below the wing, in absence of vortex breakdown (see top images of Figures 2 and 3d), have values in the range $0.02 \lesssim \Gamma^* \lesssim 0.1$.

Qualitative Visualization of Flow Patterns

In order to gain further insight into the mechanism that gives rise to the instantaneous pattern of vorticity concentrations in the outer region of the vortex, described in the foregoing as

concentrations A through D, dye visualization was undertaken. By changing the origin of the dye visualization marker, it was observed that vortices were shed from both the windward and leeward sides of the leading-edge at an axial location near the trailing-edge of the wing. Figure 4 shows dye visualization originating from a uniform layer of high-density, which was spread along the windward side of the leading-edge, and at a location near the trailing-edge. The edge is defined by the sharp, angled, gray geometry in each of the visualization images. Using this type of dye visualization, as well as other locations of dye injection, it was observed that vortices are initially shed parallel to the leading-edge of the wing, then undergo a rapid reorientation such that they are essentially vertical relative to the free-stream. This process was characterized using a sequence of dye images taken with a high-resolution digital camera. Adjacent, nearly vertical concentrations of vorticity appear to form an inverted V, the location of which is designated by the arrows in each dye image. It is suggested that the evolution of these concentrations of dye in Figure 4 gives rise to the adjacent patterns of counterrotating azimuthal vorticity A^+, A^- and so on, indicated in Figure 3d. It should be noted that rapid tilting of markers taken to represent shed vortices is evident in Figure 6 of Riley and Lowson[22], at locations further upstream of the trailing-edge, for a larger value of sweep angle, smaller angle-of-attack, and larger Reynolds number than the present values. Also evident in the dye visualization is a narrow band of lighter dye with its origin at the location designated by the arrow normal to the windward-surface of the wing. Its trajectory is of the same form as that of small-scale longitudinal steady vortices visualized by Riley and Lowson[21]. This narrow band of lighter dye forms a knot-like structure with each of the vortices shed from the leading-edge of the wing.

Downstream Evolution of Vorticity Concentrations

The issue arises as to the form of the broken-down leading-edge vortex at very high angle-of-attack and at locations downstream of the trailing-edge of the wing. In particular, the associated wavelengths and circulation of the vorticity concentrations are of interest. The representative images of Figure 5 correspond to $\alpha = 35°$. In this case, vortex breakdown occurs well upstream of the trailing-edge of the wing and the consequence for the instantaneous patterns of vorticity ω are indicated in the top image of Figure 5. Large-scale clusters of positive and negative vorticity bound the wake-like region originating from the breakdown bubble. The representative streamwise wavelength of these vortical patterns is $\lambda / D_v^{**} \sim 2$, where the vortex diameter D_v^{**} is evaluated at the trailing-edge of the delta wing, again using the definition of distance between extrema of positive and negative as defined in Section 2. The circulation of these concentrations is relatively large, on the order of $\Gamma^* = 1.27$.

In accord with the trajectories of these large-scale clusters of vorticity, relatively high levels of fluctuating vorticity ω_{rms} are generated along their paths. Moreover, the pattern of averaged velocity $< V >$ indicates a wake-like structure; the centerline velocity of the wake increases with streamwise distance downstream of the breakdown bubble.

Criteria for Onset of Vortex Breakdown and Vorticity Fluctuations

Further insight into the onset of vortex breakdown for the conditions corresponding to Figure 3c can be obtained by superposition of contours of constant averaged vorticity $< \omega >$ and constant averaged velocity $< V >$, as shown in the top image of Figure 6. This superposition of images zooms in on the region at the onset of vortex breakdown; it should be noted that intermediate contours of $< \omega >$ and $< V >$ have been omitted for purposes of clarity. Two crucial locations in the breakdown region are designated by a white dot and a black dot. The

white dot represents the location of the switch in sign of azimuthal vorticity. Referring to Figure 3c, it is the location where the abrupt transformation occurs between relatively distributed layers of positive and negative vorticity P^+ and P^- and highly concentrated regions of vorticity Q^+ and Q^-. In addition to the rapid onset of highly concentrated vorticity, the onset of vortex breakdown also involves a "switch" of the orientation of positive vorticity to a location relatively close to the wing surface. This switch is represented by concentration P^+ close to the wing surface and concentration Q^+ well away from the surface; the corresponding switch of the opposite sense occurs for P^- and Q^-. The black dot in the top image of Figure 6 represents the apparent occurrence of a stagnation point along the centerline of the vortex. Upstream of this location, the mean- (averaged) axial velocity is positive and downstream of it, it takes on negative values. We therefore conclude that the switch in sign of azimuthal vorticity, represented by the white dot, precedes the occurrence of a stagnation point at the leading portion of the breakdown bubble. This observation is in accord with the theoretical model of Brown and Lopez[13].

Actually, the time-averaged structure of vortex breakdown shown in the top image is associated with substantial fluctuations of vorticity. Contours of constant root-mean-square vorticity ω_{rms} are superposed on contours of averaged vorticity $<\omega>$ in the image at the bottom of Figure 6. A peak value of ω_{rms} occurs along the centerline of the vortex at a location coincident with the stagnation point. In fact, upstream of this location, on either side of the vortex centerline, two peak values of ω_{rms} occur. Taken together, these three peak values of ω_{rms} show that the onset of vortex breakdown is associated with large values of local vorticity fluctuations. The largest peak value of ω_{rms} is 7.92 sec^{-1}; it compares with the peak value of averaged vorticity is $<\omega> = 10.8\ sec^{-1}$. A further observation is that significant levels of ω_{rms}

occur at approximately the location of the switch in sign of averaged vorticity $< \omega >$, designated by the large white dot in the top image.

Concluding Remarks

Using an approach of global, instantaneous imaging of the leading-edge vortex from a delta wing, it has been demonstrated that multiple layers of instantaneous and averaged azimuthal vorticity can coexist over a range of angle-of-attack. From the standpoint of buffet-induced loading of aerodynamic surfaces, the instantaneous structure of these vorticity layers, and the variation of this structure with time, is of principal importance. Three basic classes of vorticity concentrations are evident. They are classified according to their physical origin in Table 1, and briefly summarized in the following:

(a) ***Concentrations of azimuthal vorticity due to a centrifugal instability of the vortex*** have relatively small values of wavelength and circulation. The wavelength normalized by the local vortex diameter is in general accord with the recent numerical simulation of Sreedhar and Garab[33] for a free vortex in absence of a leading-edge.

(b) ***Concentrations due to vortex breakdown*** have significantly larger values of wavelength, and large values of circulation. They are associated with the classical helical mode instability of breakdown.

(c) ***Concentrations due to an unsteady instability from the leading-edge*** have relatively large values of wavelength and moderate values of circulation. They apparently arise from reorientation of the unsteady layer vorticity shed from the leading-edge. In concept, their origin appears to be the same as shown by smoke visualization of the time varying instability of Riley and Lowson[4].

It should be emphasized that the wavelength and circulation of certain of the aforementioned classes of vorticity concentrations may be a function of Reynolds number. For example, class (c) is expected to scale on the thickness of the shear-layer shed from the leading-edge. This aspect deserves further consideration for all classes of concentrations. It is well known, however, that the onset of breakdown of a vortex from a sharp leading-edge is relatively insensitive to Reynolds number. This observation should be correlated with the wavelength and scale of classes of concentrations (a) and (c). The possible Reynolds number dependence may influence the relative importance of the classes of vorticity concentration for buffeting of the surface of a wing or tail. Present characterizations suggest that class (a) may not be important, in view of their relative small wavelength and circulation. In future investigations, these considerations could be incorporated with images of the flow structure in crossflow planes, in addition to the plane employed in the present study.

Table 1. Dimensionless Wavelength and Circulation of Classes of Azimuthal Vorticity Concentrations

	λ/D_v	$\Gamma^* = \Gamma/\pi\, U_{ref}\, D_v$
Concentrations arising from centrifugal instability	$1.0 \lesssim \lambda/D_v \lesssim 1.6$	$0.02 \lesssim \Gamma^* \lesssim 0.1$
Concentrations due to vortex breakdown	$1.7 \lesssim \lambda/D_v \lesssim 2.0$	$0.4 \lesssim \Gamma^* \lesssim 1.2$
Concentrations due to instability from leading-edge	$2.0 \lesssim \lambda/D_v \lesssim 3.0$	$0.1 \lesssim \Gamma^* \lesssim 0.4$

A major emphasis of this investigation has been on the instantaneous and averaged structure of the leading-edge vortex prior to, and in the vicinity of, the onset of vortex breakdown. An important, related aspect is the identification and comparison of two different criteria for the onset of vortex breakdown, and their interpretation in relation to vorticity

fluctuations. The first criterion involves the location of the switch of azimuthal vorticity, and the second involves occurrence of a stagnation point along the centerline of the vortex. It is shown that the former criterion precedes the latter, and this sequence of events is consistent with the concept of Brown and Lopez[11], who established the relationship between the change in sign of the azimuthal vorticity and the occurrence of zero axial velocity along the centerline of the vortex. Particularly interesting, however, is the occurrence of peak levels of vorticity fluctuation, i.e. rms vorticity, in relation to these criteria for onset of vortex breakdown. At the location of the stagnation point, a large peak of rms vorticity occurs. Moreover, two additional peaks occur upstream of this location, immediately following the switch in sign of the averaged azimuthal vorticity. In other words, the onset of the switch of the mean vorticity also marks the occurrence of significant levels of vorticity fluctuation. In fact, the peak values of rms vorticity at the onset of vortex breakdown are of the same order as the peak values of averaged vorticity.

Acknowledgements

The authors gratefully acknowledge the financial support of the Air Force Office of Scientific Research under Contract No. F49620-99-1-0011, monitored by Dr. Steven Walker. One of the authors, Professor Besir Sahin, would like to thank the Scientific and Technical Research Council of Turkey (TUBITAK) and NATO for their financial support.

References

[1]Gursul, I. and Xie, W., "Buffeting Flows Over Delta Wings", *AIAA Journal*, Vol. 37, No. 1, January, 1999, pp. 58-65.

[2]Earnshaw, P. B. and Lawford, J. A., "Low Speed Wind Tunnel Experiments on a Series of Sharp-Edged Delta Wings", Aeronautical Research Council, R&M 3424, August, 1964.

[3]Mabey, D. B., "Beyond the Buffet Boundary", *Aeronautical Journal*, Vol. 77, April, 1973, pp. 201-215.

[4]Riley, A. J. and Lowson, M. V., "Development of a Three-Dimensional Free Shear Layer", *Journal of Fluid Mechanics*, Vol. 369, 1998, pp. 49-89.

[5]Sarpkaya, T., "On Stationary and Travelling Vortex Breakdowns", *Journal of Fluid Mechanics*, Vol. 45, Pt. 3, 1971, pp. 545-559.

[6]Sreedhar, M. and Ragab, S., "Large Eddy Simulation of Longitudinal Stationary Vortices", *Physics of Fluids*, Vol. 6, No. 7, 1994, pp. 2501-2514.

[7]Sarpkaya, T., "Vortex Breakdown in Swirling Conical Flows", *AIAA Journal*, Vol. 9, 1971, pp. 1792-1799.

[8]Sarpkaya, T., "Effect of the Adverse Pressure Gradient on Vortex Breakdown", *AIAA Journal*, Vol. 12, No. 5, 1974, p. 607.

[9]Hall, M. G., "Vortex Breakdown", *Annual Review of Fluid Mechanics*, Vol. 4, 1972, pp. 195-218.

[10]Liebovich, S., "Structure of Vortex Breakdown", *Annual Review of Fluid Mechanics*, Vol. 10, 1978, pp. 221-246.

[11]Liebovich, S., "Vortex Stability and Breakdown: Survey and Extension", *AIAA Journal*, Vol. 22, No. 9, 1984, pp. 1192-1206.

[12]Escudier, M., "Vortex Breakdown: Observations and Explanations", *Progress in Aerospace Sciences*, Vol. 25, 1988, pp. 189-229.

[13]Brown, G. L. and Lopez, J. M., "Axisymmetric Vortex Breakdown. Part 2. Physical Mechanisms", *Journal of Fluid Mechanics*, Vol. 221, 1990, pp.553-576.

[14]Lopez, J. M. and Perry, A. D., "Axisymmetric Vortex Breakdown. Part 3. Onset of Periodic Flow and Chaotic Advection", *Journal of Fluid Mechanics*, Vol. 234, 1992, pp. 449-471.

[15]Delery, J. M., "Aspects of Vortex Breakdown", *Progress in Aerospace Sciences*, Vol. 30, 1994, pp. 1-59.

[16]Visbal, M. R., "Onset of Vortex Breakdown Above a Pitching Delta Wing", *AIAA Journal*, Vol. 32, No. 8, 1994, pp. 15768-1575.

[17]Rusak, Z., Wang, S. and Whiting, C. H., "The Evolution of a Perturbed Vortex in a Pipe to Axisymmetric Vortex Breakdown", *Journal of Fluid Mechanics*, Vol. 366, 1998, pp. 211-237.

[18]Wérle, H., "Sur L'Éclatement des Tourbillons", Note Technique N° 175, Office National D'Études et de Recherches Aérospatiales, 1971.

[19]Pagan, D. and Solignac, J. L., "Experimental Study of the Breakdown of a Vortex Generated by a Delta Wing", Rech. Aérosp., Vol. 3, 1986, pp. 29-51.

[20]Towfighi, J. and Rockwell, D., "Instantaneous Structure of Vortex Breakdown on a Delta Wing via Particle Image Velocimetry", *AIAA Journal,* Vol. 31, No. 6, 1993, pp. 1160-1162.

[21]Lin, J.-C. and Rockwell, D., "Transient Structure of Vortex Breakdown on a Delta Wing at High Angle-of-Attack", *AIAA Journal*, Vol. 33, No. 1, 1995, pp. 6-12.

[22]Visbal, M. R., "Structure of Vortex Breakdown on a Pitching Delta Wing", AIAA Paper 93-0434, January, 1993.

[23]Gad-el-Hak, M. and Blackwelder, R. F., "The Discrete Vortices from a Delta Wing", *AIAA Journal*, Vol. 23, No. 3, June, 1985, pp. 961-962.

[24]Gad-el-Hak, M. and Blackwelder, R. F., "Control of the Discrete Vortices from a Delta Wing", *AIAA Journal*, Vol. 26, No. 5, 1986, pp. 1042-1049.

[25]Lowson, M. V., "The Three Dimensional Vortex Sheet Structure on Delta Wings", in Fluid Dynamics of Three-Dimensional Turbulent Shear Flows and Transition, October, 1988, AGARD-CP-438.

[26]Gordnier, R. E. and Visbal, M. R. "Instabilities in the Shear Layer of Delta Wings", AIAA Paper 95-2281, 26th AIAA Fluid Dynamics Conference, June 19-22, 1995, San Diego, CA.

[27]Visbal, M. R and Gordnier, R. E., "Origin of Computed Unsteadiness in the Shear Layer of Delta Wings", *AIAA Journal of Aircraft*, Vol. 32, No. 5, 1995, pp. 1146-1148.

[28]Cipolla, K. and Rockwell, D., "Small-Scale Vortical Structures in Crossflow Plane of a Rolling Delta Wing", *AIAA Journal*, Vol. 36, No. 12, 1998, pp. 2276-2278.

[29]Payne, F. M., "The Structure of Leading Edge Vortex Flows Including Vortex Breakdown", Ph.D. Dissertation, University of Notre Dame, 1987.

[30]Payne, F. M., Ng, T. T., Nelson, R. C., and Schiff, L. B., "Visualization and Wake Surveys of Vortical Flow over a Delta Wing", *AIAA Journal*, Vol. 26, No. 2, February, 1988, pp. 137-143.

[31]Reynolds, G. A. and Abtahi, A. A., "Three-Dimensional Vortex Development, Breakdown, and Control", AIAA Paper No. 89-0998, March, 1989.

[32]Su, W., Liu, M. and Lui, Z., "Topological Structures of Separated Flows about a Series of Sharp-Edged Delta Wings at Angles of Attack up to 90°", Topological Fluid Mechanics,

Proceedings of the IUTAM Symposium, Cambridge, UK (eds. H. K. Moffatt and A. Tsinber), Cambridge University Press, Cambridge, 1990, pp. 395-400.

[33]Rockwell, D., Magness, C., Towfighi, J., Akin, O., and Corcoran, T., "High-Image-Density Particle Image Velocimetry Using Laser Scanning Techniques", *Experiments in Fluids*, Vol. 14, 1993, pp. 181-192.

Figures

Figure 1: Schematic of experimental system showing delta wing at high angle-of-attack and onset of vortex breakdown.

Figure 2a: Patterns of instantaneous vorticity ω, averaged vorticity $<\omega>$ and rms vorticity ω_{rms}, in comparison with averaged velocity $<V>$ at an angle-of-attack $\alpha = 24°$. Minimum and incremental values of instantaneous vorticity ω are 1 and 0.75 sec^{-1}; of averaged vorticity $<\omega>$ are 1 and 0.75 sec^{-1}; and of rms vorticity ω_{rms} 0.75 and 0.1 sec^{-1}. For contours of averaged velocity $<V>$, units of numerical values designated on contour lines are mm/sec and incremental value between contours is 2.5 mm/sec.

Figure 3a: Patterns of instantaneous vorticity ω, averaged vorticity $<\omega>$ and rms vorticity ω_{rms}, in comparison with averaged velocity $<V>$ at an angle-of-attack $\alpha = 24°$. Minimum and incremental values of instantaneous vorticity ω are 1 and 0.75 sec^{-1}; of averaged vorticity $<\omega>$ are 1 and 0.75 sec^{-1}; and of rms vorticity ω_{rms} 0.75 and 0.125 sec^{-1}. For contours of averaged velocity $<V>$, units of numerical values designated on contour lines are mm/sec and incremental value between contours is 2.5 mm/sec.

Figure 3b: Patterns of instantaneous vorticity ω, averaged vorticity $<\omega>$ and rms vorticity ω_{rms}, in comparison with averaged velocity $<V>$ at an angle-of-attack $\alpha = 30°$. Minimum and incremental values of instantaneous vorticity ω are 1 and 0.75 sec^{-1}; of averaged vorticity $<\omega>$ are 1 and 0.75 sec^{-1}; and of rms vorticity ω_{rms} 0.75 and 0.125 sec^{-1}. For contours of averaged velocity $<V>$, units of numerical values designated on contour lines are mm/sec and incremental value between contours is 2.5 mm/sec.

Figure 3c: Patterns of instantaneous vorticity ω, averaged vorticity $<\omega>$ and rms vorticity ω_{rms}, in comparison with averaged velocity $<V>$ at an angle-of-attack $\alpha = 32°$. Minimum and incremental values of instantaneous vorticity ω are 1 and 0.75 sec^{-1}; of averaged vorticity $<\omega>$ are 1 and 0.75 sec^{-1}; and of rms vorticity ω_{rms} 0.5 and 0.5 sec^{-1}. For contours of averaged velocity $<V>$, units of numerical values designated on contour lines are mm/sec and incremental value between contours is 2.5 mm/sec.

Figure 3d: Effect of angle-of-attack on patterns of instantaneous vorticity ω. Minimum and incremental values of instantaneous vorticity for all cases ω are 1 and 0.75 sec^{-1}.

Figure 4: Dye visualization of three-dimensional vortex shedding from the leading-edge of the wing, at a chordwise location near the trailing-edge. Angle-of-attack of wing $\alpha = 32°$.

Figure 5: Patterns of instantaneous vorticity ω, averaged vorticity $<\omega>$ and rms vorticity ω_{rms}, in comparison with averaged velocity $<V>$ at an angle-of-attack $\alpha = 35°$. Minimum and incremental values of instantaneous vorticity ω are 2 and 0.75 sec^{-1}; of averaged vorticity $<\omega>$ are 1 and 0.25 sec^{-1}; and of rms vorticity ω_{rms} are 2 and 0.25 sec^{-1}. For contours of averaged velocity $<V>$, units of numerical values designated on contour lines are mm/sec and incremental value between contours is 2.5 mm/sec.

Figure 6: Patterns of averaged velocity $<V>$ on averaged vorticity $<\omega>$ and rms vorticity ω_{rms} on averaged vorticity $<\omega>$ at an angle-of-attack $\alpha = 32°$. Minimum and incremental values of averaged vorticity $<\omega>$ are 1 sec^{-1} and 1.25 sec^{-1}; for rms vorticity ω_{rms} values are 1 and 0.5 sec^{-1} respectively. For contours of averaged velocity $<V>$, incremental value between contours is 10 mm/sec. Negative and positive vorticity contours are represented by short and long dashed-lines

respectively. Negative and positive velocity contours are designated by thin and thick solid lines respectively.

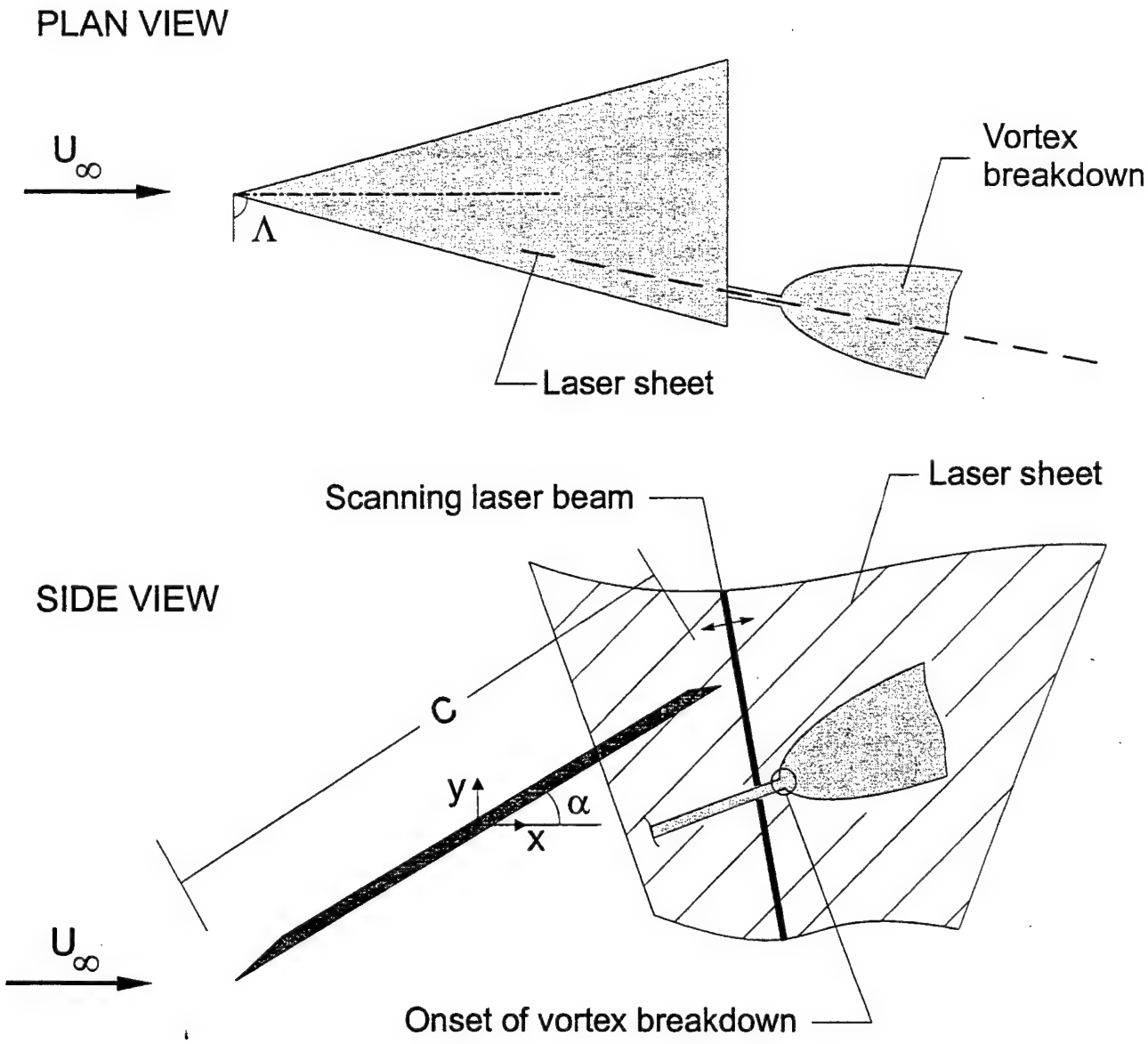

Figure 1: Schematic of experimental system showing delta wing at high angle-of-attack and onset of vortex breakdown. Scanning laser beam generates the laser sheet.

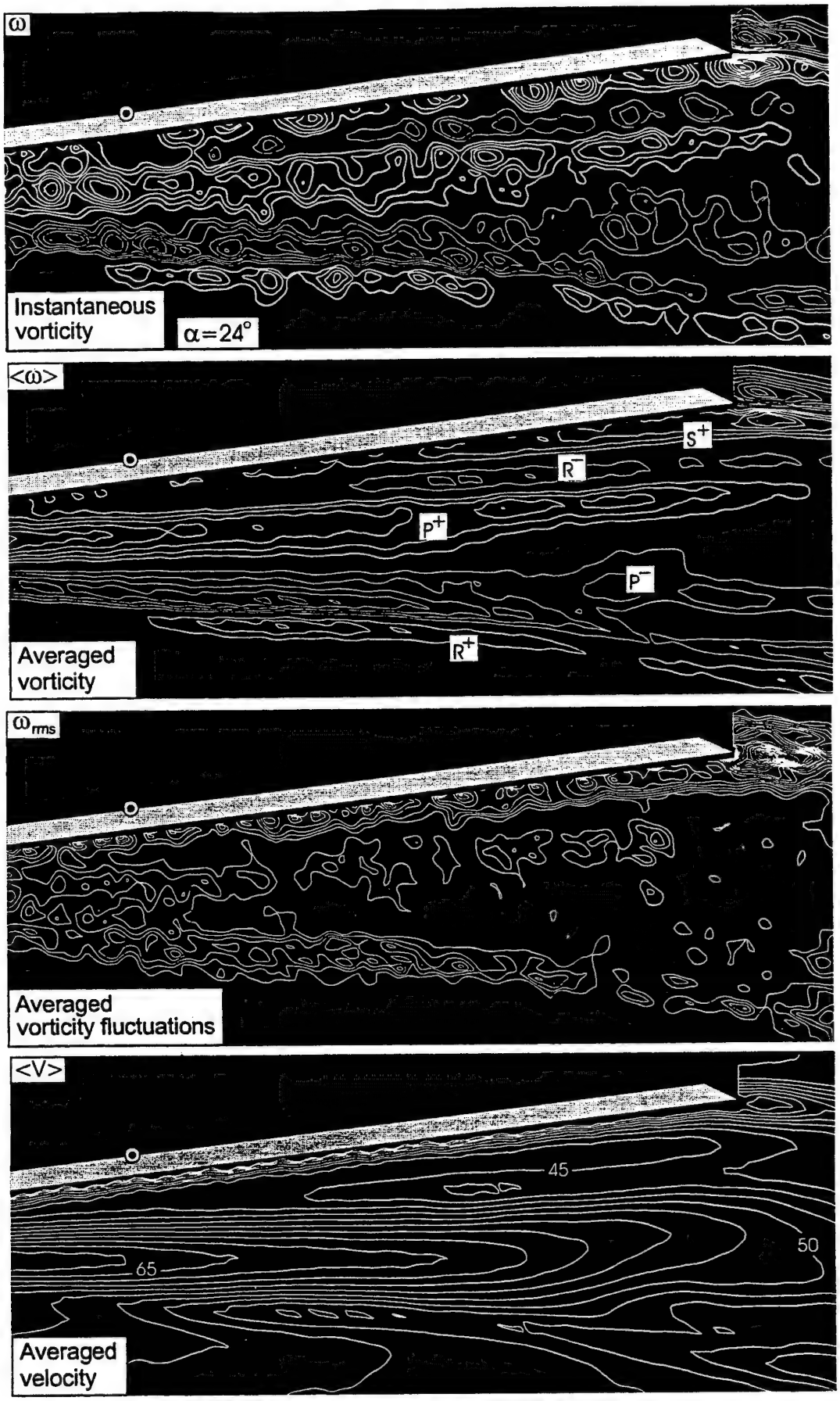

Figure 2: Patterns of instantaneous vorticity ω, averaged vorticity <ω> and rms vorticity ω_{rms}, in comparison with averaged velocity <V> at an angle-of-attack α=24°. Minimum and incremental values of instantaneous vorticity ω are 1 and 0.75 sec^{-1}; of averaged vorticity <ω> are 1 and 0.75 sec^{-1}; and of rms vorticity ω_{rms} are 0.75 and 0.1 sec^{-1}. For contours of averaged velocity <V>, units of numerical values designated on contour lines are mm/sec and incremental value between contours is 2.5 mm/sec.

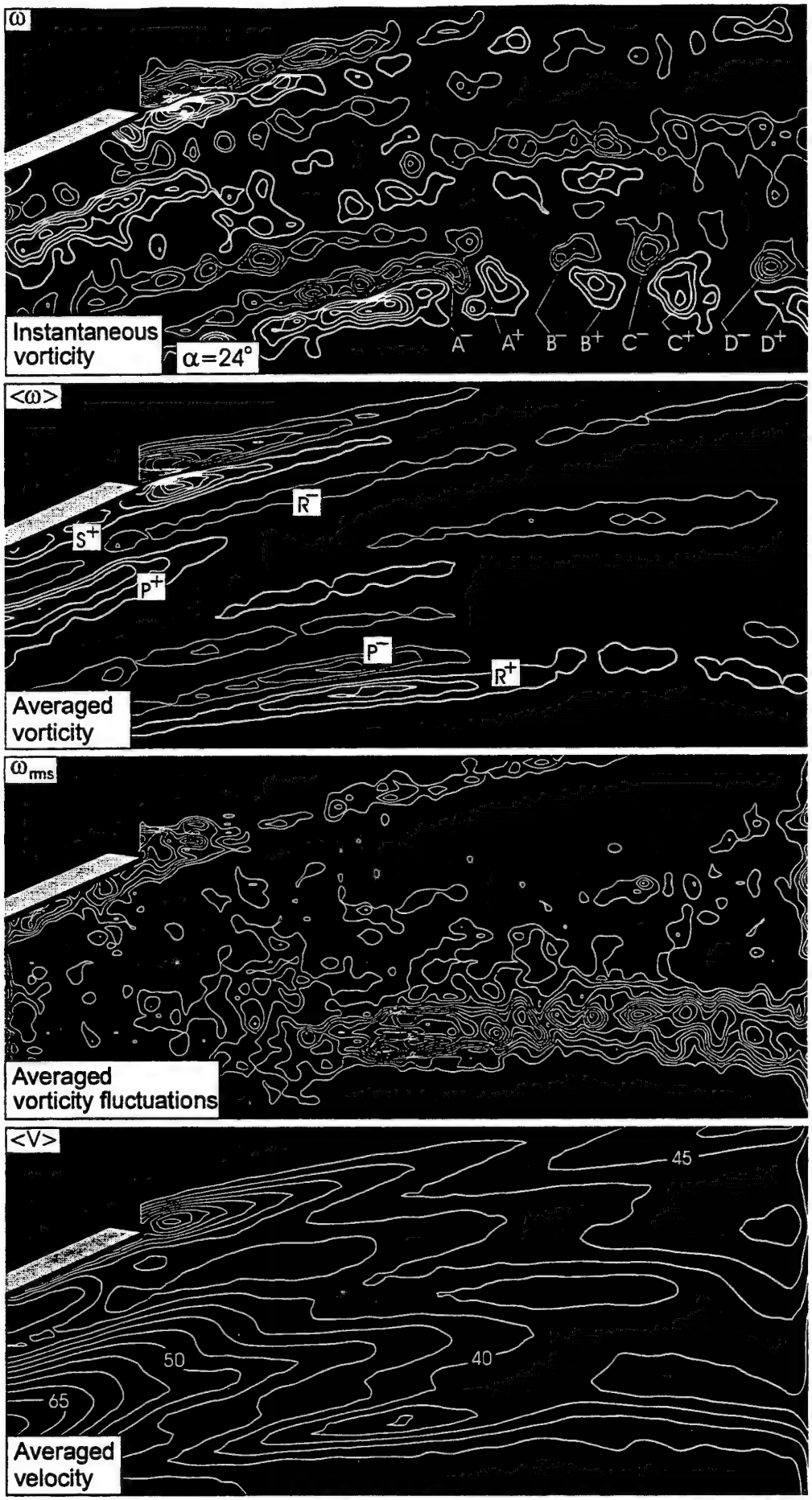

Figure 3a: Patterns of instantaneous vorticity ω, averaged vorticity <ω> and rms vorticity ω_{rms}, in comparison with averaged velocity <V> at an angle-of-attack α=24°. Minimum and incremental values of instantaneous vorticity ω are 1 and 0.75 sec^{-1}; of averaged vorticity <ω> are 1 and 0.75 sec^{-1}; and of rms vorticity ω_{rms} are 0.75 and 0.125 sec^{-1}. For contours of averaged velocity <V>, units of numerical values designated on contour lines are mm/sec and incremental value between contours is 2.5 mm/sec.

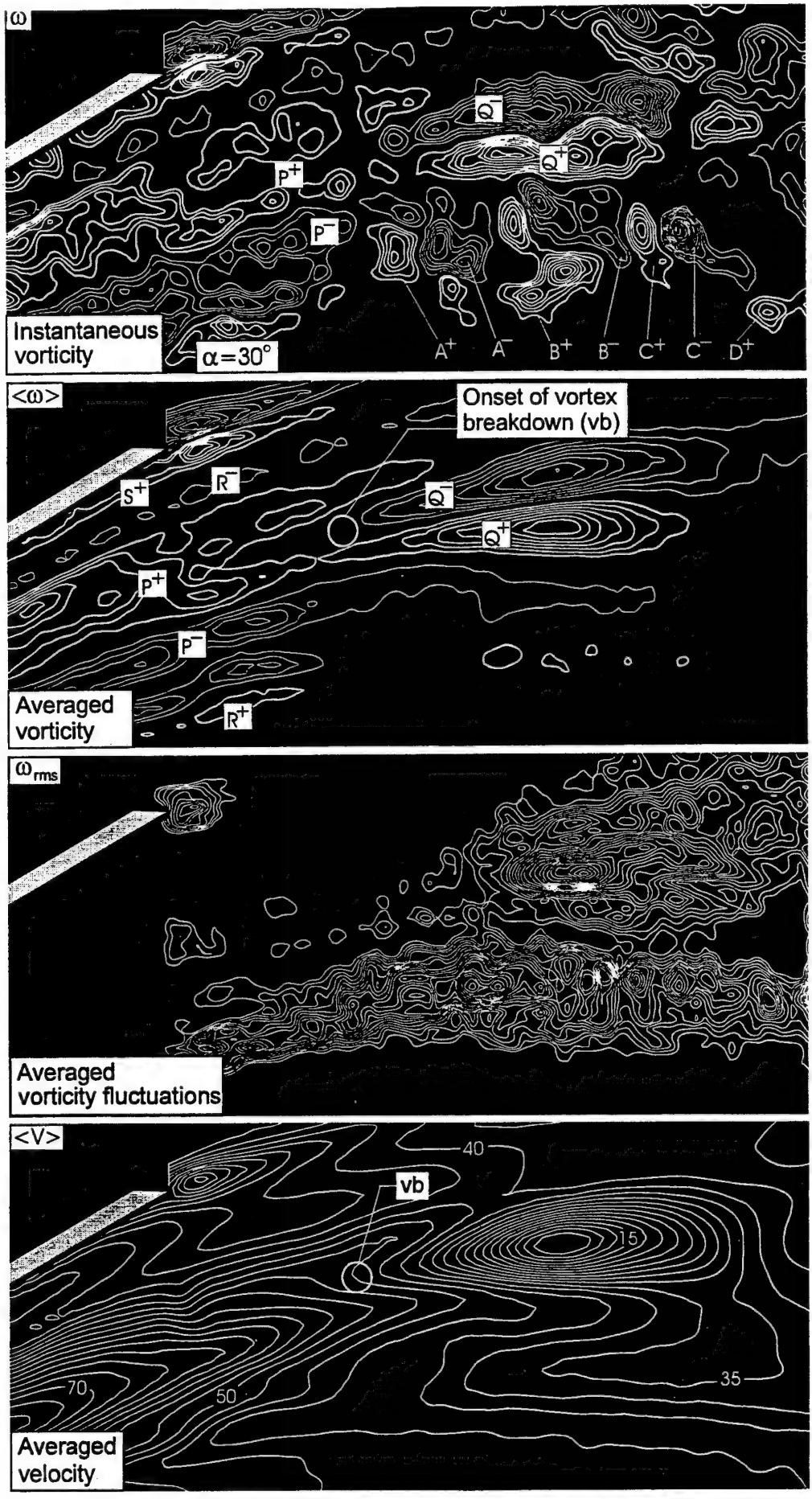

Figure 3b: Patterns of instantaneous vorticity ω, averaged vorticity <ω> and rms vorticity ω_{rms}, in comparison with averaged velocity <V> at an angle-of-attack α=30°. Minimum and incremental values of instantaneous vorticity ω are 1 and 0.75 sec^{-1}; of averaged vorticity <ω> are 1 and 0.75 sec^{-1}; and of rms vorticity ω_{rms} are 1 and 0.125 sec^{-1}. For contours of averaged velocity <V>, units of numerical values designated on contour lines are mm/sec and incremental value between contours is 2.5 mm/sec.

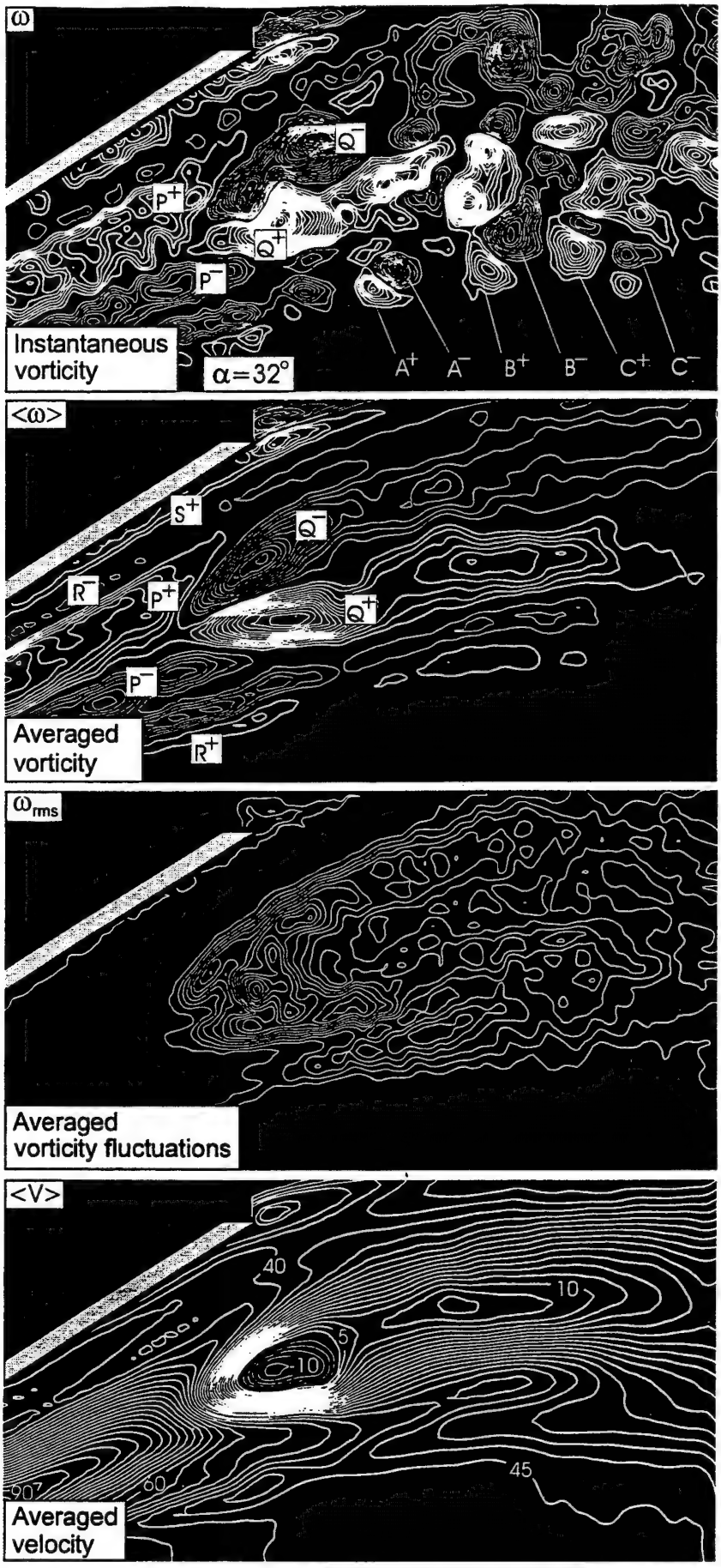

Figure 3c: Patterns of instantaneous vorticity ω, averaged vorticity <ω> and rms vorticity ω_{rms}, in comparison with averaged velocity <V> at an angle-of-attack $\alpha=32^{\circ}$. Minimum and incremental values of instantaneous vorticity ω are 1 and 0.75 sec^{-1}; of averaged vorticity <ω> are 1 and 0.75 sec^{-1}; and of rms vorticity ω_{rms} are 1 and 0.5 sec^{-1}. For contours of averaged velocity <V>, units of numerical values designated on contour lines are mm/sec and incremental value between contours is 2.5 mm/sec.

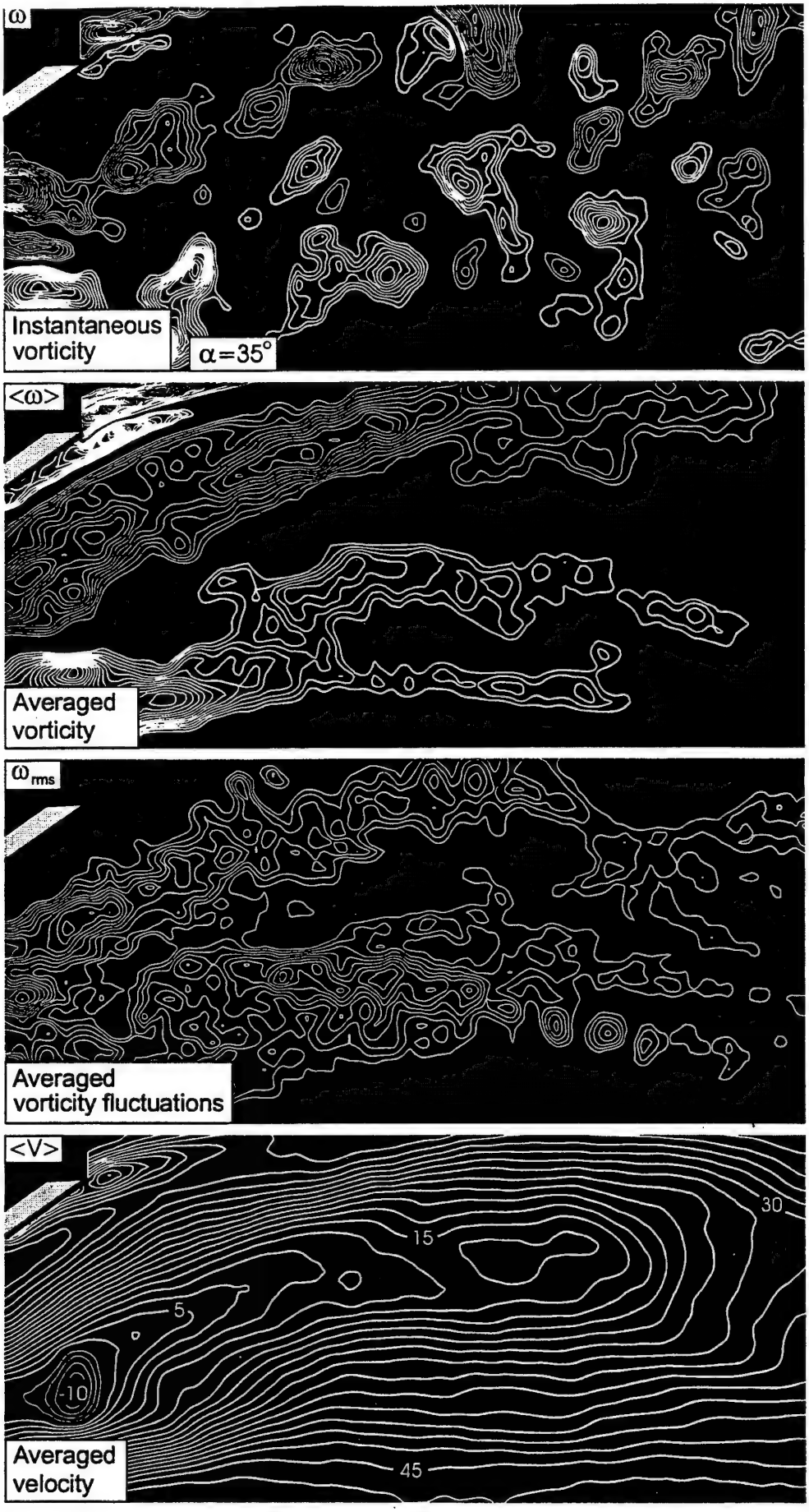

Figure 5: Patterns of instantaneous vorticity ω, averaged vorticity <ω> and rms vorticity ω_{rms}, in comparison with averaged velocity <V> at an angle-of-attack α=35°. Minimum and incremental values of instantaneous vorticity ω are 2 and 0.75 sec^{-1}; of averaged vorticity <ω> are 1 and 0.25 sec^{-1}; and of rms vorticity ω_{rms} are 2 and 0.25 sec^{-1}. For contours of averaged velocity <V>, units of numerical values designated on contour lines are mm/sec and incremental value between contours is 2.5 mm/sec.

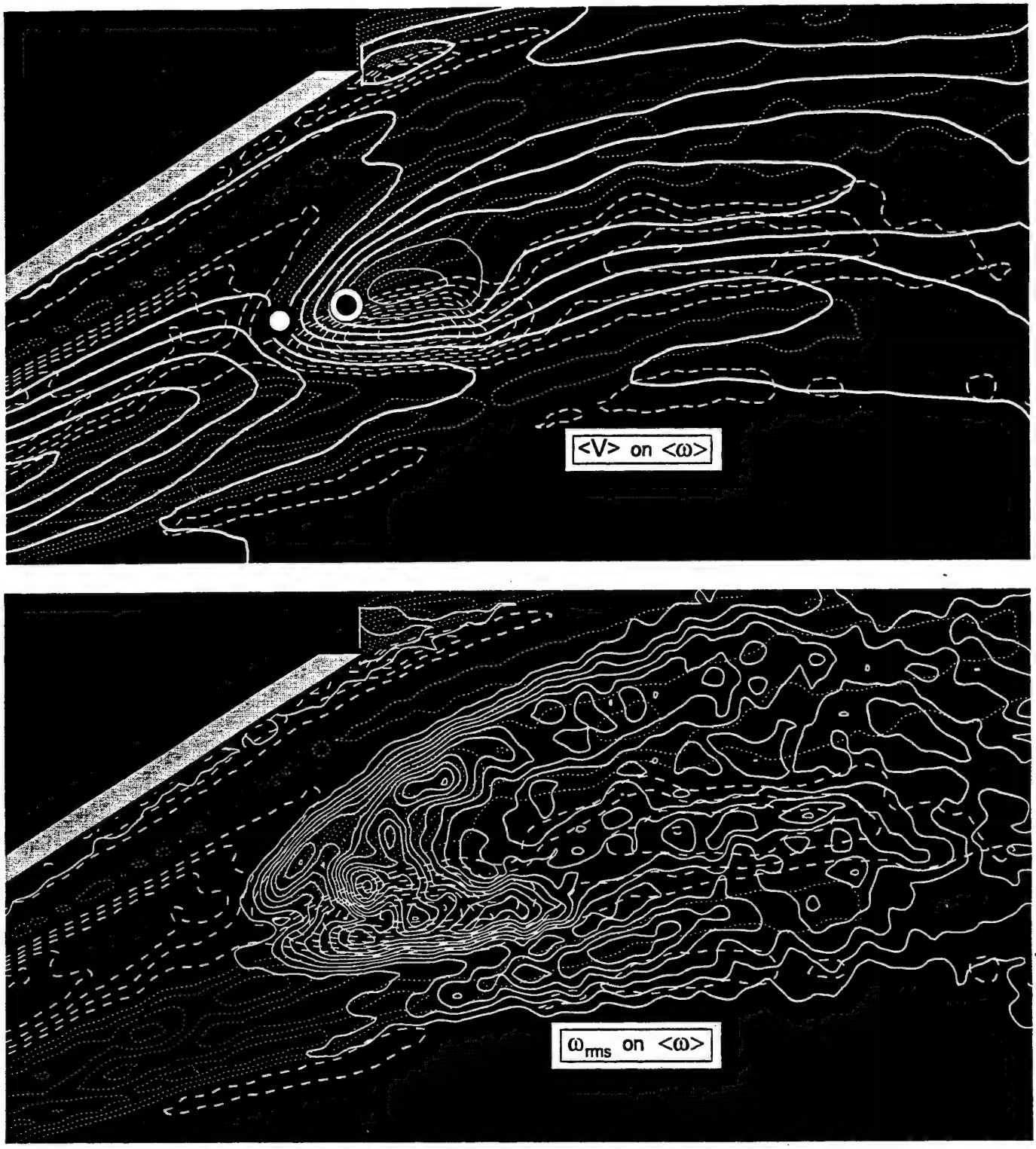

Figure 6: Patterns of averaged velocity <V> on averaged vorticity <ω> and rms vorticity ω_{rms} on averaged vorticity <ω> at an angle-of-attack $\alpha=32^{\circ}$. Minimum and incremental values of averaged vorticity <ω> are 1 sec^{-1} and 1.25 sec^{-1}; for rms vorticity ω_{rms} values are 1 and 0.5 sec^{-1} respectively. For contours of averaged velocity <V>, incremental value between contours is 10 mm/sec. Negative and positive vorticity contours are represented by short and long dashed-lines respectively. Negative and positive velocity contours are designated by thin and thick solid lines respectively.

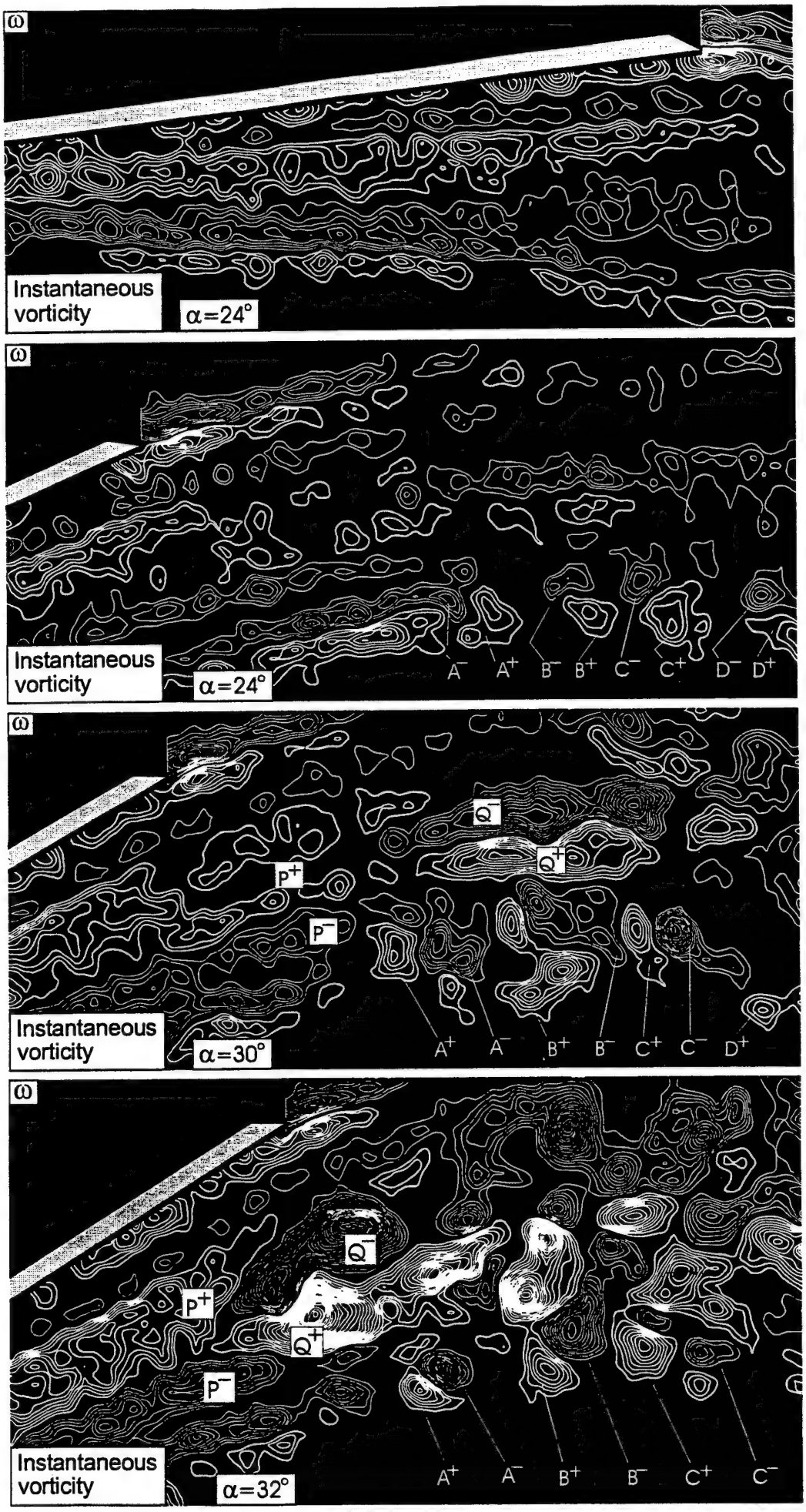

Figure 3d: Effect of angle-of-attack on patterns of instantaneous vorticity ω. Minimum and incremental values of instantaneous vorticity for all cases ω are 1 and 0.75 sec^{-1}.

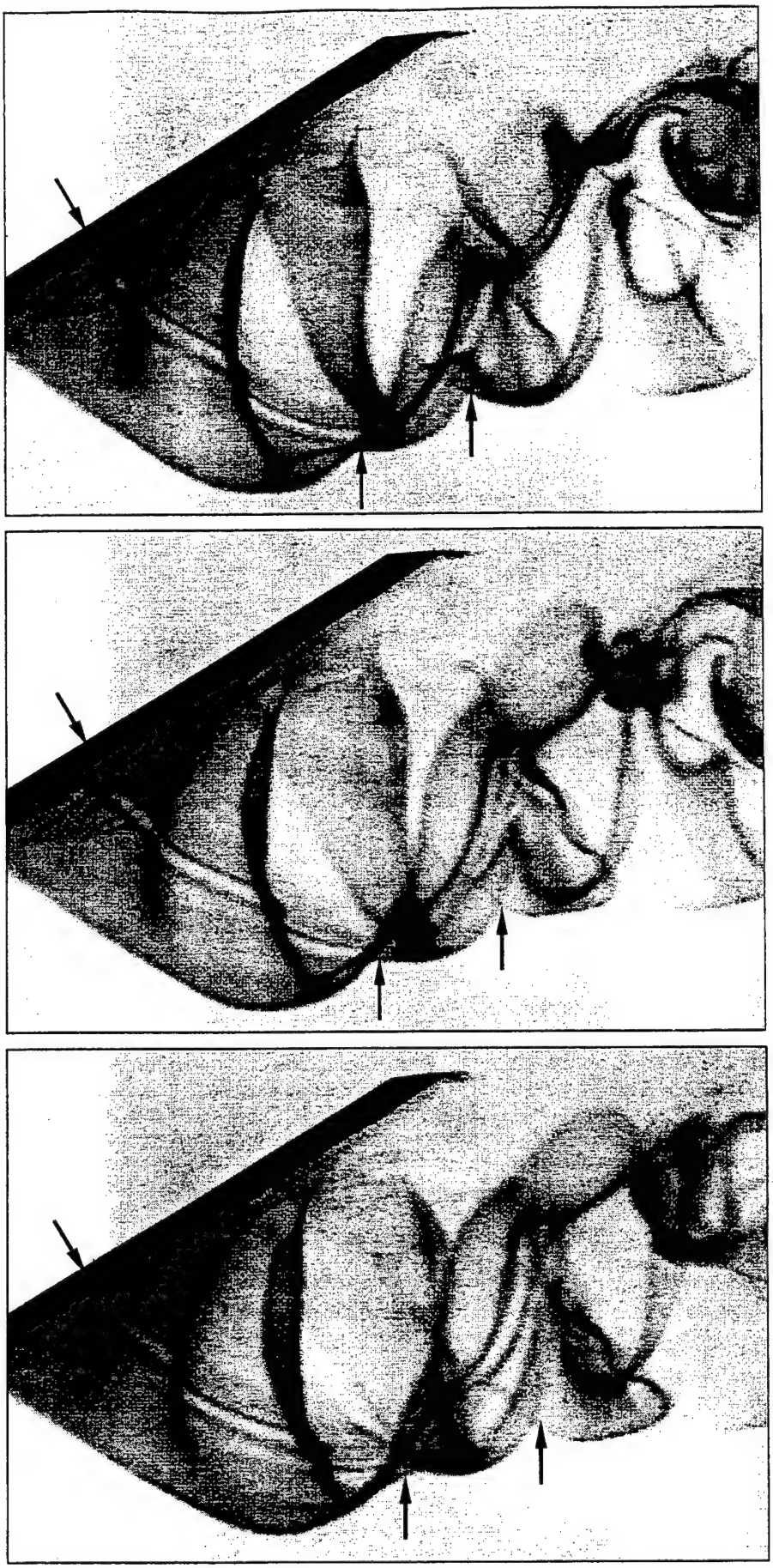

Figure 4: Dye visualization of three-dimensional vortex shedding from the leading-edge of the wing, at a chordwise location near the trailing-edge. Angle-of-attack of wing $\alpha=32^{\circ}$.

APPENDIX B

Perturbations of a Delta Wing: Control of Vortex Breakdown and Buffeting*

by

M. Özgören* and B. Sahin*

Department of Mechanical Engineering

Cukurova University

Balcali 01330 Adana

Turkey

* On leave at Lehigh University

D. Rockwell

Department of Mechanical Engineering and Mechanics

354 Packard Laboratory

19 Memorial Drive West

Lehigh University, Bethlehem, PA 18015

ABSTRACT

A delta wing is subjected to small-amplitude perturbations over a range of periods, in order to simulate leading-edge control concepts. Substantial modifications of the instantaneous and averaged structure of the leading-edge vortex are attainable, both with and without a downstream impingement plate. The features of the vortex response are characterized using a technique of high-image-density particle image velocimetry. The location of the onset of vortex breakdown can either be advanced or retarded, and the attendant changes in vortex structure are interpreted in the context of buffeting of the impingement plate. Comparison of the vortex structure with and without deployment of the plate shows a dramatic influence of the plate.

***Özgören, M. Sahin, B. and Rockwell, D. 2001 "Perturbations of a Delta Wing: Control of Vortex Breakdown and Buffeting", *AIAA Journal of Aircraft*, Vol. 38, No. 6, November-December, pp. 1040-1050.**

NOMENCLATURE

C = Chord of delta wing (mm)

D_v' = Characteristic vortex diameter (mm)

f_e = Perturbation frequency of the wing (Hz)

f_o = Frequency of vortex breakdown (Hz)

L = Distance between trailing-edge of the delta wing and leading-edge of the plate

L_p = Length of the plate (mm)

M = Magnification

N = Number of samples

Re = Reynolds number, $Re = U_\infty C/\nu$

ν = Kinematic viscosity (mm^2/sec)

T = Total time of sample (sec)

T_e = Period of wing perturbation (sec)

T_o = Period of inherent (undisturbed) vortex breakdown (sec)

U_{ref} = Reference velocity (mm/sec)

U_∞ = Freestream velocity (mm/sec)

v = Transverse velocity component (mm/sec)

V = Total velocity (mm/sec)

$\langle V \rangle$ = Averaged velocity (mm/sec)

v_{rms} = Root-mean-square of transverse velocity fluctuations (mm/sec)

W_p = Width of the plate (mm)

X_b^* = Vortex breakdown location in presence of wing perturbation (mm)

$(X_b^*)_o$ = Vortex breakdown location for stationary wing (mm)

α = Angle-of-attack of delta wing (^{o})

α_o = Amplitude of wing perturbation

$\overline{\alpha}$ = Mean angle-of-attack

$\alpha(t)$ = Dynamic angle-of-attack of delta wing (^{o})

Λ = Sweep angle of delta wing (^{o})

ν = Kinematic viscosity (mm^2/sec)

ω = Vorticity (1/sec)

$<\omega>$ = Averaged vorticity (1/sec)

ω_e = Angular velocity of wing perturbation (rad/sec)

$\Delta\omega$ = Incremental values of vorticity (1/sec)

1. INTRODUCTION

Buffeting of Tails and Plates

Interaction of vortices with aerodynamic surfaces, such as tails and plates, induces unsteady surface loading, often referred to as buffeting. Lee[1] gives an extensive overview of this area of unsteady aerodynamics. Wolfe et al.[2] correlated data from a diverse set of experiments, extending over a wide range of Reynolds and Mach number. The emphasis was on correlations of the predominant frequency of buffeting. Measurement of spectra of pressure fluctuations on either a tail or a plate are reported in the works of Washburn et al.[3], Bean and Wood[4], Canbazoglu et al.[5] and Wolfe et al.[6]. Considerable effort has focused on the buffeting of tails (fins) of F-series aircraft, with emphasis on the surface pressure loading and acceleration response. For the case of a model F-15 aircraft, Triplett[7] determined the fluctuations on the surface of the tail. Studies of model F-18 aircraft, which primarily focused on the surface

pressure spectra on tails (fins), include the works of Wentz[8], Ferman et al.[9], Zimmerman et al.[10], Shah[11], Lee and Tang[12], Martin and Thompson[13] and Lee et al.[14]. Similar types of measurements on the fin of a model F-22 aircraft were undertaken by Moses and Huttsell[15]. Luber et al.[16] addressed the role of dynamic loads on the design of aircraft. Use of active control techniques applied directly to the surface of a fin can effectively attenuate the buffet response, as demonstrated by Ashley et al.[17].

Of course, the origin of buffeting of any aerodynamic surface is the unsteady flow adjacent to it. For the case of the tail buffet problem, knowledge of the physical structure of the vortex incident upon, and its interaction with, the tail is of central importance. Breitsamter and Laschka[18,19,20] used a hot wire anemometer technique to map the fluctuating flow pattern associated with vortex breakdown in absence of a tail; they employed these data to calculate the surface loading. Beutner et al.[21] used planar Doppler velocimetry to measure the root-mean-square distributions of the unsteady flow parameters associated with impingement of a vortex upon a fin. A sequence of investigations, which employed high-image-density particle image velocimetry (PIV) involves the works of Mayori and Rockwell[22] and Wolfe et al.[6] to determine the distortion of vortex breakdown during its interaction with a thin flat plate and the investigation of Canbazoglu et al.[5,23] to define the instantaneous patterns of vortex distortion during its interaction with a tail. Related numerical investigations are not summarized here; they are provided by Rockwell[24].

The issue arises as to whether control of vortices from the leading-edges of a delta wing can provide modification of the flow field associated with buffet loading of an aerodynamic surface such as a wing or tail. In the sections that follow, various vortex control techniques are described. Then the potential for modification of the buffet flow field via vortex control is

addressed. Finally, these previous related investigations form the basis for defining the unresolved issues for the present investigation: the detailed structure of controlled vortices and their interaction with a simulated tail, i.e. a plate.

Vortex Control by Unsteady Flap or Unsteady Free-Stream

Control by a flap undergoing relatively large-amplitude transient displacement or, alternatively, periodic oscillation, is addressed by Spedding, Maxworthy and Rignot[25] and Karagounis, Maxworthy and Spedding[26]. Analogous to the approach of oscillating a flap or an entire wing is perturbation of the free stream past a stationary wing, as undertaken by Gursul, Lin and Ho[27].

Vortex Control by Axial or Tangential Blowing/Suction

Either steady or unsteady fluid injection has been employed at the leading-edge of a delta wing. Control approaches in this category are reviewed by Rockwell[28]. Steady control in the form of a single jet oriented along the axis of the vortex was addressed by Shih, Wu and Vakili[29] and Visser, Iwanski, Nelson and Ng[30], as well as by investigators cited therein. A major consequence of this approach is an increase in length of the vortex core to the onset of vortex breakdown. The effectiveness of steady tangential blowing was shown in the investigation of Wood and Roberts[31], followed by a series of investigations, including that of Celik and Roberts[32]. Flow visualization showed that blowing can effectively alter the structure of the leading-edge vortex at high angle-of-attack.

Regarding unsteady control approaches, Gad-el-Hak and Blackwelder[33] applied unsteady blowing-suction in a direction normal to a relatively thin leading-edge, and observed alteration of the initially-formed small-scale vortices from the leading-edge. Both steady and unsteady tangential blowing and suction at the leading-edge of a delta wing were addressed by Gu,

Robinson and Rockwell[34]. They show that the onset of vortex breakdown could be displaced a substantial distance downstream by use of these approaches. In a related numerical simulation, Findlay, Kern and Kwon[35], showed the effect of a steady slit-jet oriented normal to the leading-edge; changes in both the location and strength of the leading-edge vortex were attained.

Control of Vortex-Tail Interaction by Tangential Blowing

The foregoing investigations address techniques for controlling the structure of vortices. If the onset and structure of vortex breakdown can be altered, it will have important implications for buffet of, for example, a wing surface, as well as an aerodynamic appendage or a tail located in the path of the vortex. Of all of the aforementioned control approaches, only tangential blowing concepts have been employed to modify tail buffeting. Tangential blowing at the leading-edges of a delta wing can alter the buffet loading of tails, as demonstrated by Bean and Wood[4]. Moreover, Huttsell, Tinapple and Weyer[36] describe a range of investigations involving tangential blowing at a number of locations on an actual model of an aircraft, with the aim of altering the buffet-induced loading.

Vortex Control by Insertion of a Body or Edge

A type of vortex control not addressed in the previous sections involves the inherent upstream influence from a body or surface located within the vortex. Even relatively small geometries can have a significant effect. Reynolds and Abtahi[37] demonstrated that insertion of a probe in a leading-edge vortex could substantially alter the location of vortex breakdown. Furthermore, Gursul and Yang[38] showed that deployment of a control cylinder could cause the early onset of breakdown of a leading-edge vortex. Akilli, Sahin and Rockwell[39] have revealed that a small control wire, having a diameter two orders of magnitude smaller than the vortex diameter, can substantially alter the onset of breakdown. At the other extreme, if a relatively

large tail is placed in the path of a vortex and subjected to controlled perturbations, the vortex-tail interaction exhibits a coupled behavior, as demonstrated by Gursul and Xie[40]. Sahin, Akilli, Lin and Rockwell[41] have shown a conceptually similar effect for vortex interaction with an oscillating plate. They showed that vortex breakdown incident upon an oscillating plate can show markedly different patterns of vortex structure, depending upon the ratio of the perturbation frequency to the inherent frequency of vortex breakdown.

Unresolved Issues

The overall objective of the present investigation is to simulate the effect of unsteady leading-edge control, and its consequence for buffeting of surfaces located within or adjacent to the vortex. Examples of control concepts include unsteady blowing, suction, flaps, microflaps and MEMS actuators. All of these approaches alter the vorticity originating from the separation line along the leading-edge. Perturbations of the wing, and thereby its leading-edges, will alter the vorticity generation from the separation line in a fashion analogous to the aforementioned control concepts. By subjecting the wing to perturbations over a range of frequencies, it will be possible to observe the response of the vortex to an applied perturbation.

The major unresolved issues pertaining to the theme of the present investigation are: (i) the effect of small-amplitude perturbations at the leading-edges of a swept wing on the occurrence of vortex breakdown; (ii) the sensitivity of vortex breakdown to the value of perturbation frequency, relative to the inherent frequency of vortex breakdown; and (iii) the consequence of this altered vortex structure on the velocity fluctuations in the vicinity of the plate, which are central to models of buffet loading. The response of the vortex to applied perturbations should also be considered in absence of the impingement plate. Comparison with the foregoing results would show if the plate in the vortex influences the effectiveness of the

perturbations. This investigation addresses these issues using a technique of high-image-density particle image velocimetry, which allows characterization of the instantaneous and averaged patterns of vorticity and velocity.

2. EXPERIMENTAL SYSTEM AND TECHNIQUES

All experiments were performed in a large-scale water channel having a width of 927 mm and a height of 610 mm. The water height in the channel was maintained constant at a value of 559 mm. The delta wing system indicated in the schematic of Figure 1 was mounted in this test section. The wing-plate system is similar to that employed by Sahin, Akilli, Lin and Rockwell[41], for which the wing was maintained stationary and the impingement plate was subjected to controlled oscillations. The delta wing has a sweep angle of $\Lambda = 75°$, a chord $C = 222$ mm and a thickness of 3.2 mm. The bevel angle of the wing on the windward side was 34°. The plate had a length of $L_p = 162$ mm and a thickness $t_p = 6.35$ mm; its leading- and trailing-edges were beveled at angles 5° and 12° respectively. The distance between the trailing-edge of the delta wing and the leading-edge of the plate was maintained at $L = 73$ mm. The wing was subjected to small-amplitude controlled perturbations of the form $\alpha(t) = \bar{\alpha} + \alpha_o \sin \omega_e t$, in which $\omega_e = 2\pi f_e$. The period $T_e = 2\pi/\omega_e$ was varied over the interval $0.5 \text{ sec} \leq T_e \leq 2 \text{ sec}$, relative to the period $T_o = 1.6$ sec of the inherent (non-perturbed spiral ($n = 1$) mode of vortex breakdown. Values of T_o were determined from time records of dye visualization of the periodic, three-dimensional vortex pattern, at a location immediately after the onset of vortex breakdown. Over one hundred oscillation cycles were averaged to obtain the value of T_o.

The mean angle-of-attack of the wing was maintained constant at $\bar{\alpha} = 24°$. The amplitude of the wing perturbation was $\alpha_o = 1°$. Throughout the experiments, the value of free-

stream velocity was $U_\infty = 48$ mm/sec. The Reynolds number, based on chord C of the wing, was $Re = 1.07 \times 10^4$.

A technique of high-image-density particle image velocimetry allowed determination of the instantaneous flow patterns over a plane passing through the centerline of the vortex. This technique is based on a laser-scanning concept, as described by Rockwell et al.[42]. The schematic of Figure 1 shows the extent of the laser sheet generated by the scanning laser beam. The sheet was oriented such that it passed through the center of the vortex, including the region of vortex breakdown. The central feature of this scanning laser beam technique is impingement of the laser beam on a rotating polygonal mirror having eight facets. At the selected value of freestream velocity, the most effective scanning frequency of this beam was 75 Hz. In order to optimize the quality of the laser sheet generated using this approach, as well as to minimize the thickness of the sheet, which was approximately 1 mm, the laser beam was transmitted through a sequence of focusing optics prior to its impingement upon the rotating polygonal mirror.

Effective seeding of the flow with small particles is essential in order to obtain high quality images for the technique of high-image-density PIV. This seeding was accomplished by use of metallic-coated, hollow plastic spheres, which had a diameter of 14 microns.

Image acquisition involved a Canon EOS-1 camera. It effectively captured the multiply-exposed particle images generated by successive scans of the laser beam. The camera was operated at a shutter speed of 1/15 sec, and a value of f-stop of f = 5. The desired field of view of the laser sheet required a camera lens having a magnification of M = 1:4.24. Since the instantaneous flow patterns of vortex breakdown involve regions of reverse flow, it was necessary to deploy an oscillating bias mirror ahead of the camera lens in order to avoid issues associated with directional ambiguity. High-resolution 35 mm film (300 lines/mm) was

employed to record the particle images. These negatives of the particle image patterns were then digitized with a resolution of 125 pixels/mm. In order to evaluate the velocity field, a single-frame, cross-correlation technique was applied to the patterns of particle images. The most effective size of the interrogation window was 90 × 90 pixels. A fifty percent overlap was maintained, in accord with the Nyquist criterion. Approximately fifty particle images were located within the interrogation window, thereby ensuring that the criterion of high-image-density was exceeded. With the aforementioned value of magnification factor, the effective grid size in the physical plane of the laser sheet was 1.53 mm × 1.53 mm. During acquisition of the images of the flow pattern, the framing rate of the motor-driven Canon EOS-1 camera was 5.55 frames/sec. A Gaussian filter with a factor of p = 1.3 was applied to the calculated velocity field. No additional filtering of the data was carried out. The total number of velocity vectors was 5,734. The field of view of the images is 141 mm × 62 mm.

Representations of the flow pattern, to be described subsequently, involve not only instantaneous images of velocity and vorticity, but also averaged representation of these quantities, as defined by the following equations:

$$< V > = \frac{1}{N} \sum_{n=1}^{N} V_n(x,y) \tag{1a}$$

$$< \omega > = \frac{1}{N} \sum_{n=1}^{N} \omega_n(x,y) \tag{1b}$$

$$v_{rms} = \left\{ \frac{1}{N} \sum_{n=1}^{N} \left[v_n(x,y) - < v(x,y) > \right]^2 \right\}^{1/2} \tag{1c}$$

In these equations, N represents the total number of PIV images. Averaged representations were obtained by averaging a total of thirty-six images.

3. TIME-AVERAGED STRUCTURE OF VORTEX

Averaged Location of Vortex Breakdown

An overview of the consequence of wing perturbations on the averaged location of vortex breakdown in presence of the impingement plate is illustrated in Figure 2. The onset of breakdown is indicated as X_b^*, relative to its value $(X_b^*)_o$ for the case of the stationary wing. This value of $X_b^*/(X_b^*)_o$ as a function of T_e/T_o, in which T_e is the period of the wing perturbation and T_o is the inherent period of vortex breakdown. As indicated in the inset of the schematic of Figure 2, the onset of vortex breakdown X_b^* is taken to correspond to the leading-edges of the vorticity concentrations arising from the initial portion of the breakdown bubble. In Figure 2, the vertical bars at each data point correspond to the extreme values of X_b^* determined during the course of data acquisition. The filled circular symbols represent the averaged values.

It is evident that retardation of the onset of vortex breakdown occurs over a significant range of excitation period of the wing, extending approximately from $0.9 < T_e/T_o < 4.3$. Maximum retardation occurs at a ratio of approximately $T_e/T_o = 1.2$, which corresponds to a value of $f_eC/U_\infty = 7.4$. On the other hand, a rather dramatic advancement of the onset of vortex breakdown occurs at low values of T_e/T_o, with particularly large values attained in the vicinity of $T_e/T_o = 0.2$. These alterations of the onset of vortex breakdown are accompanied by substantial changes in the averaged and instantaneous structure of the breakdown process, as described in the following.

Patterns of Averaged Vorticity in Presence and Absence of Impingement Plate

Averaged contours of vorticity $<\omega>$ are shown in Figure 3a for the case where the impingement plate is deployed immediately downstream of the trailing-edge of the delta wing. Images are exhibited for the case of the stationary wing, as well as the wing subjected to small-

amplitude perturbations of angle-of-attack at period T_e. When the wing is perturbed at $T_e = 2$ sec, the onset of vortex breakdown moves downstream and the peak vorticity level along the edge of the separation bubble is significantly decreased. On the other hand, at $T_e = 1$ sec, the onset of vortex breakdown is advanced in the upstream direction, and the pattern of vorticity in the leading portion of the bubble is characterized by a high level of vorticity concentration. Further downstream along the edges of the vortex breakdown bubble, the peak values of vorticity are, however, dramatically lower than those immediately following the onset of vortex breakdown. Finally, for the case $T_e = 0.5$ sec, the onset of vortex breakdown is advanced well upstream of the location of the left boundary of the image; in fact, independent dye visualization shows that it occurs at a location of approximately 0.85C measured from the trailing-edge of the delta wing, in which C is the wing chord as illustrated in Figure 1. In this case, even though the onset of breakdown occurs relatively early, significant levels of vorticity are indeed evident along the edges of the breakdown bubble at axial locations in the vicinity of the leading-edge of the plate.

In order to determine the effect of deployment of the impingement plate, the same experiments were executed in absence of a plate. The averaged vorticity contours are shown in Figure 3b. For the case of the stationary wing, represented by the top image, only very low level vorticity contours are apparent in the central region of the vortex, and no indication of vortex breakdown is evident; in fact, independent dye visualization showed vortex breakdown to occur at a distance 2.5C downstream of the trailing-edge of the wing. At periods $T_e = 2$ sec and 1 sec of the wing, corresponding to the second and third images of Figure 3b, the patterns of averaged vorticity $<\omega>$ contrast with their counterparts in presence of the impingement edge shown in Figure 3a. The onset of vortex breakdown is not detectable in the top three images of Figure 3b.

The presence of the impingement plate therefore has a large influence on the location and controllability of vortex breakdown.

On the other hand, at the lowest value of excitation T_e = 0.5 sec, corresponding to the bottom image of Figure 3b, the onset of vortex breakdown occurs near the left boundary of the image. Comparing this image with the corresponding one of Figure 3a, it is evident that the averaged vorticity contours are relatively narrow and closely spaced, relative to the case where the edge is present. In fact, this remarkably narrow breakdown bubble in the bottom image of Figure 3b is substantially narrower than all other breakdown bubbles in presence of an impingement edge, i.e., for the case of the stationary edge T_e = 2 sec and 1 sec in Figure 3a. More specifically, compare the images in Figures 3a and 3b, for which the onset of vortex breakdown occurs at the trailing-edge of the wing. In Figure 3a, the appropriate image is at T_e = 1 sec, and in Figure 3b, it corresponds to T_e = 0.5 sec. The presence of the impingement edge, even though it is located well downstream of the onset of vortex breakdown, is associated with a rapid divergence of the vorticity layers along the edge of the breakdown bubble.

Finally, viewing the images of Figures 3a and 3b as a whole, well-defined vorticity layers are present adjacent to the bottom boundary of the images corresponding to the case of the stationary wing and the wing subjected to perturbations at T_e = 0.5 sec. These layers apparently have no relation to the innermost layers that eventually undergo breakdown. Rather, it is hypothesized that they are associated with a three-dimensional instability of the shear layers separating from the leading-edges of the wing.

Contours of Averaged Velocity in Presence and Absence of Impingement Plate

Contours of constant averaged velocity $<V>$ are shown in Figures 4a and 4b; they correspond to the averaged vorticity $<\omega>$ images of Figures 3a and 3b. The images of Figure

4a clearly show the retardation and advancement of the onset of vortex breakdown relative to the case of the stationary wing. Moreover, as shown in the first, third and fourth images of Figure 4a, corresponding to the stationary wing and the wing at T_e = 1 sec and 0.5 sec, very large velocity defects are present in the central region of the vortex breakdown bubble. A much milder defect occurs in the second image corresponding to T_e = 2 sec.

The corresponding images of Figure 4b in absence of the impingement plate show the very gradual variations of the velocity along the axis of the vortex, which is indicated by the dashed line. When comparing these velocity contours with those of Figure 4a where the impingement plate is present, it is evident that the consequence of the impingement plate is to induce very large gradients of velocity along the axis of the vortex. An exception is the case corresponding to the lowest perturbation period of the wing T_e = 0.5 sec, represented by the bottom image in Figure 4b. In this case, since the onset of vortex breakdown has been remarkably advanced due to the perturbation. As a consequence, relatively large gradients of velocity along the axis of the vortex are evident, even in absence of the impingement plate.

Variations of Maximum Averaged Vorticity in Presence of Impingement Plate

A further representation of the consequence of wing perturbations on the vortex structure is illustrated in Figure 5. In this case, the impingement plate is deployed and values of averaged vorticity $<\omega>$ are tracked along a locus corresponding to the maximum level of vorticity $<\omega>$, as indicated by the black line in the patterns of $<\omega>$ shown in the right column of Figure 5. The corresponding values of $<\omega>$ depicted in the left column of Figure 5 show the substantial influence of wing perturbation. At T_e = 2 sec, the peak vorticity is substantially reduced and the location of X/D_v' at which the broad maximum of vorticity occurs is significantly shifted downstream relative to the case of the stationary edge. On the other hand,

perturbation at T_e = 1 sec induces a sharply defined peak in vorticity at a relatively small value of X/D_v'. It is followed, however, by a relatively low level of vorticity along the edge of the breakdown bubble. Finally, for the smallest period of excitation T_e = 0.5 sec, the value of averaged vorticity indicates only a small peak and generally decays by a substantial amount along the separation bubble. Of course, one expects a well-defined peak of vorticity upstream of the left boundary of the image shown in Figure 4. That is, due to the fact that vortex breakdown is substantially advanced in the upstream direction, one expects the corresponding peak of vorticity $<\omega>$ to occur well upstream of the trailing-edge of the wing.

4. INSTANTANEOUS STRUCTURE OF VORTEX

All of the foregoing averaged features of the onset and development of vortex breakdown are, of course, a consequence of the altered instantaneous structure. Figure 6a provides an overview of instantaneous patterns of vorticity corresponding to the stationary wing and the wing subjected to perturbations T_e = 2, 1 and 0.5 sec respectively. Viewing these images as a whole, the alteration of location of vortex breakdown is generally in accord with that corresponding to the averaged patterns of vorticity $<\omega>$ shown in Figure 3a. In order to interpret the instantaneous structure in terms of instantaneous clusters of vorticity, analogous clusters indicated as A, B ... F are shown in all images in Figure 6a. The instantaneous clusters corresponding to the top image, i.e., the case of the stationary wing, represent cross-sectional cuts of the spiral mode of inherent vortex breakdown as it encounters the leading-edge of the plate. This instability is altered as indicated by the patterns of instantaneous vorticity given in the second image at T_e = 2 sec. The streamwise distance between, for example, clusters A and C is significantly reduced at T_e = 2 sec; moreover, the transverse spacing between, for example, vorticity clusters A and B is also reduced. In the third image, corresponding to T_e = 1 sec, the

patterns of vorticity take on a distinctly different form. Vorticity clusters indicated as A, B and C have become relatively elongated and inclined with respect to the centerline of the breakdown bubble. This overall pattern of instantaneous vorticity is located downstream of high levels of vorticity concentration E, D and F, due to the upstream advancement of the onset of vortex breakdown. Finally, the image at the bottom of 6a, corresponding to the lowest period $T_e = 0.5$ sec, shows closely-spaced, smaller-scale concentrations of vorticity along the edges of the breakdown bubble, in comparison with the case of the stationary edge.

Important for consideration of buffeting of the plate is the effective wavelength and propagation speed of the instantaneous vortical structures exhibited in Figure 6a. Using the instantaneous images therein, it is possible to plot the spatial variation of instantaneous vorticity along the edges of the breakdown bubble. The result is shown in Figure 6b. At each value of T_e, distributions of vorticity shown in the left column of Figure 6b were evaluated along the thin black lines in the right column of Figure 6a. Considering, first of all, the case of the stationary wing, corresponding to the top image of Figure 6b, the undisturbed, spiral mode of vortex breakdown gives rise to relatively large-scale, widely-spaced vorticity concentrations. The corresponding spatial distribution of instantaneous vorticity shown at the left of this image thereby exhibits pronounced peaks having relatively wide spacing. On the other hand, excitation at $T_e = 2$ sec induces a series of smaller-scale concentrations of vorticity. Correspondingly, the peaks and the spatial distribution are relatively closely spaced. At the period of excitation $T_e = 1$ sec, the patterns of instantaneous vorticity take on a remarkably different form. Although adjacent small-scale concentrations are induced by the excitation, they appear as inclined layers of instantaneous vorticity. As a consequence, a line passing through vorticity contours, such as that designated in Figure 6b, gives rise to relatively widely-spaced peaks. At $T_e = 0.5$ sec, the

small-scale concentrations again become approximately oriented along the indicated line, thereby producing more closely spaced peaks of the spatial distribution of vorticity.

In order to provide further insight into the space-time evolution of the patterns of instantaneous vorticity, excerpts from cinema sequences are shown in Figures 6c and 6d. Figure 6c corresponds to the case of the stationary wing and Figure 6d to the wing subjected to perturbations at T_e = 0.5 sec. In Figure 6c, the general form of the vorticity concentrations sufficiently far upstream of the impingement plate is preserved. Large changes occur, however, along the upper surface of the plate where the localized vortex formed from the tip successively interacts with vortical structures originating from the vortex breakdown process. In Figure 6d, the vorticity concentrations exhibit significant distortion, even at locations well upstream of the impingement plate, though the generally small-scale features of individual clusters are identifiable. This small-scale is, of course, associated with the low period T_e of excitation of the wing.

5. CONSEQUENCE OF VORTEX STRUCTURE ON BUFFET FLOW FIELD ALONG PLATE SURFACE

It is well known that an important parameter related to the magnitude of buffeting of aerodynamic surfaces is the transverse velocity fluctuation v_{rms}. It may be viewed as an indicator of the effective fluctuating angle of attack, in accord with the concepts recently outlined by Breitsamter and Laschka[20], and related to previous investigations of the turbulent structure of the flow field associated with the buffeting, by Breitsamter and Laschka[18,19]. In essence, sufficiently large values of v_{rms} that are properly correlated along the surface can give rise to a substantial magnitude of buffet-loading. Plots of constant contours of root-mean-square transverse velocity fluctuation v_{rms}/U_{ref} are indicated in Figure 7a. U_{ref} is the reference velocity at a location in the

freestream above the trailing-edge; its value was 48 mm/sec. The onset of vortex breakdown, which is clearly designated in the averaged vorticity contours $<\omega>$ in Figure 3a, is associated with concentrated regions of relatively high v_{rms}, evident in images corresponding to the stationary wing and the wing at T_e = 2 sec and 1 sec in Figure 7a. The patterns of velocity fluctuations v_{rms}/U_{ref} exhibited in Figure 7a indicate that the entire flow field is affected by the perturbation of the delta wing; these patterns indicate the time-averaged consequence of the instantaneous patterns shown in the foregoing image layouts. It is evident in Figure 7a that substantial distortions are induced within the interior of the vortex, and, moreover, high levels of v_{rms} occur along the exterior of the vortex, evident by the higher level contours along the bottom edges of the images corresponding to T_e = 2 sec, 1 sec and 0.5 sec in Figure 7a. Finally, note that reasonably high levels are induced in the leading-edge region of the impingement plate for all cases shown in Figure 7a.

The thin white vertical lines shown in Figure 7a indicate locations for which vertical distributions of v_{rms}/U_{ref} are plotted in Figure 7b. The upper left plot of Figure 7b, which corresponds to line K in Figure 7a, shows that, for the case of the stationary edge, a peak in v_{rms} occurs near the plane of symmetry of the breakdown bubble. This peak is generally smoothed out, and the form of the distribution is altered, at locations L, M and N where the boundary conditions of the plate surface come into play. Generally speaking, the level of v_{rms} is substantially reduced for locations K through N at the excitation condition T_e = 2 sec. At the other extreme, the very high level of v_{rms} at the large value of y'/C at location K is due to the induced vortex street from the trailing-edge of the wing at T_e = 0.5 sec. The distributions of the v_{rms} along line L, which is located immediately upstream of the leading-edge of the plate, all tend to show local minima at the leading-edge. Corresponding distributions along line M all go to

zero at the surface of the plate due, of course, to the impermeability condition. Well downstream of the leading-edge, corresponding to line N, this same general form of the v_{rms} distributions persists.

6. CONCLUDING REMARKS

Current interest in deployment of various techniques for controlling leading-edge vortex formation on delta wings that are either stationary, or undergoing a maneuver at relatively long time scales, have stimulated the present investigation, which simulates key features of leading-edge control by small-amplitude perturbations of a delta wing. The concept is that the very large unsteady pressure gradients at the leading-edge induced by small perturbations of the wing will have large consequences for instantaneous, three-dimensional patterns of vorticity generated from the edge. Indeed, the present investigation shows a substantial influence on both the averaged and instantaneous structure of the leading-edge vortex.

When the wing is perturbed in presence of an impingement plate, either retardation or advancement of the onset of averaged vortex breakdown is attainable. Particularly large values of advancement of vortex breakdown are achieved when the period of oscillation of the edge is approximately equal to the period of inherent vortex breakdown upon the corresponding stationary edge. Averaged vorticity contours show that induced vortex breakdown upstream of the edge generally results in rapid divergence of the averaged vorticity layers along the edge of the breakdown bubble. Corresponding distributions of averaged velocity show that, for both the case of the stationary and perturbed wing, large gradients of velocity are generated along the axis of the leading-edge vortex, extending from the leading-edge of the breakdown bubble to a location well within the bubble.

On the other hand, when no impingement edge is deployed, the flow patterns are dramatically different. Vortex breakdown generally occurs at locations well downstream of corresponding cases where impingement edge is deployed. Moreover, the transformation of the flow pattern in the region upstream of breakdown is a gradual one, evidenced by the relatively slow variations of velocity along the axis of the vortex. In other words, the consequence of presence of the impingement plate is not simply to induce an earlier onset of breakdown, but also to generate relatively large changes in the averaged structure of the vortex upstream of the breakdown location.

All of these features are related to alteration of patterns of instantaneous vorticity along and within the breakdown bubble. Different classes of patterns have been defined, dependent upon the excitation period T_e of the wing. Principal distinctions of these patterns are changes in the streamwise wavelength between clusters of vorticity, as well as the transverse distance between these clusters. A fruitful path for further work would be to relate these observations to wave propagation characteristics along the vortex.

The consequence of buffeting has been interpreted in terms of rms values of transverse velocity fluctuations. The effect of perturbation of the wing at a defined period T_e is shown to produce substantial differences in both the magnitude and shape of distributions of v_{rms} at locations upstream of the impingement plate. At locations well downstream of the leading-edge of the plate, however, the form of the v_{rms} distributions is compatible with the zero permeability condition of the plate, and the shape of the v_{rms} distributions is altered accordingly.

7. ACKNOWLEDGMENTS

The support of the Air Force Office of Scientific Research under Contract No. F49620-99-1-0011, monitored by Dr. Steven Walker, is gratefully acknowledged. One of the authors,

Professor Besir Sahin, would like to thank the Scientific and Technical Research Council of Turkey (TUBITAK) and NATO for their financial support.

LIST OF REFERENCES

[1]Lee, B. H. K. "Vertical Tail Buffeting of Fighter Aircraft", *Progress in Aerospace Sciences*, Vol. 36, 2000, pp. 193-279.

[2]Wolfe, S., Lin, J.-C. and Rockwell, D. "Buffeting of Fins: An Assessment of Surface Pressure Loading", *AIAA Journal*, Vol. 33, No. 11, 1995, pp. 2232-2235.

[3]Washburn, A. E., Jenkins, L. M. and Ferman, M. A., "Experimental Investigation of Vortex-Fin Interaction", AIAA Paper 93-0050, 31st Aerospace Sciences Meeting and Exhibit, January, Reno, NV, 1993.

[4]Bean, D. E. and Wood, N. J. "An Experimental Investigation of Twin Fin Buffeting and Suppression", AIAA Paper 93-0054, 31st Aerospace Sciences Meeting and Exhibit, January, Reno, NV, 1993.

[5]Canbazoglu, S., Lin, J.-C., Wolfe, S. and Rockwell, D. "Buffeting of a Fin: Distortion of the Incident Vortex", *AIAA Journal*, Vol. 33, 1995, pp. 2144-2150.

[6]Wolfe, S., Lin, J.-C. & Rockwell, D. "Buffeting at the Leading-Edge of a Flat Plate due to a Streamwise Vortex: Flow Structure and Surface Pressure Loading", *Journal of Fluids and Structures*, Vol. 9, 1995, pp. 359-370.

[7]Triplett, W. E. "Pressure Measurements on Twin Vertical Tails in Buffeting Flow, *Journal of Aircraft*, Vol. 20, 1983, pp. 920-925.

[8]Wentz, W. H., Jr. "Vortex-Fin Interaction on a Fighter Aircraft", AIAA Paper 87-8409, *Proceedings of the AIAA 5th Applied Aerodynamics Conference*, Monterey, CA, AIAA, Washington, D.C., 1987, pp. 192-399.

[9]Ferman, N. A., Patel, S. R., Zimmerman, N. H. and Gerstenkorn, G. "A Unified Approach to Buffet Response of Fighter Aircraft Empennage", *AGARD/NATO 70th Structures and Materials Meeting,* Sorento, Italy, 1990, 2-1–2-15.

[10]Zimmerman, N. H., Ferman, M. A,.Yurkovich, R. N. and Gerstenkorn, G. "Prediction of Tail Buffet Loads for Design Application", 1989, AIAA Paper 89-1378.

[11]Shah, G. H. "Wind-tunnel Investigation of Aerodynamic and Tail Buffet Characteristics of Leading-Edge Extension Modifications to the F/A-18", 1991, AIAA Paper 91-2889.

[12]Lee, B. H. K. and Tang, F. C. "Buffet Load Measurements on an F/A-18 Vertical Fin at High Angle-of-Attack", 1992, AIAA Paper 92-2127.

[13]Martin, C A. and Thompson, D. H. "Scale Model Measurements on Fin Buffet Due to Vortex Bursting on F/A-18", 1991, AGARD/CP497.

[14]Lee, B. H. K., Brown, D., Tang, F. C. and Plosenski, M. "Flow Field in the Vicinity of an F/A-18 Vertical Fin at High Angle-of-Attack", *Journal of Aircraft*, Vol. 30, 1993, pp. 69-74.

[15]Moses, Robert W. and Huttsell, Lawrence "Fin Buffeting Features of an Early F-22 Model", 2000, AIAA Paper 2000-1695.

[16]Luber, W., Becker, J. and Sensburg, O. "The Impact of Dynamic Loads on the Design of Military Aircraft", AGARD-R-815, Florence, Italy, September, 1996, 4-5, 8-1–8-27.

[17]Ashley, H., Rock, S. M., Digumarthi, R. V., Chaney, K. and Eggers Jr., A. J. "Active Control for Fin Buffet Alleviation", WL-TR-93-3099, Wright Patterson AFB, OH, January, 1994.

[18]Breitsamter, C. and Laschka, B. "Turbulent Flow Structure Associated with Vortex-Induced Fin Buffeting", *Journal of Aircraft*, Vol. 31, 1994, pp. 773-781

[19]Breitsamter, C. and Laschka, B. "Turbulent Flowfield Structure Associated with Fin Buffeting Around a Vortex-Dominated Aircraft Configuration at Sideslip", 19th Congress of the

International Council of the Aeronautical Sciences, Anaheim, CA, September, ICAS-94-4.3.2, I, 1994, pp. 768-684.

[20]Breitsamter, C. and Laschka, B. "Fin Buffet Pressure Evaluation Based on Measured Flowfield Velocities", *Journal of Aircraft*, Vol. 35, 1998, pp. 806-815.

[21]Beutner, T. J., Baust, H. N. and Meyers, J. F. "Doppler Global Velocimetry Measurements of a Vortex-Tail Interaction", *Proceedings of the International Symposium on Flow Visualization*, 7th, Seattle, ed. J. P. Crowder, 1995, pp. 418-423, New York: Begell House.

[22]Mayori, A. and Rockwell, D. "Interaction of a Streamwise Vortex with a Thin Plate: A Source of Turbulent Buffeting", *AIAA Journal*, Vol. 32, 1994, pp. 2022-2029.

[23]Canbazoglu, S., Lin, J.-C., Wolfe, S. and Rockwell, D. "Buffeting of a Fin: Streamwise Evolution of Flow Structure", *AIAA Journal of Aircraft*, Vol. 33, 1995, pp. 85-190.

[24]Rockwell, D. "Vortex-Body Interactions", *Annual Review of Fluid Mechanics*, Vol. 30, 1998, pp. 199-229.

[25]Spedding, G. R., Maxworthy, T. and Rignot, E. "Unsteady Vortex Flows Over Delta Wings", *Proceedings of Second AFOSR Workshop on Unsteady and Separated Flows*, July, Colorado Springs, CO, 1987. Frank J. Seiler Research Laboratory Report FJSRL-TR-88-0004, September, 1988, pp. 238-288.

[26]Karagounis, T., Maxworthy, T. and Spedding, G. R. "Generation and Control of Separated Vortices Over a Delta Wing by Means of Leading-Edge Flaps", AIAA Paper 89-0997, AIAA Second Shear Flow Conference, March, Tempe, AZ, 1989.

[27]Gursul, I., Lin, H. and Ho, C.-M. "Vorticity Dynamics of Two-Dimensional and Three-Dimensional Wings in Unsteady Freestream", AIAA Paper 91-0010, 29th Aerospace Sciences Meeting, January, Reno, NV, 1991.

[28]Rockwell, D. "Three-Dimensional Flow Structure on Delta Wings at High Angle-of-Attack: Experimental Concepts and Issues", AIAA Paper 93-0550, 31st Aerospace Sciences Meeting and Exhibit, January, Reno, NV, 1993.

[29]Shih, Z., Wu, J. M. and Vakili, A. D. "An Investigation of Leading-Edge Vortices on Delta Wings with Jet Blowing", AIAA Paper 87-0330, AIAA 25th Aerospace Sciences Meeting, January, Reno, NV, 1987.

[30]Visser, K. D., Iwanski, K. T., Nelson, R. C. and Ng, T. T. "Control of Leading-Edge Vortex Breakdown by Blowing", AIAA Paper 88-0504, AIAA 26th Aerospace Sciences Meeting, January, Reno, NV, 1988.

[31]Wood, M. J. and Roberts, L. "The Control of Vortical Lift on Delta Wings by Tangential Leading-Edge Blowing", AIAA Paper 87-0158, AIAA 25th Aerospace Sciences Meeting, January, Reno, NV, 1987.

[32]Celik, Z. Z. and Roberts, L. "Aircraft Control at High-Alpha by Tangential Blowing", AIAA Paper 92-0021, 30th Aerospace Sciences Meeting and Exhibit, January, Reno, Nevada, 1992.

[33]Gad-el-Hak, M. and Blackwelder, R. F. "Control of the Discrete Vortices from a Delta Wing", *AIAA Journal*, Vol. 25, 1987, pp. 1042-1049.

[34]Gu, W., Robinson, O. and Rockwell, D. "Control of Vortices on a Delta Wing by Leading-Edge Injection", *AIAA Journal*, Vol. 32, No. 7, 1993, pp. 1177-1186.

[35]Findlay, D., Kern, S. and Kwon, O. "Numerical Investigation of the Effect of Blowing on High Angle of Attack Flow Over Delta Wings", AIAA Paper 91-1809, 22nd Fluid Dynamics, Plasma Dynamics, and Lasers Conference, June, Honolulu, HA, 1991.

[36]Huttsell, L. J., Tinapple, J. A. and Weyer, R. M. "Investigation of Buffet Loading on a Scaled F-15 Twin Tail Model", AGARD Structures and Materials Panel Workshop, October, Denmark, 1997.

[37]Reynolds, G. A. and Abtahi, A. A. "Instabilities in Leading-Edge Vortex Development", AIAA Paper 87-2424, Applied Aerodynamics and Atmospheric Flight Dynamics Conference, Monterey, California, 1987.

[38]Gursul, I. and Yang, H. "Vortex Breakdown over a Pitching Delta Wing", AIAA Paper 94-0536, 32nd Aerospace Sciences Meeting and Exhibit, January, Reno, NV, 1994.

[39]Akilli, H., Sahin, B. and Rockwell, D. "Control of Vortex Breakdown by a Transversely-Oriented Wire", *Physics of Fluids*, Vol. 13, No. 2, 2001, pp. 452-463.

[40]Gusul, I. and Xie, W. "Interaction of Vortex Breakdown with an Oscillating Fin", AIAA Paper 2000-0279, 38th Aerospace Sciences Meeting and Exhibit, January, Reno, NV, 2000.

[41]Sahin, B., Akilli, H., Lin, J.-C. and Rockwell, D. 1999 "Vortex Breakdown-Edge Interaction: Consequence of Edge Oscillations", *AIAA Journal* (in press).

[42]Rockwell, D., Magness, C., Towfighi, J., Akin, O. and Corcoran, T. "High-Image-Density Particle Image Velocimetry Using Laser Scanning Techniques", *Experiments in Fluids*, Vol. 14, 1993, pp. 181-192.

LIST OF FIGURES

Figure 1: Schematics of delta wing subjected to small-amplitude perturbations about its mid-chord, which changes the structure of the leading-edge vortex and its breakdown, thereby altering the unsteady nature of vortex impingement upon the plate.

Figure 2: Time-averaged location X_b^* of onset of vortex breakdown due to small-amplitude perturbation of delta wing, normalized by the value $(X_b^*)_o$ corresponding to the stationary wing. T_e is perturbation period of delta wing and T_o is period of inherent instability mode of vortex breakdown in absence of wing perturbation. Mean and perturbation angle-of-attack are $\bar{\alpha} = 24^\circ$ and $\alpha_o = 1^\circ$. Period of natural instability of vortex breakdown is $T_o = 1.6$ sec.

Figure 3a: Contours of averaged vorticity $< \omega >$ for the stationary wing and wing subjected to small-amplitude perturbation at designated period T_e in presence of the impingement plate, relative to the period $T_o = 1.6$ sec of the inherent instability of vortex breakdown. Thick and thin lines represent respectively positive and negative vorticity. Minimum and incremental values of vorticity are $\omega_{min} = \pm 1$ sec^{-1} and $\Delta\omega = 0.5$ sec^{-1}. Nominal angle-of-attack of delta wing is $\bar{\alpha} = 24^\circ$ and amplitude of perturbation angle-of-attack is $\alpha_o = 1^\circ$.

Figure 3b: Contours of averaged vorticity $< \omega >$ for the stationary wing and wing subjected to small-amplitude perturbation at designated period T_e in absence of the impingement plate, relative to the period $T_o = 1.6$ sec of the inherent instability of vortex breakdown. Thick and thin lines represent respectively positive and negative vorticity. Minimum and incremental values of vorticity are $\omega_{min} = \pm 1$ sec^{-1} and $\Delta\omega = 0.5$ sec^{-1}. Nominal angle-of-attack of delta wing is $\bar{\alpha} = 24^\circ$ and amplitude of perturbation angle-of-attack is $\alpha_o = 1^\circ$.

Figure 4a: Contours of constant averaged velocity $< V >$ for the case of the stationary delta wing and wing subjected to small amplitude perturbation at designated period T_e, relative to period $T_o = 1.6$ sec of inherent instability of vortex breakdown in presence of the impingement plate. Numbers on contours

correspond to velocity in mm/sec; incremental value between contours is 2.5 mm/sec. Nominal angle-of-attack of delta wing is $\bar{\alpha} = 24°$ and amplitude of perturbation angle-of-attack is $\alpha_o = 1°$.

Figure 4b: Contours of constant averaged velocity $< V >$ for the case of stationary delta wing and wing subjected to small amplitude perturbation at designated period T_e, relative to period $T_o = 1.6$ sec of inherent instability of vortex breakdown in absence of the impingement plate. Numbers on contours correspond to velocity in mm/sec; incremental value between contours is 2.5 mm/sec. Nominal angle-of-attack of delta wing is $\bar{\alpha} = 24°$ and amplitude of perturbation angle-of-attack is $\alpha_o = 1°$.

Figure 5: Variation of averaged vorticity $< \omega >$ along a line corresponding to maximum positive vorticity for the case of a stationary wing and wing subjected to perturbation and angle-of-attack at period T_e, relative to the period $T_o = 1.6$ sec of the inherent instability of vortex breakdown. Coordinate X represents distance from left boundary of image and vortex diameter D_v' is a reference diameter measured after the onset of vortex breakdown in absence of wing perturbation.

Figure 6a: Patterns of instantaneous positive (thick line) and negative (thin line) vorticity corresponding to a stationary wing and wing subjected to small-amplitude perturbation at period T_e, relative to the period $T_o = 1.6$ sec of the inherent instability of vortex breakdown. Minimum and incremental values of vorticity are $\omega_{min} = \pm 1.5$ sec^{-1} and $\Delta\omega = 0.5$ sec^{-1}. Nominal angle-of-attack of delta wing is $\bar{\alpha} = 24°$ and amplitude of perturbation angle-of-attack is $\alpha_o = 1°$.

Figure 6b: Variation of instantaneous vorticity ω along a line corresponding to maximum positive vorticity for the case of the stationary wing and wing subjected to perturbation of angle-of-attack at period T_e, relative to the period $T_o = 1.6$ sec of the inherent instability of vortex breakdown. Coordinate X represents distance from the beginning of the solid line and vortex diameter D_v' is a reference diameter measured after the onset of vortex breakdown in absence of wing perturbation, as displayed in Figure 5.

Figure 6c: Excerpts from cinema sequence showing evolution of patterns of vorticity with time for the case of the stationary delta wing. Parameters are same as for Figure 6a.

Figure 6d: Patterns of instantaneous vorticity corresponding to perturbation of delta wing at period $T_e = 0.5$ sec, relative to period $T_o = 1.6$ sec of inherent instability of vortex breakdown. All parameters are same as for Figure 6a.

Figure 7a: Root-mean-square values of transverse velocity fluctuation v_{rms} for the cases of a stationary delta wing and a wing subjected to small-amplitude perturbation of angle-of-attack. Wing is perturbed at period T_e, relative to the period $T_o = 1.6$ sec of the inherent instability of vortex breakdown. Numbers on contours correspond to constant values of the dimensionless ratio v_{rms}/U_{ref}, in which U_{ref} is reference velocity. Minimum and incremental values of transverse velocity fluctuation are $v_{rms}/U_{ref} = 0.05$ and $\Delta v_{rms}/U_{ref} = 0.01$. Nominal angle-of-attack of delta wing is $\bar{\alpha} = 24°$ and amplitude of perturbation angle-of-attack is $\alpha_o = 1°$. Thin vertical lines represent locations at which distributions of v_{rms}/U_{ref} are displayed in Figure 7b.

Figure 7b: Distributions of root-mean-square of transverse velocity fluctuation v_{rms} normalized by reference velocity U_{ref} along the vertical lines designated in Figure 7a. Wing is perturbed at period T_e, relative to the period $T_o = 1.6$ sec of the inherent instability of vortex breakdown.

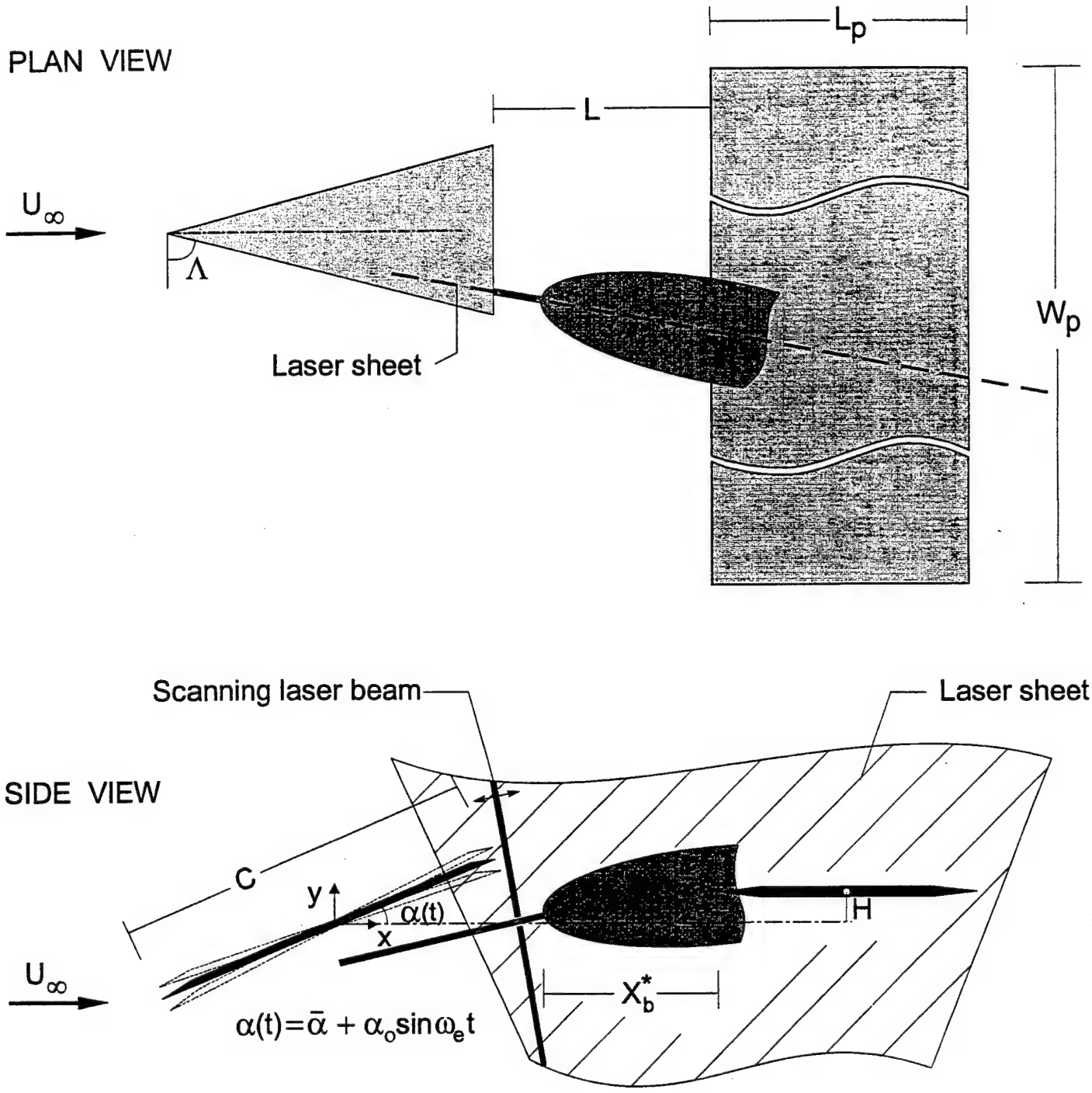

Figure 1: Schematics of delta wing subjected to small-amplitude perturbation about its mid-chord, which changes the structure of the leading-edge vortex and its breakdown, thereby altering the unsteady nature of vortex impingement upon the plate.

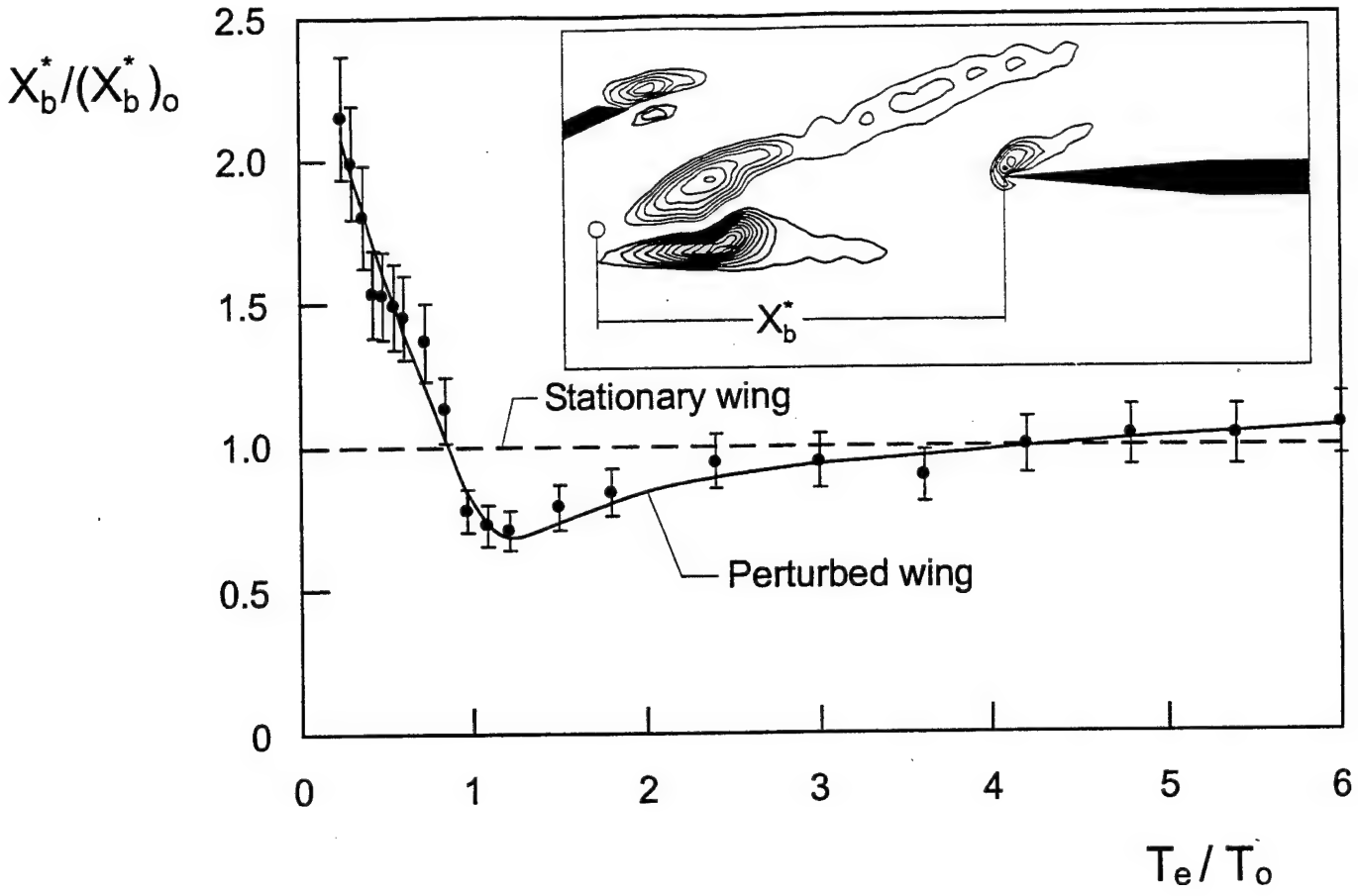

Figure 2: Time-averaged location X_b^* of onset of vortex breakdown due to small-amplitude perturbation of delta wing, normalized by the value $(X_b^*)_o$ corresponding to the stationary wing. T_e is perturbation period of delta wing and T_o is period of inherent instability mode of vortex breakdown in absence of wing perturbation. Mean and perturbation angle-of-attack are $\bar{\alpha}=24^\circ$ and $\alpha_o=1^\circ$. Period of natural instability of vortex breakdown is $T_o= 1.6$ sec.

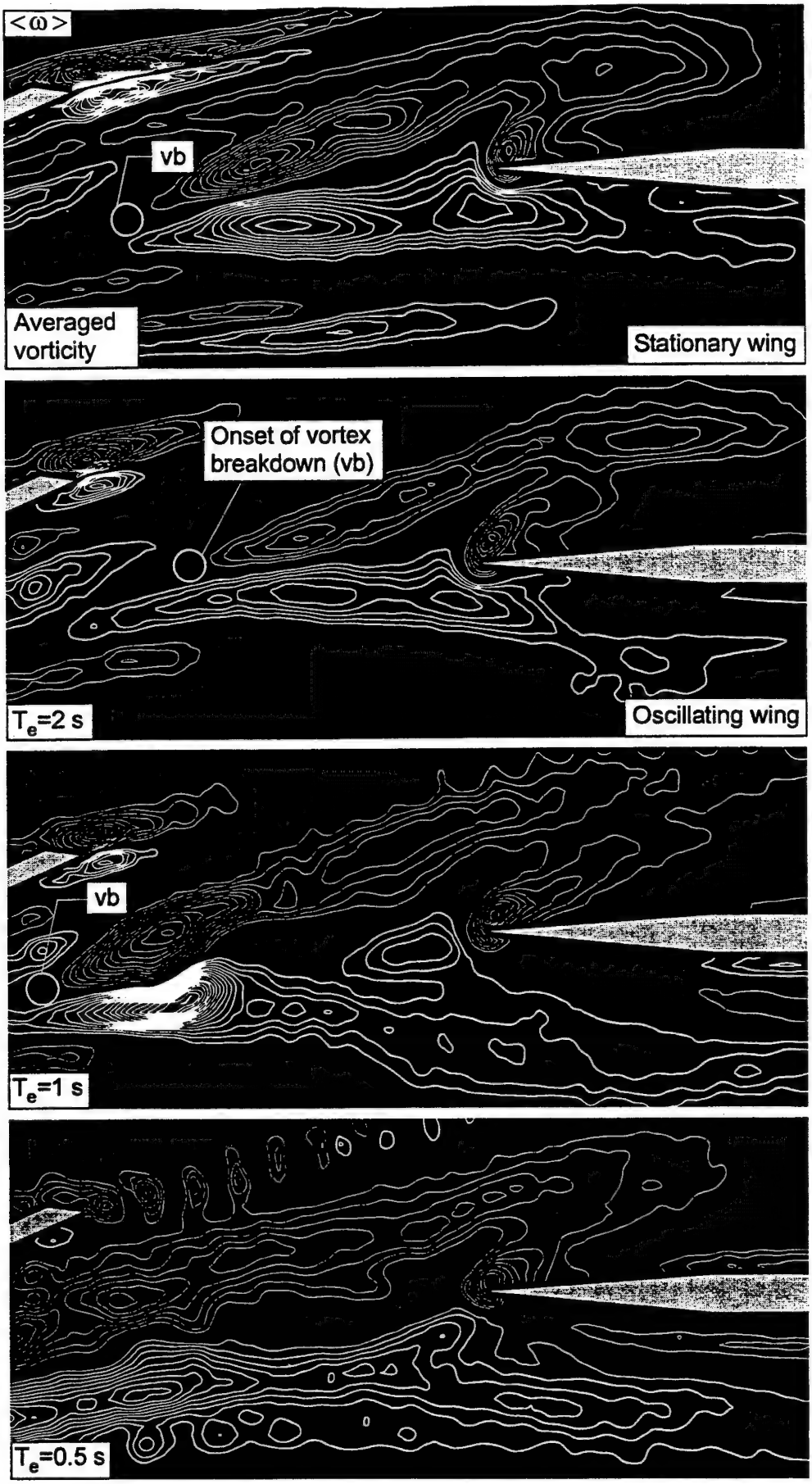

Figure 3a: Contours of averaged vorticity <ω> for the stationary wing and wing subjected to small-amplitude perturbation at designated period T_e in presence of the impingement plate, relative to the period T_o=1.6 sec of the inherent instability of vortex breakdown. Thick and thin lines represent respectively positive and negative vorticity. Minimum and incremental values of vorticity are $\omega_{min} = \pm 1$ sec^{-1} and $\Delta\omega = 0.5$ sec^{-1}. Nominal angle-of-attack of delta wing is $\bar{\alpha} = 24^\circ$ and amplitude of perturbation angle-of-attack is $\alpha_o = 1^\circ$.

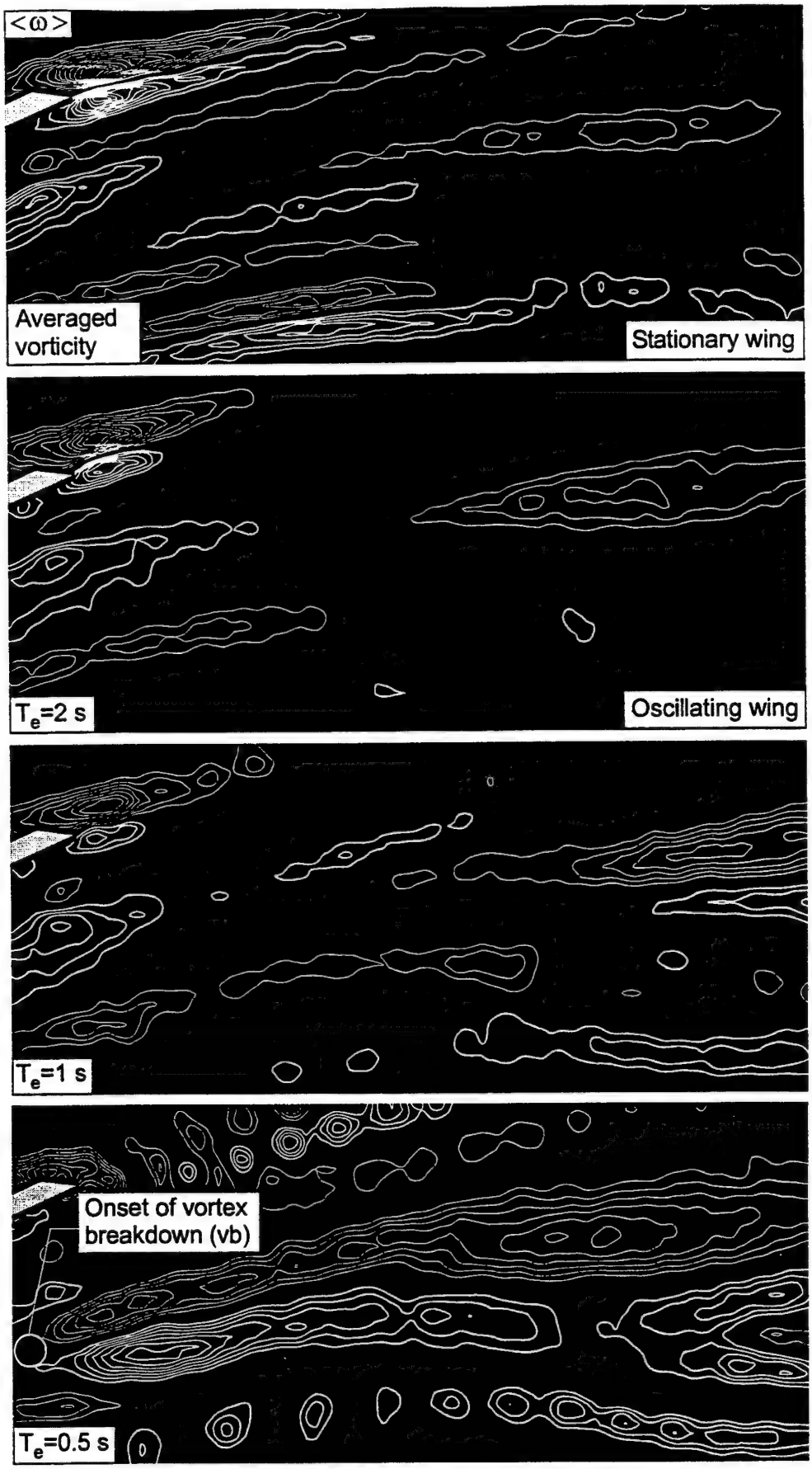

Figure 3b: Contours of averaged vorticity <ω> for the stationary wing and wing subjected to small-amplitude perturbation at designated period T_e in absence of the impingement plate, relative to the period T_o=1.6 sec of the inherent instability of vortex breakdown. Thick and thin lines represent respectively positive and negative vorticity. Minimum and incremental values of vorticity are $\omega_{min}=\pm 1$ sec^{-1} and $\Delta\omega$=0.5 sec^{-1}. Nominal angle-of-attack of delta wing is $\bar{\alpha}=24^{\circ}$ and amplitude of perturbation angle-of-attack is $\alpha_o=1^{\circ}$.

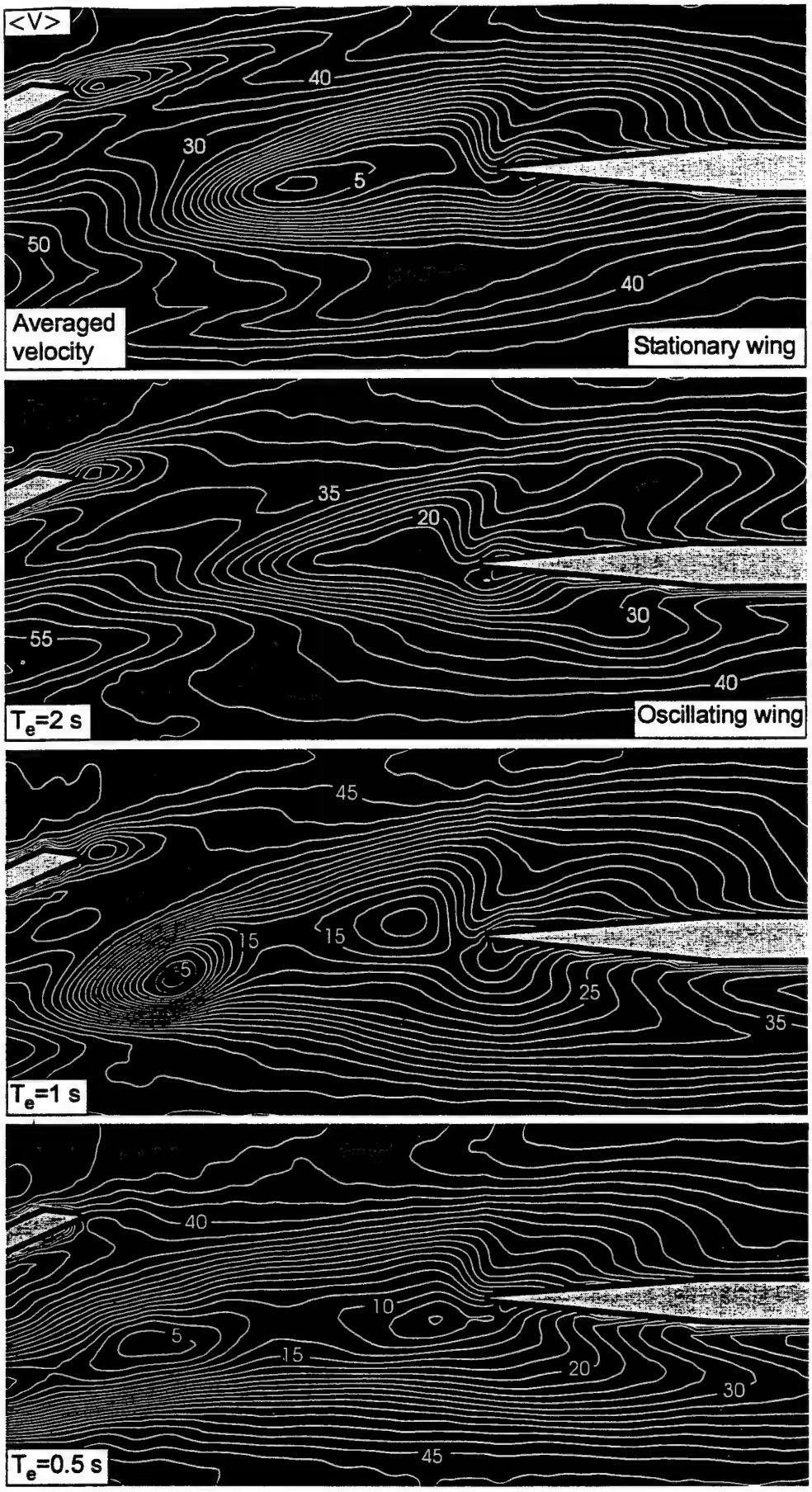

Figure 4a: Contours of constant averaged velocity <V> for the case of the stationary delta wing and wing subjected to small-amplitude perturbation at designated period T_e, relative to period T_o = 1.6 sec of inherent instability of vortex breakdown in presence of the impingement plate. Numbers on contours correspond to velocity in mm/sec; incremental value between contours is 2.5 mm/sec. Nominal angle-of-attack of delta wing is $\bar{\alpha}$= 24° and amplitude of perturbation angle-of- attack is α_o=1°.

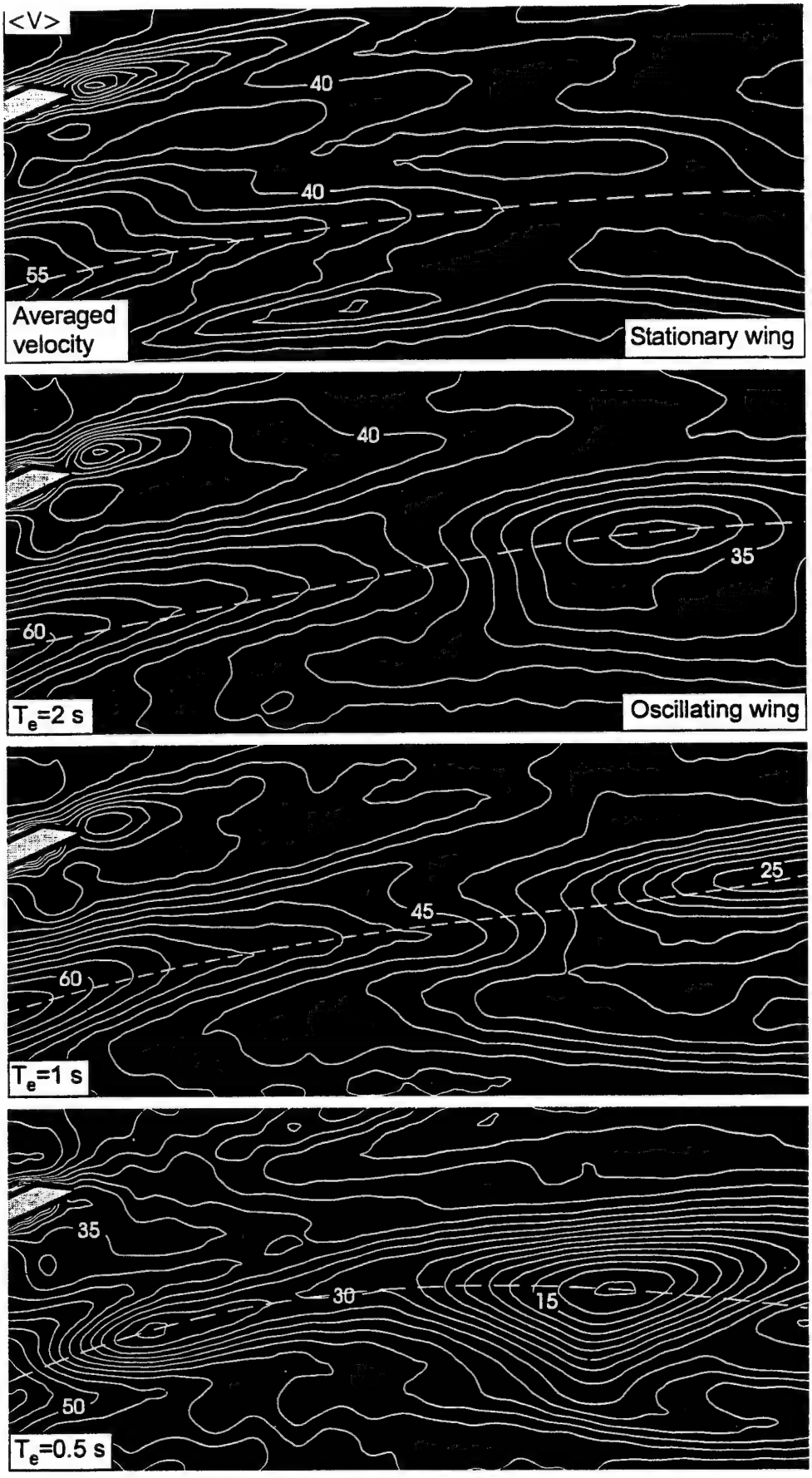

Figure 4b: Contours of constant averaged velocity <V> for the case of stationary delta wing and wing subjected to small-amplitude perturbation at designated period T_e, relative to period T_o = 1.6 sec of inherent instability of vortex breakdown in absence of the impingement plate. Numbers on contours correspond to velocity in mm/sec; incremental value between contours is 2.5 mm/sec. Nominal angle-of-attack of delta wing is $\bar{\alpha}$= 24° and amplitude of perturbation angle-of-attack is α_o=1°.

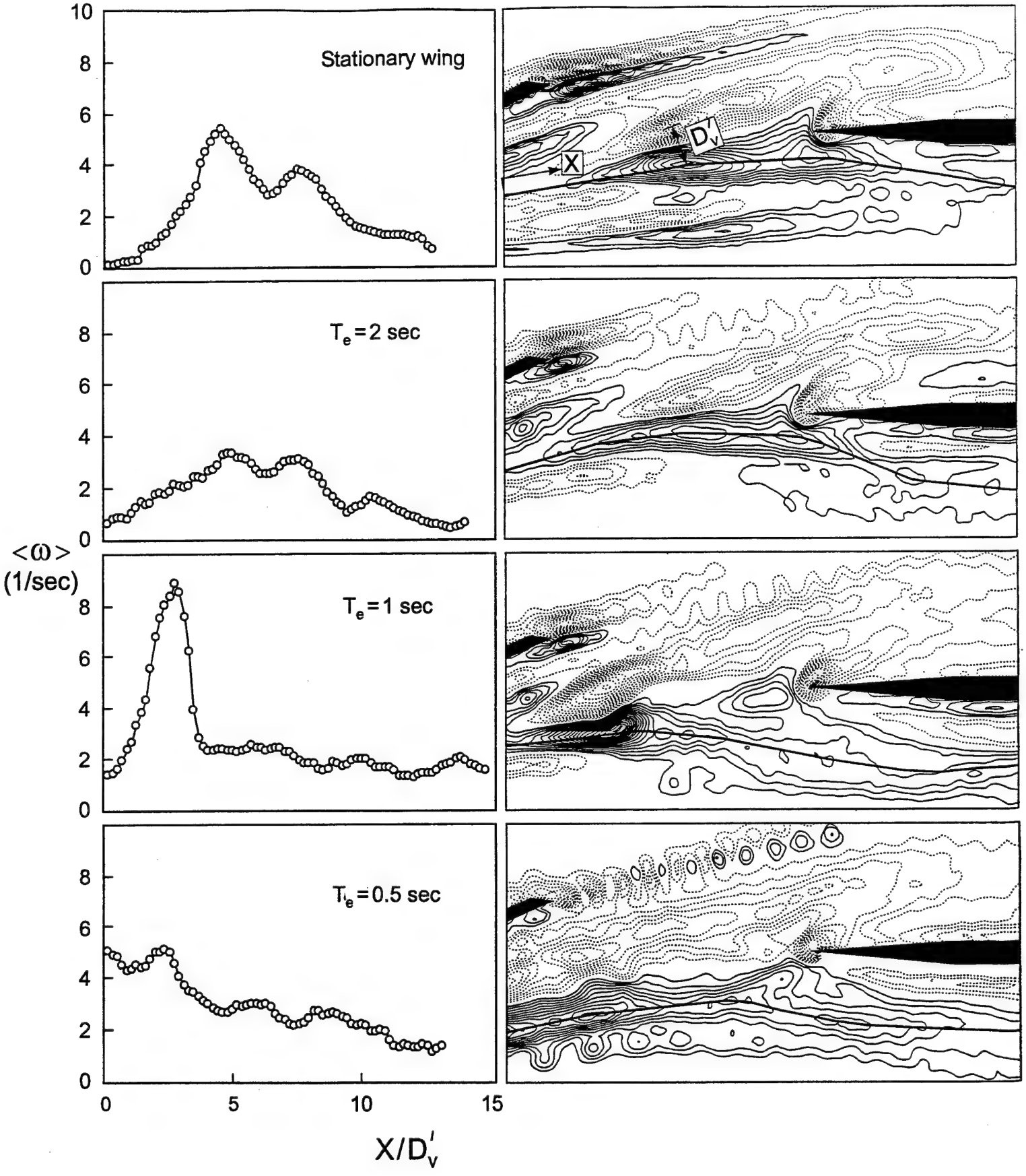

Figure 5: Variation of averaged vorticity <ω> along a line corresponding to maximum positive vorticity for the case of a stationary wing and wing subjected to perturbation of angle-of-attack at period T_e, relative to the period T_o=1.6 sec of the inherent instability of vortex breakdown. Coordinate X represents distance from left boundary of image and vortex diameter D'_v is a reference diameter measured after the onset of vortex breakdown in absence of wing perturbation.

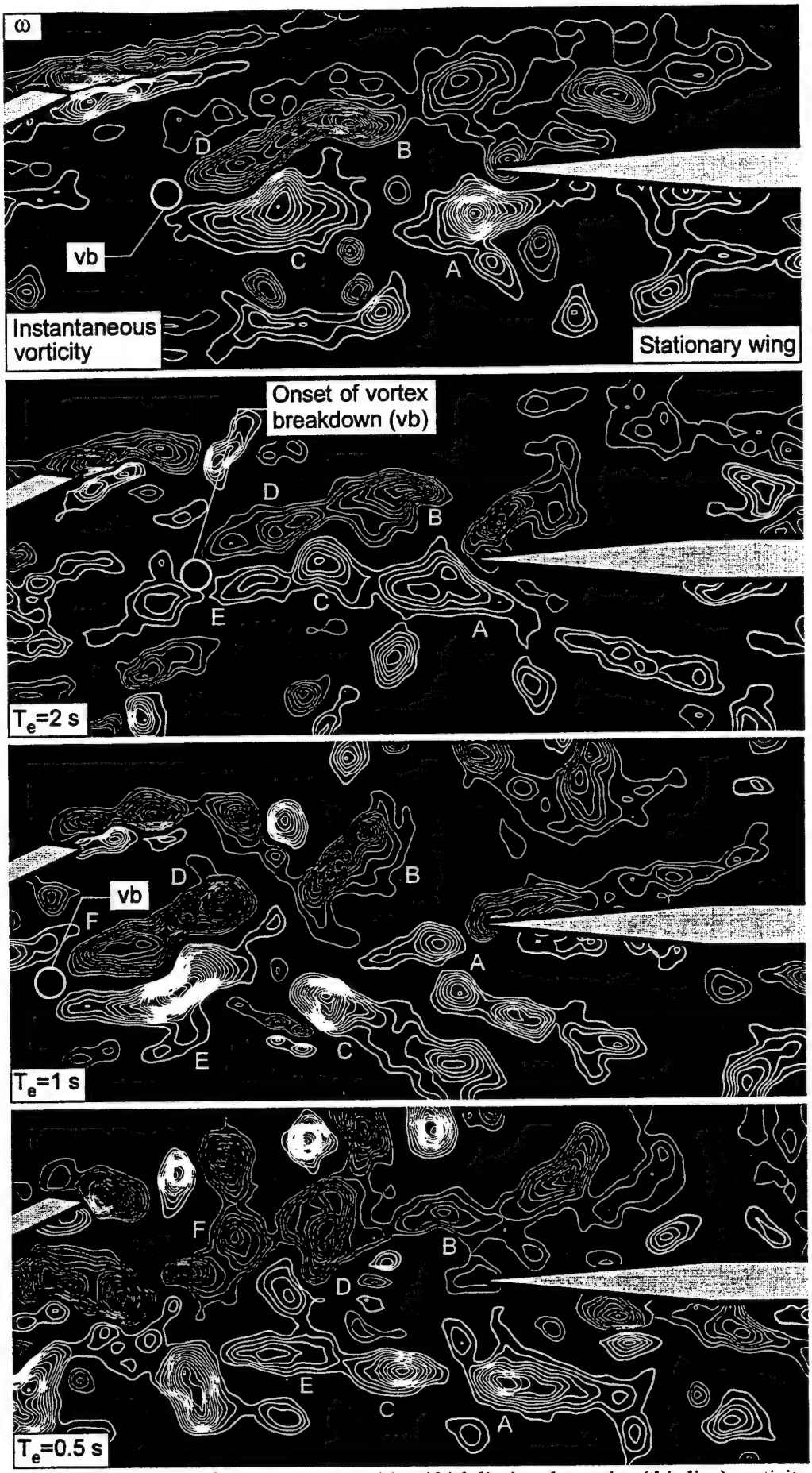

Figure 6a: Patterns of instantaneous positive (thick line) and negative (thin line) vorticity corresponding to a stationary wing and wing subjected to small-amplitude perturbation at period T_e, relative to the period T_o=1.6 sec of the inherent instability of vortex breakdown. Minimum and incremental values of vorticity are $\omega_{min} = \pm 1.5$ sec^{-1} and $\Delta\omega = 0.5$ sec^{-1}. Nominal angle-of-attack of delta wing is $\bar{\alpha} = 24^{\circ}$ and amplitude of perturbation angle-of-attack is $\alpha_o = 1^{\circ}$.

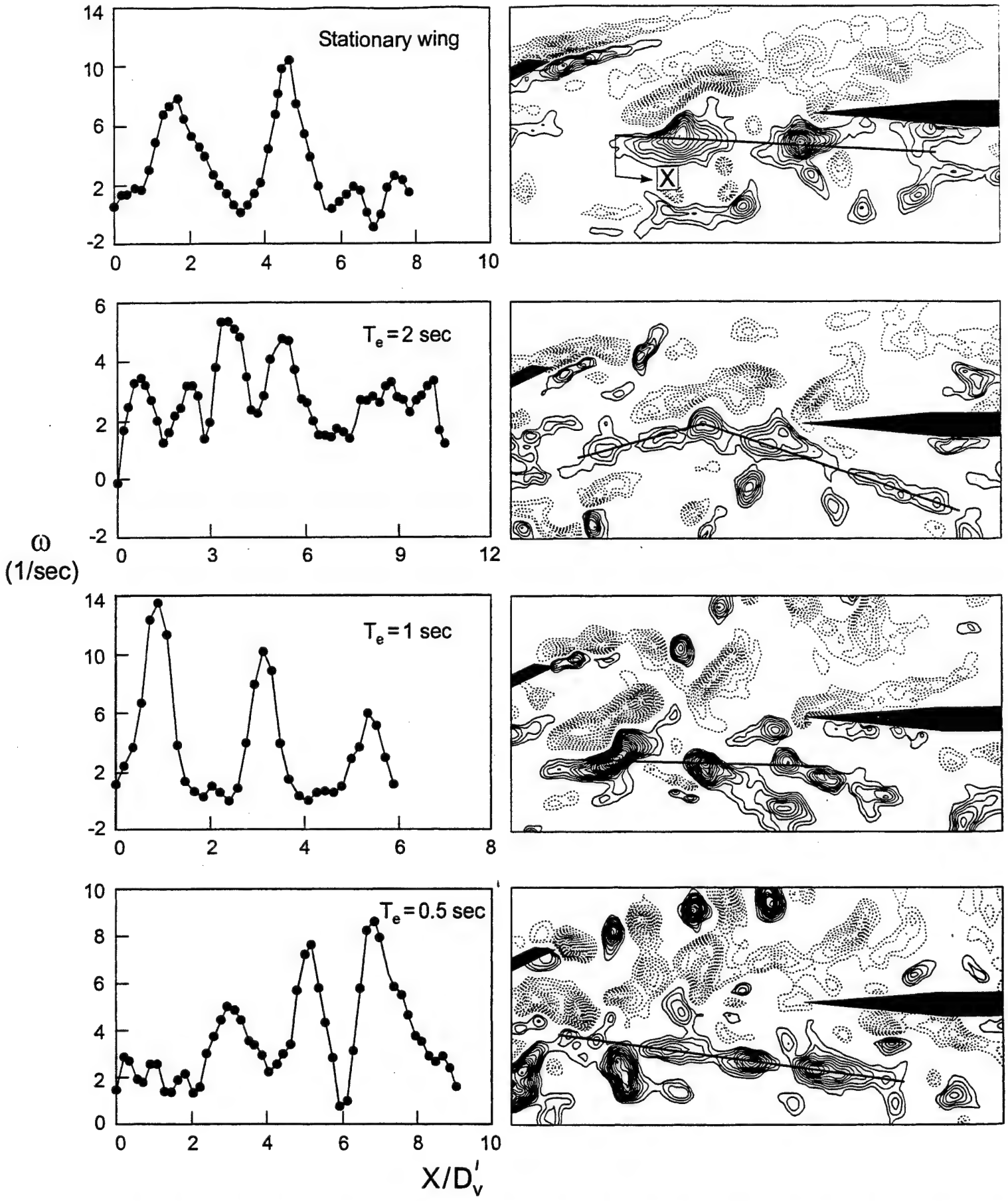

Figure 6b: Variation of instantaneous vorticity ω along a line corresponding to maximum positive vorticity for the case of the stationary wing and wing subjected to perturbation of angle-of-attack at period T_e, relative to the period T_o=1.6 sec of the inherent instability of vortex breakdown. Coordinate X represents distance from the beginning of the solid line and vortex diameter D_v' is a reference diameter measured after the onset of vortex breakdown in absence of wing perturbation, as displayed in Figure 5.

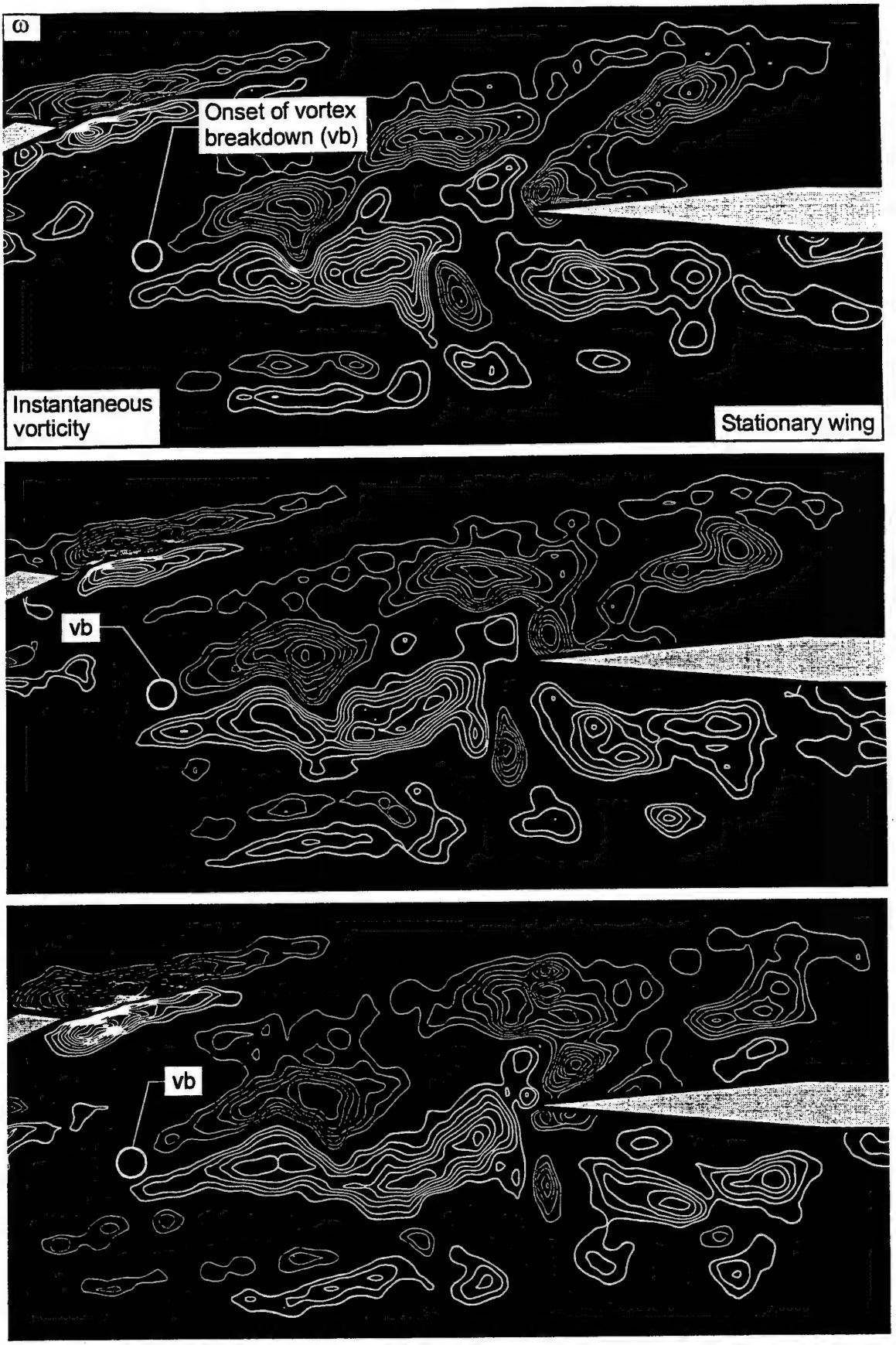

Figure 6c: Excerpts from cinema sequence showing evolution of patterns of vorticity with time for the case of the stationary delta wing. Parameters are same as for Figure 6a.

Figure 6d: Patterns of instantaneous vorticity corresponding to perturbation of delta wing at period T_e=0.5 sec, relative to period T_o=1.6 sec of inherent instability of vortex breakdown. All parameters are same as for Figure 6a.

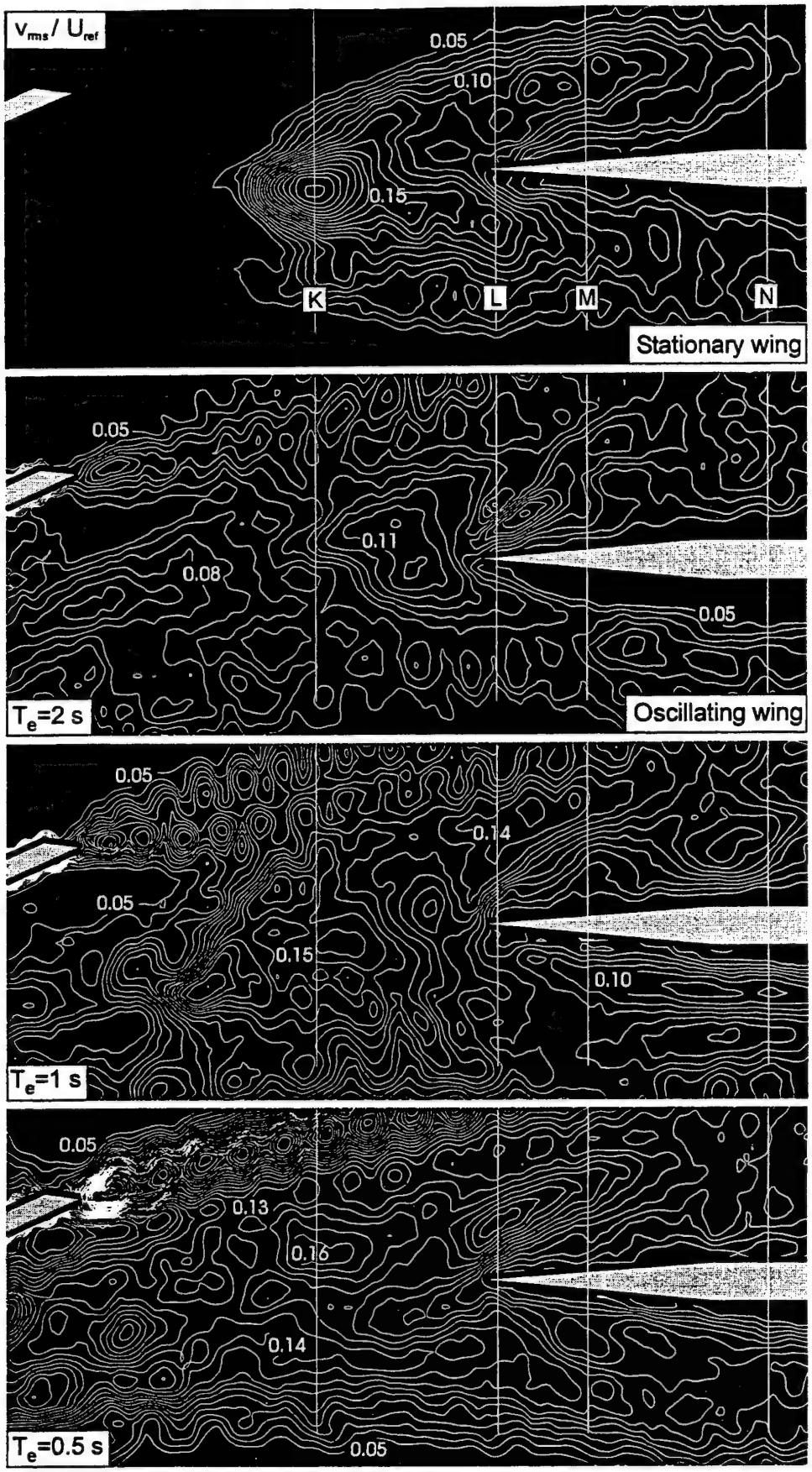

Figure 7a: Root-mean-square values of transverse velocity fluctuation v_{rms} for the cases of a stationary delta wing and a wing subjected to small-amplitude perturbation of angle-of-attack. Wing is perturbed at period T_e relative to the period T_o=1.6 sec of the inherent instability of vortex breakdown.Numbers on contours correspond to constant values of the dimensionless ratio v_{rms}/U_{ref}, in which U_{ref} is reference velocity. Minimum and incremental values of transverse velocity fluctuation are v_{rms}/U_{ref} = 0.05 and $\Delta v_{rms}/U_{ref}$= 0.01. Nominal angle-of-attack of delta wing is $\bar{\alpha}$= 24° and amplitude of perturbation angle-of-attack is α_o=1°. Thin vertical lines represent locations at which distributions of v_{rms}/U_{ref} are displayed in Figure 7b.

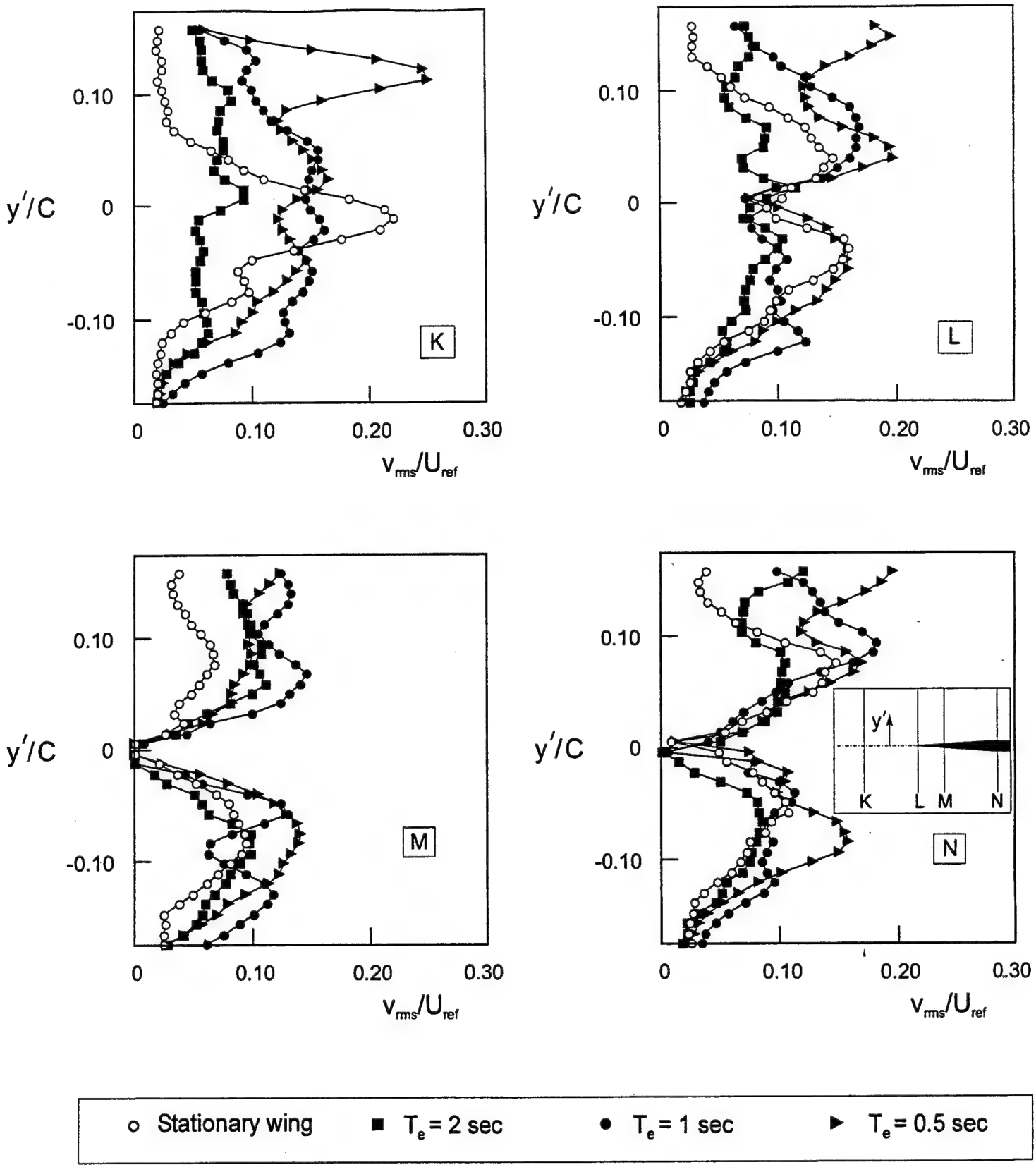

Figure 7b: Distributions of root-mean-square of transverse velocity fluctuation v_{rms} normalized by reference velocity U_{ref} along the vertical lines designated in Figure 7a .Wing is perturbed at period T_e relative to the period T_o=1.6 sec of the inherent instability of vortex breakdown.

APPENDIX C

Sahin 011701

VORTEX BREAKDOWN-EDGE INTERACTION: CONSEQUENCE OF EDGE OSCILLATIONS*

B. Sahin* and H. Akilli*
Department of Mechanical Engineering
Cukurova University
Balcali 01330 Adana
Turkey

J.-C. Lin and D. Rockwell
Department of Mechanical Engineering and Mechanics
354 Packard Laboratory, 19 Memorial Drive West
Lehigh University, Bethlehem, PA 18015

* On leave at Department of Mechanical Engineering and Mechanics, Lehigh University

ABSTRACT

A technique of high-image-density particle image velocimetry is employed to determine the instantaneous and averaged features of distortion of vortex breakdown incident upon a stationary and an oscillating leading-edge. It is demonstrated that the onset of vortex breakdown can be advanced or retarded substantially, depending upon the period of the edge oscillation relative to the inherent frequency of vortex breakdown. These features are interpreted with the aid of global representations of averaged and rms distributions of velocity, vorticity and Reynolds stress, as well as a cinema sequence of instantaneous patterns of velocity and vorticity. Moreover, instantaneous, wholefield images in a cinema sequence allow evaluation of global representations of spectra and cross-spectra, providing further insight into the central mechanisms that dictate the surface loading of the edge.

***Sahin, B., Akilli, H., Lin, J.-C. and Rockwell, D. 2001 "Vortex Breakdown-Edge Interaction: Consequence of Edge Oscillations", *AIAA Journal*, Vol. 39, No. 5, pp. 865-876.**

Nomenclature

C = chord of delta wing (mm)

D_v = characteristic vortex diameter (mm)

f = frequency (Hz)

f_o = frequency of vortex breakdown (Hz)

f_e = excitation frequency of edge of plate (Hz)

f_N = Nyquist frequency (Hz)

L_p = length of plate (mm)

M = magnification

N = number of samples

Re = Reynolds number = $U_\infty C/\nu$

S = Distance between two points for cross-spectrum evaluation

S_{ab} = magnitude of cross-spectrum

T = total sampling time (sec)

T_e = period of edge oscillation (sec)

T_o = period of inherent (undisturbed) vortex breakdown (sec)

u = horizontal component of velocity (mm/sec)

U_{ref} = reference velocity (mm/sec) = U_∞

U_∞ = freestream velocity (mm/sec)

$u'v'$ = Reynolds stress correlation

V = total velocity (mm/sec)

X_b^* = vortex breakdown location in presence of edge oscillations (mm)

$(X_b^*)_o$ = vortex breakdown location for stationary plate (mm)

α = angle-of-attack of delta wing (°)

α_p = angle-of-attack of plate (°)

ϕ_{ab} = phase shift of cross-spectrum

Λ = sweep angle of delta wing (°)

Δt = sampling time (sec)

ω = vorticity (sec^{-1})

ω_{rms} = root-mean-square of vorticity fluctuation (sec^{-1})

Γ = circulation of the vorticity concentration (mm^2/sec)

Introduction

Buffeting of aircraft tails or fins by a broken-down vortex, which has its origin at an aerodynamic surface located upstream, represents an important class of flow-structure interaction that can give rise to vibration, and potentially failure, of the tail or fin. This class of vortex-body interactions is part of a broader range of interaction phenomena, as recently reviewed by Rockwell[1]. Experimentally-based investigations have provided valuable information on the loading and response characteristics of the tail (or fin), sometimes accompanied by qualitative flow visualization. In recent years, a major emphasis, from an experimental standpoint, has focused on various combinations of the time-averaged and unsteady forces, moments and surface pressures, and surface acceleration as addressed in the works of Triplett[2], Brown, Lee and Tang[3], Lee, Brown, Ziglea and Poirel[4] and Lee and Brown[5]. A summary of recent investigations, including efforts to control buffeting, is provided by Huttsell, Tinapple and Weyer[6].

Of course, all of these features of the unsteady loading and acceleration have their genesis in the vortical flow patterns impinging upon the fin or tail. Flow visualization of the vortex structure is provided by Erickson, Hall, Banks, Del Frate, Schreiner, Hanley and Pulley[7], and Fisher, DelFrate and Richwine[8]. The velocity fluctuation fields in the vicinity of vertical tails, induced by the incident vortex, have been addressed in several investigations. Sellers, Meyers and Hepner[9] performed measurements on a model of a YF-17 aircraft, and demonstrated the occurrence of large velocity fluctuations in the vicinity of the tails. Komerath, Liou, Schwartz and Kim[10,11] considered a model of an F-15 aircraft and showed occurrence of peaks in the velocity spectra, at locations both inboard and outboard of the vertical tails, at high angle-of-attack. Breitsamter and Laschka[12] provide extensive data of the pointwise averaged velocity field in the vicinity of a fin region of a delta-canard configuration. Despite the fact that the Reynolds number was relatively high, i.e., $Re = 10^6$, spectra of the velocity field exhibited sharply defined peaks. These observations confirm the essentially inviscid nature of the fluctuating field due to vortex breakdown, and are in accord with a visualized spiral instability of vortex breakdown on a full-scale research version of the F-18 aircraft at high angle of incidence, performed by Fisher, Del Frate and Richwine[8].

Global, quantitative characterization of the flow is required for an adequate understanding of these phenomena. Imaging of vortex-plate and vortex-tail interactions, providing both global instantaneous and time-averaged information is described by Mayori and Rockwell[13], Canbazoglu, Lin, Wolfe and Rockwell[14], and Wolfe, Lin and Rockwell[15]. These investigations of vortex breakdown-surface interactions provide an essential foundation for the investigations proposed herein. An alternate type of imaging approach involving planar Doppler velocimetry, has yielded time-averaged

representations of vortex-fin interaction. Global images of selected parameters, in root-mean-square form, are given by Beutner, Baust and Meyers[16].

Numerical investigations of Rizk and Gee[17], Gee, Murman, and Schiff[18], Kandil, Sheta, and Massey[19], and Rizzetta[20] have simulated various aspects of the vortex breakdown-tail interaction in relation to the loading characteristics. Among other features pointed out by these numerical investigations, the importance of upstream influence of aeroelastic deflections of the tail on the onset of vortex breakdown has been addressed by Kandil, Sheta, and Massey[19]. Computations by Gordnier and Visbal[21,22] provide a detailed description of the instantaneous and time-averaged three-dimensional flow structure generated by the impingement of a delta wing vortex pair on a plate. Their study revealed the existence of complex separation patterns on both sides of the plate resulting from the spanwise variation in effective angle of attack, which is induced by the incoming vortex system. The vortex breakdown location was found to be sensitive to the degree of obstruction created by the stall on the plate. This mutual interaction between the incident vortex breakdown and the separated flow on the impingement surface may provide a basis for future flow control strategies.

The foregoing numerical and experimental investigations recognize the existence of a predominant spectral peak, i.e., predominant frequency component above the broadband background, due to vortex breakdown. It has important consequences for loading of the tail. This predominant frequency corresponds to the helical mode instability of the flow downstream of the onset of vortex breakdown as addressed by Garg and Leibovich[23] and Gursul[24]. Wolfe, Canbazoglu, Lin, and Rockwell[25] showed that dominant frequencies of surface pressure fluctuations on fins agree very well with those on the surface of delta wings without a fin characterized by Gursul[24]. Wolfe,

Canbazoglu, Lin, and Rockwell[25] propose a simple scaling parameter for the dominant frequency, valid over a wide range of Reynolds and Mach numbers. This relationship is further substantiated by Wolfe, Lin, and Rockwell[15] for the limiting case of direct and near-direct encounter of a broken-down vortex with a flat plate. In this investigation, pressure spectra on the plate were compared with the instantaneous structure of the incident vortex. It was shown that the dominant frequency of loading is relatively insensitive to the offset of the incident vortex. Moreover, the largest amplitude loading occurs when the maximum mean vorticity of the incident vortex is aligned with the leading-edge of the plate.

The objective of this investigation is to characterize the interaction of vortex breakdown with stationary and oscillating leading-edges using a global imaging technique. The possibility of retardation or advancement of the process of vortex breakdown, the nature of local vorticity-edge interactions, and the coupling between the flow patterns in the vicinity of the tip of the edge and the upstream development of vortex breakdown will be addressed. Moreover, spectral and cross-spectral analysis using a sequence of instantaneous, global images will be undertaken in order to determine spectral features of the incident vortex and the distorted vorticity field past the edge, which in turn dictate the unsteady loading on the edge.

Experimental System and Techniques

Experiments were performed in a large-scale water channel having a test section length of 4,928 mm, a width of 927 mm and a height of 610 mm. During the course of the experiments, the water level was maintained at 559 mm, which prevented overflow of the channel, especially during startup of the pump. The freestream velocity U_∞ was 45 mm/sec, giving a value of Reynolds number based on wing chord C, of 10,240.

As illustrated in Figure 1, a leading-edge vortex, which was generated from a delta wing, impinged upon a plate having a sharp leading-edge. The angle-of-attack of the delta wing $\alpha = 24°$ and $30°$ for the present experiments, while the plate had an angle of attack of $\alpha_p = 0°$ and $2.5°$. Unless otherwise noted, angle-of-attack is $\alpha = 29°$ for all cases. The delta wing had a chord of $C = 222$ mm and a sweep angle $\Lambda = 75°$. The thickness of the wing was 3.18 mm. It was beveled at an angle of $34°$ on its windward side. The plate had a length of $L_p = 162$ mm and a thickness $t_p = 6.35$ mm; its leading- and trailing-edges were beveled at angles of $5°$ and $12°$ respectively. The distance between the trailing-edge of the delta wing and the leading-edge of the plate was maintained at $L = 73$ mm. The onset of vortex breakdown occurred a distance X_b^* upstream of the leading-edge of the plate. For the case of the stationary edge, the breakdown occurs at $(X_b^*)_o$.

The plate was subjected to prescribed pitching oscillations about its midchord by a high resolution stepping motor, which was controlled by the laboratory microcomputer. The variation of angle-of-attack is defined as $\alpha_p(t) = \bar{\alpha}_p + (\alpha_p)_o \sin \omega_e t$, in which $\omega_e = 2\pi f_e$. Unless otherwise indicated, $\bar{\alpha}_p = 0$ and $(\alpha_p)_o = 2.5°$ for all experiments. This pitching amplitude of the plate corresponds to a tip displacement of $\pm$ 3.5 mm, relative to the vortex diameter of 8.5 mm. The period $T_e = 2\pi/\omega_e$ was varied over the interval $1 \text{ sec} \leq T_e \leq 6$ sec, relative to the period $T_o = 1.66$ sec of the inherent frequency of vortex breakdown in the spiral mode. At $T_e = 1$ sec, the vortex patterns induced at the leading-edge dominated the vortex-plate interaction, thereby providing a reasonable lower limit of T_e.

Instantaneous images of the vortex breakdown-edge interaction were acquired using a technique of high-image-density particle image velocimetry, described by Rockwell et al.[25]. The beam from a continuous wave Argon-ion laser was transmitted through an optical train, then impinged upon a rotating multi- (48) faceted mirror, in order to generate a scanning laser sheet. This sheet is indicated by the bold dashed line in the plan view of Figure 1. It was aligned with the centerline of the leading-edge vortex. The scanning frequency was adjusted to 75 Hz. In order to provide well-defined particle images for the PIV technique, the flow was seeded with 14.6 micron, metallic-coated hollow plastic spheres. At the aforementioned value of laser scanning frequency, typically four to five multiple exposures of each particle image were acquired during each shutter opening of the camera. These particle images were recorded on 35 mm high-resolution film having 300 lines/mm as specified by the manufacturer. The patterns of particle images were digitized at a resolution of 125 pixels/mm. The mean diameter of each particle image was 0.4 pixels (3.26 microns). A single frame cross-correlation technique was employed to determine the velocity field. The interrogation window had a size of 1.55 mm × 1.55 mm (90 pixels × 90 pixels) in the plane of the laser sheet. Since the magnification was M = 1:4.3, the size of the interrogation window on the film was 0.36 mm × 0.36 mm. In order to satisfy the Nyquist criterion, a 50% overlap was used during the interrogation process. Moreover, to ensure that the high-image-density criterion was satisfied, each interrogation window contained a total of approximately 40 to 60 particle images. Cinema representations of the flow were obtained by employing the maximum framing rate (5.55 frames/sec) of the 35 mm camera.

Calculation of the averaged quantities was performed according to the equations defined in the following. Each averaged parameter was determined at each spatial

coordinate (x,y) by considering the average of all instantaneous values (x,y). The terminology and definition of each of the averaged parameters are as follows:

$< V >$ = averaged (or mean) total velocity

$$< V > \equiv \frac{1}{N}\sum_{n=1}^{N} V_n(x,y) \tag{1}$$

$< u >$ = averaged value of horizontal component of velocity

$$< u > \equiv \frac{1}{N}\sum_{n=1}^{N} u_n(x,y) \tag{2}$$

$< \omega >$ = mean value of vorticity ω

$$< \omega > \equiv \frac{1}{N}\sum_{n=1}^{N} \omega_n(x,y) \tag{3}$$

ω_{rms} = root-mean-square of vorticity fluctuation

$$\omega_{rms} \equiv < \omega >_{rms} \equiv \left[\frac{1}{N}\sum_{n=1}^{N}[\omega_n(x,y) - < \omega(x,y) >]^2\right]^{1/2} \tag{4}$$

$< u'v' >$ = averaged value of Reynolds stress correlation

$$< u'v' > \equiv \frac{1}{N}\sum_{N=1}^{n}[u_n(x,y) - < u(x,y) >]\,[v_n(x,y) - < v(x,y) >] \tag{5}$$

The effect of the number of images on the foregoing averages was examined, and is described subsequently in the section entitled *Averaged Flow Patterns*.

Using the cinema sequence of instantaneous images, it was possible to construct, at arbitrary locations in the flow, the time history of velocity and vorticity, and then evaluate the spectrum and cross-spectrum using approaches similar to those employed for classical pointwise measurement techniques. The associated parameters and the

limitations of the calculated values are described in the section entitled *Spectra and Cross-Spectra Based on Instantaneous Imaging of Vortex Breakdown-Edge Interaction.* The Nyquist frequency was $f_N = 2.78$ Hz.

Vortex Breakdown-Edge Interactions

Averaged Flow Patterns

Figure 2 shows the location of the onset of vortex breakdown X_b^* due to edge oscillations. The value of X_b^* was determined from dye injection; it corresponded to an abrupt increase in the visualized cross-section of the vortex. For each period T_e of the plate excitation, six dye images were recorded on a video system, and the locations of vortex breakdown were averaged to yield a single value of X_b^*. In Figure 2, X_b^* is normalized by $(X_b^*)_o$, which represents the onset of breakdown for the stationary edge. This parameter is a function of the period T_e of the edge oscillation normalized by the period T_o of the spiral mode instability of vortex breakdown during its interaction with the stationary edge, T_e/T_o. The circular data points indicate averaged data and the vertical bars represent the maximum deviation of the self-excited excursions about these averaged values. At small values of $T_e/T_o \cong 0.25$, the onset of vortex breakdown is substantially advanced upstream as the ratio $X_b^*/(X_b^*)_o$ approaches a value of 2. As indicated by the magnitude of the vertical bars for $T_e/T_o \cong 0.25$, substantial instantaneous excursions occur about the averaged location of the vortex breakdown. On the other hand, at larger values of T_e/T_o, the onset of breakdown is remarkably retarded over a range of excitation, $1 \leq T_e/T_o \leq 2.5$. At sufficiently high values of T_e/T_o, the location of

onset of vortex breakdown approaches its value corresponding to the stationary edge; this limiting case represents a quasi-steady response. The physical basis for the advancement and retardation of the onset of vortex breakdown is addressed in the averaged and instantaneous images that follow.

Figure 3a gives contours of constant $< u > /U_{ref}$ for a range of oscillation T_e of the edge, relative to those of the stationary edge. The averaged component of streamwise velocity $< u >$ is normalized with respect to the reference velocity $U_{ref} = U_\infty$ at a location in the relatively undisturbed region of the flow. For the present series of images, it corresponds to a location x/C = 0.5 and y/C = 0.65; these coordinates are defined in Figure 1. In each of the images of Figure 3a, the maximum contour level of $< u > /U_{ref} =$ 0.6 corresponds to the outermost contour; successive contours lying within this outer one correspond to incrementally decreasing values of positive $< u > /U_{ref} = 0.1$; each is represented by a thick white line. In certain images, negative values of $< u > /U_{ref}$ are observed; they are represented by the thin white line. Viewing all of the images of Figure 3a as a whole, it is evident that a wake-like region exists upstream of the leading-edge. At locations downstream of the tip of the edge, contours of $< u > /U_{ref}$ tend to merge along the surface of the edge. The bubble-like depictions of the wake regions of Figure 3a all show the existence of a well-defined minimum immediately downstream of the leading-edge of the bubble. Moreover, for the case of the lowest period of excitation $T_e = 1$ sec, a negative pocket of $< u > /U_{ref}$ is nearly centered at the tip of the edge. For this extreme case, the leading-edge of the bubble protrudes the furthest distance upstream. It should be noted that the aforementioned effects of retardation and advancement of the onset of vortex breakdown were also clearly evident in the dye

visualization described in conjunction with Figure 2. Such visualization provides, of course, a fully three-dimensional portrayal of the modified breakdown.

Figure 3b provides a parallel set of images corresponding to contours of constant averaged vorticity $<\omega>$. All images show well-defined concentrations of positive (thick white line) and negative (thin white line) azimuthal vorticity upstream of the leading-edge. The transverse distance between the extrema of positive and negative vorticity on either side of the region of vortex breakdown is defined as the characteristic diameter D_v of the broken-down vortex. The leftmost boundaries of these vorticity contours, i.e., the leading-edges of the vorticity contour plots, are taken to define the onset of vortex breakdown, which is designated as the streamwise location of the minimum vorticity contour. This location is approximately coincident with the outermost contour of $<u>/U_{ref} = <u>/U_\infty$ exhibited in Figure 3a, which represents the edge of the wake-like region of vortex breakdown. Moreover, at the tip of the edge, a vorticity layer is formed in all images, due to the finite angle of attack α_p of the leading-edge of the plate with respect to the axis of the vortex. At sufficiently low values of excitation period $T_e = 1$ sec, highly concentrated vortices are evident on both the upper and lower sides of the leading-edge. Finally, it should be noted that remnants of the pattern of vorticity formed in the wake of the delta wing are evident in the upper left corner of each image.

Viewing the entire layout of images of Figure 3b, it is evident that the pattern of vorticity at the excitation condition $T_e = 6$ sec is very similar to that of the corresponding to the stationary edge, suggesting that an essentially quasi-steady perturbation of the vortex and its interaction with the edge are attained. This case corresponds to a ratio $T_e/T_0 = 3.5$ (compare Figure 2). When the excitation period is lowered to $T_e = 2$ sec,

corresponding to $T_e/T_o = 1.2$, the onset of vortex breakdown is substantially retarded, i.e., it moves downstream towards the tip of the edge. Moreover, the peak values of vorticity in the vortex breakdown region are dramatically reduced. The converse situation occurs for $T_e = 1$ sec, i.e., $T_e/T_o = 0.6$, for which the onset of breakdown is substantially advanced in the upstream direction. Moreover, the peak values of vorticity in the breakdown region are increased significantly relative to those for the case of a stationary edge. Remarkably high levels of peak positive and negative vorticity are generated along the upper and lower surfaces of the edge.

Figure 3c provides representations of contours of root-mean-square vorticity fluctuation ω_{rms}, corresponding to the images of Figure 3b. For the cases of the stationary edge and the edge oscillating at $T_e = 6$ sec, an extremum of ω_{rms} occurs at a location along the centerline of the region of vortex breakdown. This extremum is, however, displaced upstream of the locations of the peak value, i.e., extremum of $<\omega>$ shown in Figure 3b. This extremum is located in the shear layers of the breakdown bubble. Moreover, the maximum values of ω_{rms} appear to occur at or near the maximum negative value of $<u>/U_{ref}$, i.e., within the region of substantial velocity defect in the wakelike region of the breakdown bubble, as shown in Figure 3a. Furthermore, a distinctive feature of the vorticity pattern upstream of the stationary edge is the occurrence of vorticity fluctuations occurring in two distinct layers, one above and the other below the edge. On the other hand, no such bifurcation of the ω_{rms} contours occurs for the edge oscillation at $T_e = 6$ sec. Figure 3c also shows that, at $T_e = 2$ sec, the breakdown process is markedly retarded; significant levels of ω_{rms} do not occur upstream of the tip of the edge. Rather, relatively high values of ω_{rms} occur in the vicinity of the

tip, due to its oscillation. Finally, substantially-enhanced levels of ω_{rms} in the initial region of vortex breakdown, as well as in the vicinity of the tip of the edge, are evident at the lowest excitation period $T_e = 1$ sec.

Corresponding values of the averaged velocity correlation $<u'v'>/U_{ref}^2 = <u'v'>/U_\infty^2$ are shown in Figure 3d. The highest values of $<u'v'>/U_{ref}^2$ actually occur in the vorticity layers of the vortex breakdown region, evident by comparison with the $<\omega>$ contours of Figure 3b. For the case of the stationary edge, these peak values of $<u'v'>/U_{ref}^2$ are, however, displaced downstream of the peak values of averaged vorticity $<\omega>$. Distinguishing features of the case of the oscillating edge at $T_e = 6$ sec are the relatively high levels of $<u'v'>/U_{ref}^2$ generated at the tip and along the upper surface of the edge, in contrast to the case of the stationary edge. In fact, the important role of the edge oscillation in generating high values of $<u'v'>/U_{ref}^2$ is evident at $T_e = 1$ sec and 2 sec in Figure 3d. At $T_e = 1$ sec, large values of $<u'v'>/U_{ref}^2$ are induced well upstream of the tip of the edge.

The intent of each of the averaged images given in Figures 3a through 3d is to provide an approximate reference image. Such an image is the consequence of the time sequence of instantaneous patterns, which is addressed in the next section. The effect of the number N of instantaneous images employed to obtain the averaged image is indicated in Figure 3e for the vorticity $<\omega>$ and the velocity correlation $<u'v'>/U_{ref}^2$. The overall forms of the averaged patterns appear to converge relatively quickly; an exception appears to be the positive (thick white line) concentration of $<u'v'>/U_{ref}^2$ immediately above the tip of the leading-edge. This approximate convergence of the

overall patterns for a very limited number of cycles is apparently due to the cyclic-repetitive nature of the patterns of vorticity and velocity, and the absence of significant low frequency fluctuations. Dye visualization over a large number of oscillation cycles showed that presence of the plate inhibited the usual low frequency, streamwise excursions of vortex breakdown that occur in absence of the plate.

Instantaneous Flow Patterns

The averaged flow pattern upstream of, and at the edge, exhibited in Figures 3a through 3d, is, of course, a consequence of the time evolution of the corresponding instantaneous patterns. Key features of the instantaneous structure are given in Figures 4a and 4b, which show pairs of vorticity-velocity images. The development of instantaneous patterns of vorticity upon the stationary edge is indicated in the set of three images at the upper left of Figure 4a. Vorticity concentrations A, and C through G, all originate from the initial process of vortex breakdown upstream of the tip of the edge. On the other hand, concentration B is generated from the tip of the edge. Following the time evolution of these images, it is evident that vorticity concentrations A and C successively attempt to merge with concentration B as they pass above the edge. For the case of edge oscillation at a relatively long period $T_e = 6$ sec, shown in the bottom three rows of images of Figure 4a, the pattern of instantaneous vorticity concentrations along the upper surface of the edge again indicate interaction between vorticity concentration A originating from vortex breakdown and an elongated vorticity layer B, which has a high level of vorticity, originally formed from the tip of the edge. Along the lower surface, vorticity concentration E undergoes relatively rapid decrease in level of vorticity. Upstream of the tip of the edge, the overall pattern of instantaneous concentrations, C, F and G, is analogous to the pattern D, F and G corresponding to the stationary edge. In

other words, the upstream influence of the oscillating edge is not significant, save for possible alteration of details of the vorticity concentration.

The corresponding distributions of instantaneous velocity for both cases of the stationary and oscillating edge, exhibited in the right column of Figure 4a, show generally similar regions of large velocity defect due to the onset of vortex breakdown. The interface between the region of relatively large and low velocity corresponds to the locus of high vorticity in the corresponding patterns of vorticity. Moreover, analogous regions of high velocity gradient in the vicinity of the tip of the edge again correspond to high vorticity.

Figure 4b shows, in the top three rows of images, the consequence of edge oscillation at $T_e = 2$ sec. The patterns of instantaneous vorticity show that the onset of vortex breakdown has moved downstream substantially, and the width of the breakdown region, represented by the distance between layers of positive and negative vorticity, i.e., between concentrations C and G, is relatively narrow. Moreover, the degree of agglomeration of vorticity into larger-scale structures is not as pronounced as for the foregoing cases. The corresponding patterns of instantaneous velocity at $T_e = 2$ sec shown in the right column of Figure 4b do not show a clearly identifiable region of low velocity that would indicate a pronounced wake defect due to onset of vortex breakdown. This remarkable retardation of the onset of vortex breakdown at $T_e = 2$ sec corresponds to a value of $T_e/T_o = 1.2$ in Figure 2, which shows minimum values of $X_b^*/(X_b^*)_o \cong 0.4$. The physical origin of this averaged retardation of the onset of vortex breakdown appears to be the compatibility between the edge oscillation and the arrival of incident concentrations of vorticity. This issue is further addressed in conjunction with Figure 5.

At the smallest value of excitation T_e = 1 sec, represented in the bottom three rows of Figure 4b, the instantaneous structure of the positive and negative layers of vorticity takes on a fundamentally different form, relative to the previous cases at larger T_e. It resembles a bubble-like mode of vortex breakdown. Moreover, small-scale concentrations of vorticity are embedded in these layers. At the tip of the edge, these incident layers appear to merge with pronounced concentrations of vorticity generated at the tip of the edge. Viewed as a whole, these images suggest a close interrelationship between the pronounced concentrations of vorticity generated in the vicinity of the tip and the pattern of vortex breakdown well upstream of the tip. In essence, generation of large-scale vortices from the tip sets up an effective blockage. It is well known that the onset of vortex breakdown is highly sensitive to the scale of an obstacle placed in the flow. The vortex system at the tip therefore may be viewed as an equivalent obstacle that substantially advances the onset of vortex breakdown in the upstream direction. The corresponding patterns of instantaneous velocity shown in the right column indicate that the region of large velocity defect, associated with the onset of vortex breakdown, has moved considerably further upstream than for the cases of the stationary edge and the edge oscillating at T_e = 6 sec shown in Figure 4a. Moreover, the pattern of relatively large-magnitude velocity vectors induced near the tip of the edge is compatible with the very high levels of vorticity concentration in that region.

The effect of angle-of-attack α_p of the plate was examined, in order to ensure that the aforementioned retardation of the onset of vortex breakdown was a persistent feature. For the images shown in Figure 5, the centerline of the plate is approximately aligned with the centerline of the region of vortex breakdown, corresponding to an angle-of-attack of the plate of $\alpha_p = 2.5°$. As a consequence, as shown in the top two images of

Figure 5, leading-edge separation and the consequent generation of a vortex from the tip of the edge do not occur. The occurrence of a positive concentration of vorticity along the upper surface of the edge is simply due to clipping of the incident layer of positive vorticity during transverse undulations of the pattern of vortex breakdown. Generally speaking, the patterns of instantaneous vorticity, which are indicative of the spiral mode of vortex breakdown, have a generally similar form relative to those in the top three rows of images of Figure 4a.

For the case of edge oscillation at $T_e = 2$ sec, the process of vortex breakdown is, again, substantially retarded in a manner similar to that represented by a pattern of average vorticity in Figure 3b and instantaneous vorticity in Figure 4b. The two instantaneous patterns at the bottom of Figure 5 show instants corresponding to maximum negative and positive displacement of the edge. The important feature of the interaction between the patterns of instantaneous vorticity and the oscillating edge is the relative position of the instantaneous large-scale cluster of vorticity relative to the position at the tip of the edge. In the first (upper) image of instantaneous vorticity at $T_e = 2$ sec, the large-scale concentration of negative (thin line) vorticity is well above the tip of the edge, whereas in the second pattern of instantaneous vorticity, the large-scale concentration of positive (thick line) vorticity is well below the tip of the edge. This out-of-phase relationship between deflection of the edge and the arrival of incident concentrations of vorticity during a typical cycle of the edge oscillation appears to be a key factor that allows downstream movement, or retardation, of the vortex breakdown.

Effect of Edge Oscillation on Averaged Swirl of Component of Vorticity of Incident Vortex

The averaged patterns of vorticity of the region of vortex breakdown provide, in essence, an indication of the effective, averaged strength of the swirl component of vorticity. That is, since the patterns of vorticity represent orientations normal to the plane of the image, and the laser sheet passes through the centerline of the vortex, distributions of the swirl component of vorticity are at hand. Figure 6 shows the variation of the peak value of averaged vorticity $<\omega>$ as a function of distance along the vortex. As already suggested by the images of Figure 3b, and further shown in Figure 6, the onset of vortex breakdown gives rise to extrema of averaged vorticity along the edge of the breakdown bubble, which appear to decay rapidly with increasing streamwise distance and for regions above and below the plate. To further emphasize this point, the variation of peak vorticity was considered along the white lines indicated in each of the respective images in the insets of Figure 6. That is, these white lines correspond to the locus of peak vorticity along the lower portion of the vortex. The corresponding values of vorticity are represented by the three curves for the stationary edge, and the oscillating edge at $T_e = 6$ sec and $T_e = 2$ sec. Distance x is measured from the beginning of the white line and the characteristic vortex diameter D_v corresponds to the transverse distance between the vorticity extrema in each pattern of vortex breakdown. For the case of the stationary edge, the peak vorticity rapidly attains its maximum value at $x/D_v = 2$, then exhibits decay, followed by a secondary peak, then further decay. For $T_e = 6$ sec, a generally similar form of the curve is evident, except the secondary peak has been smoothed out by the effect of the oscillating edge on the pattern of vorticity in the vicinity of the tip of the

edge. Finally, at T_e = 2 sec, the onset of the peak value of vorticity is retarded to a location of approximately $x/D_v = 4.5$, followed by an abrupt decrease.

These variations of averaged vorticity are associated with changes in the instantaneous circulation Γ of the vorticity concentrations. Representative variations of $\Gamma/\pi D_v U_{ref}$ are shown in Figure 7 for the case of the stationary edge. Three successive cycles of the incident pattern of vorticity concentration are considered, giving rise to concentrations A_1, A_2 and A_3, as well as B_1, B_2 and B_3. To provide a guide for interpreting these variations, three images at N = 2, 6 and 8 are shown for the first cycle of incident vorticity concentrations. The cluster of vorticity A_1 actually undergoes a substantial increase in circulation, apparently due to reorientation of the distribution of vorticity vectors along the edge of the separation bubble. The originally isolated concentration A_1 in image N = 2 evolves into an elongated form, with additional vorticity on either side of it. In image N = 6, and as is evident in image N = 8, the cluster of vorticity A_1 actually consists of three identifiable concentrations. At N = 2, B_1 is shown to have a relatively high peak vorticity and thereby circulation and, at successive instants, N = 6 and 8, it undergoes very substantial decrease in circulation as it encounters and moves along the surface of the edge. This attenuation is logical, in view of the fact that the vorticity concentration is actually a cross-section of the three-dimensional concentration associated with the spiral mode of instability, and the leading-edge represents an impermeable surface, which severs the incident spiraling vortex. The plot of Figure 7 shows the quantitative variation of dimensionless circulation. The pattern of increasing circulation associated with the cluster of vorticity A and the decreasing circulation of vortex B persist in a repetitive fashion over several cycles.

Spectra and Cross-Spectra Based on Instantaneous Imaging of Vortex Breakdown-Edge Interaction

The cinema sequence of instantaneous images provides the possibility to construct spectra and cross-spectra of time-dependent velocity components, as well as vorticity. The time interval between successive frames of the cinema sequence was $\Delta t = 0.18$ sec, which corresponds to the sampling time. The corresponding value of the Nyquist frequency was $f_N = 2.78$ Hz. This value of sampling time Δt compares with the naturally occurring period of vortex breakdown, $T_o = 1.66$ sec. A total of thirty-six images was acquired over the time $T = 6.48$ sec. This value of T corresponds to a bandwidth $B_e = 0.15$ cycles/sec. Considerations for accurate calculation of spectra and cross-spectra are defined by Newland[27]. Important is the acquisition of adjacent time records which, when averaged together, can provide an increase in accuracy, relative to the case of a single record of duration T, irrespective of the length T of the original record. For the present experiment, such adjacent records were not obtained, and therefore the calculated spectra and cross-spectra must be viewed as approximate representations. The purpose of the present effort is to demonstrate the concept of calculation of spectra and cross-spectra at a large number of spatial points over the flow domain using the same time record of sequential images from a cinema sequence. That is, the time variation of velocity and vorticity at each location (x, y) is equivalent to simultaneous acquisition of time records from a very large number of probes in the flow. Despite the foregoing approximations, the predominant frequency is correct within five percent, and the spatial variations of the spectra and cross-spectra are in accord with what one expects from the larger-scale vorticity concentrations.

The loading on the leading-edge is a function of the frequency, amplitude and phase variation of the flow patterns past the edge. In order to provide a guide for

interpreting the spectra and cross-spectra, the averaged distributions of vorticity $< \omega >$ are employed. The fact that these averaged patterns provide a reasonable representation of the loci of extrema of instantaneous concentrations of vorticity is evident from the comparison of Figure 8a. It shows a superposition of averaged (solid line) and instantaneous (dashed line) vorticity for the case of the stationary edge. Examination of a series of these images from a cinema sequence shows that the instantaneous patterns of vorticity move through the averaged pattern.

Figure 8b illustrates the averaged pattern of vorticity for the case of the stationary edge. A lower value of minimum vorticity than employed in previous images. Also shown are corresponding spectra $S_u(f)$ of the streamwise velocity fluctuation u. The white dots indicate locations in the averaged vorticity pattern at which spectra were acquired. The three spectra on the left side of the image represent a location near the onset of vortex breakdown, but just upstream of the location at which averaged and fluctuating vorticity become sufficiently large. It is evident that no sharply defined peak is evident in these three spectra. On the other hand, spectra taken downstream of the extrema of averaged vorticity indicate a sharply-defined peak at f_o = 0.6 Hz, corresponding to passage of the instantaneous vorticity concentrations suggested in Figure 8a. The maximum amplitude of this spectral peak tends to occur near or at the location of maximum averaged vorticity in the corresponding image. At a location downstream of the tip of the leading-edge, spectral peaks at the natural breakdown frequency f_o = 0.6 Hz are again clearly evident. On the upper side of the tip of the leading-edge, these peaks also correspond to the frequency of shedding of the tip vortex. Figure 8b also shows spectra at two locations further downstream of the tip region. Spectra near the right boundary of the image exhibit a marked attenuation of their peaks.

This observation corresponds to the decrease in dimensionless circulation of the vorticity concentrations along the surface of the leading-edge, as addressed in Figure 7.

Cross-spectral analysis was performed for the same cinema sequence as for Figure 8b; the results are shown in Figure 9. The components of the cross-spectrum are: (i) the magnitude $S_{ab}(f_o)$ corresponding to two locations a and b separated by distance Δs; and (ii) the phase shift $\phi_{ab}(f_o)$ at the same value of separation Δs. Values of $S_{ab}(f_o)$ and $\phi_{ab}(f_o)$ were determined as a function of distance downstream of the tip of the edge along lines designated as 1^+, 2^+, ... and 1^-, 2^-, ..., above and below the edge surface respectively, for the transverse component of velocity v. Point a corresponds to the left edge of line 1^+ (and 1^- below the edge) and point b is located a distance Δs downstream of point a on line 1^+, 2^+, 3^+, or 4^+ for the region above the edge and similarly for the region below the edge. These values were determined over a rectangular grid of 16×7 points below the edge; the grid values were then interpolated to give contours of constant $S_{ab}(f_o)$ and $\phi_{ab}(f_o)$ shown in Figure 9.

The magnitude of the cross-spectrum $S_{ab}(f_o)$ in the region below the edge shows large values at the lower left corner of the plot of constant contours of $S_{ab}(f_o)$. The magnitudes of these contours generally decrease in the streamwise direction. The physical basis for this type of distortion of contours of $S_{ab}(f_o)$ is the passage of instantaneous concentrations of vorticity through this region. They induce large amplitudes of the transverse velocity fluctuation v(t), which yield large values of the magnitude of $S_{ab}(f_o)$. As these instantaneous patterns of vorticity move along the lower surface of the edge, the magnitude of their peak vorticity, and correspondingly the peak values of velocity v(t) decrease, contributing to relatively low values of $S_{ab}(f_o)$ over the

right portion of the contours of constant $S_{ab}(f_o)$. Corresponding values of phase $\phi_{ab}(f_o)$ are given in the bottom plot of Figure 9. The generally increasing values of ϕ_{ab} in the streamwise direction are in accord with the propagation of the aforementioned vortical patterns along the surface of the edge.

Above the edge, the patterns of $S_{ab}(f_o)$ and $\phi_{ab}(f_o)$ take on a more complex form, due to the localized formation of a vorticity concentration in the region immediately above the tip of the edge and, correspondingly, a distorted pattern of vorticity concentrations along its upper surface. These distortions are evident by examining the averaged contours of vorticity as shown in the middle plot of contours of constant $S_{ab}(f_o)$ above the edge; large values occur at the upper left corner, due to the process of tip vortex formation. Further distortions of the contours of $S_{ab}(f_o)$ are due to interactions between the incident vorticity concentrations rising from vortex breakdown and the concentrations associated with the tip vortex, as both move downstream of the tip region. This time sequence is indicated in Figure 4a. As a result of these types of interactions, the contours of constant phase $\phi_{ab}(f_o)$ are distorted in the manner shown in the uppermost plot of Figure 9. At locations sufficiently far downstream, the contours of constant phase $\phi_{ab}(f_o)$ take on a form more characteristic of a single row of propagating concentrations of vorticity.

Concluding Remarks

Interaction of vortex breakdown with an oscillating leading-edge gives rise to pronounced alterations of both the averaged and instantaneous structure of the incident, broken-down vortex; and substantial distortion of the vortex in the region of the leading-

edge. The latter is influenced by vorticity generation at the tip of the edge. The principal findings are as follows.

Substantial retardation, or delay, in the onset of vortex breakdown, and thereby development of large-scale concentrations of vorticity due to the helical mode of vortex breakdown, are attainable when the leading-edge is perturbed at a dimensionless time T_e (or frequency f_e) of the order of the corresponding time-scale (or frequency) of the frequency of naturally-occurring vortex breakdown. The physical origin of this retardation deserves further consideration. Possible mechanisms may be proper timing of the incident concentrations of vorticity relative to the motion of the tip of the edge and the phase shift of the distorted flow pattern along the surface of the plate.

On the other hand, remarkable advancement, i.e., upstream movement, of the onset of vortex breakdown is attainable when the period of excitation of the edge T_e is sufficiently small, or correspondingly, the excitation frequency f_e is sufficiently large. In this case, pronounced concentrations of vorticity are formed along the upper and lower surfaces of the tip of the edge, thereby providing increased blockage for the incident vortex breakdown.

Averaged patterns of vorticity, which represent the azimuthal or swirling component, show development of pronounced extrema shortly downstream of the onset of vortex breakdown, then a rapid decay as the broken-down vortex moves past the leading-edge. Root-mean-square distributions of fluctuating vorticity exhibit a pronounced extremum along the centerline of the broken-down vortex, and at an axial location that is typically located downstream of the extremum of averaged vorticity in the shear layers along the breakdown bubble.

Distributions of Reynolds stress show extrema in the shear layers bounding the region of vortex breakdown; these extrema generally occur, however, at an axial location downstream of the extrema of averaged vorticity. In the case where substantial retardation of the onset of vortex breakdown occurs, the levels of Reynolds stress are negligible upstream of the tip of the edge. On the other hand, it is demonstrated that the presence of edge oscillation gives rise to very high values of Reynolds stress in the vicinity of the tip of the edge. These levels are associated with vortex formation from the tip and, in the case of sufficiently low period T_e of the tip oscillation, i.e., sufficiently high frequency f_e, regions of high Reynolds stress protrude well upstream of the tip.

Approximate values of spectra and cross-spectra, evaluated from a time sequence of global images, show the transformation of the spectral content from the region of vortex breakdown upstream of the edge to the distorted breakdown along the surface of the edge. Pronounced spectral peaks are attenuated within a distance of six vortex diameters D_v downstream of the tip of the edge, such that broader-band background fluctuations exist in this region. Cross-spectral analysis in the vicinity of the tip of the edge provides portraits of both the cross-spectral amplitude and phase variations that dictate the effectiveness of loading of the surface of the edge.

Acknowledgements

The authors are grateful to the Air Force Office of Scientific Research for support of this investigation under Grant No. F49620-99-1-0011, monitored by Steven Walker. One of the authors, Professor Besir Sahin would like to thank the Scientific and Technical Research Council of Turkey (TUBITAK) and NATO for their financial support.

List of References

[1]Rockwell, D., "Vortex-Body Interactions", *Annual Review of Fluid Mechanics*, Vol. 30, 1998, pp. 199-229.

[2]Triplett, W. E., "Pressure Measurements on Twin Vertical Tails in Buffeting Flow", *Journal of Aircraft*, Vol. 20, No. 11, 1983, pp. 920-925.

[3]Brown, D., Lee, B. H. K., and Tang, F. C., "Some Characteristics and Effects of the F/A-18 Lex Vortices", *Vortex Flow Aerodynamics*, AGARD CP 494, 1990, pp. 30-1–30-20.

[4]Lee, B. H. K., Brown, D., Zigela, L. M., and Poirel, D., "Wind Tunnel Investigation and Flight Tests of Tail Buffet on the CF-18 Aircraft", *Aircraft Dynamic Loads Due to Flow Separation*, AGARD CP-483, 1990, pp. 1-1–1-26.

[5]Lee, B. H. K., and Brown, D., "Wind-Tunnel Studies of F/A-18 Tail Buffet", *Journal of Aircraft*, Vol. 29, No. 1, 1992, pp. 146-152.

[6]Huttsell, L. J., Tinapple, J. A. and Weyer, R. M., "Investigation of Buffet Load Alleviation on a Scaled F-15 Twin Tail Model", AGARD Structures and Materials Panel Workshop, Denmark, October, 1997.

[7]Erickson, G. E., Hall, R. M., Banks, D. W., Del Frate, J. H., Schreiner, J. A., Hanley, R. J., and Pulley, C. T., "Experimental Investigation of the F/A-18 Vortex Flows at Subsonic Through Transonic Speeds, Invited Paper", AIAA Paper 89-2222, July-August, 1989.

[8]Fisher, D. F., Del Frate, J. H., and Richwine, D. M., "In-Flight Flow Visualization Characteristics of the NASA F-18 High Alpha Research Vehicle at High Angles of Attack", SAE paper 892222, September, 1989. Also see the closely related study of Del Frate, J. H., Fisher, D. F., and Zuniga, F. A. "In-Flight Flow Visualization and Pressure

Measurements at Low Speeds on the NASA F-18 High Alpha Research Vehicle", NASA-Ames Research Center, Dryden Flight Research Facility, P. O. Box 273, Edwards, CA 93523-0273.

[9]Sellers, W. L., Meyers, J. F., and Hepner, T. E., "LDV Surveys over a Fighter Model at Moderate to High Angles of Attack", Society of Automotive Engineers TP Series Paper 88-1448, October, 1988.

[10]Komerath, N. M., Liou, S. G., Schwartz, R. J., and Kim, J. M., "Flow Over a Twin-Tailed Aircraft at Angle of Attack, Part I: Spatial Characteristics", *Journal of Aircraft*, Vol. 29, No. 3, 1992, pp. 413-420.

[11]Komerath, N. M., Liou, S. G., Schwartz, R. J., and Kim, J. M., "Flow Over a Twin-Tailed Aircraft at Angle of Attack, Part II: Temporal Characteristics", *Journal of Aircraft*, Vol. 29, No. 4, 1992, pp. 553-558.

[12]Breitsamter, C., and Laschka, B., "Turbulent Flow Structure Associated with Vortex-Induced Fin Buffeting", *AIAA Journal of Aircraft*, Vol. 31, No. 4, 1994, pp. 773-781.

[13]Mayori A., and Rockwell, D. "Interaction of a Streamwise Vortex with a Thin Plate: A Source of Turbulent Buffeting", *AIAA Journal*, Vol. 32, 1994, pp. 2022-2029.

[14]Canbazoglu, S., Lin, J.-C., Wolfe, S., and Rockwell, D., "Buffeting of Fins: Distortion of Incident Vortex", *AIAA Journal*, Vol. 33, No. 11, November, 1995, pp. 2144-2150.

[15]Wolfe, S., Lin, J.-C., and Rockwell, D., "Buffeting at the Leading-Edge of a Flat Plate Due to a Streamwise Vortex: Flow Structure and Surface Pressure Loading", *Journal of Fluids and Structures*, Vol. 9, 1995, pp. 359-370.

[16]Beutner,T. J., Baust, H. N., and Meyers, J. F., "Doppler Global Velocimetry Measurements of a Vortex-Tail Interaction", Proceedings of the 7th International

Symposium on Flow Visualization, Seattle, Washington, ed. J. P. Crowder, Begell House Inc. NY, 1995, pp. 418-423.

[17]Rizk, Y. M., and Gee, K., "Unsteady Simulation of Viscous Flow Field Around F-18 Aircraft at Large Incidence", *Journal of Aircraft*, Vol. 29, 1992, pp. 986-992.

[18]Gee, K., Murman, S. M., and Schiff, L. B., "Computational Analysis of F/A-18 Tail Buffet", AIAA Paper 95-3440, 1995.

[19]Kandil, O. A., Sheta, E. F., and Massey, S. J., "Buffet Responses of a Vertical Tail in Vortex Breakdown Flows", AIAA Paper No. 95-3464, 1995.

[20]Rizzetta, D. P., "Numerical Simulation of the Interaction Between a Leading-Edge Vortex in a Vertical Tail, AIAA Paper No. 96-2012, 27th AIAA Fluid Dynamics Conference, June 17-20, 1996, New Orleans, LA.

[21]Gordnier, R. E., and Visbal, M. R., "Numerical Simulation of the Impingement of a Streamwise Vortex on a Plate", AIAA Paper No. 97-17812, 8th AIAA Fluid Dynamics Conference, June 29-July 2, 1997, Snowmass Village, CO.

[22]Gordnier, R. E. and Visbal, M. R., "Numerical Simulation of the Impingement of a Streamwise Vortex on a Plate", *International Journal of Computational Fluid Dynamics*, Vol. 12, pp. 49-66, 1999.

[23]Garg, A. K., and Leibovich, S., "Spectral Characteristics of Vortex Breakdown Flowfields", *Physics of Fluids*, Vol. 22, No. 11, November, pp. 1979, 2053-2064.

[24]Gursul, I., "Unsteady Flow Phenomena Over Delta Wings at High Angle-of-Attack", *AIAA Journal*, Vol. 32, No. 2, February, 1994, pp. 225-231.

[25]Wolfe, S., Canbazoglu, S., Lin, J.-C., and Rockwell, D., "Buffeting of Fins: An Assessment of Surface Pressure Loading", *AIAA Journal*, Vol. 33, No. 11, 1995, pp. 2232-2235.

[26]Rockwell, D., Magness, C, Towfighi, J., Akin, O., and Corcoran, T., "High Image-Density Particle Image Velocimetry Using Laser Scanning Techniques", *Experiments in Fluids*, Vol. 14, 1993, pp. 181-19.

[27]Newland, D. E., Random Vibrations, Spectral and Wavelet Analysis, 3rd Edition, Longman Group Ltd., England, 1993.

List of Figures

Figure 1: Plan and side views of experimental system. Delta wing is stationary and impingement plate oscillates according to $\alpha_p(t) = \overline{\alpha}_p + (\alpha_p)_o \sin\omega_e t$. The impingement plate extends along the entire span of the test section.

Figure 2: Plot of averaged location of onset of vortex breakdown as a function of dimensionless period of oscillation of impingement plate. X_b^* represents distance upstream of tip of edge at which breakdown occurs when edge oscillates and $(X_b^*)_o$ is distance when edge is stationary. T_e is period of edge oscillation, and T_o is natural frequency of vortex breakdown. The vertical bar on each data point represents the deviation of the vortex breakdown position from its averaged value, as determined from six dye visualization images. Angle of attack of delta wing is $\alpha = 24°$. Mean and fluctuating angle of attack of impingement plate are respectively $\overline{\alpha}_p = 0°$ and $(\overline{\alpha}_p)_o = 2.5°$ according to $\alpha_p(t) = \overline{\alpha}_p + (\alpha_p)_o \sin\omega_e t$.

Figure 3a: Contours of constant averaged streamwise velocity $< u >$ normalized by reference velocity U_{ref} for the case of a stationary edge and an edge oscillating at defined period T_e. For all images, maximum and incremental values of average velocity $< u >/U_{ref}$ are respectively 0.6 and 0.1.

Figure 3b: Images representing contours of constant averaged vorticity $< \omega >$ for the case of the stationary edge and an edge oscillating at prescribed period T_e. For all images, the minimum and incremental values of $< \omega >$ are $\pm$ 2 and 0.75 sec^{-1}.

Figure 3c: Contours of constant fluctuating vorticity ω_{rms} for stationary edge and edge oscillating at defined T_e. For all images, the minimum and incremental values of ω_{rms} are 1.5 and 0.5 sec^{-1}.

Figure 3d: Images representing contours of constant $< u'v' >/U_{ref}^2$ for a stationary edge and an edge oscillating at defined values of period T_e. For all images, minimum and incremental values of $< u'v' >/U_{ref}^2$ are respectively $\pm$ 0.0025 and 0.0025.

Figure 3e: Effect of number N of instantaneous images on averaged vorticity $< \omega >$ and velocity $< u'v' >$ for the case of the stationary plate.

Figure 4a: Excerpts from cinema sequences showing patterns of instantaneous vorticity and distributions of velocity vectors for the case of a stationary edge and an edge oscillating at $T_e = 6$ sec. For all images, the minimum and incremental values of instantaneous vorticity ω are respectively $\pm$ 2 and 0.75 sec^{-1}. Natural frequency of vortex breakdown is $T_o = 1.66$ sec.

Figure 4b: Excerpts from cinema sequences showing patterns of instantaneous vorticity and distributions of velocity vectors for the case of an edge oscillating at $T_e = 2$ sec and 1 sec. For all images, the minimum and incremental values of instantaneous vorticity ω are respectively $\pm$ 2 and 0.75 sec^{-1}. Natural frequency of vortex breakdown is $T_o = 1.66$ sec.

Figure 5: Patterns of averaged and instantaneous vorticity for a stationary and oscillating leading-edge in the case where the axis of the incident vortex breakdown is aligned with the centerline of the leading-edge. For both averaged and instantaneous images, the minimum and incremental values of vorticity are respectively $\pm$ 2 and 0.75 sec^{-1}. Angle-of-attack of delta wing is $\alpha = 30°$.

Figure 6: Variation of averaged vorticity $< \omega >$ as a function of dimensionless distance x/D_v. Values of $< \omega >$ are along the white line, corresponding to the locus of the vorticity extremum.

Figure 7: Variation of dimensionless circulation Γ as a function of frame number N of a cinema sequence for representative, large-scale vorticity concentrations A and B.

Figure 8a: Superposition of averaged (solid line) and instantaneous (dashed line) contours of constant vorticity for a case of vortex breakdown incident upon a stationary edge. Minimum and incremental values of vorticity are respectively $\pm$ 2 and 0.75 sec^{-1}.

Figure 8b: Spectra $S_u(f)$ as a function of location in incident vortex breakdown and along surface of edge. Image at center shows contours of constant averaged vorticity $< \omega >$ and white dots represent locations at which spectra were acquired. Frequency at which spiral mode of vortex breakdown occurs is f = 0.6 cycles/sec.

Figure 9: Representations of magnitude $S_{ab}(f)$ and phase $\phi_{ab}(f)$ of cross-spectrum of transverse velocity fluctuation v(t) for the case of vortex breakdown incident upon stationary edge.

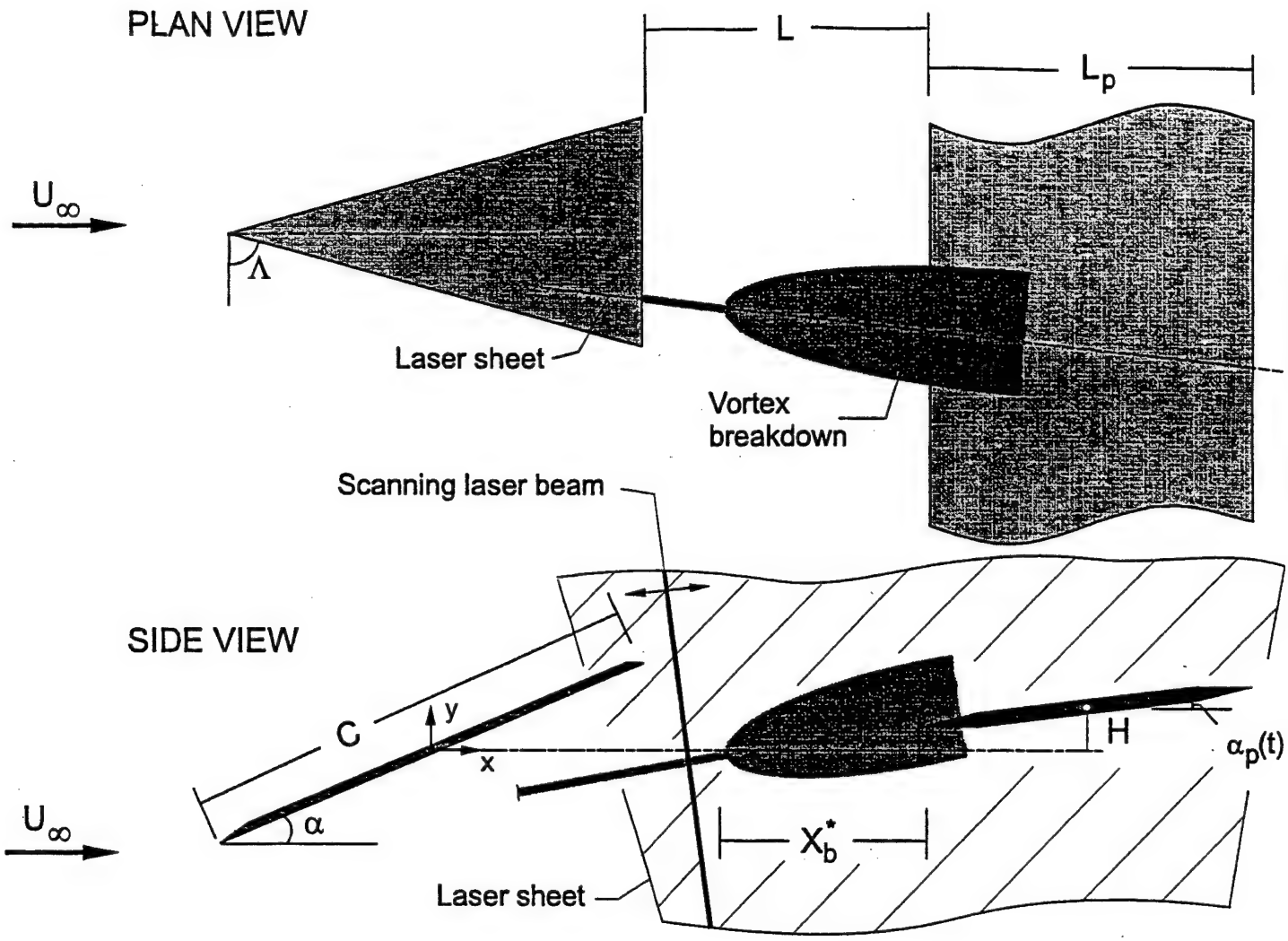

Figure 1: Plan and side views of experimental system. Delta wing is stationary and impingement plate oscillates according to $\alpha_p(t) = \bar{\alpha}_p + (\alpha_p)_o \sin\omega_e t$. Plate extends across entire span of test section.

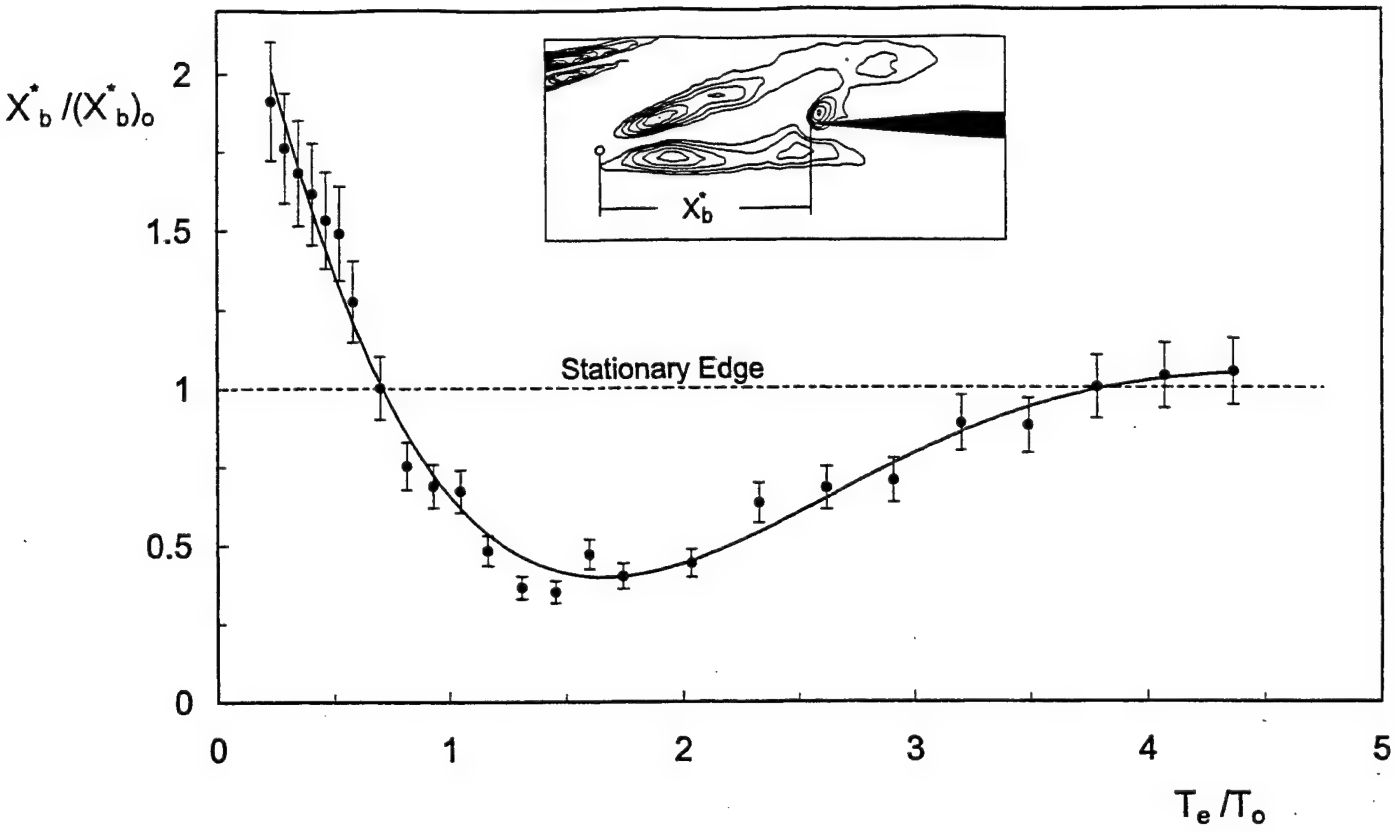

Figure 2: Plot of averaged location of onset of vortex breakdown as a function of dimensionless period of oscillation of edge of impingement plate. X^*_b represents distance upstream of tip of edge at which breakdown occurs when edge oscillates and $(X^*_b)_o$ is distance when edge is stationary. T_e is period of edge oscillation, and T_o is natural frequency of vortex breakdown. Angle of attack of delta wing is $\alpha=24^\circ$. Mean and fluctuating angle of attack of impingement plate are respectively $\bar{\alpha}_p=0^\circ$ and $(\alpha_p)_o=2.5^\circ$ according to $\alpha_p(t)=\bar{\alpha}_p+(\alpha_p)_o \sin\omega_e t$

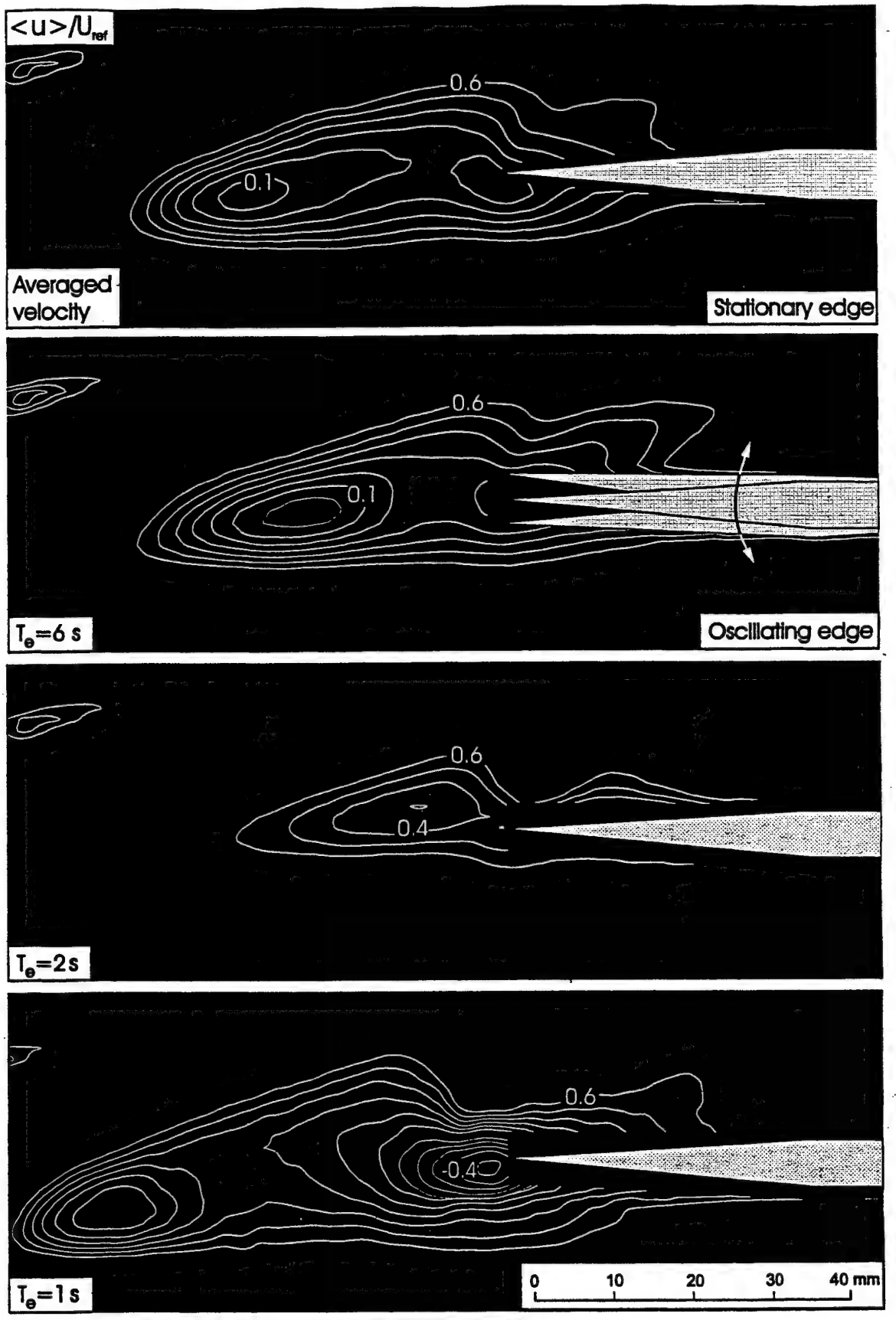

Figure 3a: Contours of constant averaged streamwise velocity $< u >$ normalized by reference velocity $U_{ref} = U_\infty$ for the case of a stationary edge and an edge oscillating at defined period T_e. Values of $T_e = 6$, 2 and 1 sec correspond to $T_e/T_o = 3.61$, 1.20, and 0.6, in which T_o is the period of the spiral mode of natural vortex breakdown. Plate is subjected to oscillations according to $\alpha_p = \bar{\alpha}_p + (\alpha_p)_o \sin\omega_e t$; $\bar{\alpha}_p = 0$ and $(\alpha_p)_o = 2.5$. Schematic shows extreme positions of oscillating edge. For all images, maximum and incremental values of average velocity $< u > / U_{ref}$ are respectively 0.6 and 0.1.

Figure 3b: Images representing contours of constant averaged vorticity $< \omega >$ for the case of the stationary edge and an edge oscillating at prescribed period T_e. Values of T_e = 6, 2 and 1 sec correspond to T_e/T_o = 3.61, 1.20, and 0.6, in which T_o is the period of the spiral mode of natural vortex breakdown. Oscillation parameters are same as for Figure 3a. For all images, the minimum and incremental values of $< \omega >$ are respectively ±2 and 0.75 sec^{-1}.

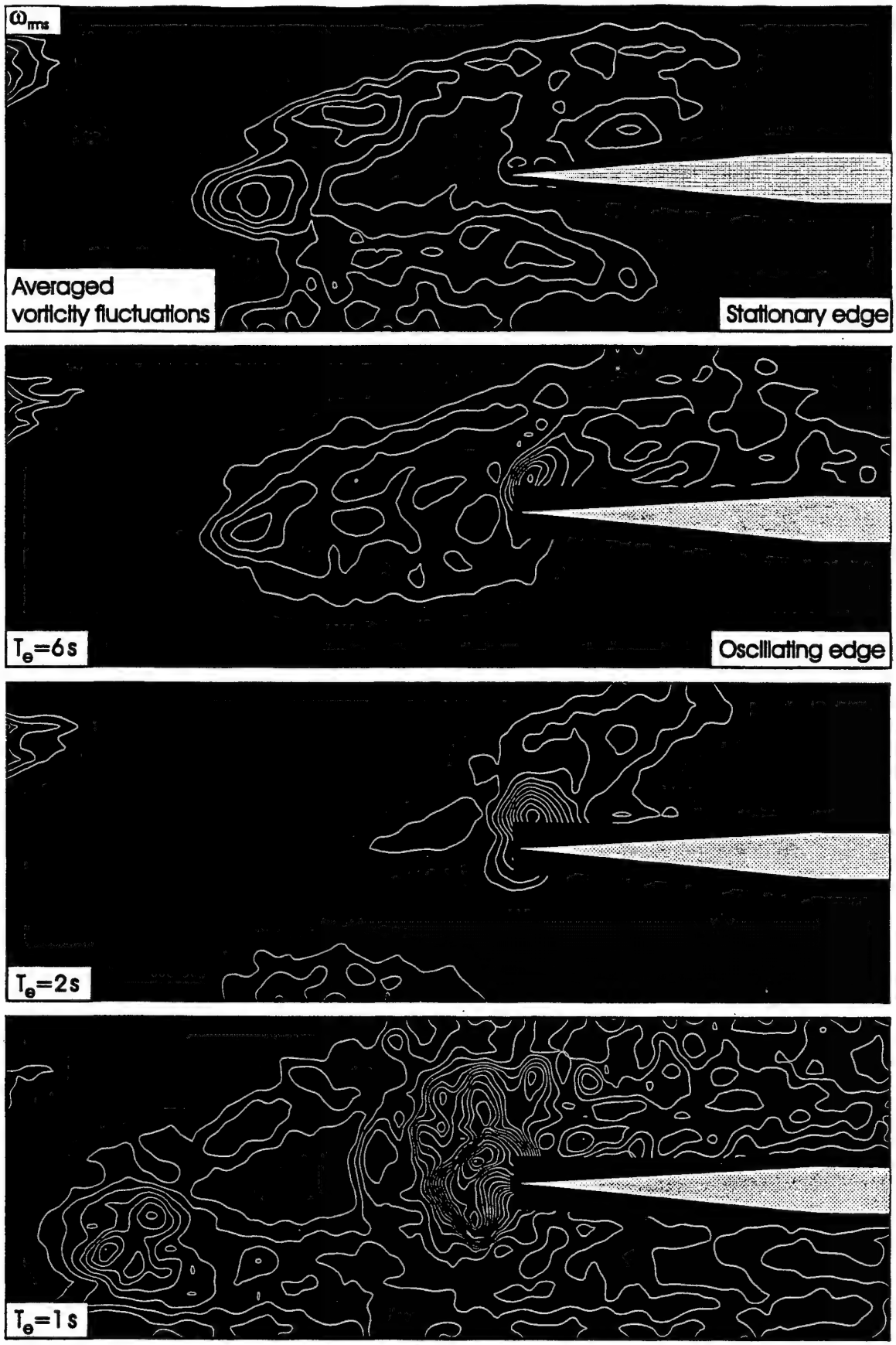

Figure 3c: Contours of constant fluctuating vorticity ω_{rms} for stationary edge and edge oscillating at prescribed period T_e. Values of T_e= 6, 2 and 1 sec correspond to T_e/T_o= 3.61, 1.20, and 0.6, in which T_o is the period of the spiral mode of natural vortex breakdown. Oscillation parameters are same as for Figure 3a. For all images, the minimum and incremental values of ω_{rms} are respectively 1.5 and 0.5 sec^{-1}.

Figure 3d: Images representing contours of constant $< u'v' >/U^2_{ref}$ for a stationary edge and an edge oscillating at prescribed values of period T_e. Values of $T_e = 6$, 2 and 1 sec correspond to $T_e/T_o = 3.61$, 1.20, and 0.6, in which T_o is the period of the spiral mode of natural vortex breakdown. Oscillation parameters are same as for Figure 3a. For all images, minimum and incremental values of $< u'v' >/U^2_{ref}$ are respectively ± 0.0025 and 0.0025.

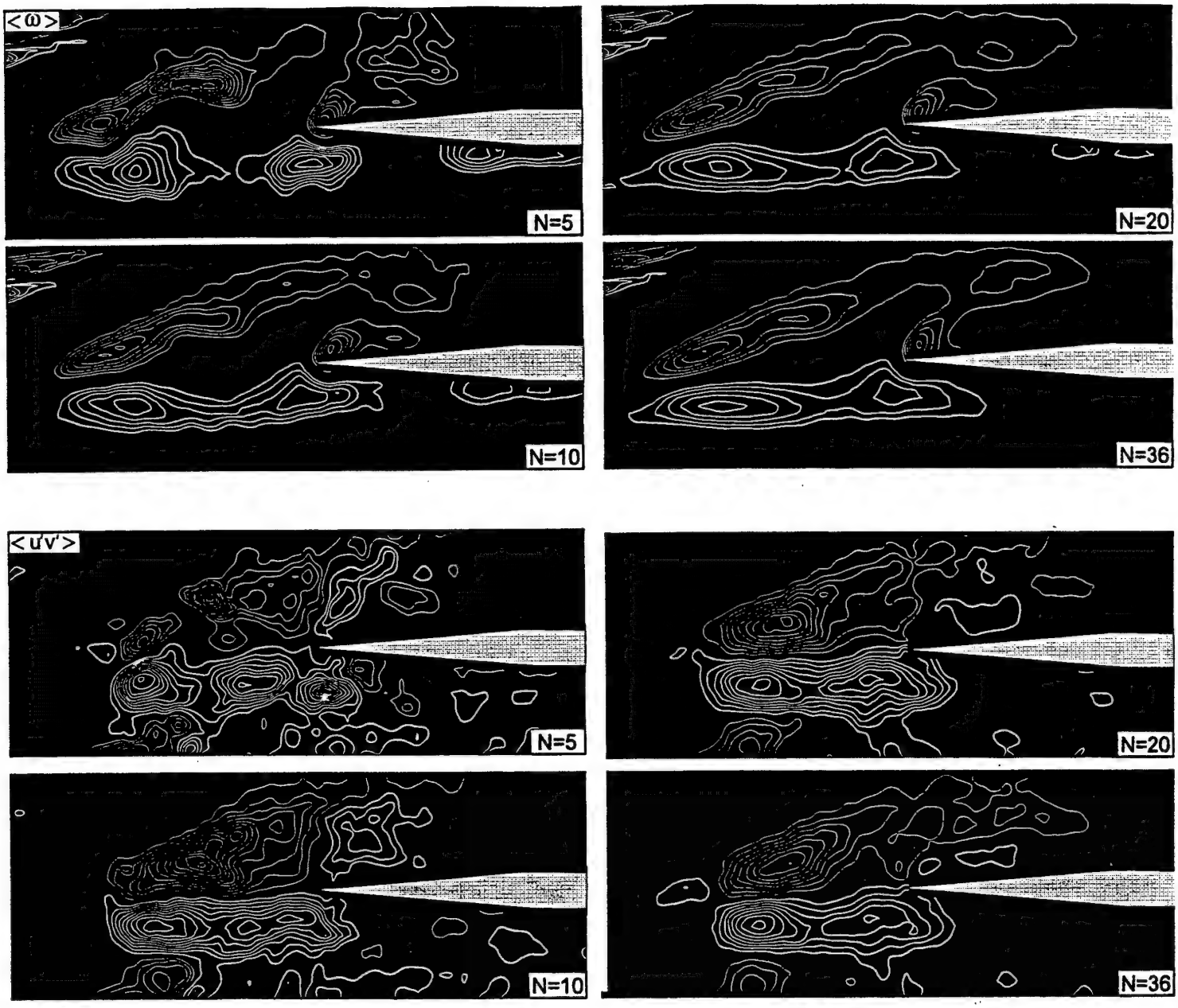

Figure 3e: Effect of number N of instantaneous images on averaged image of vorticity $<\omega>$ and velocity correlation $<u'v'>$ for the case of the stationary plate.

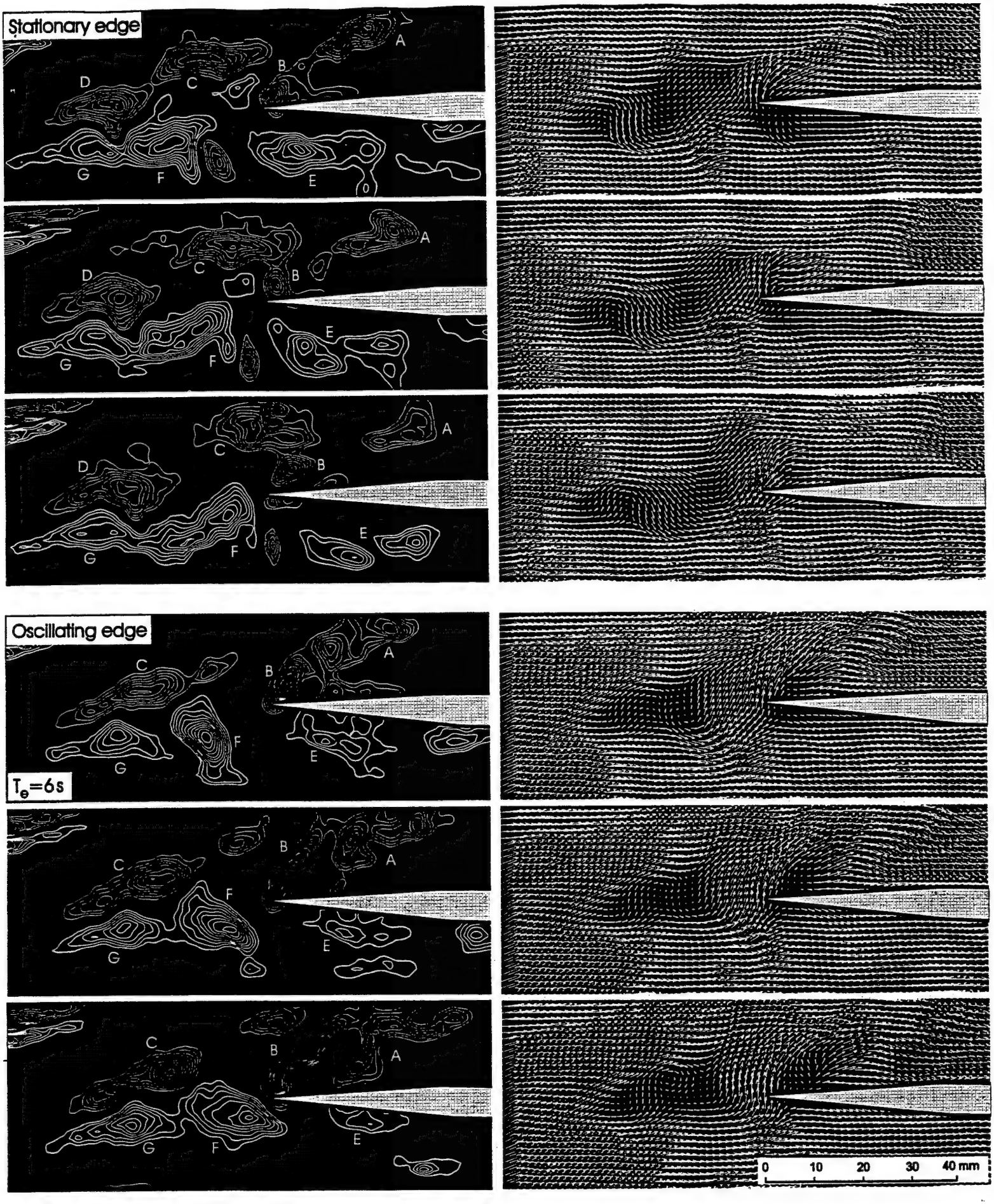

Figure 4a: Excerpts from cinema sequences showing patterns of instantaneous vorticity and distributions of velocity vectors for the case of a stationary edge and an edge oscillating at $T_e = 6$ sec. In each series, the time between images is 0.18 sec. For all images, the minimum and incremental values of instantaneous vorticity ω are respectively ± 2 and 0.75 sec^{-1}. Natural frequency of vortex breakdown is T_o=1.66 sec.

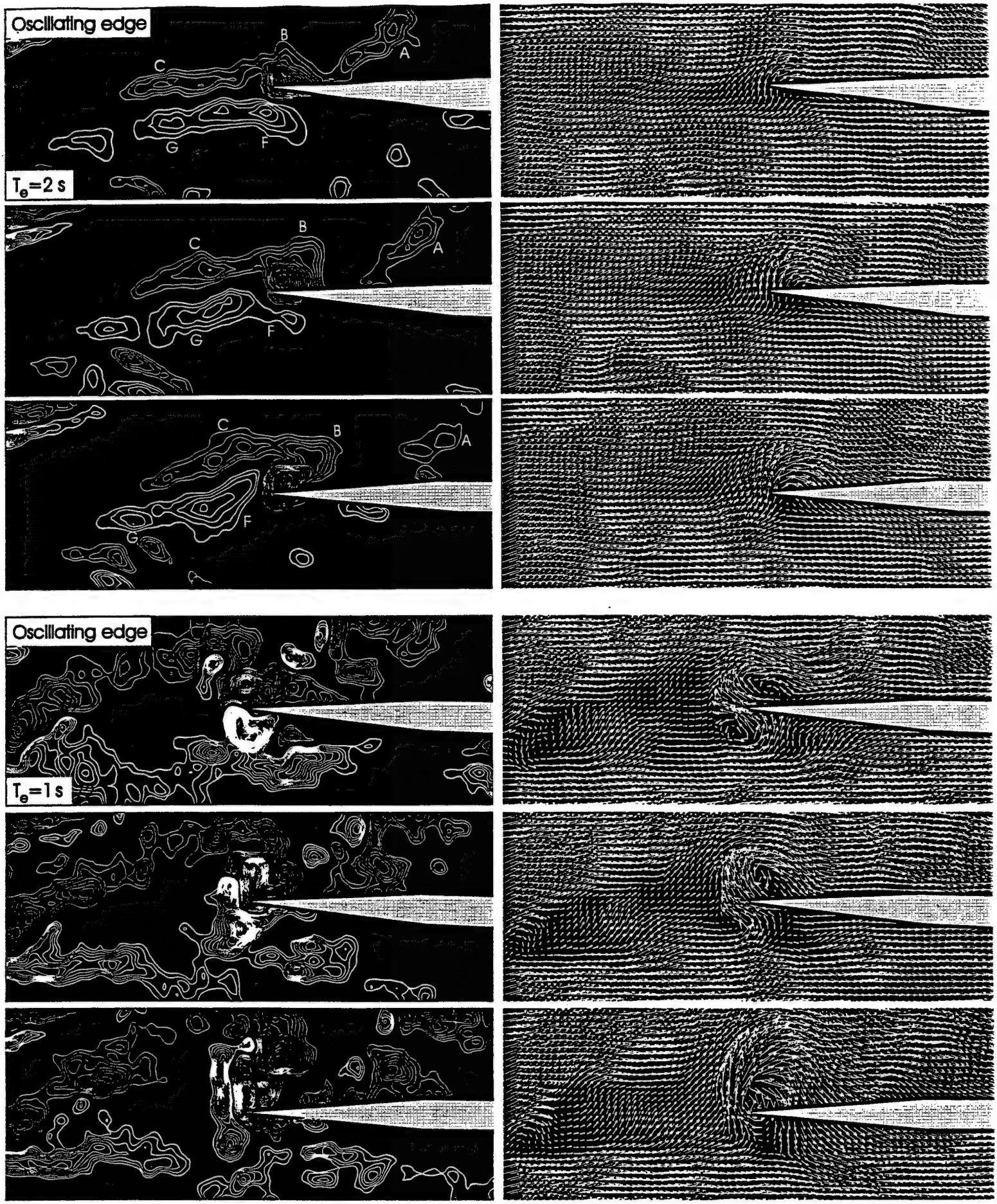

Figure 4b: Excerpts from cinema sequences showing patterns of instantaneous vorticity and distributions of velocity vectors for the case of an edge oscillating at $T_e = 2$ sec and 1 sec. For all images, the minimum and incremental values of instantaneous vorticity ω are respectively ± 2 and 0.75 sec^{-1}. Natural frequency of vortex breakdown is T_o=1.66 sec.

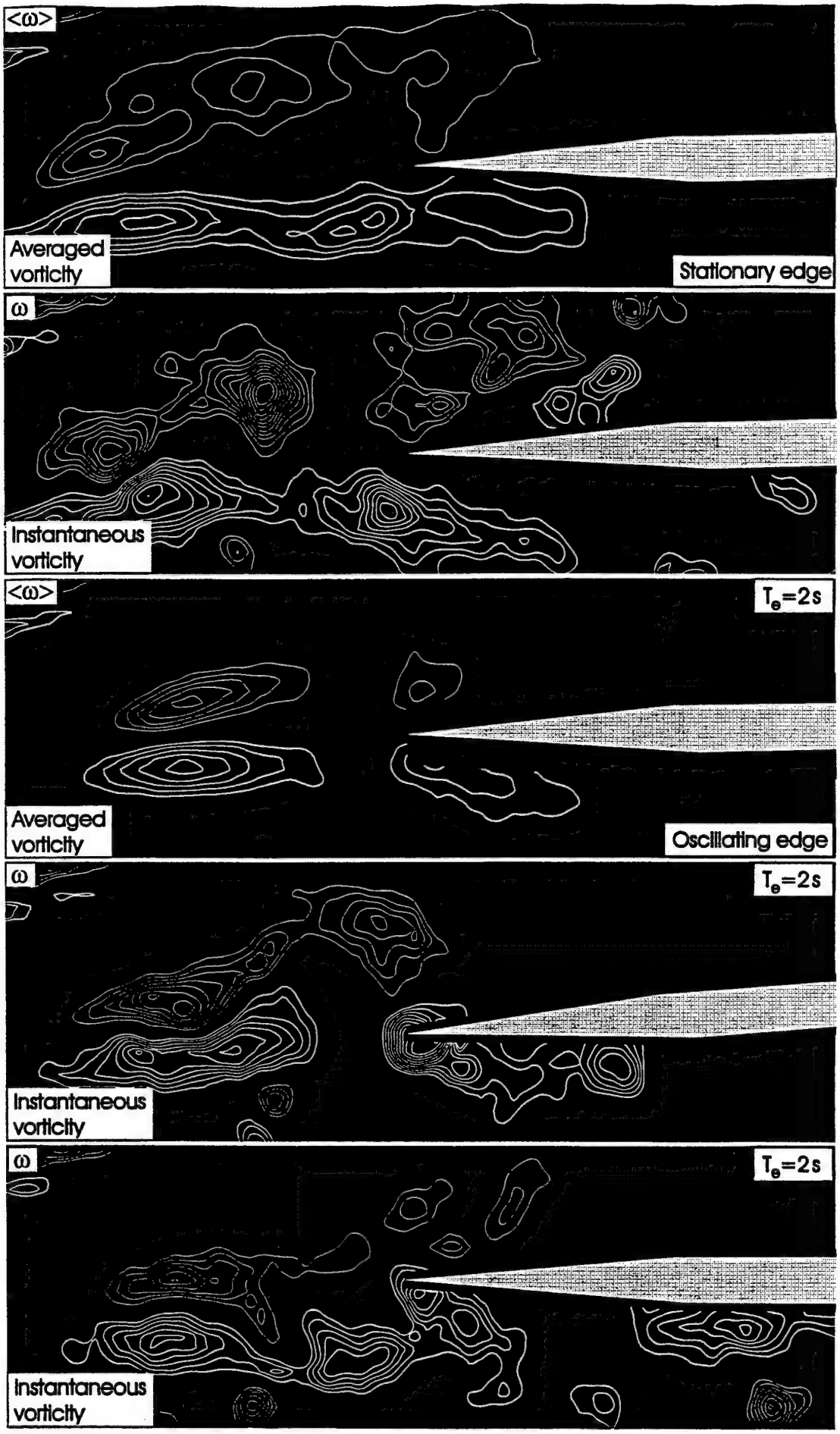

Figure 5: Patterns of averaged and instantaneous vorticity for a stationary and an oscillating leading-edge in the case where the axis of the incident vortex breakdown is aligned with the centerline of the leading-edge. For both averaged and instantaneous images, the minimum and incremental values of vorticity are respectively ±2 and 0.75 sec^{-1}.

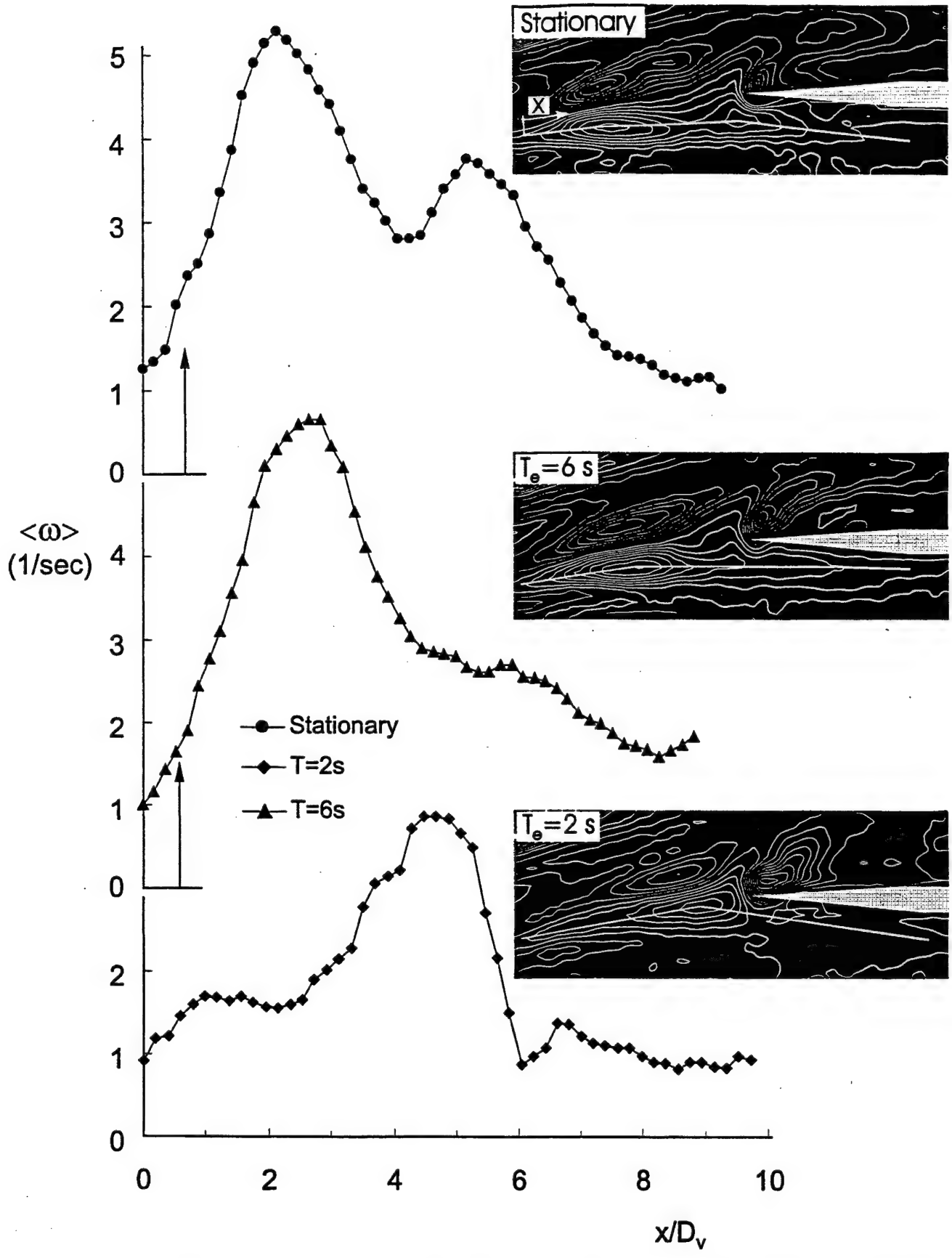

Figure 6: Variation of averaged vorticity $<\omega>$ as a function of dimensionless distance x/D_v. Values of $<\omega>$ are along the white line, corresponding to the locus of the vorticity extremum.

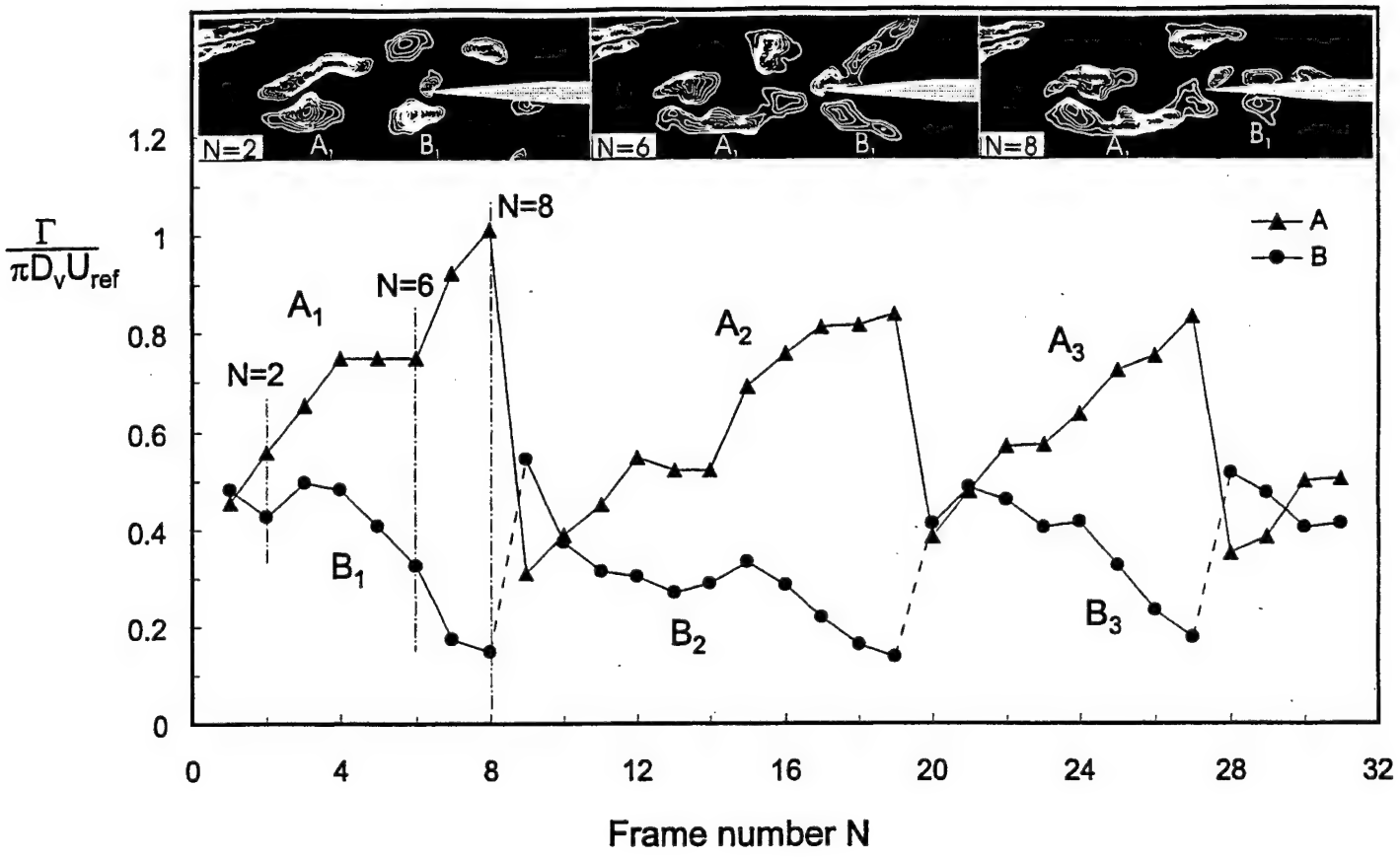

Figure 7: Variation of dimensionless circulation Γ as a function of frame number N of a cinema sequence for representative, large-scale vorticity concentrations A and B.

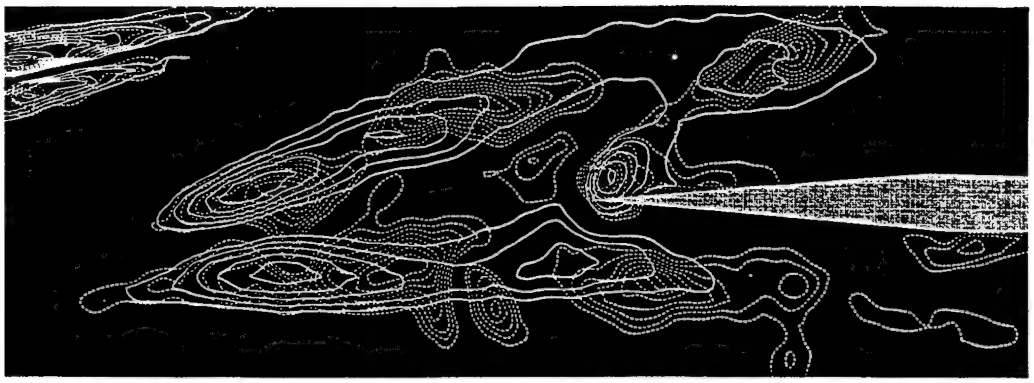

Figure 8a: Superposition of averaged (solid line) and instantaneous (dashed line) contours of constant vorticity for the case of vortex breakdown incident upon a stationary edge. Minimum and incremental values of vorticity are respectively ±2 and 0.75 sec^{-1}.

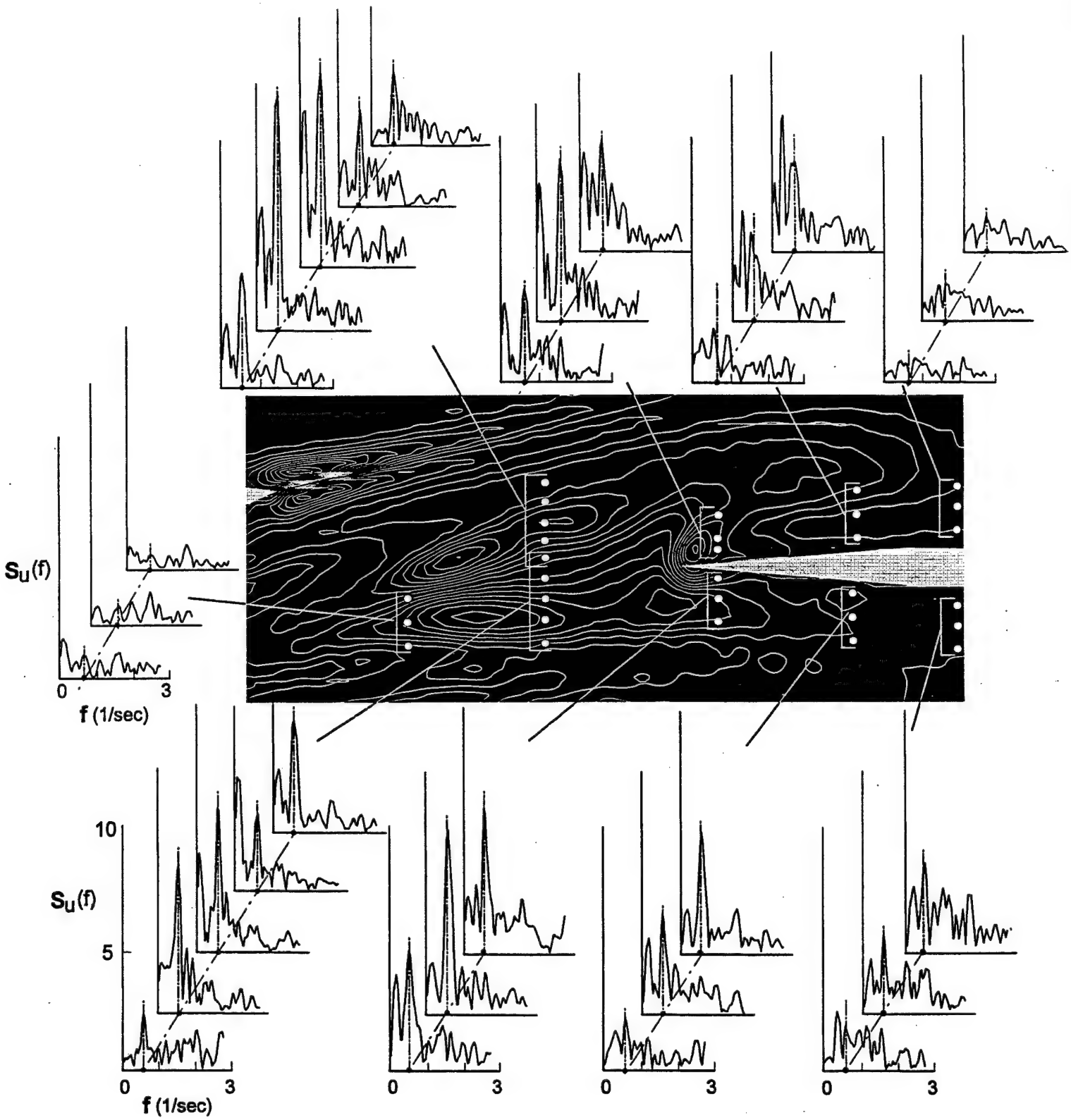

Figure 8b: Spectra $S_u(f)$ as a function of location in incident vortex breakdown and along surface of stationary edge. Image at center shows contours of constant averaged vorticity $<\omega>$ and white dots represent locations at which spectra were acquired. Frequency at which spiral mode of vortex breakdown occurs is f=0.6 cycles/sec.

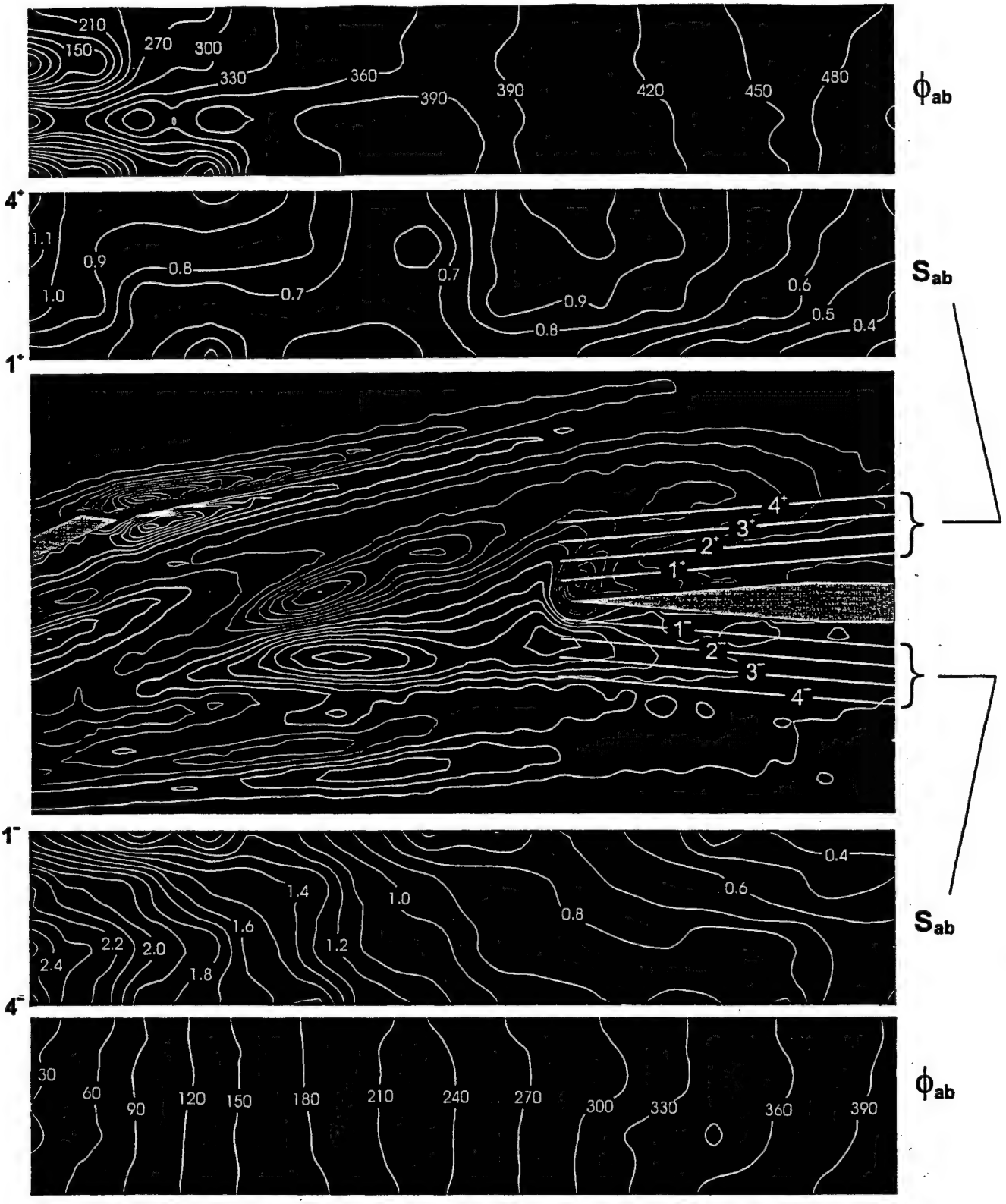

Figure 9: Representations of magnitude $S_{ab}(f)$ and phase $\phi_{ab}(f)$ of cross-spectrum of streamwise velocity fluctuation for the case of vortex breakdown incident upon a stationary edge.

APPENDIX D

Akilli-1 102000

CONTROL OF VORTEX BREAKDOWN BY A TRANSVERSELY-ORIENTED WIRE*

by

H. Akilli* and B. ahin*
Department of Mechanical Engineering
Cukurova University
Balcali 01330 Adana
Turkey

D. Rockwell
Department of Mechanical Engineering
and Mechanics
354 Packard Laboratory
19 Memorial Drive West
Lehigh University, Bethlehem, PA 18015

* On leave at Department of Mechanical Engineering and Mechanics, Lehigh University

ABSTRACT

A small wire oriented orthogonally to the axis of the leading-edge vortex on a delta wing at high angle-of-attack generates substantial changes in the vortex structure, which is characterized using a technique of high-image-density particle image velocimetry. A wire having a diameter two orders of magnitude smaller than the diameter of the leading-edge vortex prior to the onset of vortex breakdown can substantially advance the onset of breakdown by as much as fifteen vortex diameters. Depending upon the dimensionless diameter of the wire and wire location along the axis of the vortex, the onset of vortex breakdown can occur either upstream or downstream of the wire. Contours of constant velocity indicate that the rate of decrease of streamwise velocity along the centerline of the vortex is substantially enhanced, even for locations well upstream of the wire, relative to the case of vortex breakdown in absence of a wire. Patterns of instantaneous vorticity in presence of the wire typically exhibit a form characteristic of either a spiral- or bubble-like mode of breakdown that occurs in absence of the wire.

***Akilli, H., Sahin, B. and Rockwell, D. 2001 "Control of Vortex Breakdown by a Transversely-Oriented Wire", *Physics of Fluids*, Vol. 13, No. 2, pp. 452.263.**

I. INTRODUCTION

Breakdown of the leading-edge vortices from a delta wing has been a phenomenon of long-standing importance, and has received considerable attention over the past four decades. The occurrence of vortex breakdown as a function of geometry and angle-of-attack on a delta wing has been addressed by Lambourne and Bryer[1], Lowson[2], Wentz and Kohlman[3] and others. An overview of the averaged location of vortex breakdown in relation to geometrical parameters of the delta wing, in the context of previous investigations, is provided by Lowson and Riley[4]. Of course, the unsteady features of vortex breakdown have important implications for buffeting phenomena, as recognized early on by Earnshaw and Lawford[5], Mabey[6] and a variety of other investigations described by Gursul and Xie[7]. In the event that the delta wing undergoes unsteady motion, the nature of the vortex breakdown is altered. The most predominant feature is a phase shift between the motion of the wing and the onset of breakdown, as shown by Wolffelt[8], Gilliam *et al.*[9], Reynolds and Abtahi[10], Hudson *et al.*[11], Thompson[12], Magness *et al.*[13], Atta and Rockwell[14], LeMay *et al.*[15], Jarrah[16], Ashley *et al.*[17], and Rockwell[18]; all of the foregoing investigations have been for pitching motion. Analogous types of phase shift of breakdown occur for rolling motion of the wing as shown by Hanff and Huang[19], Ng *et al.*[20] and Cipolla *et al.*[21].

Conceptual features of the complex nature of vortex breakdown, interpreted in the context of experiments, theory and numerical simulations are provided by the reviews and assessments of Sarpkaya[22,23,24], Hall[25], Liebovich[26,27], Escudier[28], Brown and Lopez[29], Lopez and Perry[30], Delery[31] and Wang and Rusak[32].

From an experimental standpoint, recent efforts have addressed the global, instantaneous features of vortex breakdown. Towfighi and Rockwell[33] and Lin and Rockwell[34] show that an essential feature of vortex breakdown on a stationary delta wing and a wing in unsteady motion was a switch in sign of the azimuthal vorticity; this concept was first advanced in the theoretical model of Brown and Lopez[29].

Control of the location of the onset of vortex breakdown, either on stationary wings or wings in unsteady motion, has received less attention. Rockwell[18] provides an overview of approaches to controlling breakdown using concepts such as steady and unsteady leading-edge blowing and deployment of flaps. More recent efforts have

focused on blowing from the trailing-edge of the delta wing as described by Helin and Watry[35], Ding and Shih[36] and Vorobieff and Rockwell[37,38].

Very little attention has been devoted to passive control techniques for altering the onset of vortex breakdown. A possibility involves insertion of a body within the vortex core. The promise of such an approach is foretold by an observation of Reynolds and Abtahi[10]; they altered the onset of vortex breakdown by insertion of a probe in the vortex from a delta wing. Moreover, Gursul and Yang[39] observed that deployment of a relatively large control cylinder, having a diameter of approximately 5% of the wing chord, could cause premature breakdown of a leading-edge vortex. A particularly intriguing issue, and one that has substantial practical importance, is whether relatively small obstacles can substantially alter the onset of breakdown. The objective of this investigation is to examine the consequence of deployment of a very small wire oriented transverse to the axis of the vortex. Global patterns of vorticity and velocity are employed to characterize the changes of location and structure breakdown.

II. EXPERIMENTAL SYSTEMS AND TECHNIQUE

Experiments were performed in a large-scale, free-surface water channel having a cross-section of 927 mm × 610 mm. During the course of all experiments, the water was maintained at a height of 559 mm. The delta wing was mounted at mid-depth of the water channel. A general schematic of the wing arrangement is given in Figure 1. It had a sweep angle of $\Lambda = 75°$, a chord of C = 222 mm and a thickness of 3.2 mm. The leading-edge of the wing was beveled at 34° on the windward side. For the present experiment, the angles-of-attack were $\alpha = 25°$ and 30°. The free-stream velocity was 48 mm/sec, giving a value of Reynolds number $Re = 1.0 \times 10^4$.

A small diameter wire was located at a prescribed location along the axis of the leading-edge vortex. As indicated in Figure 1, the orientation of the wire was orthogonal to the vortex axis. It was supported by two vertical rods, each having a diameter of 9 mm. The distance L between these supports was 485 mm; it was sufficiently large compared to the span S of the trailing-edge of the wing, such that the wakes from these wire supports did not influence the flow development on the delta wing. The entire arrangement of the wire support and the transverse wire could be traversed to an arbitrary

location, thereby allowing placement of the wire at any location along the axis of the vortex. For the present experiment, the wire was traversed over the range of $0.2 \leq X_w/C \leq 1.2$ at seventeen different stations. The wire was of plastic material and had a diameter $D_w = 0.14$ mm, 0.5 mm and 0.8 mm. Using the diameter $D_v = 7$ mm as the normalizing length scale, the dimensionless wire diameter takes values $D_w/D_v = 0.02$, 0.07 and 0.11. The diameters D_w and D_v are indicated in the schematic of Figure 1. In addition, D_v is shown in the representative image at the bottom of Figure 1; it is the distance between extrema of azimuthal vorticity prior to the onset of vortex breakdown. The reference value of diameter D_v, which is employed for all normalization herein, is defined at the location 0.6 C for $\alpha = 30°$.

During experiments, a consistent procedure was followed in order to carefully assess the effect of wire insertion on the onset of vortex breakdown. First of all, as a reference case, the yaw angle of the wing was carefully adjusted over small intervals, within 1°, in order to achieve vortex breakdown at essentially the same streamwise location on either side of the delta wing; this symmetry of the vortex breakdown was attainable within an uncertainty of 5mm. When the wire was inserted, it tended to promote symmetry of the vortex breakdown position on either side of the delta wing.

In order to quantitatively characterize the effect of wire insertion at the onset of vortex breakdown, a laser-scanning version of high-image-density particle image velocimetry was employed (Rockwell *et al.*[40]). For this approach, the laser illumination involved generation of a vertical scanning laser sheet by, first of all, transmitting the laser beam through a system of steering and focusing optics, then onto a polygonal rotating mirror having eight facets. The mirror rotated at a frequency of 15.6 Hz, thereby providing an effective scanning frequency of 125 Hz. The flow was seeded with metallic-coated hollow plastic spheres having a characteristic diameter of 14 microns. Images could be acquired with laser power illuminations as low as a few watts; in the present experiments, however, a laser output of 15 watts was employed.

Particle images were photographed using a Canon EOS-1 camera, which was motor-driven. The shutter speed was 1/25 sec and the f-stop was f = 4.5. The magnification M of the camera lens was M = 1:4.6. In order to preclude issues associated with directional ambiguity, a rotating bias mirror was placed in front of the camera lens at an angle of 45° to its optical axis. High-resolution 35 mm film (300 lines millimeter)

allowed adequately resolved particle images. The 35 mm negatives were digitized using a Nikon digitizer at a resolution of 125 pixels/mm. A single-frame cross-correlation technique was employed in order to evaluate the patterns of particle images, thereby yielding the velocity field. An interrogation window of 90 × 90 pixels was employed in order to satisfy the Nyquist sampling criterion and an overlap ratio of 50% was employed. Approximately 40 to 60 particle images were located within this window, in order to satisfy the high-image-density criterion. The effective grid size on the film was 0.36 × 0.36 mm. Taking the magnification factor M into account, the actual grid size in the physical plane of the laser sheet was 1.67 mm × 1.67 mm. The overall field of view in the plane of the laser sheet was 100 mm × 155 mm.

III. OVERVIEW OF RESPONSE OF ONSET OF VORTEX BREAKDOWN TO INSERTION OF WIRE

Figure 2 shows the change in location of onset of vortex breakdown ΔX^* as a function of wire location X_w downstream of the apex of the wing. This parameter ΔX^*, which represents the displacement of the onset of vortex breakdown is, in essence, the difference between the location of vortex breakdown in absence of the wire relative to that with the wire present, as indicated in a schematic at the upper right of Figure 2. The diameter of the vortex D_v prior to the onset of vortex breakdown, as well as the wing chord C, are employed as normalizing parameters. For the smallest wire diameter $D_w/D_v = 0.02$, it is possible to attain a maximum displacement of the onset of breakdown of $\Delta X^*/D_v = 15$. For the largest wire diameter $D_w/D_v = 0.11$, the maximum value is $\Delta X^*/D_v = 23$. Irrespective of the wire diameter, when the location of the wire X_w is moved downstream of the apex, the displacement of breakdown $\Delta X^*/D_v$ continuously increases until a maximum, limiting value is attained in the range $0.5 \leq X_w/C \leq 0.7$. Further increases in wire location X_w yield a decrease in the value of $\Delta X^*/D_v$.

At relatively small values of X_w/C in Figure 2, corresponding to a wire location near the apex of the wing, relatively large changes of $\Delta X^*/D_v$ are attainable for small changes of wire location $\Delta X_w/C$. This slope is defined as $G = [\Delta X^*/D_v]/[\Delta X_w/C]$. Moreover, it is evident that, at least for the two smallest wires $D_w/D_v = 0.02$ and 0.07, relatively high values of negative G are also attainable at large X_w/C. In fact, G has its

maximum-negative value at a location $X_w/C = 1.0$, corresponding to the trailing-edge of the wing. It is known that naturally-occurring vortex breakdown, in absence of a wire, is highly sensitive to the sudden change in boundary conditions imposed at the trailing-edge of the wing (Cipolla and Rockwell[41]), so attempts to passively control the breakdown location via the small wire appear to be enhanced by the sudden change in conditions of the trailing-edge. On the other hand, the large value of G observed at small values near the apex of the wing, i.e., at small values of X_w/C is most likely due to a different mechanism that involves low values of the swirl ratio Ω of the vortex, is, in essence, the ratio of the characteristic circumferential velocity to axial velocity.

Figure 3 shows the location of the onset of vortex breakdown relative to the location of the wire, i.e., ΔX_b. It is given as a function of distance of the wire X_w from the apex of the wing. Vortex diameter D_v and wing chord C are employed as normalizing parameters. Irrespective of the wire diameter D_w/D_v, the value of ΔX_b rapidly decreases as the location of the wire X_w is moved downstream of the apex of the wing until, at a given value of X_w, the onset of vortex breakdown is coincident with the location of the wire, corresponding to $\Delta X_b = 0$. At larger values of X_w, relatively mild changes in ΔX_b are observed. For the two largest wire diameters, $D_w/D_v = 0.07$ and 0.11, the negative values of ΔX_b observed at larger values of X_w/C signify that the wire is actually located downstream of the onset of vortex breakdown, i.e., within the breakdown bubble. Furthermore, taking an overview of the plots exhibited in Figure 3, it is evident that the maximum slope $[\Delta X_b/D_v]/[\Delta X_w/D_v]$ is large for values of $\Delta X_b/D_v > 0$. In essence, this means that large changes of $\Delta X_b/D_v$ are attainable only as long as the onset of breakdown occurs downstream of the wire location.

IV. GLOBAL CHARACTERIZATION OF LOCALIZED DEPLOYMENT OF SMALL WIRE

Figure 4a shows the consequence of the smallest wire of dimensionless diameter $D_w/D_v = 0.02$, in which D_w and D_v are respectively the diameters of the wire and the vortex prior to the onset of vortex breakdown. The patterns of instantaneous positive (thick line) and negative (thin line) vorticity of Figure 4a represent the azimuthal component of vorticity.

Herein, vortex breakdown is taken to occur at the location where the azimuthal vorticity changes sign. Referring to the top image of Figure 4a, it occurs at the location indicated by the circular symbol. Upstream of this location, positive (thick line) vorticity occurs in the upper region of the image, while negative (thin line) vorticity occurs in the bottom region. Downstream of the circular symbol representing the onset of vortex breakdown (vb), positive vorticity occurs in the lower part of the image and negative vorticity in the upper part. This switch in sign of vorticity is more clearly evident in the other images shown in Figure 4a. The origin of this criterion is the theory of Brown and Lopez[29]. It was confirmed using PIV imaging in the investigation of Towfighi and Rockwell[33]. As will be illustrated subsequently, this approximate criterion also corresponds to the onset of a rapid decrease of the streamwise velocity at the leading-edge of the wake-like breakdown bubble. It should be noted that the location of vortex breakdown in absence of a wire, represented by the top image of Figure 4a, is downstream of the trailing-edge of the wing, i.e., $X_{vb}/C = 1.2$. As shown in the second image, when the wire is inserted at a location corresponding to the trailing-edge of the wing, $X_w/C = 1.0$, the onset of vortex breakdown (vb) occurs at the location of the wire. If the wire is successively moved upstream to locations $X_w/C = 0.8$ and 0.6, shown in the bottom two images of Figure 4a, the onset of vortex breakdown occurs at an increasing distance downstream of the wire. This trend is, in fact, shown in the overview plot of Figure 2. For all cases shown in Figure 4a, the patterns of positive and negative vorticity concentrations exhibit an alternating wake-like form analogous to patterns of Kármán vortices shed from a two-dimensional cylinder. In fact, the vorticity concentrations are sectional cuts through the spiral mode of the three-dimensional instability associated with vortex breakdown. Moreover, it should be noted that this pattern of vorticity concentrations is very similar to that occurring in absence of a wire. This observation suggests that the presence of a wire does not generate vorticity of significantly large scale to alter the pattern of vorticity associated with the inherent vortex breakdown process.

Figure 4b shows averaged contours of constant velocity component $< V >$, based on five instantaneous images. Since the deviations of the instantaneous velocity contours from image to image are not substantial, the consequence of limited averaging is simply to smooth out small-scale irregularities of the velocity field. For all images, the aforementioned onset of vortex breakdown (vb), defined on the basis of vorticity, occurs

at the onset of a particularly rapid decrease in the magnitude of $< V >$ along the centerline of the vortex, i.e., at the leading-edge of the wake-like separation bubble. The traditionally defined location of breakdown is designated as vb^*; it corresponds to a stagnation point. An interesting consequence of insertion of the wire is substantially closer spacing of the contours of constant $< V >$ at locations upstream of the wire. That is, the magnitude of $< V >$ decreases much more rapidly along the centerline of the vortex when the wire is present, relative to the case of no wire. In fact, this effect extends well upstream of the wire location.

Figure 5a shows patterns of instantaneous vorticity for the case of a larger wire, represented by $D_w/D_v = 0.11$. In this case, the onset of vortex breakdown (vb) actually occurs upstream of the wire. Remarkable is the fact that the wire location is within the breakdown bubble, evident from images corresponding to $X_w/C = 0.8$ and 1.0. The location of the wire and the initial region of the breakdown bubble are not evident in the image corresponding to $X_w/C = 0.4$, since they lie to the left of the field of view of the image. It is interesting, however, to note that the wake-like region downstream of the onset of vortex breakdown remains relatively narrow for a substantial distance at $X_w/C = 0.4$. In fact, if one defines this diameter as the transverse distance between extrema of positive and negative vorticity, it has a smaller value than the value of characteristic vortex diameter D_v prior to the onset of vortex breakdown in the top three images of Figure 5a. Finally, it should be pointed out that presence of this larger diameter wire can induce a bubble-like, as opposed to a spiral-like, instability of the initial region of vortex breakdown, as evident in the image at $X_w/C = 0.8$.

The corresponding patterns of averaged velocity $< V >$ are portrayed in Figure 5b. For the case of no wire, represented by the top image, the decay of $< V >$ along the centerline of the vortex is relatively mild. On the other hand, when the wire is present, it is evident from images at $X_w/C = 0.8$ and 1.0 that relatively rapid decrease of $< V >$ along the centerline occurs at locations upstream of the onset of vortex breakdown (vb). In the limiting case, where vortex breakdown occurs outside the field of view, corresponding to the bottom image at $X_w/C = 0.4$ in Figure 5b, the pattern of contours of $< V >$ takes on a fundamentally different form and the occurrence of the region of very low velocity within the breakdown bubble actually is further downstream than that for the wire at $X_w/C = 0.8$. A particularly remarkable observation concerns the location of the

wire relative to the region of very low velocity within the breakdown bubble. As is evident in the images at $X_w/C = 0.8$ or 1.0, the equilibrium position of the breakdown bubble has adjusted itself such that wire is coincident with a region of very low, or even negative velocity $< V >$.

A comparison of the effect of dimensionless wire diameter D_w/D_v is shown in Figure 6a. The images in the left column correspond to angle-of-attack $\alpha = 30°$ and those in the right column to $\alpha = 25°$. Moreover, for the left column of images, the wire is located immediately downstream of the trailing-edge, corresponding to $X_w/C = 1.2$, whereas in the right column it is located at the trailing-edge, $X_w/C = 1.0$. Considering first the images in the left column, it is evident that an increase in wire diameter moves the onset of vortex breakdown upstream. As a consequence, the wire location, which, in fact, is fixed at a given geometrical position, becomes, in a relative sense, embedded further within the breakdown bubble. For the smaller angle-of-attack, indicated by the images in the right column taken at a relatively low angle-of-attack $\alpha = 25°$, this effect is less dramatic, but nevertheless discernible.

Figure 6b shows corresponding patterns of velocity $< V >$. As already suggested by previous image layouts, the insertion of the wire and the consequent earlier onset of vortex breakdown (vb) results in a more rapid decrease of the $< V >$ along the vortex centerline. In addition, even when the wire is located well within the breakdown bubble in a region of low or centrally zero velocity, it produces severe modification of the velocity field relative to the case of no wire present.

Figure 7a shows the consequence of variations in wire diameter D_w/D_v for the case of relatively low angle-of-attack $\alpha = 25°$ of the delta wing. In contrast to the previous sets of images at higher angle-of-attack α, irrespective of the value of D_w/D_v, the onset of vortex breakdown (vb) always occurs downstream of the wire. For the case of the smallest wire $D_w/D_b = 0.02$, a remarkably large distance exists between the wire location and the onset of breakdown (vb). Further increases in D_w/D_v bring the onset of vortex breakdown (vb) further upstream until it nearly coincides with the wire location. A further interesting observation is the relatively small diameter of the so-called breakdown bubble at this low angle-of-attack. As is particularly evident in the bottom image corresponding to $D_w/D_v = 0.11$, the transverse distance between vorticity layers is

remarkably narrow and extends for a substantial distance downstream from the onset of vortex breakdown. From this pattern of the vorticity layers, it is not possible to assert that a well-defined spiral mode of vortex breakdown occurs, at least over the initial region of the breakdown bubble.

The contours of constant $< V >$, exhibited in Figure 7b, further attest to the unusual nature of these induced breakdown patterns, relative to their counterparts occurring at high angle-of-attack and described in the foregoing. For the smallest diameter wire $D_w/D_v = 0.02$, the decay of the magnitude of $< V >$ upstream of the onset of vortex breakdown is still relatively mild and of the same general form as for the case of no wire, represented by the top image. On the other hand, when the wire diameter reaches a sufficiently large value $D_w/D_v = 0.11$, indicated in the bottom image of Figure 7b, the decay of $< V >$ upstream of vortex breakdown is indeed more rapid.

CONCLUDING REMARKS

The onset of breakdown of the vortices from the leading-edge of a delta wing can be substantially altered by insertion of a wire oriented orthogonally to the axis of the vortex. Even when the wire has a diameter two orders of magnitude smaller than the characteristic diameter of the leading-edge vortex prior to the onset of vortex breakdown, substantial changes can be effected. These alterations of vortex breakdown have been quantitatively assessed using a technique of high-image-density particle image velocimetry, which provides interpretation of the vortex structure using patterns of vorticity and velocity contours.

In an overall sense, it is demonstrated that the effectiveness of a wire of given diameter is a strong function of the location of the wire along the axis of the vortex. Relatively large changes of onset of vortex breakdown are attainable in two principal regions. The first region is immediately downstream of the apex of the wing, where the ratio of the characteristic azimuthal to axial velocity of the vortex is relatively small. The other principal region of high sensitivity corresponds to the location of the wire at or near the trailing-edge of the wing, except for relatively large wire diameter; in this region, the vortex is subjected to a sudden change in boundary conditions.

Moreover, the location of the onset of vortex breakdown can occur either upstream or downstream of the wire. When the position of the wire is moved downstream of the apex, the distance between the wire and the onset of vortex breakdown rapidly decreases until a limiting value is attained, such that the breakdown position is coincident with the wire location. Further increase in displacement of the wire from the apex produces onset of vortex breakdown upstream of the wire, provided the wire diameter is sufficiently large. Remarkably, even when the wire is located downstream of the onset of vortex breakdown and well within the breakdown bubble where the local velocity is small, it can still induce a significant change in the location of vortex breakdown relative to the case of no wire.

A still further observation concerns patterns of contours of constant velocity. They show that presence of the wire induces a substantially more rapid decay of the centerline velocity at locations upstream of vortex breakdown, relative to the case of no wire. That is, two effects occur simultaneously: the onset of vortex breakdown moves upstream and the rate of decay of the centerline velocity well upstream of breakdown increases. In fact, this alteration is evident at locations well upstream of the wire.

The overall form of the wire-induced vortex breakdown is significantly different when the angle-of-attack of the wing is sufficiently small, i.e., $\alpha = 25°$. That is, the patterns of vorticity and velocity exhibit distinctive forms, relative to those occurring at sufficiently large angle-of-attack, $\alpha = 30°$, for which the breakdown patterns take on more conventional forms. When breakdown is induced at $\alpha = 25°$, the characteristic diameter of the breakdown bubble is relatively small, and the distance between the wire location and the onset of vortex breakdown is relatively large.

It is well known that the two predominant modes of vortex breakdown at high angle-of-attack, and in absence of a wire, are the spiral and bubble modes. For the range of parameters in the present investigation, the spiral mode was generally predominant. The issue arises as to how the presence of the wire influences the existence of the spiral mode, and whether a bubble mode is attainable. For the instantaneous patterns of vorticity provided herein, occurrence of a spiral mode corresponds to an alternating pattern of positive and negative azimuthal vorticity concentrations immediately following the onset of vortex breakdown. Generally speaking, most images taken in presence of the wire exhibit a pattern of vorticity concentrations having alternating sign, thereby

indicating presence of the spiral mode. Representative examples are shown in the bottom two images of Figure 4a. On the other hand, for certain wire diameters and locations, it is possible to occasionally observe a pattern of vorticity corresponding to a bubble mode of vortex breakdown, as exhibited, for example, in the bottom right image of Figure 6a. In this case, the concentrations of vorticity are essentially symmetrical with respect to the centerline of the vortex. Finally, it should be noted that hybrid patterns of vorticity, involving a mixture of the purely spiral and bubble mode patterns could be detected. Such patterns involve, immediately after the onset of vortex breakdown, symmetrical concentrations of vorticity about the centerline, which rapidly degenerate to an asymmetrical, alternating pattern of vorticity. Such a pattern might be termed a mixed-mode, in that it embodies the feature of a bubble type breakdown in the initial region, followed by a spiral mode. An example of this mixed mode is shown in the second image of Figure 4a.

Examination of the patterns of instantaneous vorticity provided herein shows no indication of localized, small-scale concentrations of vorticity shed from the wire, at least within the limits of the spatial resolution of the imaging technique. In fact, as described in the preceding paragraph, the patterns of vorticity are suggestive of a spiral mode, bubble mode, or a mixture of these two modes. In other words, the overall patterns of vorticity concentrations are, for the most part, similar to those observed in vortex breakdown from wings having various geometrical parameters and angles-of-attack. Although the presence of the wire may influence the predisposition towards one particular mode, the basic, recognizable features of the initial region of vortex breakdown seem to be generally preserved. These observations suggest a mechanism(s) involving upstream influence from the wire and/or its steady wake. Leibovich[27] reviews a variety of theoretical concepts for occurrence of vortex breakdown, among them a criticality criterion. In the context of the works of Squire[42] and Benjamin[43], he emphasizes the importance of considering the evolving vortex core, rather than a core of the columnar type; the evolving core allows disturbances to spread upstream of a source located in the downstream region of the flow. A downstream disturbance can generate waves, the longest of which moves most rapidly, and potentially can make it up to the critical location. Furthermore, the theoretical assessment of Wang and Rusak[32], including their previous works cited therein, along with the study of Rusak *et al.*[44], provide a basis for

describing upstream influence. In essence, for a suitable range of swirl ratio of the vortex, disturbances can propagate upstream, and are eventually manifested in the form of a stable state of vortex breakdown. These interpretations deserve further consideration, in the context of the present observations. In doing so, it should be kept in mind that the images exhibited herein represent the equilibrium position of the onset of vortex breakdown relative to the location of the wire, i.e., attainment of a steady state condition. It would be desirable, in further experiments, to employ a technique that allows abrupt insertion of the wire at a given location in the vortex, and to observe the transient response leading to the eventual state of stationary vortex breakdown.

ACKNOWLEDGEMENTS

This research program was sponsored by the Air Force Office of Scientific Research and monitored by Dr. Steven Walker under Contract No. F49620-99-1-0011. One of the authors, Professor Besir Şahin, would like to thank the Scientific and Technical Research Council of Turkey (TUBITAK) and NATO for their financial support.

LIST OF REFERENCES

[1] N. C. Lambourne and D. W. Bryer, "The bursting of leading edge vortices – some observations and discussion of the phenomenon", Aeronautical Research Council R&M 3282, April (1961).

[2] M. V. Lowson, "Some experiments with vortex breakdown", *Journal of the Royal Aeronautical Society* **68**, 343 (1964).

[3] W. H. Wentz, Jr. and D. L. Kohlman, D. L., "Vortex breakdown on slender sharp edged wings", *Journal of Aircraft* **8**, 156 (1971).

[4] M. V. Lowson and A. J. Riley, "Vortex breakdown control by delta wing geometry", *Journal of Aircraft* **32**, 832 (1995).

[5] P. B. Earnshaw and J. A. Lawford, "Low speed wind tunnel experiments on a series of sharp-edged delta wings", Aeronautical Research Council, R&M 3424, August.

[6] D. B. Mabey, "Beyond the buffet boundary", *Aeronautical Journal* **77**, 201 (1973).

[7] I. Gursul and W. Xie, W., "Buffeting flows over delta wings", *AIAA Journal* **37**, 58 (1999).

[8] K. W. Wolffelt, "Investigation of the movement of vortex burst position with dynamically changing angle of attack for a schematic delta wing in water tunnel with correlation to similar studies in a wind tunnel", AGARD Conference Proceedings CP-413, NATO Advisory Group for Aerospace Research and Development (1986).

[9] F. Gilliam, J. Wissler and M. Robinson, "Visualization of unsteady separated flow about a pitching delta wing", AIAA Paper 87-0240 (1987).

[10] G. A. Reynolds and A. A. Abtahi, "Instabilities in leading-edge vortex development", AIAA Paper 87-2424 (1987).

[11] L. J. Hudson, P. I. King and M. David, "Flow separation and vortex bursting locations on wings pitching at constant rates", AIAA Paper 89-2160 (1986).

[12] D. H. Thompson, "A water tunnel study of vortex breakdown over wings with highly swept leading edges", Australian Defence Scientific Service, Aeronautical Research Laboratories, Aerodynamics Note 356, May (1975).

[13] C. M. Magness, O. Robinson and D. Rockwell, "Control of leading-edge vortices in a delta wing", AIAA Paper 89-0999 (1989).

[14] R. Atta and D. Rockwell, "Leading-edge vortices on a pitching delta wing", *AIAA Journal* **28**, 995 (1990).

[15]S. P. LeMay, S. M. Batill and R. C. Nelson, "Leading-edge vortex dynamics on a pitching delta wing", *Journal of Aircraft* **27**, 131 (1990).

[16]M. A. M. Jarrah, "Visualization of the flow about a delta wing maneuvering in pitch at very high angle dynamics", ASME Publication FED **92**, edited by J. A. Miller and D. P. Telionis, American Society of Mechanical Engineers, New York, 109 (1990).

[17]H. Ashley, J. Katz, M. A. Jarrah and T. Vaneck, "Survey of research on unsteady aerodynamic loading of delta wings", *Journal of Fluids and Structures* **5**, 363 (1991).

[18]D. Rockwell, "Three-dimensional flow structure on delta wings at high angle of attack: experimental concepts and issues", AIAA Paper 93-0550 (1993).

[19]E. S. Hanff and X. Z. Huang, "Roll-induced cross-loads on a delta wing at high incidence", AIAA Paper 91-3223 (1991).

[20]T. T. Ng, G. N. Malcolm and L. C. Lewis, "Experimental study of vortex flows over delta wings in a wing-rock motion", *Journal of Aircraft* **29**, 598 (1992).

[21]K. Cipolla, A. Liakopoulos and D. Rockwell, "Quantitative imaging in proper orthogonal decomposition of flow past a delta wing", *AIAA Journal* **36**, 1247 (1998).

[22]T. Sarpkaya, "On stationary and traveling vortex breakdowns", *Journal of Fluid Mechanics* **45**, 545 (1971).

[23]T. Sarpkaya, T., "Vortex breakdown in swirling conical flows", *AIAA Journal* **9**, 1792 (1971).

[24]T. Sarpkaya, "Effect of the average pressure gradient on vortex breakdown", *AIAA Journal* **12**, 602 (1974).

[25]M. G. Hall, "Vortex breakdown", *Annual Review of Fluid Mechanics* **4**, 195 (1972).

[26]S. Leibovich, "Structure of vortex breakdown", *Annual Review of Fluid Mechanics* **10**, 221 (1978).

[27]S. Leibovich, "Vortex stability and breakdown: survey and extension", *AIAA Journal* **22**, 1192 (1984).

[28]M. Escudier, "Vortex breakdown: observations and explanations", *Progress in Aerospace Sciences* **25**, 189 (1988).

[29]G. L. Brown and J. M. Lopez, "Axisymmetric vortex breakdown. Part 2: Physical mechanisms", *Journal of Fluid Mechanics* 221, 553 (1990).

[30]J. M. Lopez and A. D. Perry, "Axisymmetric vortex breakdown. Part 3. Onset of periodic flow and chaotic advection", *Journal of Fluid Mechanics* 234, 449 (1992).

[31]J. M. Delery, "Aspects of vortex breakdown", *Progress in Aerospace Sciences* **30**, 1 (1994).

[32]S. Wang and Z. Rusak, "The dynamics of a swirling flow in a pipe and transition to axisymmetric vortex breakdown", *Journal of Fluid Mechanics* **340**, 177 (1997).

[33]J. Towfighi and D. Rockwell, "Instantaneous structure of vortex breakdown on a delta wing via particle image velocimetry", *AIAA Journal* **31**, 1160 (1993).

[34]J.-C. Lin and D. Rockwell, "Transient structure of vortex breakdown on a delta wing at high angle-of-attack", *AIAA Journal* **33**, 6 (1995).

[35]H. E. Helin and C. W. Watry, "Effects of trailing-edge entrainment on delta wing vortices", *AIAA Journal* **32**, 802 (1994).

[36]Z. Ding and C. Shih, "Trailing-edge jet control of the leading-edge vortices of a delta wing", *AIAA Journal* **34**, 2641 (1996).

[37]P. Vorobieff and D. Rockwell, "Multiple-actuator control of vortex breakdown on a pitching delta wing", *AIAA Journal* **34**, 2184 (1996).

[38]P. Vorobieff and D. Rockwell, "Vortex breakdown on pitching delta wing: Control by intermittent trailing-edge blowing", *AIAA Journal* **36**, 585 (1998).

[39]I. Gursul and H. Yang, "Vortex breakdown over a pitching delta wing", AIAA Paper 94-0536, 32nd Aerospace Sciences Meeting and Exhibit, January 10-13, Reno, NV (1994).

[40]D. Rockwell, C. Magness, J. Towfighi, O. Akin and T. Corcoran, "High image-density particle image velocimetry using laser scanning techniques", *Experiments in Fluids* **14**, 181 (1993).

[41]K. Cipolla and D. Rockwell, "Instantaneous crossflow topology on a delta wing in presence of vortex breakdown", *AIAA Journal of Aircraft* **35**, 218 (1998).

[42]H. B. Squire, "Analysis of the 'vortex breakdown' phenomenon", *Miszellaneen der Angewandten Mechanik*, Berlin, Akademie-Verlag, 306 (1960).

[43]T. B. Benjamin, "Theory of the vortex breakdown phenomenon", *Journal of Fluid Mechanics*, **14**, 593 (1962).

[44]Z. Rusak, S. Wang and C. H. Whiting, "The evolution of a perturbed vortex in a pipe to axisymmetric vortex breakdown", *Journal of Fluid Mechanics* **366**, 211 (1998).

FIGURE CAPTIONS

Figure 1: Overview of delta wing and wire arrangement. Field of view of image of leading-edge vortex from delta wing is indicated by rectangle. Length of field of view corresponds to 0.7C.

Figure 2: Change in location of onset of vortex breakdown ΔX^* as a function of location X_w of wire. Vortex diameter D_v prior to vortex breakdown and wing chord C are employed as normalizing parameters. Each curve corresponds to a given value of dimensionless wire diameter D_w/D_v; the zero reference line is indicated for each value of D_w/D_v. Angle of attack α of delta wing is $\alpha = 30°$.

Figure 3: Change in location of onset of vortex breakdown ΔX_b relative to position of wire as a function of wire location X_w. Vortex diameter D_v prior to vortex breakdown and wing chord C are employed as normalizing parameters. Each curve corresponds to a given value of dimensionless wire diameter D_w/D_v. Lines of zero $\Delta X_b/D_v$ are indicated for each value of D_w/D_v. Angle of attack α of delta wing is $\alpha = 30°$.

Figure 4a: Effect of wire location X_w/C on patterns of instantaneous vorticity in vicinity of onset of vortex breakdown (vb) for a wire diameter D_w relative to the vortex diameter D_v of $D_w/D_v = 0.02$. Minimum and incremental values of vorticity are $\omega_{min} = \pm 2$ sec^{-1} and $\Delta\omega = 0.75$ sec^{-1}. Thick and thin lines represent respectively positive and negative vorticity. Angle of attack of delta wing is $\alpha = 30°$. Wire is represented by a small white dot. The diameter of this dot is magnified by a factor of two relative to the scale of the vortex, i.e. scale of vorticity patterns. Length of each image corresponds to 0.7C.

Figure 4b: Effect of wire location X_w/C on contours of constant velocity $< V >$ in vicinity of onset of vortex breakdown (vb) as defined by vorticity criterion. Location of vortex breakdown vb^* corresponds to attainment of zero velocity along centerline of vortex. For all cases, ratio of wire diameter D_w to vortex diameter D_v is $D_w/D_v = 0.02$. Numbers of contours of $< V >$ indicate values of velocity in mm/sec; increment between contours is 5 mm/sec. Angle of attack of delta wing is $\alpha = 30°$. Wire is represented by a small white dot. The diameter of this dot is magnified by a factor of two relative to the scale of the vortex.

Figure 5a: Effect of wire location X_w/C on patterns of instantaneous vorticity in vicinity of onset of vortex breakdown (vb) for a wire diameter D_w relative to the diameter D_v of the vortex core of $D_w/D_v = 0.11$. Minimum and incremental values of vorticity are $\omega_{min} = \pm 2$ sec^{-1} and $\Delta\omega = 0.75$ sec^{-1}. Angle of attack of delta wing is $\alpha = 30°$. Wire is represented by a small white dot.

Figure 5b: Effect of wire location X_w/C on contours of constant velocity $< V >$ in vicinity of onset of vortex breakdown (vb) for a wire diameter D_w relative to the vortex core diameter D_v of $D_w/D_v = 0.11$. Units of $< V >$ are mm/sec and incremental value is 5 mm/sec. Angle of attack of delta wing is $\alpha = 30°$. Wire is represented by the small white dot.

Figure 6a: Effect of ratio of wire diameter D_w to diameter D_v of vortex core on patterns of instantaneous positive (solid line) and negative (thin line) vorticity associated with change of onset of vortex breakdown. Left column of images corresponds to angle of attack $\alpha = 30°$ and right column to $\alpha = 25°$. Minimum and incremental values of vorticity are $\omega_{min} = \pm 2$ sec^{-1} and $\Delta\omega = 0.75$ sec^{-1}. Wire is represented by a small white dot. For $D_w/D_v = 0.02$, dot is magnified by factor of two relative to its actual scale. For other values of D_w/D_v, dot is shown to scale. Length of each image corresponds to 0.45C.

Figure 6b: Effect of ratio of wire diameter D_w to diameter D_v of vortex core on contours of constant velocity $< V >$ at two different values of angle of attack of delta wing. Left column of images corresponds to angle of attack $\alpha = 30°$ and right column to $\alpha = 25°$. Units of $< V >$ are mm/sec and increment between contours is 5 mm/sec. Wire is represented by a small white dot. For $D_w/D_v = 0.02$, dot is magnified by factor of two relative to its actual scale. For other values of D_w/D_v, dot is shown to scale. Length of each image corresponds to 0.45C.

Figure 7a: Effect of ratio of wire diameter D_w to diameter D_v of vortex on patterns of instantaneous vorticity associated with change of location of onset of vortex breakdown (vb) at low angle of attack $\alpha = 25°$ of delta wing. Minimum and incremental values of vorticity are $\omega_{min} = \pm 2\ sec^{-1}$ and $\Delta\omega = 0.75\ sec^{-1}$. Wire is represented by a small white dot. For $D_w/D_v = 0.02$, dot is magnified by factor of two relative to the scale of the vortex. For other values of D_w/D_v, dot is shown to scale. Length of each image corresponds to 0.7C.

Figure 7b: Effect of ratio of diameter of wire D_w to diameter D_v of vortex core on patterns of constant velocity associated with change of location of onset of vortex breakdown (vb) at low angle of attack $\alpha = 25°$ of delta wing. Units of $< V >$ are mm/sec and incremental value is 5 mm/sec. Wire is represented by a small white dot. For $D_w/D_v = 0.02$, dot is magnified by factor of two relative to the scale of the vortex. For other values of D_w/D_v, dot is shown to scale. Length of each image corresponds to 0.7C.

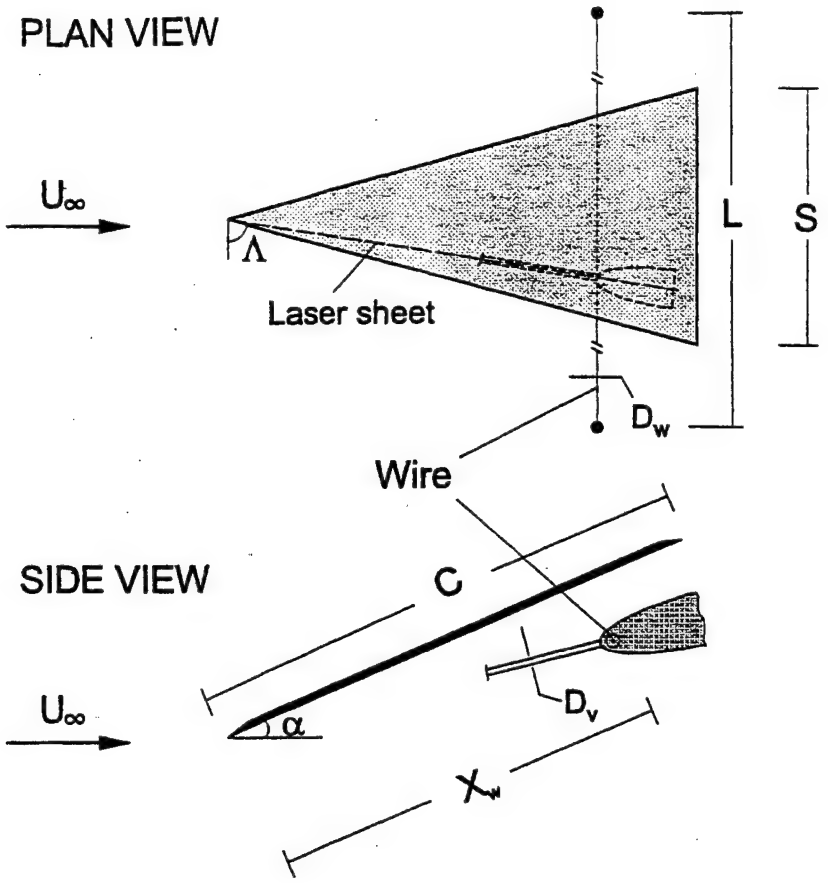

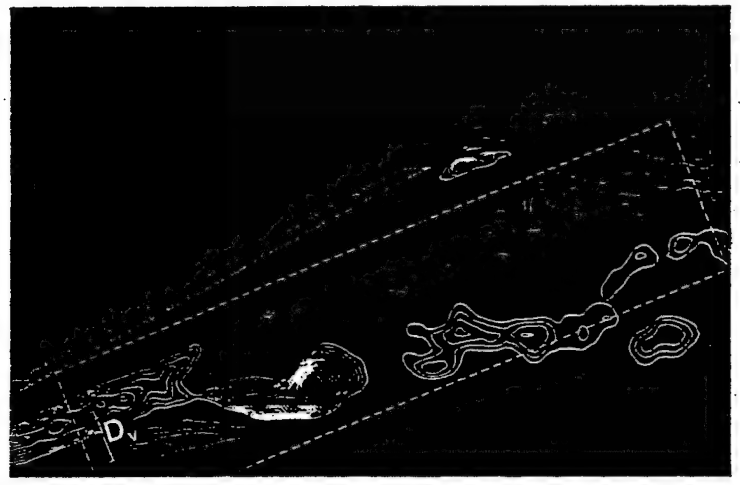

Figure 1: Overview of delta wing and wire arrangement. Field of view of image of leading-edge vortex from delta wing is indicated by rectangle. Length of field of view corresponds to 0.7C.

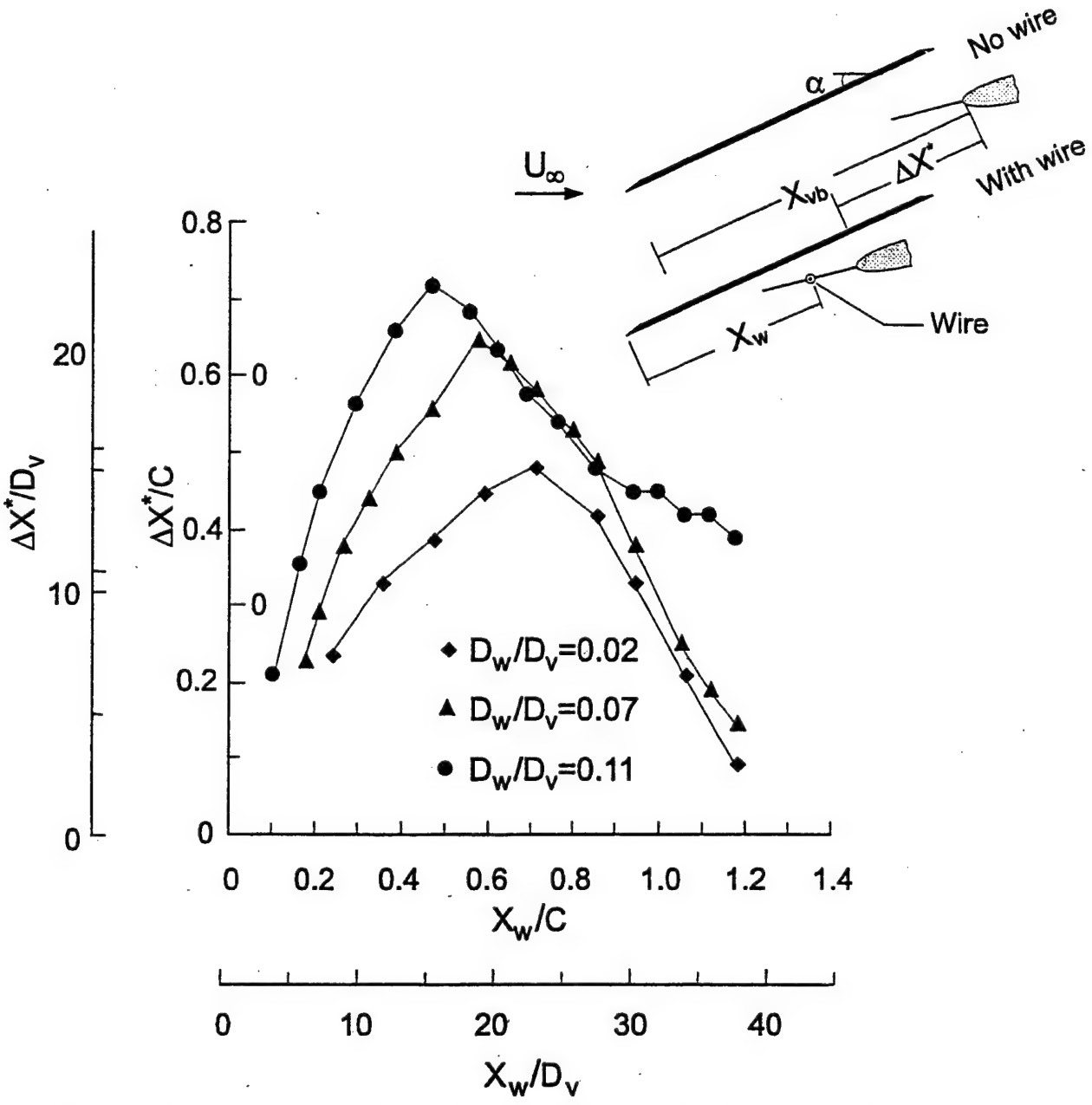

Figure 2: Change in location of onset of vortex breakdown ΔX^* as a function of location X_w of wire. Vortex diameter D_v prior to vortex breakdown and wing chord C are employed as normalizing parameters. Angle of attack α of delta wing is $\alpha = 30°$.

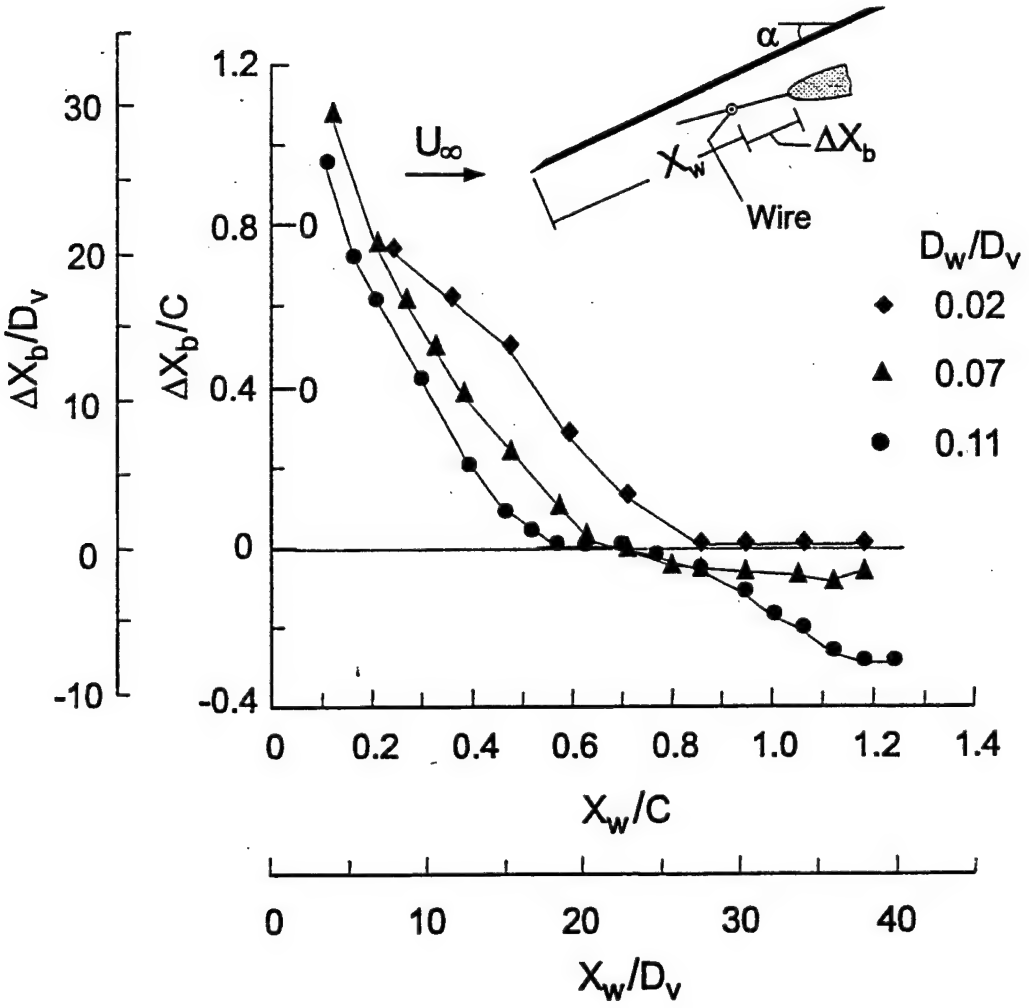

Figure 3: Change in location of onset of vortex breakdown ΔX_b relative to position of wire as a function of wire location X_w. Vortex diameter D_v prior to vortex breakdown and wing chord C are employed as normalizing parameters. Angle of attack α of delta wing is $\alpha = 30°$.

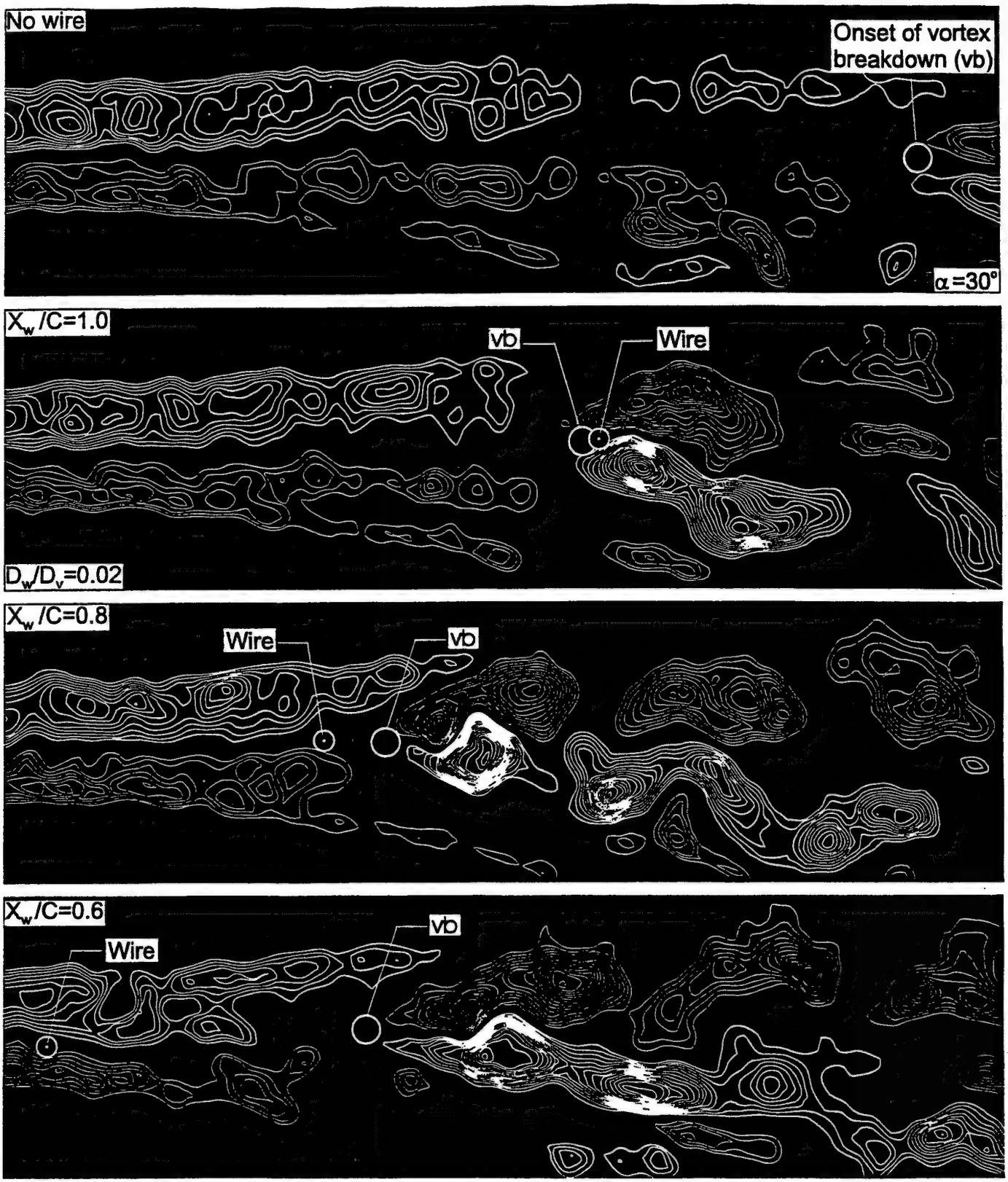

Figure 4a: Effect of wire location X_w/C on patterns of instantaneous vorticity in vicinity of onset of vortex breakdown (vb) for a wire diameter D_w relative to the vortex diameter D_v of $D_w/D_v = 0.02$. Minimum and incremental values of vorticity are $\omega_{min} = \pm 2\ sec^{-1}$ and $\Delta\omega = 0.75\ sec^{-1}$. Thick and thin lines represent respectively positive and negative vorticity. Angle of attack of delta wing is $\alpha = 30°$. Wire is represented by a small white dot. The diameter of this dot is magnified by a factor of two relative to the scale of the vortex, i.e. scale of vorticity patterns. Length of each image corresponds to 0.7C.

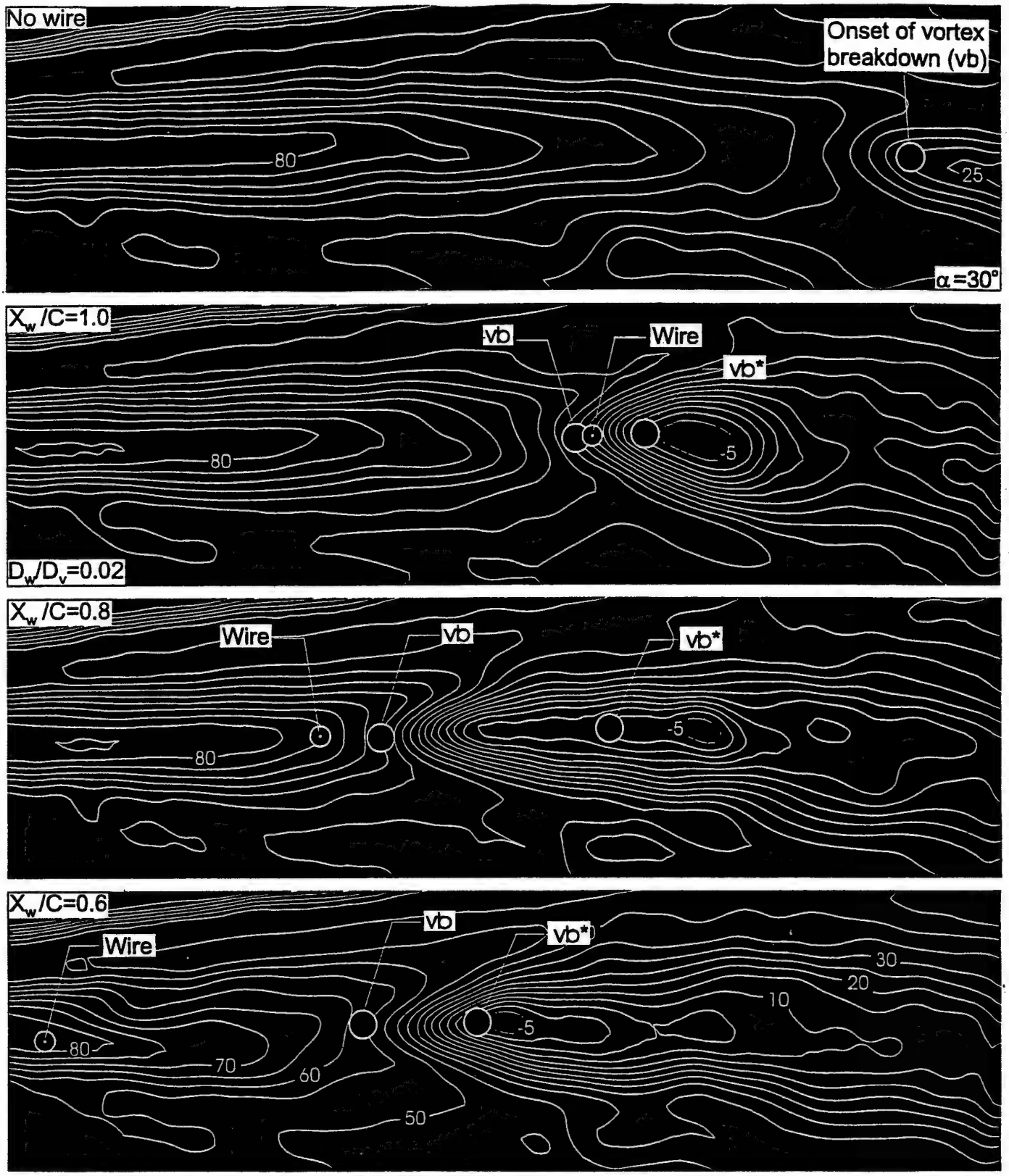

Figure 4b: Effect of wire location X_w/C on contours of constant velocity $<V>$ in vicinity of onset of vortex breakdown (vb) as defined by vorticity criterion. Location of vortex breakdown vb* corresponds to attainment of zero velocity along centerline of vortex. For all cases, ratio of wire diameter D_w to vortex diameter D_v is $D_w/D_v = 0.02$. Numbers of contours of $<V>$ indicate values of velocity in mm/sec: increment between contours is 5 mm/sec. Angle of attack of delta wing is $\alpha=30°$. Wire is represented by a small white dot. The diameter of this dot is magnified by a factor of two relative toits actual size.

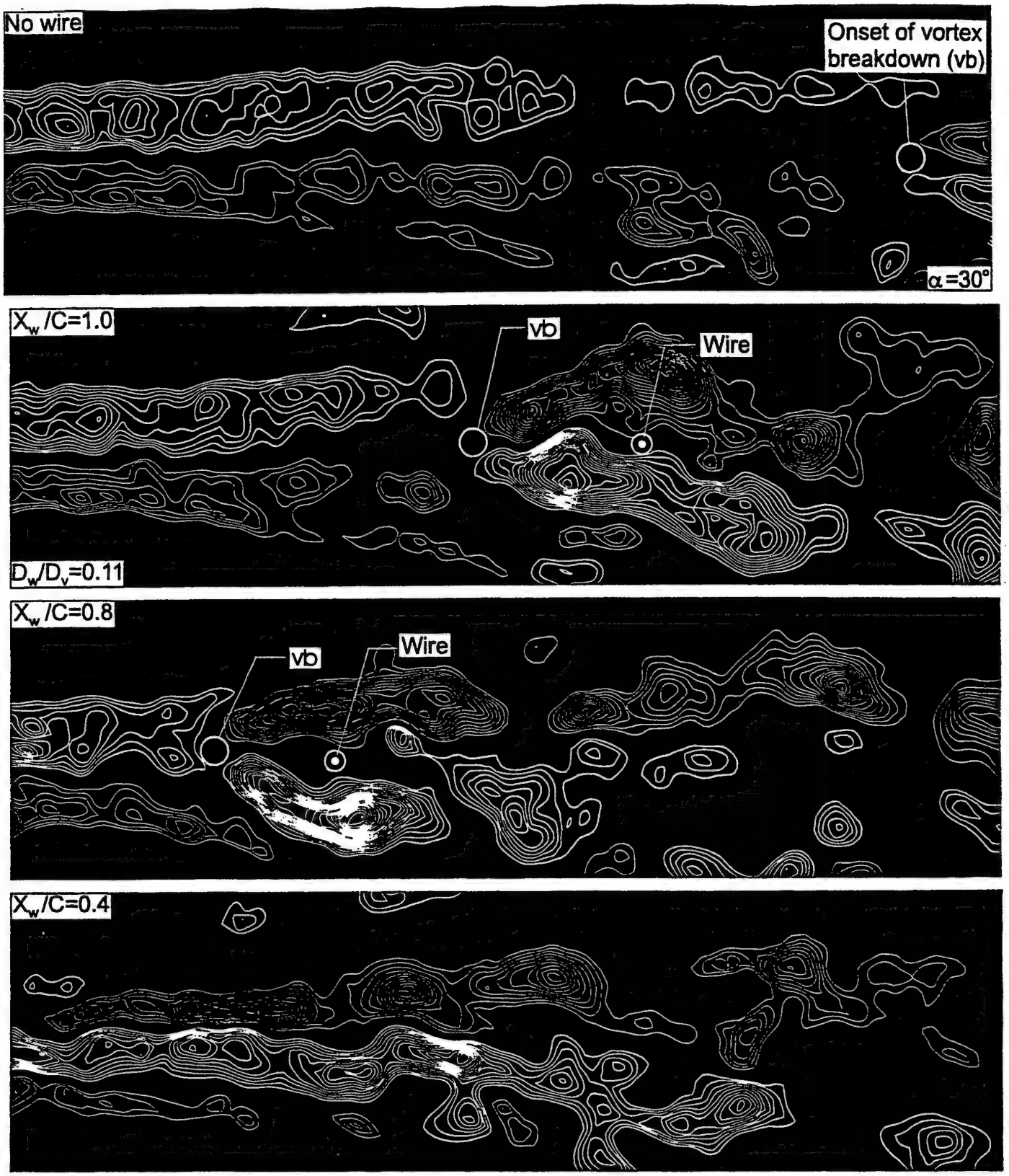

Figure 5a: Effect of wire location X_w/C on patterns of instantaneous vorticity in vicinity of onset of vortex breakdown (vb) for a wire diameter D_w relative to the diameter D_v of the vortex core of $D_w/D_v = 0.11$. Minimum and incremental values of vorticity are $\omega_{min} = \pm 2\ sec^{-1}$ and $\Delta\omega = 0.75\ sec^{-1}$. Angle of attack of delta wing is $\alpha = 30°$. Wire is represented by the small white dot.

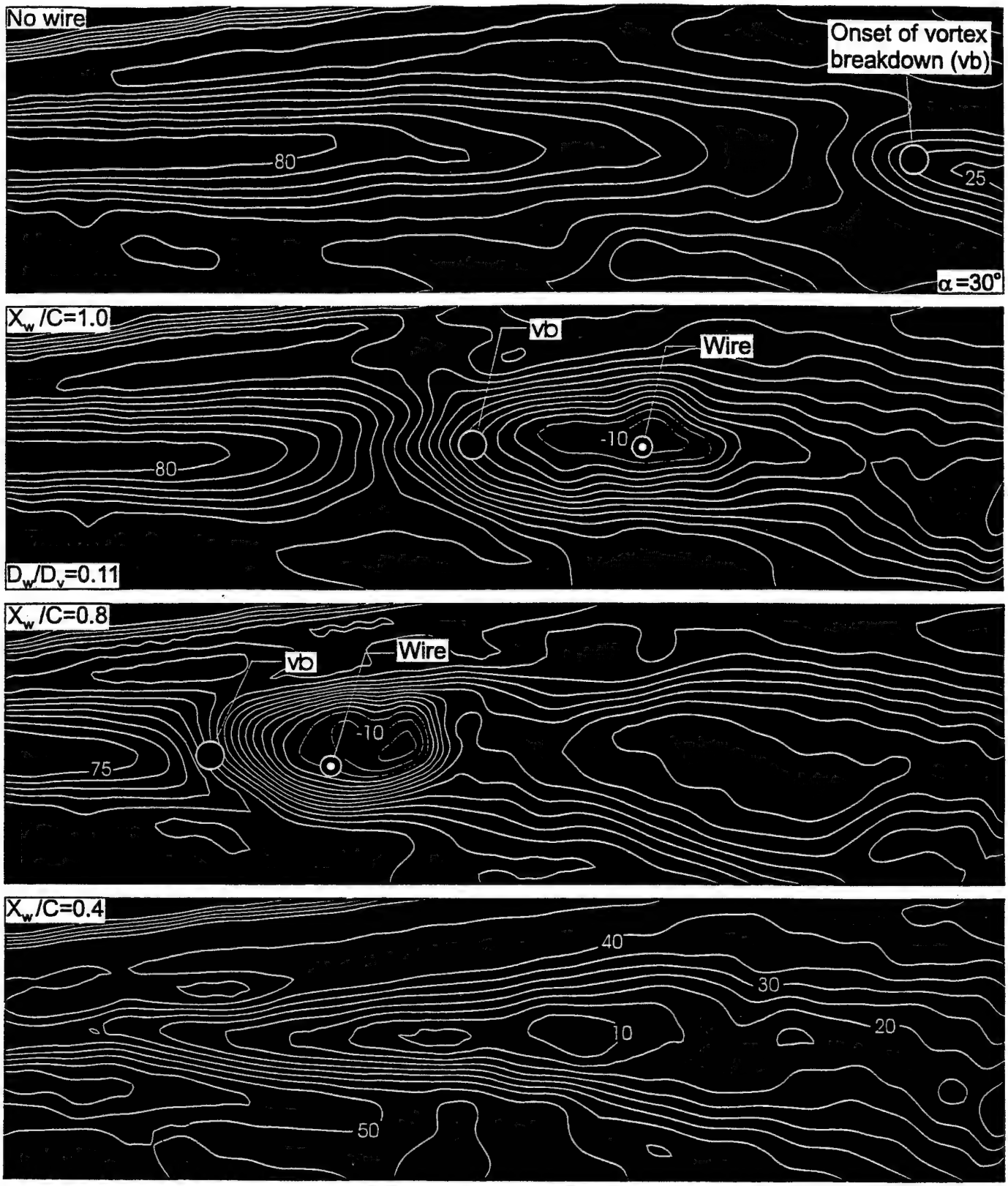

Figure 5b: Effect of wire location X_w/C on contours of constant velocity $< V >$ in vicinity of onset of vortex breakdown (vb) for a wire diameter D_w relative to the vortex core diameter D_v of $D_w/D_v = 0.11$. Units of $< V >$ are mm/sec and incremental value is 5 mm/sec. Angle of attack of delta wing is $\alpha = 30°$. Wire is represented by the small white dot.

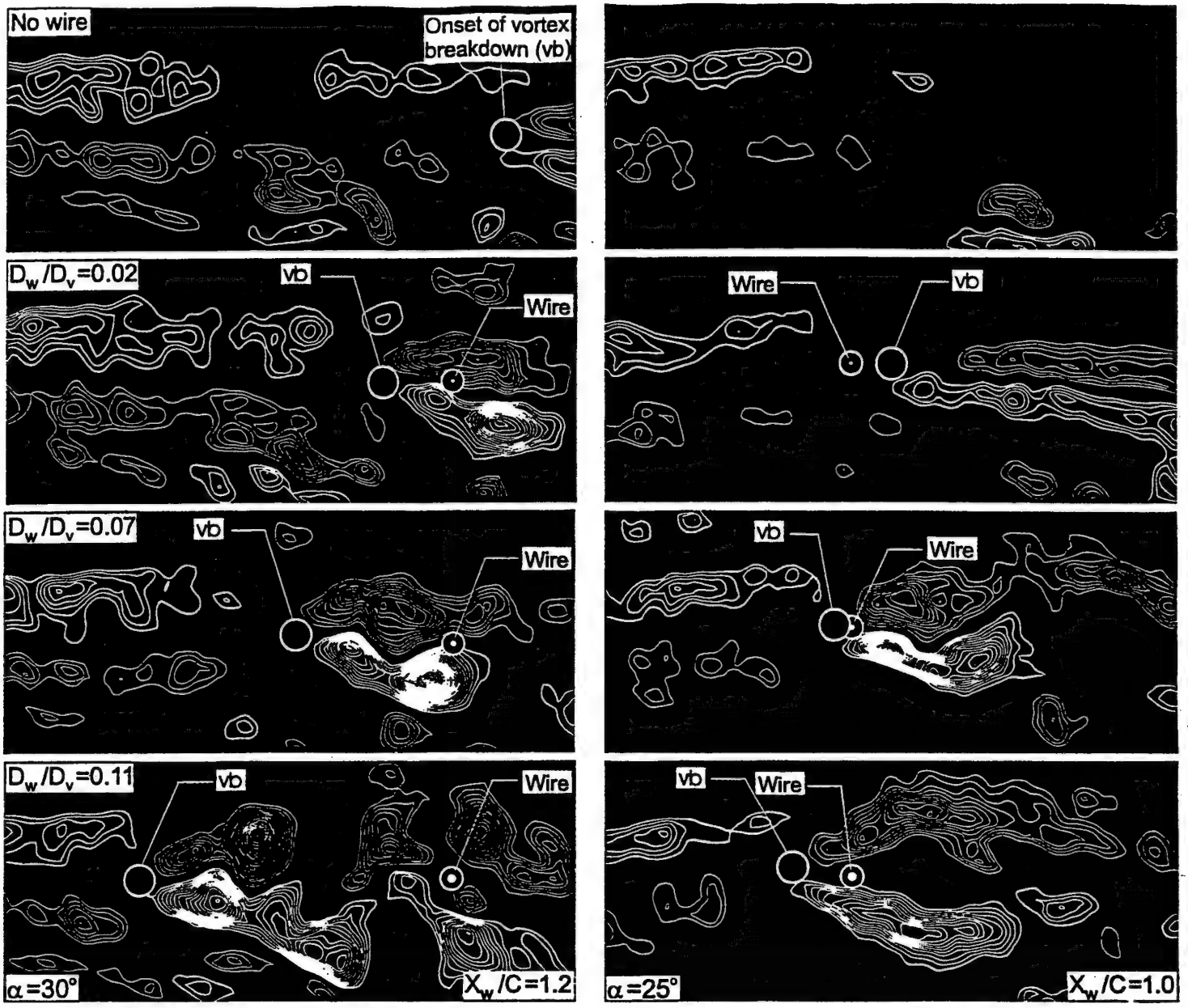

Figure 6a: Effect of ratio of wire diameter D_w to diameter D_v of vortex core on patterns of instantaneous positive (solid line) and negative (thin line) vorticity associated with change of onset of vortex breakdown. Left column of images corresponds to angle of attack $\alpha = 30^\circ$ and right column to $\alpha = 25^\circ$. Minimum and incremental values of vorticity are $\omega_{min} = \pm 2 sec^{-1}$ and $\Delta\omega = 0.75\ sec^{-1}$. Wire is represented by a small white dot. For D_w/D_v=0.02, dot is magnified by factor of two relative to its actual scale. For other values of D_w/D_v, dot is shown to scale. Length of each image corresponds to 0.45C.

APPENDIX E

Özgören-3 FIN 061101

VORTEX BREAKDOWN FROM A PITCHING DELTA WING INCIDENT UPON A PLATE: FLOW STRUCTURE AS THE ORIGIN OF BUFFET LOADING

by

M. Özgören* and B. Sahin*

Department of Mechanical Engineering

Cukurova University

Balcali 01330 Adana

Turkey

* On leave at Lehigh University

D. Rockwell

Department of Mechanical Engineering and Mechanics

354 Packard Laboratory

19 Memorial Drive West

Lehigh University, Bethlehem, PA 18015

A delta wing is subjected to both static and dynamic variations of angle-of-attack; the vortices from the wing impinge upon a stationary plate. A technique of high-image-density particle image velocimetry is employed to compare the patterns of vortex development with and without the impingement plate. For the limiting case of static variations of angle-of-attack, the presence of the plate exerts a large influence on the onset of vortex breakdown. In contrast, dynamic (unsteady) variation of angle-of-attack yields changes of breakdown location that are generally similar for cases with and without the impingement plate. The detailed structure of the vortex breakdown-plate interaction is represented by patterns of instantaneous velocity and vorticity, which serve as the origin of buffet-induced loading of the surface of the plate.

*** Özgören, M., Sahin, B., and Rockwell, D. 2002 *Journal of Fluid Mechanics.***

1. INTRODUCTION

1.1 BUFFETING OF TAILS AND PLATES: SURFACE LOADING

Buffeting of aerodynamic surfaces, especially vortex breakdown incident upon the tail of an aircraft, as well as a simulated tail in the form of a plate, has received considerable attention during the last decade. A comprehensive review is provided by Lee (2000). Wolfe *et al.* (1995a) assessed a variety of experiments extending over a wide range of Reynolds and Mach number, and correlated the predominant frequency of buffeting. Investigations that involved measurement of pressure spectra on either a tail or a plate include those of Bean & Wood (1993), Washburn *et al.* (1993), Canbazoglu *et al.* (1995a) and Wolfe *et al.* (1995b). Substantial effort has been devoted to characterization of the surface pressure loading and acceleration response and tails of F-series aircraft. Triplett (1983) determined the fluctuations on the tail of a Model F-15 aircraft. Wentz (1987), Ferman *et al.* (1990), Zimmerman *et al.* (1989), Shah (1991), Lee & Tang (1992), Martin & Thompson (1991) and Lee *et al.* (1993) characterized the surface pressure spectra on tails of Model F/A-18 aircraft. Moses & Huttsell (2000) performed similar types of measurements on the fin of a Model F-22 aircraft. Luber *et al.* (1996) assessed the impact of dynamic loads on the design of aircraft. Finally, the buffet response of a fin can be effectively alleviated by active control of its surface, as shown by Ashley *et al.* (1994).

The focus of the foregoing investigation has been, for the most part, on measurement of localized surface loading, with the intent of calculating the dynamic response of the surface. Links between the physics of the nonstationary flow patterns and the surface loading have not been pursued.

1.2 CONTROL OF BUFFET FLOW FIELD AND BUFFET LOADING

Although implementation of various types of control techniques for altering the performance of aircraft has been extensively pursued, relatively few investigations have explicitly addressed the consequence of flow control on buffeting of a tail. Bean and Wood (1993) employed tangential blowing at a leading-edge and observed the buffet loading of a tail. Huttsell *et al.* (1997) employed tangential blowing techniques on actual aircraft configurations to control tail buffeting. Sheta *et al.* (2000) undertook a numerical simulation of various tangential blowing techniques as a means to attenuate the buffet of a twin-tail configuration. Özgören *et al.* (2000) employed small-amplitude perturbations of a delta wing, with the intent of simulating control at the leading-edges of a stationary wing, and characterized the buffet flow field along the leading-edge of a plate. Whereas all of the previous investigations aim to control buffeting by manipulating the vortex at, or close to, its origin, Sahin *et al.* (2000) and Gursul & Xie (2000) employed respectively small-amplitude perturbations of the leading-edge of the plate and larger amplitude perturbations of an actual tail. Due to an apparent upstream influence, the incident vortex and its interaction with the aerodynamic surface were altered accordingly.

Generally speaking, the effect of large amplitude, low frequency motion of a wing on the buffet loading of a downstream aerodynamic surface has not been pursued. Complex maneuvers of an actual aircraft typically occur at relatively low dimensionless frequencies, in comparison with dimensionless frequencies of either vortex breakdown or a shear layer instability from the leading-edge of the wing. Knowledge of the flow distortion along the aerodynamic surface due to these interactions would be insightful.

1.3 PHYSICS OF INTERACTION OF VORTEX BREAKDOWN WITH A TAIL, FIN OR PLATE

An understanding of the buffet loading of an aerodynamic surface requires insight into the unsteady flow field of the region of vortex breakdown as it encounters a tail (fin) or plate. Breitsamter & Laschka (1994a,b; 1998) employed hot wire anemometry to characterize in detail the fluctuating flow field of the region of vortex breakdown in absence of a tail. Beutner *et al.* (1995) used a technique of planar Doppler velocimetry to determine the root-mean-square patterns of the flow field due to vortex-fin interaction. In a series of investigations employing high-image-density particle image velocimetry (PIV), Mayori & Rockwell (1994) and Wolfe *et al.* (1995b) characterized the distortion of vortex breakdown upon encounter with a thin flat plate and Canbazoglu *et al.* (1995a,b) used a similar approach to characterize the instantaneous patterns of the distortion due to interaction with a tail.

Further insight into the physics of vortex- and vortex breakdown-tail (fin) interaction is provided by the numerical investigations of Rizk & Gee (1992), Gee *et al.* (1995), Kandil *et al.* (1995), Rizetta (1996), Kandil & Sheta (1998) and Gordnier & Visbal (1997). Gordnier & Visbal (1997) demonstrate the mechanism of partitioning of the incident vortex due to its direct encounter with the leading-edge of a plate.

Insight into the relationship between the nonstationary flow patterns along an aerodynamic surface, e.g., the tail of an aircraft, and the buffet loading of the surface is provided by the measurements and model of Breitsamter & Laschka (1994a,b; 1998). They relate the local loading of the surface to the fluctuating angle-of-attack associated with the turbulence at a given location above the surface. The local angle-of-attack varies with time according to the ratio of the local vertical to horizontal velocity. The

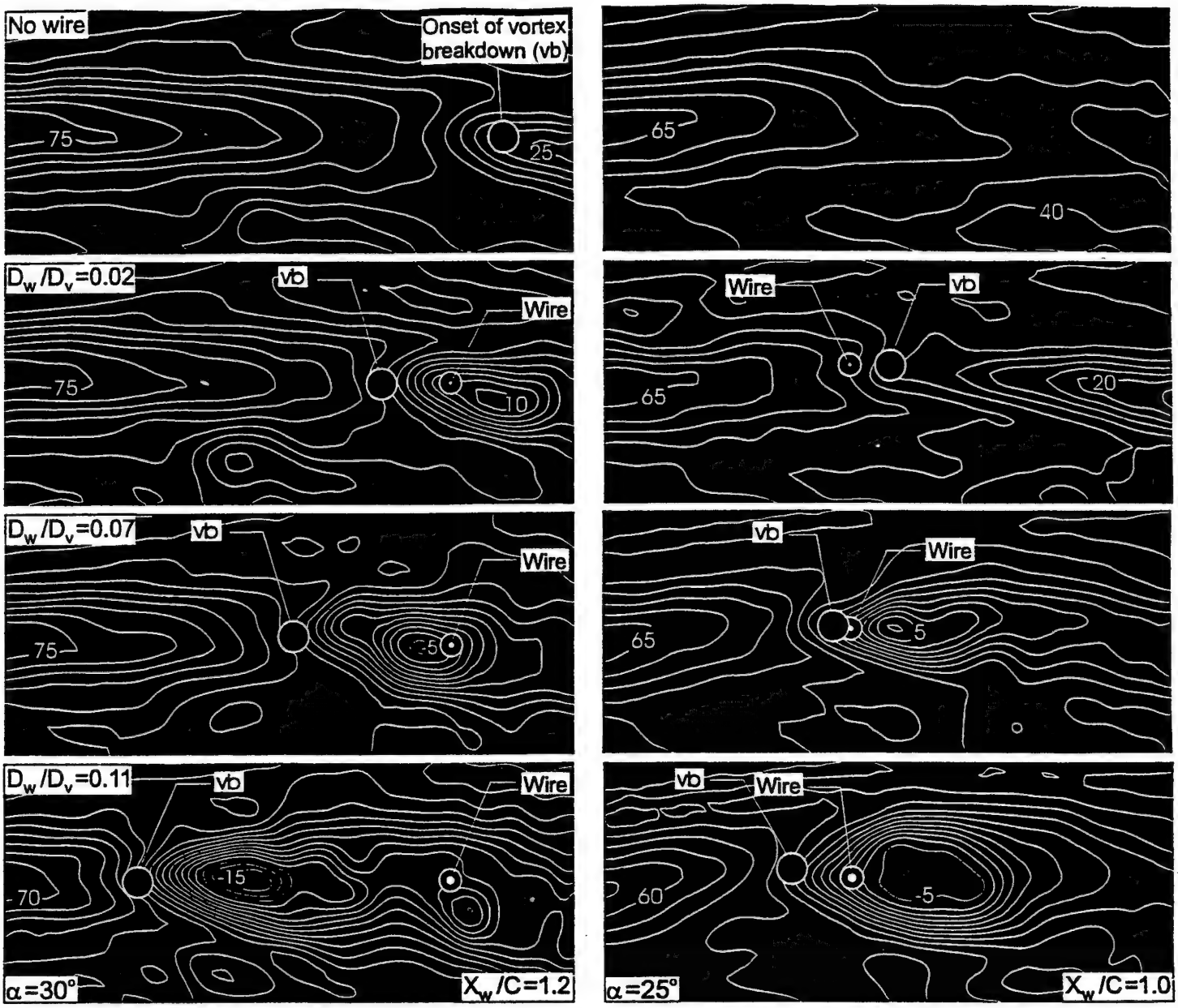

Figure 6b: Effect of ratio of wire diameter D_w to diameter D_v of vortex core on contours of constant velocity $< V >$ at two different values of angle of attack of delta wing. Left column of images corresponds to angle of attack $\alpha = 30^\circ$ and right column to $\alpha = 25^\circ$. Units of $< V >$ are mm/sec and increment between contours is 5 mm/sec. Wire is represented by a small white dot. For D_w/D_v=0.02, dot is magnified by factor of two relative to its actual scale. For other values of D_w/D_v, dot is shown to scale. Length of each image corresponds to 0.45C.

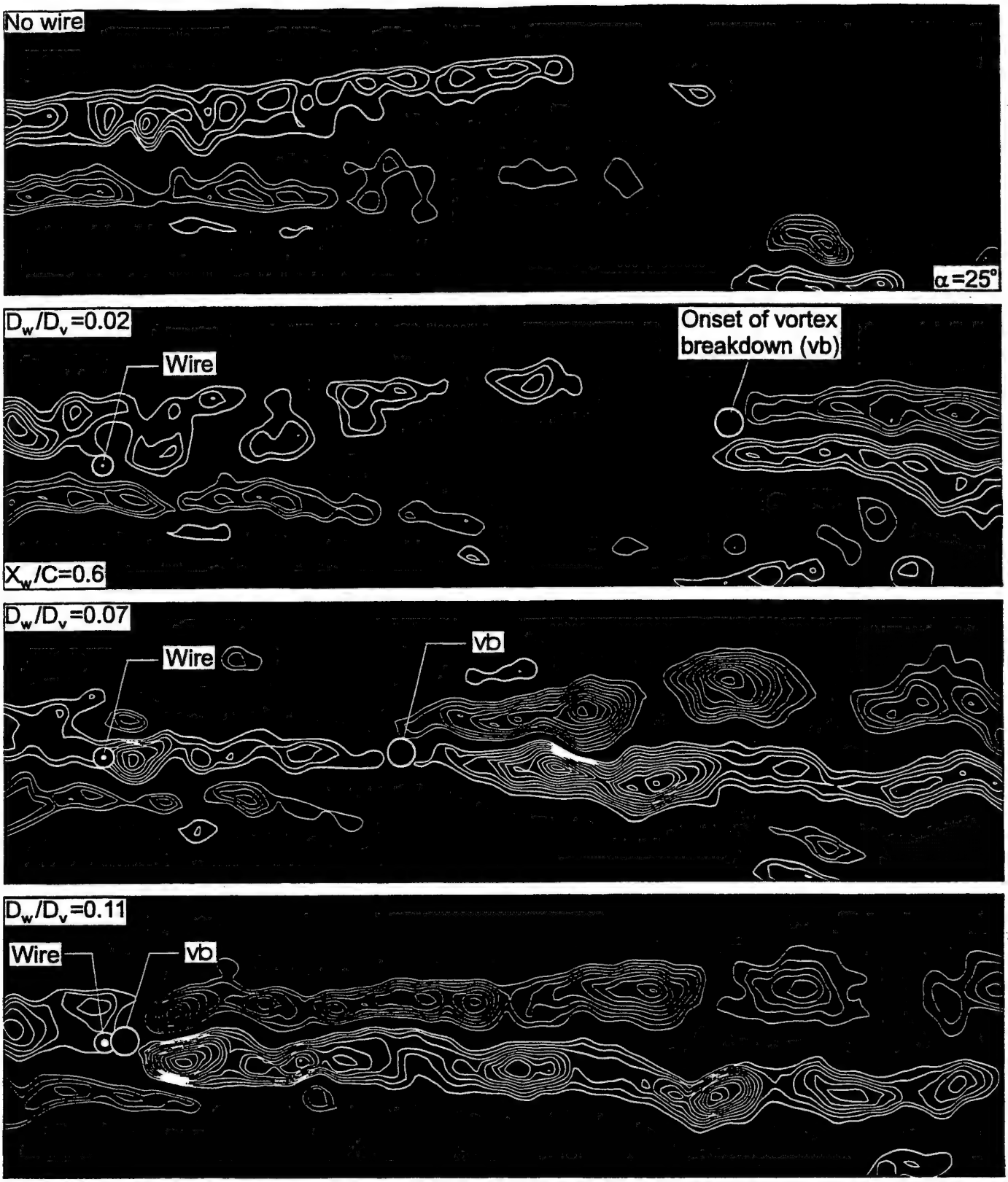

Figure 7a: Effect of ratio of wire diameter D_w to diameter D_v of vortex on patterns of instantaneous vorticity associated with change of location of onset of vortex breakdown (vb) at low angle of attack $\alpha = 25^\circ$ of delta wing. Minimum and incremental values of vorticity are $\omega_{min} = \pm 2$ sec^{-1} and $\Delta\omega = 0.75$ sec^{-1}. Wire is represented by a small white dot. For D_w/D_v=0.02, dot is magnified by factor of two relative to the scale of the vortex. For other values of D_w/D_v, dot is shown to scale. Length of each image corresponds to 0.7C.

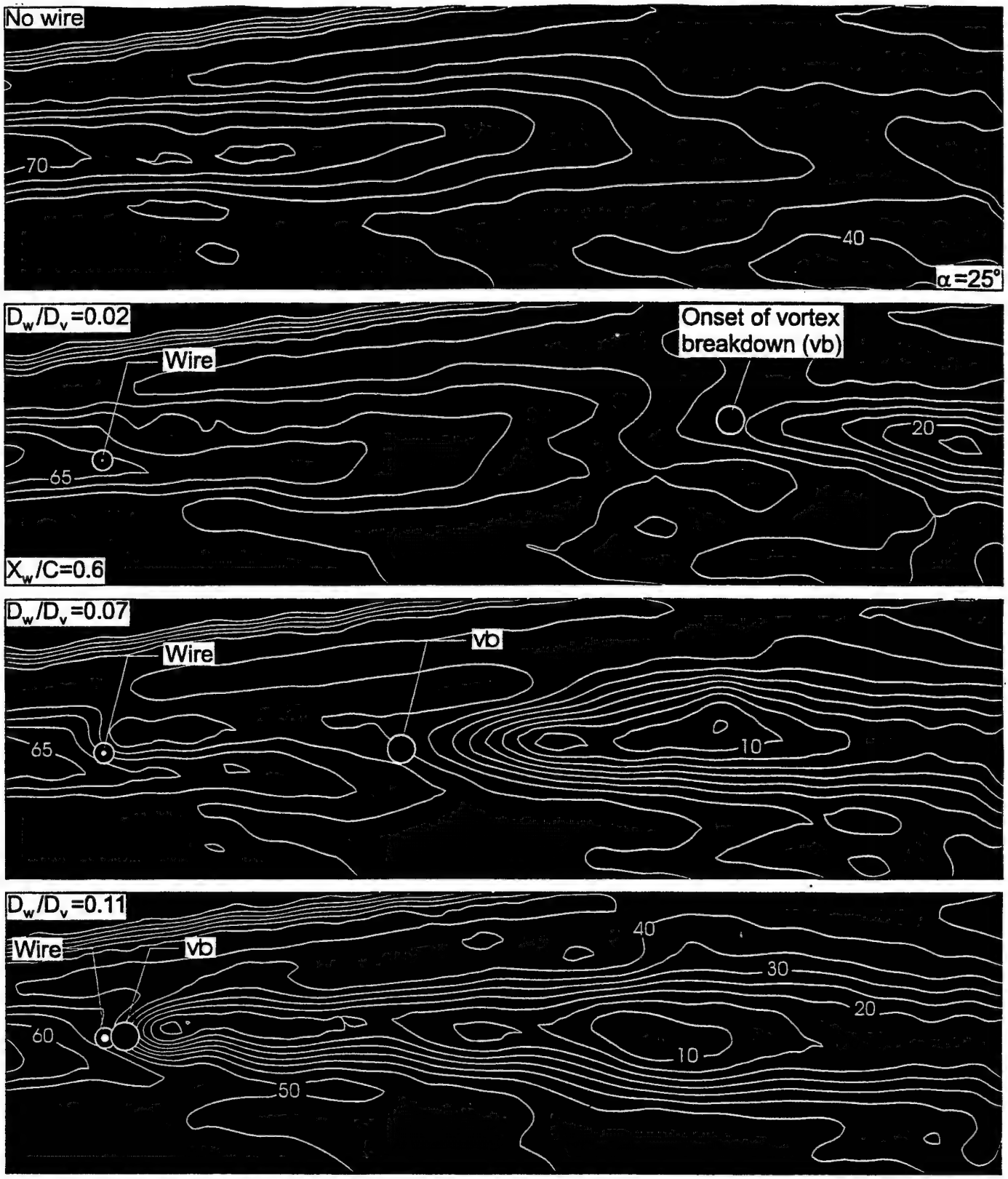

Figure 7b: Effect of ratio of diameter of wire D_w to diameter D_v of vortex core on patterns of constant velocity associated with change of location of onset of vortex breakdown (vb) at low angle of attack $\alpha = 25^\circ$ of delta wing. Units of $< V >$ are mm/sec and incremental value is 5 mm/sec. Wire is represented by a small white dot. For D_w/D_v=0.02, dot is magnified by factor of two relative to the scale of the vortex. For other values of D_w/D_v, dot is shown to scale. Length of each image corresponds to 0.7C.

central link is an analogy to the Kuessner (1954) integral, which relates the loading on a body to fluctuations of angle-of-attack. An important assumption is that flow separation does not occur along the surface. Generally speaking, knowledge of the fluctuating velocity immediately above the surface can yield a basis for understanding the loading of the surface.

1.4 UPSTREAM INFLUENCE ON VORTEX BREAKDOWN DUE TO A BODY OR SURFACE LOCATED WITHIN THE VORTEX

A body or an aerodynamic surface located within the path of a vortex can potentially alter the onset of vortex breakdown, relative to the case of the free vortex. As a consequence, the state of the vortex breakdown incident upon a tail or fin may be altered relative to that based strictly on consideration of a freely evolving vortex in absence of a body or surface. Reynolds & Abtahi (1987) and Gursul & Yang (1994) showed that a probe and a moderate-sized cylinder could advance the onset of vortex breakdown. Akilli *et al.* (2001) demonstrated that a wire of diameter approximately two orders of magnitude smaller than the vortex diameter can substantially influence the onset of vortex breakdown. These observations, which involve stationary bodies inserted into the vortex, are complemented by those that employ unsteady motion of a tail (Gursul & Xie, 2000) and perturbations of the leading-edge of the plate (Sahin *et al.*, 2000) to control the location of vortex breakdown.

An important issue is the effect of the centerline of an incident, broken-down vortex; it may modify the vortex at locations upstream of the leading-edge of a plate or tail. That is, the degree of upstream influence, and thereby alteration of the incident vortex, is expected to be largest when the vortex centerline and the leading-edge are

aligned, and diminished when they are offset. The physics of his phenomenon should be quantitatively assessed.

1.5 PHASE LAG OF VORTEX BREAKDOWN DUE TO LARGE-AMPLITUDE MOTION OF A WING, FLAP OR EXTENSION

A delta wing that undergoes relatively large-amplitude variations of, for example, angle-of-attack, gives rise to unsteady development of the vortex. The influence of a body or aerodynamic surface in the path of a vortex may alter this unsteady development; very little is known of this influence. In absence of such an obstruction, it is well known that the onset of vortex breakdown lags the motion of the wing (Rockwell, 1993). Gursul (2000) has reviewed this phase lag concept and provided a model for its occurrence. Relevant investigations involving motion of a delta wing in absence of a downstream obstruction include those of Lowson (1964), Woffelt (1987), Atta & Rockwell (1987, 1990), Reynolds & Abtahi (1987), LeMay *et al.* (1990), Magness (1991), Thompson *et al.* (1991), Miau *et al.* (1992), Greenwell & Wood (1994), Gursul & Yang (1995) and Myose *et al.* (1997). Analogous phase lags occur when a flap or wing extension undergoes unsteady motion, as investigated by Deng & Gursul (1997) and Yang & Gursul (1997).

This concept of phase lag is important for buffet loading of aerodynamic surfaces. The streamwise and transverse locations of vortex breakdown, as it impinges upon a plate or tail, are expected to lag the motion of the wing or aerodynamic surface, e.g., LEX, from which it is generated. The nature of this type of phase lag has not been investigated.

1.6 UNRESOLVED ISSUES AND OBJECTIVES

The following issues remain unclarified. First of all, a direct comparison of the physics of vortex breakdown with and without a tail (or plate) has not yet been undertaken. More

explicitly, the manner in which the location and structure of vortex breakdown are modified in presence of an aerodynamic surface for the case of a static wing and a static tail (or plate) has remained unexplored. Second, in the event that the wing undergoes pitching motion, the manner in which presence of a stationary tail or plate located downstream of the wing influences the phase lag of vortex breakdown, relative to the case of no tail (or plate), has remained uninvestigated. Third, the pitching motion of a wing will produce corresponding cross-stream excursions of the location of vortex breakdown relative to a stationary tail (or plate) located downstream of the wing. The modification of the vortex breakdown-plate encounter has not been addressed. One expects large changes in the velocity field that induces buffet loading. These changes will occur in relation to distortion of patterns of vorticity, and this interrelationship requires clarification.

The aim of the present investigation is to employ a technique of high-image-density particle image velocimetry in two planes, one aligned with the axis of the vortex and the other aligned with the cross-flow plane, in order to determine the underlying physics of the issues defined in the foregoing.

2. EXPERIMENTAL SYSTEM AND TECHNIQUES

Experiments were undertaken in a water channel test section having a height of 610 mm and a width of 927 mm. The depth of the water was maintained constant at a value of 559 mm. An overview of the delta wing-plate configuration is illustrated in Figure 1. It is similar to the arrangement used by Sahin *et al.* (2000), for the case where the wing was maintained stationary, and the impingement plate was subjected to small-amplitude controlled oscillations, and by Özgören *et al.* (2000), for which the wing was perturbed at

small amplitude and high frequency and the impingement plate was maintained stationary. The essential characteristics of this system are as follows. The delta wing has a chord C = 222 mm, a thickness of 3.2 mm and a sweep angle $\Lambda = 75°$. The wing was beveled on the windward side at an angle of 34°. Regarding the impingement plate, it had a chordwise length of L_p = 162 mm and a thickness t_p = 6.3 mm; the leading-edge was beveled at an angle of 5°, and the trailing-edge at 12°. The plate was oriented horizontally in order to examine the effect of the vertical offset of the centerline of the vortex, relative to the leading-edge of the plate, during pitching motion of the wing. During a complex maneuver of an aircraft, such variations of offset are expected to occur. Furthermore, a long plate was employed in order to preclude possible coupling between the leading- and trailing-edge regions. During the entire set of experiments, the distance between the trailing-edge of the delta wing and the leading-edge of the plate was kept at L = 73 mm. This distance allowed vortex breakdown to occur upstream of the leading-edge of the plate, over a range of angle-of-attack α of the wing.

Previous investigations have focused on small perturbations of the wing or plate, with the aim of altering the vortex structure at and near the inherent instability frequency of vortex breakdown. In contrast, the focus of the present experiment is on relatively low frequency, large amplitude pitching motion of the wing, with the goal of determining the overall hysteresis effects of vortex breakdown in conjunction with the features of the flow-plate interaction associated with buffet loading. The pitching motion of the wing was according to $\alpha(t) = \bar{\alpha} + \alpha_o \sin\omega_e t$, which $\omega_e = 2\pi f_e$. The frequency of the pitching motion was maintained constant at f_e = 0.044 c/s. This frequency was more than an order of magnitude lower than the inherent frequency of vortex breakdown, yet was large

enough to allow highly repetitive variations of the time-dependent $x_b(t)$ of vortex breakdown. Moreover, the amplitude of the pitching motion was $\alpha_o = 10°$ for all cases. These excitation parameters corresponded to a value of reduced frequency $k = \pi f_e C/U_\infty = 0.74$. Several values of mean angle-of-attack $\bar{\alpha} = 20°$, 24° and 30° were used for cases where the wing was subjected to pitching motion. For cases where static variations of angle-of-attack were considered, the values of angle-of-attack were $\bar{\alpha} = 24°$ to 30° were employed. The value of freestream velocity was $U_\infty = 42$ mm/sec, corresponding to a Reynolds number based on chord C of $Re = 9.34 \times 10^4$. It is well known that the onset of vortex breakdown is relatively insensitive to the value of Reynolds number. The interaction of vortex breakdown with the leading-region of the impingement plate, the large-scale features of the distortion are expected to be governed primarily by inviscid phenomena, though, of course, the development of the surface boundary layer along the plate and details of possible eruption processes may exhibit a sensitivity to Reynolds number.

Preliminary experiments involved dye injection, in order to determine the location and general structure of vortex breakdown. Moreover, dye was also used to determine the hysteresis of breakdown location as a function of unsteady variations of angle-of-attack. Dye was allowed to seep through a hole on the leeward side of the apex. It marked the centerline of the vortex, and at the onset of breakdown, the width of the dye region increased abruptly. For the case of vortex breakdown from the stationary wing in absence of the impingement plate, well known, low frequency excursions of the vortex breakdown position about an averaged value were observed. In order to account for these excursions, images of the breakdown location were captured at instants corresponding to

the maximum value of breakdown location X_b and the minimum value of X_b. Three independent experiments were performed in order to determine three values of minimum and three values of maximum X_b. Then, these values were averaged to obtain the values of X_b shown in the plots herein. The maximum deviation from the average value of X_b was 0.076C at the minimum value of angle-of-attack α = 28° and decreased to a substantially smaller value of 0.028C at the maximum angle-of-attack α = 45°. On the other hand, the presence of the impingement plate stabilized the location of vortex breakdown, and a maximum deviation of 0.03C was observed for all values of α. The uncertainty in detection of the vortex breakdown position was insignificant relative to the aforementioned deviations, which are inherent features of the vortex unsteadiness. Images were recorded on high-resolution film, then digitized at 125 pixels/mm in order to determine the breakdown position. The parallax effect was accounted for by use of simple trigonometric relations.

High-image-density particle image velocimetry was employed to determine the instantaneous flow patterns. These patterns were characterized over two principal planes, as illustrated in the schematic of Figure 1. One plane was coincident with the centerline of the vortex. The other plane was parallel to the leading-edge of the plate; it provided a representation of the vortex structure in the crossflow plane. These two locations of the laser sheet are referred to as side and end views respectively.

Figure 2 shows an overview of the lasers, optical components and camera systems employed for the laser sheets corresponding to the side and end views. For the side view, an Argon-ion laser beam of 1 mm diameter passed through an optical train, and eventually impinged upon a rotating polygonal mirror, which had eight facets. This

configuration generated a laser beam scanning at a rate of 75 Hz. This scanning beam generated a laser sheet, which was coincident with the centerline of the vortex breakdown. The sheet appears as a bold line in the plan view. Seeding of the flow involved metallic-coated particles, which had a nominal diameter of 14 microns. They were illuminated by the scanning laser beam, and their images were recorded using a film-based camera. The camera was operated at a shutter speed of 1/15 sec and an f-stop, f = 5. High-resolution film of 300 lines/mm was used. In order to avoid issues associated with directional ambiguity, a bias mirror was located immediately in front of the camera lens. This arrangement provided positive displacements of all particle image patterns recorded on the film. The film was digitized at a resolution of 125 pixels/mm, then interrogated to determine the instantaneous velocity field.

On the other hand, for the end view imaging, which was done independently, a technique of DPIV was employed. The laser illumination source was a double-pulsed Yag laser, and the laser sheet was generated by a cylindrical lens. Images were recorded on a digital camera having a resolution of 1008 × 1018 pixels. The image acquisition was at a rate of 30 frames per second, corresponding to 15 pairs of images per second. A frame-to-frame correlation technique was employed to calculate the velocity field.

For the case of the film-based PIV technique, the area of the interrogation corresponded to 90 pixels × 90 pixels, and approximately 40-60 particle images were located within this area. For the DPIV approach, the interrogation area was 32 pixels × 32 pixels; it contained approximately 15 to 25 particle images. In accord with the Nyquist criterion, a 50% overlap was employed for successive interrogations.

For the side view (film-based PIV approach), the magnification was M = 1:4.52, which gave an effective grid size of 1.63 mm × 1.63 mm on the physical plane of the laser sheet. Images of the flow pattern were acquired at a framing rate of 1.55 frames/sec. Concerning the end view (DPIV technique), the magnification was M = 1:7.72, which corresponded to an effective grid size of 2.07 mm × 2.07 mm in the plane of the laser sheet.

The field of view of the acquired images was 151.3 mm × 97.3 mm for the side view and 124.4 × 126.5 mm for the end view. The total number of velocity vectors was approximately 5,734 for the side view and 3,782 for the end view. A Gaussian filter with a factor p = 1.3 was applied to calculate the velocity field. No additional filtering of the data was carried out.

As described in the investigation of Özgören *et al.* (2000), averaged representations of velocity and vorticity were obtained by averaging images of the flow pattern. In order to obtain averaged images, a total of N images were averaged at a given location (x, y). The average values of velocity and vorticity, as well as the root-mean-square values of velocity, were obtained according to the following equations:

$$< V > = \frac{1}{N} \sum_{n=1}^{N} V_n(x,y) \tag{1a}$$

$$< \omega > = \frac{1}{N} \sum_{n=1}^{N} \omega_n(x,y) \tag{1b}$$

$$v_{rms} = \left\{ \frac{1}{N} \sum_{n=1}^{N} [V_n(x,y) - < v(x,y) >]^2 \right\}^{1/2} \tag{1c}$$

$$w_{rms} = \left\{ \frac{1}{N} \sum_{n=1}^{N} [w_n(x,y) - < w(x,y) >]^2 \right\}^{1/2} \tag{1d}$$

3. ONSET AND DEVELOPMENT OF VORTEX BREAKDOWN WITH AND WITHOUT IMPINGEMENT PLATE

Stationary wing. Figure 3a shows the onset of vortex breakdown X_b normalized the by wing chord C as a function of static angle-of-attack α. For these experiments, the value of α was adjusted, the flow was allowed to attain equilibrium, and the value of the vortex breakdown position X_b was determined via the dye injection technique described in Section 2. For all experiments, the plate was located at a distance of y_p /C = 0.14 above the pitching axis of the wing. This location provided direct impingement of the central portion of the vortex breakdown region upon the leading-edge of the plate at an angle-of-attack $\alpha = 24°$. As indicated in Figure 3a, when the plate is present, and the angle-of-attack is lower than approximately $\alpha = 32°$, the vortex breakdown position is advanced in the upstream direction. That is, it occurs at a lower value of X_b/C, relative to the case without the plate. Over this range of α, the offset between the centerline of the vortex and the leading-edge of the plate is minimal, as indicated in the images of averaged vorticity in the left column of Figure 3b. In these images, the onset of vortex breakdown *vb* is defined to occur at the leading-edges of the contours of constant positive and negative vorticity. This definition is in accord with the theoretical basis of Brown and Lopez (1990), whereby the onset of breakdown corresponds to a switch in sign of azimuthal vorticity. At $\alpha = 24°$, vortex breakdown does not occur within the field of view when the plate is absent. In presence of the plate, it is located near the trailing-edge. At $\alpha = 30°$, breakdown occurs just downstream of the trailing-edge without the plate. With the plate present, it moves out of the field of view to a location well upstream of the trailing-edge.

The upstream advancement of the breakdown position relative to the case of no edge, evident by comparison of the left and right columns of Figure 3b, is in accord with the observations of Reynolds & Abtahi (1987) and Gursul & Yang (1994), who placed a probe and a moderate-sized cylinder along the centerline of the vortex. Furthermore, Akilli *et al.* (2001) found that a wire two orders of magnitude smaller than the vortex diameter could have a similar effect when oriented orthogonal to, but coincident with, the centerline of the vortex. All of these observations are related to the upstream transmission of disturbances through the vortex, as described in previous theoretical works summarized by Akilli *et al.* (2001). These works include Leibovich (1984), Wang & Rusak (19978) and Rusak *et al.* (1998).

On the other hand, for higher values of α, $\gtrsim 32°$ in Figure 3a, the difference between values of X_b/C with and without the plate is relatively small. For $\alpha > 32°$ in Figure 3a, the offset between the vortex centerline and the plate becomes large (compare $\alpha = 35°$ and $\alpha = 30°$ in Figure 3c). As a consequence, the upstream transmission of information is not as effectively accomplished. Furthermore, the onset of breakdown moves closer to the apex of the wing at larger α; in this limiting case, breakdown seems to be primarily controlled by the vortex characteristics immediately downstream of the apex.

The averaged images of Figures 3b were obtained from instantaneous images of the type shown in Figure 3c. The left column of images corresponds to cases with the plate and the right column to the cases without the plate. Consider, first of all, the images in the left column. At the lowest angle-of-attack $\alpha = 24°$, the onset of vortex breakdown occurs immediately downstream of the trailing-edge of the wing, and patterns of

instantaneous positive (thick white line) and negative (thin white line) indicate a staggered arrangement of vorticity concentrations that represent the helical mode of instability. Subsequent interaction with the leading-edge of the plate yields substantial distortion. At $\alpha = 30°$, vortex breakdown occurs at a significant distance upstream of the trailing-edge of the plate and is not evident in the field of view. Large-scale clusters of vorticity concentrations are evident as they interact with the plate. Finally, at $\alpha = 35°$, the onset of breakdown (not visible) occurs even further upstream. Furthermore, the wakelike region of breakdown is shifted upward, such that almost the entire pattern of vorticity is above the plate. For the images in the right column of Figure 3c, corresponding to the case without the impingement plate, vortex breakdown does not occur within the field of view at $\alpha = 24°$. It is located well downstream of the trailing-edge of the wing (compare to the image of Figure 3b). Only low-level, small-scale concentrations of vorticity are evident. At $\alpha = 30°$, breakdown does occur, and it gives rise to a staggered arrangement of vorticity concentrations, which are similar in concept to those at $\alpha = 24°$ with the plate present. At $\alpha = 35°$, the onset of vortex breakdown is a substantial distance upstream of the trailing-edge of the wing. The wake-like structure of the vortex breakdown region is associated with larger-scale concentrations of vorticity.

Pitching wing. From the plot of Figure 3a, along with the images shown in Figures 3b and 3c, it is evident that the presence of the impingement plate can substantially alter the onset of vortex breakdown for the case of the stationary wing. An important issue is whether this type of influence extends to vortex breakdown generated from a pitching delta wing.

Figure 4 shows the instantaneous location of vortex breakdown $X_b(t)$ normalized by the wing chord C as a function of the instantaneous angle-of-attack $\alpha(t)$ for cases without and with the impingement plate. In absence of a plate, it is well known that the onset of vortex breakdown lags the motion of the wing, and the end consequence is the generation of the type of dynamic hysteresis loops of vortex breakdown shown in Figure 4. These loops are shown for three values of mean angle-of-attack $\overline{\alpha}$ = 20°, 24° and 30°. At the two lowest values of $\overline{\alpha}$ = 20° and 24°, data were not acquired during a portion of the downstroke. Remarkable is the fact that, for all values of $\overline{\alpha}$, the difference between the instantaneous locations of vortex breakdown $X_b(t)/C$ with and without the plate is relatively small. A discernible exception occurs at the highest values of $\alpha(t)$ at the largest mean angle-of-attack $\overline{\alpha}$ = 30°. It is therefore evident that the dynamic nature of the vortex breakdown process and thereby the phase lag are not significantly influenced by presence of the impingement plate, at least in a general sense.

Figures 5a and 5b represent respectively cases with and without the impingement plate. They show instantaneous patterns of vorticity corresponding to dynamic variations of angle-of-attack $\alpha(t)$ for a mean angle-of-attack $\overline{\alpha}$ = 30°. In each layout, images are shown for three successive instants during the oscillation cycle. Moreover, in each of the images of Figures 5a and 5b, the instantaneous angle-of-attack $\alpha(t)$ is indicated at the upper right corner, as is the dimensionless time $t^* = tU_\infty/C$. Consider, first of all, the top image of Figure 5a, which corresponds to α = 30°. The location of vortex breakdown *vb* is within the field of view and near the trailing-edge. The centerline of the vortex breakdown region, which is defined by patterns of positive and negative azimuthal vorticity, is slightly above the leading-edge of the plate. In the second image,

corresponding to $\alpha = 39.5°$, the centerline of the vortex breakdown is located above the plate, and in the third image at $\alpha = 23.4°$, it is approximately aligned with the leading-edge. These images can be compared with those of Figure 5b, which represent cases without the plate. It is evident that the onset of vortex breakdown, when it is detectable, is located slightly further downstream for the case without the impingement plate.

The issue arises as to the insensitivity of the dynamic variations of the vortex breakdown position $X_b(t)$ versus angle-of-attack $\alpha(t)$; that is, these variations of $X_b(t)$ are very similar for cases with and without the impingement plate. During a given pitching cycle, the offset of the vortex centerline with respect to the leading-edge of the plate varies substantially, as shown in Figure 5a for the case of the impingement plate. In essence, this means that the location of vortex breakdown X_b does not have the opportunity to relax to an equilibrium state, unlike the aforementioned case of vortex breakdown from a stationary wing incident upon a plate. That is, the vortex dynamics appears to be controlled primarily by the wing motion, rather than by the upstream influence from the region of the impingement plate.

These observations of the vortex breakdown characteristics for the case of the pitching wing provide a basis for assessment of the corresponding end views of the vortex breakdown/plate interaction, which are addressed in the next section.

4. EVOLUTION OF VORTEX-PLATE INTERACTION IN CROSSFLOW PLANE: PATTERNS OF VORTICITY

Patterns of instantaneous vorticity ω and averaged vorticity $<\omega>$, as well as corresponding velocities V and $<V>$, are shown in the images of Figures 6 and 7 for the crossflow planes defined in the schematics of Figures 1 and 2. The streamwise location

of the crossflow laser sheet is designated by the thin, vertical white line in Figure 5a. The angle-of-attack α and the dimensionless time t^* elapsed during the pitching cycle are designated on each set of images. Furthermore, the location x_s of vortex breakdown for each image set can be determined for each value of α from Figure 4.

Figures 6a and 6b directly compare the contours of constant instantaneous vorticity ω (left column) and averaged vorticity $<\omega>$ (right column) for successive values of instantaneous angle-of-attack $\alpha(t)$ and dimensionless time $t^* = tU/C$. Images of averaged vorticity $<\omega>$ were obtained by considering a total of four images at each respective phase of the oscillation cycle of the pitching delta wing. These images, which emphasize the large-scale, repetitive vortical structures, are intended to serve as a guide for interpretation of instantaneous patterns of ω. Contours of $<\omega>$ clearly show the positive (thick white line) and negative (thin white line) projections of streamwise vorticity for the two principal vortices and their distortion upon encounter with the plate. Examination of the images of Figures 6a and 6b reveal a number of phenomena, as described in the following.

4.1 GENERATION OF CONCENTRATIONS AND LAYERS OF SECONDARY VORTICITY ADJACENT TO SURFACE OF PLATE

Considering the images of Figures 6a and 6b, especially the instantaneous representations above the surface of the plate, a concentration of positive vorticity immediately adjacent to the surface of the plate often appears beneath a corresponding concentration of negative vorticity, and conversely. These concentrations appear somewhat randomly in spatial position from one image to the next. . In concept, the generation of a vorticity concentration from a solid surface due to a concentration of vorticity of opposite sign

above the surface is well documented in a range of investigations, as summarized by Doligalski *et al.* (1994).

On the other hand, in the region below the plate, well-defined layers of distributed vorticity are clearly evident when a significant fraction of the incident vortex system is partitioned below the plate. That is, at angle-of-attack $\alpha = 25.6°$, well-defined layers of vorticity are evident along the lower surface of the plate and, in fact, these layers persist in subsequent images in Figures 6a and 6b. Such layers are clearly evident in images of both ω and $< \omega >$.

4.2 SPACING OF MAJOR CONCENTRATIONS OF VORTICITY ABOVE AND BELOW THE PLATE

Consider the images of averaged vorticity $< \omega >$ in Figures 6a and 6b. As the value of dimensionless time t^* increases, an increasing fraction of the incident vorticity concentrations is partitioned to the region beneath the plate. For all values of $t^* = tU/C$, the distance between these concentrations remains relatively large. On the other hand, the remaining portions that are partitioned to the region above the plate move relatively close together at larger values of t^*. This difference in spacing between vortices on the upper and lower sides of the plates is apparently due to vortex induction. The coexistence of the actual vortices with their corresponding image vortices within the plate results in a tendency for the upper vortex system to move together and the lower system to move apart. This effect was suggested in the limiting situation of a stationary wing and plate in the investigation of Mayori & Rockwell (1994). In addition, the numerical simulation of Gordnier & Visbal (1997), for a stationary wing and plate system, shows a similar difference in spacing between the partitioned vortices on the upper and lower sides of the plate.

4.3 SIMULTANEOUS PRESENCE OF SMALL- AND LARGE-SCALE CONCENTRATION OF VORTICITY

The instantaneous patterns of vorticity of Figures 6a and 6b, especially those extending from $t^* = 2.55$ to 4.16, show small-scale concentrations of vorticity of opposite sense intermingled with the large-scale concentrations. In the averaged images, especially those extending from $t^* = 2.55$ to 3.18, it is evident that the small-scale vorticity concentrations of opposite sense exist in the region between the two large-scale, primary vortices. The origin of these small-scale vortical structures may be due to two sources. First of all, prior to encounter with the plate, concentration of vorticity may arise about the periphery of each large-scale vortex from the three-dimensionality of the breakdown process. Second, periodic eruption of the surface boundary layer induced by the large-scale vortex adjacent to the plate can lead to successive, small-scale vorticity concentration, in the manner described by Gordnier & Visbal (1995) and Cipolla & Rockwell (1998).

5. EVOLUTION OF VORTEX-PLATE INTERACTION IN CROSSFLOW PLANE: PATTERNS OF VELOCITY

The images of Figures 7a and 7b show instantaneous V and averaged $< V >$ patterns of velocity vectors corresponding to the contours of constant vorticity exhibited in Figures 6a and 6b. The major features of these patterns are described in the following.

5.1 HALF-SADDLE DISTRIBUTIONS OF VELOCITY: CONVERGENCE OF PATTERNS OF VELOCITY VECTORS AT THE PLANE OF SYMMETRY.

Consider the patterns of averaged velocity $< V >$ shown in the right columns of Figures 7a and 7b. At the highest angle-of-attack $\alpha = 32.7°$, which occurs at $t^* = 2.55$, the large-scale vortex system is associated with a pattern of velocity vectors that converges at the vertical plane of symmetry of the plate. According to topological concepts based on

critical point theory, this pattern corresponds to a half-saddle point at the locations where the corresponding streamlines would meet at an elevation immediately adjacent to the plate. Away from the surface of the plate, the velocity vectors are directed upwards. This general pattern along the upper surface of the plate persists, with some irregularities, to $\alpha = 20°$, corresponding to $t^* = 4.16$. Over the time span from $t^* = 2.55$ to 4.16, the saddle point drifts to the left, then to the right at $t^* = 4.82$. This observation suggests a low frequency variation of the saddle point location. At larger values of $\alpha = 20.7°$ and 22.7°, a saddle point adjacent to the surface of the plate is not so well-defined.

5.2 STAGNATION REGIONS OF PATTERNS OF VELOCITY VECTORS: DIVERGENCE OF PATTERNS AT PLANE OF SYMMETRY

As increasing fractions of the incident vortex system are partitioned below the plate, a stagnation region forms along the lower surface of the plate. It is located midway between the centers of the swirl patterns of velocity vectors. This stagnation pattern is first evident at $\alpha = 25.6°$ and becomes more sharply defined at subsequent values of α in Figures 7a and 7b. To be sure, the corresponding streamline pattern would also exhibit a half-saddle point analogous to that observed along the upper surface of the plate; on the lower side of the plate, the corresponding streamlines are directed away from, rather than towards, the vertical plane of symmetry. In this section, this region is referred to as a stagnation region, since it represents a region of very low velocity magnitude, relative to that occurring on the upper side of the plate.

5.3 INSTANTANEOUS DEVIATIONS FROM THE AVERAGED PATTERNS OF VELOCITY

The concepts of half-saddle point and a stagnation region, which were defined on the basis of the averaged images shown in the right columns of Figures 7a and 7b, are, in some cases, discernible in the corresponding patterns of instantaneous velocity as well.

The patterns of instantaneous velocity can exhibit substantially more complex forms, especially for the region above the plate. For example, at $\alpha = 25.6°$, the instantaneous pattern of V does not exhibit a single, well-defined half-saddle. Rather, the simultaneous presence of a number of vorticity concentrations along the plate produces several adjacent swirl patterns of velocity vectors. Additional patterns of distortion are shown at the other values of α in the left columns of Figures 7a and 7b. The buffet model of Breitsamter & Laschke (1994, 1998) requires the instantaneous vertical component of velocity v, in conjunction with the instantaneous out-of-plane velocity component w at representative spatial locations along the surface of the plate, with the assumption of no significant flow separation from the surface. It is evident that the large variation with time t^* of the instantaneous patterns of Figures 7a and 7b will yield substantial fluctuations of the v component of the buffet velocity. Moreover, the spanwise correlation of the v component fluctuations is not necessarily dictated by a single length scale, e.g., the spanwise distances between the largest scale vortical structures. The patterns of velocity suggest multiple scales of the swirl patterns of velocity vectors.

6. INTERRELATIONSHIP BETWEEN PATTERNS OF VORTICITY AND VELOCITY: CONSEQUENCE FOR BUFFET VELOCITY DISTRIBUTIONS

Taken together, the patterns of velocity and vorticity described in Figures 6 and 7 have important consequences for the vortex-induced loading of the surface of the plate. As shown in the preceding sections, the type of imaging performed in this investigation allows acquisition of a sequence of velocity images, then extraction of the spatial distribution of vertical, or normal, velocity as a function of time. The potential for employing this velocity component as an input to a buffet model is described in Section

1.3. In turn, these patterns of velocity can be directly compared to the corresponding patterns of vorticity, in order to reveal how distortion of the vortical structures is related to the patterns of vertical buffet velocity. Our present considerations are twofold. First of all, the aim is to assess the relationship between the instantaneous distributions of vorticity and the corresponding instantaneous patterns of vertical velocity. Second, the sensitivity of the spatial distributions of buffet velocity to distance from the surface of the plate will be addressed.

6.1 EFFECT OF VORTEX PARTITIONING ON PATTERNS OF VORTICITY IN RELATION TO PATTERNS OF VERTICAL BUFFET VELOCITY

Figure 8 shows a direct comparison of patterns of instantaneous vorticity ω and vertical velocity v at two critical instants during the vortex-plate interaction. The top row corresponds to the situation where the vortex system is located above the surface of the plate, and the bottom row of images to the scenario where the incident vortices have been split upon encounter with the plate. In the image at the upper left, large-scale vortical structures are generally discernible and, between them, smaller-scale concentrations of positive and negative vorticity are evident. The corresponding distribution of vertical velocity at the upper right indicates a substantial magnitude of upward (positive) vertical velocity in the region between the two large-scale concentrations of vorticity. Near the left and right boundaries of the image, a region of high downward vertical velocity exists above the surface of the plate. It is evident that the small-scale concentrations of vorticity between the large-scale vortical structures do not produce local changes in sign of the vertical buffet velocity; rather, its sign everywhere corresponds to the induced velocity between the largest vortical structures.

For the case where the vortex system is split upon its encounter with the plate, as shown in the bottom row of images of Figure 8, a distinctly different pattern of vertical velocity distribution exists. Along the upper surface of the plate, the vertical velocity is positive upward, due primarily to the induced updraft between the two concentrations of vorticity. Only very low-level regions of negative vertical velocity exist on either side of this positive region. This contrasts with the image at the upper right of Figure 8. It is therefore evident that partitioning of the incident vortex system, which is represented by the lower set of images, yields a region of large vertical velocity between them, and insignificant vertical velocity exterior to them. Along the lower surface of the plate, a broadly distributed, lower level region of upward (positive) vertical velocity is evident in the central portion of the image and regions of negative vertical velocity exist near the boundary of the image. This type of pattern does not exist along the lower surface of the plate for the case where the vortex system remains above the surface of the plate, as in the top row of images.

6.2 VARIATION OF DISTRIBUTIONS OF VERTICAL BUFFET VELOCITY WITH DISTANCE FROM SURFACE OF PLATE

It is envisioned that a typical model for the buffet loading will require the distribution of buffet velocity along a constant elevation from the surface. The issue then arises as to the sensitivity of the velocity magnitude, as well as its overall distribution, to the displacement from the plate surface. Figure 9a shows the instantaneous distribution of vertical buffet velocity for the case where the vortex system remains above the plate. Four horizontal white lines designate reference heights for evaluation of the velocity distribution. They are indicated as y = 70, 75, 80, and 85. In the plots shown at the

bottom of Figure 9a, the distributions of the vertical buffet velocity v versus z have a generally similar form, but with significantly different peak magnitudes.

Figure 9b represents the case where the incident vortex system is split by the plate. For both the regions above and below the plate, the general form of the vertical velocity distributions, as a function of distance from the surface of the plate, is again similar, but with differing magnitudes. Above the plate, for example, the peak positive value of buffet velocity at y = 85 substantially exceeds that at y = 70. Below the plate, along the line closest to the plate, i.e., y = 55, the magnitude of v becomes very small and the general form of the distribution is substantially distorted, relative to the distributions of y = 50 though 40.

Based on these observations of Figures 9a and 9b, it appears that a zonally-averaged distribution of buffet velocity might be an appropriate representation of its effective magnitude and distribution. That is, a spatially-averaged vertical velocity over a finite horizontal band would alleviate limitations associated with consideration along a single elevation from the surface of the plate.

7. CONCLUDING REMARKS

Techniques of high-image-density particle image velocimetry have led to the instantaneous and averaged patterns of velocity and vorticity associated with vortex breakdown, and its interaction with a stationary impingement plate. Vortex generation from both a stationary and a pitching delta wing has been considered. Images of the flow have been acquired in two principal planes: a plane coincident with the axis of the leading-edge vortex and a plane parallel to the leading-edge of the impingement plate. Representations of the flow in these planes provide insight into the streamwise evolution

of the vortex, including the occurrence of vortex breakdown and its interaction with the plate.

The case of the stationary delta wing and a stationary plate has served as a reference for characterization of the vortex-plate interaction. The locations of vortex breakdown, both in presence of the impingement plate and in absence of the plate, have been determined for incremental changes in angle-of-attack of the wing. It is demonstrated that, over a substantial range of angle-of-attack, the streamwise location of vortex breakdown is substantially different for the case with and without the impingement plate. This observation is conceptually similar to previous experiments, which have demonstrated an upstream movement of the onset of vortex breakdown due to placement of a probe, moderate-sized cylinder, or very small wire within or across the vortex. Taken together with the present results, it is clear that disturbances, which originate at the location of the leading-edge of the plate propagate upstream through the noncolumnar vortex to alter the steady-state location of vortex breakdown. This view is supported by the theoretical findings described in Section 3.

When the wing is subjected to pitching motion, the induced phase shift between the wing motion and the onset of vortex breakdown induces hysteresis loops of vortex breakdown position versus angle-of-attack. Remarkably, these loops are generally similar for cases with and without the impingement plate. In other words, despite the fact that wing motion induces a change in the vertical offset of vortex breakdown with respect to the leading-edge of the plate, the time variation of the axial location of breakdown along the vortex core is similar to the variation in absence of a plate. The consequence is essentially equivalent hysteretic-loops of breakdown position versus angle-of-attack are

generated. This equivalence of cases with and without the impingement plate is apparently due to the fact that the location of vortex breakdown never comes to an equilibrium state during its encounter with the leading-edge of the plate, due to the continuous variations of the vertical offset of the vortex centerline.

When the wing undergoes pitching motion, the vertical position of the incident vortex(ices) upon the plate, and thereby the mechanism of vortex-plate interaction, varies substantially during the pitching cycle. The incident vortex system is partitioned into two subsystems above and below the plate over a substantial range of angle-of-attack. The two vortices above the plate tend to merge together, while those below the plate move apart. In addition, a given vortex adjacent to the plate can induce either a distributed vorticity layer, or a vorticity concentration, depending upon the scale and circulation of the primary vortex.

These features of the partitioned vorticity field are also interpreted in terms of space-time distributions of vertical (transverse) velocity above and below the plate. According to the model of Breitsamter & Laschke (1994a,b; 1998), which is described in Section 1.3, these velocity distributions adjacent to the top and bottom surfaces of the plate can eventually be considered to determine the buffet-induced loading, provided the corresponding streamwise velocities are accounted for, and the effects of flow separation are not significant. The focus of the present investigation is on determination of the basic classes of patterns and topologies of both averaged and instantaneous fields of velocity vectors, in relation to fundamental types of vorticity patterns. Furthermore, the magnitude and form of the instantaneous distributions of velocity are assessed as a function of distance from the surface of the plate. The magnitude of the vertical

component of the buffet velocity distribution is found to be sensitive to the elevation from the top or bottom surface of the plate, but the overall form of the distributions is generally preserved. It is recommended that a zonally-averaged distribution of velocity be considered in order to characterize the normal buffet velocity. This aspect could be accounted for in the next generation of this work, which could employ a cinema version of particle image velocimetry to determine the space-time variations of both the vertical and horizontal velocity fields as a basis for implementation of a model for the buffet loading.

ACKNOWLEDGMENTS

The support of the Air Force Office of Scientific Research under Contract No. F49620-99-1-0011, monitored by Dr. Steven Walker, is gratefully acknowledged. One of the authors, Professor Besir Sahin, would like to thank the Scientific and Technical Research Council of Turkey (TUBITAK) and NATO for their financial support.

REFERENCES

AKILLI, H., SAHIN, B. & ROCKWELL, D. 2001 Control of vortex breakdown by a transversely-oriented wire. *Physics of Fluids* **13**, 452-463.ASHLEY, H., ROCK, S. M., DIGUMARTHI, R. V., CHANEY, K. & EGGERS Jr., A. J. 1994 Active control for fin buffet alleviation. WL-TR-93-3099, Wright Patterson AFB, OH, January.

ATTA, R. & ROCKWELL, D. 1987 Hysteresis of vortex development and breakdown on an oscillating delta wing. *AIAA Journal* **25**, 1512-1513.

ATTA, R. & ROCKWELL, D. 1990 "Leading-Edge Vortices on a Pitching Delta Wing. *AIAA Journal* **28**, 995-1004.

BEAN, E. G. & WOOD N. J. 1993 An experimental investigation of twin fin buffeting and suppression. AIAA Paper No. 93-0054, 31st Aerospace Sciences Meeting and exhibit, January 11-14, Reno, NV.

BEUTNER, T. J., BAUST, H. N. & MEYERS, J. F. 1995 Doppler global velocimetry measurements of a vortex-tail interaction. Proceedings of the International Symposium on Flow Visualization, 7th, Seattle, ed. J. P. Crowder, pp. 418-423, New York: Begell House.

BREITSAMTER, C. & LASCHKA, B. 1994a Turbulent flow structure associated with vortex-induced fin buffeting. *Journal of Aircraft* **31**,773-781

BREITSAMTER, C. & LASCHKA, B. 1994b Turbulent flowfield structure associated with fin buffeting around a vortex-dominated aircraft configuration at sideslip. 19th Congress of the International Council of the Aeronautical Sciences, Anaheim, CA, September, ICAS-94-4.3.2, **I**, 768-684.

BREITSAMTER, C. & LASCHKA, B. 1998 Fin buffet pressure evaluation based on measured flowfield velocities. *Journal of Aircraft* **35**, 806-815.

BROWN, G. L. AND LOPEZ, J. M. 1990 Axisymmetric vortex breakdown. Part 2: Physical mechanisms. *Journal of Fluid Mechanics* **221**, 553-576.

CANBAZOGLU, S., LIN, J.-C., WOLFE, S. & ROCKWELL, D. 1995a Buffeting of a fin: Distortion of the incident vortex. *AIAA Journal* **33**, 2144-2150.

CANBAZOGLU, S., LIN, J.-C., WOLFE, S. & ROCKWELL, D. 1995b Buffeting of a fin: Streamwise evolution of flow structure. *AIAA Journal of Aircraft* **33**, 85-190.

CIPOLLA, K. M. & ROCKWELL, D. 1998 Small-scale vortical structures in crossflow plane of a rolling delta wing. *AIAA Journal* **36**, 2276-2278.

DENG, Q. & GURSUL, I. 1997 Vortex breakdown over a delta wing with oscillating leading edge flaps. *Experiments in Fluids* **23**, 347-352.

DOLIGALSKI, T. L., SMITH, C. R. & WALKER, J. D. A. 1994 Vortex interactions with walls. *Annual Review of Fluid Mechanics* **26**, 573-616.

FERMAN, N. A., PATEL, S. R., ZIMMERMAN, N. H. & GERSTENKORN, G. 1990 A unified approach to buffet response of fighter aircraft empennage. *AGARD/NATO 70th Structures and Materials Meeting,* Sorento, Italy, 2-1–2-15.

GEE, K., MURMAN, S. M. & SCHIFF, L. F. 1995 Computational analysis of F/A-18 tail buffet. AIAA Paper No. 95-3440.

GREENWELL, D. I. & WOOD, N. J. 1994 Some observations on the dynamic response to wing motion of the vortex burst phenomenon. *Aeronautical Journal* February, 49-59.

GORDNIER, R. E. & VISBAL, M. R. 1995 Instabilities in the shear layer of delta wings. AIAA Paper 95-2281, June.

GORDNIER, R. E. & VISBAL, M. R. 1997 Numerical simulation of the impingement of a streamwise vortex on a plate. AIAA Paper No. 97-1781, 28th AIAA Fluid Dynamics Conference, 4th AIAA Shear Flow Control Conference, June 29-July 2, Snowmass, CO. Also see 1999 *International Journal of Computational Fluid Dynamics*, **12**, 49-66.

GURSUL, I. 2000 A proposed mechanism for the time lag of vortex breakdown location in unsteady flows. AIAA Paper No. 2000-0787, 38th Aerospace sciences Meeting and Exhibit, 10-13 January, Reno, NV.

GURSUL, I. & YANG, H. 1994 Vortex breakdown over a pitching delta wing. AIAA Paper 94-0536, 32nd Aerospace Sciences Meeting and Exhibit, January, Reno, NV.

GURSUL, I. & YANG, H. 1995 On fluctuations of vortex breakdown location. *Physics of Fluids* **7**, 229-231.

GURSUL, I. & XIE, W. 2000 Interaction of vortex breakdown with an oscillating fin. AIAA Paper 2000-0279, 38th Aerospace Sciences Meeting and Exhibit, January, Reno, NV.

HUTTSELL, L. J., TINAPPLE, J. A. & WEYER, R. M. 1997 Investigation of buffet loading on a scaled f-15 twin tail model. AGARD Structures and Materials Panel Workshop, October, Denmark.

KANDIL, O. A., SHETA, E. F. & MASSEY, S. J. 1995 Buffet responses of a vertical tail in vortex breakdown flows. AIAA paper No. 95-3464.

KANDIL, O. A. & SHETA, E. F. 1998 Coupled and uncoupled bending-torsion responses of twin-tail buffet. *Journal of Fluids and Structures* **12**, 677-701.

KUESSNER, H. G. 1954 A general method for solving problems of the unsteady lifting surface theory in a subsonic range. *Journal of the Aeronautical Sciences* **21**, 17-26.

LEE, B. H. K. 2000 Vertical tail buffeting of fighter aircraft. *Progress in Aerospace Sciences* **36**, 193-279.

LEE, B. H. K. & TANG, F. C. 1992 Buffet load measurements on an F/A-18 vertical fin at high angle-of-attack. AIAA Paper 92-2127.

LEE, B. H. K., BROWN, D., TANG, F. C. & PLOSENSKI, M. 1993 Flow field in the vicinity of an F/A-18 vertical fin at high angle-of-attack. *Journal of Aircraft* **30**, 69-74.

LEIBOVICH, S. 1984 Vortex stability and breakdown: Survey and extension. *AIAA Journal* **22**, 1192-1206.

LEMAY, S. P., BATILL, S. M. & NELSON, R. C. 1990 Leading-edge vortex dynamics on pitching delta wing. *Journal of Aircraft* **27**, 131-138.

LOWSON, M. V. 1964 Some experiments with vortex breakdown. *Journal of the Royal Aeronautical Society* **68**, 343.

LUBER, W., BECKER, J. & SENSBURG, O. 1996 The impact of dynamic loads on the design of military aircraft. AGARD-R-815, Florence, Italy, September 4-5, 8-1–8-27.

MAGNESS, C., ROBINSON, O. & ROCKWELL, D. 1993 Instantaneous topology of the unsteady leading-edge vortex at high angle-of-attack. *AIAA Journal* **31**, 1384-1391.

MARTIN, C A. & THOMPSON, D. H. 1991 Scale Model Measurements on Fin Buffet Due to Vortex Bursting on F/A-18", AGARD/CP497.

MAYORI, A. & ROCKWELL, D. 1994 Interaction of a streamwise vortex with a thin plate: a source of turbulent buffeting. *AIAA Journal* **32**, 2022-2029.

MIAU, J. J., CHANG, R. C., CHOU, J. H., & LIN, C. K. 1992 Nonuniform motion of leading-edge vortex breakdown on ramp pitching delta wings. *AIAA Journal* **30**, 1691-1702.

MOSES, ROBERT W. & HUTTSELL, LAWRENCE 2000 Fin buffeting features of an early F-22 model. AIAA Paper No. 2000-1695.

MYOSE, R. Y., LEE, B. K., HAYASHIBARA, S. & MILLER, L. S. 1997 Diamond, cropped, delta and double-delta wing vortex breakdown during dynamic pitching. *AIAA Journal* **35**, 567-569.

ÖZGÖREN, M., SAHIN, B. & ROCKWELL, D. 2000 Perturbations of a delta wing: control of vortex breakdown and buffeting. Submitted to *AIAA Journal of Aircraft.*

REYNOLDS, G. A. & ABTAHI, A. A. 1987 Instabilities in leading-edge vortex development. AIAA Paper 87-2424, Applied Aerodynamics and Atmospheric Flight Dynamics Conference, Monterey, CA.

RIZK, Y. M. & GEE, K. 1992 Unsteady simulation of viscous flow field around f-18 aircraft at large incidence. *Journal of Aircraft* **29**, 986-992.

RIZZETTA, D. P. 1996 Numerical simulation of the interaction between a leading-edge vortex in a vertical tail. AIAA Paper No. 96-2012. Presented at AIAA Fluid Dynamics Conference, 27th, New Orleans, LA.

ROCKWELL, D. 1993 Three-dimensional flow structure on delta wings at high angle-of-attack: Experimental concepts and issues. AIAA Paper No. 93-0550. Presented at 31st Aerospace Science Meeting & Exhibit, January 11-14, Reno, NV.

SAHIN, B., AKILLI, H., LIN, J.-C. & ROCKWELL, D. 2000 Vortex breakdown-edge interaction: Consequence of edge oscillations. *AIAA Journal* (in press).

SHAH, G. H. 1991 Wind-tunnel investigation of aerodynamic and tail buffet characteristics of leading-edge extension modifications to the F/A-18. AIAA Paper 91-2889.

SHETA, ESSAM F., HARRAND, VINCENT J. & HUTTSELL, LAWRENCE J. 2000 Active vortical flow control for alleviation of twin-tail buffet of generic fighter aircraft. AIAA 38th Aerospace Sciences Meeting and Exhibit, January 10-13, Reno, NV. AIAA Paper No. 2000-0906.

THOMPSON, S. A., BATILL, S. M. & NELSON, R. C. 1991 Separated flowfield on a slender wing undergoing transient pitching motions. *Journal of Aircraft* **28**, 480-495.

TRIPLETT, W. E. 1983 Pressure measurements on twin vertical tails in buffeting flow. *Journal of Aircraft* **20,** 920-925.

WANG, S. & RUSAK, Z. 1997 The dynamics of a swirling flow in a pipe and transition to axisymmetric vortex breakdown. *Journal of Fluid Mechanics* **340**, 177-223.

RUSAK, Z., WANG, S. & WHITING, C. H. 1998 The evolution of a perturbed vortex in a pipe to axisymmetric vortex breakdown. *Journal of Fluid Mechanics* **366**, 211-237.

WASHBURN, A.E., JENKINS, L. M. & FERMAN, M. A. 1993 Experimental investigation of vortex-fin interaction. AIAA Paper 93-0050.

WENTZ, W. H., Jr. 1987 Vortex-fin interaction on a fighter aircraft. *Proceedings of the AIAA 5th Applied Aerodynamics Conference*, Monterey, CA, AIAA, Washington, D.C., 392-399 (AIAA Paper 87-4909).

WOFFELT, K. W. 1987 Investigation of the movement of vortex burst position with dynamically changing angle of attack for a schematic delta wing in water tunnel with

correlation to similar studies in a wind tunnel. *Aerodynamic and Related Hydrodynamic Studies Using Water Facilities.* AGARD-CP-413.

WOLFE, S., LIN, J.-C. & ROCKWELL, D. 1995a Buffeting of fins: An assessment of surface pressure loading", *AIAA Journal*, Vol. 33, No. 11, pp. 2232-2235.

WOLFE, S., LIN, J.-C. & ROCKWELL, D. 1995b Buffeting at the leading-edge of a flat plate due to a streamwise vortex: Flow structure and surface pressure loading. *Journal of Fluids and Structures* **9**, 359-370.

YANG, H. & GURSUL, I. 1997 Vortex breakdown over unsteady delta wings and its control. *AIAA Journal* **35**, 571-574.

ZIMMERMAN, N. H., FERMAN, M. A,.YURKOVICH, R. N. & GERSTENKORN 1989 Prediction of tail buffet loads for design application. AIAA Paper No. 89-1378.

LIST OF FIGURES

Figure 1: Schematics of delta wing subjected to large-amplitude, low frequency pitching motion about its midchord, which leads to alteration of the structure of the leading-edge vortex, its breakdown, and its impingement upon a stationary plate. Mean and perturbation angles-of-attack are $\bar{\alpha} = 30°$ and $\alpha_o = 10°$ respectively. Reduced frequency is $k = \pi f_e C/U_\infty = 0.74$.

Figure 2: Imaging systems for high-image-density PIV (side view) and DPIV (end view).

Figure 3a: Variation of location of vortex breakdown with static angle-of-attack of stationary wing. Breakdown locations are compared in presence and in absence of impingement plate.

Figure 3b: Contours of averaged vorticity $<\omega>$ in presence of the impingement plate (left column) and in absence of the impingement plate (right column). In presence of the impingement plate, minimum and incremental values of averaged vorticity $<\omega>$ are $\omega_{min} = \pm 1$ sec^{-1} and $\Delta\omega = 0.5$ sec^{-1} respectively. In absence of the impingement plate, minimum and incremental values of averaged vorticity $<\omega>$ are $<\omega_{min}> = \pm 1$ sec^{-1} and $<\Delta\omega> = 0.75$ sec^{-1}.

Figure 3c: Contours of instantaneous vorticity ω in presence of the impingement plate (left column) and in absence of the impingement plate (right column). Minimum and incremental values of instantaneous vorticity ω are $\omega_{min} = \pm 1.5$ sec^{-1} and $\Delta\omega = 0.75$ sec^{-1} respectively for all angles-of-attack in presence of the impingement plate. In absence of the impingement plate, minimum and incremental values of instantaneous vorticity ω for

$\alpha = 24°$ and $30°$ are respectively $\omega_{min} = \pm 1$ sec^{-1} and $\Delta\omega = 0.75$ sec^{-1}, and for $\alpha = 35°$ are $\omega_{min} = \pm 2$ sec^{-1} and $\Delta\omega = 0.75$ sec^{-1}.

Figure 4: Comparison of dynamic hysteresis loops of vortex breakdown as a function of angle-of-attack in presence of the impingement plate and in the absence of the impingement plate. Amplitude of pitching motion is $\alpha_o = 10°$ and reduced frequency is $k = \pi f_e C/U_\infty = 0.74$ for all cases.

Figure 5a: Patterns of positive (thick line) and negative (thin line) vorticity for pitching motion of delta wing in presence of the impingement plate. Minimum and incremental values of instantaneous vorticity are $\omega_{min} = \pm 1.5$ sec^{-1} and $\Delta\omega = 0.75$ sec^{-1} respectively. Mean angle-of-attack of delta wing $\bar{\alpha} = 30°$ and amplitude pitching of motion is $\alpha_o = 10°$. Reduced frequency is $k = \pi f_e C/U_\infty = 0.74$ and dimensionless time $t^* = tU_\infty/C$.

Figure 5b: Patterns of positive (thick line) and negative (thin line) vorticity for pitching motion of delta wing in absence of the impingement plate. Minimum and incremental values of instantaneous vorticity are $\omega_{min} = \pm 1.5$ sec^{-1} and $\Delta\omega = 0.75$ sec^{-1} respectively. Mean angle-of-attack of delta wing $\bar{\alpha} = 30°$ and amplitude pitching of motion is $\alpha_o = 10°$. Reduced frequency is $k = \pi f_e C/U_\infty = 0.74$ and dimensionless time $t^* = tU_\infty/C$.

Figure 6a: Cross-section of vortex breakdown-plate interaction at a location $0.185L_p$ downstream of the leading-edge of the plate, corresponding to the thin vertical line in Figure 5a. Delta wing is pitching at reduced frequency $k = \pi f_e C/U_\infty = 0.74$. Instantaneous vorticity contours (left column) and averaged vorticity contours (right column) are represented as a function of angle-of-attack α of the wing and dimensionless time $t^* = tU_\infty/C$. Patterns of positive (thick line) and negative (thin line) vorticity are depicted. Minimum and incremental values of instantaneous vorticity are respectively

$\omega_{min} = \pm 1$ sec^{-1} and $\Delta\omega = 0.5$ sec^{-1}; and of averaged vorticity $<\omega>$ are $<\omega_{min}> = \pm 0.5$ sec^{-1} and $<\Delta\omega> = 0.35$ sec^{-1}. Mean angle-of-attack and pitching motion amplitude of delta wing are $\overline{\alpha} = 30°$ and $\alpha_o = 10°$.

Figure 6b: Cross-section of vortex breakdown-plate interaction at a location $0.185L_p$ downstream of the leading-edge of the plate, corresponding to the thin vertical line in Figure 5a. Delta wing is pitching at reduced frequency $k = \pi f_e C/U_\infty = 0.74$. Instantaneous vorticity contours (left column) and averaged vorticity contours (right column) are represented as a function of angle-of-attack α of the wing and dimensionless time $t^* = tU_\infty/C$. Patterns of positive (thick line) and negative (thin line) vorticity are depicted. Minimum and incremental values of instantaneous vorticity are respectively $\omega_{min} = \pm 1$ sec^{-1} and $\Delta\omega = 0.5$ sec^{-1}; and of averaged vorticity $<\omega>$ are $<\omega_{min}> = \pm 0.5$ sec^{-1} and $<\Delta\omega> = 0.35$ sec^{-1}. Mean angle-of-attack and pitching motion amplitude of delta wing are $\overline{\alpha} = 30°$ and $\alpha_o = 10°$.

Figure 7a: Cross-section of vortex breakdown-plate interaction at a location $0.185L_p$ downstream of the leading-edge of the plate, corresponding to the thin vertical line in Figure 5a. Delta wing is pitching at reduced frequency $k = \pi f_e C/U_\infty = 0.74$. Instantaneous vorticity fields (left column) and averaged vorticity fields (right column) are shown for variations of angle-of-attack α of the wing and dimensionless time $t^* = tU_\infty/C$. Mean angle-of-attack and pitching amplitude of delta wing are $\overline{\alpha} = 30°$ and $\alpha_o = 10°$.

Figure 7b: Cross-section of vortex breakdown-plate interaction at a location $0.185L_p$ downstream of the leading-edge of the plate, corresponding to the thin vertical line in Figure 5a. Delta wing is pitching at reduced frequency $k = \pi f_e C/U_\infty = 0.74$.

Instantaneous velocity fields (left column) and averaged velocity fields (right column) are shown for variations of angle-of-attack α of the wing and dimensionless time $t^* = tU_\infty/C$. Mean angle-of-attack and pitching amplitude of delta wing are $\overline{\alpha} = 30°$ and $\alpha_o = 10°$.

Figure 8: Contours of instantaneous vorticity (left column) and instantaneous vertical velocity (right column). Minimum and incremental values of instantaneous vorticity ω are $\omega_{min} = \pm 1$ sec^{-1} and $\Delta\omega = 0.5$ sec^{-1} respectively. For vertical velocity v contours, $v_{min} = \pm 5$ (mm/sec) and $\Delta v = 2.65$ (mm/sec) respectively.

Figure 9a: Contours of instantaneous vertical velocity v (top image) and distributions of v along horizontal lines indicated in image. Instantaneous angle-of-attack is $\alpha = 32.7°$ and dimensionless time is $t^* = tU_\infty/C = 2.55$. Minimum and incremental values of instantaneous vertical velocity contours in image are $v_{min} = \pm 5$ (mm/sec) and $\Delta v = 2.5$ (mm/sec) respectively. Dimensions of v are mm/sec and z is mm.

Figure 9b: Contours of instantaneous vertical velocity v (top image) and distributions of v along horizontal lines indicated in image. Instantaneous angle-of-attack is $\alpha = 32.7°$ and dimensionless time is $t^* = tU_\infty/C = 2.55$. Minimum and incremental values of instantaneous vertical velocity contours in image are $v_{min} = \pm 5$ (mm/sec) and $\Delta v = 2.5$ (mm/sec) respectively. Dimensions of v are mm/sec and z is mm.

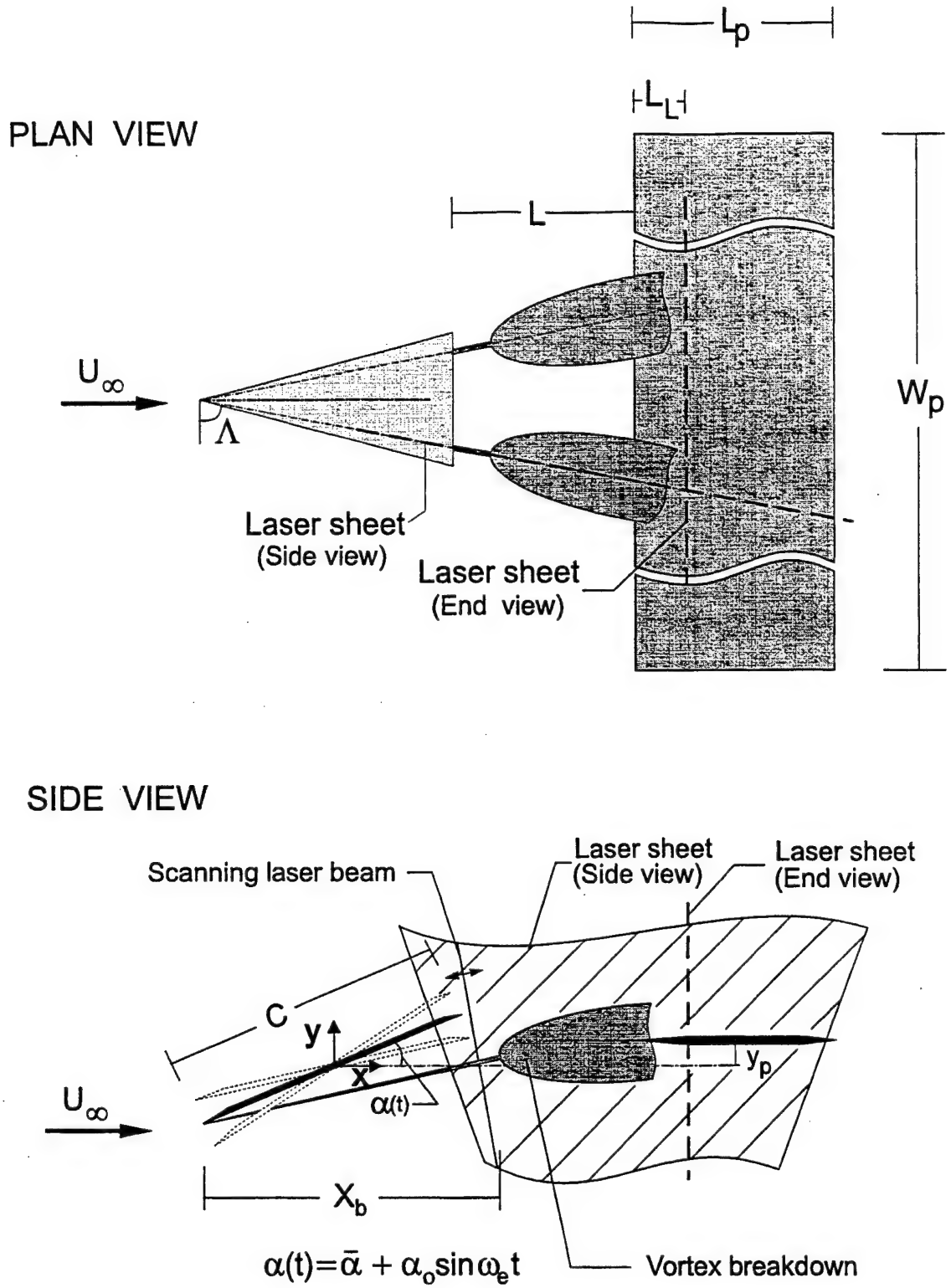

Figure 1: Schematics of delta wing subjected to large-amplitude, low frequency pitching motion about its midchord, which leads to alteration of the structure of the leading-edge vortex, its breakdown, and its impingement upon a stationary plate. Mean and perturbation angles-of-attack are $\bar{\alpha}=30^\circ$ and $\alpha_o=10^\circ$ respectively. Reduced frequency is $k = \pi f_e C/U_\infty = 0.74$.

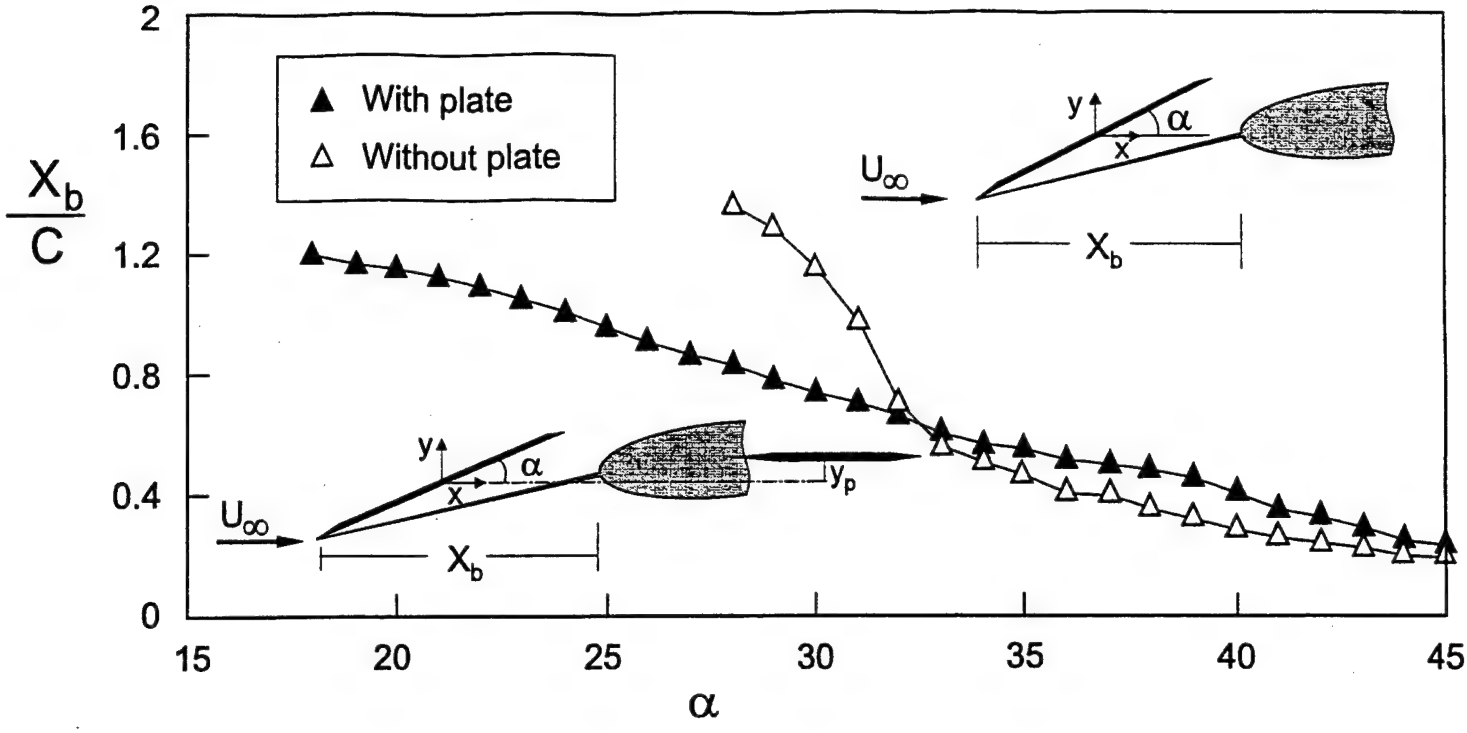

Figure 3a: Variation of location of vortex breakdown with static angle-of-attack of stationary wing. Breakdown locations are compared in presence and in absence of impingement plate.

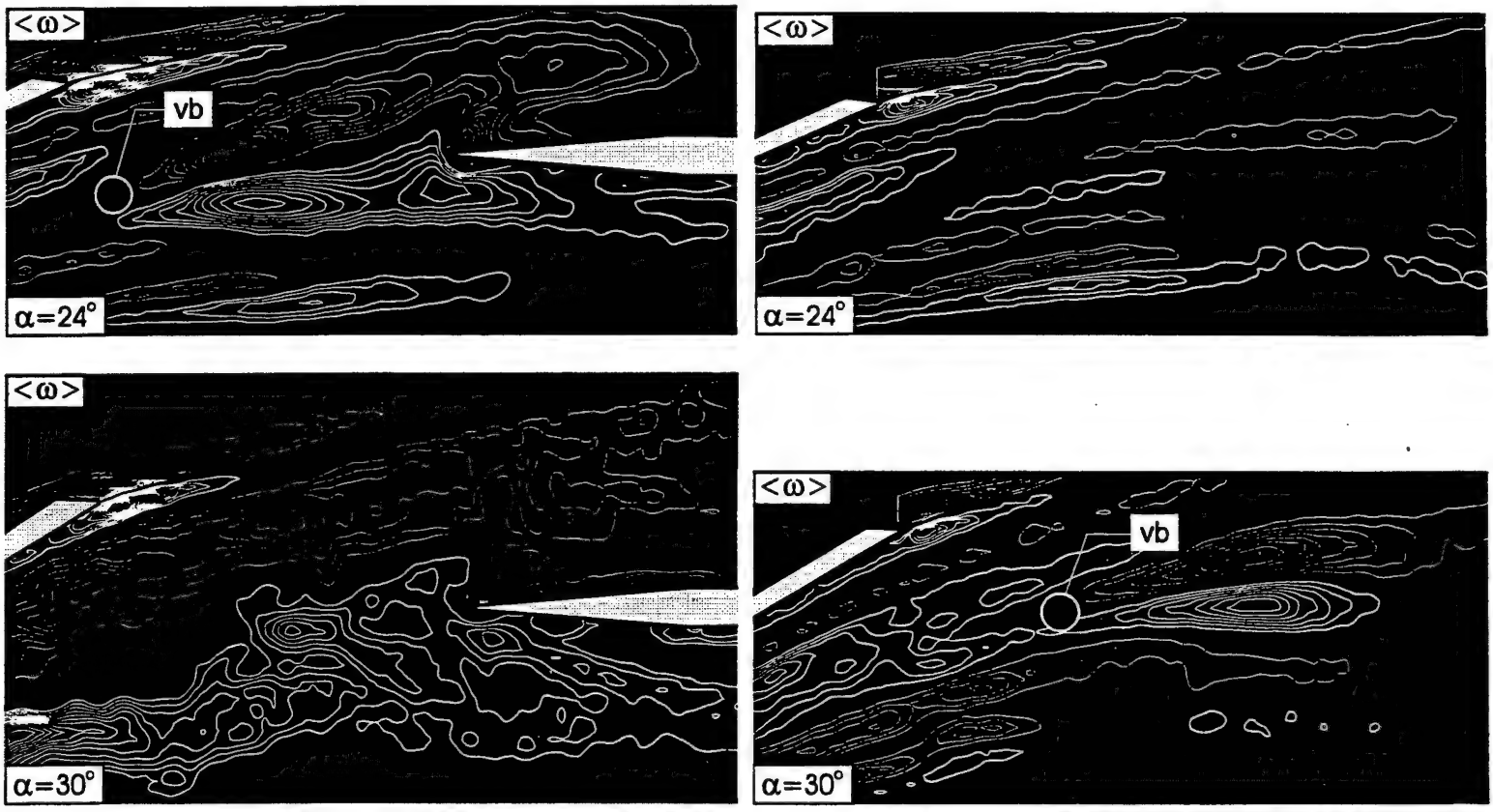

Figure 3b: Contours of averaged vorticity <ω> in presence of the impingement plate (left column) and in absence of the impingement plate (right column). In presence of the impingement plate, minimum and incremental values of averaged vorticity <ω> are $\omega_{min} = \pm 1$ sec^{-1} and $\Delta\omega = 0.5$ sec^{-1} respectively. In absence of the impingement plate, minimum and incremental values of averaged vorticity <ω> are $<\omega_{min}> = \pm 1$ sec^{-1} and $<\Delta\omega> = 0.75$ sec^{-1}.

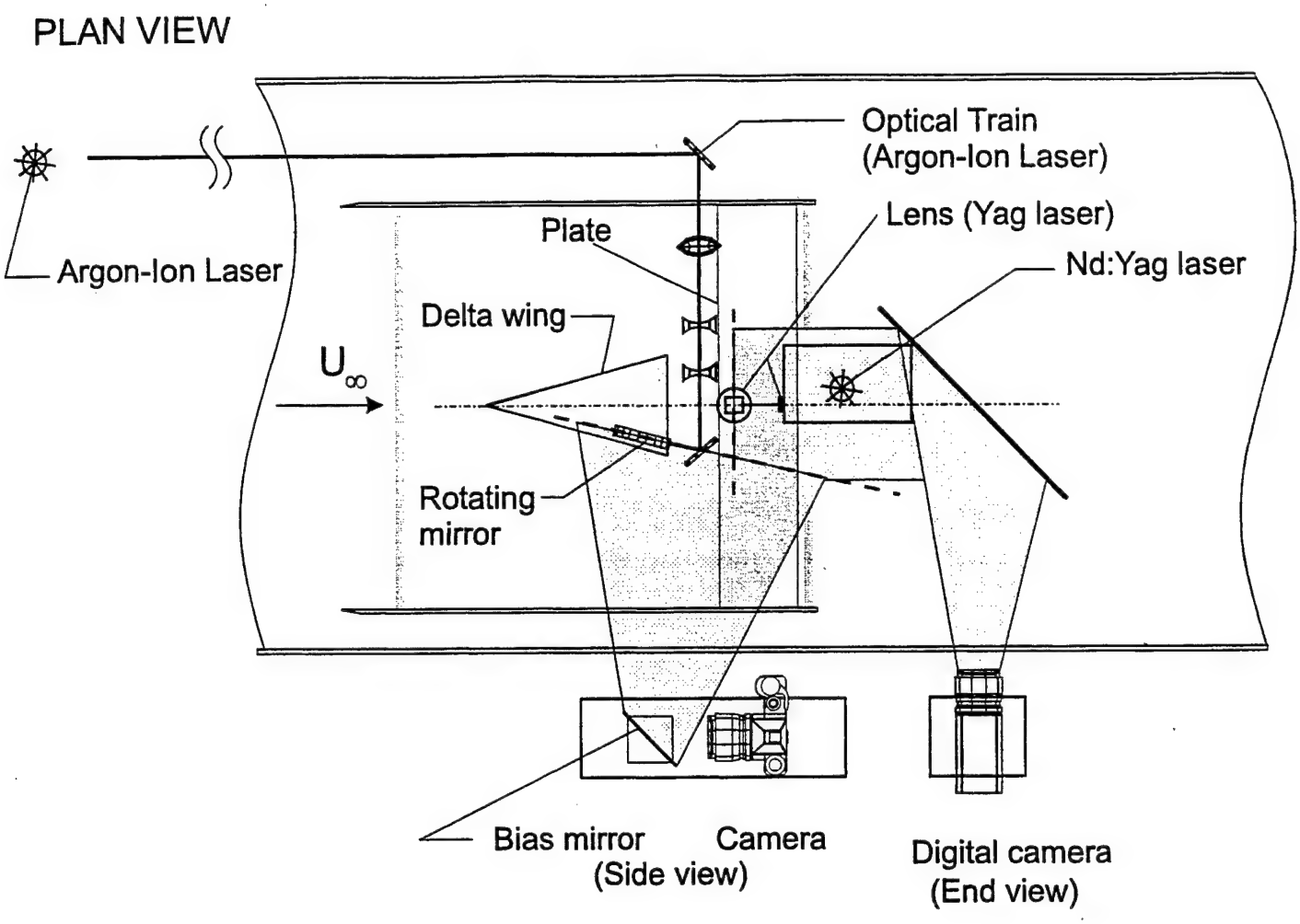

Figure 2: Imaging systems for high- image-density PIV (side view) and DPIV (end view).

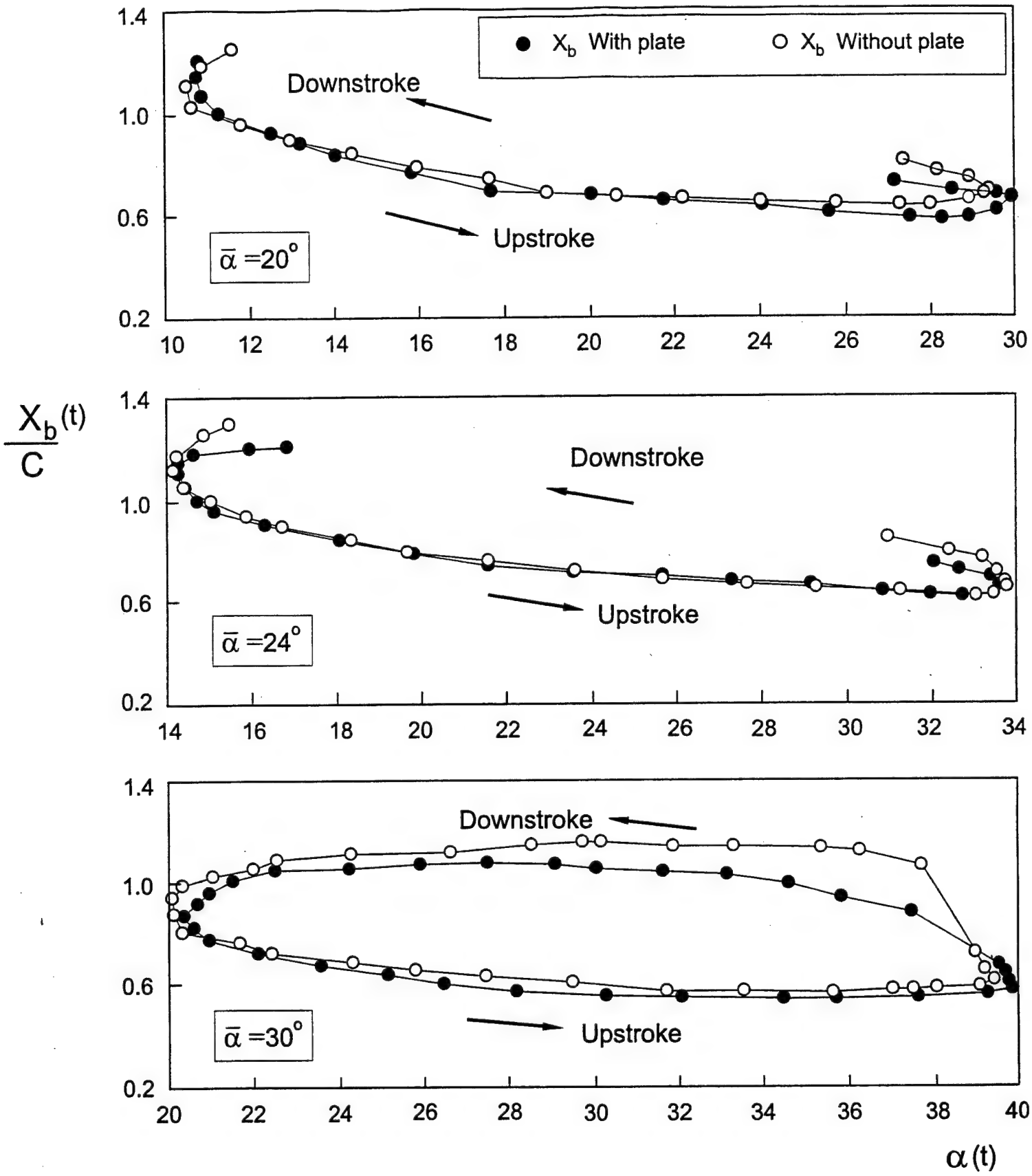

Figure 4: Comparison of dynamic hysterisis loops of vortex breakdown as a function of angle-of-attack in presence of the impingement plate and in the absence of the impingement plate. Amplitude of pitching motion is α_o=10° and reduced frequency is k = $\pi f_e C/U_\infty$ = 0.74 for all cases.

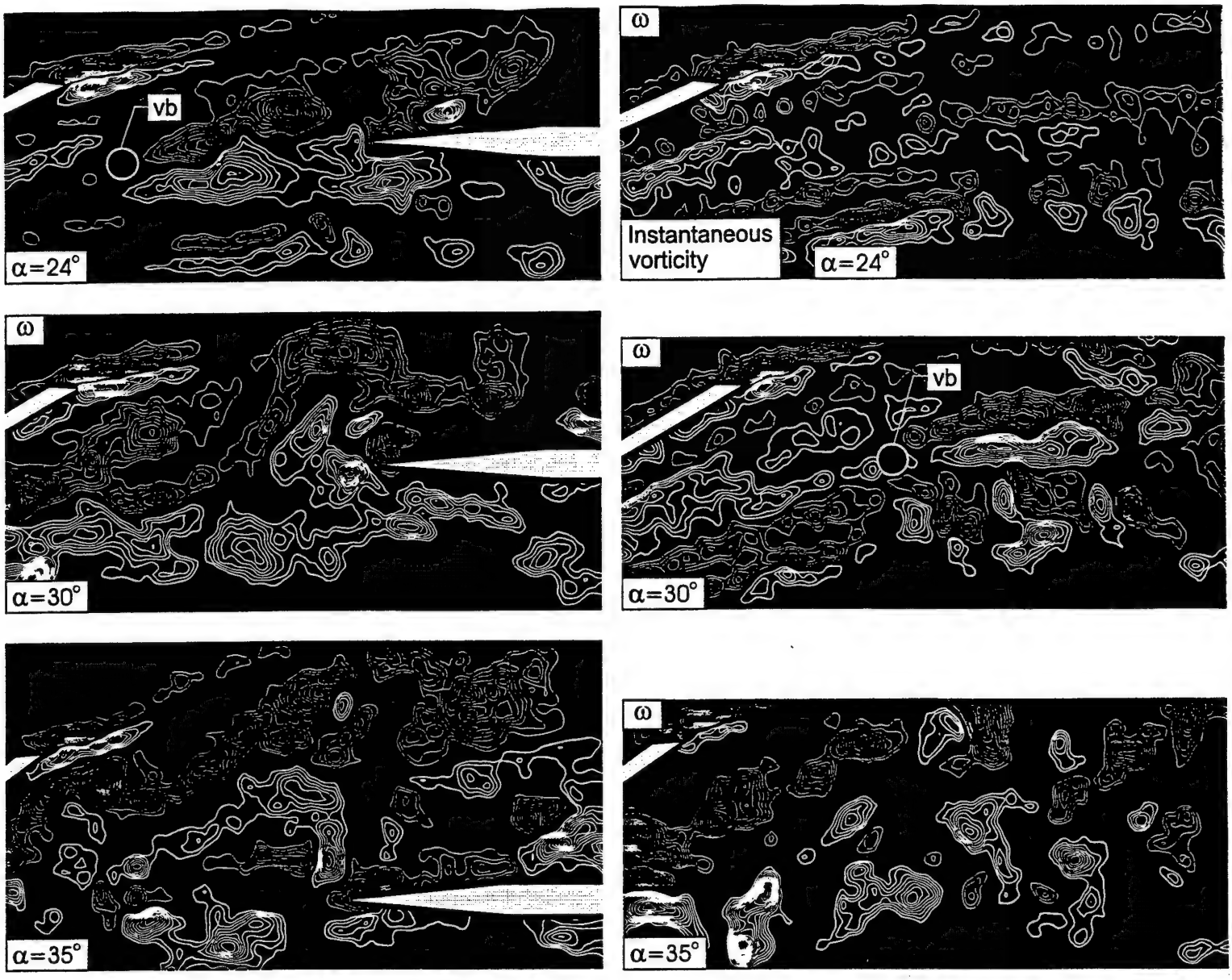

Figure 3c: Contours of instantaneous vorticity ω in presence of the impingement plate (left column) and in absence of the impingement plate (right column). Minimum and incremental values of instantaneous vorticity ω are $\omega_{min} = \pm 1.5\ sec^{-1}$ and $\Delta\omega = 0.75\ sec^{-1}$ respectively for all angles-of-attack in presence of the impingement plate. In absence of the impingement the plate, minimum and incremental values of instantaneous vorticity ω for $\alpha=24^{\circ}$ and 30° are respectively $\omega_{min} = \pm 1\ sec^{-1}$ and $\Delta\omega = 0.75\ sec^{-1}$, and for $\alpha=35^{\circ}$ are $\omega_{min} = \pm 2\ sec^{-1}$ and $\Delta\omega = 0.75\ sec^{-1}$.

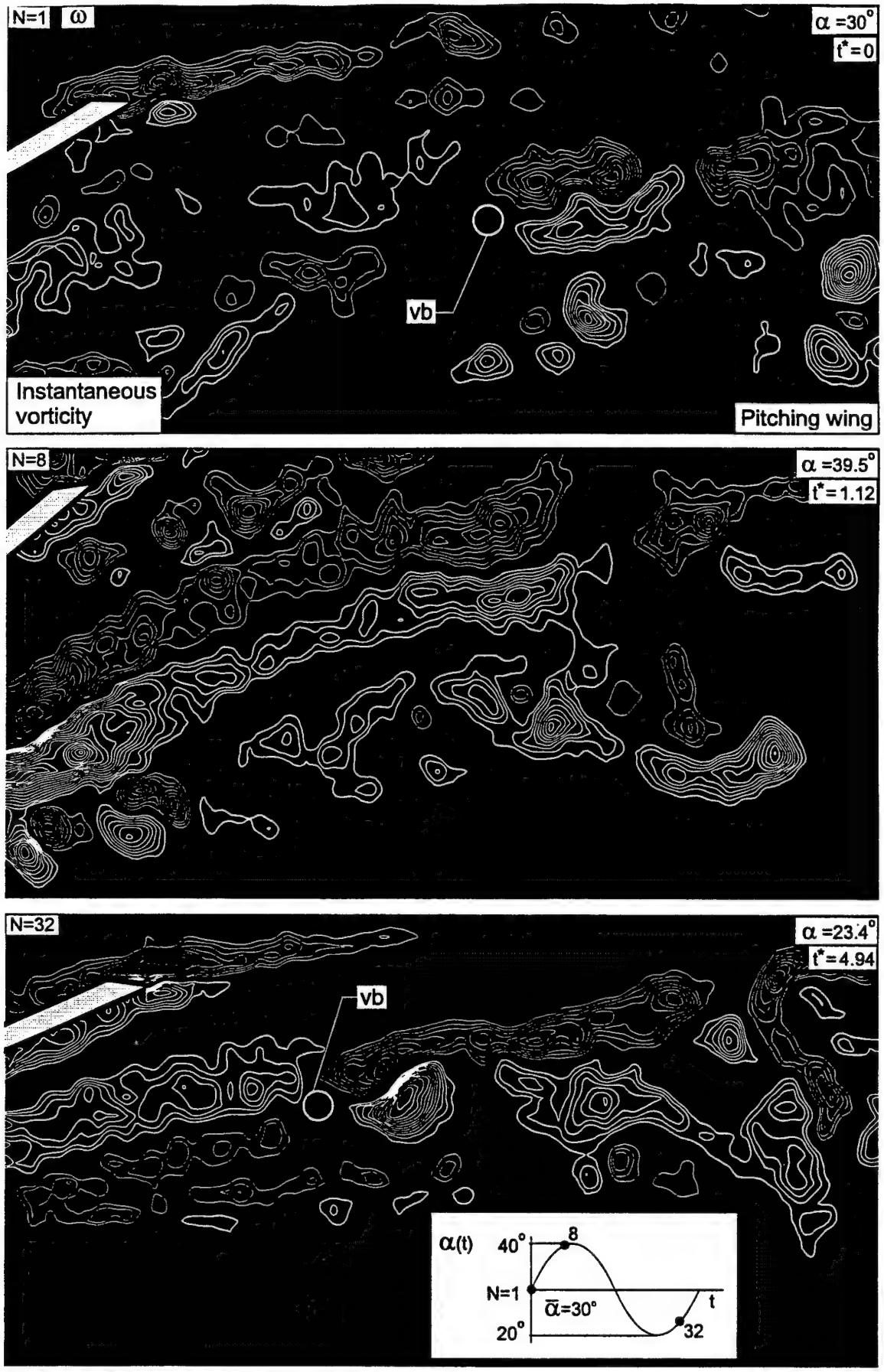

Figure 5b: Patterns of positive (thick line) and negative (thin line) vorticity for pitching motion of delta wing in absence of the impingement plate. Minimum and incremental values of instantaneous vorticity are $\omega_{min} = \pm 1.5$ sec^{-1} and $\Delta\omega = 0.75$ sec^{-1} respectively. Mean angle-of-attack of delta wing $\bar{\alpha} = 30^{\circ}$ and amplitude of pitching motion is $\alpha_o = 10^{\circ}$. Reduced frequency is $k = \pi f_e C/U_\infty = 0.74$ and dimensionless time $t^* = tU_\infty/C$.

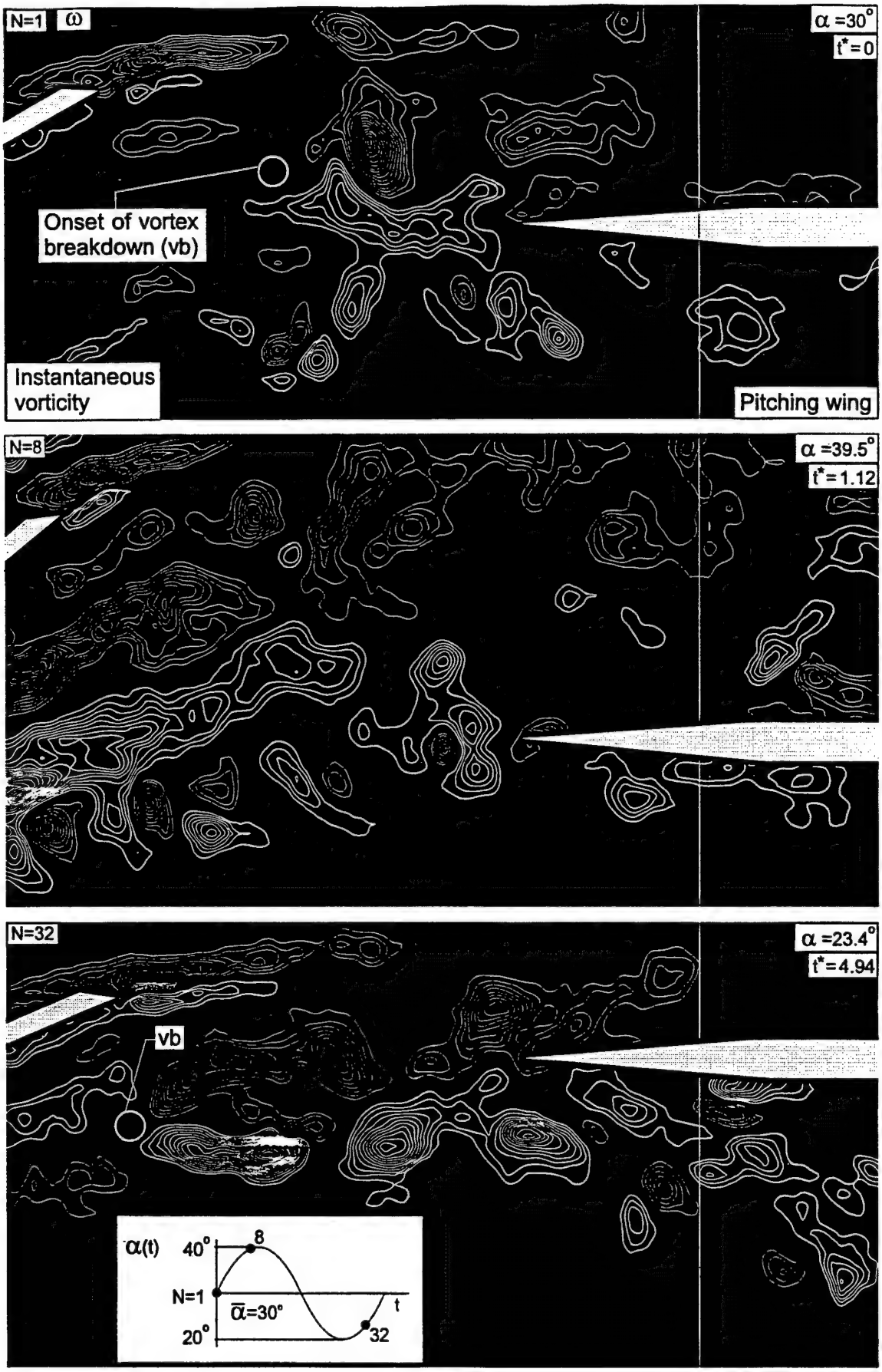

Figure 5a: Patterns of positive (thick line) and negative (thin line) vorticity for pitching motion of delta wing in presence of the impingement plate. Minimum and incremental values of instantaneous vorticity are $\omega_{min} = \pm 1.5$ sec^{-1} and $\Delta\omega = 0.75$ sec^{-1} respectively. Mean angle-of-attack of delta wing $\bar{\alpha} = 30^{\circ}$ and amplitude of pitching motion is $\alpha_o = 10^{\circ}$. Reduced frequency is $k = \pi f_e C/U_\infty = 0.74$ and dimensionless time $t^* = tU_\infty/C$.

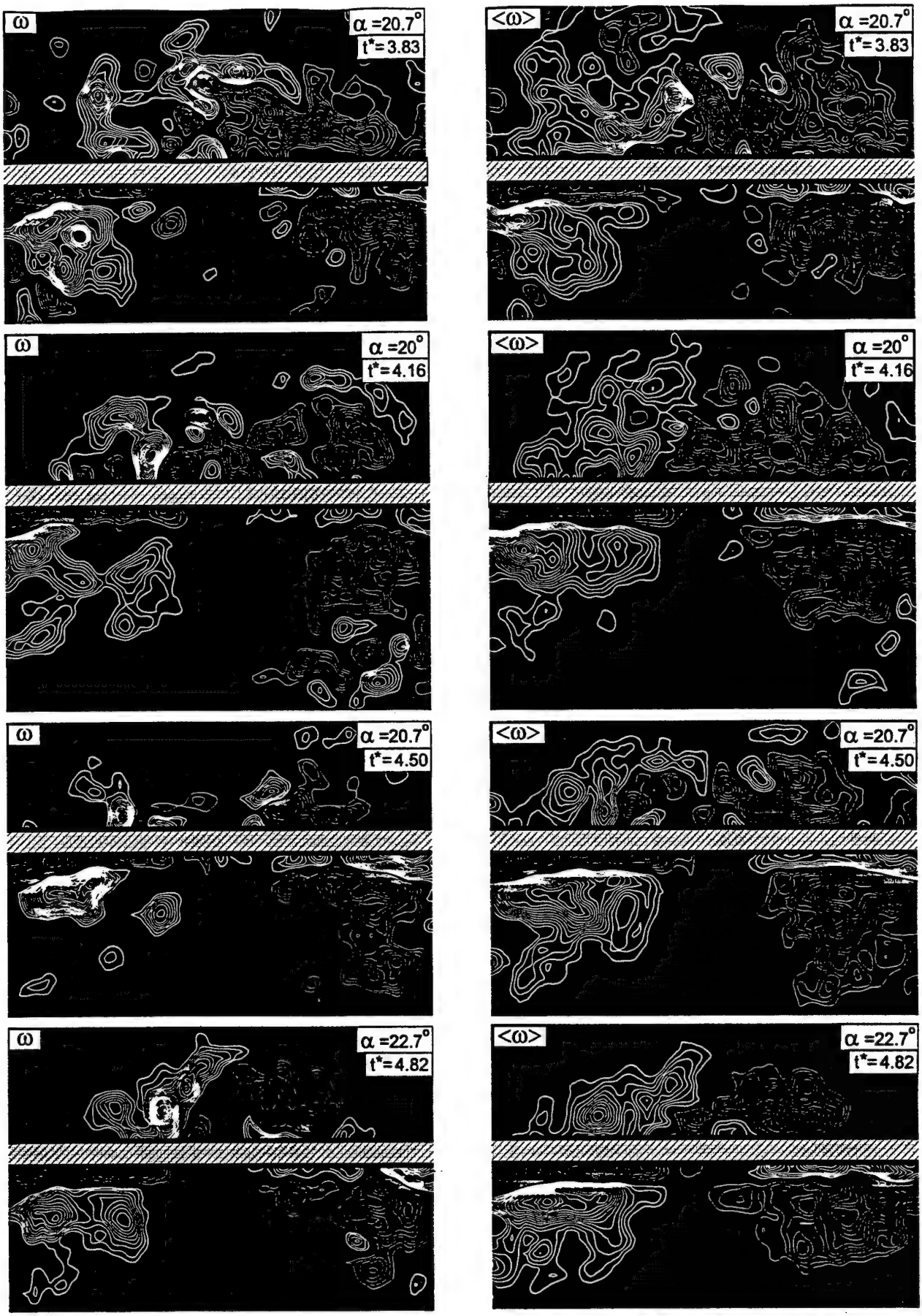

Figure 6b: Cross-section of vortex breakdown-plate interaction at a location $0.185L_p$ downstream of the leading-edge of the plate, corresponding to the thin vertical line in Figure 5a. Delta wing is pitching at reduced frequency $k = \pi f_e C/U_\infty = 0.74$. Instantaneous vorticity contours (left column) and averaged vorticity contours (right column) are represented as a function of angle-of-attack α of the wing and dimensionless time $t^* = tU_\infty/C$. Patterns of positive (thick line) and negative (thin line) vorticity are depicted. Minimum and incremental values of instantaneous vorticity are respectively $\omega_{min} = \pm 1\ sec^{-1}$ and $\Delta\omega = 0.5\ sec^{-1}$; and of averaged vorticity $<\omega>$ are $<\omega_{min}> = \pm 0.5\ sec^{-1}$ and $<\Delta\omega> = 0.35\ sec^{-1}$. Mean angle-of-attack and pitching motion amplitude of delta wing are $\bar{\alpha} = 30°$ and $\alpha_o = 10°$.

Figure 6a: Cross-section of vortex breakdown-plate interaction at a location $0.185L_p$ downstream of the leading-edge of the plate, corresponding to the thin vertical line in Figure 5a. Delta wing is pitching at reduced frequency $k = \pi f_c C/U_\infty = 0.74$. Instantaneous vorticity contours (left column) and averaged vorticity contours (right column) are represented as a function of angle-of-attack α of the wing and dimensionless time $t^* = tU_\infty/C$. Patterns of positive (thick line) and negative (thin line) vorticity are depicted. Minimum and incremental values of instantaneous vorticity are respectively $\omega_{min} = \pm 1\ sec^{-1}$ and $\Delta\omega = 0.5\ sec^{-1}$; and of averaged vorticity $<\omega>$ are $<\omega_{min}> = \pm 0.5\ sec^{-1}$ and $<\Delta\omega> = 0.35\ sec^{-1}$. Mean angle-of-attack and pitching motion amplitude of delta wing are $\bar{\alpha} = 30°$ and $\alpha_o = 10°$.

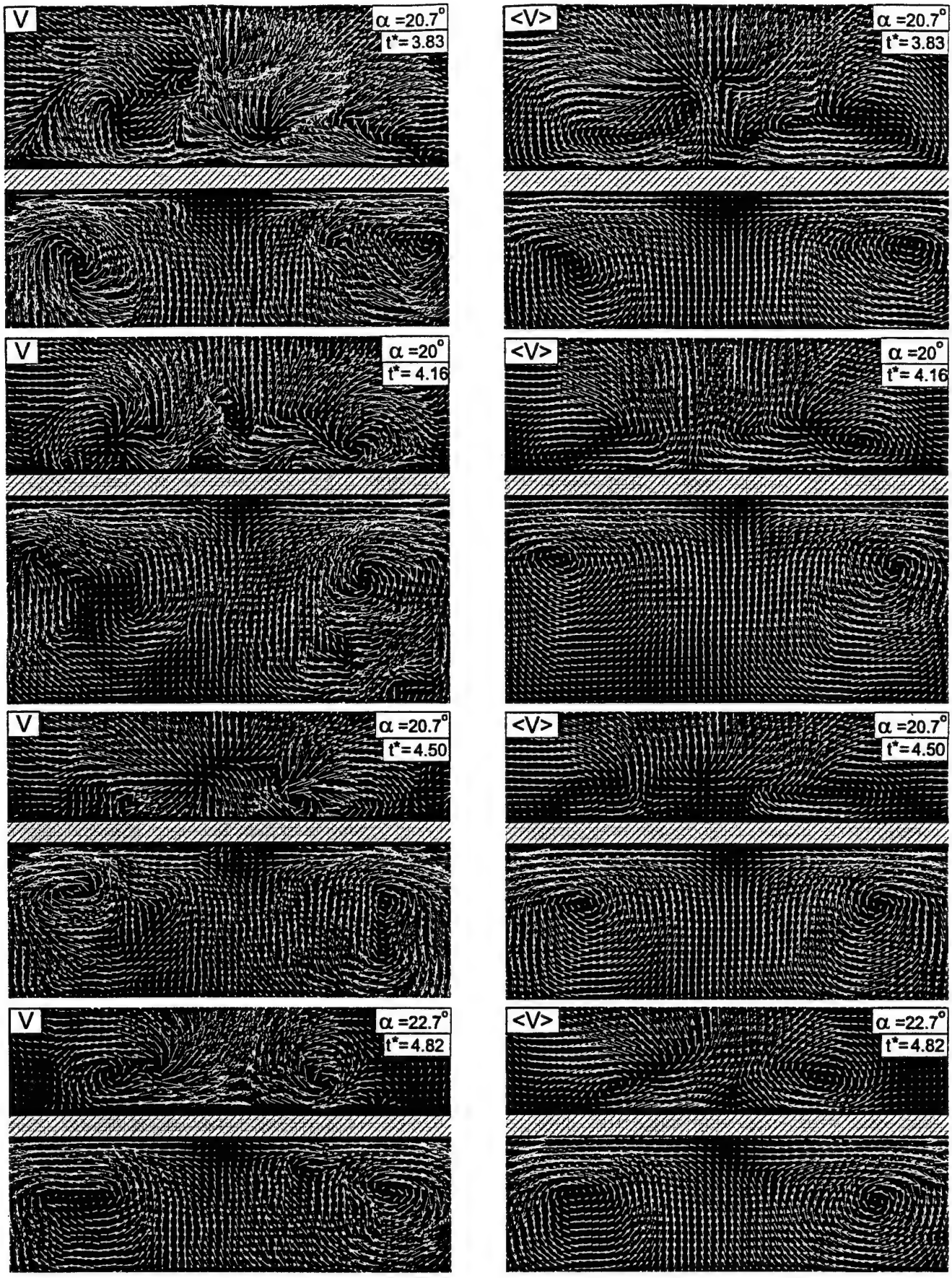

Figure 7b: Cross-section of vortex breakdown-plate interaction at a location $0.185L_p$ downstream of the leading-edge of the plate, corresponding to the thin vertical line in Figure 5a. Delta wing is pitching at reduced frequency $k = \pi f_e C/U_\infty = 0.74$. Instantaneous velocity fields (left column) and averaged velocity fields (right column) are shown for variations of angle-of-attack α of the wing and dimensionless time $t^* = tU_\infty/C$. Mean angle-of-attack and pitching amplitude of delta wing are $\bar{\alpha}= 30^\circ$ and $\alpha_o=10^\circ$.

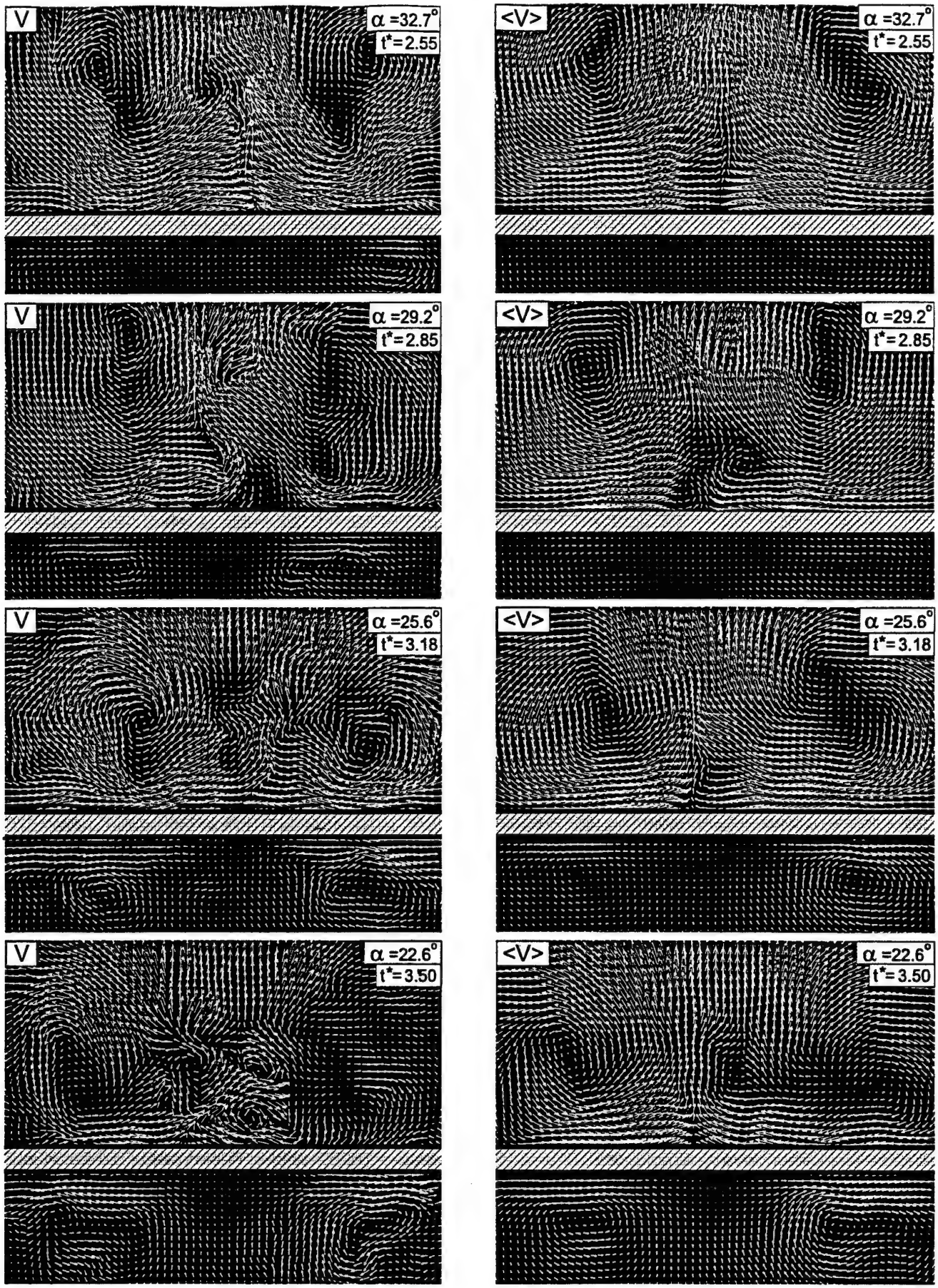

Figure 7a: Cross-section of vortex breakdown-plate interaction at a location $0.185L_p$ downstream of the leading-edge of the plate, corresponding to the thin vertical line in Figure 5a. Delta wing is pitching at reduced frequency $k = \pi f_e C/U_\infty = 0.74$. Instantaneous velocity fields (left column) and averaged velocity fields (right column) are shown for variations of angle-of-attack α of the wing and dimensionless time $t^* = tU_\infty/C$. Mean angle-of-attack and pitching amplitude of delta wing are $\bar{\alpha}=30^\circ$ and $\alpha_o=10^\circ$.

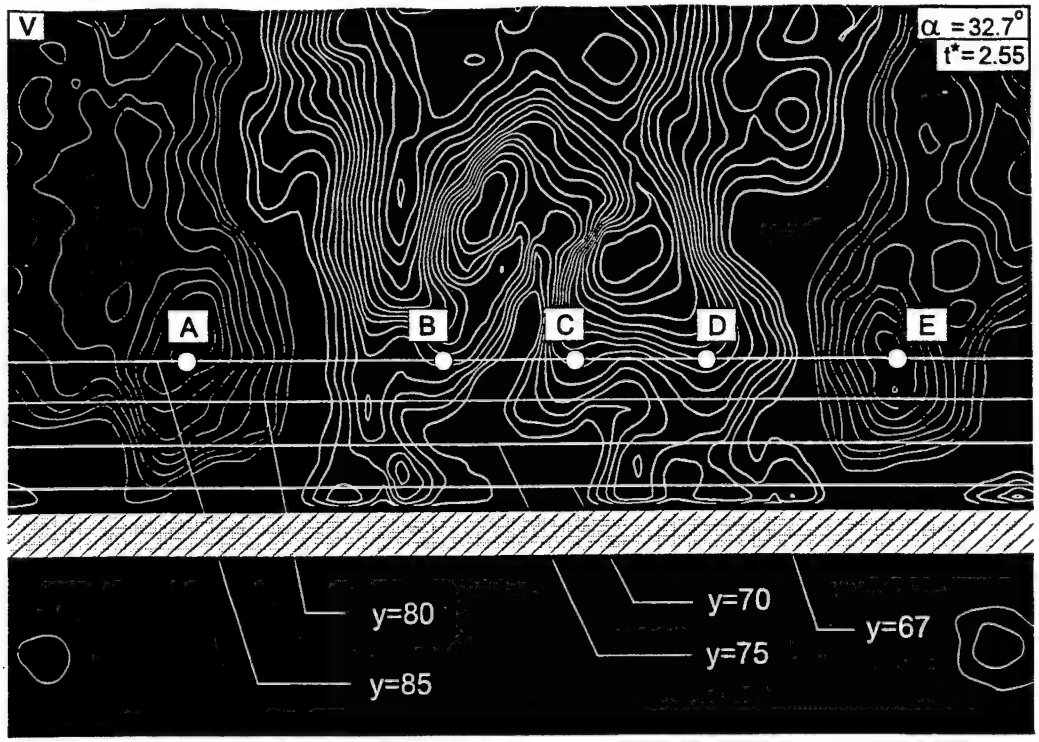

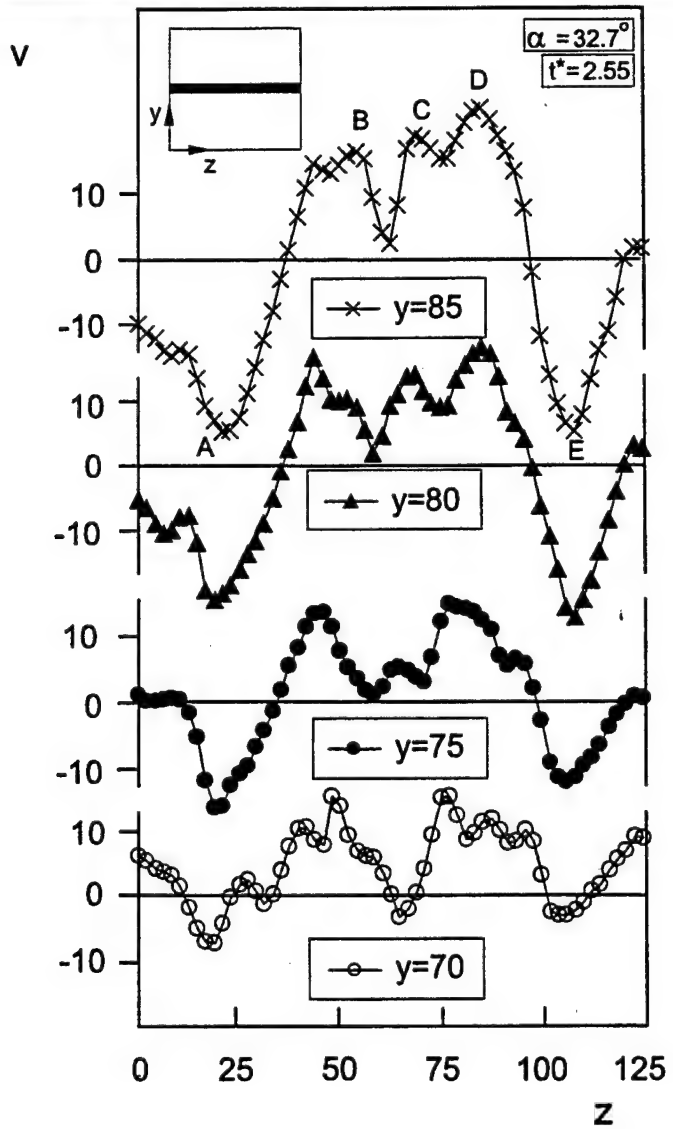

Figure 9a: Contours of instantaneous vertical velocity v (top image) and distributions of v along horizontal lines indicated in image. Instantaneous angle-of-attack is $\alpha = 32.7^{\circ}$ and dimensionless time is $t^{*} = tU_{\infty}/C = 2.55$. Minimum and incremental values of instantaneous vertical velocity contours in image are $v_{min} = \pm 5$ (mm/sec) and $\Delta v = 2.5$ (mm/sec) respectively. Dimensions of v are mm/sec and z is mm.

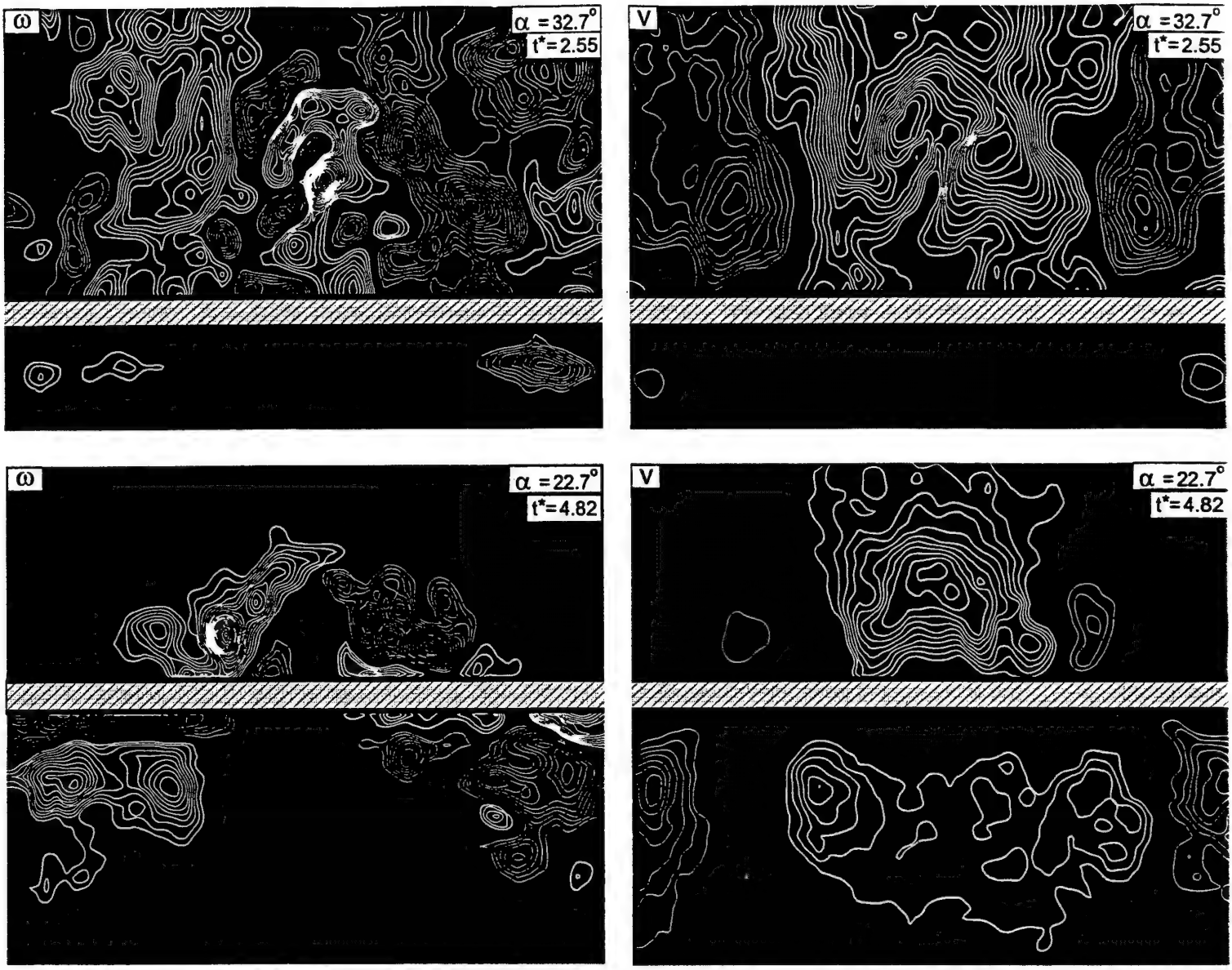

Figure 8: Contours of instantaneous vorticity (left column) and instantaneous vertical velocity (right column). Minimum and incremental values of instantaneous vorticity ω are $\omega_{min} = \pm 1\ sec^{-1}$ and $\Delta\omega = 0.5\ sec^{-1}$ respectively. For vertical velocity v contours, $v_{min} = \pm 5$ (mm/sec) and $\Delta v = 2.5$ (mm/sec) respectively.

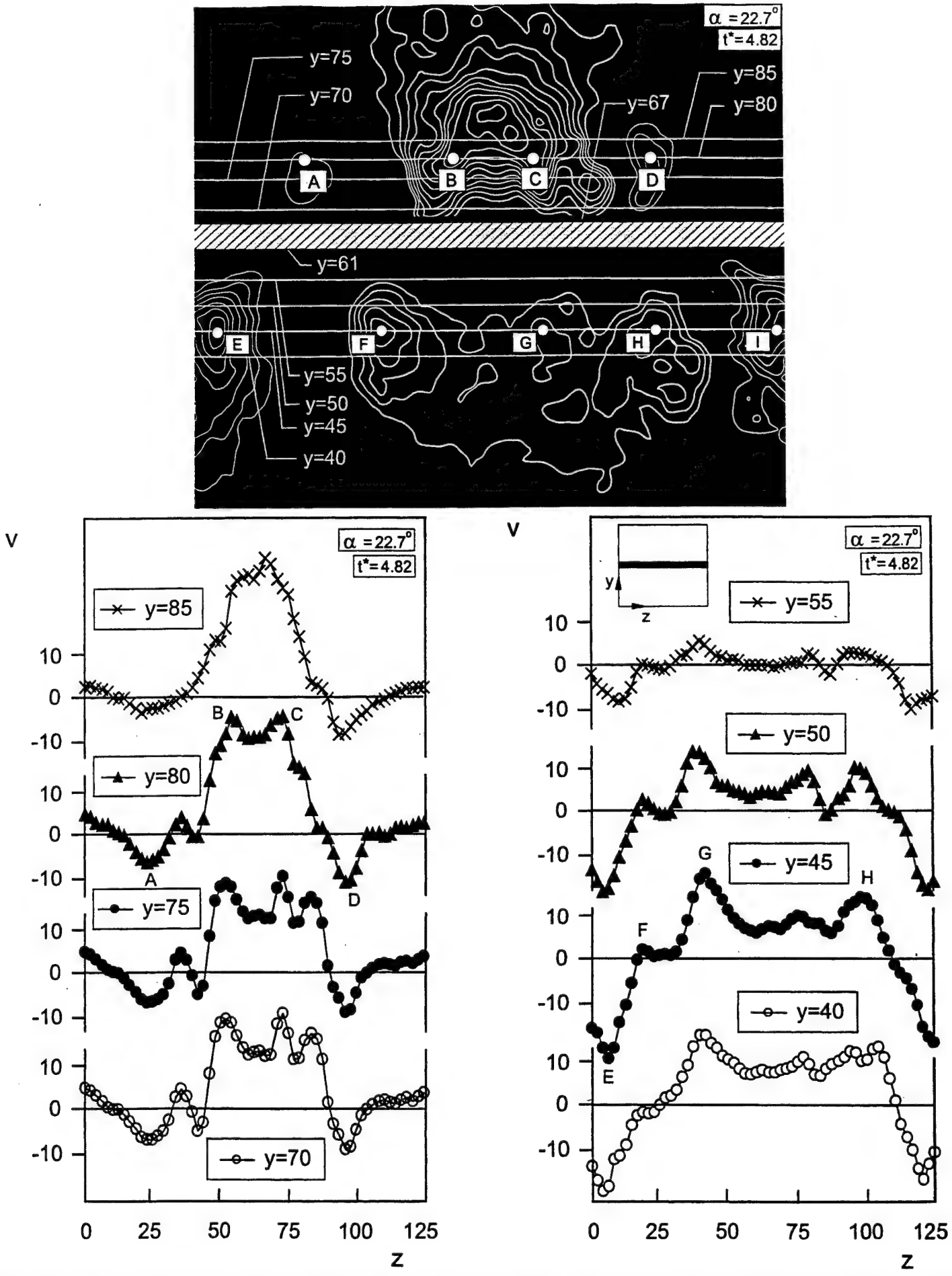

Figure 9b: Contours of instantaneous vertical velocity v (top image) and distributions of v along horizontal lines indicated in image. Instantaneous angle-of-attack is $\alpha = 22.7^{\circ}$ and dimensionless time is $t^{*} = tU_{\infty}/C = 4.82$. Minimum and incremental values of instantaneous vertical velocity contours in image are $v_{min} = \pm 5$ (mm/sec) and $\Delta v = 2.5$ (mm/sec) respectively. Dimensions of v are mm/sec and z is mm.

APPENDIX F

Akilli-2 FIN 102201

CONTROL OF VORTEX BREAKDOWN BY A COAXIAL WIRE*

by

H. Akilli* and B. Sahin*
Department of Mechanical Engineering
Cukurova University
Balcali 01330 Adana
Turkey

D. Rockwell
Department of Mechanical Engineering
and Mechanics
354 Packard Laboratory
19 Memorial Drive West
Lehigh University, Bethlehem, PA 18015

* On leave at Department of Mechanical Engineering and Mechanics, Lehigh University

ABSTRACT

A very small diameter wire is tethered from the apex of a delta wing and nominally aligned with the centerline of the leading-edge vortex. The wire can alter both the onset and structure of vortex breakdown. A technique of high-image-density particle image velocimetry allows acquisition of patterns of instantaneous and averaged vorticity and velocity, which reveal the relationship between: advancement of vortex breakdown towards the apex of the wing; and corresponding changes of patterns of vorticity and velocity contours. The diameter of the wire is one percent of the core diameter of the pre-breakdown vortex. It is possible to alter the onset of vortex breakdown by as much as approximately one chord length of the wing. A critical parameter is the length of the wire, which is normalized by: the chord of the wing; or the distance to onset of vortex breakdown in absence of the wire. Once a critical length of the wire is attained, further increases in length have no effect on the onset of breakdown. This effect is interpreted in terms of abrupt changes in patterns of vorticity and streamwise gradients of velocity along the central region of the vortex. It is possible to attain a switch in sign of azimuthal vorticity and a wakelike region of the vortex, in absence of a stagnation point.

INTRODUCTION

Vortex breakdown on stationary and moving delta wings has been the subject of intense research for over three decades. The range of investigations characterizing the onset of vortex breakdown is provided in the Introduction of a recent complementary manuscript of Akilli *et al.*[1], which addressed control of breakdown via a transversely oriented wire. The focus of the present investigation is on deployment of a coaxial wire, nominally aligned with the axis of a leading-edge vortex, with the intent of inducing early onset of vortex breakdown and thereby altering the spectral content and scales of the

*** Akilli, H., Sahin, B. and Rockwell, D. 2002 *Physics of Fluids.***

turbulence generated in the vortex breakdown region. In turn, this alteration is expected to have important consequences for buffeting of aerodynamic surfaces, as described in the early investigations of Earnshaw and Lawford[2] and Mabey[3], as well as in more recent investigations summarized by Gursul and Xie[4], Lee[5], Sahin *et al.*[6], and Özgören *et al.*[7].

Substantial effort has been devoted to controlling the onset of vortex breakdown on delta wings at high angle-of-attack. Rockwell[8] reviewed control approaches, which include stationary and oscillating leading-edge flaps, and steady and unsteady blowing applied either tangentially to, or in-line with, the leading-edge. Rather than exerting control at the leading-edge of the wing, it has been demonstrated that blowing from the trailing-edge can substantially alter the location of vortex breakdown, as demonstrated by Helin and Watry[9] and Ding and Shih[10]. A combined approach of actuation of leading-edge flaps and trailing-edge blowing was undertaken by Vorobieff and Rockwell[11,12]; this type of dual control during the pitching maneuver of the wing can substantially alter the phase shift between the wing motion and the onset of vortex breakdown. Recent efforts to implement control schemes on an actual aircraft are described by Huttsell *et al.*[13].

In contrast to the aforementioned control approaches, very little effort has been devoted to deployment of small-scale geometries within the vortex to control the onset of breakdown. Akilli *et al.*[1] have demonstrated that a wire oriented transversely to the centerline of the leading-edge vortex, and having a diameter two orders of magnitude smaller than the vortex diameter, can substantially influence the onset of vortex breakdown. These results demonstrate the surprising effectiveness of small-scale obstacles, and complement previous observations of Reynolds and Abtahi[14] and Gursul and Yang[15], who employed a relatively large-scale probe and cylinder respectively. In view of the promising results obtained with the transversely-oriented wire, the issue arises as to whether a coaxial wire tethered from the apex of the delta wing can also provide effective control. The objective of this investigation is to characterize alterations of the onset and structure of vortex breakdown for a wire diameter two orders of magnitude smaller than the diameter of the vortex core. Moreover, the sensitivity to wire length and angle-of-attack of the wing variations will be addressed. In doing so, a technique of high-image-density particle image velocimetry will provide global images of

the velocity and vorticity fields, thereby yielding a quantitative basis for interpreting the effects of this type of control.

EXPERIMENTAL SYSTEM AND TECHNIQUES

All experiments were undertaken in a large-scale water channel having a test section width of 927 mm, height of 610 mm and length of 4928 mm. The water elevation in the channel was maintained at 559 mm. The flow speed in the test section was maintained at 65 mm/sec.

An overview of the delta wing arrangement with a deployed wire is shown in Figure 1. The wing had a chord C = 222 mm and a sweep angle of $\Lambda = 75°$. All experiments were performed at a Reynolds number Re based on chord C of $U_\infty C/\nu$ = 14,792. During experiments, the angle-of-attack α was varied over the range $15° \leq \alpha \leq 35°$. This was accomplished by rotation of the delta wing about its midchord. The wing was held in position by a vertical sting extending from the upper surface of the wing through the free-surface of the water channel. This sting, which had a streamlined leading-edge, was 3 mm thick and 35 mm long in the streamwise direction.

As indicated in the schematics of Figure 1, a wire of diameter D_w was tethered from the leading-edge of the delta wing. For all experiments, $D_w = 0.1$ mm. The value of D_w is normalized by the diameter D_v of the vortex prior to the onset of vortex breakdown. As a reference, the value of D_v at an angle-of-attack $\alpha = 30°$ is employed. This representative diameter is designated as $(D_v)_r$. For all data illustrated herein, $D_w/(D_v)_r = 0.01$. During experiments, the length of the wire L_w was varied. Two normalization scales are employed to represent the dimensionless wire length: the chord C of the delta wing; and the distance from the tip of the wing to the onset of vortex breakdown in absence of a wire, designated as $(X_b)_o$. The wire lengths are then L_w/C and $L_w/(X_b)_o$.

In this investigation, only the leading-edge vortex subjected to control by deployment of the wire was characterized using quantitative imaging. Dye visualization was employed to examine both leading-edge vortices simultaneously, in order to preclude ambiguous interpretation due to competition between the onset of vortex breakdown of the leading-edge vortices on either side of the wing. By maintaining the wing at a very

small, but finite, yaw angle $\beta < 1°$, it was possible to ensure that the onset of breakdown on the opposite side of the wing always occurred well downstream of breakdown of the leading-edge vortex of interest, thereby ensuring that there was no coupling between the leading-edge vortices. Qualitative visualization of vortex breakdown was accomplished using dye visualization. Dye entered the wing through a tap located on the windward (upstream) side of the delta wing adjacent to the sting attachment. The dye then proceeded through the interior of the wing to the apex, where it seeped into the leading-edge vortices. This procedure of injecting dye ensured that the flow in the apex region remained undisturbed during the injection process. The onset of vortex breakdown was defined at the abrupt increase in diameter of the dye marker; an average of a total of five of these instantaneous locations gave the time-averaged location of the onset of vortex breakdown. This approach led to the plots of Figures 2 and 3, which represent the change of vortex breakdown due to presence of the wire.

A laser scanning approach to high-image-density particle image velocimetry, as summarized by Rockwell *et al.*[16], was employed to quantitatively assess the vortex breakdown artificially induced by the wire. The experimental system and approach were very similar to those of Akilli *et al.*[1]. The beam from a continuous wave Argon laser operating at a power output of 15 watts was transmitted through a system of steering mirrors and focusing lenses. This conditioned beam then impinged upon a rotating mirror having eight facets. The purpose of the rotating mirror was to generate a rapidly scanning laser beam. The mirror was controlled to rotate at a frequency of 18.75 Hz; the corresponding value of scanning frequency was therefore 150 Hz. The flow was seeded with metallic-coated hollow plastic spheres of diameter of 14 microns. Due to the rapidly scanning laser, as many as three to four multiply exposed particle images were acquired.

A Canon EOS-1 N RS camera was employed to photograph the patterns of particle images. The f-stop was $f = 4.5$ and the shutter speed was 1/30 sec. The magnification was adjusted in order to provide adequate spatial resolution for the critical region of vortex breakdown. This consideration led to a value of magnification $M = 1{:}4.86$. Regions of vortex breakdown, such as those of interest in the present investigation, are typically associated with localized reverse flows. It was therefore necessary to employ a rotating bias mirror, in order to avoid difficulties due to directional

ambiguity. The bias mirror was located immediately in front of the camera lens at an angle of 45° to the optical axis.

The multiply-exposed particle images were recorded on 35 mm film having a high resolution of 300 lines per millimeter. In turn, the negatives of the film were digitized at a resolution of 125 pixels/mm. As described in the work of Akilli *et al.*[1], as well as previous works cited therein, a single-frame cross-correlation technique was invoked to evaluate the patterns of particle images. The size of the interrogation window was 90 × 90 pixels; an overlap of 50% was employed. To ensure that the high-image-density criterion was satisfied, approximately 40 to 60 particle images were present within the interrogation window.

The actual grid size in the physical plane of the laser sheet was 1.75 mm × 1.75 mm, which is related to the effective grid size on the film of 0.36 × 0.36 mm by the magnification factor M. The field of view of the images shown herein is indicated by the rectangular box defined by the dashed lines of Figure 1; the original image was cropped alnong its top and bottom edges to yield the view of Figure 1. This box is shown to scale relative to the length C of the delta wing. Its length was 0.7 C. It is approximately aligned with the centerline of the leading-edge vortex. Moreover, the leading-edge of the field of view is located a distance of 0.4 C downstream of the tip of the apex of the delta wing.

OVERVIEW OF RESPONSE OF VORTEX BREAKDOWN

Figure 2 shows the response of vortex breakdown to deployment of the wire. As described in the foregoing, the location of breakdown was obtained via dye visualization. The schematics of Figure 2 define X_b as the distance from the tip of the wing to the onset of vortex breakdown in presence of a wire of length L_w. In absence of the wire, the onset of vortex breakdown occurs at a distance designated as $(X_b)_o$. This difference in location of breakdown is shown for a range of angle-of-attack $15° \leq \alpha \leq 35°$. It is evident that when the wire length L_w/C is as small as 0.5, a substantial change in onset of breakdown is generally attainable. At this nominal value of L_w/C, small increases in wire length produce large changes in the location of breakdown until an asymptotic condition is

attained for a wire length L_w/C of the order of unity. This trend does not occur, however, for the highest angle-of-attack $\alpha = 35°$.

For all values of α, increases of wire length beyond $L_w/C \cong 1$ produce only mild changes in the onset of breakdown. In this range, it is possible to generalize the sensitivity of the breakdown response as a function of angle-of-attack. The highest sensitivity, corresponding to the largest change of the parameter $[(X_b)_o - X_b]/C$ occurs at $\alpha = 15°$ and, for successively higher values of α, smaller changes occur until, at $\alpha = 35°$, the least sensitive response is evident.

An alternate length scale for normalization of the wire length L_w is the distance $(X_b)_o$ to the onset of vortex breakdown in absence of a wire. Figure 3 shows the data of Figure 2 plotted according to this normalization. For lower values of angle-of-attack $15° \leq \alpha \leq 25°$, the difference in breakdown location $[(X_b)_o - X_b]/C$ attains an approximately asymptotic value at $L_w/(X_b)_o \cong 0.5$. At higher values of $\alpha = 30°$ and 35°, somewhat larger values of dimensionless wire length $L_w/(X_b)_o$ are required to attain the asymptotic condition.

STRUCTURE OF VORTEX BREAKDOWN IN PRESENCE OF WIRE

The physical features of the altered leading-edge vortex in presence of a wire, relative to the case of no wire, are shown in Figure 4. The top image (a) shows contours of instantaneous positive (thick line) and negative (thin line) vorticity ω without deployment of the wire, while the remaining three images provide different representations of the flow in presence of the wire: (b) contours of averaged vorticity $< \omega >$; (c) contours of averaged velocity $< V >$; and (d) averaged velocity vectors. In all cases, the dimensionless wire length was $L_w/C = 1.14$ and angle-of-attack was $\alpha = 30°$. For the averaged images, a total of five instantaneous images were employed; the intent was not to provide a statistical average, but to show a smoothed version of the velocity fields in direct comparison with the corresponding pattern of vorticity. Image (a) clearly indicates that, in absence of the wire, there is no significant disruption of the patterns of vorticity. In contrast, when the wire is deployed as shown in the second image (b), the onset of vortex breakdown *vb* appears within the field of view of the image. It is located well upstream of the end of the wire, which is designated as *eow*.

In all of the images presented herein, the location of onset of vortex breakdown is defined to occur at the switch in sign of azimuthal vorticity. This criterion originates from the theoretical description of Brown and Lopez[17]. Prior to the onset of breakdown, the positive (white) vorticity occurs in the upper part of the second image of Figure 4, while after breakdown, it occurs in the lower part. The converse holds for the patterns of negative vorticity. Note the concentrations of negative (gray) vorticity.

Further features of this vortex breakdown are evident in Figure 4c. It shows a large decrease in magnitude of the contours of averaged velocity $< V >$ along the axis of the vortex. Downstream of breakdown, indicated by the symbol *vb*, very low values of $< V >$ are evident. These features are compared with the pattern of velocity vectors $< V >$ in Figure 4d. As evident in images 4b through 4d, a distinguishing feature of this artificially-induced vortex breakdown is the lack of formation of a large-scale breakdown "bubble", which is characteristic of vortex breakdown or "bursting" that naturally occurs at higher angle-of-attack. Moreover, no stagnation point is indicated in either image 4c or 4d.

Finally, it is evident from all images in Figure 4 that the onset of vortex breakdown (*vb*) occurs well upstream of the end of the wire (*eow*). The issue arises as to whether it is possible to manipulate the location of vortex breakdown by alterations of the dimensionless wire length L_w/C.

Figure 5a exhibits the effect of wire length. In all images, the end of the wire (*eow*) and the onset of vortex breakdown (*vb*) are clearly indicated; the schematic of the wire is, however, omitted. For a small wire length $L_w/C = 0.46$, which is represented in the second image, the onset of vortex breakdown is again defined by a switch in sign of the azimuthal vorticity contours. In this case, breakdown actually occurs well downstream of the end of the wire. This process of vortex breakdown is vaguely defined. The positive and negative vorticity layers downstream of vortex *vb* are actually embedded within a set of positive and negative layers that appear to represent an extension of the pre-breakdown layers. When the length of the wire is increased to $L_w/C = 0.69$, as shown in the third image of Figure 5a, the switch in sign of the azimuthal vorticity at the location *vb* becomes sharply defined; for this case, vortex breakdown occurs upstream of the end of the wire. Finally, for the longest wire length $L_w/C = 1.14$,

displayed in the fourth image of Figure 5a, the location of breakdown is again well defined. It occurs well upstream of the end of the wire. Considering the images of Figure 5a as a group, it is clear that an increase in wire length L_w/C promotes an upstream advancement of the onset of breakdown.

Corresponding contours of constant velocity $< V >$ are shown in Figure 5b. For the wire length $L_w/C = 0.46$, the change in velocity $< V >$ along the central portion of the vortex is relatively mild, in contrast to the large gradients of $< V >$ for the dimensionless wire length $L_w/C = 0.69$. This observation is in accord with the sharply defined occurrence of breakdown based on patterns of instantaneous vorticity in the image at $L_w/C = 0.69$ in Figure 5a, relative to the slowly evolving process of breakdown at $L_w/C = 0.46$ in Figure 5a. Moreover, as shown in the bottom two images of Figure 5b, a sufficiently long wire length $L_w/C = 0.69$ or 1.14 is associated not only with large gradients of $< V >$ along the central portion of the vortex, but also the rapid occurrence of a region of very low, but not negative, velocity immediately downstream of the breakdown position *vb*.

The effect of a lower value of angle-of-attack $\alpha = 25°$ is shown in Figure 6. The same general trends occur as for the case $\alpha = 30°$ exhibited in Figure 5a. That is, the onset of vortex breakdown becomes more sharply defined for longer values of wire length L_w/C, with the wire length $L_w/C = 1.14$ yielding a sharply defined location of switch of azimuthal vorticity, indicated by the circular symbol and the designation *vb*. Evident in all images of Figure 6 is the particularly small transverse distance between positive (thick line) and negative (thin line) vorticity layers downstream of the onset of breakdown. This transverse distance is of the same order, or even smaller than, the corresponding distance upstream of breakdown. The typical distance between the layers downstream of breakdown is $0.7\ D_v$ for the wire length $L_w/C = 0.57$.

A still further decrease in angle-of-attack to $\alpha = 20°$ produces the patterns of vortex breakdown exhibited in Figure 7. These patterns exhibit the same general trend as observed in Figures 5a and 6. For the shortest wire $L_w/C = 0.57$, however, vortex breakdown does not appear to occur within the field of view. At $L_w/C = 0.69$, a considerable void of high-level vorticity exists between the pre-breakdown vorticity layers and the onset of breakdown. For a sufficiently long wire length $L_w/C = 1.14$, a

well-defined switch in azimuthal vorticity at the location *vb* is particularly evident. Corresponding contours of constant velocity $< V >$ (not shown) indicate extremely mild variations along the core of the vortex for the wire lengths $L_w/C = 0.57$ and 0.69. In contrast, relatively well-defined gradients of $< V >$ occur along the core for $L_w/C = 1.14$. Furthermore, it is again evident that the layers of positive and negative vorticity downstream of breakdown are closely spaced, and large-scale concentrations of vorticity do not form at breakdown.

A direct comparison of the effect of angle-of-attack for a fixed wire length is shown in Figure 8a. For all images, the length of the wire is $L_w/C = 0.57$. For this length, large changes in the location of vortex breakdown occur for small changes of wire length, evident from the plot of Figure 2. Comparing the three images of $\alpha = 20°$, 25° and 30°, the effect of increasing α is to not only to advance the onset of vortex breakdown in the upstream direction, but also to induce a more sharply defined switch in the azimuthal vorticity contours. These overall trends are reflected in the contours of constant velocity $< V >$ of Figure 8b.

A similar type of comparison is shown in Figure 9a, but in this case the wire is sufficiently long, $L_w/C = 1.14$, such that it corresponds to the onset of the asymptotic region of the plot of Figure 2. That is, the length of the wire is sufficiently long such that a small increase or decrease about the nominal value of $L_w/C = 1.1$ induces relatively mild changes in the onset of breakdown. As a consequence, the location of onset of breakdown *vb* changes little when α is varied. Moreover, in all cases, the switch of patterns of instantaneous vorticity at breakdown is well defined. The corresponding plots of velocity $< V >$ of Figure 9b show the occurrence of a well-defined pocket of low velocity, i.e., a wake region. A further discernible trend is as follows. As angle-of-attack α increases, the central portion of this low velocity pocket migrates upstream towards the onset of breakdown *vb*, which corresponds to the switch in sign of vorticity.

CONCLUDING REMARKS

A small diameter wire tethered from the apex of a delta wing, and aligned coaxially with the center of the leading-edge vortex, can induce substantial advancement of the onset of vortex breakdown. The diameter of the wire is two orders of magnitude

smaller than the characteristic diameter of the vortex prior to the onset of vortex breakdown. Alterations of not only the location of breakdown, but also the structure of the vortex are evident using dye visualization and images obtained from a technique of high-image-density particle image velocimetry.

For sufficiently small values of wire length, i.e., approximately one-half the wing chord, the change in onset of breakdown is highly sensitive to the wire length. For a sufficiently long wire, i.e., the order of the wing chord or larger, the change in breakdown location is relatively insensitive to wire length. The largest changes in onset of breakdown occur at smaller values of angle-of-attack. At sufficiently high angle-of-attack, the consequence of the wire is relatively minor, irrespective of wire length. An alternate normalization for the wire length is the distance from the wing apex to the onset of vortex breakdown in absence of the wire. This normalization shows that small changes in wire length generate large changes in the location of breakdown when the wire length is less than approximately one-half the breakdown length in the absence of the wire.

Patterns of azimuthal vorticity, as well as velocity, show the changes in the structural form of breakdown due to presence of the wire. The occurrence of a switch in sign of azimuthal vorticity at the location of breakdown is shown to be an inherent feature for all cases of breakdown that are artificially induced by the wire. The onset of breakdown can occur either downstream or upstream of the end of the wire. The former occurs at smaller values of wire length. In this case, the onset of breakdown is vaguely defined, because the demarcation of the patterns of vorticity at the switch in sign of azimuthal vorticity is not sharply defined. On the other hand, when vortex breakdown occurs upstream of the end of the wire, which tends to be the case for longer wire lengths, the switch in sign of azimuthal vorticity is sharply defined. A remarkable feature of all patterns of wire-induced breakdown is the relatively narrow width of the breakdown region, which is defined as the transverse distance between the centers of the positive and negative vorticity layers. This width is typically the same order as or, remarkably, even smaller than the width prior to the onset of breakdown.

Corresponding patterns of velocity further elucidate the aforementioned trends exhibited by patterns of vorticity. It is shown that a sharply-defined switch in sign of

vorticity is associated with large streamwise gradients of velocity along the core of the vortex and occurrence of a low velocity pocket immediately downstream of the onset of breakdown. On the other hand, for shorter wire lengths and/or lower values of angle-of-attack, the switch in sign of azimuthal vorticity may not be so clearly defined, the gradient of velocity along the core of the vortex is relatively mild, and the evolution to a state of breakdown therefore occurs relatively slowly along the axis of the vortex. In fact, the onset of zero velocity, i.e., occurrence of a stagnation point, along the axis of the vortex does not occur, even though a wake-type defect of the velocity is evident.

ACKNOWLEDGMENTS

The authors gratefully acknowledge the financial support of the Air Force Office of Scientific Research under Grant No. F49620-99-1-0011, monitored by Dr. Steven Walker. One of the authors, Professor Besir Sahin, would like to thank the Scientific and Technical Research Council of Turkey (TUBITAK) and NATO for their financial support.

LIST OF REFERENCES

[1] H. Akilli, B. Sahin, and D. Rockwell, "Vortex breakdown on a delta wing: Control by a transversely-oriented wire", *Physics of Fluids* **13** (2), 452-463 (2000).

[2] P. B. Earnshaw and J. A. Lawford, "Low speed wind tunnel experiments on a series of sharp-edged delta wings", Aeronautical Research Council, R&M 3424, August (1964).

[3] D. B. Mabey, "Beyond the buffet boundary", *Aeronautical Journal* **77** (April), 201-215 (1973).

[4] I. Gursul and W. Xie, "Buffeting flows over delta wings", *AIAA Journal* **37** (1), 58-65 (1999).

[5] B. H. K. Lee, "Vortical tail buffeting of fighter aircraft", *Progress in Aerospace Sciences* **36**, 193-279 (2000).

[6] B. Sahin, H. Akilli, J.-C. Lin and D. Rockwell, "Vortex breakdown-edge interaction: consequence of edge oscillations", *AIAA Journal* **39** (5), 865-876 (2001).

[7] M. Özgören, B. Sahin and D. Rockwell, "Structure of leading-edge vortices on a delta wing at high angle-of-attack", *AIAA Journal* (in press).

[8] D. Rockwell, "Three-dimensional flow structure on delta wings at high angle of attack: experimental concepts and issues", AIAA Paper 93-0550 (1993).

[9] H. E. Helin and C. W. Watry, "Effects of trailing-edge entrainment on delta wing vortices", *AIAA Journal* **32** (4), 802-804 (1994).

[10] Ding, Z. and Shih, C. 1996 "Trailing-Edge Jet Control of the Leading-Edge Vortices of a Delta Wing", *AIAA Journal*, Vol. 34, No. 12, pp. 2641-2644.

[11] P. Vorobieff and D. Rockwell, "Multiple-actuator control of vortex breakdown on a pitching delta wing", *AIAA Journal* **34** (10), 2184-2186 (1996).

[12] P. Vorobieff and D. Rockwell, "Vortex breakdown on pitching delta wing: Control by intermittent trailing-edge blowing", *AIAA Journal* **36** (4), 585-589 (1998).

[13] Huttsell, L. J., Tinapple, J. A. and Weyer, R. M. 1997 "Investigation of Buffet Load Alleviation on a Scaled F-15 Twin Tail Model", AGARD Structures and Materials Panel Workshop, Denmark, October.

[14] G. A. Reynolds and A. A. Abtahi, "Instabilities in leading-edge vortex development", AIAA Paper 87-2424 (1987).

[15]I. Gursul and H. Yang, "Vortex breakdown over a pitching delta wing", AIAA Paper 94-0536, 32nd Aerospace Sciences Meeting and Exhibit, January 10-13, Reno, NV (1994).

[16]D. Rockwell, C. Magness, J. Towfighi, O. Akin and T. Corcoran, "High image-density particle image velocimetry using laser scanning techniques", *Experiments in Fluids* **14**, 181-192 (1993).

[17]G. L. Brown and J. M. Lopez, "Axisymmetric vortex breakdown. Part 2: Physical mechanisms", *Journal of Fluid Mechanics* 221, 553 (1990).

LIST OF FIGURES

Figure 1: Overview of delta wing showing concept of small wire of diameter D_w and length L_w aligned with axis of the leading-edge vortex having a pre-breakdown diameter of D_v. Leading end of wire is tethered from tip of apex of wing. Field of view of image corresponds to 0.7C.

Figure 2: Change of location of onset of vortex breakdown $[X_b)_o - X_b]/C$ due to insertion of wire as a function of dimensionless length of wire L_w/C; C is chord of wing. In all cases, diameter of wire D_w normalized by reference diameter $(D_v)_r$ of vortex is $D_w/(D_v)_r = 0.01$. $(D_v)_r$ is diameter of vortex prior to onset of vortex breakdown at angle of attack $\alpha = 30°$.

Figure 3: Change of location of onset of vortex breakdown $[X_b)_o - X_b]/C$ due to insertion of wire as a function of length of wire $L_w/(X_b)_o$. Normalization parameter $(X_b)_o$ is distance from apex to onset of vortex breakdown in absence of wire. For all cases, diameter of wire D_w normalized by reference vortex diameter $(D_v)_r$ is $D_w/(D_v)_r = 0.01$. $(D_v)_r$ is diameter of vortex prior to onset of vortex breakdown at angle of attack $\alpha = 30°$.

Figure 4: Overview of effect of wire on onset of vortex breakdown. Image (a) corresponds to instantaneous patterns of vorticity in absence of wire, and image (b) to instantaneous vorticity with wire. Wire extends from tip of apex of delta wing to location indicated by triangle and designated as end of wire (eow). Location of onset of vortex breakdown (vb) based on a vorticity criterion is designated by the circular symbol. Positive and negative vorticity are indicated by thick and thin lines respectively. Minimum and incremental values of vorticity are $\omega_{min} = \pm 2\ sec^{-1}$ and $\Delta\omega = 0.7\ sec^{-1}$. Image (c) represents contours of constant velocity <V>. Numbers on designated contours correspond to velocity in units of mm/sec. Image (d) shows corresponding pattern of actual velocity vectors.

Length of wire L_w normalized by wing chord C is $L_w/C = 1.14$. Diameter of wire D_w normalized by reference diameter $(D_v)_r$ is $D_w/(D_v)_r = 0.01$. In above images, diameter of wire is drawn to scale relative to the scale of the vortex, i.e., relative to scale of patterns of vorticity and contours of constant velocity. Length of each PIV image is 0.7C, in which C is chord of delta wing. Angle of attack of delta wing is $\alpha = 30°$.

Figure 5a: Effect of wire length L_w/C on patterns of instantaneous vorticity in vicinity of onset of vortex breakdown (vb) indicated by the circular symbol. End of wire is indicated by triangle and designated as eow. Diameter of wire D_w normalized by reference diameter $(D_v)_r$ of vortex is $D_w/(D_v)_r = 0.01$. For all images, minimum and incremental values of vorticity are $\omega_{min} = \pm 2\ sec^{-1}$ and $\Delta\omega = 0.7\ sec^{-1}$. Positive vorticity is indicated by thick lines and negative vorticity by thin lines. Angle of attack of delta wing is $\alpha = 30°$.

Figure 5b: Effect of wire length L_w normalized by chord C on contours of constant velocity <V> in the vicinity of onset of vortex breakdown (vb). End of wire is indicated by triangle and designated as eow. Diameter of wire D_w normalized by reference

diameter $(D_v)_r$ of vortex is $D_w/(D_v)_r = 0.01$. Numbers on designated contours correspond to magnitude of velocity <V> in mm/sec. Increment between contours is 5 mm/sec. Angle of attack of delta wing is $\alpha = 30°$.

Figure 6: Effect of wire length L_w/C on patterns of instantaneous vorticity in vicinity of onset of vortex breakdown (vb) indicated by the circular symbol. End of wire is indicated by triangle and designated as eow. Diameter of wire D_w normalized by reference diameter $(D_v)_r$ of vortex is $D_w/(D_v)_r = 0.01$. For all images, minimum and incremental values of vorticity are $\omega_{min} = \pm 2$ sec^{-1} and $\Delta\omega = 0.7$ sec^{-1}. Positive vorticity is indicated by thick lines and negative vorticity by thin lines. Angle of attack of delta wing is $\alpha = 30°$.

Figure 7a: Effect of wire length L_w/C on patterns of instantaneous vorticity in vicinity of onset of vortex breakdown (vb) indicated by the circular symbol. End of wire is indicated by triangle and designated as eow. Diameter of wire D_w normalized by reference diameter $(D_v)_r$ of vortex is $D_w/(D_v)_r = 0.01$. For all images, minimum and incremental values of vorticity are $\omega_{min} = \pm 2$ sec^{-1} and $\Delta\omega = 0.75$ sec^{-1}. Positive vorticity is indicated by thick lines and negative vorticity by thin lines. Angle of attack of delta wing is $\alpha = 30°$.

Figure 7b: Effect of wire length L_w normalized by chord C on contours of constant velocity <u> in the vicinity of onset of vortex breakdown (vb). End of wire is indicated by triangle and designated as eow. Diameter of wire D_w normalized by reference diameter $(D_v)_r$ of vortex is $D_w/(D_v)_r = 0.01$. Numbers on designated contours correspond to magnitude of velocity <u> in mm/sec. Increment between contours is 7.5 mm/sec. Angle of attack of delta wing is $\alpha = 20°$.

Figure 8a: Effect of angle-of-attack α on patterns of vorticity in vicinity of onset of vortex breakdown due to insertion of wire. End of wire (eow) is designated by the triangular symbol, while the onset of vortex breakdown (vb) is designated by the circular symbol. For all images, minimum and incremental values of vorticity are $\omega_{min} = \pm 2$ sec^{-1} and $\Delta\omega = 0.75$ sec^{-1}. For all cases, length of wire L_w normalized by chord C is $L_w/C = 0.57$. Diameter of wire D_w normalized by reference diameter $(D_v)_r$ of vortex is $D_w/(D_v)_r = 0.01$.

Figure 8b: Effect of angle-of-attack α on onset of vortex breakdown (vb) represented by contours of constant velocity <V>. End of wire (eow) is designated by the triangular symbol, while the onset of vortex breakdown (vb) is designated by the circular symbol. Numbers on contour lines represent magnitude of velocity in mm/sec. For all cases, length L_w of wire normalized by chord C is $L_w/C = 0.57$. Diameter of wire D_w normalized by reference diameter $(D_v)_r$ of vortex is $D_w/(D_v)_r = 0.01$.

Figure 9a: Effect of angle-of-attack α on patterns of vorticity in vicinity of onset of vortex breakdown due to insertion of wire. End of wire (eow) is designated by the triangular symbol, while the onset of vortex breakdown (vb) is designated by the circular symbol. For all images, minimum and incremental values of vorticity are $\omega_{min} = \pm 2$ sec^{-1}

and $\Delta\omega = 0.75\ sec^{-1}$. For all cases, length of wire L_w normalized by chord C is $L_w/C = 1.14$. Diameter of wire D_w normalized by reference diameter $(D_v)_r$ of vortex is $D_w/(D_v)_r = 0.01$.

Figure 9b: Effect of angle-of-attack α on onset of vortex breakdown (vb) represented by contours of constant velocity <V>. End of wire (eow) is designated by the triangular symbol, while the onset of vortex breakdown (vb) is designated by the circular symbol. Numbers on contour lines represent magnitude of velocity in mm/sec. For all cases, length L_w of wire normalized by chord C is $L_w/C = 1.14$. Diameter of wire D_w normalized by reference diameter $(D_v)_r$ of vortex is $D_w/(D_v)_r = 0.01$.

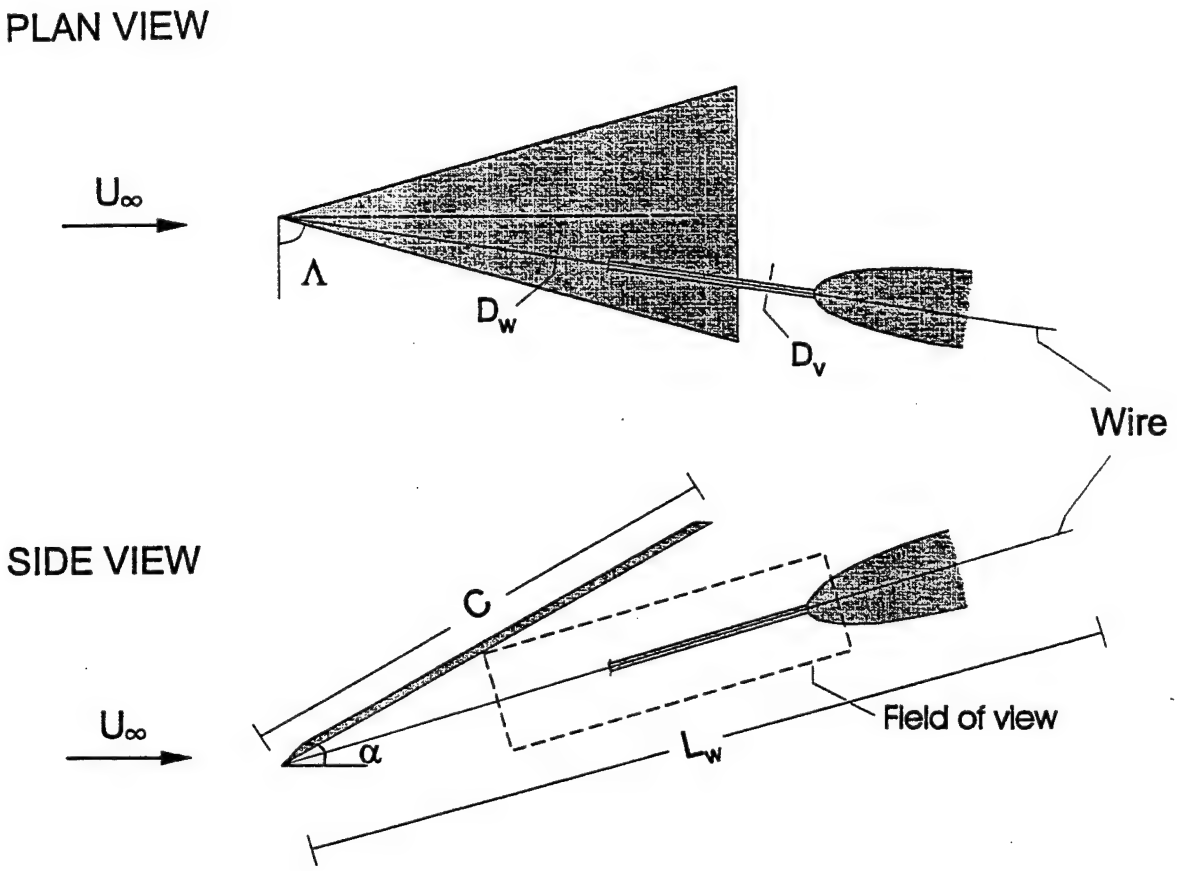

Figure 1: Overview of delta wing showing concept of small wire of diameter D_w and length L_w aligned with axis of the leading-edge vortex having a pre-breakdown diameter of D_v. Leading end of wire is tethered from tip of apex of wing. Field of view of image corresponds to 0.7C.

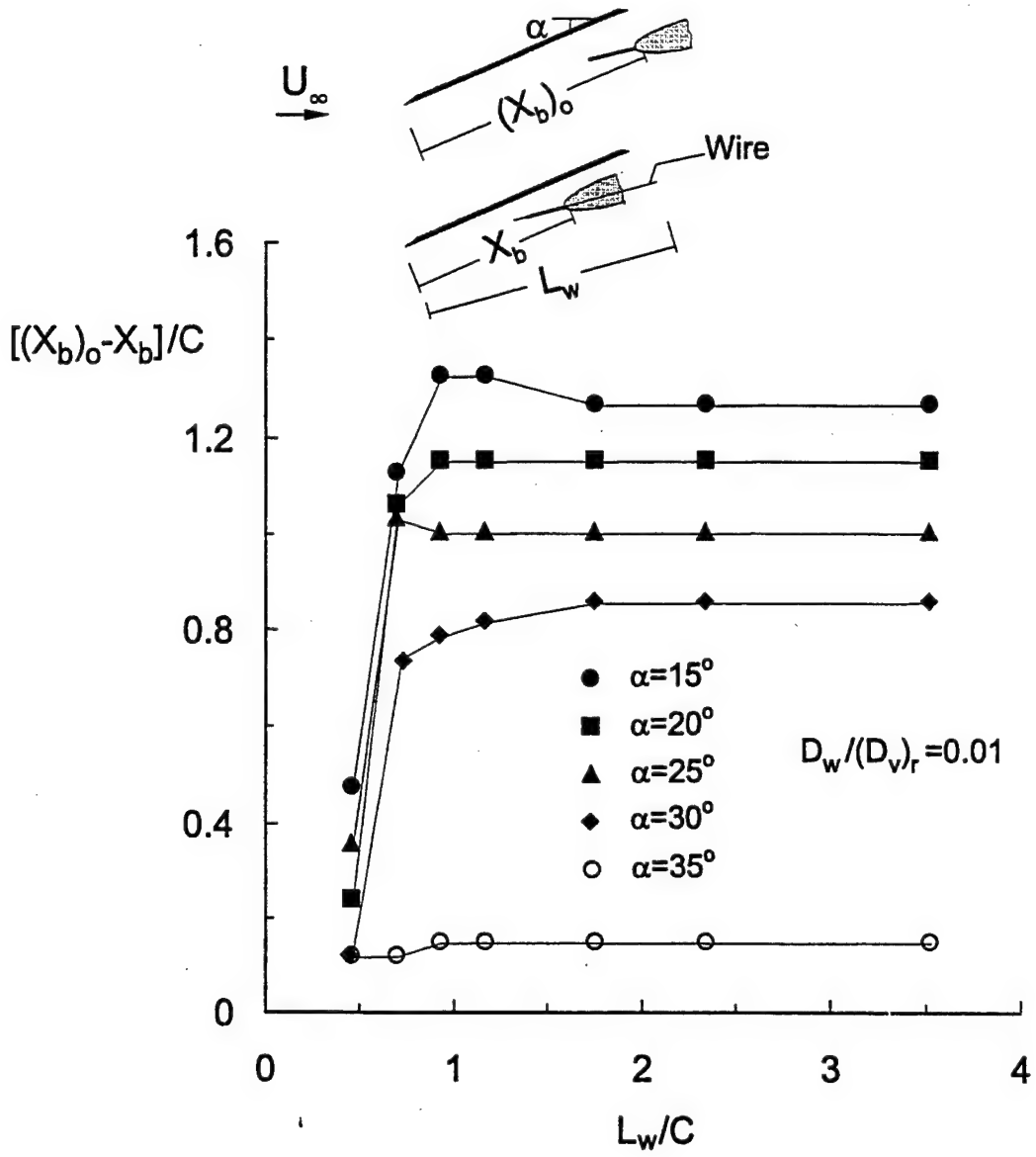

Figure 2: Change of location of onset of vortex breakdown $[(X_b)_o - X_b]/C$ due to insertion of wire as a function of dimensionless length of wire L_w/C; C is chord of wing. In all cases, diameter of wire D_w normalized by reference diameter $(D_v)_r$ of vortex is $D_w/(D_v)_r = 0.01$. $(D_v)_r$ is diameter of vortex prior to onset of vortex breakdown at angle of attack $\alpha = 30°$.

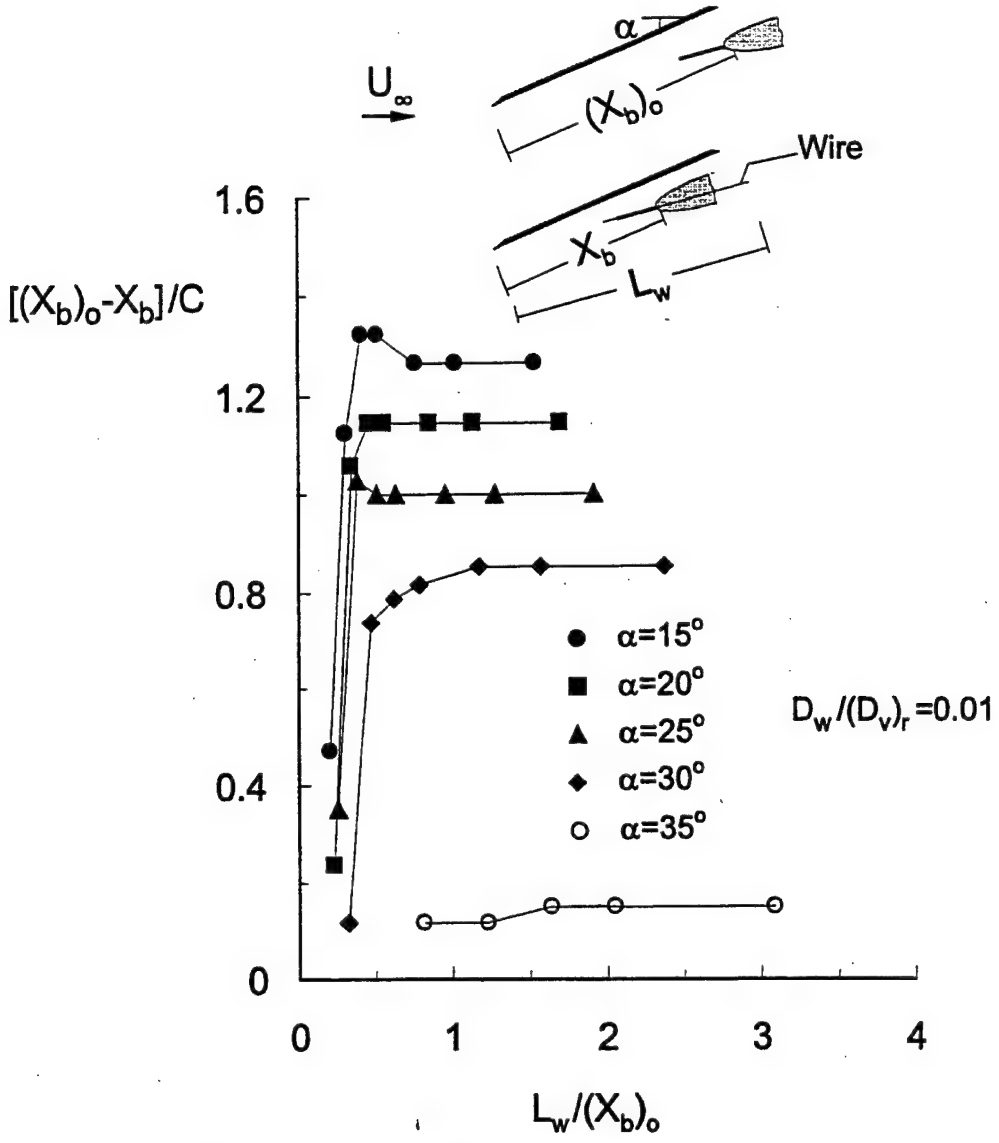

Figure 3: Change in location of onset of vortex breakdown $[(X_b)_o - X_b]/C$ due to insertion of wire as a function of length of wire $L_w/(X_b)_o$. Normalization parameter $(X_b)_o$ is distance from apex to onset of vortex breakdown in absence of wire. For all cases, diameter of wire D_w normalized by reference vortex diameter $(D_v)_r$ is $D_w/(D_v)_r = 0.01$. $(D_v)_r$ is diameter of vortex prior to onset of breakdown at angle of attack $\alpha = 30°$.

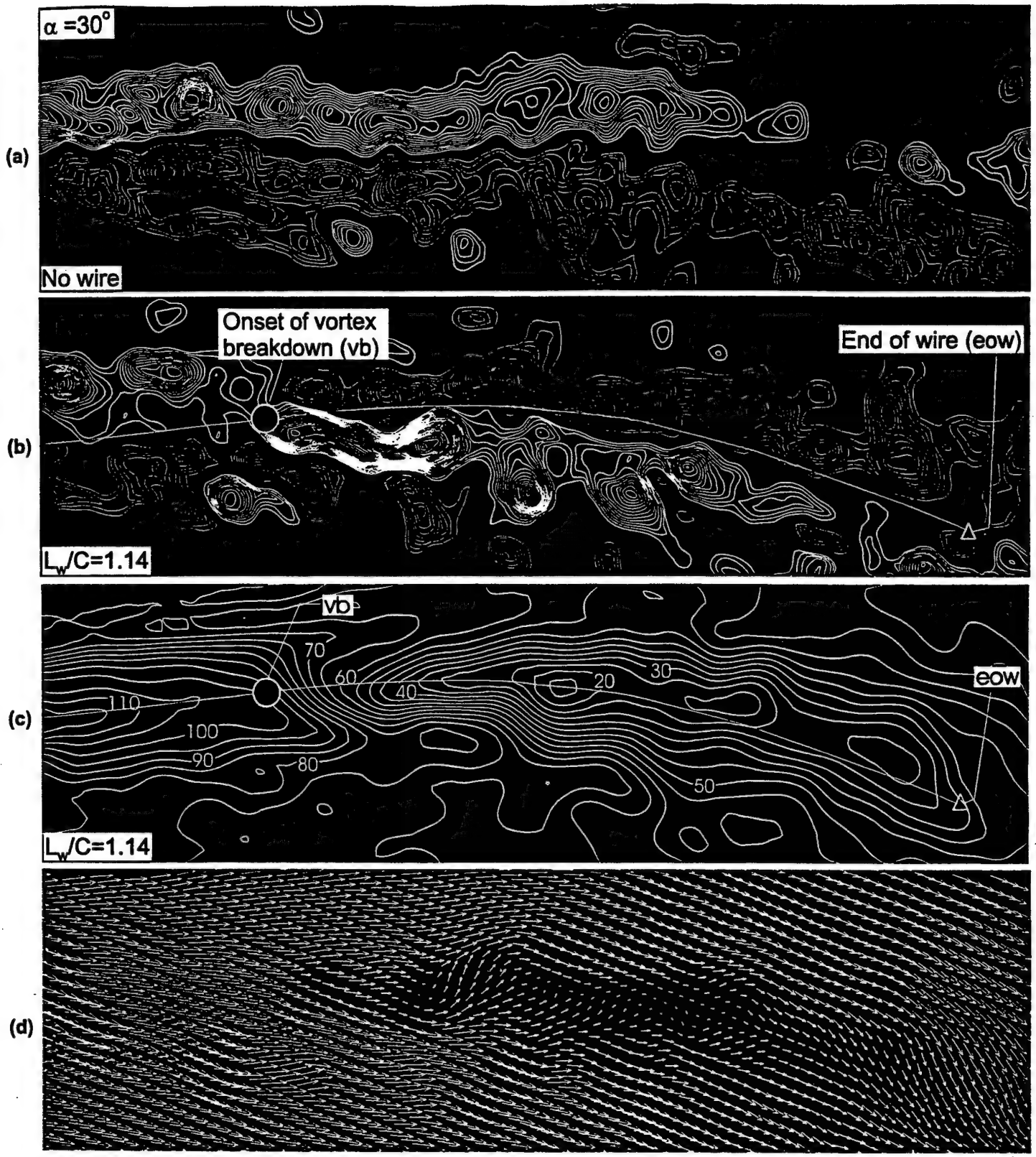

Figure 4: Overview of effect of wire on onset of vortex breakdown. Image (a) corresponds to instantaneous patterns of vorticity in absence of wire, and image (b) to instantaneous vorticity with wire. Wire extends from tip of apex of delta wing to location indicated by triangle and designated as end of wire (eow). Location of onset of vortex breakdown (vb) based on a vorticity criterion is designated by the circular symbol. Positive and negative vorticity are indicated by thick and thin lines respectively. Minimum and incremental values of vorticity are $\omega_{min} = \pm 2\text{sec}$ and $\Delta\omega = 0.75\text{sec}^{-1}$. Image (c) represents contours of constant velocity $< V >$. Numbers on designated contours correspond to velocity in units of mm/sec. Image (d) shows corresponding pattern of actual velocity vectors.

Length of wire L_w normalized by wing chord C is $L_w/C = 1.14$. Diameter of wire D_w normalized by reference diameter $(D_v)_r$ is $D_w/(D_v)_r = 0.01$. In above images, diameter of wire is drawn to scale relative to the scale of the vortex, i.e., relative to scale of patterns of vorticity and contours of constant velocity. Length of each PIV image is 0.7C, in which C is chord of delta wing. Angle of attack of delta wing is $\alpha = 30^{\circ}$.

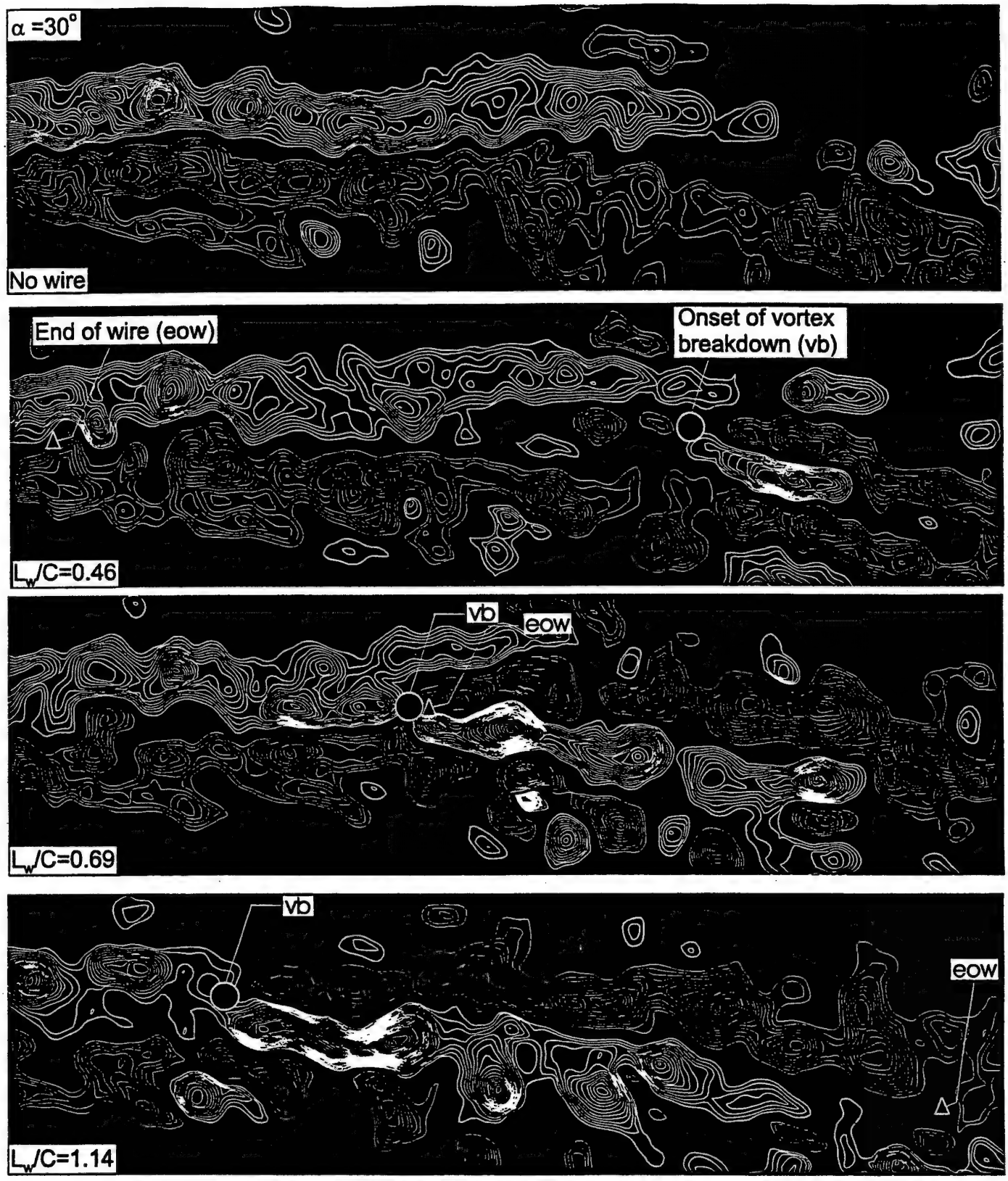

Figure 5a: Effect of wire length L_w/C on patterns of instantaneous vorticity in vicinity of onset of vortex breakdown (vb) indicated by the circular symbol. End of wire is indicated by triangle and designated as eow. Diameter of wire D_w normalized by reference diameter $(D_v)_r$ of vortex is $D_w/(D_v)_r = 0.01$. For all images, minimum and incremental values of vorticity are $\omega_{min} = \pm 2\ sec^{-1}$ and $\Delta\omega = 0.75 sec^{-1}$. Positive vorticity is indicated by thick lines and negative vorticity by thin lines. Angle of attack of delta wing is $\alpha = 30°$.

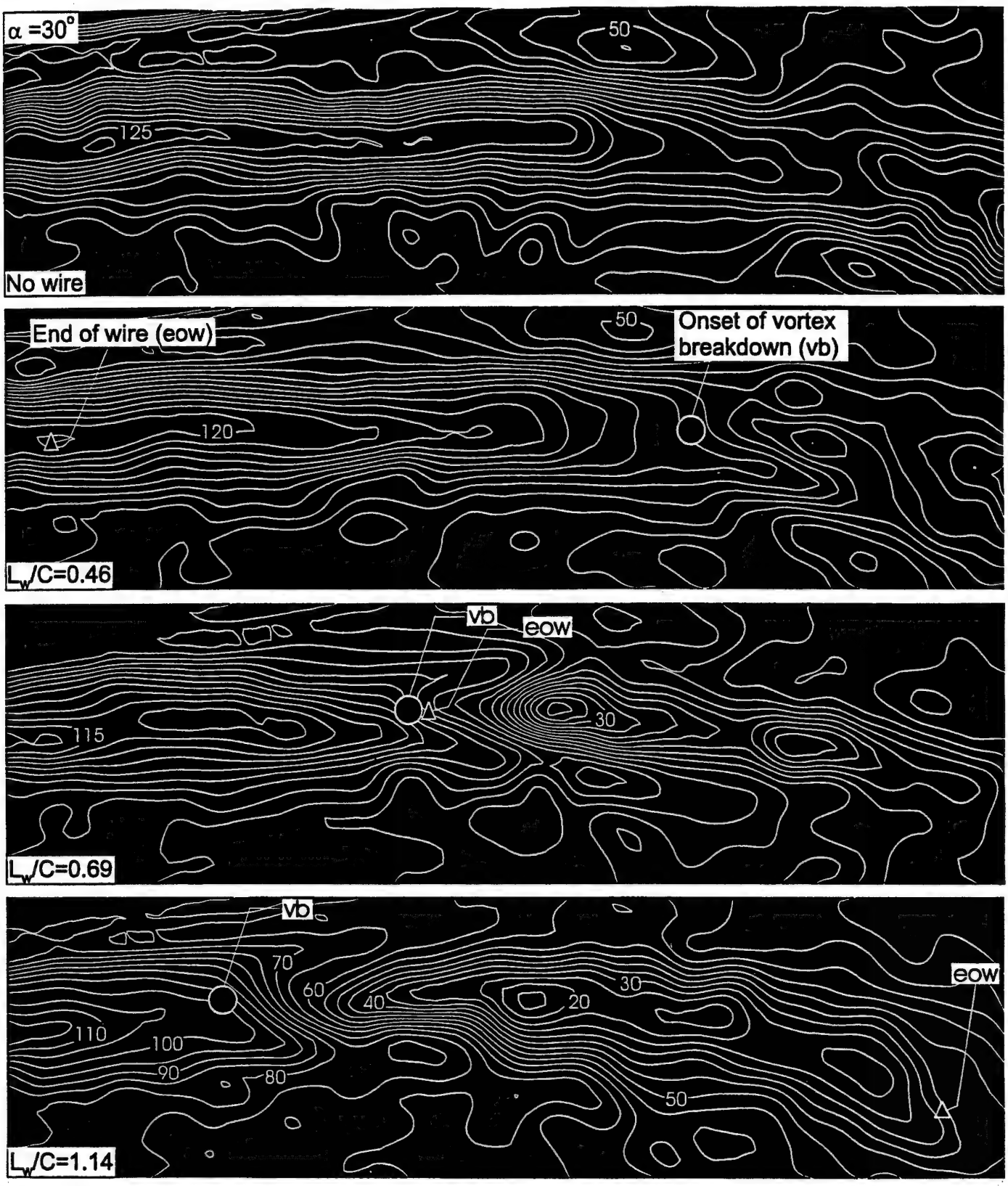

Figure 5b: Effect of wire length L_w normalized by chord C on contours of constant velocity $<V>$ in the vicinity of onset of vortex breakdown (vb). End of wire is indicated by triangle and designated as eow. Diameter of wire D_w normalized by reference diameter $(D_v)_r$ of vortex is $D_w/(D_v)_r = 0.01$. Numbers on designated contours correspond to magnitude of velocity $<V>$ in mm/sec. Increment between contours is 5 mm/sec. Angle of attack of delta wing is $\alpha = 30°$.

Figure 6: Effect of wire length L_w/C on patterns of instantaneous vorticity in vicinity of onset of vortex breakdown (vb) indicated by the circular symbol. End of wire is indicated by triangle and designated as eow. Diameter of wire D_w normalized by reference diameter $(D_v)_r$ of vortex is $D_w/(D_v)_r = 0.01$. For all images, minimum and incremental values of vorticity are $\omega_{min} = \pm 2\ sec^{-1}$ and $\Delta\omega = 0.75 sec^{-1}$. Positive vorticity is indicated by thick lines and negative vorticity by thin lines. Angle of attack of delta wing is $\alpha = 25°$.

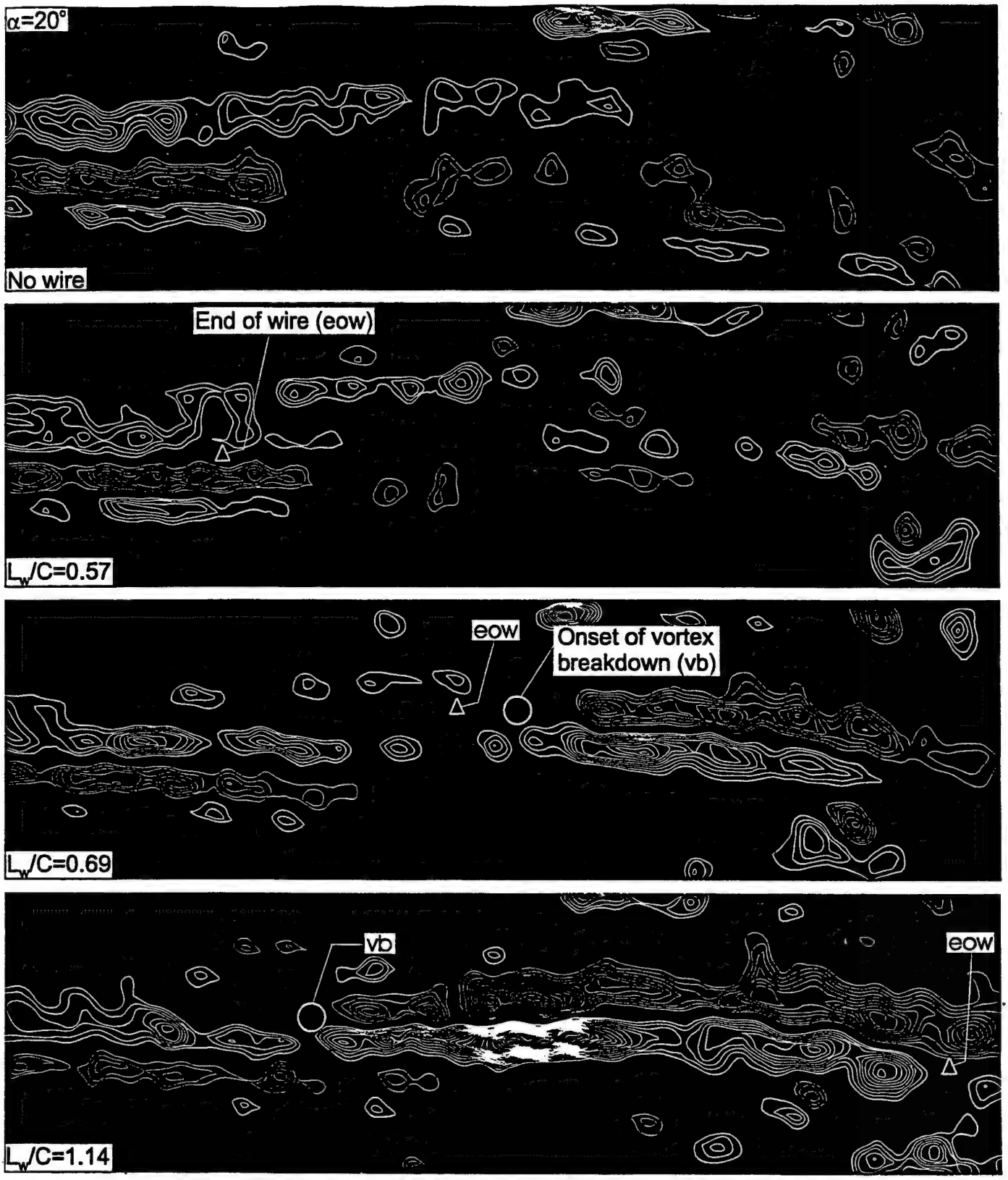

Figure 7: Effect of wire length L_w/C on patterns of instantaneous vorticity in vicinity of onset of vortex breakdown (vb) indicated by the circular symbol. End of wire is indicated by triangle and designated as eow. Diameter of wire D_w normalized by reference diameter $(D_v)_r$ of vortex is $D_w/(D_v)_r = 0.01$. For all images, minimum and incremental values of vorticity are $\omega_{min} = \pm 2\ sec^{-1}$ and $\Delta\omega = 0.75 sec^{-1}$. Positive vorticity is indicated by thick lines and negative vorticity by thin lines. Angle of attack of delta wing is $\alpha = 20°$.

Figure 8a: Effect of angle of attack α on patterns of vorticity in vicinity of onset of vortex breakdown due to insertion of wire. End of wire (eow) is designated by the triangular symbol, while the onset of vortex breakdown (vb) is designated by the circular symbol. For all images, minimum and incremental values of vorticity are $\omega_{min} = \pm 2\ sec^{-1}$ and $\Delta\omega = 0.75 sec^{-1}$. For all cases, length of wire L_w normalized by chord C is $L_w/C = 0.57$. Diameter of wire D_w normalized by reference diameter $(D_v)_r$ of vortex is $D_w/(D_v)_r = 0.01$.

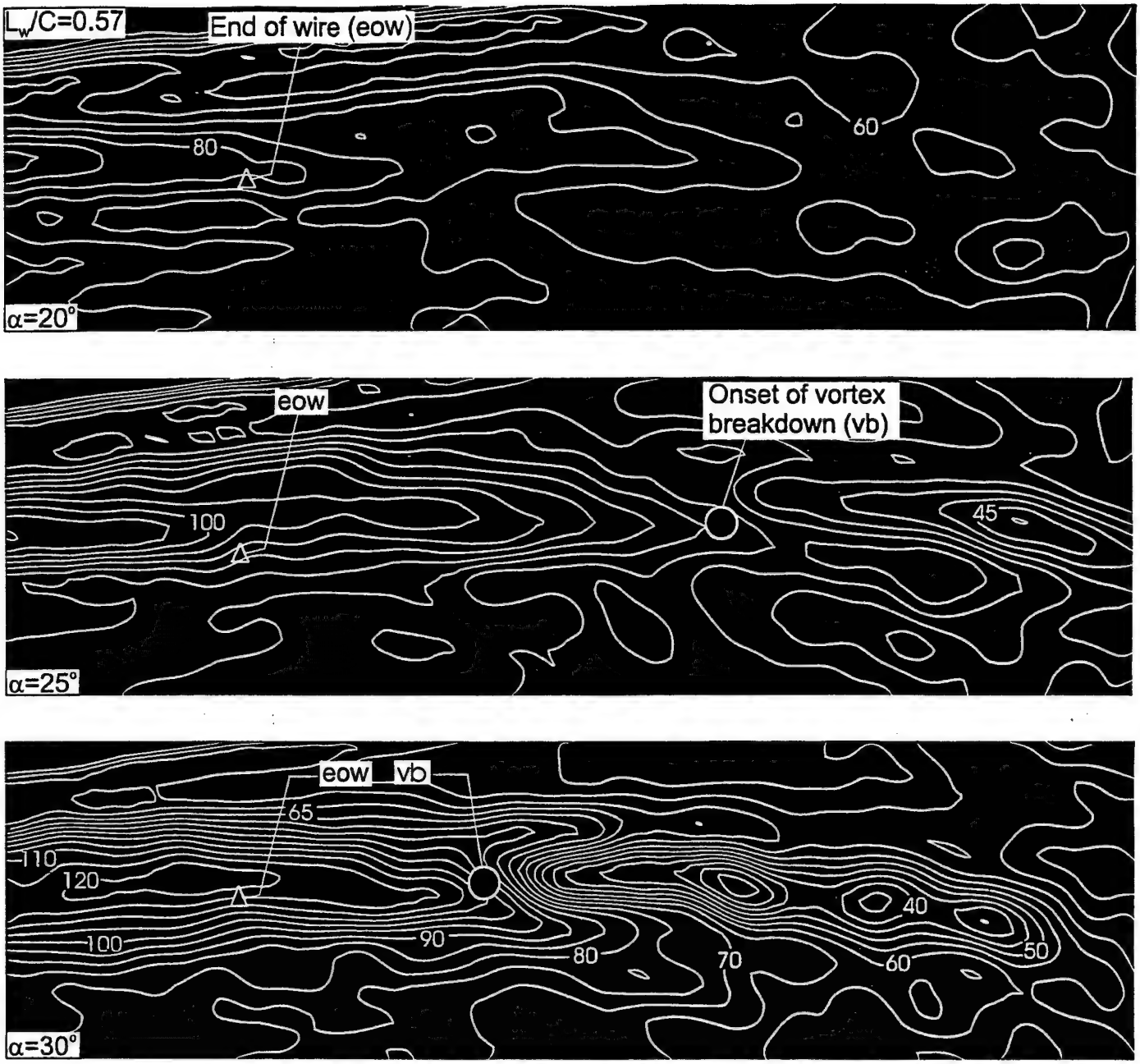

Figure 8b: Effect of angle of attack α on onset of vortex breakdown (vb) represented by contours of constant velocity $< V >$. End of wire (eow) is designated by the triangular symbol, while the onset of vortex breakdown (vb) is designated by the circular symbol. Numbers on contour lines represent magnitude of velocity in mm/sec. For all cases, length L_w of wire normalized by chord C is $L_w/C = 0.57$. Diameter of wire D_w normalized by reference diameter $(D_v)_r$ of vortex is $D_w/(D_v)_r = 0.01$.

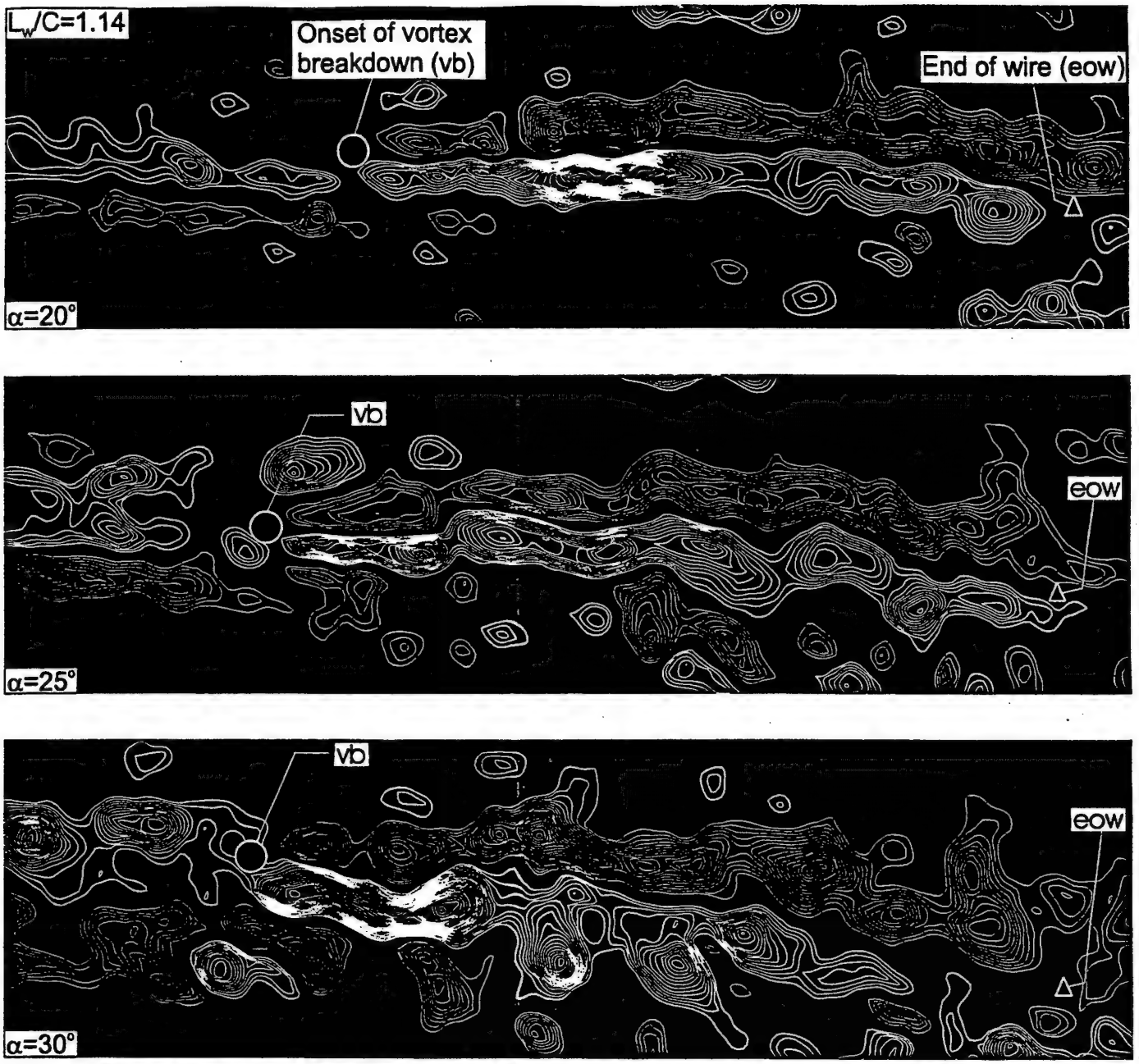

Figure 9a: Effect of angle of attack α on patterns of vorticity in vicinity of onset of vortex breakdown due to insertion of wire. End of wire (eow) is designated by the triangular symbol, while the onset of vortex breakdown (vb) is designated by the circular symbol. For all images, minimum and incremental values of vorticity are $\omega_{min} = \pm 2$ sec^{-1} and $\Delta\omega = 0.75$sec^{-1}. For all cases, length of wire L_w normalized by chord C is $L_w/C = 1.14$. Diameter of wire D_w normalized by reference diameter $(D_v)_r$ of vortex is $D_w/(D_v)_r = 0.01$.

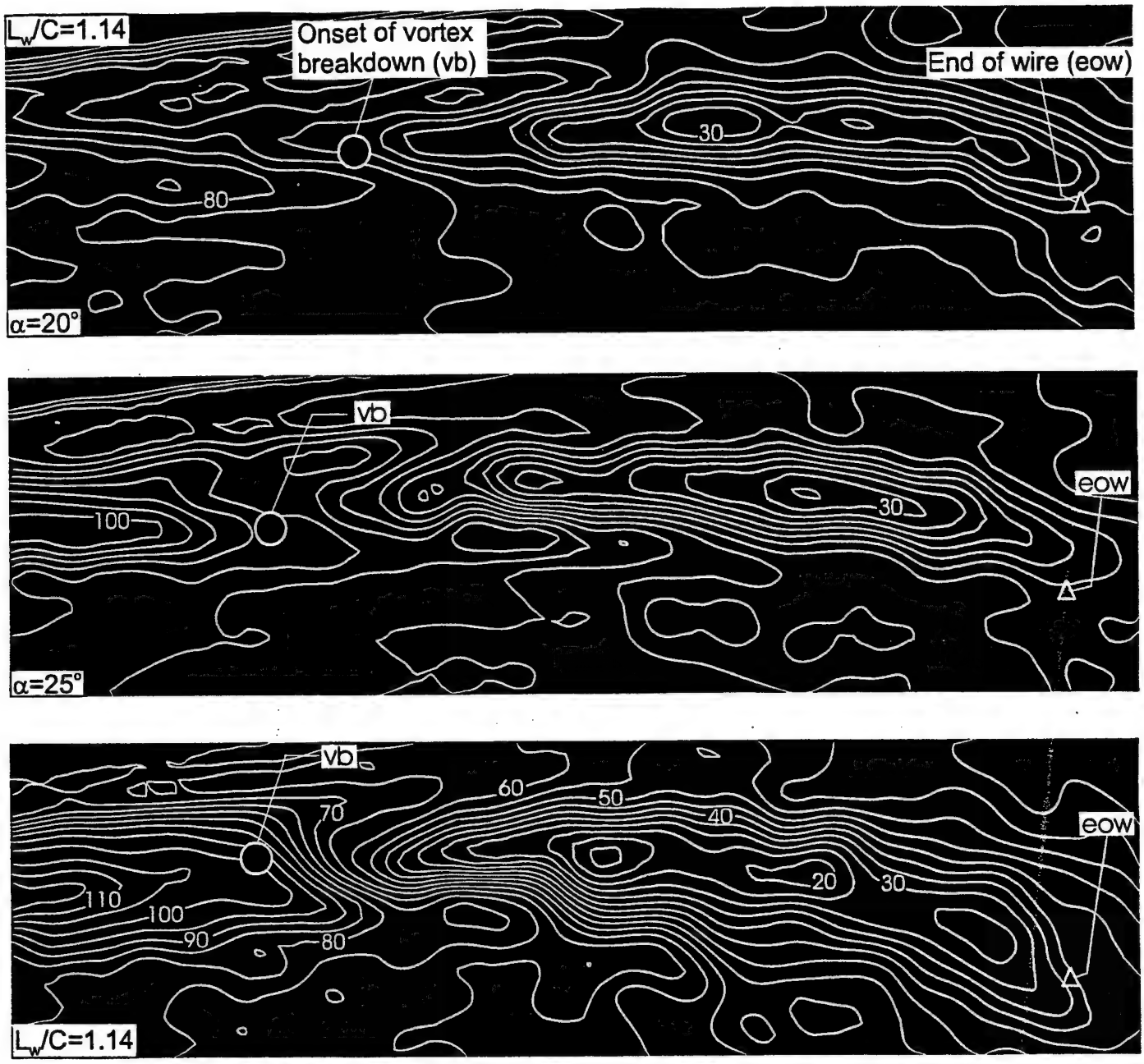

Figure 9b: Effect of angle of attack α on onset of vortex breakdown (vb) represented by contours of constant velocity $<V>$. End of wire (eow) is designated by the triangular symbol, while the onset of vortex breakdown (vb) is designated by the circular symbol. Numbers on contour lines represent magnitude of velocity in mm/sec. For all cases, length L_w of wire normalized by chord C is $L_w/C = 1.14$. Diameter of wire D_w normalized by reference diameter $(D_v)_r$ of vortex is $D_w/(D_v)_r = 0.01$.

APPENDIX G

PIV99 011700

Keynote Lecture, Third International Workshop on Particle Image Velocimetry, University of California, Santa Barbara, September 16-18, 1999. Extended version of manuscript originally prepared August 5, 1999.

IMAGING OF UNSTEADY SEPARATED FLOWS: GLOBAL APPROACHES TO NEW INSIGHT*

by

Donald Rockwell
Department of Mechanical Engineering and Mechanics
354 Packard Laboratory, 19 Memorial Drive West
Lehigh University, Bethlehem, PA 18015

ABSTRACT Quantitative characterization of unsteady, separated flows is central to understanding the physics of flow-structure interactions, which can give rise to vibration and noise generation. Global, instantaneous representations, obtained from high-image-density particle image velocimetry, can provide a basis for identification and classification of flow patterns. Moreover, these representations allow direct links to established theoretical concepts, which can be expressed in terms of vorticity. Case studies of vortex-dominated flows are addressed using these approaches, with the aim of defining challenges and future prospects.

1 Introduction

Unsteady separated flows are an inherent feature of a wide class of flow-structure interactions that involve wakes, jets and mixing layers. Related configurations include, for example, steady flow or an unsteady wave past a bluff body, flow in a jet-edge system and flow past a cavity or other geometric discontinuity. Blake (1986), Blevins (1990), Naudascher and Rockwell (1994), and Howe (1998) address the engineering interpretation and analytical modeling of flow-induced vibrations of, and noise generation

***Rockwell, D. 2000 "Imaging of Unsteady Separated Flows: Global Approaches to New Insight", *Experiments in Fluids*, Vol. 29, No. 7, pp. S255-S273.**

from, these systems. Rockwell (1998a) provides a recent overview of the underlying physics and unresolved issues.

Traditional approaches to characterizing flow-structure interactions have typically involved extensive measurement of overall forces, as well as distributions of surface pressure and acceleration. In most cases, these methods involve time-averaged representations, such as root-mean-square values or spectral distributions. An understanding of the physics of the loading is typically based on a form of qualitative flow visualization. Over the years, these approaches have yielded considerable insight and guidance for modeling not only the loading of a stationary body, but also the coupled interaction between a vibrating body, the associated noise generation and the surrounding flow. With the advent of quantitative imaging approaches, such as particle image velocimetry (PIV), the aforementioned characterization of surface forces, pressures and accelerations, can be presented in parallel with instantaneous representations of the flow patterns, i.e., patterns of velocity, vorticity, and streamlines, as recently summarized by Rockwell (1998b). Quantitative representations of the flow invite comparison with various classes of numerical simulation, which, of course, has proved to be a productive route. Assessment of these types of experimental-numerical comparisons, as well as strictly experimental studies that yield quantitative representations of the flow, lies outside the scope of the present overview. Rather, the emphasis herein is on description of: (a) selected frameworks for identification and classification of complex flows characteristic of flow-structure interactions; and (b) direct links to theoretical formulations that describe the consequences for unsteady loading and noise generation of unsteady separated flows. These approaches are illustrated for various classes of vortex-structure interaction, with the aim of stimulating further investigations in this direction.

2 Framework for identification and classification of flow patterns

The vast majority of flow-structure interactions are associated with generation of coherent patterns of the flow structure, often in conjunction with a broadband background. Coherent features of the flow arise from the elastic motion of a portion of a solid

boundary, such as a panel of an aircraft wing or a ship hull, or motion of an entire body, especially those having cylindrical configurations, such as tall buildings, risers, offshore platforms, towing cables, and heat exchanger tubes. Even in absence of motion of a boundary or body, the occurrence of self-excited acoustic resonance, such as that occurring in an organ pipe, a long pipeline-cavity system, or even within a cavity configuration, can enhance the degree of organization of separated flow patterns. Finally, in certain situations, combinations of elastic motion and acoustic resonance can work together to yield identifiable, coherent flow patterns. The nature of these coherent patterns, and the degree to which they coexist with, or dominate, broadband features of the flow, can provide a direct indication of the degree of "lock-on" of a self-excited vibration or acoustic resonance phenomenon. An immediate priority is therefore to address possible frameworks for eduction of coherent vortical structures in separated flows.

In recent decades, substantial advances have been made in techniques for identification and classification of coherent structures, in both free and bounded flows, with emphasis on deployment of one or more pointwise sensors, e.g., hot wire/film probes and LDA probes. Bonnet et al. (1998) provide a comprehensive overview and critique of a range of approaches applied to free turbulent shear flows. These approaches include: topological methods; proper orthogonal decomposition; conditional sampling; wavelets; pattern recognition; stochastic estimation; and full field methods, such as pseudoflow visualization. Bonnet et al. (1998) give an extensive list of citations that describe these methods. They include: Adrian (1975); Antonia (1981); Glauser and George (1992); Lesieur (1993); Berkooz et al. (1993); Hussain (1993); Kevlahan et al. (1993); and Adrian et al. (1996).

The technique of high-image-density particle image velocimetry (PIV) has seen rapid development in recent years. To date, relatively little effort has been devoted to pattern identification and interpretation using the aforementioned techniques, despite their promise foretold by accomplishments using pointwise approaches. Herein, emphasis is on two types of frameworks for identification and classification: topological concepts; and proper orthogonal decomposition. Both of these frameworks have been employed in

conjunction with PIV and, hopefully, will provide motivation for application of other classes of coherent structure identification.

2.1
Topological concepts incorporating critical point theory

Topological concepts, based on critical point theory, can provide a means of classification and interpretation of, for example, patterns of skin friction lines along a surface and streamlines away from the surface. Conceptual overviews, as well as summaries of related investigations, are given by Hunt et al. (1978), Tobak and Peake (1982), Perry and Chong (1987), Chong et al. (1990), Moffatt and Tsinober (1990), and Dallmann et al. (1995).

For a given flow field, it is possible to define critical points as points where the slope of streamlines is indeterminate, and the velocity is zero in an appropriate reference frame. Representative critical points include, for example, foci and saddle points. Of course, complete knowledge of the flow obtained from a theoretical or numerical simulation allows a full topological description, as described in the investigation of Oswatitsch (1958). He provided the first classification of critical points, on a systematic basis, by using solutions of the continuity and Navier-Stokes equations. Early experimental investigations, e.g., Maskell (1955) and other investigations reviewed by Tobak and Peake (1982) and Perry and Chong (1987), focused on surface flow patterns in the form of skin friction lines or limiting streamlines near a solid surface, and revealed central features of three-dimensional separation. The power of deducing flow patterns adjacent to a surface on the basis of surface patterns is markedly evident in the investigation of Hunt et al. (1978). Related topological rules are defined by Hunt et al. (1978) and Tobak and Peake (1982). Regarding quantitative measurement of flow patterns both adjacent to and well away from a surface, the flying hot wire technique of Perry and his colleagues has yielded important insight into the phase-averaged structure of the flow; related works are summarized by Perry and Chong (1987). Further interpretations of flow topology based on pointwise measurements are given by Bonnet et al. (1998).

Irrespective of whether numerical or experimental investigations are employed for topological characterization of flows, misinterpretations may arise unless proper caution is exercised. For example, a pattern of sectional streamlines on a given cross-section of the

flow is often employed to identify "vortices". Dallmann and Schulte-Werning (1990) emphasize that interpretation depends strongly on the selected sequence of cross-sections. Only a sequence of "Poincaré-sections" provides the correct information. Such sections provide visualization of the intersection with the singular stream- or vorticity-surfaces. Furthermore, the nonuniqueness of the cross-flow topologies of three-dimensional vortical flows due, among other features, to axial compression and stretching, is evaluated by Visbal and Gordnier (1994). Unsteadiness of the flow can provide additional complexities for interpretation of the flow topology; a critical view is given by Dallman et al. (1995). Finally, sufficient spatial resolution is necessary for adequate definition of, for example, streamline topology and the associated critical points. As shown by Lin and Rockwell (1997), the effective grid size employed in PIV imaging can have a marked effect on the patterns of vorticity, associated circulation, and patterns of streamline topology. In fact, one can see, in the recent literature, inconsistent interpretations of streamline patterns based on either PIV or PTV. The most evident fallacy is representation of an inherently three-dimensional vortex flow by a pattern of concentric streamlines, as opposed to the correct interpretation of a stable or unstable focus and an associated spiral pattern of streamlines.

PIV with adequate spatial resolution can provide the spatial distribution of velocity over an entire plane at a given instant, and thereby the instantaneous flow topology at that instant. Magness et al. (1993) determined the instantaneous sectional streamline pattern over the crossflow plane on a delta wing at high angle of attack, as illustrated in Figure 1. The jitter in the streamline patterns is due to inherent turbulent fluctuations. Nevertheless, the definition of node N and saddle S points is consistent with topological rules (see schematic in inset). In fact, this type of characterization leads to an unexpected, nonclassical focus. It is unstable at the nodal location N_1, corresponding to an outward-spiral of the streamline pattern, which is now recognized to be an inherent feature of vortex flow at high angle of attack.

A fascinating prospect is application of topological concepts to a fully-turbulent boundary layer flow, which may exhibit vortical structures of varying degrees of coherence. Important in this case is, again, consideration of the instantaneous topological

features of the flow. Zong et al. (1998) have employed a high resolution PIV technique to detect the focus-type regions over a given crossflow plane, as illustrated in Figure 2. The darkened regions represent values of a two-dimensional discriminate that lie below a given threshold value, which is close to zero.

2.2 Proper orthogonal decomposition

Proper orthogonal decomposition (POD) provides a basis for characterizing organized spatial characteristics in a flow, i.e. coherent structures. POD approaches are useful in design and simulation of flow control systems, since they provide a compact description of the system dynamics.

The POD approach is attributable to Lumley (1967). An assessment of this approach is given by Berkooz et al. (1993), which includes a description of POD-weighted-residuals for describing system dynamics. Further aspects are described in the recent investigation of Liakopoulos et al. (1997). Particularly relevant to our present considerations is the version of POD referred to as snapshot POD, defined by Sirovich (1987). In essence, snapshot POD is based on sequence of instantaneous spatial fields acquired at different times.

As part of an assessment of the application of pointwise measurement techniques to the eduction of coherent structures, Bonnet et al. (1998) describe, with the aid of numerical simulation, POD representations of a free turbulent shear flow. The reconstructed POD modes involved use of Taylor's hypothesis, with a spatially constant transport velocity. This leads to the terminology of "frozen" snapshots of the flow patterns, allowing transformation of the time coordinate into a streamwise coordinate.

PIV techniques provide the opportunity to acquire instantaneous, spatial representations of the flow. Furthermore, cinema PIV techniques, as described by Vogel and Lauterborn (1988) and Lin and Rockwell (1994, 1997), can lead to a sequence of images of high temporal resolution, relative to the predominant time scale of the flow structure. Alternately, video or digital camera systems, which typically have lower framing rates when the spatial resolution is higher, can provide temporally resolved descriptions of slow flows as described, for example, by Huang (1994) and Noca et al.

(1999). The potential therefore exists to apply the concepts of snapshot POD to a highly-resolved time sequence of instantaneous images. Huang (1994) first applied truly snapshot POD, in the spirit proposed by Sirovich (1987), to the separated flow past a backward-facing step using a video-based approach. Comparisons of patterns of velocity vectors and vorticity contours with POD reconstructions, based on a varying number of modes, clearly showed the usefulness of this approach.

Cipolla et al. (1998) employed the snapshot POD technique for characterizing the flow past a delta wing. Figure 2 compares reconstructed velocity fields and patterns of vorticity with the original PIV data in the crossflow plane. A reconstruction based on only three eigenmodes provides a remarkably reasonable description of the pattern of velocity vectors and the major features of the contours of constant vorticity, especially those associated with the primary leading-edge vortex. Further application of the snapshot POD technique (Cipolla et al., 1998) yielded insight into the unsteady fluctuations of the vortex structure, which are associated with fluctuations in the location of vortex breakdown. Finally, it should be noted that an important link exists between this snapshot POD technique and the aforementioned topological concepts described in Section 2.1. The streamline pattern in a crossflow plane can be constructed using a small number of eigenfunctions, as demonstrated by Cipolla et al. (1998). These observations clearly indicate the capability of POD to yield a high compression ratio, while still retaining the important features of the flow pattern.

3
Direct links to theoretical, vorticity-based concepts

Unsteady separated flows typically exhibit an underlying degree of coherence and are particularly well-suited to comparison with theoretical models of varying degrees of complexity. Well-defined vortical structures are likely to emerge if, as described in the foregoing, either elastic motion of a boundary or acoustic resonant phenomena are present. Theoretical models, which describe the physical consequences of instantaneous vortical structures, can serve as an important complement to the approaches described in Section 2.

It is well recognized that formulation of models on the basis of vorticity provides the most complete and unambiguous description of complex flows. Yet, the most experimental investigations have relied on pointwise measurements of velocity, at single or multiple locations, typically in conjunction with flow visualization. These types of approaches have obviously yielded important new insight. The issue arises as to how the next generation of advances in our understanding of separated flows can benefit from PIV imaging, which can yield spatial distributions of vorticity over an entire plane at a given instant and, in the case of cinema PIV, a temporarily resolved sequence of such images. Over the years, theoretical frameworks have been established for determining loading and noise characteristics. In order to obtain closure, it is necessary to know the instantaneous distributions of a flow parameter, preferably vorticity, over a spatial domain and the succession of such distributions with time. Even in cases where complete closure or sufficient accuracy cannot be attained, it may be possible to estimate those features of the flow physics that dominate loading and noise generation.

In the following, we consider a number of vorticity-based concepts and their relation to vortex generation and interaction, which, in turn, serve as the origin of flow-induced vibration and noise. They include: (i) vorticity amplification, which is central to vortex formation and its control; (ii) force-vorticity relations, which are essential for determining vortex-induced forces; (iii) vorticity-acoustic coupling formulations, which provide a basis for determining forces and sound generation due to vortex impingement; and (iv) vorticity evolution and switching, which is associated with vortex generation in swirling flows and the eventual onset of vortex breakdown, which, in turn, induces surface loading.

3.1
Vorticity amplification: A basis for vortex formation and its control

The development of vortices in unsteady separated flows is traceable to the amplification of small disturbances. The history of unstable free shear flows is wide and diverse, but recent theoretical developments provide a basis for unifying our perspective. Huerre and Monkewitz (1990) classify instabilities as local and global and, furthermore, interpret the local instability in terms of the response to an impulse. If the localized disturbances move

both in the upstream and downstream directions and extend over the entire region of the parallel flow, the flow is absolutely unstable (AU). If, on the other hand, the disturbances are swept away from the location of application of an impulse disturbance, the flow is viewed to be convectively unstable (CU). From a practical perspective, convectively unstable flows are extremely sensitive to small amplitude disturbances, whereas absolutely unstable flows, which typically culminate in robust, limit-cycle oscillations, exhibit relative insensitivity to applied perturbations. A prevalent flow configuration for investigating convectively and absolutely (globally) unstable flows is the flow past a cylinder, shown in the simplified schematic of Figure 4. Even in absence of the small-scale shear-layer vortices, the possibility of an absolutely unstable wake and the consequent formation of Kármán vortices is a central feature. At sufficiently high Reynolds number, small-scale vortical structures are evident in the separating shear layer, and are termed shear-layer vortices, Bloor-Gerrard vortices or Kelvin-Helmholtz vortices, all of which are appropriate terminologies. The existence of these small-scale vortical structures can alter the mean flow characteristics of the near-wake and thereby the conditions for which the flow becomes absolutely unstable. Regions of convectively unstable and absolutely unstable flows in the near-wake are described by Huerre and Monkewitz (1990) and Oertel (1990).

The onset of shear-layer vortices occurs in a manner similar to the widely-investigated instabilities of mixing layers and jets, as summarized in the review of Ho and Huerre (1984). It is abundantly evident, from the range of investigations cited therein, that remarkable advances have been made in our understanding of these convectively-unstable flows by use of pointwise measurements techniques, i.e., hot wire/film anemometry and laser-Doppler anemometry, often in conjunction with qualitative flow visualization. To characterize the rapid growth of a disturbance, the accepted practice has been to characterize the variation of amplitude of the velocity fluctuation in the streamwise direction; or, alternately, to integrate the kinetic energy, based on the fluctuation component, across the shear layer. It is then possible to consider the variation of this integrated energy in the streamwise direction. The question therefore arises as to

how PIV imaging can provide a more direct, and perhaps more insightful, representation of a convectively-unstable flow.

Generally speaking, the major physical issues are represented in Figure 1. The possible coexistence of small-scale vorticity concentrations in the separating shear layer, and the onset of a global (absolute) instability leading to large-scale Kármán-like vortices presents a particularly complex flow system. Moreover, since the onset of small-scale vortices in the separating shear layer is extremely sensitive to small disturbances, the question arises as to the possible control of the large-scale Kármán vortices by manipulation of the small-scale structures. In other words, the mechanism of indirect control of the Kármán vortices is important from a practical standpoint. The possibility of global, instantaneous imaging of the near-wake can yield progress towards resolution of these issues.

A first step in the application of PIV imaging to the onset of small-scale vortex formation on the separating shear layer is depicted in Figure 4. Attention is directed to that portion of the layer where the small-scale vortical structures are well developed. The overview image of Figure 5a shows the manner in which they agglomerate to form the large-scale Kármán vortices. A close-up view of the pattern of instantaneous vorticity in the bottom shear layer is exhibited in the top image of Figure 5b. The first few concentrations of vorticity on the left side of the image tend to exhibit features of a spatially periodic, i.e., neutral, vortex system. In this case, it is possible to directly compare with the theoretical, vorticity-based model of Stuart (1967) for a spatially periodic mixing layer, which allows specification of an arbitrary concentration of vorticity. Then, this link to the vorticity-based model of Stuart (1967), can be employed to physically interpret the magnitude of the Reynolds stress due to the small-scale vortices, as shown by Chyu and Rockwell (1996). According to the model of Stuart (1967), a single row of vortical structures exists in a mixing layer of velocity ratio $R = (U_1 - U_2)/(U_1 + U_2)$, in which U_1 and U_2 are the velocities on the high and low speeds of the shear layer. If the concentration of vorticity is represented by the parameter α, x and y are spatial coordinates, and t is time, the vorticity is given as:

$$\omega = -R \frac{(1-\alpha^2)}{(\cosh y + \alpha \cos(x-t))^2} . \qquad (1)$$

The middle and bottom images of Figure 5b show instantaneous streamlines in a reference frame moving at one-half the free-stream velocity and in a laboratory frame. An important by-product of the vorticity-based theory of Stuart (1967), as demonstrated by Gursul and Rockwell (1991), is proper interpretation of instantaneous streakline patterns as a function of degree of concentration of vorticity. The spatial extent of the streakline visualization marker is actually inversely related to the degree of concentration of vorticity.

Further aspects of the relationship between the development of the small-scale shear layer vortices and the Kármán vortices, depicted in the schematic of Figure 4, have been pursued by Chyu and Rockwell (1996). Since the small-scale, shear-layer vortices are highly sensitive to small amplitude disturbances, it is possible to indirectly manipulate the formation length of the large-scale vortices by application of suitable perturbations that alter the small-scale vortices. For the set of images shown in Figure 5c, the cylinder was subjected to very small amplitude transverse perturbations at the inherent frequency of formation of the small-scale shear-layer vortices. Pronounced concentrations of positive and negative vorticity from the lower and upper surfaces of the cylinder are evident in the left image. By considering the original, instantaneous velocity field, and subjecting it to a spatial filtering process, such that only the largest scales remain, yields the pinwheel type of pattern of velocity vectors shown in the middle image. Now, if this spatially-filtered velocity field is used to construct the corresponding streamline pattern, and this pattern is superposed on the original patterns of instantaneous vorticity, the result is as shown in the right image. This type of approach, which attempts to link small- to large-scale vortical structures is, in principle, applicable to other classes of unsteady separated flows.

3.2
Force-vorticity relations

The forces exerted on a body can be related to the change in the vorticity field surrounding the body as, for example, described by Wu (1981) and Lighthill (1986). A simplified schematic, which defines the relevant terminology, is given in Figure 6. Furthermore, substantial progress in the area of numerical simulations has provided links

between patterns of vorticity surrounding the body and forces on the body. These approaches include discrete vortex methods, direct numerical simulations and large-eddy simulations; a summary of these advances is beyond the scope of this assessment.

Traditional experimental approaches for characterizing the forces on a body, such as a circular cylinder, have involved direct measurement of unsteady forces, or, alternately, measurement of surface pressure and its integration to yield the time variation of the forces. The relationship between vorticity and forces has been largely based on qualitative visualization of the vortex formation process in the near-wake of a body, which, of course, accounts for neither the space-time variations of the vortical structures in the downstream regions of the flow nor the vorticity variations in the layer adjacent to the body. Nevertheless, these types of approaches have provided important and valuable insight, which no doubt will serve as an anchor for application of more sophisticated imaging techniques.

The objectives, which, in essence, have been addressed in recent investigations, are as follows. First of all, in the laboratory environment, it is desirable to determine the relationship between selected concentrations of vorticity and their contribution to the overall forces on the body via space-time imaging. In doing so, it is desirable to evaluate the force contributions based on a flow domain of minimum extent surrounding the body. This requires new types of force-vorticity formulations, more specifically, implementation of a control volume approach, which can incorporate vorticity, momentum or surface flux techniques. Finally, a consequence of these objectives is determination of the relation between the unsteady forces on the body and the time-averaged or mean forces. So, in essence, the aim of our present considerations is to relate the generation and evolution of defined concentrations of vorticity to unsteady forces acting on a cylinder using models of varying levels of sophistication in conjunction with flow imaging.

The simplest and most direct theoretical representation is that of a system of point vortices in the wake of the cylinder. The extended Blasius theorem, described by Milne-Thomson (1960), has been employed to determine the instantaneous drag D and lift L. The explicit derivation of Sarpkaya (1963, 1968) yields, for example, the following expression for the instantaneous lift:

$$L = -\rho \sum_{k=1}^{m} \Gamma_k (-U - u_k + u_{k_i}) - \rho \sum_{k=1}^{m} p_{k_i} \frac{\partial \Gamma_k}{\partial t} \qquad (2)$$

in which U is the time-dependent velocity of the ambient flow, Γ_k and u_k are the circulation and velocity in the x-direction of the k vortex, while u_{k_i} and p_{k_i} are the velocity and location of the corresponding image vortex. Equation (2), which was formulated with the intent of employing numerical simulation via a discrete vortex method(s), assumes that the actual vorticity is concentrated at a point; in concept, however, distributed vorticity can be represented by a cluster of a large number of such discrete vortices. The first link between equation (2) and experimental visualization of a vortex system was provided by Maull and Milliner (1978), who investigated oscillatory flow past a cylinder. They asserted that the principal features of the time-dependent variations of L and D could be reasoned on the basis of movement of clusters of the dye about the cylinder; in doing so, they represented each visualized vortex by a single point vortex. Ikeda and Yamamoto (1981) employed a technique of particle streak visualization to determine the instantaneous circulation of shed vortices and, using a form of equation (2), aimed to calculate the cylinder loading. Particle streak visualization is still a popular technique, and interpretation of visualized patterns requires great care. This type of approach, as well as any other that yields velocity distributions and attempts to identify the existence of vortices, is subject to the well-known issue of reference-frame dependence of the pattern of velocity vectors and, of course, the corresponding streamline patterns as well, as recently assessed by Lin and Rockwell (1997). That is, for a given underlying pattern of vorticity, there are non-unique distributions of velocity. This well-recognized feature should motivate the experimentalist to employ vorticity-based models and simulation techniques as a framework for interpreting quantitative images.

An approach that fully accounts for the distributed nature of vorticity is described by Wu (1981) and Lighthill (1986). The interpretation of Lighthill (1986) was motivated by loading of off-structures, and he assumed that the details of the vorticity field would be provided by a numerical simulation of the flow. As described by Lighthill, the instantaneous force on a body is related to the change with respect to time of the moment

of distributed vorticity about the body. For a three-dimensional flow, the expression for the instantaneous force vector is:

$$\underline{F} = -\frac{1}{2}\rho\frac{d}{dt}\int_V \underline{x}\wedge\underline{\omega}\,dV. \tag{3}$$

In this equation, the position vector of a fluid element is defined as $\underline{x}$, the vorticity of the element is $\underline{\omega}$, and the volume surrounding the body is designated as V. Using a PIV technique, Lin and Rockwell (1996) experimentally determined the distribution of vorticity clusters about a body undergoing sinusoidal oscillation in quiescent fluid, then employed equation (3) to determine the variation of instantaneous lift. More recently, Zhu et al. (1999) have employed a similar approach for the case of a cylinder undergoing transient motion beneath a free-surface. This experiment was designed to account for an important restriction of equation (3), i.e., all previously generated vorticity must be accounted for. It is therefore necessary that all of the vorticity generated from the cylinder remains within the field of view of the PIV imaging system. The thrust of the investigation of Zhu et al. (1999) was to identify those concentrations of vorticity that contribute most substantially to instantaneous lift and drag. Equation (3) can be recast in the form

$$C_D\underline{i} + C_L\underline{j} = \frac{d}{dt}\{(M^*_\omega)_D\underline{i} + (M^*_\omega)_L\underline{j}\} \tag{4a}$$

where

$$(M^*_\omega)_L = \frac{\int_A x\,\omega_z\,dA}{\frac{1}{2}U^2D} \qquad \text{and}$$

$$(M^*_\omega)_D = \frac{-\int_A y\,\omega_z\,dA}{\frac{1}{2}U^2D} \tag{4b}$$

To provide a physical basis for interpreting the force coefficients as a function of the change of moment of vorticity M^*_ω with time, the approximation $\Delta M^*_\omega/\Delta t$ is employed. Using this simplification, it is possible to illustrate, for a fixed time interval Δt, the manner in which the moment of vorticity changes from frame to frame of a PIV cinema sequence. Actually, the detailed physics is best conveyed by considering the change in the

distribution of moment of vorticity throughout space. At a given point, we have $(M_\omega)_L = \int x\omega_z \, dA / \frac{1}{2} U^2 D$ for the lift component. An analogous expression holds for the drag component. Figure 7 shows instantaneous patterns of $(M_\omega)_L$ and $(M_\omega)_D$ for two widely-spaced frames N = 15 and 18 of a cinema sequence. The corresponding distributions of difference moments of vorticity between these frames, designated as $(\Delta M_\omega)_L$ and $(\Delta M_\omega)_D$, are illustrated at the bottom of Figure 7. Further interpretation of images of this type allows identification of the degree to which each of the concentrations of vorticity contributes to L and D.

A challenge in finally calculating the instantaneous values of lift L and drag D is the limited time resolution Δt afforded by cinema PIV approaches that employ sufficiently large format high resolution film. In contrast to numerical simulations, where relatively high time resolution is attainable, substantial error can be induced in evaluating the time derivatives of equation (4a). In the investigation of Zhu et al. (1999), the primary intent was to identify those vorticity concentrations that contributed to the forces. With this motivation, moments of vorticity $(M^*_\omega)_L$ and $(M^*_\omega)_D$ were compared with time integrals of lift and drag coefficients, i.e., $\int C_L dt$ and $\int C_D dt$. These integrals were determined from independent force measurements and show remarkably good agreement with the moments of vorticity M^*_ω. Alternately, if extremely long time scales are employed for the generation and development of vortical structures, as posed in the experiment of Noca et al. (1997), then reasonable time derivatives may be calculated. The aim of their investigation was not to compare calculated with measured forces, but to demonstrate the self-consistency of a force calculation approach, described subsequently.

The theoretical concept advocated by Wu (1981) and Lighthill (1986) has recently been extended by Noca et al. (1997) to account for the fact that all of the previously generated vorticity may not be within the field of view of a PIV imaging system. Their approach involved a control volume, which focused on vorticity-based representations, and involved elimination of the pressure term. Details of the derivation are given by Noca (1996). The fact that this general approach is physically sound was demonstrated using the high-resolution Lagrangian numerical technique of Koumoutsakos and Leonard

(1995). A clear advantage and, in fact, a primary motivation, of the vorticity-based approaches as defined in the foregoing is that a direct relationship between the space-time development of the vorticity field and the body loading is clearly evident. A source of uncertainty is, however, accurate calculation of the vorticity over the region of interest. The question therefore arises as to whether a momentum-based, as opposed to a vorticity-based, approach would be fruitful. Unal et al. (1997) formulated a control volume technique based on momentum concepts. It has its genesis in the generalized theoretical framework of Wu (1981) whose analytical developments describe the loading of single and multiple bodies. The approach of Unal et al. (1997) is complemented by the parallel study of Noca (1997) and Noca et al. (1999). In their investigations, a different, momentum-based control-volume derivation was pursued; presumably, it is equivalent to that of Unal et al. (1997). The control volume equation of Unal et al. (1997) is

$$\underline{F} = -\frac{d}{dt}\int_{V_F} \rho\,\underline{u}\,dV - \oint_{S_E} [\rho\underline{u}(\underline{n}\cdot(\underline{u}-\underline{u}_s)) + p\underline{n} - \underline{\tau}]\,ds, \qquad (5)$$

in which V_F is the fluid volume bounded by the exterior surface S_E of the control volume, and $\underline{u}$ and $\underline{u}_s$ are the respective velocities of the fluid and the control volume surface. In essence, this equation states that the contributions to the force are: (i) the time rate change of the momentum within the control volume; (ii) the net momentum flux across the boundaries of the control surface; (iii) the instantaneous pressure force acting on the control surface; and (iv) the instantaneous shear force on the control surface. PIV imaging allows the spatial distribution of the velocity field to be determined at each successive instant of time, thereby yielding evaluation of terms (i) and (ii). Term (iii) is determined by integrating the x and y momentum equations and the shear stress associated with term (iv) is determined from definitions of τ_{yx} and τ_{xy}. This general approach was verified using a vortex-in-cell technique of solving the vorticity transport equation, as described by Graham (1988) and Meneghini and Bearman (1995). A detailed comparison of time-dependent variation of lift coefficient determined from cinema PIV images and independent force measurements is given by Unal et al. (1997).

Recent, intriguing developments conveyed in the work of Noca et al. (1999) assess various control volume representations, which encompass the entire domain within the

control volume and external to the body surface. They compare the consequence of location of the control volume boundaries and position vectors relative to the flow pattern determined via DPIV, as shown in Figure 3. Within this context, Noca et al. (1999) formulate a so-called flux equation, as opposed to the momentum equation. The flux equation, in its time-dependent form, can yield time-dependent forces from PIV data acquired only on an arbitrary surface surrounding the entire body. The relevant equation is:

$$\underline{F} = \oint_{S(t)} \hat{\underline{n}} \cdot \underline{\underline{\gamma}}_{flux}\, ds - \oint_{S_b(t)} \hat{\underline{n}} \cdot (\underline{u} - \underline{u}_s)\underline{u} dS - \frac{d}{dt}\int_{S_b(t)} \hat{\underline{n}} \cdot (\underline{u}\underline{x}) dS$$

$$\underline{\underline{\gamma}}_{flux} = \frac{1}{2}u^2\underline{\underline{I}} - \underline{u}\underline{u} - \frac{1}{N-1}\underline{u}(\underline{x} \wedge \underline{\omega}) + \frac{1}{N-1}\underline{\omega}(\underline{x} \wedge \underline{u}) \qquad (6)$$

$$-\frac{1}{N-1}\left[\left(\underline{x} \cdot \frac{\partial \underline{u}}{\partial t}\right)\underline{\underline{I}} - \underline{x}\frac{\partial \underline{u}}{\partial t} + (N-1)\frac{\partial \underline{u}}{\partial t}\underline{x}\right] + \frac{1}{N-1}[\underline{x} \cdot (\nabla \cdot \underline{\underline{T}})\underline{\underline{I}} - \underline{x}(\nabla \cdot \underline{\underline{T}})] + \underline{\underline{T}}$$

in which $\underline{F}$ is the force on the body, S(t) and $S_b(t)$ are the surfaces of the control volume and body respectively, $\underline{u}$ and $\underline{u}_s$ are the flow and body velocities, $\underline{x}$ is position vector, $\underline{\underline{T}}$ is the viscous stress tensor, and N = 2 and 3 for two and three-dimensional flows respectively. They caution on the range of applicability of their approach, in that an effective "moment arm" may generate large terms in cases where larger domains or smaller force coefficients are involved. Using DPIV data for the case of a jerking cylinder, as represented by the PIV image of Figure 8, Noca et al. (1999) demonstrated self-consistency between their momentum-equation and flux-equation formulations. Although no comparisons were made with independent force measurements, the self-consistency check attests to the promise of this approach.

3.3
Vorticity-acoustic coupling formulations: Role of vortex impingement and generation of forces and sound

The impingement of vortical structures on edges and corners in jet-edge and cavity systems can give rise to unsteady loading of the edge or corner, as well as relatively large amplitude sound. The elements of a typical impingement system are given in Figure 9. As

illustrated, the interaction of concentrations of vorticity gives rise to an upstream influence, which perturbs the separating flow in the sensitive region of the nozzle lip. This perturbation is amplified in the free-shear layer of the jet, giving rise to concentrations of vorticity. The underlying physics and unresolved issues related to this type of jet-edge system, which are also generic to a wider class of cavity configurations, are described by Powell (1961), Rockwell and Naudascher (1979), Blake (1986), Rockwell (1998a), and Howe (1998).

From an experimental standpoint, the traditional approaches have been to characterize the amplifying convective instability wave in the separated shear layer using pointwise measurements. Typically, a phase-referencing technique is employed, whereby the amplitude and phase of the predominant, single frequency undulation is characterized as a function of spatial position throughout the quasi-laminar shear layer. Central to most previous investigations has been use of flow visualization, in order to determine the development of concentrations of vorticity and the manner in which they are distorted as they interact with the edge. Many investigations of this class of flows have focused on surface force or pressure measurements, sometimes accompanied by pointwise velocity measurements. For example, Schachenmann and Rockwell (1980, 1982) decomposed the velocity fluctuations of the resonant acoustic mode and the hydrodynamic vorticity-based fluctuations using a combination of pressure and velocity measurements in a simple linear model. The underlying, quantitative physics of the patterns of vorticity was, however, not addressed. Over the years, simple kinematic models have been a popular means of representing flow-acoustic oscillations, i.e., coupling between vortices formed in the shear layer of a jet or a mixing layer and the acoustic resonant mode(s) of an adjacent resonator. Knowledge of parameters such as the convective wave speed in the unstable shear layer is required, and they either have been assumed or approximated from linearized stability theory.

The objectives for the present series of investigations, involving global, instantaneous PIV imaging, address the key elements of the system of Figure 9. First of all, coherent undulations and eventual vortex formation in a jet formed from a fully-developed turbulent channel flow is a key issue. Although it has been generally accepted

that such coherent vortices can arise in presence of acoustic resonance or elastic boundaries, the purely hydrodynamic disturbance amplification on a turbulent background has remained unclarified. Furthermore, the flow distortion in the vicinity of the edge will give rise to a form of upstream influence that is dictated by the nature of distortion of patterns of vorticity in the edge region. Whether this upstream influence takes the form of a di- or multi-pole source-like region has remained unclarified. Finally, when the type of system shown in Figure 9 occurs in presence of an acoustic resonator, say at the mouth of an organ pipe or adjacent to a side branch cavity, the excitation of the acoustic resonator, in conjunction with the organized undulations of the jet or shear layer, typically involving vortex formation, serves as a source of acoustic power. In turn, the magnitude of the acoustic power generation determines the degree to which the flow tone lock-on is attainable for the shear layer-resonator system.

To date, it has not been possible to quantitatively characterize a central feature of flow-acoustic coupling, i.e., the magnitude of the acoustic power generation, on a purely experimental basis. Howe (1975, 1980, 1984) clearly established the link between the coexisting vorticity (hydrodynamic) and acoustic fields necessary for effective acoustic power generation. According to his formulation, the instantaneous acoustic power P is given by:

$$P = -\rho_o \int_V \underline{u} \cdot (\underline{\omega} \wedge \underline{V})\, dV \qquad (7)$$

in which $\underline{u}$ is the vector acoustic velocity at a given point, $\underline{\omega}$ is vorticity, $\underline{V}$ is the vector hydrodynamic velocity, and $\underline{\omega} \wedge \underline{V}$ is a cross-product. Hourigan et al. (1990) have employed smoke visualization to determine the trajectory of a given vorticity concentration, in conjunction with the discrete vortex formulation of the space-time evolution of the concentrations. Using this approach of qualitative flow visualization and inviscid numerical simulation, along with a finite element calculation of the resonant acoustic field velocity $\underline{u}$ for the configuration of an axisymmetric cavity, they reasoned the essential features leading to effective acoustic power generation. Further investigation of this class of flow-acoustic coupling involves, for example the work of Bruggeman et al. (1991) who employed Howe's interpretation to deduce features of acoustic power

generation due to vortex interaction with the corner of a closed side branch. Moreover, Kriesels et al. (1995) employ qualitative visualization in conjunction with a discrete vortex method to relate physical features of the acoustic power generation to the vortex-corner interaction in a similar side branch arrangement.

It is, of course, highly desirable to determine the magnitude of the instantaneous acoustic power P from direct knowledge of the spatial distribution of vorticity $\underline{\omega}$. Assuming that the acoustic field and hydrodynamic (vorticity-based) field can be linearly decomposed for purposes of this calculation, the issue becomes determination of the vector quantity $\underline{\omega} \times \underline{V}$ according to equation (7).

A configuration inherent to a number of flow-acoustically coupled systems is an unstable impinging jet, which is typically quasi-laminar in, for example, an organ pipe arrangement. To illustrate the central issues associated with the hydrodynamic aspects of equation (7), consider the situation of a turbulent jet impinging upon an edge. It has been demonstrated recently (Lin and Rockwell, 1999) that, due to feedback from the jet-edge interaction, the initial turbulence of the jet is rapidly overshadowed by the amplification of the most unstable mode of the jet, provided that one views the disturbance as growing in an inviscid manner on the turbulent background. The end consequence is generation of large-scale vortical structures in the vicinity of the edge, as shown in the images of velocity and vorticity in Figure 10. Small-scale concentrations of vorticity embedded within the large-scale concentration; they arise from a small-scale inviscid instability during separation of the shear layer at the nozzle lip. Using the type of imaging described in Figure 10, it should be possible to formulate an integrated experimental approach that will couple the amplifying disturbances in the shear layer, distortion of the vorticity patterns at the edge/corner, the loading on the edge and thereby the nature of the upstream influence. Our present considerations focus on the generation of acoustic power P defined by equation (7).

Using the pattern of vorticity and the corresponding instantaneous distribution of velocity of Figure 10, the quantity $\underline{\omega} \times \underline{V}$ can be calculated; the distribution in the vicinity of the edge is illustrated in the bottom image of Figure 10. It is evident that the large-scale cluster of vorticity above the edge is associated with a sink-like pattern of $\underline{\omega} \times \underline{V}$

vectors. On the other hand, all other vorticity concentrations produce vectors that are largely oriented in the positive or negative vertical direction. Significant contributions arise from the small-scale vortical structures in the jet shear layers. Viewing the pattern of $\underline{\omega} \times \underline{V}$ as a whole, the fact that these vectors are oriented predominantly in the vertical direction suggests that local components $\underline{u}$ of the resonant acoustic mode oriented in the vertical direction will provide particularly large contributions to the acoustic power P, because the value of the dot product in equation (5) is maximum. Of course, it is necessary to construct images of this type shown in Figure 10 over the complete cycle of the jet oscillation, and to consider their phase shift, relative to the cyclic variation of the acoustic wave field $\underline{u}$, in order to calculate the total effective acoustic power P.

A similar approach, involving cinema PIV, can be employed to characterize the more complex flow of unstable oscillations past a cavity. Typical images are shown in Figure 11. The upper image shows the entire region of the shear layer across the mouth of the cavity and the recirculation region within it, while the bottom three images show patterns of velocity vectors viewed in various reference frames, corresponding to the laboratory frame (top image) and frames moving at 0.25 and 0.50 of the freestream velocity. The overview of the cavity flow shown in the top image indicates the relationship between ejected fluid near the corner of the cavity, and a jet-like flow along the vertical and bottom walls of the cavity, which eventually modulates the separating shear layer from the leading-corner. This type of upstream influence, which occurs over a relatively long time scale, is not to be confused with the type of upstream influence depicted schematically in Figure 9, which occurs essentially instantaneously for low Mach number flows and may be interpreted in terms of Biot-Savart induction. The important message associated with the top image of Figure 11 is that, since the approach boundary layer is fully-turbulent, organized undulations of the separating shear layer are attainable, due to upstream influence. The bottom three images show various representations of the small- and large-scale vortical structures, which are evident to varying degrees, depending upon the reference frame. The corresponding patterns of vorticity (not shown) indicate that a large-scale concentration of vorticity is nearly coincident with the trailing-corner of the cavity and, at this instant, the pressure at the corner takes on a large negative value.

3.4
Vorticity evolution and breakdown in swirling flows: Origin of surface forces

Swirling vortex flows occur above a delta wing, in pipes, and within intakes and exhaust configurations of rotating machinery systems. When the ratio of the swirl to axial velocity reaches a critical value, the onset of vortex breakdown occurs, giving rise to pronounced undulations that have important consequences for unsteady loading. The many, complex aspects of vortex breakdown are assessed by Hall (1972), Leibovich (1978, 1984), Escudier (1988) and Brown and Lopez (1990).

Experimental approaches have focused primarily on use of pointwise measurements, most reliably laser-Doppler anemometry, often coupled with qualitative flow visualization. These investigations have provided important insight, and have led, for example, to characterization of the ratio of the characteristic azimuthal to axial component of velocity, the location of vortex breakdown, and the averaged structure of turbulence in the breakdown region. Moreover, critical insight into the spectral content as a function of distance downstream of vortex breakdown has been attainable.

Major unresolved issues are centered on both the time-averaged and instantaneous structure of the breakdown region. First of all, a suitable criterion for onset of breakdown is called for. Observations in the literature suggest that the occurrence of a zero axial velocity, i.e., a stagnation point, along the axis of vortex may not be an adequate indicator. A vorticity-based criterion can provide a useful, and perhaps more universal, complement. In fact, Brown and Lopez (1990) have formulated a relationship between the variation of vorticity in the region of vortex breakdown and the change in axial velocity along the centerline of the vortex:

$$w(o,z) = \frac{1}{2}\int_{-\infty}^{\infty}\int_{0}^{\infty} \frac{\sigma^2 \eta(\sigma, z')}{\left[\sigma^2 + (z - z')^2\right]^{3/2}} d\sigma\, dz', \qquad (8)$$

in which w(o,z) is the axial velocity on the centerline of the vortex at the axial location z, and η is the azimuthal vorticity at radial location σ. The PIV investigation of Towfighi and Rockwell (1993) showed that the onset of vortex breakdown was in accord with a switch in sign of azimuthal vorticity, a concept that is inherent to the theory of Brown and Lopez (1990). Unclarified aspects of the breakdown region involve comparison of the

and Q^+ further from the wing and conversely for P^- and Q^-, is in accord with the concept of Brown and Lopez (1990), described by equation (8).

It appears that two representative criteria for the onset of vortex breakdown can be defined. A direct comparison of criteria based on averaged velocity $<V>$ and vorticity $<\omega>$ is shown in the image of Figure 14, which gives a superposition of $<V>$ on $<\omega>$. In order to facilitate a clear comparison, the incremental values of $<V>$ and $<\omega>$ are larger than those exhibited in Figure 13. Two dots are shown on this image. The upstream (white) dot corresponds to the onset of vortex breakdown based on a vorticity criterion, i.e., the location of switch in sign of azimuthal vorticity. The downstream (black) dot corresponds to the location of the stagnation point on the axis of the leading-edge vortex. We therefore conclude that the switch in sign of azimuthal vorticity precedes the occurrence of a stagnation point. Consideration of a range of parameters, including variations in angle of attack and use of control techniques to externally stimulate the onset of vortex breakdown, show that the criterion based on the switch in sign of azimuthal vorticity provides a reliable indicator of the onset of a wake-like region, whereas the criterion based on occurrence of a stagnation point is less consistent. These criteria are currently under further investigation.

Essential for characterizing the unsteady loading of the surface of the wing, as well as tails or other aerodynamic appendages in the path of the vortex is the time-dependent structure of vortex breakdown. A representative instantaneous image, which gives contours of constant instantaneous vorticity ω, is shown in Figure 15. On the whole, regions of vorticity P^+ and P^- are relatively distributed, but contain detectable small-scale structures, apparently due to centrifugal effects. Regions Q^+ and Q^- actually involve a pattern of alternating positive and negative extrema of vorticity along the central portion of the vortex; this structure is representative of the helical-type instability of the breakdown region. Along the exterior of the vortex, definable pairs A^+, A^- and so on evolve in the region immediately downstream of the trailing-edge of the wing; they are due to a three-dimensional vortex formation process from the edge of the wing, indicated by three-dimensional dye visualization. It is evident that significant buffeting, or unsteady loading, of an aerodynamic appendage will be induced over nearly the entire transverse

extent of the broken-down vortex, due to these different classes of vorticity concentrations. Using this type of instantaneous imaging, it is possible to determine spectra and cross-spectra by employing a series of instantaneous images, thereby providing links to traditional buffet models and a rational means for improving them.

4 Quantitative flow visualization

The frameworks and links to theoretical concepts described in Sections 2 and 3 are often preceded by preliminary visualization, which may take one of two general forms: visualization using a marker, such as dye or smoke; or visualization based on PIV imaging. In addition, simultaneous marker visualization and PIV may be employed in certain situations. It is appropriate to briefly comment on these types of visualization, since they often serve as a decision point for more incisive stages of an investigation.

Marker visualization in unsteady, separated flow typically takes the form of one or more streaklines. Alternately, timelines may be generated from a hydrogen bubble or smoke wire. Consider, for example, generation of a streakline. If it emanates from a location where the fluctuating vorticity is zero, and the effects of diffusion are minimal, then a reasonable representation of the pattern of vorticity can be expected. If, on the other hand, these conditions are not satisfied, then a number of fallacies may arise. Hama (1962) demonstrated misinterpretations of streakline patterns due to injection at various elevations in an unsteady shear layer. Representative difficulties include the apparent amplification of the disturbance when, in reality, the disturbance was prescribed as neutral, and an apparent variation of wavelength at various elevations across a free-shear layer when, in actuality, only a single wavelength exists in the actual flow. In a similar spirit, Williams and Hama (1980) show that the presence of waves in a shear flow at two different frequencies, with arbitrary phase between them, can give rise to misinterpretations of vortex-vortex interaction patterns. Kurosaka and Sundaram (1986) exhibit false interpretations of growth of vortex strength for an isolated vortex in a Kármán street of vortices based on streakline visualization. Cimbala (1984) and Cimbala et al. (1988) emphasize the importance of diffusion of a smoke marker. In downstream regions of the flow, well-defined vortices appear to be present when, in reality, they do not

exist. Gursul, Lusseyran and Rockwell (1990) bring forth difficulties in interpreting visualization with finite-thickness markers. The influence of thinning and thickening of visualization markers, the consequences of amplifying and decaying disturbance fields on visualization, and the effects of reference frames on visualized vortical flows are critiqued for both streaklines and timelines. In a further study, Gursul and Rockwell (1991) show the unexpected result of changes in concentration of vorticity in vortices having a constant value of circulation. The visualization marker actually spreads over an increased area of the flow as the degree of concentration increases.

A global, quantitative imaging technique, such as PIV, directly provides patterns of instantaneous velocity and vorticity; moreover, it is straightforward to examine patterns of instantaneous velocity or streamlines in various reference frames. In fact, if a properly time resolved sequence of such PIV images is acquired, it is possible, in principal, to reconstruct the streaklines, pathlines, and timelines of the flow patterns and compare them directly with the underlying patterns of vorticity. Even with this sort of quantitative approach to visualization, however, difficulties in interpretation may arise, especially with regard to interpretation of patterns of velocity and streamlines in various reference frames. This issue is linked to the challenge of defining a "vortex", which is addressed by Lugt (1979), who proposes a criterion based on examination of time variations of flow patterns in selected reference frames. Furthermore, interpretation of the existence of a vortex is central to topological concepts based on critical point theory, as described in Section 2; this aspect is addressed in a number of references cited therein, e.g., Chong et al. (1990).

5
Concluding Remarks

The technique of particle image velocimetry shows great promise for in-depth characterization of unsteady separated flows in the area of flow-induced vibration and noise generation and, no doubt, in allied topics as well. The intent of this overview is to suggest the use of frameworks and links to theories, which hopefully will provide a stimulus for development of new types of evaluation and interpretation of PIV images, extending well beyond quantitative visualization.

APENDIX H

OSCILLATIONS OF A TURBULENT JET INCIDENT UPON AN EDGE*

by

J.-C. Lin and D. Rockwell

Department of Mechanical Engineering and Mechanics

354 Packard Laboratory, 19 Memorial Drive West

Lehigh University

Bethlehem, PA 18015

***Lin, J.-C. and Rockwell, D. 2001 "Oscillations of a Turbulent Jet Incident Upon an Edge", *Journal of Fluids and Structures*, Vol. 15, No. 6, pp. 791-829.**

Running Headline: Oscillations of a Turbulent Jet

All correspondence to:

D. Rockwell
Department of Mechanical Engineering and Mechanics
354 Packard Laboratory, 19 Memorial Drive West
Lehigh University
Bethlehem, PA 18015
Telephone: 610-758-4107
Fax: 610-758-4041
Email: dor0@lehigh.edu

SUMMARY

For the case of a jet originating from a fully turbulent channel flow and impinging upon a sharp edge, the possible onset and nature of coherent oscillations has remained unexplored. In this investigation, high-image-density particle image velocimetry and surface pressure measurements are employed to determine the instantaneous, whole-field characteristics of the turbulent jet-edge interaction in relation to the loading of the edge.

It is demonstrated that even in absence of acoustic resonant or fluid-elastic effects, highly coherent, self-sustained oscillations rapidly emerge above the turbulent background. Two clearly identifiable modes of instability are evident. These modes involve large-scale vortices that are phase-locked to the gross undulations of the jet and its interaction with the edge, and small-scale vortices, which are not phase-locked. Time-resolved imaging of instantaneous vorticity and velocity reveals the form, orientation, and strength of the large-scale concentrations of vorticity approaching the edge in relation to rapid agglomeration of small-scale vorticity concentrations. Such vorticity field-edge interactions exhibit rich complexity, relative to the simplified pattern of vortex-edge interaction traditionally employed for the quasi-laminar edgetone. Furthermore, these interactions yield highly nonlinear surface pressure signatures. The origin of this nonlinearity, involving coexistence of multiple frequency components, is interpreted in terms of large- and small-scale vortices embedded in distributed vorticity layers at the edge. Eruption of the surface boundary layer on the edge due to passage of the large-scale vortex does not occur; rather apparent secondary vorticity concentrations are simply due to distension of the oppositely-signed vorticity layer at the tip of the edge.

The ensemble-averaged turbulent statistics of the jet quickly take on an identity that is distinct from the statistics of the turbulent boundary layer in the channel. Large increases in Reynolds stress occur due to onset of the small-scale concentrations of vorticity immediately downstream of separation; substantial increases at locations further downstream arise from development of the large-scale vorticity concentrations.

1. INTRODUCTION

Impingement of a low Reynolds number planar jet upon an edge is well known to give rise to coherent, self-sustained oscillations. The essential features of jet-edge interaction are generic to a broader range of configurations, including oscillations of an axisymmetric jet impinging upon a plate, oscillations of a shear layer along the mouth of the cavity, and other related systems reviewed by Rockwell & Naudascher (1978, 1979), Rockwell (1983, 1998), Blake & Powell (1986), Crighton (1992) and Howe (1997). Ordered jet-edge oscillations, which have been characterized in various fashions during the past half century for initially laminar jets, date from the early studies of Brown (1937a,b), and include those of Nyborg (1954), Powell (1961), Karamcheti *et al.* (1969), Holger *et al.* (1977, 1980), Lepicovsky & Ahuja (1983), as well as experimental and theoretical investigations of the foregoing authors.

Measurement of the magnitude of the force on the edge and the associated sound field were first addressed by Powell (1961). Holger *et al.* (1980) formulated a vortex model for the force, which led to prediction of the sound pressure. Characterization of the flow physics of these initially laminar jet-edge interactions has involved qualitative smoke and dye visualizations, often with pointwise velocity measurements. Karamcheti *et al.* (1969) determined streamwise variations of the velocity fluctuation amplitude and phase along the jet. Kaykayoglu & Rockwell (1986) determined the detailed distribution of instantaneous pressure along the surface of the edge and demonstrated that the effective location of the force on the edge was not at the tip, but downstream of the tip at a distance corresponding to a significant fraction of the unstable wavelength of the incident jet. Furthermore, the complex, multiple-frequency content of the interaction at the edge is manifested in a corresponding upstream influence, as shown in the experiments of Lucas & Rockwell (1984).

The variation of the dimensionless frequencies of oscillation of laminar jets as a function of impingement distance is summarized by Karamcheti *et al.* (1969), also included in Naudascher & Rockwell (1979), and more recently, by Holger *et al.* (1977), Crighton (1992), and Howe (1997). For all data addressed therein, the conditions at the nozzle exit were laminar. These studies, which represent investigations using both air and water as working fluids, exhibit remarkably similar variations of fL/U with L/H. Distinct stages 1, 2, and 3 of the oscillation are evident. For a given set of data, it is clear that spectral components corresponding to two simultaneous states of oscillation may occur.

The central elements of the flow physics that give rise to self-sustained oscillations were first put forth by Powell (1961), and they have served as a framework for subsequent investigations, as assessed by Holger *et al.* (1977), Rockwell & Naudascher (1979), Rockwell (1983, 1998), and Crighton (1992) and Howe (1997). These elements are, in a general sense: amplification of the disturbance in the jet, giving rise to transverse undulations; interaction of the undulating jet with the leading-edge, inducing unsteady loading on the edge; upstream influence from the edge to the sensitive (receptive) region of separation at the jet nozzle exit; and conversion of this upstream influence to an unstable perturbation in the jet shear-layer.

The present investigation addresses these issues using a global technique to determine the instantaneous structure of the jet, in relation to measurement of the surface loading on the edge.

2. EXPERIMENTAL SYSTEM AND TECHNIQUES

Experiments, which were performed using a large-scale jet-edge apparatus housed within a water channel system, involved particle image velocimetry, in conjunction with pointwise surface pressure measurements. The experimental system and techniques are described in the following.

2.1 EXPERIMENTAL SYSTEM

A large-scale water channel housed the jet-edge system. The water channel has a test section 610 mm wide × 610 mm deep, and a length of 4,572 mm. This main test section is preceded by a contraction having an inlet width of 18,289 mm; the corresponding contraction ratio is therefore 3:1. A honeycomb-screen system is located at the inlet of the contraction, in order to minimize the free-stream turbulence, which is typically less than 0.1%.

Inlet Contraction. The jet-edge test section was located within the water channel test section in the manner indicated in Figure 1. Its overall length was 6,553 mm. The principal components are an inlet contraction, a flow development channel, the edge system and the outflow section. As illustrated in the plan view of Figure 1, the deployment of two flow barriers, on either side of the test section, precluded flow through the gap between the jet-edge test section and the water channel test section. In essence, this barrier system created a large reservoir of very low velocity water, which was drawn into the inlet contraction, in the manner depicted by the pattern of arrows in the plan view. Inclusion of a honeycomb at the upstream end of the inlet contraction provided a significant pressure drop, and ensured that the flow entering the inlet contraction was essentially uniform, except for viscous layers adjacent to the wall of the jet-edge test section. The contraction ratio of the inlet contraction was 20:1.

Flow Development Channel. In order to ensure that a fully-developed turbulent boundary layer was attained, a flow development channel, having a width of 3,175 mm and a height $2H = 25.4$ mm, was specified. This corresponds to a channel length to height

Based on extensive studies of nominally laminar jet-edge interactions, cited in the foregoing, it is possible to define a number of unresolved issues:

(i) Even for the case where the jet is initially laminar, the detailed structure of its oscillation and interaction with the edge are unclarified. All previous related investigations have focused on qualitative flow visualization, along with pointwise measurements of velocity within the undulating jet, force on the edge, and sound pressure away from the edge. Classical flow visualization, e.g., dye and smoke injection and particle streak measurements, can, in many instances, give rise to misinterpretations of the actual, underlying vorticity field, as assessed by Gursul *et al.* (1990) and Gursul & Rockwell (1991). The detailed, quantitative structure of the jet-edge interaction is, of course, crucial for determining the force on the edge, the upstream influence, and the sound pressure.

(ii) The potential for emergence of organized jet oscillations from a fully-turbulent channel flow has not yet been explored. In the event that organized oscillations do exist, it is unclear whether a predominant large-scale instability, or both small- and large-scale instabilities, i.e. vortices, occur on a random background. Moreover, the development of patterns of vortical structures upstream of, and immediately adjacent to, the impingement edge is unresolved. The traditional view is that a fully-evolved jet vortex street approaches the edge; yet the presence of the edge is expected to continuously influence the vorticity distribution and trajectory of a typical vortex

(iii) The consequence of the turbulent jet-edge interaction on the surface loading of the edge has not been addressed. In particular, it is unknown whether the spectral content of these surface fluctuations is broad- or narrow-band, in absence of acoustic resonant/fluid-elastic effects. Moreover, both the maximum amplitude and the origin of nonlinearity of the pressure fluctuations on the upper and lower sides of the edge has not been related to the evolution of the instantaneous velocity and vorticity fields.

(iv) The nature of the rapid transformation from the turbulence statistics of the unseparated channel flow to the statistics of the jet is undefined. Furthermore, the character of the turbulence statistics in the tip region of the edge, which is related to the source-like behavior in that region, is unclarified.

were continuously monitored. Both of these criteria were effective in ensuring that the jet-edge encounter was essentially a symmetrical one during the course of all experiments.

Particularly important is inclusion of a surface plate, which was in contact with the free-surface, and prevented undesirable generation of free-surface perturbations. In fact, in absence of the surface plate, substantial free-surface standing wave modes could be induced; they contaminated the fundamental hydrodynamics of the jet-edge interaction. This surface plate extended well downstream of the jet-edge arrangement, as illustrated in Figure 1.

Outflow Section. Resistance between the jet-edge section and the main exhaust reservoir of the water channel system was provided by the honeycomb arrangement shown in Figure 1. A surface plate, which prevented contamination by oscillations of the free-surface, extended from the channel exit to the location of the honeycomb. Downstream of the honeycomb, porous foam was placed in contact with the free-surface. This foam arrangement extended to the inlet of the exhaust reservoir. The foam further ensured damping of perturbations induced by the organized jet-edge oscillations.

Impingement Edge. The impingement edge, which is illustrated in Figure 1, was made entirely of Plexiglas. It had an included angle of 19°, a thickness of 18 mm, and a span of 457 mm, thereby extending across the entire test section. Pressure taps of diameter 0.726 mm were located at a distance of 7.62 mm downstream of the tip of the edge. One tap was located on the top surface and another on the bottom surface. The taps were at the same spanwise location. These lines, which were actually small milled channels having a square cross-section of 1.5 mm × 1.5 mm, terminated in the transducer box, which housed the two high sensitivity pressure transducers. Two PCB Model No. 106B50 pressure transducers were employed. They were custom-manufactured for long-term immersion in water. The natural frequency of the transmission line-cavity-pressure transducer system was determined, by transient testing, to be 30.5 Hz, which is a factor of approximately 15 higher than the predominant frequency of the jet-edge oscillation. Evaluation of the damping coefficient during the transient response experiments indicated that the maximum distortions of the pressure magnitude and phase were within 0.5 %.

ratio of 125:1 and a span to height ratio of 18:1 determined from the summary of Niederschulte (1989) on conditions for attainment of fully-developed channel flows.

In order to abruptly trip the boundary layer at the inlet to the flow development channel, two brass rods of diameter 2.4 mm were affixed to the bottom and top walls of the channel, at a location immediately downstream of the channel inlet. This trip is similar in concept to that employed by Niederschulte (1989), and promotes the rapid onset of transition. In addition, a special boundary layer trip section was employed in the present channel. It consisted of a pattern of hemispheres of varying diameter, mounted on both the bottom and top walls of the channel. The length of this boundary layer trip section was 203 mm. Its leading-edge was located a distance of 152 mm downstream of the channel inlet. Extensive dye visualization showed that the combination of the inlet trip cylinders and the boundary layer trip section promoted very rapid onset of a turbulent channel flow. Full details of this trip section are described by Johansson & Smith (1983) and Rockwell & Lin (1996).

Jet-Edge System. The edge system, indicated in Figure 1, involved a sharp leading-edge made of Plexiglas; details are described subsequently. The edge was suspended by four support posts, in the form of brass rods of 12.7 mm diameter. These four rods connected the Plexiglas edge to a Plexiglas plate located outside the test section. The junction of the rod with the plate was stabilized via a flange welded to the rod. This support system for the edge ensured that edge vibrations did not occur. It also allowed vertical adjustment of the edge, in order to ensure symmetry of the jet-edge encounter as well as translation of the edge along the test section, thereby providing variation of impingement distance L. In order to fine-tune the symmetry of the flow along the lower and upper sides of the edge, an adjustable plate system was incorporated. The length of each of these adjustable plates was 457 mm. The plate angles, θ_1 and θ_2, could be altered. During the course of the experiment, their nominal values were $31.5° \leq \theta \leq 41°$. In absence of these adjustable plates, large-scale, very low velocity recirculation zones could build up at that location of the test section, and bias the jet-edge interaction to an asymmetrical state. During all experiments, the jet-edge interaction was continuously visualized using dye and laser sheet visualization. Moreover, the upper and lower instantaneous surface pressures on the edge

resolution, extending over a number of cycles of the jet-edge oscillation, a motor-driven Canon camera was employed; it had a maximum framing rate of nine frames/sec. During both types of cinema image acquisition, the pressure signals at the lower and upper taps along the surface of the edge were acquired simultaneously. This approach allowed a direct correlation between the induced surface pressure and the dynamics of the unsteady, impinging jet. Details of these cinema techniques, involving synchronization of the framing camera with the components of the image and data acquisition systems, as well as representative images, are given by Lin & Rockwell (1998).

Proper selection of the magnification factors of the lenses on the Nikon F-4, Hulcher and Canon cameras was critical, since the magnification factor is, in the end, related to the effective grid size of the pattern of velocity vectors. For the case of the turbulent channel flow, for which only the Nikon F-4 camera was employed, the magnification was 1:1.17. It provided a sufficiently small grid size such that a total of 60 data points could be attained across the 25.4 mm channel flow. For photographing the jet-edge oscillations, using the Nikon F-4, Hulcher, and Canon cameras, magnifications M in the range $1{:}5.45 \leq M \leq 1{:}5.78$ were employed.

Implementation of all camera systems required a means of precluding directional ambiguity of the acquired particle images. An oscillating bias mirror, i.e. an image shifting mirror, was located in front of the camera lens of both the Nikon F-4 and the Hulcher cinema cameras. The angular displacement of the mirror was triggered during each shutter opening, thereby imparting a constant bias displacement of all particle images recorded on the film. This bias was then removed during the interrogation process. The angular displacement of the mirror was of the order of 0.01°, in order to avoid any type of systematic distortion of the recorded pattern of particle images, which would be present for finite rotation angle of the mirror.

A Nikon digitizing system allowed each 35 mm negative to be digitized at a relatively high resolution of 125 pixels per millimeter. Subsequently, these patterns of digitized images were evaluated using a single-frame, cross-correlation technique. This approach provided an instantaneous velocity vector at each interrogation location. A standard, 50% overlap of the interrogation areas was employed. For the channel flow, the effective grid size, in the plane of the laser sheet, i.e., the distance between velocity vectors, was

2.2 EXPERIMENTAL TECHNIQUES

High-Image-Density PIV Technique. A laser-scanning version of high-image-density PIV, described in detail by Rockwell *et al.* (1993), was employed in the present experiments. Illumination was provided by a laser, of the continuous wave Argon-ion type. It had a maximum output of 25 watts. In essence, a scanning laser sheet was generated by impingement of the focused laser beam on a rotating polygon mirror. Details of the optical arrangement are described in the following.

This laser beam was transmitted through a laser-optical arrangement, which was mounted on a rail system. The optics could therefore be translated along the streamwise direction. Moreover, an additional rail allowed translation in the cross-stream direction. A beam-steering mirror and convex and concave lenses, having focal lengths f = 300 and 100 mm respectively were fixed to the translating table. The multi-faceted rotating mirror, from which the incident beam was reflected to produce a scanning sheet, along with a focusing singlet and a second beam steering mirror, were mounted on a circular table, which could be rotated to any angular position. This optical system allowed the laser beam to be focused to a sufficiently narrow waist, to provide a beam diameter in the measurement region of interest of approximately 1 mm.

The rotating mirror had 48 facets. The effective scanning rate of the laser beam was accomplished by controlling its speed of rotation. The scanning frequency was 624 cycles/sec for imaging of the jet-edge flow and 1,529 cycles/sec for imaging of the channel flow. Proper selection of this frequency is critical, in order to optimize the displacement between the multiply-exposed images of particles, which had a diameter of 12 microns.

A Nikon F-4 camera with a motor drive was employed to obtain still photos of the turbulent channel flow and the jet-edge oscillation. For the purposes of these experiments, corresponding to randomly-acquired images, the camera was triggered externally and the motor-driven capability of the camera was not employed. High resolution 35 mm film with an effective resolution of 300 lines/mm was used. A second camera system, a Hulcher cinema camera, was employed for image acquisition highly resolved in time. This image sequence is referred to hereafter as the highly resolved cinema sequence, corresponding to a maximum framing rate of forty frames per second. Images were recorded on 100 foot spools of 35 mm film. Finally, for a cinema sequence of lower time

using two analog filters, one for each of the pressure transducers was done in the low-pass mode, with a cut-off frequency of 10 Hz.

3. TURBULENT CHANNEL FLOW

The fully-developed turbulent channel flow was characterized by acquisition of images at the location upstream of the channel exit defined in Section 2. In a typical image, approximately 5,800 velocity vectors were obtained. Representative instantaneous velocity fields are given for two different reference frames in Figure 2a.

To determine the time-averaged statistics of the turbulent channel flow, a total of 20 PIV images were acquired at random times. The minimum time spacing was 10 sec, much longer than the estimated time scale of the largest eddy in the channel flow, i.e., of the order of 0.066 sec. For evaluation of all averaged and statistical quantities, the variation of the velocity with coordinate x was considered at a given value of y in a specified image. This provided, for a given image, values of mean velocity components $\overline{u}$ and $\overline{v}$, the corresponding rms values u_{rms} and v_{rms}, as well as the velocity correlation $\overline{u'v'}$. Then, by averaging these values obtained from all images, final statistics were obtained. This approach is the same as that employed by Liu *et al.* (1991) and Rockwell & Lin (1996).

Extensive consideration was given to the detailed LDA measurements of Niederschulte (1989), which extended over the range of Reynolds number $2{,}457 \leq Re \leq 18{,}339$ based on half-channel width. For the present experiments, the corresponding value was Re = 5,472, and the closest value of Niederschulte (1989) is Re = 2,777; therefore, comparisons were made at Re = 2,777. It should also be noted that Liu *et al.* (1991) have carried out a high resolution PIV study of the same channel flow as Niederschulte (1989). Their data agree closely with those of Niederschulte (1989), and therefore are not repeated here. Finally, we note that Kim *et al.* (1987) have performed a direct numerical simulation of the turbulent statistics of a fully-developed in channel flow. The Reynolds number of their DNS calculations corresponds to Re = 2,800. These calculation results were also used as a basis for comparison.

The top plot of Figure 2b shows a direct comparison of the time-averaged velocity $\overline{u}$ normalized with respect to the maximum velocity $\overline{U}_m$ at the center of the channel. This comparison includes: the present investigation; the LDA data of Niederschulte (1989); and

0.42 mm. For the case of the jet-edge images, obtained with the Nikon F-4, Hulcher and Canon cameras, the effective grid sizes Δ were in the range $1.82 \leq \Delta \leq 2.08$ mm.

After post-processing of the raw velocity field, spurious (outlying) vectors were removed, then blank regions were filled using an established bilinear interpolation technique. The number of spurious vectors in the flow field never exceeded 0.5 percent of the total vectors. A Gaussian filter, with an exponent $p = 1.3$, was employed to smooth the velocity field, without inducing a significant distortion over the scales of interest in the present study. Landreth & Adrian (1990) provide an assessment of these interpolation and filtering techniques.

Two image areas were employed for acquisition of PIV images of the approach turbulent channel flow and the jet-edge oscillation. They are defined with respect to an (x,y) coordinate system, having its origin on the centerline and at the exit of the channel. The image area employed for characterizing the turbulent channel flow had an aspect ratio of approximately 1.5:1. Its left and right boundaries were located at distances $x = -172$ mm and -132 mm respectively. The image area used for the overview of the jet-edge oscillations also had an aspect ratio of approximately 1.5:1. This view was employed for the randomly-acquired sequence of images, and the cinema sequences with high and low time resolution. For these three experiments, the average locations of the left and right boundaries were respectively: $x = -2.2$ mm, 174.1 mm; $x = -2.3$ mm, 168.2 mm; and $x = -3.6$ mm, 172.6 mm.

Pressure Measurements. The time histories of the pressure and velocity fluctuations were acquired at critical locations specified with respect to the aforementioned coordinate system. Appropriate analog filtering and amplification were employed. The sampling time allowed resolution of all dominant frequency components, up to the fourth harmonic of the fluctuation induced by the jet-edge oscillation. Signals were transmitted through the A/D board of the host microcomputer. The nondimensional frequency spectrum was computed using an FFT technique. The total acquisition time of each velocity and pressure record corresponded to, for example, 256 cycles of the predominant jet-edge oscillation at 1.26 Hz. The values of effective sampling time Δt and sampling frequency Δf are indicated in the figures corresponding to each of the time traces and spectra. Filtering

distributed peaks are evident between these higher harmonics, and a broadly distributed subharmonic of the fundamental, occurring approximately at f = 0.61 Hz, is apparent.

Extensive diagnostic experiments were conducted in order to determine the variation of the predominant spectral components over a range of L/H extending from approximately the onset of the self-excited oscillation to attainment of its maximum amplitude. These spectra are shown for extreme values of L/H in Figures 3a and 3b. All spectra exhibit predominance of the fundamental component, whose frequency decreases with increasing L/H, as well as at least at two or three higher harmonics.

Examination of the spectra of the peaks of the fundamental component in the spectra of Figures 3a and 3b, with variations in impingement length L/H, reveals the following characteristics: onset of pronounced jet-edge oscillations at L/H = 6.0 (below this value of L/H, sharply defined peaks were not detectable in the pressure spectra); a rapid increase in amplitude from L/H = 6.0 to 11.0 (not shown herein); attainment of maximum amplitude at L/H = 11.0 (not shown), followed by generally decreasing amplitude at larger values L/H; and, finally, occurrence of predominant oscillations only in the fundamental mode over the entire range of impingement length L/H up to 15.0. These trends are in remarkable accord with the measured variation of the total force F as a function of impingement length L/H measured by Powell (1961) for a low Reynolds number jet at Re = 346.

The frequencies of each of the discernible spectral components in Figures 3a and 3b, as well as components at intermediate values of L/H, were evaluated and plotted as dimensionless frequency fL/U as a function of L/H. The result is shown in Figure 4. Present data are compared with low Reynolds number, quasi-laminar air and water jets impinging upon an edge. Whereas the fundamental component k = 1 of the present study, occurring approximately at fL/U = 0.5 lines up well with the first stage n = 1 of the classical laminar jet oscillation, the higher harmonic components k = 2,3 of the present study are not coincident with the second and third stages n = 2,3 of the laminar jet oscillation. This suggests that, in the present case of turbulent jet-edge interaction, the higher modes are due to strong nonlinearity of the jet-edge oscillation. On the other hand, for the laminar jet, the basic pattern of the local jet-edge interaction region undergoes

the DNS simulation of Kim *et al.* (1987). The bottom plot of Figure 2b shows the velocity correlation component of the Reynolds stress, i.e. $\overline{u'v'}$, normalized with respect to the square of the wall friction velocity $u_* = 17.5$ mm/sec. In both plots, the agreement is acceptable in view of the difference in Reynolds number and the limited number of images employed in the averaging.

Further evaluation of the images provided distributions of u_{rms}/u_* and v_{rms}/u_* across the channel. Moreover, in order to confirm the existence of a well-defined log layer, data were evaluated to demonstrate existence of a logarithmic region extending from approximately $y^+ = 20$ to 150. Finally, verification of an inertial subrange within the turbulent channel flow was accomplished by undertaking a spectral analysis based on the PIV images. The classical $n = -5/3$ slope was evident over a substantial range of dimensionless frequency fH/u_*. Detailed distributions are given by Rockwell & Lin (1997).

4. JET-EDGE OSCILLATIONS: SURFACE PRESSURE FLUCTUATIONS

The time history of the jet-edge interaction was characterized using a variety of pointwise pressure and velocity measurements, as described by Rockwell & Lin (1997). Preliminary experiments to determine the principal oscillation characteristics were carried out by varying the impingement length L. Then, the optimum value of L was determined after considering the strength of the pressure fluctuations, in conjunction with optimization of the field of view and magnification factor of the PIV measurements. The value of dimensionless impingement length eventually chosen corresponds to $L/H = 10$, in which H is the channel half-width.

Pressure spectra were acquired at a relatively large number of values of L/H; only selected spectra are exhibited in Figures 3a and 3b. The plot at the upper left of Figure 3a shows the spectral amplitude plotted on logarithmic coordinates. It shows the degree of predominance of the organized components relative to the background. The fundamental component at $f = 1.35$ Hz extends about one and one-half decades above the background. Well-defined peaks up to the fourth harmonic are evident. In addition, rather broadly

fundamental alterations with increasing stage number (Brown, 1937; Lucas & Rockwell, 1984).

5. JET-EDGE OSCILLATIONS: INSTANTANEOUS STRUCTURE

5.1 RANDOMLY-ACQUIRED IMAGES

Thirty-six images were randomly acquired over a long time span. The minimum time between each of these images was > 10 sec, which is at least a factor of ten longer than the shortest period of the predominant (fundamental) component of the self-sustained jet-edge oscillation. In the following, the instantaneous images of vorticity and velocity in different reference frames provide insight into the instantaneous structure of the jet-edge interaction that, in turn, allows physical interpretation of the time-averaged statistics addressed in Section 6.

Examination of the entire sequence of thirty-six randomly-acquired images shows that essential features of the time-dependent oscillation could be reconstructed using a limited number of images. This is possible due to the highly coherent oscillations at the predominant (fundamental) component, already evident in pressure spectra of Figures 3a and 3b. Figure 5 shows such a reconstruction corresponding to three successive instants. First of all, tracking the large-scale cluster of negative vorticity in the lower part of the image, it moves downstream beneath the edge with increasing time. Correspondingly, the positive layer of vorticity is deflected upward and simultaneously undergoes coalescence of positive vorticity into the initial stages of a large-scale cluster, which eventually will take the mirror image form of the large-scale negative cluster. This positive layer of vorticity is severed at the tip of the edge, particularly evident in the middle image. After this severing occurs, the layer of positive vorticity moves downstream along the lower surface of the impingement edge. An inherent feature of both the positive and negative vorticity layers is the rapid onset of small-scale vortical structures immediately downstream of the nozzle exit. They are addressed in detail subsequently.

Comparison of the overall, global structure of the initially-turbulent jet with the low Reynolds number (laminar) jet of Lucas & Rockwell (1984) is given in Figure 6a. The dye visualization image shown superposed on the corresponding PIV images taken at the same phase of the jet oscillation cycle exhibit a remarkable similarity to the overall global

characteristics of the instantaneous PIV images. For example, the top dye image indicates: formation of a large-scale vortex, which is approximately centered at the tip of the edge; severing of the upper layer of the jet by the tip of the edge; and upward deflection of the jet centerline immediately upstream of the tip of the edge. All of these features are evident in the PIV image. Corresponding global similarities are evident in the low Reynolds number dye photo and high Reynolds number PIV image shown at the bottom of Figure 6a.

Figure 6b shows remarkable similarity between the low Reynolds number air jet of Brown (1937) and the instantaneous PIV image: formation of an elongated, large-scale concentration of vorticity in the upper layer of the jet, at a location upstream of the tip; upward deflection of the jet centerline in that region; and formation of a large-scale vortex of opposite sense centered immediately downstream of the tip. These global features exhibit similar features despite the differences in working fluid and initial conditions of the jet.

5.2 CINEMA ACQUISITION OF IMAGES

Cinema sequences were acquired using two different cameras and nominal framing rates. For the first cinema sequence yielding a highly time resolved series of images, the Hulcher camera operating at 40 frames per second was employed. The intent of this series is to show the evolution of both the small and large-scale vortical structures, in relation to the variation of the instantaneous pressure traces along the upper and lower surfaces of the impingement edge. For the second cinema sequence, the intent was to generate a phase-referenced series of images; the motor-driven Canon camera was employed at a framing rate of 8.8 frames per second. These images, acquired over approximately five cycles of the jet oscillation, allow characterization of the degree to which time evolution of the vortical structures in the jet is repetitive from cycle to cycle.

Highly Time-Resolved Cinema Sequence. First, representative features of the jet-edge interaction are described at crucial instants during the oscillation cycle. Figure 7 shows the pressure trace acquired during the cinema sequence; the dots indicate the instants at which three representative images were processed, in order to show transformation from the minimum to maximum values of the pressure p_u on the upper surface of the edge and simultaneously from the maximum to minimum of pressure p_ℓ on the lower surface of the

edge. The spectra corresponding to these two traces are indicated at the bottom of Figure 7. Due to the substantial nonlinearity of these pressure traces, the middle point on the upper trace p_u does not lie midway between the points of minimum and maximum amplitude. On the other hand, for the pressure signal p_ℓ acquired along the lower surface, the three points are approximately equally spaced.

Instantaneous images at these three instants are shown in Figures 8a through 8c. In each figure, the uppermost image corresponds to contours of constant vorticity, the middle image to the velocity field measured in the laboratory frame, and the bottom image to the velocity field viewed in the reference frame moving at ~0.5 $\overline{U}_m$, where $\overline{U}_m$ is the maximum (centerline) velocity at the exit of the channel. In Figure 8a, the pressure on the upper surface of the edge is maximum-negative, and that on the bottom surface is maximum-positive. At this instant, the upper image showing the patterns of vorticity reveals that the large-scale concentration of positive (solid line) vorticity has just passed over the pressure tap on the upper surface of the edge. Correspondingly, a moderate-scale positive concentration of vorticity is located immediately upstream of the tip of the edge. The pattern of velocity vectors shown in the middle image clearly indicates the downward deflection of the jet in the vicinity of the leading-edge, and occurrence of a large-scale swirl pattern above the edge, due to the large-scale concentration of vorticity. In the bottom image, representing the velocity field in the moving reference frame, the velocity vectors are directed towards the surface of the edge at the location of the lower pressure tap and generally away from the edge at the location of the upper tap. Moreover, the large-scale swirl pattern of velocity vectors is again clearly evident.

For the next instant, represented in Figure 8b, the pressure on the upper surface is nearly at its maximum-positive value, while that on the lower surface is approximately zero. The pattern of vorticity concentrations indicates that the moderate-scale cluster of positive (solid line) vorticity collides with the edge and, in fact, appears to be severed in the region of the tip of the edge. At this instant, the large-scale negative concentration of vorticity is nearly centered beneath the lower pressure tap. The corresponding velocity field in the laboratory frame, shown in the middle image, indicates the severe upward deflection of the jet immediately upstream of the leading-edge, and downward deflection in the region beneath the surface of the edge. In the bottom image, which shows the

instantaneous velocity field in the reference frame moving with 0.5 $\overline{U}_m$, it is evident that the velocity vectors adjacent to the upper surface of the edge are directed downwards.

Finally, in Figure 8c, the instantaneous pressures on the upper and lower surfaces are maximum-positive and -negative respectively. The patterns of instantaneous vorticity indicate a small-scale concentration of positive (solid line) vorticity above the upper surface of the edge, and a large-scale concentration of negative vorticity beneath the tap on the lower surface. In the reference frame moving at $0.5\,\overline{U}_m$ represented in the image at the bottom of Figure 8c, the velocity vectors impinge upon the upper surface of the edge at a location approximately corresponding to the upper pressure tap.

Now that the general features of the flow physics corresponding to maximum-positive and negative peaks of pressure are clarified, it is appropriate to examine in greater detail the jet oscillation and its interaction with the edge. This is done by considering a segment of the pressure trace of Figure 7, in the vicinity of t = 4.5 sec. This segment is represented in a radically expanded form in Figure 9. These expanded segments of the upper p_u and lower p_ℓ traces emphasize the nonlinearity of the pressure signal.

The complete sequence of images corresponding to this cinema sequence is given by Rockwell & Lin (1997). Here we show a sequence of four images, acquired at a rate of forty frames per second, in order to illustrate the time-resolved development of the jet and its interaction with the edge.

The patterns of vorticity given in Figure 10 show increased agglomeration of vorticity into the large-scale negative (dashed line) concentration on the lower side of the jet. Simultaneously, the large-scale concentration of positive (solid line) vorticity moves downstream of the tip of the edge. Although it is possible to track certain small-scale concentrations of vorticity from one image to the next or, in some cases for several images, the exact form of these concentrations has a short half-life, no doubt due to small-scale three-dimensional effects, which are inevitable in separated flows of this type. Even though the large-scale development of the vortical structures was observed to be remarkably two-dimensional across the span of the jet, as evidenced by preliminary, qualitative dye visualization, it is unavoidable that the small-scale structures embedded within the oscillating jet experience three-dimensional distortion.

Comparing the expanded pressure trace of Figure 9 with the patterns of vorticity of Figure 10, the following features are evident over the time span represented by images 171 through 174. Due to the nonlinearity of the pressure signals on the upper and lower surfaces of the edge, the pressure on the upper surface decreases substantially, while that on the lower surface exhibits only a mild positive increase. Correspondingly, the images of Figure 10 show that: (i) the large-scale positive (solid line) vortical structure moves downstream from the tip; and (ii) the layer of negative (dashed line) vorticity, previously severed at the tip of the edge prior to image 171, generally moves downstream along the upper and lower surfaces of the edge. The concentrations of negative vorticity between the large-scale positive vortex and the outer surface of the edge are not to be confused with what one might expect if the circulation of the large-scale vortex is sufficiently large, namely eruption of the surface boundary layer and formation of a negative region of vorticity. This scenario does not occur for the interactions illustrated in Figure 10 and the apparent secondary negative vortex is simply due to severing of the incident layer of negative vorticity in the leading region of the edge. A conceptually similar interpretation can be inferred from the images of Figures 5, 6a and 8b.

Coexisting instabilities in the oscillating jet. Consideration of all of the aforementioned images reveals, first of all, development of an instability that results in a large-scale concentration of vorticity in the vicinity of the leading-edge. This observation suggests that the jet oscillation arises from the inviscid amplification of an unstable disturbance in the jet. If this is indeed the case, then it should be possible to approximate the dimensionless frequency of oscillation on the basis of the inviscid stability analyses described by Sato (1960), Betchov & Criminale (1966), and Bajaj & Garg (1977). The value of frequency predicted on the basis of inviscid analysis will be influenced by the detailed shape of the unsteady velocity distribution and whether inviscid temporal or spatial analysis is employed. On the basis of these previous studies, it is possible to infer an approximate dimensionless oscillation frequency of $\varpi = 2\pi fH/U = 0.3$. For the fundamental $k = 1$ mode shown in the plot of Figure 3.5, the dimensionless frequency fL/U has a representative value of $fL/U = 0.42$, corresponding to a value of $\varpi = 0.27$. We therefore see remarkable agreement between inviscid theory applied to the organized, fundamental component of the oscillation growing on the turbulent background of the jet.

The above-mentioned comparisons between pressure traces and the formation of large-scale concentrations of vorticity have revealed that the pressure signatures, formation of large-scale vorticity concentrations, and the overall undulation of the jet are highly organized and repetitive. The alternating, out-of-phase formation of the large-scale structures along the lower and upper sides of the jet is sustained by the upstream influence or feedback from the edge region, which, in turn, exerts an out-of-phase, dipole-like perturbation of the transverse velocity fluctuation at the frequency corresponding to the large-scale concentrations of vorticity. So, in essence, this means that the initial perturbations in the vicinity of the channel exit associated with development of the large-scale concentrations are essentially π-out-of-phase on the lower and upper sides of the shear layer (Powell, 1961; Stabuli & Rockwell, 1987).

Coexisting with these large-scale vortical structures are small-scale concentrations of vorticity, which rapidly develop immediately downstream of the separation corners of the channel exit, evident in all of the aforementioned images exhibiting contours of constant vorticity. In fact, the agglomeration of a number of the small-scale concentrations of vorticity make up the large-scale concentrations. The identity of these smaller scales persists, in some cases, well after the large-scale concentrations become evident. In contrast to the aforementioned large-scale structures, the initial development of the small-scale concentrations of vorticity, which occurs at a much higher frequency, is not subjected to a rhythmic, out-of-phase upstream influence. In other words, the small-scales in the shear layers immediately downstream of the channel exit develop freely without local "forcing" associated with the upstream influence. The consequences are two-fold: the evolution of the small-scale concentrations is not as distinct and organized as for the large-scale concentrations; and the phase shift between the development of the small-scale concentrations on the lower and upper sides of the jet has no particular fixed value.

In order to emphasize these points, spatial distributions of instantaneous vorticity were extracted from the instantaneous cinema images 171 through 174 of Figure 10. The result is shown in Figure 11. The upper set of instantaneous vorticity distributions is along a horizontal line emanating from the upper corner of the channel exit and the bottom set is correspondingly along a line from the bottom corner. This space-time portrayal exhibits significant irregularity, arising primarily from the aforementioned lack of external "forcing"

of the small-scale concentrations of vorticity, resulting in local three-dimensionality and an early tendency towards vortex merging. As a visual guide, inclined dashed lines, all having the same slope, indicate families of peak values of vorticity and the manner in which they change with time. The movement of the peak value of vorticity in the downstream direction provides the phase speed c_v of the small-scale concentrations of vorticity. This information can be combined with the averaged wavelength between small-scale concentrations to give a typical frequency $fc_v/\lambda = 15.6$ Hz. In dimensionless terms, $\omega = 2\pi fH/\overline{U}_m = 2.82$.

It is therefore evident that this predominant frequency of formation of the small-scale concentrations of vorticity lies well above the aforementioned frequency of the large-scale concentrations, which scales on the overall jet half-width H. It is clear from the images of instantaneous vorticity that the small-scale concentrations are confined to a narrow band of the shear layer in the immediate vicinity of the corner of the channel exit. In turn, the slope of the time-averaged velocity profile $d\overline{u}/dy$ in this region is very large, due to the existence of the fully-developed turbulent channel flow. As a consequence, the local vorticity thickness $\delta_\omega = \Delta\overline{U}/(d\overline{u}/dy)_{max}$, in which $\Delta\overline{U}$ is the velocity difference across the shear layer, will be small relative to that occurring in a fully-evolved jet shear layer well downstream of the nozzle exit, where the large-scale vortical structures develop. Further efforts should evaluate δ_ω and interpret dimensionless frequencies in accord with the theory of Huerre & Monkewitz (1990). This origin of the small-scale vortical structures should then be assessed in conjunction with pre-existing, small-scale structures in the turbulent shear flow upstream of separation.

Interpretation of large-scale vortex interaction with leading edge. An early model for the onset and development of the jet oscillation in a jet-edge system was advanced by Powell (1969), who recognized the importance of unstable disturbance amplification in the jet and by Holger *et al.* (1977), who accounted for the growth and interaction of the large-scale vortex street with the edge, in order to predict the frequency and hydrodynamic feedback originating at the edge. A schematic of the model of Holger *et al.* (1977) is given in the inset (bottom) of Figure 12. In essence, they take the vortex street to be fully-formed by the time it reaches the edge. It is evident, however, from the vorticity

distributions of the foregoing images of Figures 5, 6, and 8 that the large-scale vortices have highly distributed vorticity and a non-circular form. The evolution of a cluster of vorticity corresponding to formation of a single large-scale vortex as a function of time is illustrated in Figure 12. It is evident that the terminal state, represented by the vortex from image 184, is a well-defined vortex with a dimensionless circulation $\Gamma^* = \Gamma/\pi \overline{U}_m 2H = 1.11$. Using this value of Γ^* as a reference, and working backwards in time through images 181, 177, and 171, the location of the cut-off of the upstream boundary of the large-scale vortex was adjusted to give the same value of Γ^* as for the terminal vortex in image 184. This procedure allows reconstruction of the time evolution of a defined cluster of vorticity having a constant value of circulation. In image 171, the vorticity is relatively concentrated in a thin, highly-elongated layer and, with increasing time, evolves towards a larger-scale cluster of vorticity in images 174 and 177. Simultaneously, the cluster of vorticity rotates in the clockwise direction, particularly evident in image 181 and, finally, in image 184, the major axis of the elliptically-shaped pattern of vorticity is nearly vertical. On the basis of these observations, it is evident that the large-scale vortex continues to evolve in form and orientation, even as it encounters the tip region of the edge; moreover, the location of the centroid of the vorticity concentration measured from the plane of symmetry of the edge, increases with time.

An important observation concerns the possible shedding of a secondary vortex in the tip region of the edge. Examination of, for example, the vorticity distribution in the vicinity of the tip of the edge in Figure 10 shows a region of positive vorticity immediately below the surface of the edge and above the large-scale negative concentration of vorticity. This positive vorticity is simply that on the opposite (upper) side of the jet; it has not agglomerated into a large-scale vortex, but has been severed at the tip of the edge. In other words, the large-scale negative vortex of Figure 10 has not induced shedding of a vortex either from the tip of the edge, which was considered to be a key component of the jet edge interaction by Curle (1953), or from the continuous surface of the edge, as may occur for different configurations of vortex-edge interaction, as shown by Jefferies & Rockwell (1996). In fact, positive vorticity can exist simultaneously on both the lower and upper sides of the edge due to severing of the upper vorticity layer at the tip.

Relation of vortex-edge interaction to potential generation of acoustic power. The instantaneous hydrodynamic field represented by the vorticity distributions of Figure 10, as well as by the corresponding velocity distributions (Lin & Rockwell, 1998), play a central role in determining the acoustic power generation, in the event that a resonant acoustic field exists simultaneously with the hydrodynamic field. According to the formulation of Howe (1975, 1980, 1984), the instantaneous acoustic power generation P is given by:

$$P = -\rho \int_{\forall} < (\boldsymbol{\omega} \times \mathbf{V}) \cdot \mathbf{u} > d\forall \qquad (1)$$

in which $\mathbf{u}$ is the vector acoustic velocity at a given point, $\mathbf{V}$ is the vector hydrodynamic velocity and $\boldsymbol{\omega} \times \mathbf{V}$ is the curl of the vorticity with the hydrodynamic velocity. It should be noted that this relation is relevant to any sufficiently long wavelength sound wave, not just resonant ones. Hourigan, Welsh, Thompson & Stokes (1990) have physically interpreted eqn. (1) for the occurrence of resonance in the configuration of a baffle-cavity using smoke visualization in conjunction with a discrete vortex simulation.

The aim of our present considerations is to interpret the hydrodynamic contribution $\boldsymbol{\omega} \times \mathbf{V}$ using instantaneous spatial representations of $\boldsymbol{\omega}$ and $\mathbf{V}$. It should be kept in mind that if the jet exists in a mode of resonant coupling with a resonator, its structure will be modified relative to that shown herein. The intent of the present evaluation is to demonstrate the nature of $\boldsymbol{\omega} \times \mathbf{V}$ for a representative turbulent jet. The distribution of vectors $\boldsymbol{\omega} \times \mathbf{V}$ for the present jet-edge interaction is shown in the region of the edge for images 171 and 173 in Figure 13. In image 171, the large-scale vortical structure above the edge generates a sink-like pattern of vectors, whereas all other vorticity concentrations produce predominantly vectors oriented in the positive or negative vertical direction. Particularly notable are the substantial contributions from the small-scale vortical structures, including those along the upper surface of the impingement edge. In image 173, the clusters of vectors along the edge surface are particularly pronounced and, furthermore, the large-scale structure above the edge loses its sink-like character. The importance of the small-scale concentrations of vorticity in generating substantial magnitudes of $\boldsymbol{\omega} \times \mathbf{V}$ is evident in both images 171 and 173. Moreover, these images, which exhibit vectors oriented predominantly in the vertical direction, suggest that resonant acoustic waves having velocities $\mathbf{u}$ oriented in the vertical direction will provide

particularly large contributions to the acoustic power P, since the value of the dot product in equation (1) will be maximum. The converse holds for a resonant wave oriented in the horizontal direction.

Phase-referenced representations of vortex-edge interactions. As noted in the foregoing, a cinema sequence having lower temporal resolution, but extending over approximately nine complete cycles of oscillation, was acquired in order to determine the degree to which the jet structure was phase-locked from cycle to cycle. Complete details, along with sets of images, are given by Rockwell & Lin (1997). Figure 14 shows a sequence of images, each acquired at the same phase of the instantaneous pressure signal on the lower surface of the impingement edge. This phase-referenced condition corresponds to frame numbers N = 3, 10, 17 and 24. In all images, a large-scale concentration of negative (dashed line) exists on the lower side of the jet at a location just upstream of the impingement edge. Moreover, the positive layer of vorticity, originating at the channel exit and exhibiting a train of small-scale vorticity concentrations, intersects the tip of the edge. Remarkable is the fact that an extremum of the small-scale concentrations of positive vorticity centered at the tip of the edge is well-defined in all images. Finally, a portion of the large-scale concentration of vorticity on the upper surface of the edge is evident in all images. It is evident that the large-scale vorticity concentrations are generally phase-repetitive, i.e., tend to occur at approximately the same location with a generally similar form of each of the images. With the exception of the small-scale concentration at the tip of the edge, there is no such phase consistency or phase-locking of the small-scale concentrations of vorticity.

6. ENSEMBLE-AVERAGED STATISTICS OF JET-EDGE INTERACTION

In order to determine the averaged statistics of the jet-edge interaction, both the randomly-acquired and cinema sequences of images were employed. The procedure was the same for both sequences. In essence, successive images were "stacked" such that at a given coordinate (x,y), the instantaneous values of velocity u,v were determined at that coordinate location. Then, using the equations defined in the following, the various statistical representations were calculated. For the randomly-acquired sequence, this involved a total of thirty-six images at a minimum time interval of ten sec. The time scale

of the jet oscillation is of the order of 1 sec, so the minimum sampling interval is approximately a factor of ten larger. This random sampling is typical of that employed in turbulent flows. An example is the averaged turbulent statistics of a turbulent jet impinging upon a plate involving eleven images (Landreth & Adrian, 1990). For the cinema sequence with low time resolution, it involved a total of 35 images, acquired at a nominal spacing of 114 ms, over a total number of five cycles, i.e. 5T, in which T is the period of the jet oscillation. The equations employed for determining the ensemble-averaged statistics are defined as follows:

$< V >$ ≡ averaged (or mean) total velocity

$$< V > \equiv \frac{1}{N}\sum_{n=1}^{N} V_n(x,y) \tag{6.1}$$

Similar definitions hold for the horizontal u and vertical v velocity components and for the vorticity ω. For the fluctuating components:

u_{rms} = root-mean-square of u component fluctuation

$$u_{rms} \equiv < u >_{rms} \equiv \left[\frac{1}{N}\sum_{n=1}^{N}\left[u_n(x,y) - < u(x,y) >\right]^2\right]^{1/2}, \tag{6.2}$$

and similarly for the root-mean-square of the v component fluctuation, v_{rms}. For the Reynolds stress:

$< u'v' >$ = averaged value of Reynolds stress correlation

$$< u'v' > \equiv \frac{1}{N}\sum_{n=1}^{N}\left[u_n(x,y) - < u(x,y) >\right]\left[v_n(x,y) - < v(x,y) >\right] \tag{6.3}$$

We emphasize that, unlike some ensemble-averaging processes, no phase reference or phase trigger was employed. Rather, in the case of the randomly-acquired images, the camera was triggered at an arbitrary time, so long as the interval between images was greater than ten seconds. Likewise, for the cinema series, no phase condition was employed. For the cinema sequence, the spacing between successive images employed in the ensemble-averaging process is of the order of 1/10th the predominant period of the jet oscillation.

Since markedly different criteria were employed for the acquisition of images, i.e., random versus continuous cinema, a direct comparison of the averaged quantities should provide an indication of the degree of convergence. For this reason, averaged images

obtained from the cinema sequence are directly compared with those from the randomly-acquired series in the figures that follow. Each figure contains two averaged images. The top one corresponds to that obtained from the cinema sequence, while the lower one represents the randomly-sampled (acquired) sequence.

The ensemble-average of the total velocity V in the laboratory frame is shown in Figure 15. In this image, as well as in all subsequent ensemble-averaged representations, the region in the immediate vicinity of the edge has been blanked out, due to uncertainties associated with image registration. The patterns of vectors exhibited in Figure 15 are generally antisymmetrical with respect to the plane of symmetry of the edge. The ensemble-averaged vorticity of Figure 16 exhibits very high levels of $<\omega>$ in the immediate vicinity of the corners of the channel exit. This averaged vorticity overshadows the remarkably low levels of vorticity in the vicinity of the impingement edge.

Contours of constant u_{rms} are shown in normalized form in Figure 17. Relatively high levels are attained in the shear layers of the jet, especially at a location approximately three nozzle widths downstream of the channel exit. In addition, high levels occur on the upper and lower sides of the edge, at a location immediately downstream of the tip.

Corresponding contours of v_{rms}, normalized with respect to the maximum velocity, are given in Figure 18. They also exhibit relatively high values in the vicinity of the tip of the edge. In this case, a particularly large magnitude is centered at the tip. In comparison, the foregoing extrema of the u_{rms} contours are located immediately downstream of the tip adjacent to the upper and lower surfaces.

The ensemble-averaged Reynolds stress patterns of Figure 19 exhibit large values of $<u'v'>$ in the shear layers of the jet at a distance approximately three to four nozzle widths downstream of the nozzle exit. These high values of $<u'v'>$ are clearly due to the large amplitude, transverse undulation of the jet. In addition, extrema of Reynolds stress are evident on the upper and lower sides of the tip region of the edge, again due to the severe flow distortion in that region, arising from the jet-edge interaction. In the region immediately downstream of the nozzle exit, local extrema of Reynolds stress occur due to the onset of small-scale vortices.

It is of interest to compare these extreme values of Reynolds stress with those occurring within the turbulent channel flow. Referring to Figure 2, the nominal value of

peak Reynolds stress is approximately at 0.8 u_*^2, which corresponds to 0.0013 $\overline{U}_m^2$. The extreme values of ensemble-averaged Reynolds stress in the three primary regions of Figure 13 are: 0.006 $\overline{U}_m^2$ in the region immediately downstream of the nozzle exit, induced by the small-scale vortex formation; 0.020 $\overline{U}_m^2$ in the jet shear layers at a location three to four nozzle widths downstream of the channel exit; and 0.047 $\overline{U}_m^2$ immediately in the vicinity of the tip of the edge. It is therefore evident that the averaged peak Reynolds stresses in each of these three regions exceed by factors of approximately 5, 15, and 40 the maximum Reynolds stress in the channel flow. This observation underscores the powerful influence of instabilities leading to both small-scale and large-scale vortex formation, which in turn are associated with the large-scale undulations of the jet.

7. CONCLUDING REMARKS

Self-sustained oscillation of a planar jet impinging upon an edge has long been recognized as a generic type of flow-structure interaction. Previous related investigations have focused on relatively low values of Reynolds number for which the jet is initially laminar at the nozzle exit. Even in this limiting case of the undulating laminar jet, quantitative aspects of the flow physics, especially the interaction region near the tip of the edge, which dictates the edge loading and thereby the upstream influence, have remained unclarified. The present investigation addresses the more complex case of a jet formed from a fully-turbulent channel flow. The issues of whether self-sustained oscillations can occur and the related unsteadiness of the jet have been pursued. In doing so, the instantaneous structure of the initially-turbulent jet, the instantaneous loading on the edge, and the averaged turbulence statistics of the jet-edge system have been characterized using a global imaging approach. It should be emphasized that, in the present experiment, the unsteadiness of the jet-edge system is strictly hydrodynamic. That is, it occurs in absence of acoustic, or analogous free-surface, resonant modes of the flow system; moreover, fluid elastic effects are not present. Both of these phenomena are considered parasitic for our present purposes in that they can greatly enhance coherent oscillations through coupling effects.

The principal findings are summarized in the following.

7.1 INSTANTANEOUS STRUCTURE OF THE INITIALLY-TURBULENT JET

It has been demonstrated that the jet formed from a fully-turbulent channel flow exhibits highly-organized, self-sustained oscillations. The major features of the jet evolution have been characterized using images of vorticity and velocity, acquired with adequate temporal resolution, in order to determine the time history of the unsteadiness. In essence:

(a) The jet supports two clearly identifiable modes of instability of drastically-different scales. The large-scale, global mode involves formation of vortices that scale on the overall thickness of the jet. The frequency of these vortices is well approximated by application of inviscid stability theory to the averaged turbulent background flow. The small-scale, local mode gives rise to a train of small vortices having a frequency and wavelength much larger and smaller respectively than those of the large-scale vortices. It may scale on the local vorticity thickness of the inner region of the boundary layer at the separation edge; further theoretical assessment is required. Interpretation in conjunction with small-scale structures in the approach turbulent boundary layer is needed.

(b) The two-scale instability of the impinging turbulent jet is, in some respects, analogous to the two-scale instability in the near-wake of a circular cylinder at sufficiently high Reynolds number, as represented by the comparison of Figure 20. In the case of the wake, small-scale vortices formed in the thin shear layer immediately downstream of separation coalesce to form the large-scale Kármán vortices. For both the impinging turbulent jet and the turbulent near-wake of the cylinder, the large-scale vortices emerge as highly coherent vortical structures. For the near-wake, it is well known that existence of a global (absolute) instability promotes the onset of highly robust, limit cycle oscillations, which correspond to generation of the large-scale vortices (Huerre & Monkewitz, 1990). The upstream influence required to attain these large-scale oscillations is inherent to the concept of the global or absolute instability, which accommodates an upstream wave.

On the other hand, for the impinging turbulent jet, the jet instability is convective, as opposed to absolute, but the presence of the impingement edge and the consequent upstream influence to the sensitive region of the shear layer at separation allows

highly coherent, large-scale vortical structures to be sustained in a manner directly analogous to the Kármán wake of a cylinder. This equivalence is addressed for quasi-laminar jets and wakes by Chomaz *et al.* (1988) and Rockwell (1990). For the present case of the impinging turbulent jet, the initially-developing shear layer from the channel exit is modulated by the upstream influence arising from the jet-edge interaction. This influence may be approximated, for purposes of discussion, as a dipole-like source located near the tip of the impingement edge. It is dominated by the frequency of the large-scale vortex interaction with the edge. As a consequence, the small-scale vortical structures initially formed from the corners of the channel exit, which have a much higher frequency, develop in a much less organized, non-repetitive fashion, evident by constructing space-time distributions of vorticity. They rapidly coalesce to form the large-scale vortical structures, in a manner similar to the phenomenon on collective coalescence observed for large amplitude forcing of jets in absence of an impingement edge (Ho & Huang, 1982; Rockwell, 1972).

(c) Confirmation of the concept of inviscid disturbance amplification on the turbulent background of the jet is evident by comparison of the overall form of the jet undulation and large-scale vortex development with the corresponding case of an initially-laminar jet, qualitatively visualized with dye or smoke. The gross form of the jet patterns is remarkably similar, again emphasizing the importance of upstream influence or feedback in promoting the emergence of large-scale, phase-repetitive vortices.

7.2 JET-EDGE INTERACTION AND INSTANTANEOUS LOADING OF EDGE

The quasi-periodic pressure fluctuations on the surfaces of the edge have been related to the instantaneous velocity and vorticity fields in the vicinity of the edge. The major findings are as follows:

(a) The interaction of the large-scale vortices with the edge is more complex than the traditionally-assumed case of a fully-evolved vortex street impinging upon the edge. Such vortices evolve from initially elongated patches of distributed vorticity that have an essentially horizontal major axis. These elliptically-shaped clusters of vorticity continue to develop as they interact with the edge, undergoing simultaneous translation and tilting such that their major axes tend towards a nearly vertical

orientation. Simultaneously, the centroid of these large-scale concentrations is increasingly displaced from the plane of symmetry of the edge. The dimensionless circulation of the large-scale clusters of vorticity, based on the centerline velocity of the channel flow and the width of the channel, is $\Gamma^* = \Gamma/\pi \overline{U}_m 2h \cong 1$.

(b) Along the surface of the edge, at a location immediately downstream of the tip, the large-scale vorticity concentration and smaller-scale concentrations of opposite sense are observed. The small-scale concentrations do not, however, arise from the classical scenario of boundary layer eruption from the surface of the edge to form so-called secondary vortices (Curle, 1953); rather, they are simply due to partitioning of the shear layer from the opposite side of the jet by the tip of the impingement edge.

(c) The surface pressure fluctuations on either side of the edge are highly nonlinear, involving rapid changes with pressure on one surface, while simultaneously, mild changes in pressure occur along the opposite surface. This nonlinearity takes the form of higher harmonic components in the spectra of the surface pressure fluctuations. Such multiple spectral peaks are, however, not due to multiple concentrations of large-scale vortices, as observed by Lucas & Rockwell (1984) for the corresponding case of the laminar jet. Rather, they are due to the complex type of vortex pattern described in (b).

(d) This type of nonlinearity, and the associated form of the spectral distribution of the fluctuating surface pressures, is preserved over a wide range of impingement length L normalized by the nozzle half-width H. Appropriate scaling of the frequency of the surface pressure fluctuation involves fL/H, in analogy with that employed for the classical laminar-jet interactions. The importance of the impingement length scale L is due to the feedback, or upstream influence, which occurs essentially instantaneously from the impingement edge to the sensitive region of the shear layer in the vicinity of the nozzle exit. The convective time scale corresponding to development of the vortex system over distance L accounts for the variation of the absolute value of frequency f of the fundamental mode of the surface pressure and thereby development of the large-scale vortices in the jet. An important distinction relative to the laminar jet is the apparent lack of occurrence of successive stages of oscillation, which are well known to occur in accord with increasingly complex patterns of large-scale

vortices immediately upstream of and at the tip of the impingement edge. Such stage-like behavior does not appear to occur for the turbulent jet; rather, the nonlinear nature of the jet-edge interaction induces the higher order harmonics.

(e) In the event that the jet-edge oscillation would occur in presence of a resonant acoustic mode of a confined system, evaluation of the hydrodynamic integrand of the integral expressing the acoustic power reveals substantial contributions from both large- and small-scale concentrations of vorticity in the vicinity of the impingement edge. This evaluation shows that resonant acoustic modes oriented transverse to the jet-edge will produce the maximum acoustic power for a given magnitude of acoustic velocity.

7.3 TURBULENCE STATISTICS OF JET

The statistics of the jet rapidly take on an identity distinct from the turbulent boundary layer in the channel. Due to separation of flow from the exit of the channel, which is characterized by inflection points in the averaged velocity profile, rapid amplification of disturbances occurs, leading to highly-correlated velocity fluctuations in the streamwise and transverse directions. As a consequence:

(a) The averaged Reynolds stresses in the initial formation region of the jet, due to formation of small-scale vortices, exceeds that of the turbulent boundary layer within the channel by a factor of five. Further downstream in the jet, the onset of large-scale vortex formation is associated with averaged values of Reynolds stress of the order of fifteen times that in the channel boundary layer. Finally, in regions of local interaction of the jet with the tip of the edge, the Reynolds stress can be of the order of forty times that of the initially turbulent boundary layer.

(b) Large values of averaged Reynolds stresses in the tip region of the edge are associated with peak values of the rms velocity fluctuations. The transverse component v_{rms} exhibits peak values at the tip of the edge, while the streamwise component u_{rms} shows two peak values located immediately downstream of the tip of the edge, one on the upper surface and the other on the lower surface.

8. ACKNOWLEDGEMENTS

The authors are pleased to acknowledge the partial support of the National Science Foundation under Grants No. CTS-9422432 and CTS-9803734, as well as the Office of Naval Research with Grants No. N00014-94-1-0815, P00001 and N00014-94-1-1183, NASA-Langley Research Center under Grant No. NAG-1-1885, and the Air Force Office of Scientific Research, Grant No. F49620-99-1-0011. The authors benefited from the contributions of Matthew Reiss during the experimental phase of this investigation.

9. LIST OF REFERENCES

BAJAJ, A. K. & GARG, V. K. 1977 Linear stability of jet flows. *Transactions of the ASME, Journal of Applied Mechanics* **44**, 378-384.

BETCHOV, R. & CRIMINALE, W. O. 1966 Spatial instability of the inviscid jet and wake. *The Physics of Fluids* **9** (2), 359-362.

BLAKE, W. K. & POWELL, A. 1986 The development of contemporary views of flow-tone generation. In *Recent Advances in Aeroacoustics* (ed. A. Krothapali and C A. Smith), 247-325, Springer-Verlag:New York.

BROWN, G. B. 1937a The vortex motion causing edge tones. *Proceedings of the Physical Society of London* **49**, 493-507.

BROWN, G. B. 1937b The mechanism of edge-tone production. *Proceedings of the Physical Society of London* **49**, 508-521.

CHOMAZ, J. M., HUERRE P. & REDEKOPP, L. T. 1988 Bifurcations to local and global modes in spatially-developing flows. *Physical Review Letters* **60** (1), 25-28.

CHYU, C.-K. & ROCKWELL, D. 1996 Near-wake structure of an oscillating cylinder: effect of controlled Kelvin-Helmholtz vortices. *Journal of Fluid Mechanics* **322**, 21-49.

CRIGHTON, D. G. 1992 The jet-edge tone feedback cycle; linear theory for the operating stages. *Journal of Fluid Mechanics* **234**, 361-392.

CURLE, N. 1953 The mechanics of edge-tones. *Proceedings of the Royal Society of London A* **216**, 412-424.

GURSUL, I., LUSSEYRAN, D. & ROCKWELL D. 1990 On interpretation of flow visualization of unsteady shear flows. *Experiments in Fluids* **9**, 257-266.

GURSUL, I. & ROCKWELL, D. 1991 Effect of concentration of vortices on streakline patterns. *Experiments in Fluids* **10**, 294-296.

HO, C.-M. & HUANG, L. S. 1982 Subharmonics and vortex merging in mixing layers. *Journal of Fluid Mechanics* **119**, 443-473.

HOLGER, D. K., WILSON, T. A. & BEAVERS, G. S. 1977 The fluid mechanics of the edge tone. *Journal of the Acoustical Society of America* **62**, 1116-1128.

HOLGER, D. K., WILSON, T. A. & BEAVERS, G. S. 1980 The amplitude of edgetone sound. *Journal of the Acoustical Society of America* **67**, 1507-1511.

HOURIGAN, K., WELSH, M. C., THOMPSON, M. C. & STOKES, A. N. 1990 Aerodynamic sources of acoustic resonance in a duct with baffles. *Journal of Fluids and Structures* **4**, 345-370.

HOWE, M. S. 1975 Contributions to the theory of aerodynamic sound with application to excess jet noise and the theory of the flute. *Journal of Fluid Mechanics* **71**, 625-673.

HOWE, M. S. 1980 The dissipation of sound at an edge. *Journal of Sound and Vibration* **70**, 407-411.

HOWE, M. S. 1984 On the absorption of sound by turbulence and other highly dynamic flows. *Journal of Applied Mathematics* **32**, 187-209.

HOWE, M. S. 1997 Edge, cavity and aperture tones at very low Mach numbers", *Journal of Fluid Mechanics* **330**, 61-84.

HUERRE, P. 1984 Perturbed free shear layers. *Annual Review of Fluid Mechanics* **16**, 365-424.

HUERRE, P. & MONKEWITZ, P. A. 1990 Local and global instabilities of spatially developing flows. *Annual Review of Fluid Mechanics* **22**, 473-537.

JEFFERIES, R. & ROCKWELL, D. 1996 Interactions of a vortex with an oscillating leading-edge. *AIAA Journal* **34** (11), 2448-2450.

JOHANSSON, J. B. & SMITH, C. R. 1983 The effects of cylindrical surface modifications on turbulent boundary layers. Report FN-3, Department of Mechanical Engineering and Mechanics, Lehigh University, Bethlehem, Pennsylvania, U.S.A.

KARAMCHETI, K., BAUER, A. B., SHIELDS, W. L., STEGEN, G. R. & WOOLLEY, J. P. 1969 Some features of an edge-tone flow field", NASA HQ Conference, Basic Aeronautical Noise Research, NASA Special Publication 207, 275-304.

KAYKAYOGLU, R. & ROCKWELL, D. 1986 Unstable jet-edge interaction. Part I. Instantaneous pressure fields at single frequency. *Journal of Fluid Mechanics* **169**, 125-149.

KIM, J., MOIN, P. & MOSER, R. 1987 turbulent statistics in fully developed channel flow at low Reynolds number. *Journal of Fluid Mechanics* **177**, 133-166.

LANDRETH, C. C. & ADRIAN, R. J. 1990 Impingement of a low Reynolds number circular jet onto a flat plate at normal incidence. *Experiments in Fluids* **9**, 74-84.

LEPICOVSKY, J. & AHUJA, K. K. 1983 some new results on edge tone oscillations in high speed subsonic jets. AIAA Paper No. 83-0665.

LIN, J.-C. & ROCKWELL, D. 1998 Cinema PIV and its application to impinging vortex systems. Article FEDSM 98-5270, *Proceedings of ASME Fluids Engineering Division Summer Meeting*, June 21-25, Washington, D.C.

LIU, Z.-C., LANDRETH, C. C., ADRIAN, R. J. & HANRATTY, T. J. 1991 High resolution measurement of turbulent structure in a channel with particle image velocimetry. *Experiments in Fluids* **10**, 301-312.

LUCAS, M. & ROCKWELL, D. 1984 Self-excited jet: upstream modulation and multiple frequencies. *Journal of Fluid Mechanics* **147**, 333-352.

MONKEWITZ, P. & HUERRE, P. 1982 Influence of the velocity ratio on the spatial instability of mixing layers. *Physics of Fluids* **24** (7), 1137-1143.

NIEDERSCHULTE, M. 1989 Turbulent flow through a rectangular channel. Ph.D. Dissertation, Department of Theoretical and Applied Mechanics, University of Illinois at Urbana-Champaign.

NYBORG, W. L 1954 Self-maintained oscillations of the jet in a jet-edge system. *Journal of the Acoustical Society of America* **26**, 174-182.

POWELL, A. 1961 On the edge tone. *Journal of the Acoustical Society of America* **33**, 395-409.

ROCKWELL, D. 1972 External excitation of planar jets. *Journal of Applied Mechanics* **39** (4), 883-890.

ROCKWELL, D. 1983 Oscillations of impinging shear layers. Invited Lecture, 20th Aerospace Sciences Meeting of AIAA, January, 1981, Orlando, FL; AIAA Paper 81-0047; also see *AIAA Journal* **21**, 645-664.

ROCKWELL, D. 1990 Active control of globally-unstable separated flows. *Proceedings of International Symposium of ASME FED: Unsteady Fluid Dynamics* (ed. J. A. Miller and D. P. Telionis) **92**, 379-394.

ROCKWELL, D. 1998 Vortex-body interactions. Invited contribution to *Annual Review of Fluid Mechanics* **30**, 199-229.

ROCKWELL, D. & LIN, J. C. 1996 *Experimental data for computational fluid dynamic simulations of fluid oscillators: cavity flow. Volumes 1 and 2.* Fluid Mechanics

Laboratories Report R01, ``1996, Department of Mechanical Engineering and Mechanics, Lehigh University, Bethlehem, Pennsylvania, U.S.A.

ROCKWELL, D. & LIN, J. C. 1997 *Experimental data for computational fluid dynamics simulation of fluid oscillators: jet-edge flow.* Fluid Mechanics Laboratories Report R01, 1997, Department of Mechanical Engineering and Mechanics, Lehigh University, Bethlehem, Pennsylvania, U.S.A.

ROCKWELL, D., MAGNESS, C., TOWFIGHI, J., AKIN, O. & CORCORAN, T. 1993 High-image-density particle image velocimetry using laser scanning techniques. *Experiments in Fluids* **14**, 181-192.

ROCKWELL, D. & NAUDASCHER E. 1978 Review - self-sustaining oscillations of flow past cavities. Transactions of the ASME, *Journal of Fluids Engineering* **100** (June), 152-165.

ROCKWELL, D. & NAUDASCHER E. 1979 Self-sustained oscillations of impinging free-shear layers. *Annual Review of Fluid Mechanics* **11**, 67-94.

Sato, H. 1960 The stability and transition of a two-dimensional jet. *Journal of Fluid Mechanics* **7**, 53-80.

STAUBLI, T. & ROCKWELL D. 1987 Interaction of an unstable planar jet with an oscillating leading-edge. *Journal of Fluid Mechanics* **176**, 135-167.

LIST OF FIGURES

Figure 1: Overview of jet-edge system.

Figure 2a: Instantaneous velocity fields of turbulent channel flow shown in reference frames moving with the maximum velocity $\overline{U}_m$ (top image) and spatially-averaged velocity $\overline{U}_M$ (bottom image).

Figure 2b: Variation of mean velocity distribution across the channel (top plot) and Reynolds stress normalized by friction velocity (bottom plot). Present PIV measurements are compared with LDA measurements of Niederschulte (1989) and direct numerical simulation (DNS) of Kim et al. (1987).

Figure 3a: Spectra of pressure fluctuation on lower surface of impingement edge as a function of dimensionless impingement distance. Inset shows typical spectrum plotted on a logarithmic scale.

Figure 3b: Spectra of pressure fluctuation on lower surface of impingement edge as a function of dimensionless impingement distance.

Figure 4: Comparison of variations of dimensionless frequency with dimensionless impingement distance for present and previous investigations. For the present study of an initially turbulent jet, all four detectable spectral peaks k = 1, 2, 3, and 4 are represented. Previous studies, which typically exhibit modes n = 1, 2, and 3, involve laminar jet formation from the nozzle exit.

Figure 5: Comparison of vorticity distributions at three successive phases of the jet oscillation. Images are from the randomly-acquired series. Minimum vorticity $\omega_{min} = \pm 10$; incremental vorticity $\Delta\omega = 5$ sec^{-1}.

Figure 6a: Comparison of instantaneous distributions of vorticity with the qualitative dye visualization of Lucas and Rockwell (1984) for the case of an initially laminar jet at Re = 300. $\omega_{min} = \pm 10$ sec^{-1}. $\Delta\omega = 5$ sec^{-1}.

Figure 6b: Comparison of instantaneous distribution of vorticity with the qualitative smoke visualization of Brown (1937) at a value of Reynolds number Re = 183. Minimum vorticity level $\omega_{min} = \pm 10$ sec^{-1} and $\Delta\omega = 5$ sec^{-1}.

Figure 7: Pressure traces corresponding to highly-resolved cinema sequence. Instants at which three representative images were acquired are represented by circular symbols. These images show the transformation from minimum to maximum pressure on the upper surface of the edge and maximum to minimum pressure on the lower surface of the edge. Sampling time is $\Delta t = 0.005$ sec.

Figure 8a: Comparison of vorticity, velocity in the laboratory frame and velocity in a frame moving at 0.50 $\overline{U}_m$ for the cinema sequence. $\omega_{min} = 10$ sec^{-1} and $\Delta\omega = 5$ sec^{-1}. Images represent transformed versions of those of Lin and Rockwell (1998).

Figure 8b: Comparison of vorticity, velocity in the laboratory frame and velocity in a frame moving at 0.50 $\overline{U}_m$ for the cinema sequence. $\omega_{min} = 10$ sec^{-1} and $\Delta\omega = 5$ sec^{-1}.

Figure 8c: Comparison of vorticity, velocity in the laboratory frame and velocity in a frame moving at 0.50 $\overline{U}_m$ for the cinema sequence. $\omega_{min} = 10$ sec^{-1} and $\Delta\omega = 5$ sec^{-1}.

Figure 9: Expanded segment of pressure trace of Figure 7, which emphasizes the highly time-resolved image acquisition in the vicinity of maximum negative pressure p_u on the upper surface and maximum positive pressure p_ℓ on the lower surface of the edge. Sampling time is $\Delta t = 0.005$ sec.

Figure 10: Excerpts from the cinema sequence showing instantaneous patterns of vorticity leading to occurrence of maximum negative pressure p_u on the upper surface and maximum positive pressure p_ℓ on the lower surface. Images correspond to numbers 171 through 174, designated on the pressure data of Figure 9. Time resolution between images is $\delta t/T = 0.03$, in which T is the period of the jet oscillation. Images represent transformed versions of those of Lin and Rockwell (1998).

Figure 11: Spatial distributions of vorticity along horizontal lines extending from the corners of the channel exit for sequential instants of time corresponding to images 171 through 174. Inclined dashed lines are intended to serve as a guide for identifying common peaks or valleys, corresponding to maxima and minima of vorticity concentrations. These data were extracted from the images of Figure 10.

Figure 12: Evolution of a defined cluster of vorticity, which eventually evolves into a large-scale vortex as it encounters the impingement edge. Images were extracted from the same cinema sequence as Figure 10. Horizontal reference lines correspond to the plane of symmetry of the jet-edge system, i.e., the line passing through the tip of the edge. The dimensionless circulation Γ^* is constant for all clusters of vorticity.

Figure 13: Contours of constant vorticity for images 171 (top) and 173 (bottom) of the cinema sequence of Figure 10 and corresponding vectors of the quantity $\underline{\omega} \wedge \underline{V}$ of the acoustic power integral.

Figure 14: Representative images of the phase-referenced vorticity field excerpted from cinema sequence; each image corresponds approximately to occurrence of zero instantaneous pressure p_ℓ on the lower surface of the impingement edge.

Figure 15: Ensemble-averaged distribution of total velocity $< V >$ shown in laboratory reference frame. Top image is from cinema sequence and bottom image is from randomly-acquired sequence.

Figure 16: Contours of ensemble-averaged vorticity, $< \omega >$. Top image is from cinema sequence and bottom image is from randomly-acquired sequence. Minimum vorticity $\omega_{min} = \pm 10$ sec^{-1} and incremental vorticity $\Delta\omega = 5$ sec^{-1}.

Figure 17: Contours of constant root-mean-square of the streamwise component of the velocity fluctuation, u_{rms}, normalized with respect to the maximum velocity at the centerline $\overline{U}_m$. Minimum contour is 0.02 and increments are 0.02. Top image is from cinema sequence and bottom image is from randomly-acquired sequence.

Figure 18: Contours of constant root-mean-square of the transverse component of the velocity fluctuation, v_{rms}, normalized with respect to the maximum velocity $\overline{U}_m$ at the centerline. Minimum contour is 0.02 and incremental values are 0.02. Top image is from cinema sequence and bottom image is from randomly-acquired sequence.

Figure 19: Contours of constant ensemble-averaged Reynolds stress, $< u'v' >$, normalized by square of maximum velocity $\overline{U}_m^2$. Top image is from cinema sequence and bottom image is from randomly-acquired sequence. Minimum contour is 0.002 and the increment between contours is 0.002.

Figure 20: Comparison of the near-wake of a circular cylinder and the jet in a jet-edge system. Both exhibit the rapid development of small-scale vorticity concentrations due to a localized instability immediately downstream of separation of the shear layer. The Reynolds number for the flow past the cylinder, based on cylinder diameter, is 10,000 (from Chyu and Rockwell, 1996). Note that the bottom shear layer from the circular cylinder exhibits a train of small-scale vortices that roll up to form the Kármán vortex. For the jet-flow, the Reynolds number, based on nozzle width, is 10,944.

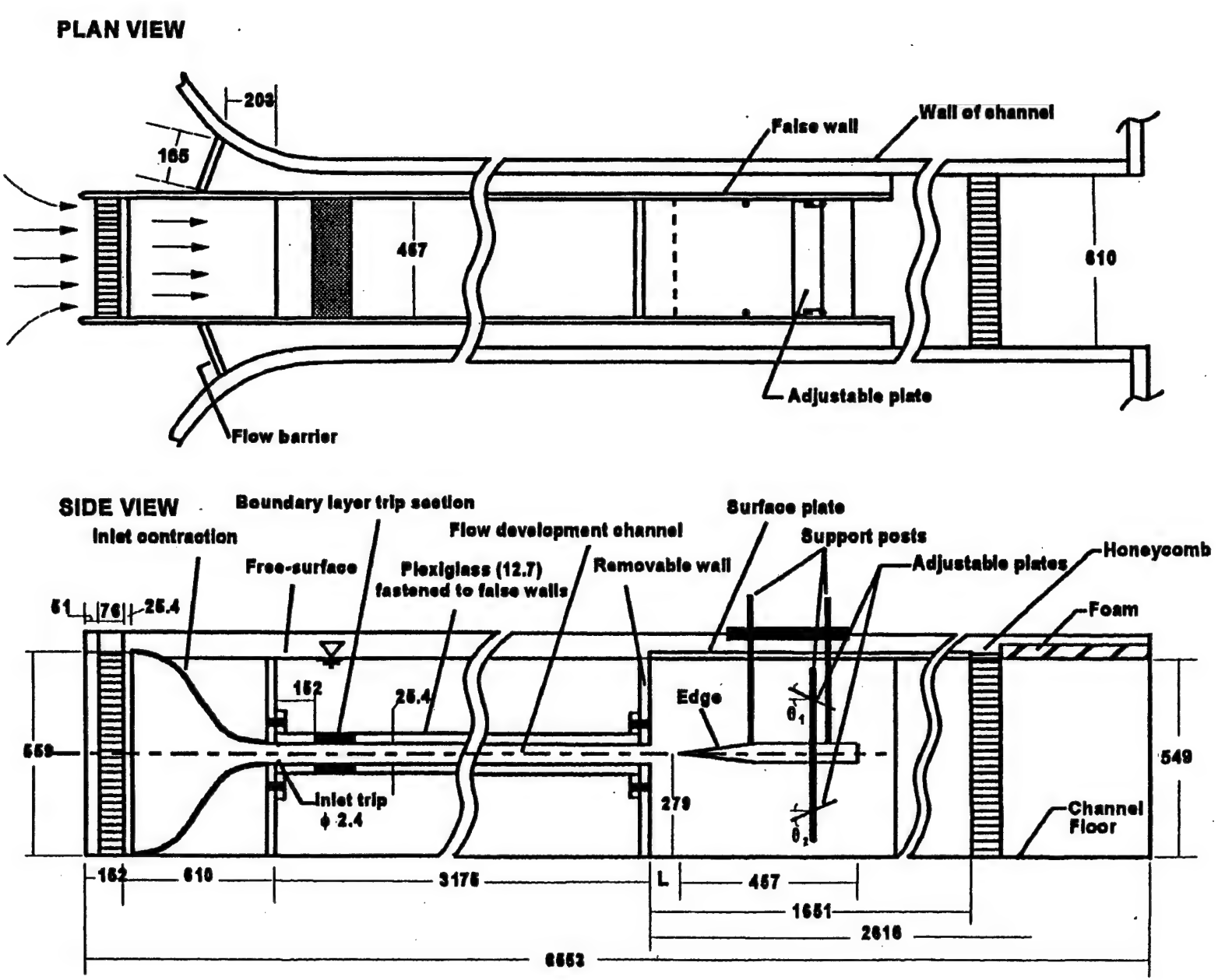

Figure 1: Overview of jet-edge system. All dimensions in millimeters

Figure 2a: Instantaneous velocity fields of turbulent channel flow shown in reference frames moving with the maximum velocity $\overline{U}_m$ (top image) and spatially-averaged velocity $\overline{U}_M$ (bottom image).

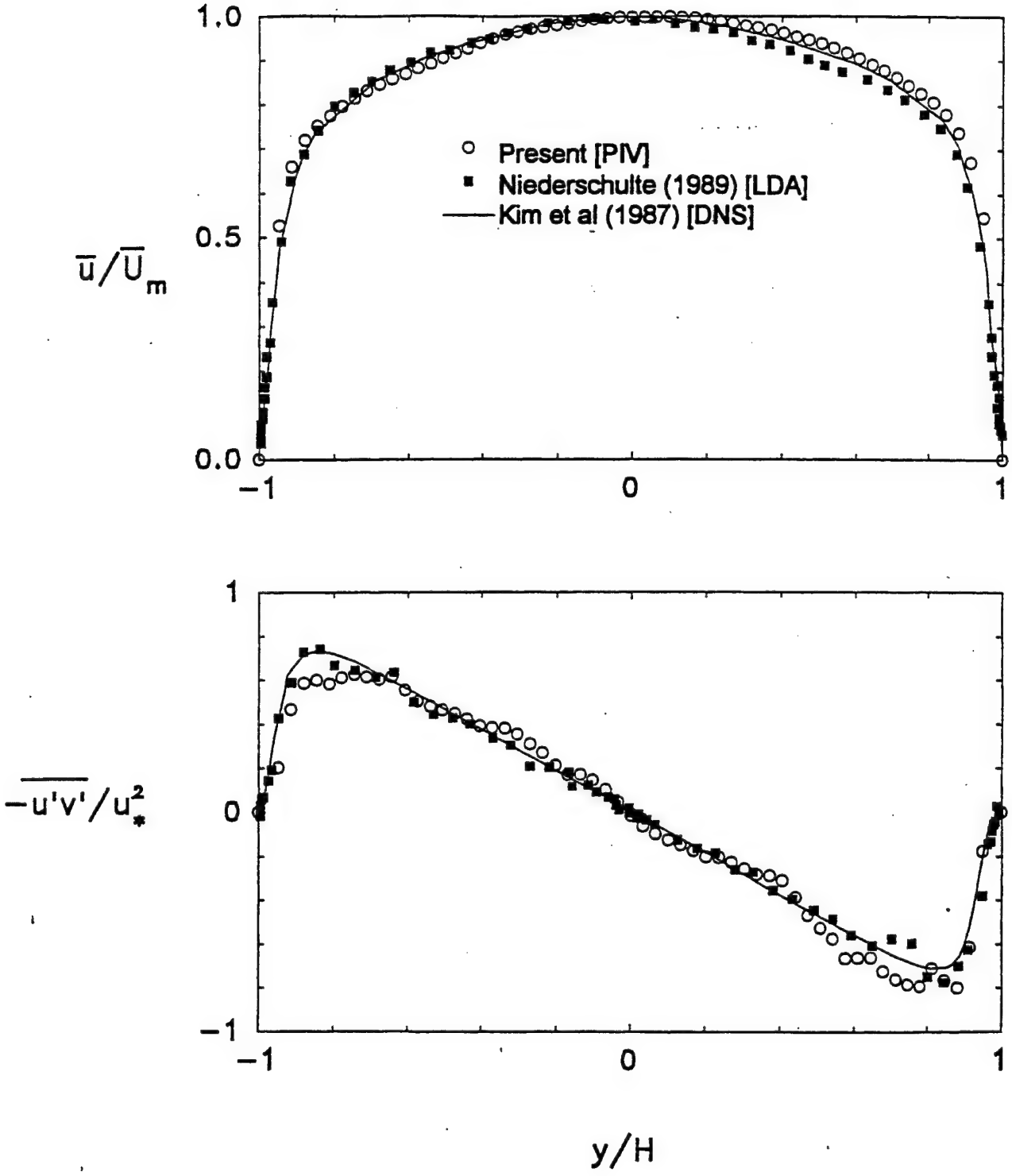

Figure 2b: Variation of mean velocity distribution across the channel (top plot) and Reynolds stress normalized by friction velocity (bottom plot). Present PIV measurements are compared with LDA measurements of Niederschulte (1989) and direct numerical simulation (DNS) of Kim et al. (1987).

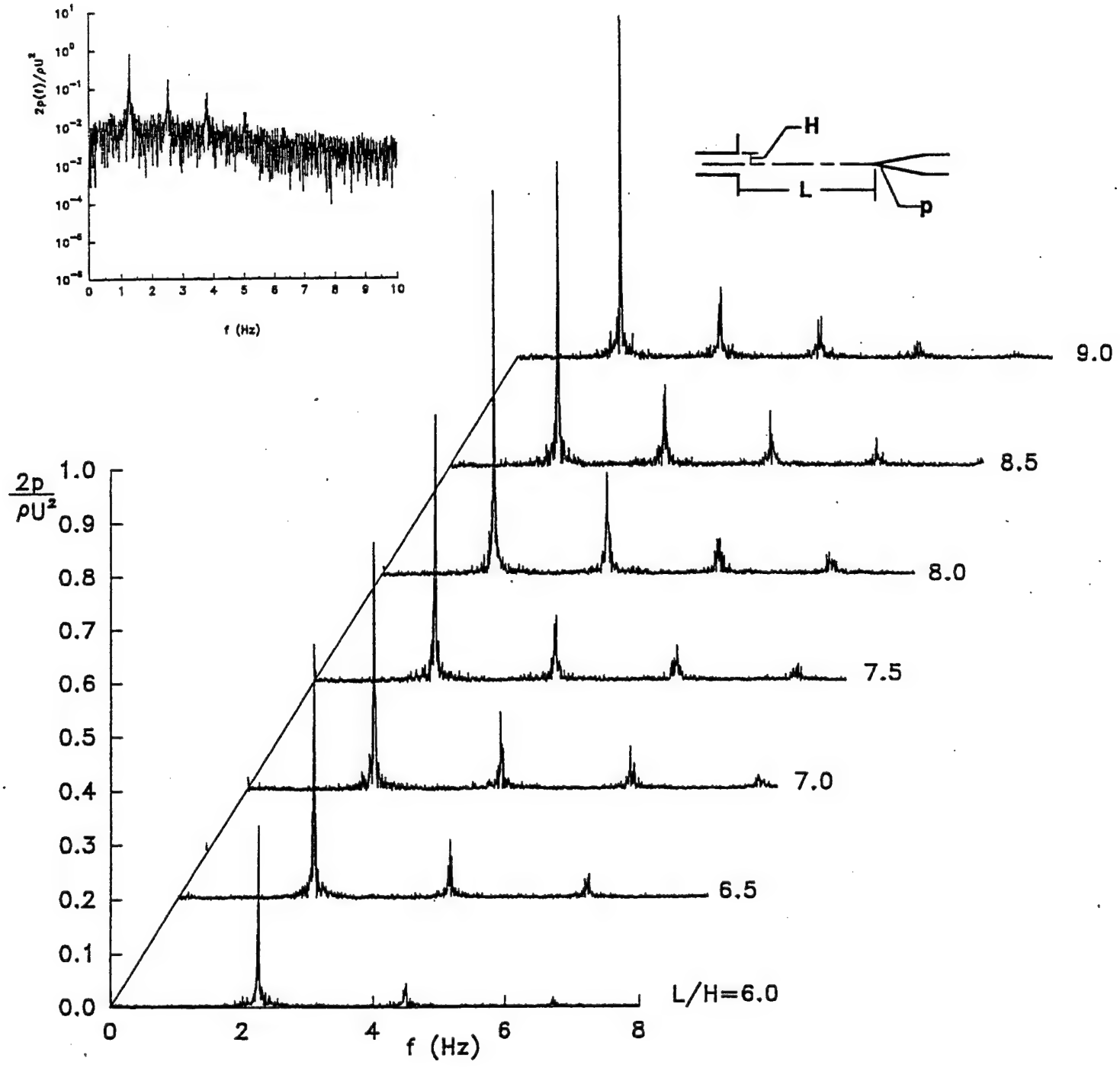

Figure 3a: Spectra of pressure fluctuation on lower surface of impingement edge as a function of dimensionless impingement distance. Inset shows typical spectrum plotted on a logarithmic scale.

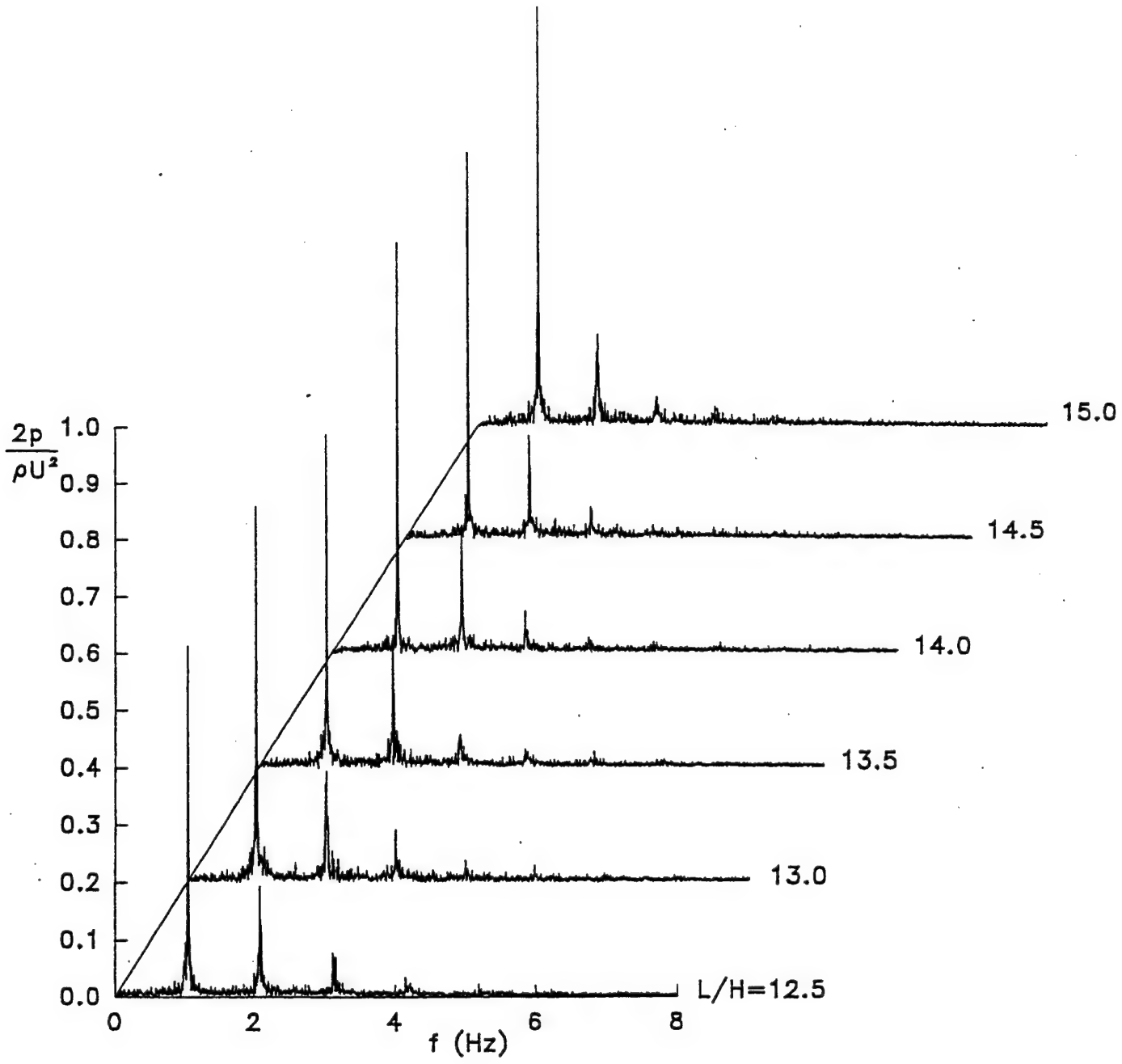

Figure 3b: Spectra of pressure fluctuation on lower surface of impingement edge as a function of dimensionless impingement distance.

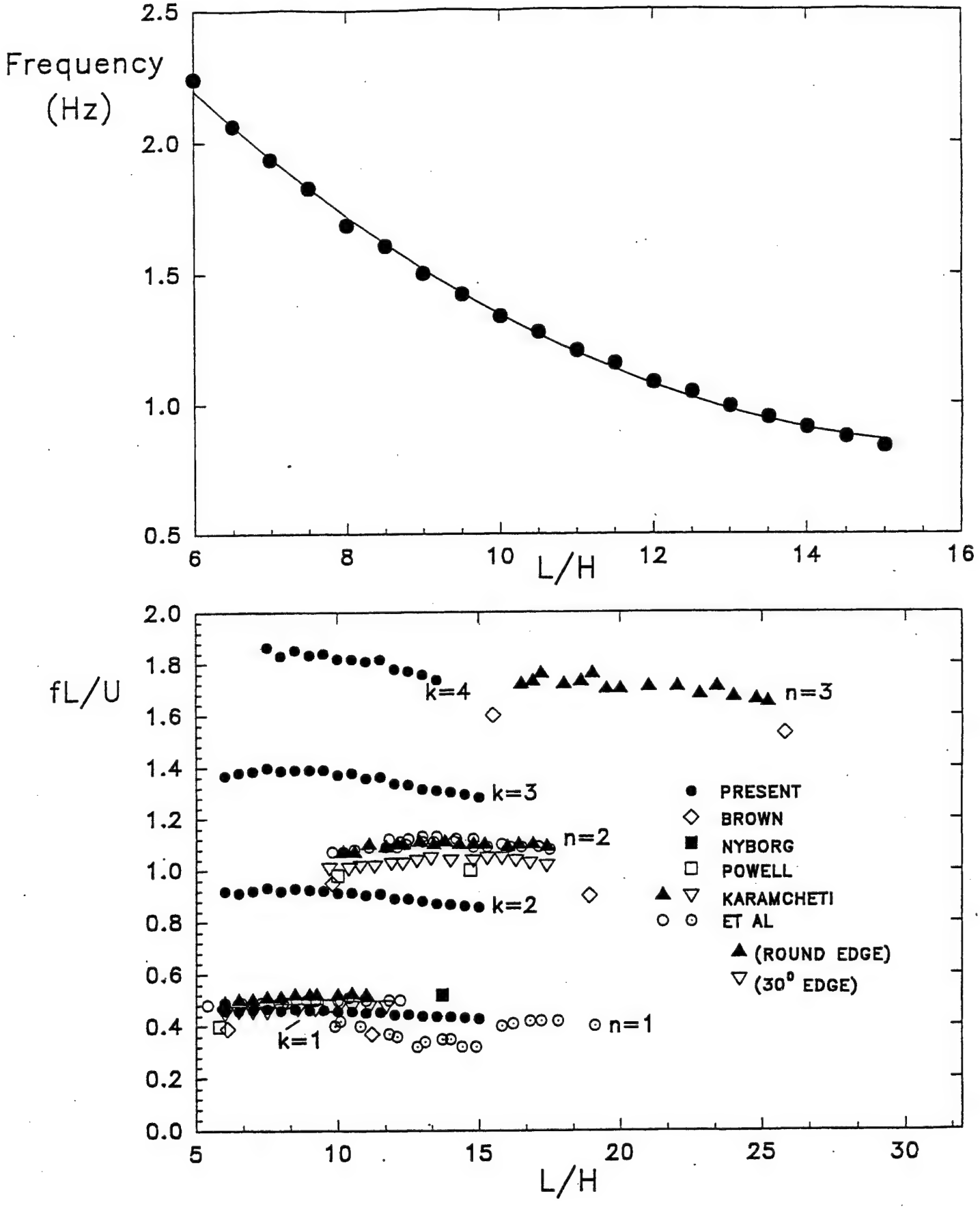

Figure 4: Comparison of variations of dimensionless frequency with dimensionless impingement distance for present and previous investigations. For the present study of an initially turbulent jet, all four detectable spectral peaks k = 1, 2, 3, and 4 are represented. Previous studies, which typically exhibit modes n = 1, 2, and 3, involve laminar jet formation from the nozzle exit.

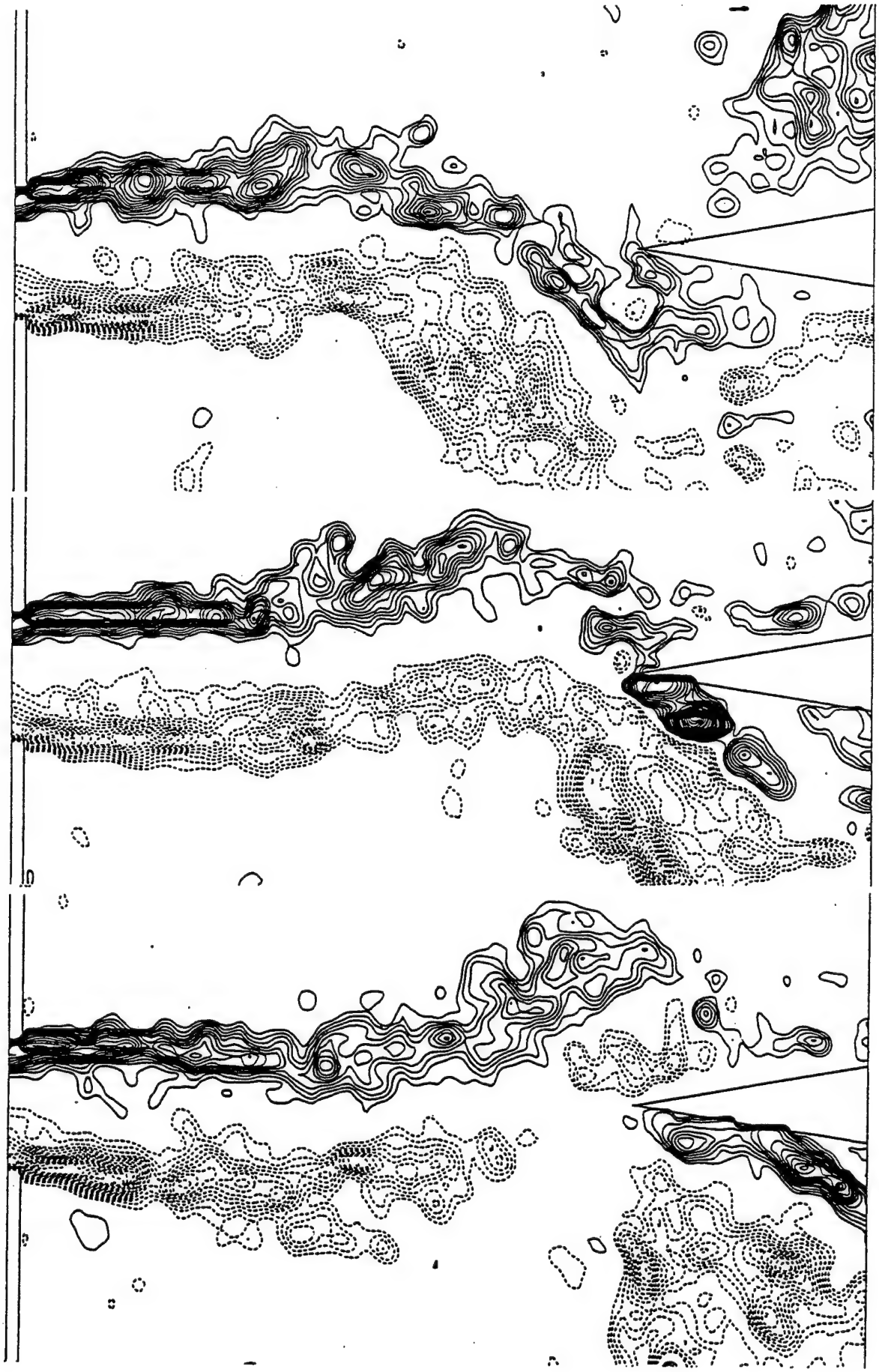

Figure 5: Comparison of vorticity distributions at three successive phases of the jet oscillation. Images are from the randomly-acquired series. Minimum vorticity $\omega_{min} = \pm 10$; incremental vorticity $\Delta\omega = 5$ sec^{-1}.

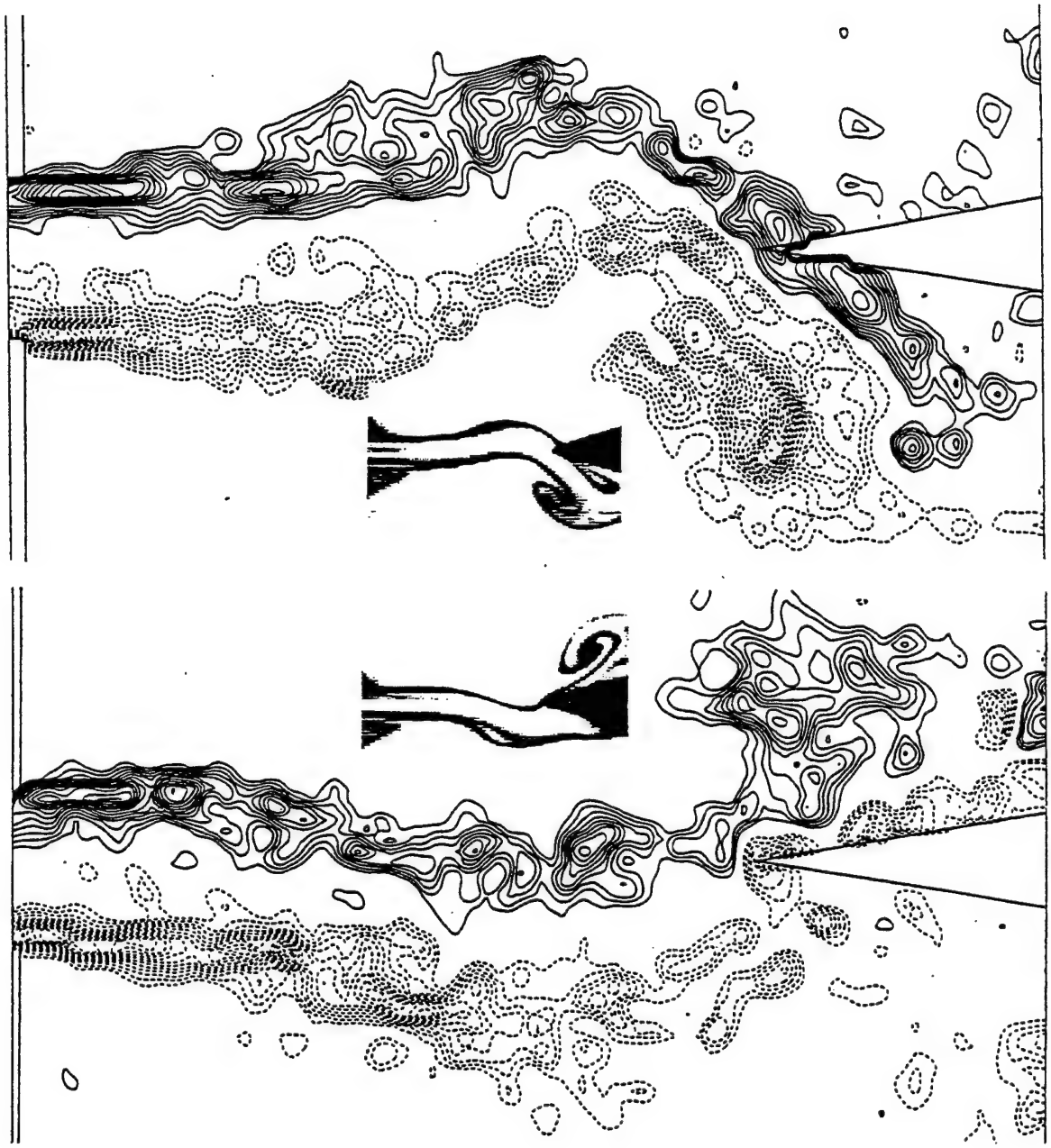

Figure 6a: Comparison of instantaneous distributions of vorticity with the qualitative dye visualization of Lucas and Rockwell (1984) for the case of an initially laminar jet at Re = 300. $\omega_{min} = \pm 10$ sec^{-1}. $\Delta\omega = 5$ sec^{-1}.

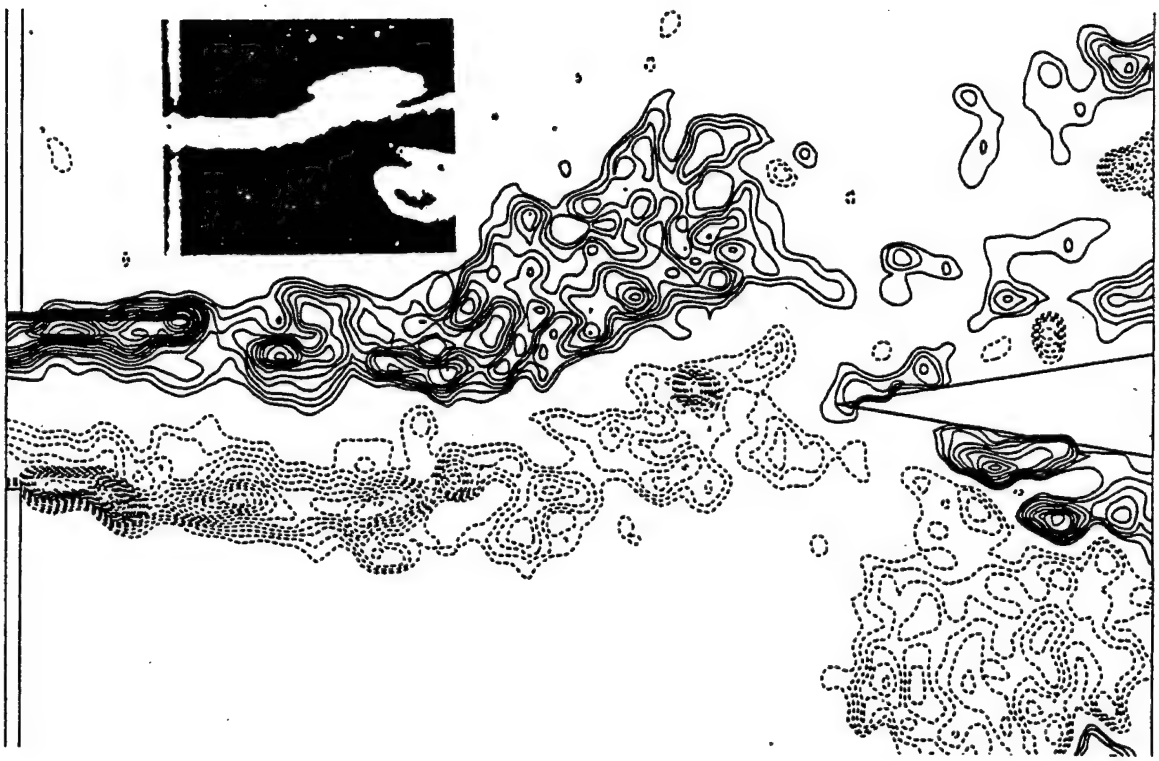

Figure 6b: Comparison of instantaneous distribution of vorticity with the qualitative smoke visualization of Brown (1937) at a value of Reynolds number Re = 183. Minimum vorticity level $\omega_{min} = \pm 10$ sec^{-1} and $\Delta\omega = 5$ sec^{-1}.

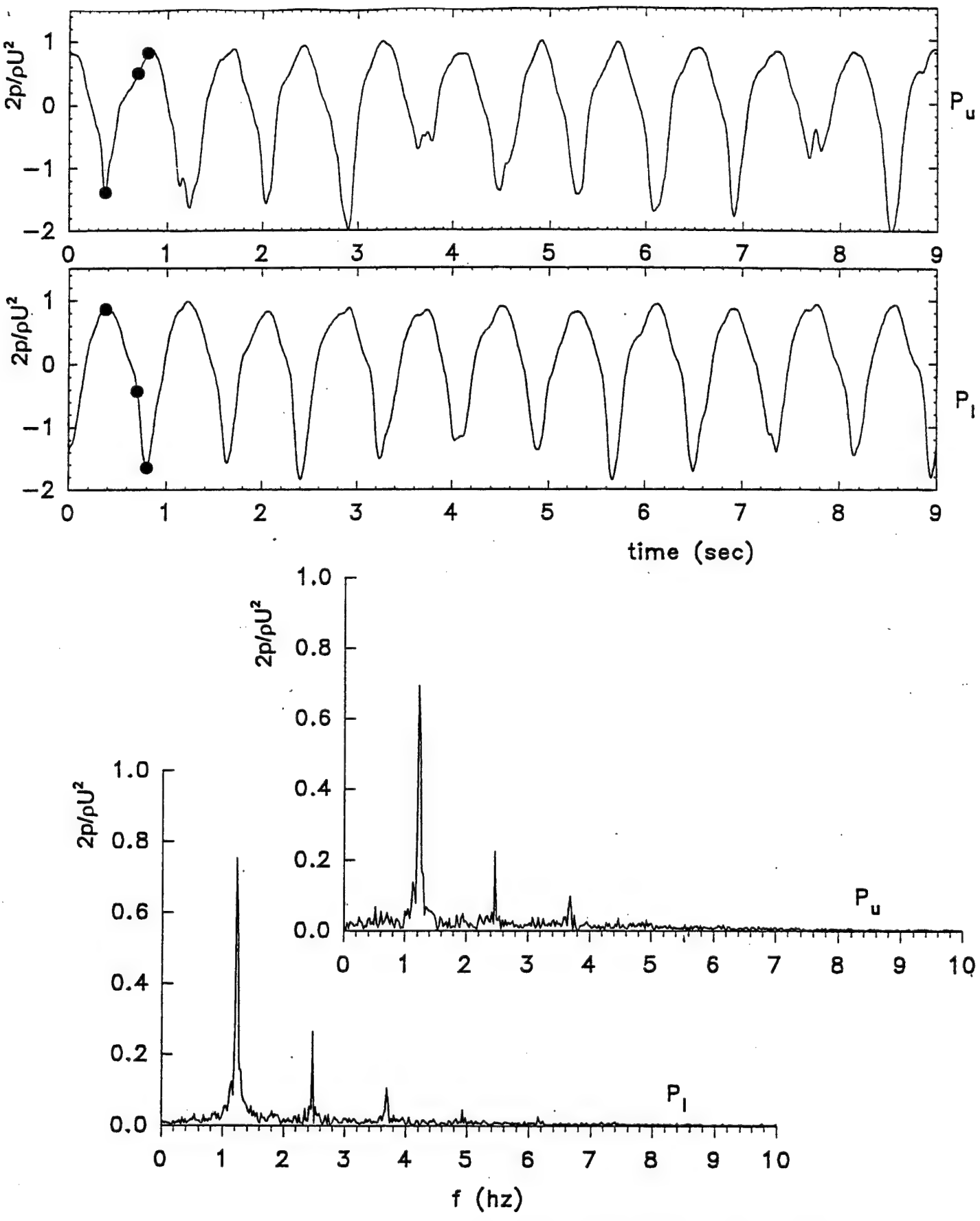

Figure 7: Pressure traces corresponding to highly-resolved cinema sequence. Instants at which three representative images were acquired are represented by circular symbols. These images show the transformation from minimum to maximum pressure on the upper surface of the edge and maximum to minimum pressure on the lower surface of the edge. Sampling time is $\Delta t = 0.005$ sec.

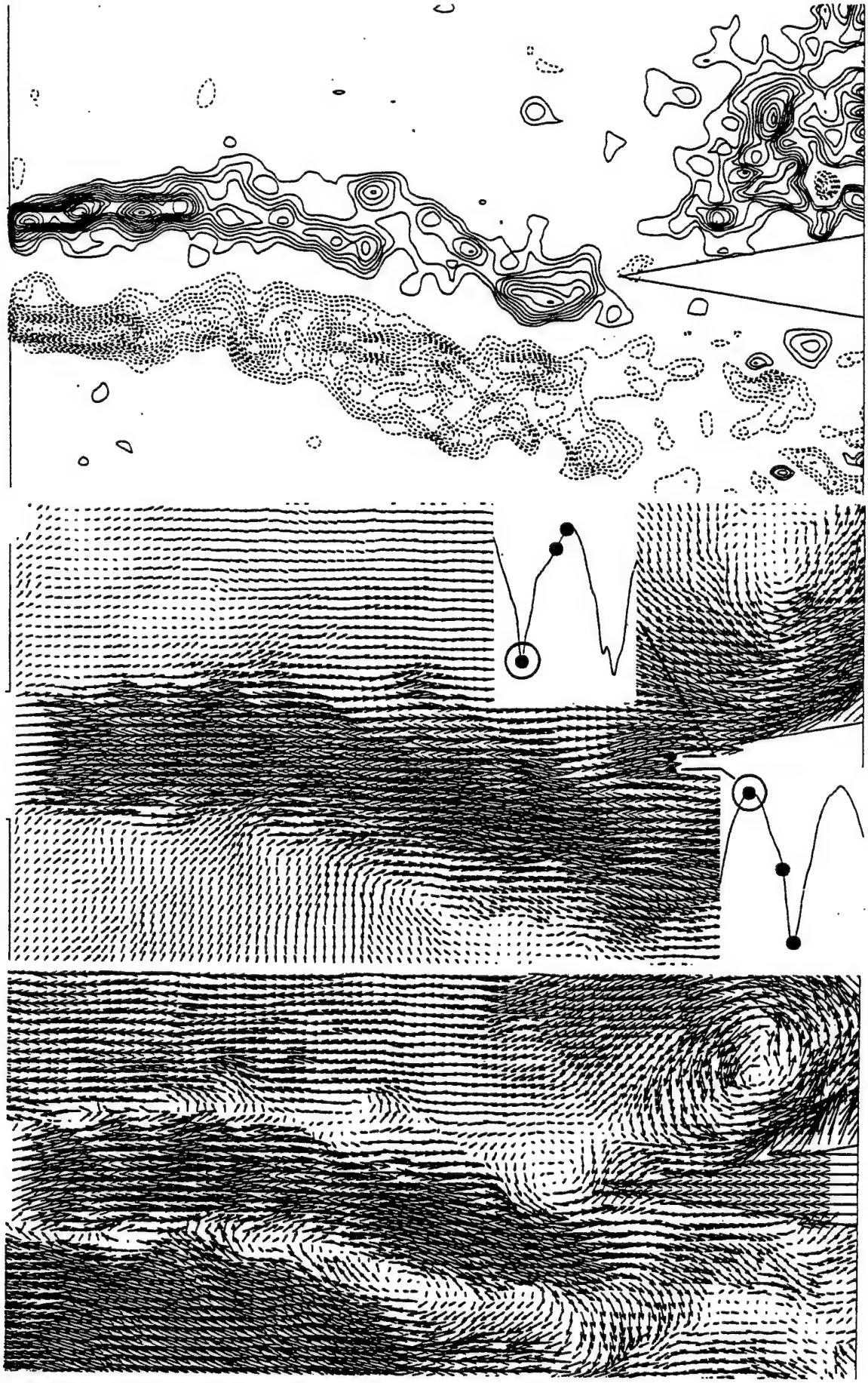

Figure 8a: Comparison of vorticity, velocity in the laboratory frame and velocity in a frame moving at 0.50 $\overline{U}_m$ for the cinema sequence. $\omega_{min} = 10$ sec^{-1} and $\Delta\omega = 5$ sec^{-1}. Images represent transformed versions of those of Lin and Rockwell (1998).

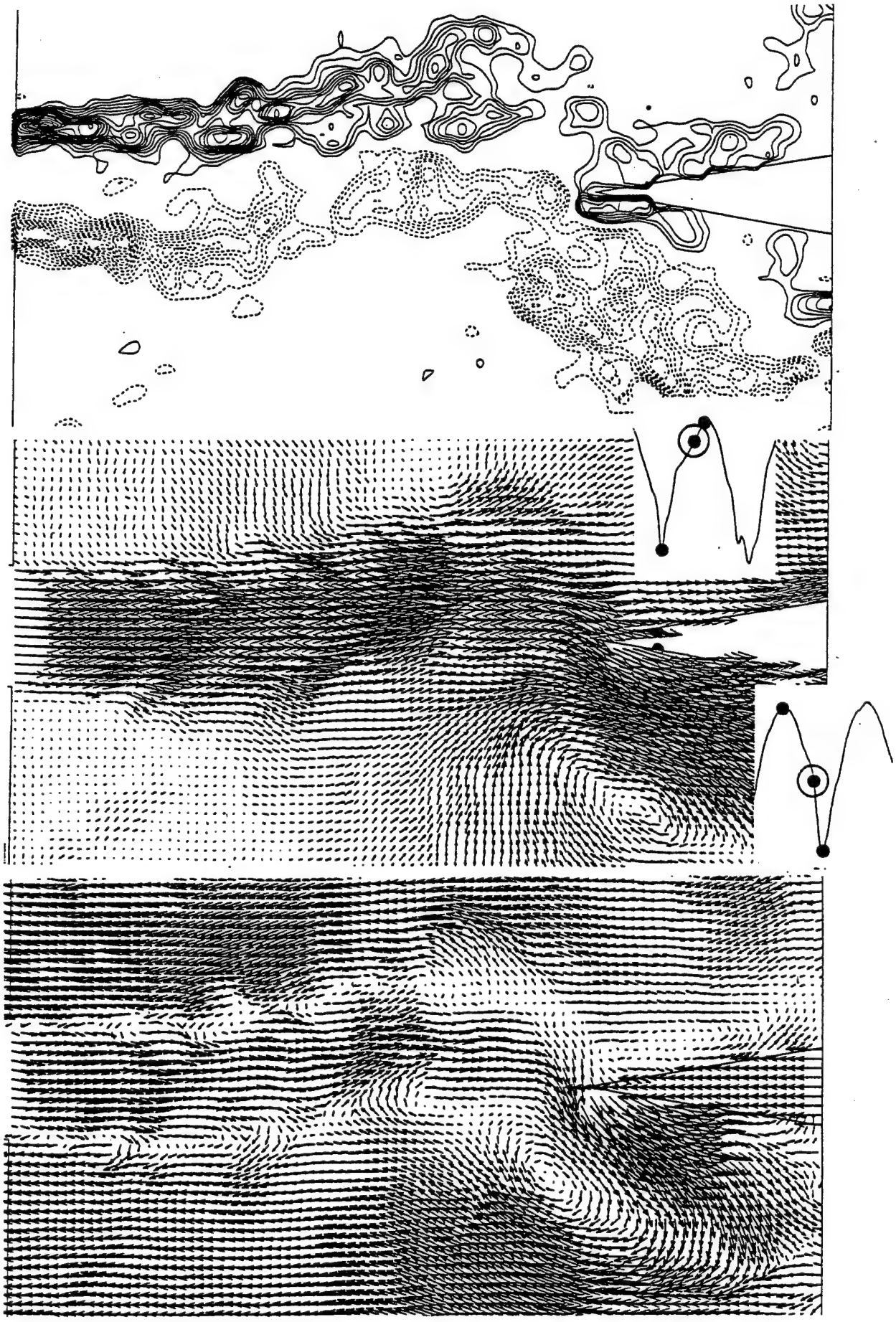

Figure 8b: Comparison of vorticity, velocity in the laboratory frame and velocity in a frame moving at 0.50 $\overline{U}_m$ for the cinema sequence. $\omega_{min} = 10$ sec^{-1} and $\Delta\omega = 5$ sec^{-1}.

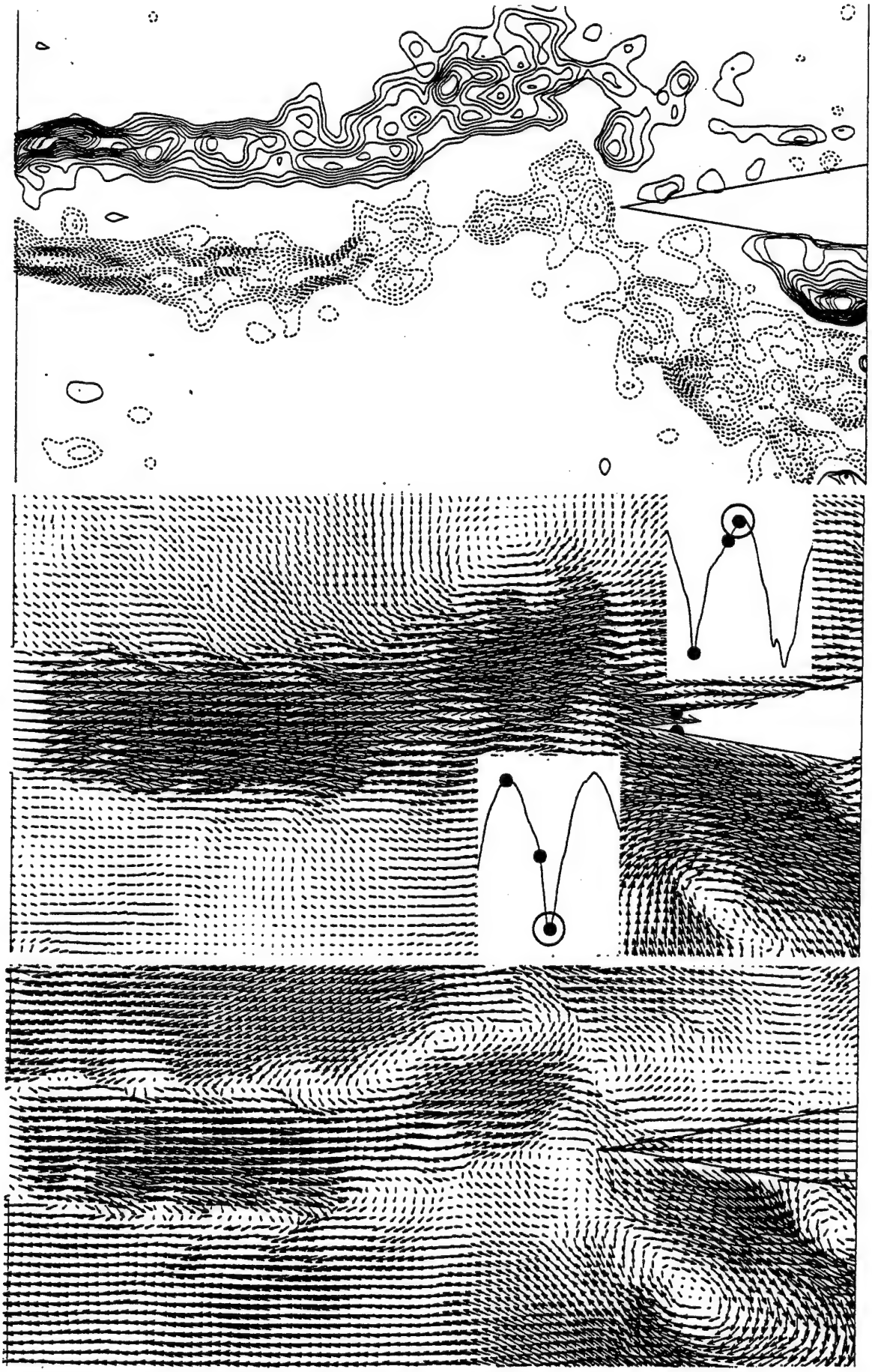

Figure 8c: Comparison of vorticity, velocity in the laboratory frame and velocity in a frame moving at 0.50 $\overline{U}_m$ for the cinema sequence. $\omega_{min} = 10\ sec^{-1}$ and $\Delta\omega = 5\ sec^{-1}$.

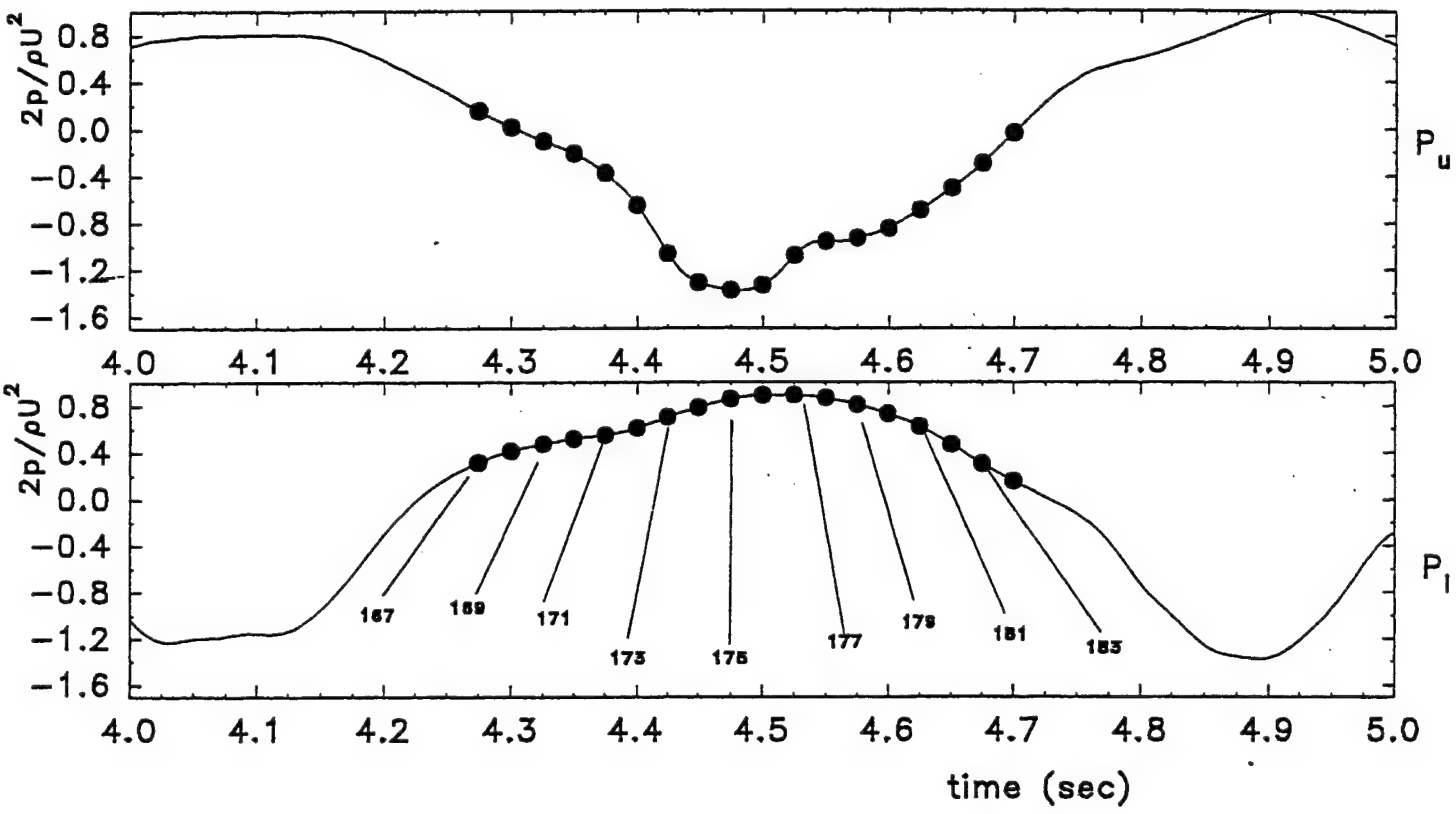

Figure 9: Expanded segment of pressure trace of Figure 7, which emphasizes the highly time-resolved image acquisition in the vicinity of maximum negative pressure p_u on the upper surface and maximum positive pressure p_ℓ on the lower surface of the edge. Sampling time is $\Delta t = 0.005$ sec.

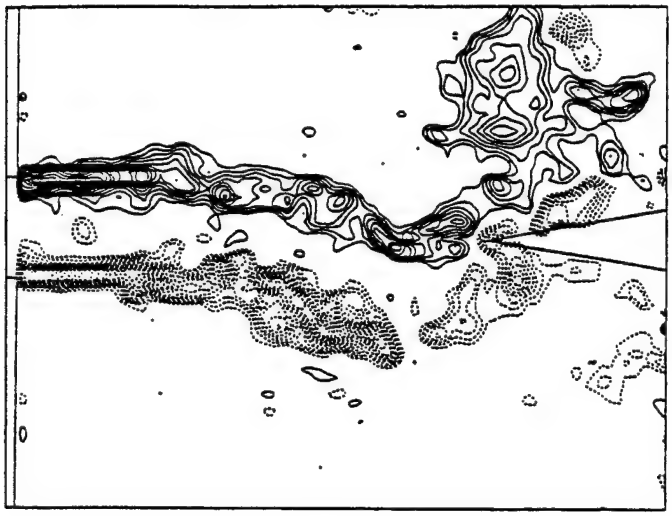

Image 171

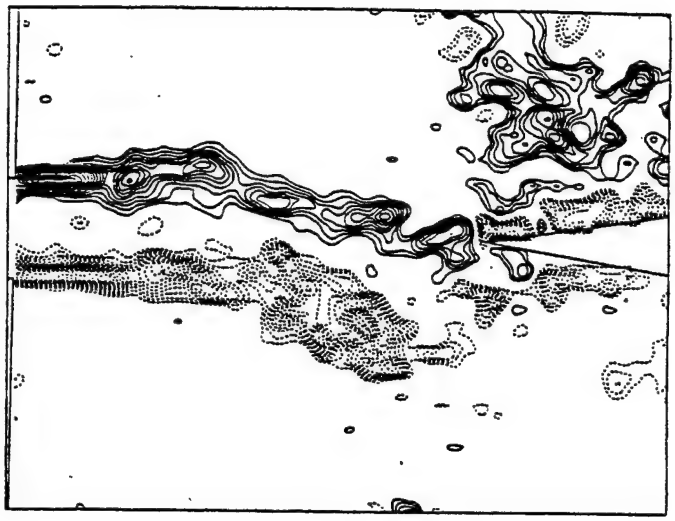

173

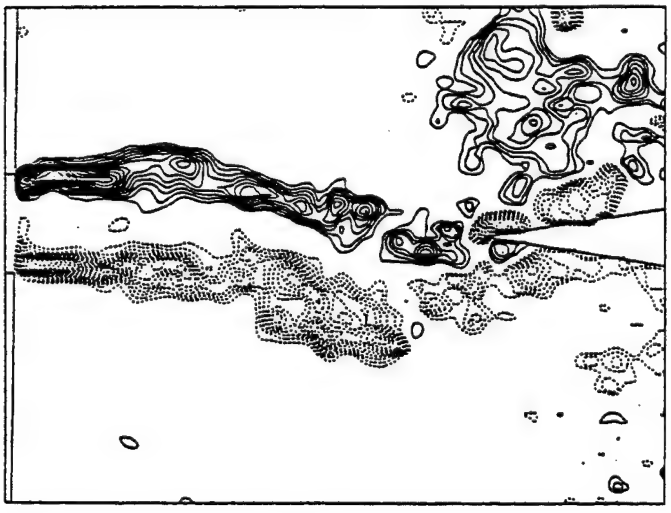

172

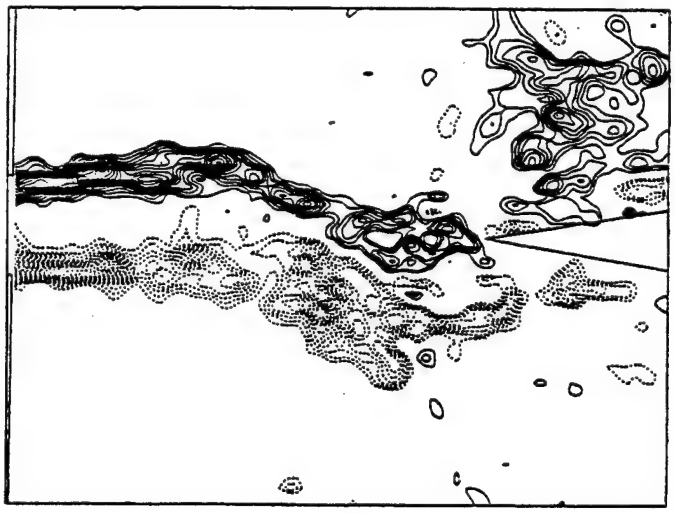

174

Figure 10: Excerpts from the cinema sequence showing instantaneous patterns of vorticity leading to occurrence of maximum negative pressure p_u on the upper surface and maximum positive pressure p_ℓ on the lower surface. Images correspond to numbers 171 through 174, designated on the pressure data of Figure 9. Time resolution between images is $\delta t/T = 0.03$, in which T is the period of the jet oscillation. Images represent transformed versions of those of Lin and Rockwell (1998).

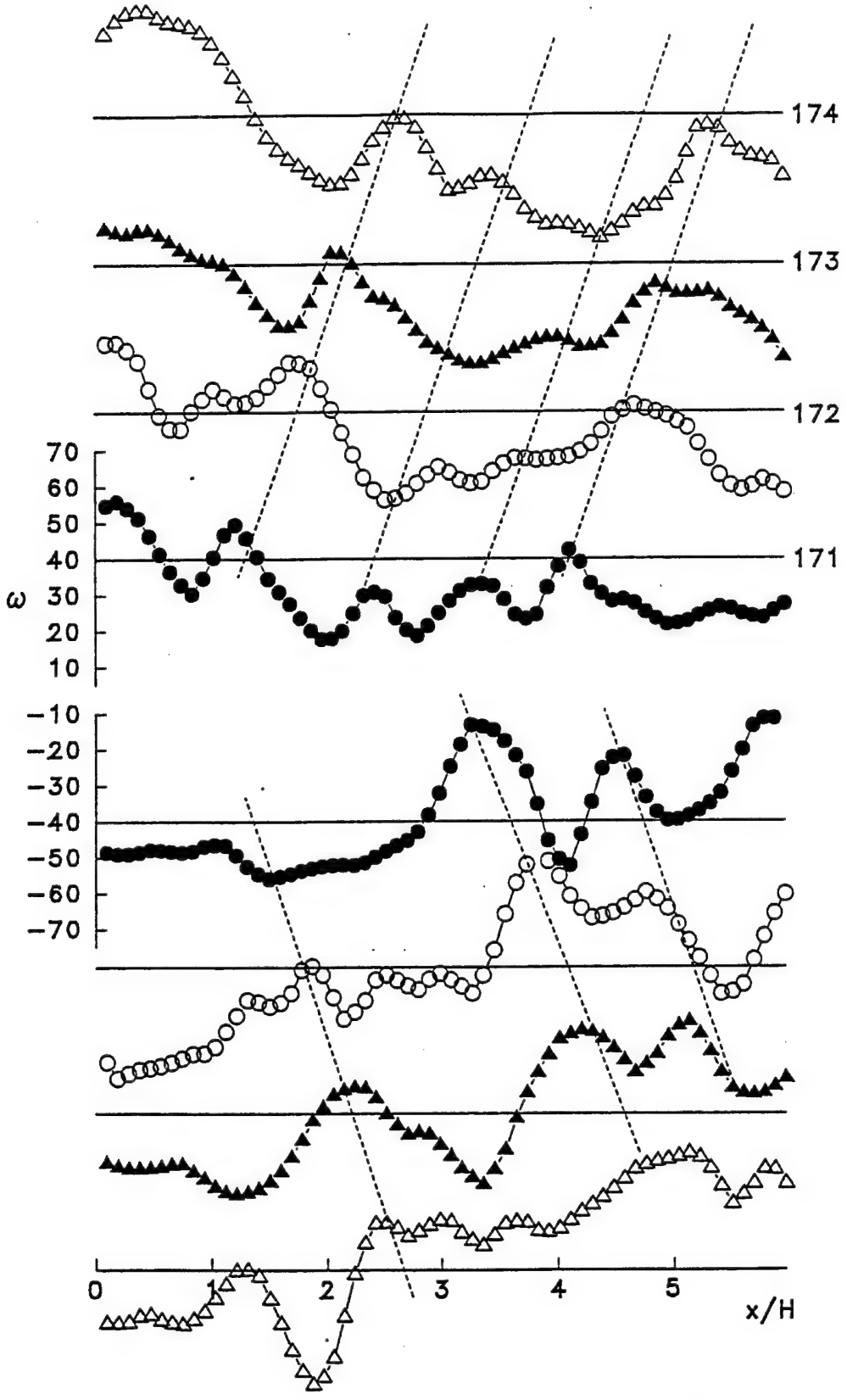

Figure 11: Spatial distributions of vorticity along horizontal lines extending from the corners of the channel exit for sequential instants of time corresponding to images 171 through 174. Inclined dashed lines are intended to serve as a guide for identifying common peaks or valleys, corresponding to maxima and minima of vorticity concentrations. These data were extracted from the images of Figure 10.

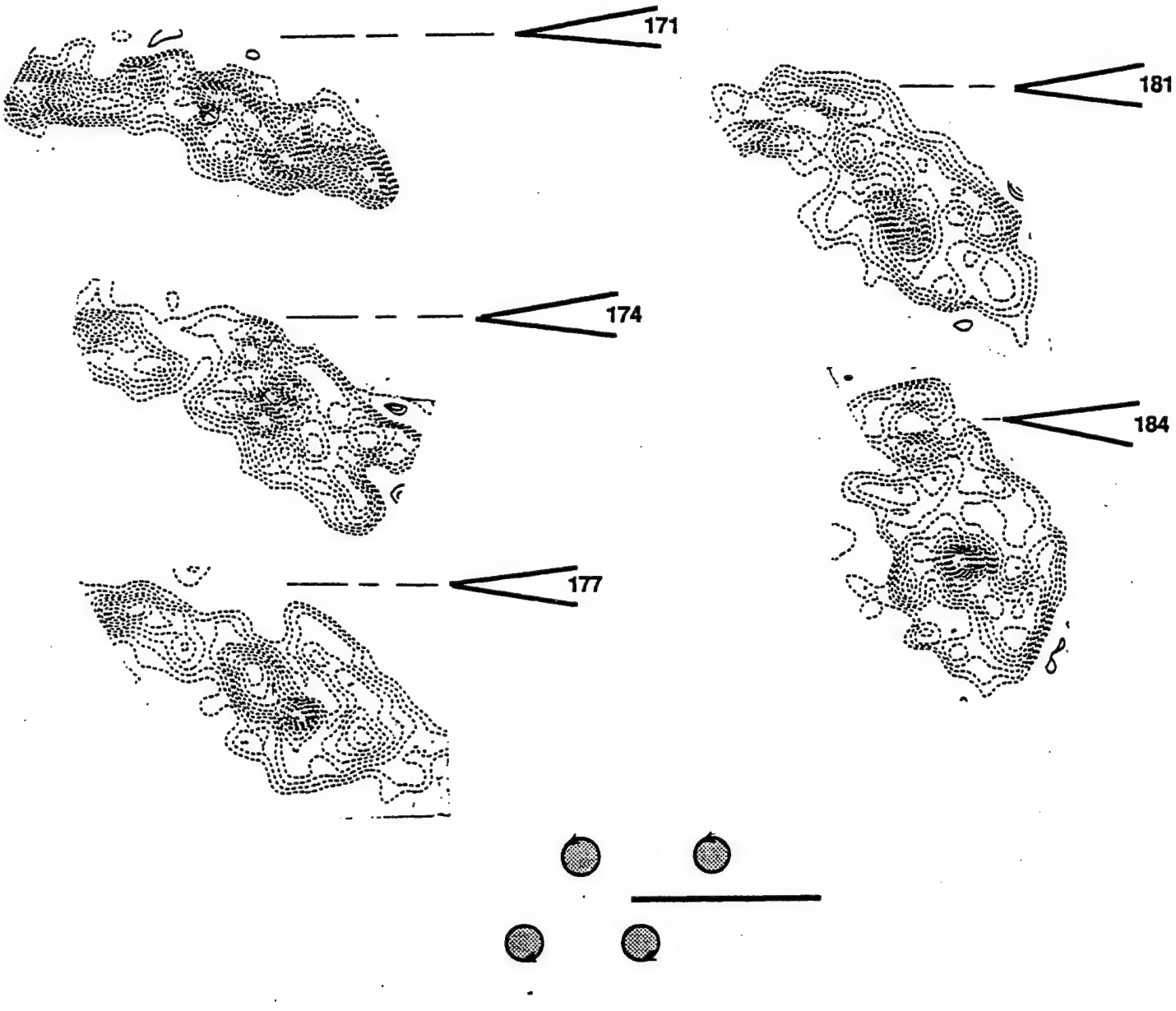

Figure 12: Evolution of a defined cluster of vorticity, which eventually evolves into a large-scale vortex as it encounters the impingement edge. Images were extracted from the same cinema sequence as Figure 10. Horizontal reference lines correspond to the plane of symmetry of the jet-edge system, i.e., the line passing through the tip of the edge. The dimensionless circulation Γ^* is constant for all clusters of vorticity.

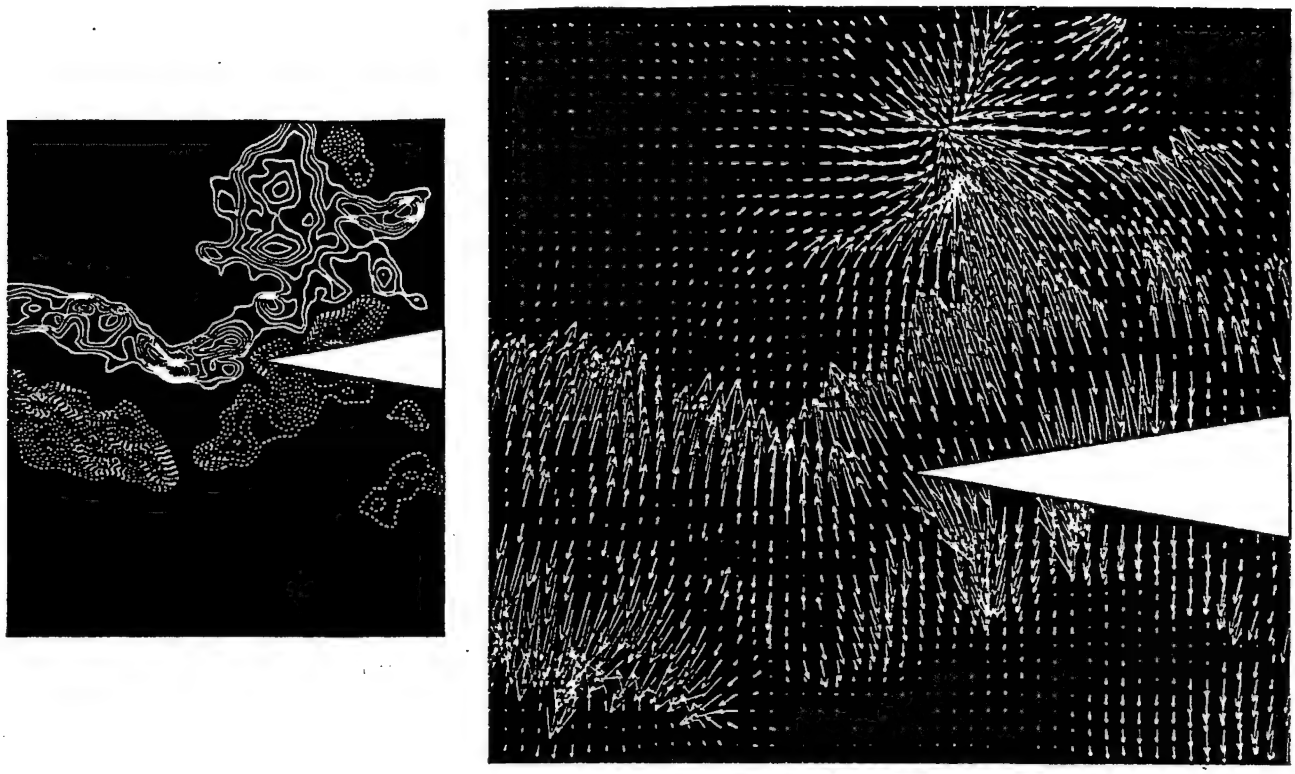

171

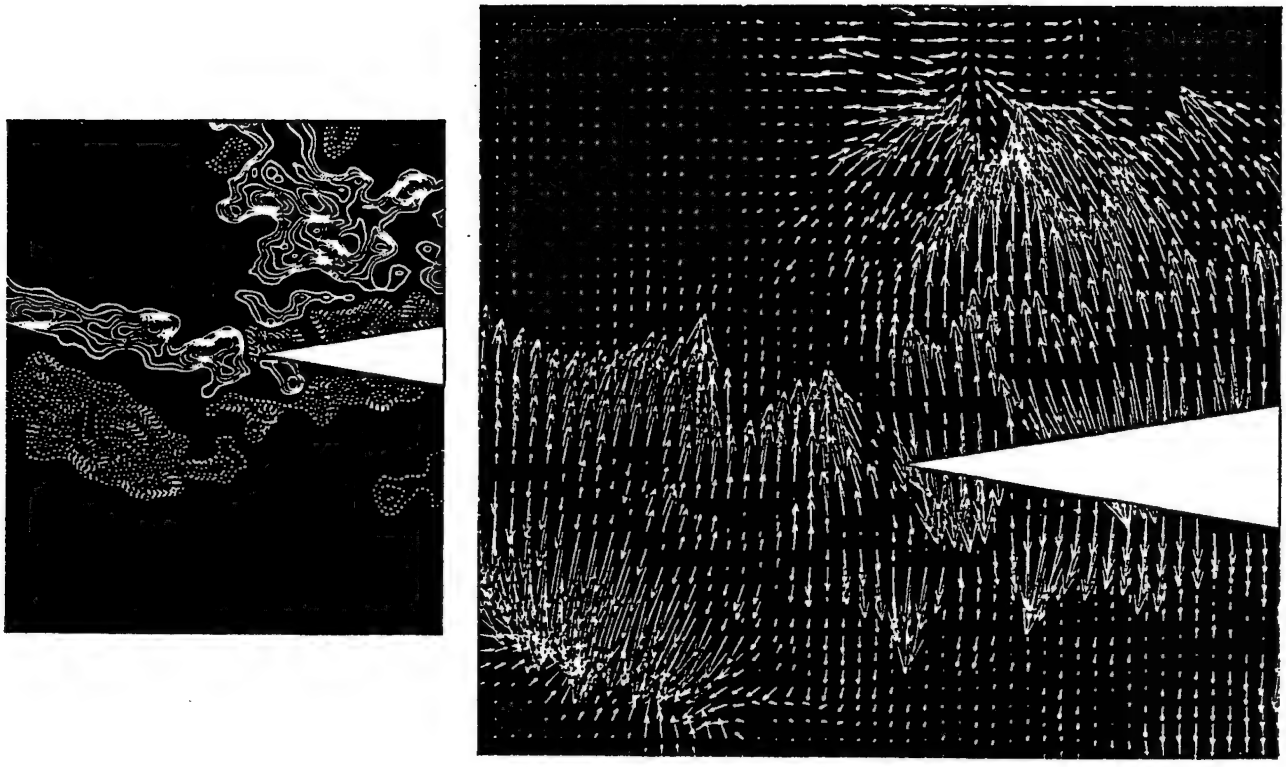

173

Figure 13: Contours of constant vorticity for images 171 (top) and 173 (bottom) of the cinema sequence of Figure 10 and corresponding vectors of the quantity $\underline{\omega} \wedge \underline{V}$ of the acoustic power integral.

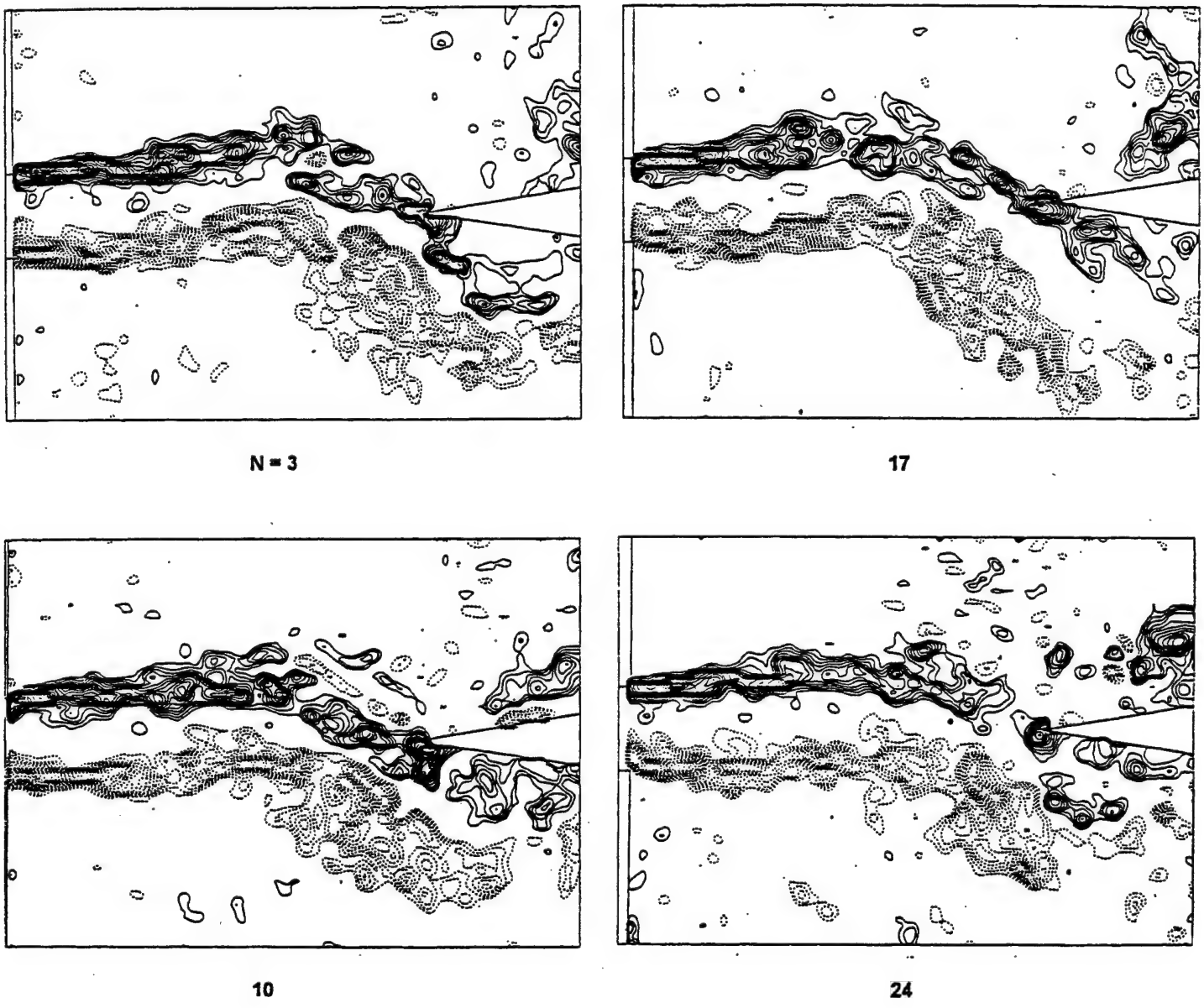

Figure 14: Representative images of the phase-referenced vorticity field excerpted from cinema sequence; each image corresponds approximately to occurrence of zero instantaneous pressure p_ℓ on the lower surface of the impingement edge.

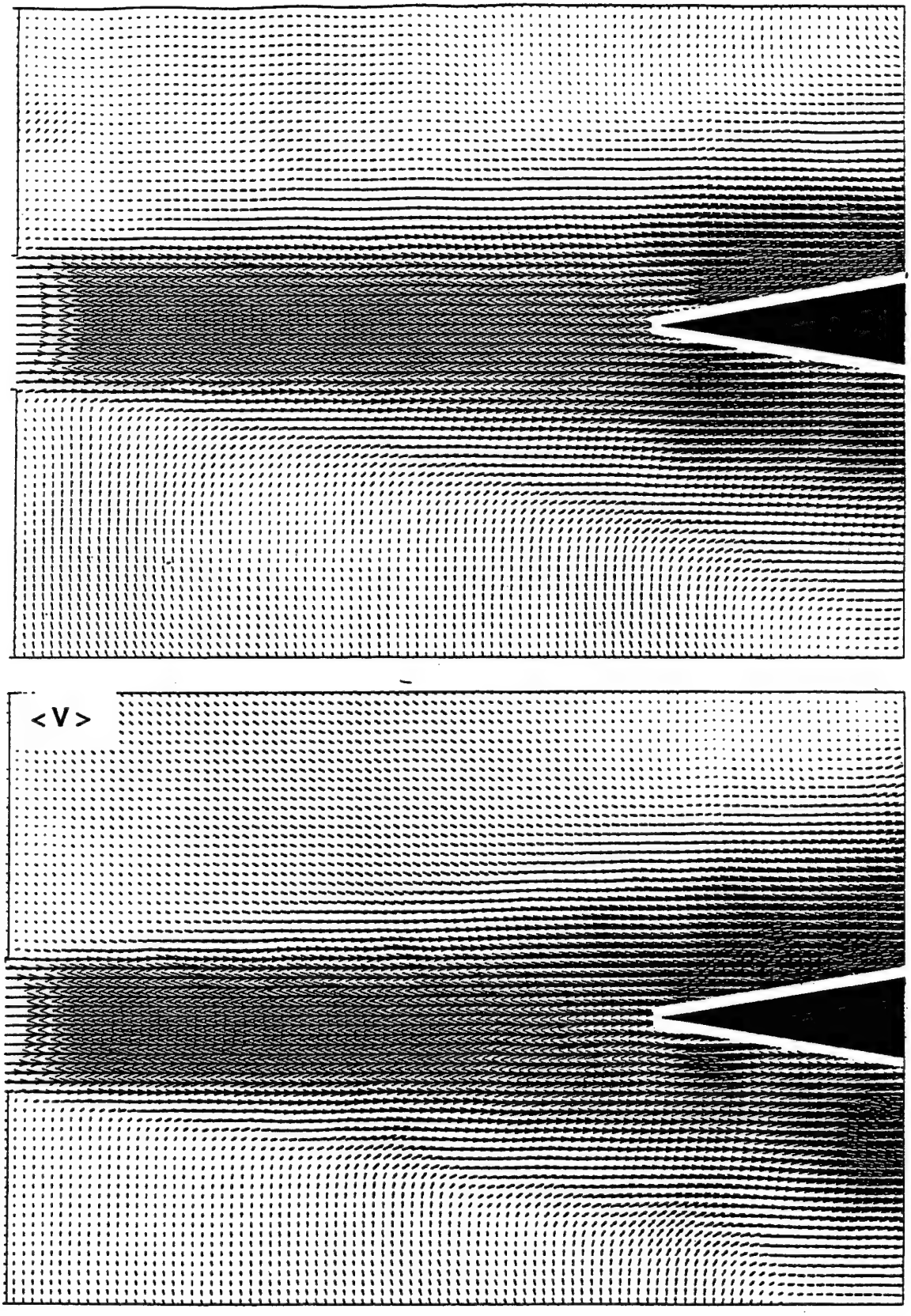

Figure 15: Ensemble-averaged distribution of total velocity $< V >$ shown in laboratory reference frame. Top image is from cinema sequence and bottom image is from randomly-acquired sequence.

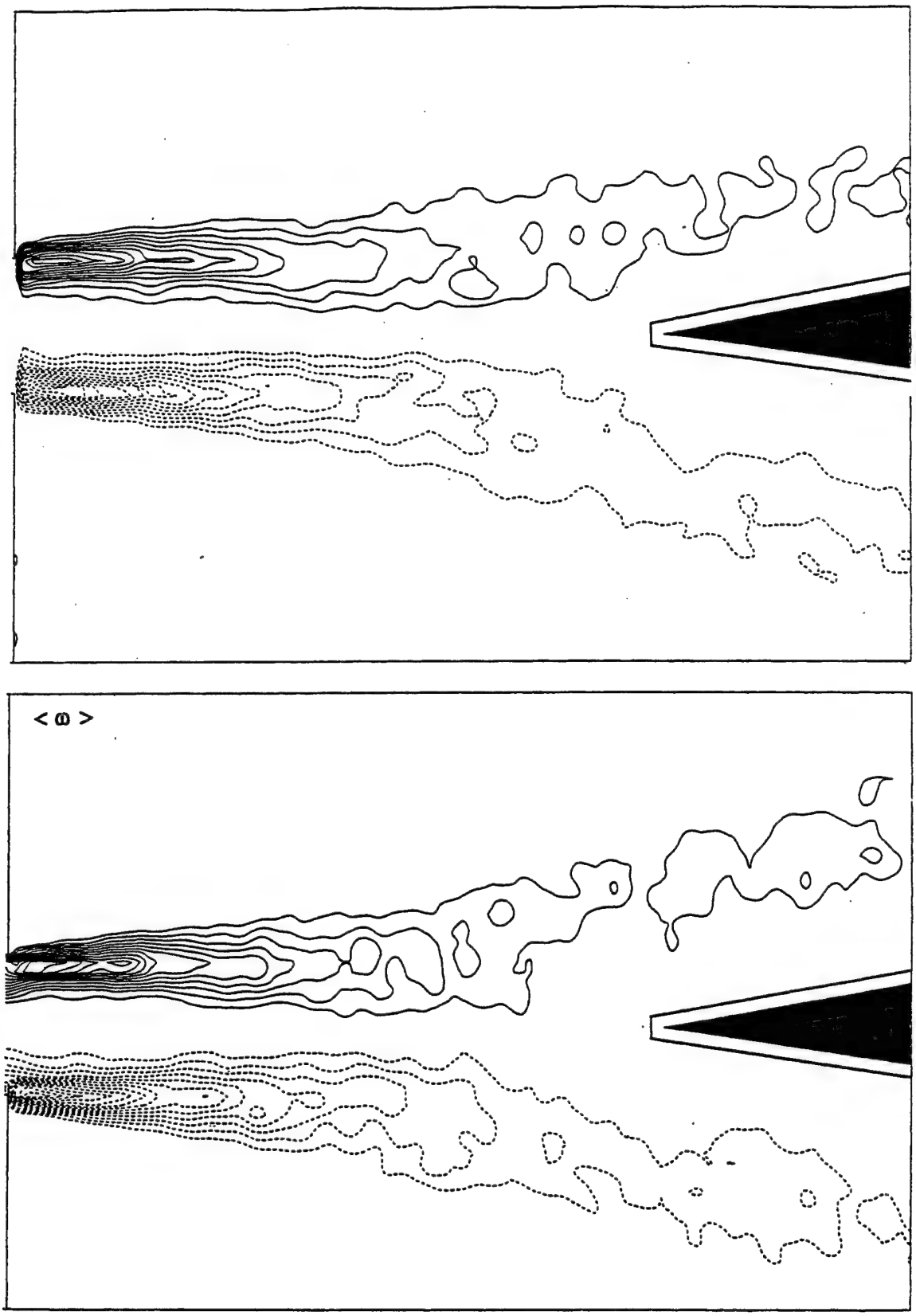

Figure 16: Contours of ensemble-averaged vorticity, $< \omega >$. Top image is from cinema sequence and bottom image is from randomly-acquired sequence. Minimum vorticity $\omega_{min} = \pm 10$ sec^{-1} and incremental vorticity $\Delta\omega = 5$ sec^{-1}.

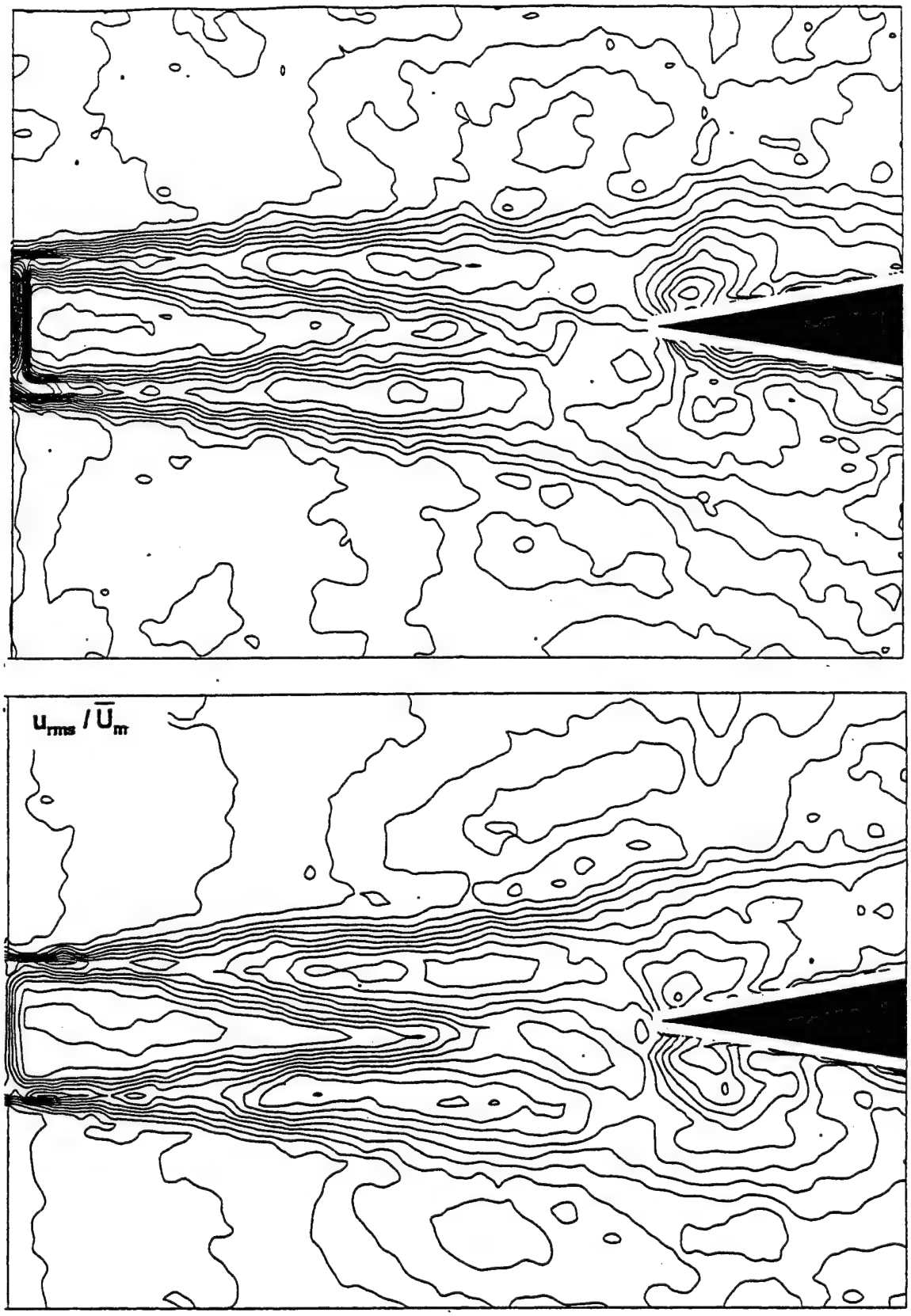

Figure 17: Contours of constant root-mean-square of the streamwise component of the velocity fluctuation, u_{rms}, normalized with respect to the maximum velocity at the centerline $\overline{U}_m$. Minimum contour is 0.02 and increments are 0.02. Top image is from cinema sequence and bottom image is from randomly-acquired sequence.

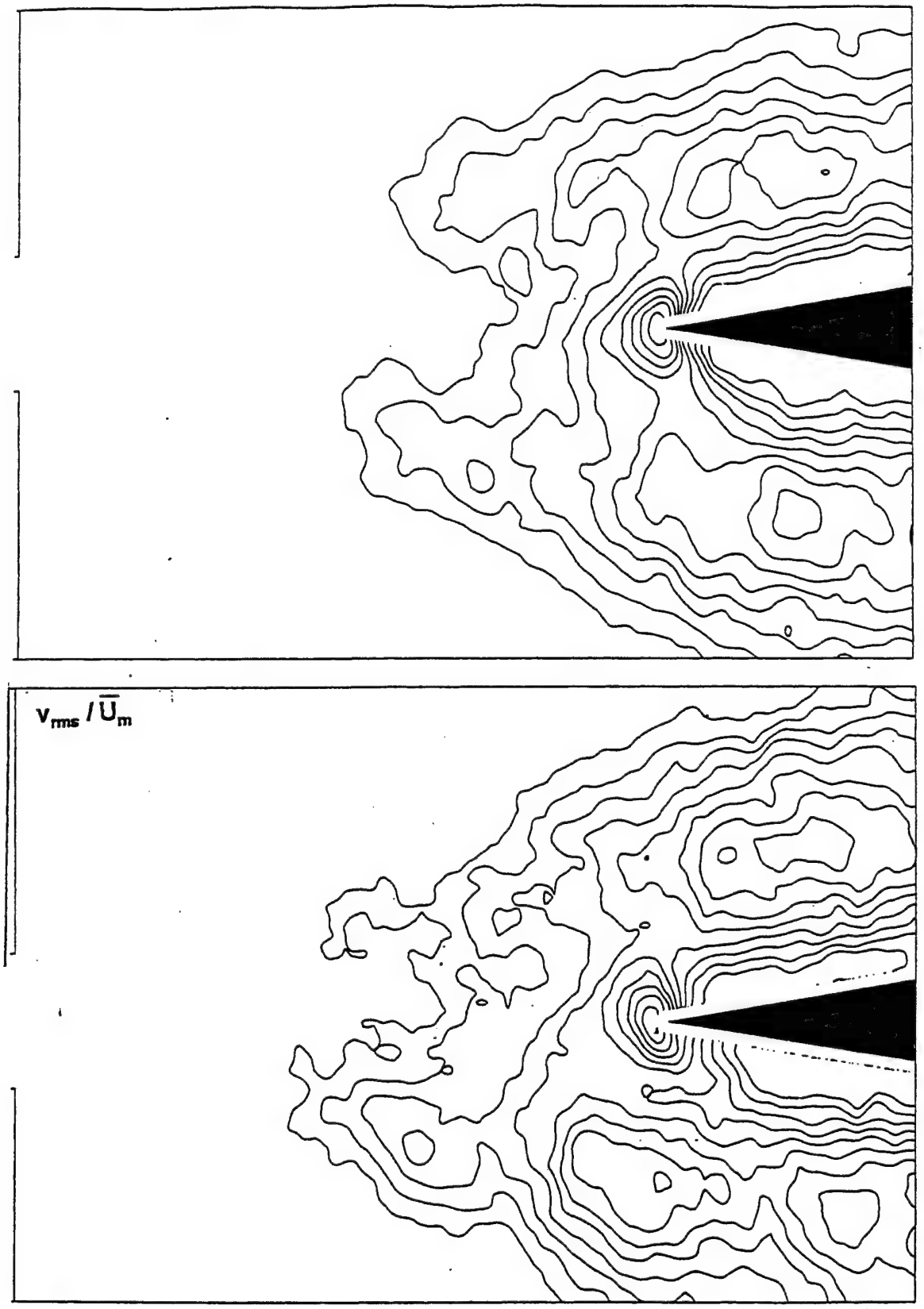

Figure 18: Contours of constant root-mean-square of the transverse component of the velocity fluctuation, v_{rms}, normalized with respect to the maximum velocity $\overline{U}_m$ at the centerline. Minimum contour is 0.02 and incremental values are 0.02. Top image is from cinema sequence and bottom image is from randomly-acquired sequence.

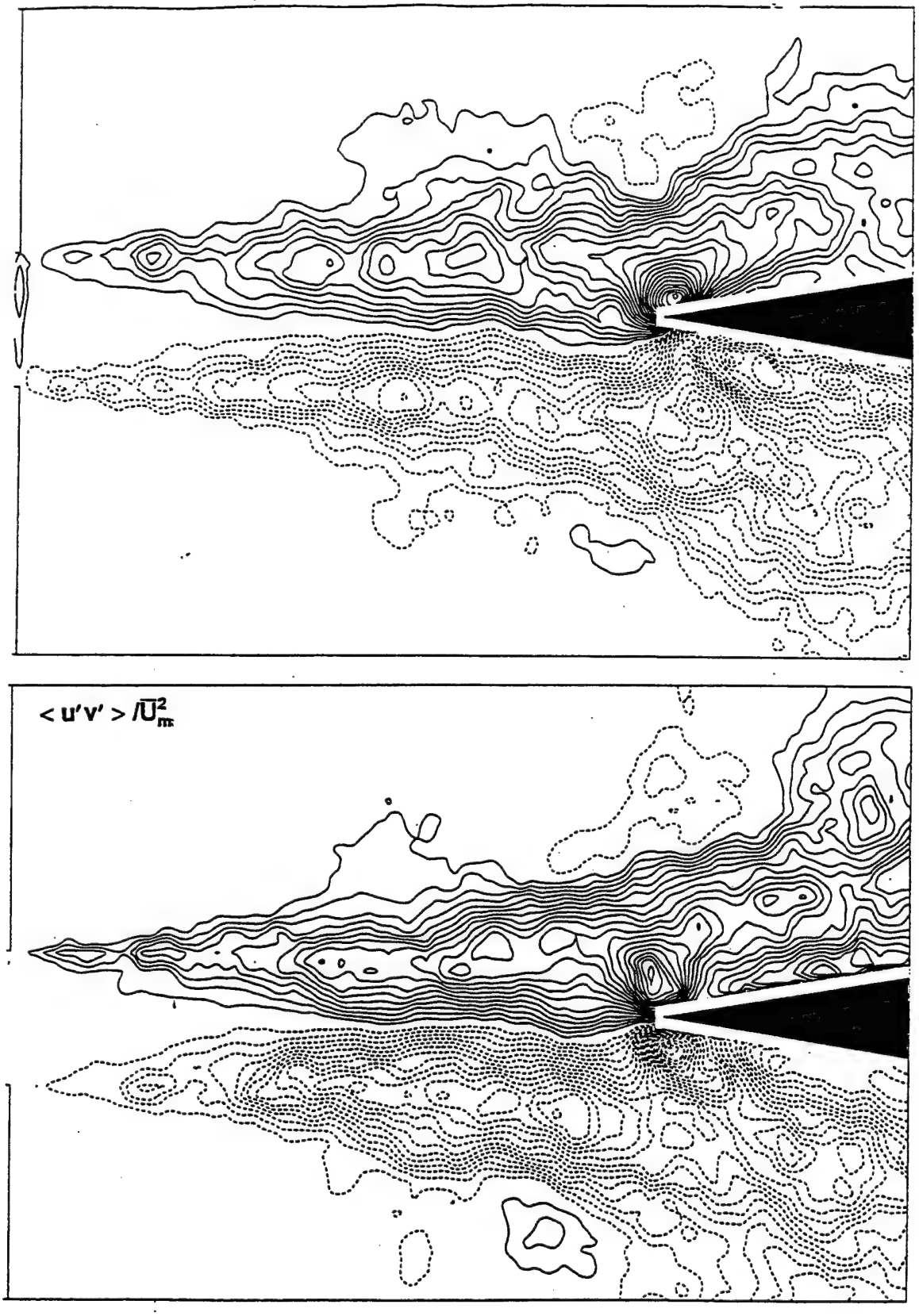

Figure 19: Contours of constant ensemble-averaged Reynolds stress, $< u'v' >$, normalized by square of maximum velocity $\overline{U}^2_m$. Top image is from cinema sequence and bottom image is from randomly-acquired sequence. Minimum contour is 0.002 and the increment between contours is 0.002.

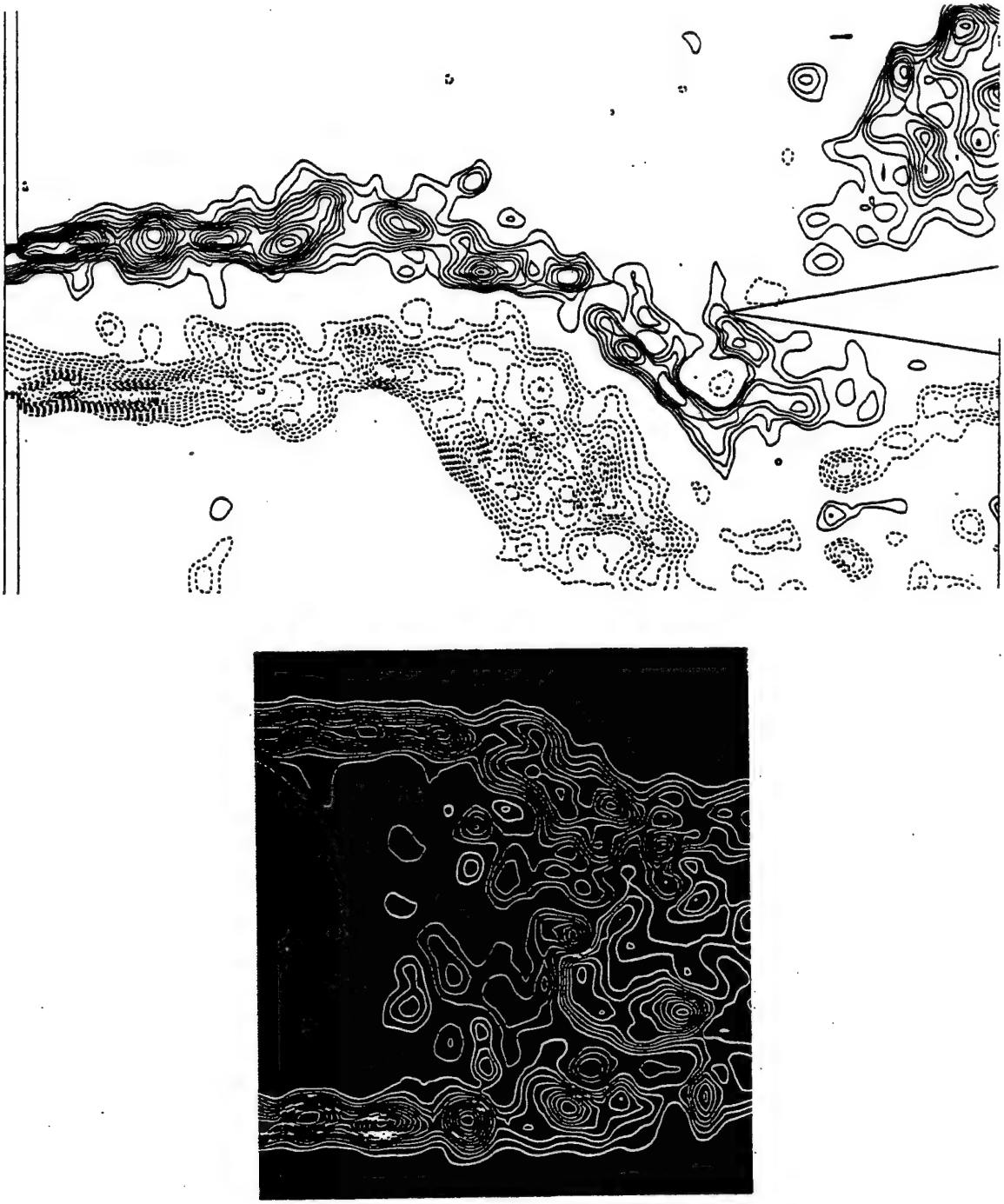

Figure 20: Comparison of the near-wake of a circular cylinder and the jet in a jet-edge system. Both exhibit the rapid development of small-scale vorticity concentrations due to a localized instability immediately downstream of separation of the shear layer. The Reynolds number for the flow past the cylinder, based on cylinder diameter, is 10,000 (from Chyu and Rockwell, 1996). Note that the bottom shear layer from the circular cylinder exhibits a train of small-scale vortices that roll up to form the Kármán vortex. For the jet-flow, the Reynolds number, based on nozzle width, is 10,944.

APPENDIX I

lin org osc 082100

ORGANIZED OSCILLATIONS OF AN INITIALLY-TURBULENT FLOW PAST A CAVITY*

by

J.-C. Lin[1] and D. Rockwell[2]
Lehigh University, Bethlehem, Pennsylvania 18015

Abstract

The unsteady flow structure due to a turbulent boundary layer past a rectangular, open cavity is characterized using a cinematographic technique of high-image-density particle image velocimetry. Organized small- and large-scale vortical structures emerge above the turbulent background in absence of mechanisms that typically enhance the organized nature of such shear flows: acoustic resonance; Mach wave reflections; and elastic effects of the cavity boundary. The large-scale vortical structures induce ordered pressure fluctuations at the impingement corner of the cavity; their magnitude and phase shift are characterized using simultaneous imaging and pressure measurements. Within the cavity, a jet-like flow occurs along the cavity walls, and it eventually modulates the separating shear layer at the leading-corner of the cavity. The nature of this wall jet flow is a function of the impingement process at the trailing corner of the cavity. Calculation of the turbulence statistics based on flow images reveals that the turbulence in the separated shear layer along the mouth of the cavity and in the jet-like flow within the cavity rapidly dominate the turbulent structure of the inflow.

Nomenclature

L = cavity length

W = cavity depth

U_∞ = freestream velocity

***Lin, J.-C. and Rockwell, D. 2001 "Organized Oscillations of an Initially Turbulent Flow Past a Cavity", *AIAA Journal,* Vol. 39, No. 6, pp. 1139-1151.**

---

[1] Research Associate, Department of Mechanical Engineering and Mechanics, 354 Packard Laboratory, Memorial Drive West, Lehigh University, Bethlehem, PA 18015.

[2] Paul B. Reinhold Professor, Department of Mechanical Engineering and Mechanics, 354 Packard Laboratory, Memorial Drive West. Lehigh University, Bethlehem, PA 18015. Member AIAA.

19

19

P	=	instantaneous pressure
ω	=	vorticity
u	=	streamwise (x) component of instantaneous velocity
u'	=	velocity fluctuation in x direction
v	=	transverse (y)
v'	=	velocity fluctuation in y direction
x,y	=	coordinates
t	=	time
β	=	fundamental of most unstable frequency of cavity shear layer
$\beta/2$	=	subharmonic of most unstable frequency of cavity shear layer
δ	=	boundary layer thickness
$( )_{rms}$	=	root-mean-square
$\overline{( )}$	=	time-averaged

I. Introduction

Flow past an open cavity is known to give rise to self-sustained oscillations in a wide variety of configurations, including slotted-wall, wind and water tunnels, slotted flumes, bellows-type pipe geometries, high-head gates and gate slots, aircraft components and internal piping systems. These cavity-type oscillations are the origin of coherent and broadband sources of noise and, if the structure is sufficiently flexible, flow-induced vibration as well. Moreover, depending upon the state of the cavity oscillation, substantial alterations of the mean drag may be induced. In the following, the state of knowledge of flow past cavities, based primarily on laminar inflow conditions, is described within a framework based on the flow physics. Then, the major unresolved issues for this class of flows will be delineated.

Self-excited cavity oscillations have generic features, which are assessed in detail in the reviews of Rockwell and Naudascher[1,2], Rockwell[3], Howe[4] and Rockwell[5]. These features, which are illustrated in the schematic of Figure 1, are: (i) interaction of a vorticity concentration(s) with the downstream corner; (ii) upstream influence from this corner interaction to the sensitive region of the shear layer formed from the upstream corner of the cavity; (iii) conversion of the

upstream influence arriving at this location to a fluctuation in the separating shear layer; and (iv) amplification of this fluctuation in the shear layer as it develops in the streamwise direction. In view of the fact that inflow shear-layer in the present investigation is fully turbulent, item (iv) is of particular interest. It is generally recognized, at least for laminar conditions at separation from the leading-corner of the cavity, that the disturbance growth in the shear layer can be described using concepts of linearized, inviscid stability theory, as shown by Rockwell[6], Sarohia[7], and Knisely and Rockwell[8]. As demonstrated by Knisely and Rockwell[8], on the basis of experiments interpreted with the aid of linearized theory, not only the fundamental component of the shear layer instability may be present, but a number of additional, primarily lower frequency components can exist as well. In fact, the magnitude of these components can be of the same order as the fundamental. These issues have not been addressed for the case of a fully-turbulent inflow and its separation from the leading corner of the cavity.

Related numerical simulations

In addition to the major elements contributing to onset of vortical structures in the separated shear-layer, as described in the foregoing, the possible modulation effect of the unsteady recirculating flow within the cavity should be addressed. Possible coupling between the unsteady flow structure within the cavity, in the form of recirculating eddies, and the unstable shear layer along the mouth of the cavity, has been the focus of a number of numerical investigations in recent years. Ghaddar, Korczak, Mikic and Patera[9] simulated the incompressible flow in periodically grooved channels by direct numerical simulation. A single, weak recirculating vortex is observed within the cavity. Najm and Ghoniem[10] employ a vortex simulation technique. They show that, for relatively short cavities, the roll-up of the instability of the separating shear layer is a dominant mode of oscillation, whereas for sufficiently long cavities, low frequency eddies within the cavity appear to dominate the oscillation mechanism. Pereira and Sousa[11] use a finite difference numerical scheme with temporal discretization. Patterns of instantaneous streamlines and vorticity contours within the cavity suggest a relationship to the unstable shear layer past the cavity. More recently, Pereira and Sousa[12] combine the results of their unsteady numerical simulation with pointwise laser-Doppler measurements at crucial locations in the cavity and suggest, for their particular cavity configuration and flow conditions, that coupling occurs between the shear layer and the dynamics of the recirculation flow field within the cavity. Most recently, Takakura, Higashino,

Yoshizawa, and Ogawa[13] have employed a large eddy simulation to determine the unsteady features of supersonic flow past a cavity. Their instantaneous patterns of velocity vectors within the cavity, at a time corresponding to inflow into the cavity at the impingement corner, exhibit a wall jet flow along the vertical and bottom faces of the cavity, which provides a mechanism for recirculation flow. The issue arises as to whether a fully-turbulent inflow at essentially zero Mach number gives rise to organized, large-scale recirculation zones within the cavity; if so, the manner in which they mimic the foregoing simulation is unclear.

Overview of available experimental information

Over the past few decades, considerable attention has been given to experimental characterization of self-sustained oscillations of impinging shear layers. These studies have been centered on pointwise measurements of pressure and/or velocity in qualitative flow visualization using dye, smoke or Schlieren techniques.

Visualization of the vortex interaction with the leading-edge of an impingement surface has been carried out by Ziada and Rockwell[14,15] and Tang and Rockwell[16] for the cases of a sharp impingement edge and the sharp corner of a cavity, respectively. Severe distortion of the incident vortices can occur and, in some cases, generation of secondary (counter) vortices plays a key role. Correspondingly, measurements of the fluctuating force on a wedge by Ziada and Rockwell[14] and pressure fluctuations on the surface of the corner by Tang and Rockwell[16] have shown the relationship between the phase of the induced force/pressure, the distortion of the incident vortex, and the generation of secondary vortices. Considerable insight has been provided by these visualization studies, which must be interpreted in accord with the issues and potential fallacies of qualitative flow visualization, as assessed by Gursul and Rockwell[17,18] and Gursul, Lusseyran, and Rockwell[19]. To complement qualitative visualization of the unsteady flow field immediately upstream and along the edge, Gursul and Rockwell[17] and Graf and Durgin[20] employ phase-averaged, phase-Doppler anemometry techniques to determine the cycle-averaged velocities adjacent to the edge for an elliptical leading-edge and a cavity-corner respectively.

Measurement of velocity fluctuations in the unsteady shear layer have been carried out using point-wise hot-wire, hot film and laser-Doppler anemometry techniques. Woolley and Karamecheti[21] determine the variation of the phase and amplitude of the velocity fluctuation along the shear layer of an impinging jet of a jet-edge system and Sarohia[7] characterized

equivalent quantities for the analogous oscillating shear layer of a shallow open cavity. Knisely and Rockwell[8] and Schachenmann and Rockwell[22] characterized the multiple frequency components and the streamwise distributions of organized wave amplitude and phase along open rectangular and closed axisymmetric cavities respectively. Gharib and Roshko[23] determined features of the velocity field in relation to the overall drag on the cavity. More recently, Pereira and Sousa[12], have obtained velocity spectra at selected locations in the cavity shear layer. These pointwise measurements, which have advanced our understanding of this class of flows, provide the stimulus for global, instantaneous measurements of the instantaneous flow structure.

Major unresolved physical and experimental issues

Essentially all quantitative measurements of the unsteady flow between the upstream (leading) corner in the downstream corner of the cavity have involved time-averaged or phase-averaged pointwise measurements. Even for the case of an initially laminar boundary layer at the upstream separation location, substantial "jitter", or cycle-to-cycle variation of the flow pattern, can occur for a typical cavity oscillation. Especially when the inflow boundary layer is transitional or turbulent, its coexistence with potentially coherent oscillations can generate very significant cycle-to-cycle variations of the flow pattern. It is therefore productive to obtain instantaneous measurements of the velocity field over the entire region of the flow. Such global realization would provide a physical basis for interpretation of various types of time-, ensemble-, and phase-averages of the flow structure. A further advantage is that instantaneous pressure fluctuations along the surface of the cavity can be directly related to instantaneous, global variations of the flow pattern. To date, this approach has not been undertaken, even for the simplest case of an initially-laminar flow at separation.

Impingement of a quasi-coherent, turbulent shear layer upon the downstream corner of the cavity will result in severe distortion of the incident vortical structures. These so-called turbulent vortices will have a range of scales. Instantaneous, global insight into the vortex distortion process is called for.

Amplification of disturbances in the separated turbulent shear layer along the cavity may involve coexisting instabilities, characteristic of a wide range of length scales present in the separating turbulent boundary layer and different characteristic thicknesses of the separating flow. The interaction of these instabilities in the evolving shear layer, i.e., small- and large-scale

interacting vortical structures, can most effectively be clarified using instantaneous, global representations of the flow structure, which has not yet been undertaken.

Within the cavity, existence of unsteady, recirculating flow is expected to occur in a highly modulated fashion, driven by the unsteady impingement process at the downstream (trailing) corner of the cavity. The instantaneous structure of these large-scale recirculating flows, and the manner in which they modulate the separating shear layer from the upstream (leading) corner of the cavity has not been addressed in a global, instantaneous sense.

Objectives

The overall goal of the present investigation is to address the unresolved issues defined in the foregoing. In general, this involves determining the instantaneous, global flow structure past and within a cavity due to an inflow turbulent boundary layer. The possible instantaneous, global states of the flow will be related to instantaneous pressure fluctuations on the downstream corner of the cavity. Furthermore, the time-averaged turbulence statistics will be interpreted in terms of these instantaneous flow patterns.

II. Experimental System and Techniques

Experiments were performed in a large-scale water channel, using combinations of surface pressure measurements and particle image velocimetry, which yielded global representations of the velocity and vorticity fields. The overall experimental system and quantitative measurement techniques are described in the following.

Experimental System

The free-surface water channel had a test section 36 inches wide × 24 inches deep. The total length of the test section was 20 feet. For the present experiments, the free-surface of the water was maintained at a height of 16.5 inches. This test section is preceded by a large contraction, having an inlet width of 6 feet; its contraction ratio is 2:1. An arrangement of honeycombs and screens is located upstream of the contraction; it minimized the free-stream turbulence, which is less than 0.1%. The freestream velocity was 10.53 inches/second.

The cavity test section, which was custom designed and constructed for the present experiments, was housed within the main test section of the water channel. Figure 2 shows the overall configuration and dimensions of the cavity section. It had an internal width of 18 inches

and an overall length of 130 inches. It is bounded on either side by vertical false walls extending from the floor of the water channel to a height equal to the upper edge of the channel test section. The cavity test section is preceded by a special inlet contraction, which has two purposes. First of all, it facilitates attainment of a higher velocity at the inlet of the cavity test section. Second, through use of a special gap arrangement between the inlet contraction and the leading-edges of the false walls of the cavity test section, it was possible to attain essentially parallel inflow into the leading region of the cavity test section (see plan view of Figure 2). This configuration is crucial, in that it precludes separation of the boundary layers along the interior surfaces of the false walls.

The major components of the cavity test section, most evident in the side view of Figure 2, involve a long flat plate, the cavity with an adjustable length L, and a deflection plate. A central objective of this unique facility is attainment of a turbulent boundary layer approaching the cavity. While experiments on flat plate boundary layers are abundant, the concept of employing such a plate with a rather complicated cavity arrangement had not been, up to the point of this experiment, attempted in any investigation. An important condition that must be satisfied is attainment of a stagnation point of the incident freestream at the tip of the elliptical leading-edge of the flat plate, having an aspect ratio of 4:1. This condition is essential if the boundary layer along the plate is to develop in a similar fashion as in a so-called infinite free-stream. Due to the difference in resistance between the regions above and below the flat plate, the stagnation point will, in the absence of any control device, be located along the lower surface of the elliptical edge, and induce a separation bubble along the upper surface of the leading-edge. This difficulty was overcome by employing a deflection plate at a location downstream of the cavity. It imposes an overall resistance on the upper region of the flow, such that the stagnation point is moved to the tip of the leading-edge of the plate generating the boundary layer.

In order to promote a fully-turbulent boundary-layer, the trip section was located immediately downstream of the leading-edge of the plate. Details of this trip section are described by Johansen and Smith[24]. Small (0.13 inch) and large (10.1 inch) diameter Plexiglas hemispheres were arranged in a spatially periodic pattern across the entire span of the plate. In the study of Johansen and Smith[24], this configuration was found to generate a well-posed turbulent boundary layer for the same value of flow velocity and effective plate length as employed in the present study.

Further details of the cavity system are described by Rockwell and Lin[25]. The laser sheet used for PIV was located at the midspan of the cavity test section. It was transmitted through the laser windows. These windows were 1/16 inch thick strips of Plexiglas, which were flush with the external surfaces of the cavity section. This thin Plexiglas minimizes laser refraction and transmission losses. The length L of the cavity was adjustable up to a maximum value of 16 inches. The effective depth W of the cavity was maintained constant of W = 4 inches for all experiments.

A transducer block built into the impingement corner housed a PCB high sensitivity transducer (Model No. 106B50), which measured the pressure fluctuations at the impingement corner of the cavity. It is described by Rockwell and Lin[25]. The pressure tap was located along the vertical face of the cavity corner at a distance of 0.13 inches below the corner and displaced a lateral distance of 0.57 inches. The transient response of this pressure tap-line-transducer system has a resonant frequency of 31 Hz, well above the frequencies of interest of this experiment, i.e., of the order of 1.0 Hz. The damping coefficient corresponded to maximum distortions of 0.5% of the pressure magnitude and phase.

Techniques of high-image-density particle image velocimetry

A custom-designed laser-optical arrangement was employed for generating the laser sheet employed for PIV measurements, based on the laser scanning concept described by Rockwell, Magness, Towfighi, Akin and Corcoran[26]. The entire optical system was mounted on a system of rails, allowing it to be translated to a specified location beneath the test section. A beam steering mirror and convex and concave lenses, having focal lengths f = 300 and 100 mm respectively, were fixed to this translating table. To facilitate further focusing and alignment of the rotating, multi-faceted mirror, it, along with a focusing singlet and a second beam steering mirror were all mounted on a circular table, which could be rotated to any angular position, relative to the large, translating table. In essence, this system allows the laser beam to be focused to a relatively narrow waist, with minimal distortion of the wave front less than $\lambda/10$ over the central region of the beam. With this particular lens combination, it was possible to attain the minimum waist of the laser beam at the half-vertical depth of the water channel test section. Simultaneously, the beam had a sufficiently small diameter as it impinged upon the face of a multi-faceted mirror, so that only one of the mirror facets was illuminated at a given instant of time.

The rotating mirror had seventy-two facets. Its speed of rotation was controlled by an external driver unit, such that the effective scanning frequency of the laser beam, 156.2 cycles/sec, generated optimum displacement between the multiply-exposed particle images during PIV experiments. The effective thickness of the scanned laser sheet formed by the scanning laser was 1.5 mm.

The laser beam emanated from a continuous wave Argon-ion having a variable output up to approximately 25 watts. For most of the experiments described herein, the effective output power of the laser was maintained at 15 watts. The water was seeded with metallic-coated particles having a diameter of 12 microns. Multiply-exposed images of these particles were recorded on high resolution film, having an effective resolution of 300 lines/mm. Two different types of 35 mm film cameras were employed during the course of this investigation. The first was a Nikon F-4 camera, which was employed for still photos of the inflow turbulent boundary layer and the cavity oscillation. The second camera was a Hulcher cinema camera, having a maximum framing rate of 60 frames per second. Extensive evaluation of the characteristic time scales of the cavity oscillation, in conjunction with the available lighting of the laser sheet, showed that a framing rate of 10 frames per second was optimal. Images were recorded on one hundred foot spools of 35 mm film. The pressure signal was recorded simultaneously during the cinema recording, in order to allow a direct correspondence between the pressure fluctuation at the corner of the cavity and the dynamics of the impinging shear layer. Full details of this cinema system are given by Lin and Rockwell[27].

For both camera systems, a rotating bias mirror, i.e. an image shifting mirror, was located in front of the camera lens, which had magnifications of 1:7.57 and 1:7.74. The mirror was oriented at an angle of 45°, and its angular displacement was triggered during each shutter opening, in order to impart a constant bias displacement of all particle images, which was removed during the interrogation process. The angular displacement of the mirror was of the order of 0.01°, in order to preclude systematic distortion effects of the pattern of particle images induced by finite rotation angle of the mirror.

Each 35 mm negative was digitized at a resolution of 125 pixels per millimeter. Then, these digitized image patterns were subjected to a single frame, cross-correlation technique, in order to provide the instantaneous velocity vector at each interrogation location. A 50% overlap of

interrogation areas was employed. The effective grid size in the plane of the laser sheet, i.e. the distance between velocity vectors, was 0.36 mm.

Post-processing of the raw velocity field involved, first of all, removal of bad vectors, then filling the blank location using a classical bilinear interpolation. The velocity field was smoothed using a Gaussian filter having an exponent p = 1.3. These interpolation and filtering techniques are well known and described in detail by Landreth and Adrian[28].

Pressure and Velocity Measurements

Time traces of the pressure fluctuations were acquired with a PCB pressure transducer having a sensitivity of 500 mv/psi. During experiments, the pressure signal was subjected to analog filters and electronic amplifiers. The sampling time was $\Delta t = 0.004$ sec, in order to adequately resolve all the dominant frequencies. The signal was transmitted to the A/D board of the host microcomputer, stored in digital form, allowing reconstruction of the time traces, as well as computation of the power spectral density using an FFT technique. The total acquisition time T of each velocity and pressure record depended upon the particular experiment. Its value, along with the effective sampling time Δt and sampling frequency Δf are specified in conjunction with each of the time traces and spectra presented in the following.

III. Inflow Turbulent Boundary Layer

The turbulent boundary layer approaching the cavity was characterized upstream of the separation corner of the cavity. Using the coordinates (x,y) centered at the separation point of the leading corner of the cavity, PIV images were acquired over the spatial domain extending from $x = -10.31$ inches to $x = -14.87$ inches and from $y = 0.018$ to 3.02 inches. A typical instantaneous velocity field, in a reference frame of observation of 0.8 U_∞, where U_∞ is the freestream velocity, is shown at the top of Figure 3.

A total of thirty-eight PIV images were acquired at random times, with a minimum spacing of 60 sec. The variation of the velocity with coordinate x was considered at a given y in a specified image, and the values of the mean velocity components $\overline{u}$, $\overline{v}$, the corresponding fluctuation components u_{rms} and v_{rms}, as well as the velocity correlation $\overline{u'v'}$, were determined for that image. Then, by averaging these values in all thirty-eight images, the final statistical

values were obtained. This approach is described by Liu, Landreth, Adrian and Hanratty[29] and Westerweel, Draad, van der Hoevern and van Oord[30].

Figure 3 shows the variation of the mean, fluctuation and correlation quantities across the boundary layer. For these data, the boundary layer thickness $\delta = 1.80$ inches, the displacement thickness $\delta^* = 0.27$ inches, momentum thickness $\theta = 0.197$ inches, and the shape factor $H = \delta^*/\theta = 1.37$. The Reynolds number based on momentum thickness was $Re_\theta = 1{,}371$. At this value of Re_θ, Johansen and Smith[28] obtained $H = 1.37$ via single point hot film measurement.

Comparison of these distributions with those of Klebanoff [31] (see also Schlichting[32], acquired using a hot wire anemometer, indicates remarkably good agreement. Further details and comparisons of the turbulent boundary-layer structure are given by Rockwell and Lin[25]. To demonstrate that a well-defined log layer exists within the turbulent boundary layer, the raw data of the present study, in the form $\overline{u}/U_\infty$ versus y (in mm) was plotted on semi-log coordinates. A well-defined log region was shown to exist.

Moreover, to ascertain that a well-defined inertial subrange existed within the turbulent boundary layer, the PIV data were further evaluated. For each of the thirty-eight images, the spectrum was evaluated at a distance 0.91 inches from the wall corresponding to 0.5 δ, in which δ is the boundary layer thickness, also represented by the symbol δ_{995}. The technique for evaluation of the spectra is described in Section II. In essence, at each elevation from the wall, the entire sequence of u or v velocity components was considered from the left to the right boundary of the image. This sequence is, in essence, interpreted as a time sequence, leading to a frequency spectrum. Spectra for both the streamwise u' and cross-stream v' fluctuations were calculated. Figure 4 shows the well-known slope in the inertial subrange, $n = -5/3$, on the spectrum. It extends over the range $20 \leq 2\pi f\, \delta_{995}/U_\infty \leq 10^2$. This range of agreement is remarkably coincident with, for example, the normalized plot of Bradshaw[33]. At lower values of dimensionless frequency, however, there is a degree of scatter within the data, due to the fact that the averaging process did not include a sufficiently large number of images. Furthermore, at relatively high values of dimensionless frequency, the spectra of Figure 4 are meaningless, due to the fact that the spatial resolution Δx of the PIV image cannot properly represent the smallest scales of the turbulence.

IV. Instantaneous Flow Structure and Pressure Fluctuations

Sequences of instantaneous PIV images were obtained using two approaches. The first involved a cinema PIV sequence. In this case, images were acquired at a framing rate of ten frames per second, yielding a total of 167 images with a time increment $\Delta t = 0.1$ seconds between them. The second approach involved random acquisition of 77 images, whereby the camera was triggered at an arbitrary time, with the only constraint that the interval between successive images exceeded 60 seconds, which is approximately a factor of 12 longer than the period of the lowest, coherent spectral component at 0.2 Hz.

In order to establish the relationship between the fluctuation pressure at the trailing-corner and the distortion of the flow structure in that region, the pressure at tap B was acquired simultaneously with the cinema PIV series. The time trace is shown in Figure 5. The framing rate of the cinema sequence is 10 frames/sec and the first image of the cinema sequence corresponds to the instant $t = 0.1$ sec in the time trace of pressure. Subsequent images in the cinema sequence correspond to $t = 0.2$, $t = 0.3$ sec and so on in the pressure trace. A complete collection of the cinema images is given in Rockwell and Lin[25]. In the following, selected images and corresponding pressure traces are shown to illustrate the major features of the cavity oscillation.

The time trace of the pressure fluctuations shown in Figure 5 exhibits substantial modulation of the period between successive peaks. It is possible to identify portions of the trace that have a peak to peak spacing corresponding to the fundamental β and subharmonic $\beta/2$ of the most unstable frequency of the shear layer. These modes are designated as $1/\beta$ and $2/\beta$. The circle symbols indicated at the minimum or maximum values of the pressure trace correspond to the cinema images that are examined in detail in the following.

Comparison of the pressure at the impingement corner with the instantaneous vorticity and velocity distributions is given in Figure 6a. The position of the pressure tap is 0.13 inches below the tip of the corner. At the instant shown in Figure 6a, the pressure has a maximum-negative value. Correspondingly, the cluster of vorticity has its center approximately coincident with the location of the pressure tap. The impinging vortex is actually made up of layers of small-scale vortical structures. The overall diameter of this vortex is of the order of one-half the cavity length. The corresponding velocity field suggests an upward-oriented outflow from the cavity at the trailing-corner. This apparent outflow is, of course, associated with the arrival of the cluster

of vorticity at the corner. Within the cavity, jet-like flow along the vertical and bottom wall is clearly evident. Moreover, the upward oriented velocity field over the first half of the cavity length is in accord with the large entrainment demands over the initial extent of the separated shear layer formed from the leading-corner of the cavity.

Of course, it is well-known that the interpretation of patterns of velocity vectors and streamlines is dependent upon the reference frame of observation. For this reason, the velocity field of the separated layer and its impingement upon the corner of the cavity is visualized in not only the laboratory frame, but also frames moving at 0.25 and 0.50 U_∞ as shown in Figure 6b. At a frame velocity of 0.25 U_∞, the swirl patterns of velocity vectors correspond well to the concentrations of vorticity shown in Figure 6a. In Figure 6b, the extent of the distorted vortex upstream of, and above, the trailing-corner of the cavity, in accord with the cluster of vorticity in Figure 6a, is particularly evident.

In Figure 7, the incident cluster of vorticity is located just upstream of the corner. The small-scale concentrations that make up the large-scale structure are identified, in an approximate sense, by the dashed circle. In this case, the instantaneous pressure takes on its maximum-positive value, and the velocity field in the vicinity of the corner shows a downward deflection and formation of a pronounced, jet-like flow along the vertical wall of the cavity.

Instantaneous patterns of velocity and vorticity for the cavity oscillation in a mode corresponding to approximately the subharmonic frequency $\beta/2$ are shown in Figures 8 and 9 for the maximum-negative and -positive values of pressure at the impingement corner. Figure 8 shows images corresponding to the maximum-negative pressure peak, where the center of the vorticity cluster is nearly coincident with the location of the pressure tap at the corner. In this case, the velocity field exhibits a particularly violent ejection of fluid out of the cavity, drawn upward by rotation of the large-scale cluster of vorticity as it encounters the corner. In Figure 9, corresponding to the maximum-positive pressure peak, the cluster of incident vorticity is located upstream of the cavity face. The interesting feature of this particular vortex-corner interaction is that the entire extent of the flow, from the bottom of the cavity to the separated shear layer, is part of a large-scale swirl pattern, suggesting coupling between the large-scale cluster of vorticity approaching the corner and the recirculation flow in the right half of the cavity.

Viewing the relationship between the large-scale clusters of vorticity in the vicinity of the corner and the induced pressure at the corner, shown in Figures 6 through 9, the common feature

is that when the center of the large-scale vorticity cluster is approximately coincident with the cavity corner, a maximum-negative pressure is induced at the corner, whereas when it is at a location just upstream of the corner, the pressure takes on its maximum-positive value. These observations are in accord with those of Tang and Rockwell[16] for the case of an unstable laminar shear layer, which generated identifiable vortical structures that impinged upon the corner of the cavity. From the present study, it appears that this process of vortex-corner interaction is associated with substantial variations in outflow and inflow into the cavity as the vortex approaches and is severely distorted in the corner. Further consideration of this detailed interaction should provide insight into the character of the pressure source(s) that is crucial in determining the upstream influence and, especially at higher Mach number, the nature of the radiated sound pattern.

Regarding the flow field within the cavity, Figure 10 compares the instantaneous velocity of Figure 9 with the calculation of Takakura, Higashino, Yoshizawa, and Ogawa[13], for which the flow exterior to the cavity was supersonic. Nevertheless, the overall features of the velocity pattern within the cavity are remarkably similar: (i) the large magnitudes of the velocity vectors, oriented downward and away from the vertical face of the cavity; (ii) the jet-like flow along the bottom wall of the cavity, having a nearly discontinuous leading-front, i.e., the magnitude of the front edge of this jet-like flow abruptly decreases in magnitude; (iii) an upward jet-like flow along the vertical face of the leading-corner of the cavity; and, finally, (iv) a pronounced recirculating, vortex-like, flow over the right-half of the cavity, extending from the bottom wall to the separated shear layer.

Comparison of a representative image from the cinema sequence with an excerpt from the unsteady numerical simulation of Pereira and Sousa[12] is given in Figure 11. In making this comparison, an image from the cinema sequence was selected to match the phase of the oscillatory shear-layer of the numerical simulation. Both images of Figure 11 exhibit: (i) small-scale vorticity concentrations immediately downstream of separation from the leading-corner of the cavity; (ii) appearance of an initial cluster of vorticity; (iii) a thin, elongated region of vorticity between this impinging vortex and the small-scale clusters of vorticity located upstream of it; and (iv) an approximately vertical orientation of a large-scale cluster of vorticity as it encounters the trailing-corner of the cavity. It should be noted, however, that the patterns of recirculating vortices within the cavity are significantly different.

V. Averaged Flow Structure

Representations of the averaged flow pattern were obtained by averaging a series of instantaneous images of the type shown in Section 4. The first averaging involved consideration of the entire set of images in the cinema sequence. A total of 167 images was acquired at a time interval $\Delta t = 0.1$ sec between images. Accounting for the fact that 167 images were acquired, then the total time of acquisition corresponds to 16.7 sec. Recall from the cinema pressure trace, as well as other related traces, that the cavity oscillation appears to exhibit a competition between the fundamental at approximately 1.0 Hz and the subharmonic at about 0.5 Hz. This means that the cinema signal corresponds to 16.7 cycles of the fundamental and 8.35 cycles of the subharmonic.

The second type of average involved randomly selected images, as opposed to foregoing sequence of images, which were closely-spaced in time. A total of 77 images were acquired for this averaging. In this case, the minimum Δt between images was 60 sec., which was approximately a factor of 12 longer than the period corresponding to the lowest organized component in the spectrum, i.e., the component at approximately 0.2 Hz. This random sampling is typical of that employed in turbulent flows. An example is the averaged turbulent statistics of a turbulent jet impinging upon a plate involving 11 images (Landreth and Adrian[34]).

Calculation of the averaged quantities was performed according to the equations listed below. Each averaged parameter was calculated at each spatial coordinate (x,y) by considering the average of all instantaneous values (x,y). The terminology for each of the averaged parameters and the dimensionless equation employed to determine the averaged parameter are as follows:

$< V >$ ≡ averaged (or mean) total velocity

$$< V > \equiv \frac{1}{N}\sum_{n=1}^{N} V_n(x,y) \tag{5.1}$$

$< u >$ = averaged value of streamwise component of velocity

$$< u > \equiv \frac{1}{N}\sum_{n=1}^{N} u_n(x,y) \tag{5.2}$$

$< v >$ = averaged value of transverse component of velocity

$$< v > \equiv \frac{1}{N}\sum_{n=1}^{N} v_n(x,y) \tag{5.3}$$

$< \omega >$ = mean value of vorticity ω

$$< \omega > \equiv \frac{1}{N} \sum_{n=1}^{N} \omega_n(x,y) \tag{5.4}$$

$< u'v' >$ = averaged value of Reynolds stress correlation

$$< u'v' > \equiv \frac{1}{N} \sum_{n=1}^{N} [u_n(x,y) - < u(x,y) >][v_n(x,y) - < v(x,y) >] \tag{5.5}$$

The averaging process involved, in essence, stacking a series of instantaneous images in evaluating the averaged parameter at a given location (x,y). This type of average is referred to as an ensemble-average. We emphasize that, unlike some ensemble-averaging processes, no phase reference or phase trigger was employed. Rather, in the case of the randomly-acquired images, the camera was triggered at an arbitrary time, so long as the interval between images was greater than 60 sec. For the cinema series, no phase condition was employed. It is important to realize, however, that, for the cinema series, the time spacing between successive images employed in the ensemble-averaging process is 0.1 sec, which corresponds to approximately 1/10th of the fundamental instability frequency β and 1/2 of the lowest coherent spectral component at 0.2 Hz.

Since markedly different criteria were employed for the acquisition of images corresponding to the two types of averages described in the foregoing, a direct comparison of the averaged quantities should provide an indication of the degree of convergence. For this reason, averaged images obtained from the cinema series are directly compared with those from the randomly-acquired series in Figures 12 through Figure I4. Each figure contains two averaged images. The top one corresponds to that obtained from the cinema sequence, while the lower one represents the randomly-sampled (acquired) sequence.

When examining and comparing the images of Figures 12 through 14, issues related to the process of image acquisition should be kept in mind. Narrow shadow regions exist immediately above the leading- and trailing-corners of the cavity. Whereas the bilinear interpolation process was effective in providing accurate distributions of velocity through the shadow region above the trailing-corner, no attempts were made to refine the distortion due to the shadow region above the leading-corner of the cavity. The width of this shadow region is 0.008 L, where L is the cavity length. This region is not essential to understanding the central physical features of interest herein; moreover, the characteristics of the inflow boundary layer are already known from independent boundary layer measurements taken well upstream of the

cavity. It is also evident, in a number of the averaged images, that the outline of the cavity is slightly tilted relative to the horizontal. This is simply due to the fact that, especially for the cinema camera, it was very difficult to perfectly align the bottom wall of the cavity with the lower boundary of the field of view. This slight tilting does not, however, affect the quality or accuracy of the PIV data.

Averaged (mean) velocity

Comparison of the averaged total velocity $< V >$ for the cinema and randomly-acquired image sequences, corresponding to the top and bottom images respectively, is given in Figure 12. It is evident that these patterns of $< V >$ are remarkably similar. It should be noted that the apparent difference in the first line of velocity vectors in the turbulent boundary layer, emanating from the leading-corner of the cavity, is simply due to a different starting point for construction of these velocity vectors. Particularly interesting is the flow in the immediate vicinity of the corner of the cavity. It makes an abrupt transition from vectors that are predominantly oriented in the vertical direction, to those that are essentially in the horizontal direction, over a very small distance. This occurs at a streamwise location immediately downstream of the leading-corner of the cavity, and corresponding to large values of mean vorticity. This severe distortion of the mean flow, which occurs over a relatively small characteristic thickness is most likely linked to the rapid onset of the small-scale vortical structures, which appear immediately downstream of the leading-corner of the cavity, evident, for example, in Figures 6a and 8. In the vicinity of the trailing-corner of the cavity, the continuous line of velocity vectors that impinges directly upon the vertical face of the cavity, at a location immediately below the trailing-corner, represents the averaged stagnation streamline. Below this line, flow is into the cavity. This downward-deflected flow forms a jet that continues along the bottom surface of the cavity. Eventually this fluid is drawn upward towards the separating shear layer along the mouth of the cavity, in order to satisfy entrainment demands. Overall, the flow pattern in the right half of the cavity appears to exhibit a large-scale recirculation flow, which might loosely be termed a recirculation vortex.

This averaged pattern of total velocity $< V >$ in the cavity, more specifically, the large-scale recirculating vortex, is in accord with certain features of recent numerical simulations. The occurrence of a single, large-scale vortex is discernible in the averaged streamline patterns (with superposed pressure intensity contours) of Takakura, Higashino, Yoshizawa, and Ogawa[13]. Moreover, the time sequence of instantaneous streamline patterns of Pereira and Sousa (1993)

suggests, when averaged, that a single, large-scale vortex would dominate. The instantaneous streamline plots of the subsequent study of Pereira and Sousa[12] (not shown) exhibit a second, weaker vortex.

Averaged vorticity

Contours of constant averaged vorticity $< \omega >$ are indicated in Figure 13. Concerning the region of the separated layer extending from the leading- to the trailing-corner of the cavity, it is evident that the vorticity levels dominate those of the background turbulent boundary layer. Very high levels of vorticity are generated immediately downstream of the corner, where the flow makes an abrupt transformation from an attached to a separated layer. Regarding the region within the cavity, positive vorticity of significant magnitude extends well upstream along the bottom wall of the cavity.

Velocity correlation

Distributions of the velocity correlation $< u'v' >$ are given in Figure 14. In the separated shear layer between the leading- and trailing-corners of the cavity, small-scale regions of relatively high correlations of $< u'v' >$ suggest the existence of a number of small-scale vortical structures along the shear layer, already evident in, for example, the vorticity distributions in Section 4. The peak values of $< u'v' >/U_\infty^2$ in this separated layer are of the order of 10^{-2}. This value compares with the peak value in a free, turbulent mixing-layer of about 2×10^{-2} (Fiedler, Dziomba, Mensing, and Rösgen[35]). They exceed the maximum values in the approach turbulent boundary layer by a factor of approximately 7 (compare Figure 3). This observation again suggests dominance of the dynamics of the separated shear layer over the background turbulent boundary layer. Within the cavity, along the vertical face, large amplitudes of the $< u'v' >$ correlation of opposite sign occur over nearly its entire extent. By comparison with the mean velocity $< V >$ plots of Figure 12, it can be seen that the extrema of these $< u'v' >$ contours occur along the edge of the jet-like flow along the vertical face. Hussain[36] has shown, for a free axisymmetric, that either positive or negative regions of Reynolds stress may occur due to vortex interactions; counter-gradient average momentum transport is therefore possible. Similarly, high levels of $< u'v' >$ occur along the bottom wall of the cavity; again, the location of these extrema approximately correspond to the edge of the jet-like flow. The loci of these extrema along the edge of the wall jet within the cavity are directly analogous to that along the bottom edge of the

separated layer extending from the leading- to the trailing-corner of the cavity, and are in accord with the well-known observation of high levels of Reynolds stress occurring along the edge of a separated layer, due to generation of vortical structures in that region (Fiedler, Dziomba, Mensing, and Rösgen[35]).

VI. Assessment of Major Results

This investigation, which has provided instantaneous images of the flow structure, allows insight well beyond that attainable using traditional experimental techniques involving, for example, dye visualization, smoke injection and hydrogen bubble visualization. The quantitative velocity and vorticity fields and their evolution with time provide the basis for image evaluation with an eye towards identifying key pressure sources. The major features of the unsteady separated shear-layer along the cavity, its interaction with the corner of the cavity, and the corresponding flow within the cavity have been revealed, and their primary features will dictate the nature of the unsteady pressure field immediately adjacent to and well away from the cavity configuration.

In the following, summaries and assessments of the principal regions of the flow are provided.

Structure of separated shear-layer along cavity

Instantaneous images of the vorticity field reveal that the separated shear-layer exhibits two categories of coherent vortical structures. The first involves small-scale concentrations of vorticity, which are rapidly formed from the leading-corner of the cavity, and have a wavelength substantially smaller than the cavity length. The second takes the form of a large-scale cluster of vorticity, which actually results from agglomeration of the small-scale concentrations. The typical wavelength between these large-scale structures is of the order of the cavity length, and their development appears to be analogous to the roll-up of vortices in a laminar shear layer past a cavity at substantially lower values of Reynolds number.

These observations suggest the existence of two instabilities in the cavity shear layer. The initial, small-scale instability is expected to scale with a local thickness immediately in the vicinity of the leading-corner of the cavity. An approach to predicting the most unstable frequency of the inner region of the shear layer involves use of the vorticity thickness $\delta_\omega = (U_1 -$

$U2)/(dU/dy)_{max}$, in which U_1 and U_2 are the velocities on the upper and lower sides of the inner portion of the free layer at a location immediately downstream of separation and $(dU/dy)_{max}$ is the maximum value of vorticity within the layer. Using this characteristic thickness, one could determine the most unstable frequency of the small-scale vortical structures immediately downstream of separation from the leading-corner of the cavity. This approach directly shows the consequence of the very high level of mean vorticity at the leading-corner of the cavity. Now consider the instability leading to formation of the large-scale clusters of vorticity, which is of the convective type, and is reinforced through feedback from the vortex-corner impingement to the upstream (leading-) corner of the cavity. The formation of these large-scale vorticity clusters occurs at the dimensionless frequency β. If we employ the momentum thickness θ_0 of the turbulent boundary layer at separation, and view it as an approximation to the value of θ at a representative downstream location, where this larger scale instability develops, it is possible to account for the entire transverse extent of the shear layer in predicting the frequency β. According to linear stability theory for a convective-type instability, the dimensionless frequency should be $\beta = f\theta/U_\infty = 0.017$. Using the value of θ at separation, i.e. θ_0, and the free-stream velocity U_∞ defined in Section 2, the predicted frequency is $f = 0.908$ Hz, which is very close to the typical peaks having a spacing corresponding to approximately 1.0 Hz in the time traces of Figure 5. Moreover, the subharmonic component $\beta/2$ has a frequency roughly half the value in the time traces. It is important to note that the classical process of successive vortex coalescence leading to larger scale vortical structures in a free shear layer originates with an instability at dimensionless frequency $\beta \cong 0.017$ when the boundary layer is laminar. The estimated frequency of the aforementioned small-scale vortices gives a value of β nearly an order of magnitude larger when the momentum thickness θ_0 is employed at separation.

On the other hand, immediately downstream of the leading-corner, the value of peak mean vorticity drops substantially (again, compare Figure 13). If we approximate the so-called free-stream velocity on the lower side of the separated layer U_2 as equal to zero and that along the upper side U_1 as remaining relatively constant with streamwise distance at a value U_∞, it follows that the vorticity thickness δ_ω in the immediate vicinity of the corner will be substantially lower than that in the region downstream of the corner. In turn, the predicted instability frequency for the small-scale vortex formation from the corner will be substantially higher than that in the

region downstream of the corner, which is more characteristic of the global-type instability of the entire separated layer.

An additional mechanism that may produce the patterns of small-scale vortical structures at the leading-corner of the cavity is the existence of hairpin vortices in the fully turbulent boundary layer upstream of the leading-corner of the cavity. Multiple hairpin structures having a streamwise spacing of the order of one-tenth the boundary layer thickness are evident in the PIV images of Figures 7 through 9. This possibility should be investigated further in conjunction with the aforementioned mechanism of a small-scale instability.

The foregoing mechanisms of vortex formation in the separated shear layer coexist with and, in some cases may be coupled with, the large-scale patterns of recirculating flow within the cavity. Recent numerical simulations of Pereira and Sousa[12] and Najm and Ghoniem[10] specifically address the potential role of the large-scale vortex within the cavity. In fact, by viewing this region of the flow as a nonlinear dynamical system, it is possible to define a mechanism of instability due to the recirculating vortex system. The degree of predominance of this type of instability is not completely resolved. It is evident, however, by inspection of a time sequence of instantaneous images, that the velocity and pressure signals exhibit substantial modulation, or even intermittency, which may be due, at least in part, to the character of the recirculating flow within the cavity. We note, that in the low Reynolds number study of Knisely and Rockwell[8], involving flow past a cavity, that the spectra of the velocity and pressure fluctuations can exhibit a substantial number of peaks due to modulation phenomena. From the standpoint of shear layer stability, an important finding from their study is that several of the spectral components can simultaneously satisfy the phase-locking criterion between the leading- and trailing-corners of the cavity, emphasizing the importance of the instability mechanism of the separated shear layer.

The importance of the onset and development of clusters of vorticity, associated with the inherent instability of the shear-layer, is further evident from examination of the contours of constant dimensionless Reynolds stress of Figure 14. The peak values overshadow those of the inflow turbulent boundary layer, due to the coherent development of vortical structures in the separated layer.

Structure of shear-layer interaction with corner of cavity

The instantaneous velocity and vorticity fields presented herein provide the first quantitative definition of the distortion of the shear layer, more specifically of the large-scale clusters of vorticity as they encounter the corner of the cavity. As these clusters of vorticity interact with the corner, it is possible to identify large variations in inflow and outflow, to and from, the interior of the cavity. This information should be helpful in formulating models for the source of pressure fluctuations at the corner that are crucial in determining the far field sound radiation. The importance of considering different reference frames of observation of the instantaneous velocity field has been emphasized. Depending upon the frame, different features of the cavity shear layer are emphasized. Further assessment of the data in the vicinity of the cavity corner should involve: (i) calculation of pressure source terms; and (ii) construction of instantaneous streamline patterns in various reference frames, then with the aid of critical point theory, interpreting the time-variation of critical points in conjunction with magnitudes of pressure source terms in that region.

By simultaneously recording the pressure trace at the impingement corner with the cinema PIV sequence, it has been possible to determine the phase relationship between the arrival and distortion of the large-scale clusters of vorticity and the maxima and minima of the pressure fluctuations at the corner. The issue arises as to what types of geometrical modifications of the corner could serve as a basis for attenuation of the surface pressure fluctuations in that region.

The classical, time-averaged viewpoint of a cavity flow is that suggested in the averaged images of Figure 12. By constructing tangents to the velocity vectors, it is possible to identify a stagnation or reattachment streamline at the corner. Any given instantaneous image, however, does not show existence of such a reattachment line, rather the distortion of the incident vortical structures in that region, in conjunction with instantaneous inflow or outflow provide a very different picture than the averaged representation. This sort of interpretation is important for a wider class of separated and reattaching flows, such as that behind a backward facing step.

Structure of flow within cavity

The flow pattern within the cavity is dominated by a jet-like flow along the vertical wall of the trailing-corner, then in the upstream direction along the bottom wall of the cavity. This jet-like flow is a sort of wall jet, having a boundary layer on one side and a free, separated layer on its other side. This free shear-layer exhibits detectable vortical structures, which serve as a source of substantial velocity fluctuations and represent the loci of maximum velocity

correlations $< u'v' >$. In general, the flow rate associated with this jet-like flow into the cavity must satisfy the entrainment demands of the separated shear layer between the leading- and trailing-corners of the cavity. In many of the instantaneous images, this upward-oriented entrainment flow is evident along a substantial length of the separated layer. In addition, however, an upward-oriented, jet-like flow along the vertical face of the leading-corner of the cavity influences the initial development of the separating turbulent boundary layer. Unsteadiness of this upward-oriented jet no doubt contributes to the modulated character of the separated layer.

A number of admissible patterns of instantaneous, recirculation vortices can occur within the cavity. These recirculation vortices tend to occupy the right half of the cavity. In the limiting case, the swirl pattern of velocity vectors associated with this recirculation vortex extends from the bottom wall of the cavity to the separated layer, suggesting a coupling between the recirculation vortex and the large-scale cluster of vorticity that impinges upon the cavity corner. Further analysis of the data should provide insight into the possibility of such coupling.

VII. Conclusions

The central findings of the present investigation are as follows:

(1) A fully turbulent inflow, in the form of a turbulent boundary layer separating from the leading-corner of the cavity, can evolve into a pattern of organized vortical structures. Two extreme scales of these structures have been identified. The largest-scale structures scale according to the momentum thickness of the time-averaged velocity distribution at the leading-corner of the cavity. The corresponding dimensionless frequency of formation of these large vortical structures is in close agreement with that predicted from inviscid stability theory. In addition, organized vortical structures of a much smaller scale form from the leading-corner of the cavity. In this region the mean vorticity is very high and the corresponding local vorticity thickness of the separated layer will be relatively small, thereby promoting formation of small-scale vortical structures at relatively high frequency. The possible role of pre-existing vortical structures in the approach turbulent boundary layer, and their relation to those observed from the leading-corner of the cavity remains for further investigation.

(2) The separated shear layer exhibits a complex modulated structure, evident in not only the instantaneous PIV images, but also in the time traces of the pressure signal at impingement. The latter exhibits both amplitude- and frequency-modulated features, but, generally speaking, such traces exhibit periods corresponding to the fundamental and subharmonic of the instability mode associated with formation of the largest-scale vortical structures. The physical origin of this modulation is, at least in part, due to a modulated, jet-like return flow within the recirculation zone of the cavity. A front of such a jet is produced when a portion of the unsteady shear layer is deflected downward into the cavity at the location of the impingement corner.

(3) The time-averaged characteristics of the shear layer along the cavity, as well as recirculating flow within the cavity, are expressed in terms of Reynolds stresses, time-Reynolds stresses, vorticity and velocity. It is demonstrated that the Reynolds stresses of the shear layer along the cavity rapidly dominates those of the approach turbulent boundary layer. The patterns of averaged vorticity show that the region of separation from the leading-corner of the cavity dominates all other regions of the flow field, including the shear layer along the cavity and the recirculating flow within the cavity.

VIII. Acknowledgements

The authors gratefully acknowledge the partial support, in the form of research instrumentation and equipment, from National Science Foundation Grants, CTS-9422432 and CTS-9803734, Office of Naval Research Grant N00014-1-0815, and the Air Force Office of Scientific Research, Grant No. F49620-00-1-0009.

IX. List of References

[1]Rockwell, D. and Naudascher, E., "Review - Self-Sustaining Oscillations of Flow Past Cavities", *Transactions of the ASME, Journal of Fluids Engineering*, Vol. 100, June, 1978, pp. 152-165.

[2]Rockwell, D. and Naudascher, E., "Self-Sustained Oscillations of Impinging Free Shear Layers", *Annual Review of Fluid Mechanics*, Vol. 11, 1979, pp. 67-94.

[3]Rockwell, D., "Invited Lecture: Oscillations of Impinging Shear Layers", *AIAA Journal*, Vol. 21, No. 5, 1983, pp. 645-664.

[4]Howe, M. S., "Edge, Cavity, and Aperture Tones at Very Low Mach Numbers", *Journal of Fluid Mechanics*, Vol. 33, 1997, pp. 61-84.

[5]Rockwell, D., "Vortex-Body Interactions", *Annual Review of Fluid Mechanics*, Vol. 30, 1998, pp. 199-229.

[6]Rockwell, D., "Prediction of Oscillation Frequencies Due to Unstable Flow Past Cavities", Transactions of the ASME, *Journal of Fluids Engineering*, Vol. 99, June, 1977, pp. 294-300.

[7]Sarohia, V., "Experimental Investigation of Oscillations in Flows Over Shallow Cavities", *AIAA Journal*, Vol. 15, No. 7, July, 1977, pp. 984-991.

[8]Knisely, C. and Rockwell, D., "Self-Sustained Low-Frequency Components in an Impinging Shear Layer", *Journal of Fluid Mechanics*, Vol. 116, 1982, pp. 157-186.

[9]Ghaddar, N. K., Korczak, K. Z., Mikic, B. B. and Patera, A. T., "Numerical Investigation of Incompressible Flow in Grooved Channels. Part 1. Stability and Self-Sustained Oscillations", *Journal of Fluid Mechanics*, Vol. 163, 1986, pp. 99-127.

[10]Najm, H. N. and Ghoniem, A. F., "Numerical Simulation of the Convective Instability in a Dump Combustor", *AIAA Journal*, Vol. 29, No. 6, June, 1991, pp. 911-919.

[11]Pereira, J. C. F. and Sousa, J. M. M., "Finite Volume Calculations of Self-Sustained Oscillations in a Grooved Channel", *Journal of Computational Physics*, Vol. 106, 1993, pp. 19-29.

[12]Pereira, J. C. F. and Sousa, J. M. M., "Experimental and Numerical Investigation of Flow Oscillations in a Rectangular Cavity", *Transactions of the ASME, Journal of Fluids Engineering*, Vol. 117, March, 1995, pp. 68-74.

[13]Takakura, Y., Higashino, F., Yoshizawa, T. and Ogawa, S., "Numerical Study on Unsteady Supersonic Cavity Flows", AIAA Paper 96-2092, 27th AIAA Fluid Dynamics Conference, June 17-20, 1996, New Orleans, LA.

[14]Ziada, S. and Rockwell, D., "Vortex-Leading Edge Interaction", *Journal of Fluid Mechanics*, Vol. 118, 1982a, pp. 79-107.

[15]Ziada, S. and Rockwell, D., "Oscillations of an Unstable Mixing Layer Impinging Upon a Wedge", *Journal of Fluid Mechanics*, Vol. 124, 1982b, pp. 307-334.

[16]Tang, Y.-P. and Rockwell, D., "Instantaneous Pressure Fields at a Corner Associated with Vortex Impingement", *Journal of Fluid Mechanics*, Vol. 126, 1983, pp. 187-204.

[17]Gursul, I. And Rockwell, D., "Vortex Street Impinging Upon and Elliptical Leading-Edge", *Journal of Fluid Mechanics*, Vol. 211, 1990, pp. 211-242.

[18]Gursul, I. and Rockwell, D., "Effect of Concentration of Vortices on Streakline Patterns", *Experiments in Fluids*, Vol. 10, 1991, pp. 294-296.

[19]Gursul, I., Lusseyran, D., and Rockwell, D., "On Interpretation of Flow Visualization of Unsteady Shear Flows", *Experiments in Fluids*, Vol. 9, 1990, pp. 257-266.

[20]Graf, H. R. and Durgin, W. W., "Measurement of a Non-Steady Flow Field in the Opening of a Resonating Cavity Excited by Grazing Flow", *Journal of Fluids and Structures*, Vol. 7, 1993, pp. 387-400.

[21]Woolley, J. P. and Karamcheti, K., "Role of Jet Stability in Edge-Tone Generation", *AIAA Journal*, Vol. 12, November, 1974, pp. 1457-1458.

[22]Schachenmann, A. and Rockwell, D., "Self-Generation of Organized Waves in an Impinging Turbulent Jet at Low Mach Numbers", *Journal of Fluid Mechanics*, Vol. 117, 1982, pp. 425-441.

[23]Gharib, M. and Roshko, A., "The Effect of Flow Oscillations on Cavity Drag", *Journal of Fluid Mechanics*, Vol. 177, 1987, pp. 501-530.

[24]Johansen, J. B. and Smith, C. R., "The Effects of Cylindrical Surface Modifications on Turbulent Boundary Layers", Report FM-3, Department of Mechanical Engineering and Mechanics, Lehigh University, Bethlehem, PA., April, 1983.

[25]Rockwell, D. and Lin, J.-C., "Experimental data for computational fluid dynamic simulations of fluid oscillators: cavity flow. Volumes 1 and 2", Fluid Mechanics Laboratories Report R01, 1996, Department of Mechanical Engineering and Mechanics, Lehigh University, Bethlehem, Pennsylvania, U.S.A., 1996.

[26]Rockwell, D., Magness, C., Towfighi, J., Akin, O. and Corcoran, T., "High Image-Density Particle Image Velocimetry Using Laser Scanning Techniques", *Experiments in Fluids*, Vol. 14, 1993, pp. 181-192.

[27]Lin, J.-C. and Rockwell, D., "Cinema PIV and Its Application to Vortex-Surface Interactions", Proceedings of ASME Fluids Engineering Division Summer Meeting, Manuscript No. FEDSM 98-5720, June 21-25, 1998, Washington, D.C.

[28]Landreth, C. C. and Adrian, R. J., "Measurement and Refinement of Velocity Data Using High-Image-Density Analysis in Particle Image Velocimetry", Applications of Laser Anemometry to Fluid Mechanics (eds., R. Adrian, T. Asanuma, D. Durão, F. Durst, and J. Whitelaw), Springer-Verlag, NY, 1989, pp. 484-497.

[29]Liu, Z.-C., Landreth, C. C., Adrian, R. J. and Hanratty, T. J., "High Resolution Measurement of Turbulent Structure in a Channel with particle Image Velocimetry", *Experiments in Fluids*, Vol. 10, 1991, pp. 301-312.

[30]Westerweel, J., Draad, A. A., van der Hoevern, J. G. Th. and van Oord, J., "Measurement of Fully-Developed Turbulent Pipe Flow with Digital Particle Image Velocimetry", *Experiments in Fluids*, Vol. 20, 1996, pp. 165-177.

[31]Klebanoff, P. S., "Characteristics of Turbulence in a Boundary Layer with Zero Pressure Gradient", NACA Report 1247, 1995.

[32]Schlichting, H., Boundary-Layer Theory (7th Edition), McGraw-Hill Book Company, NY, 1979, p. 567.

[33]Bradshaw, P., An Introduction to Turbulence and Its Measurement, Pergaman Press, NY, 1971.

[34]Landreth, C. C. and Adrian, R. J., "Impingement of a Low Reynolds Number Turbulent Circular Jet onto a Flat Plate at Normal Incidence", *Experiments in Fluids*, Vol. 9, 1990, pp. 74-84.

[35]Fiedler, H. E., Dziomba, B., Mensing, P. and Rösgen, T., "Initiation, Evolution, and Global Consequences of Coherent Structures in Turbulent Shear Flows", Lecture Notes in Physics, Vol. 136, Springer-Verlag, 1981, pp. 219-251.

[36]Hussain, A. K. M. F., "Coherent Structures and Studies of Perturbed and Unperturbed Jets", Role for Coherent Structures in Modelling Turbulence and Mixing (ed. J. Jimenez), Lecture Notes in Physics, No. 136, Springer Verlag, pp. 252-291.

X. List of Figures

Figure 1: Principle elements of self-sustaining oscillations of turbulent flow past a cavity.

Figure 2: Overview of cavity test section located within main test section of water channel.

Figure 3: Representative image of instantaneous velocity field of turbulent boundary layer viewed in a reference frame moving at 0.8 U_∞; and variation of the mean $\bar{u}$ and fluctuating u_{rms} and v_{rms} velocities and the velocity correlation $-\overline{u'v'}$ across the boundary layer, all normalized by the freestream velocity U_∞.

Figure 4: Spectra of velocity fluctuations in the turbulent boundary layer, as obtained from PIV data. The spectra were evaluated at a distance of 0.91 inches from the wall corresponding to 0.5δ, where $\delta = \delta_{995}$ is the boundary layer thickness.

Figure 5: Time trace of pressure at impingement corner acquired simultaneously with the cinema PIV series. The framing rate of the cinema sequence is ten frames/sec and the first image of cinema sequence corresponds to t = 0.1 sec in the trace of pressure. Subsequent images correspond to t = 0.2, 0.3 sec and so on in pressure trace.

Figure 6a: Instantaneous distributions of velocity and vorticity during cavity oscillation in a mode corresponding approximately to the fundamental frequency β of the cavity shear layer. At the instant shown, the pressure at the corner has its maximum negative value.

Figure 6b: Instantaneous distributions of velocity and vorticity during cavity oscillation in a mode corresponding approximately to the fundamental frequency β of the cavity shear layer. At the instant shown, the pressure at the corner has its maximum negative value. The velocity field is shown in reference frames moving at 0.25 and 0.50 U_∞, in which U_∞ is the freestream velocity.

Figure 7: Instantaneous distributions of velocity and vorticity during cavity oscillation in a mode corresponding approximately to the fundamental frequency β of the cavity shear layer. At the instant shown, the pressure at the corner has its maximum positive value.

Figure 8: Instantaneous distributions of velocity and vorticity during cavity oscillation in a mode corresponding approximately to the subharmonic frequency $\beta/2$ of the most amplified component β of the cavity shear layer. At the instant shown, the pressure at the corner has its maximum negative value. (Images represent transformed version of those of Lin and Rockwell[27].)

Figure 9: Instantaneous distributions of velocity and vorticity during cavity oscillation in a mode corresponding approximately to the subharmonic frequency $\beta/2$ of the most amplified, fundamental component β of the cavity shear layer. At the instant shown, the pressure at the corner has its maximum positive value.

Figure 10: Comparison of representative instantaneous velocity field in cavity [top image] with instantaneous velocity field calculated using a large-eddy simulation technique by Takakura et al. (1996) [bottom image]. For the calculated flow, the flow region exterior to the cavity is supersonic.

Figure 11: Comparison of representative instantaneous vorticity distribution in the oscillating shear layer [top image] with the instantaneous vorticity distribution numerically calculated by Pereira and Sousa (1995) [bottom image]. For numerically-calculated images, solid lines are vorticity contours and dashed lines are instantaneous streamlines.

Figure 12: Distributions of averaged velocity $< V >$ based on cinema sequence [top image] and randomly-acquired sequence [bottom image].

Figure 13: Contours of constant averaged vorticity $< \omega >$ corresponding to cinema sequence [top image] and randomly-acquired sequence [bottom image] of PIV images. Minimum positive and negative contour levels correspond to ± 2 sec^{-1} and incremental level to 2 sec^{-1}.

Figure 14: Contours of constant Reynolds stress normalized by the free-stream velocity $< u'v' > / U_\infty^2$ for cinema sequence [top image] and randomly-acquired sequence [bottom image] of PIV images. Minimum contour level corresponds to 0.0005 and incremental level is 0.0005.

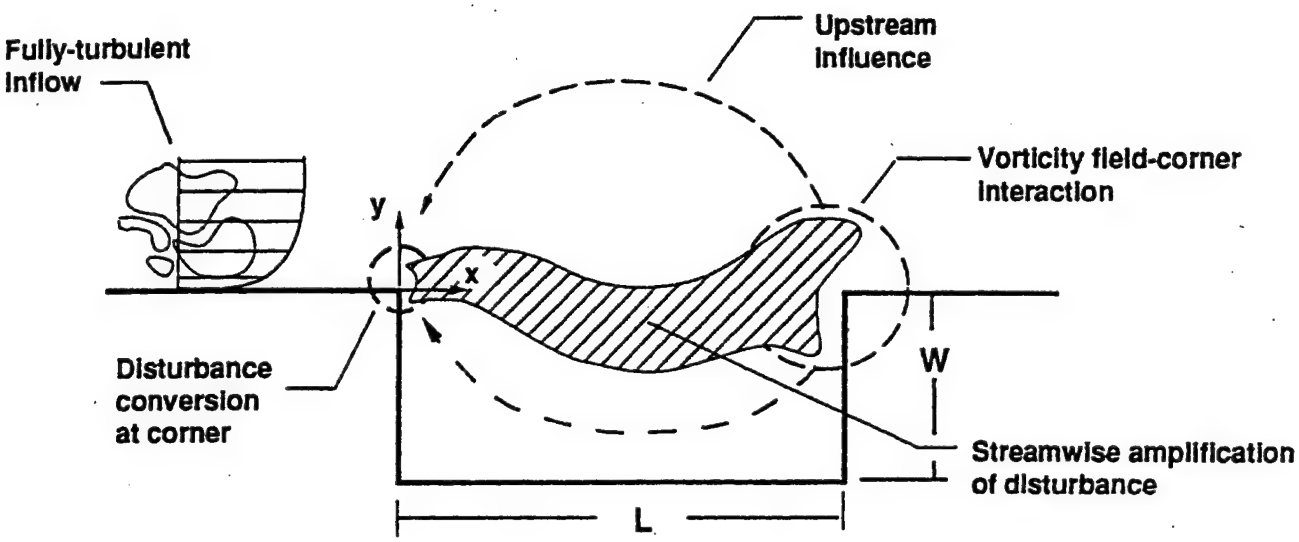

Figure 1: Principal elements of self-sustaining oscillations of turbulent flow past a cavity.

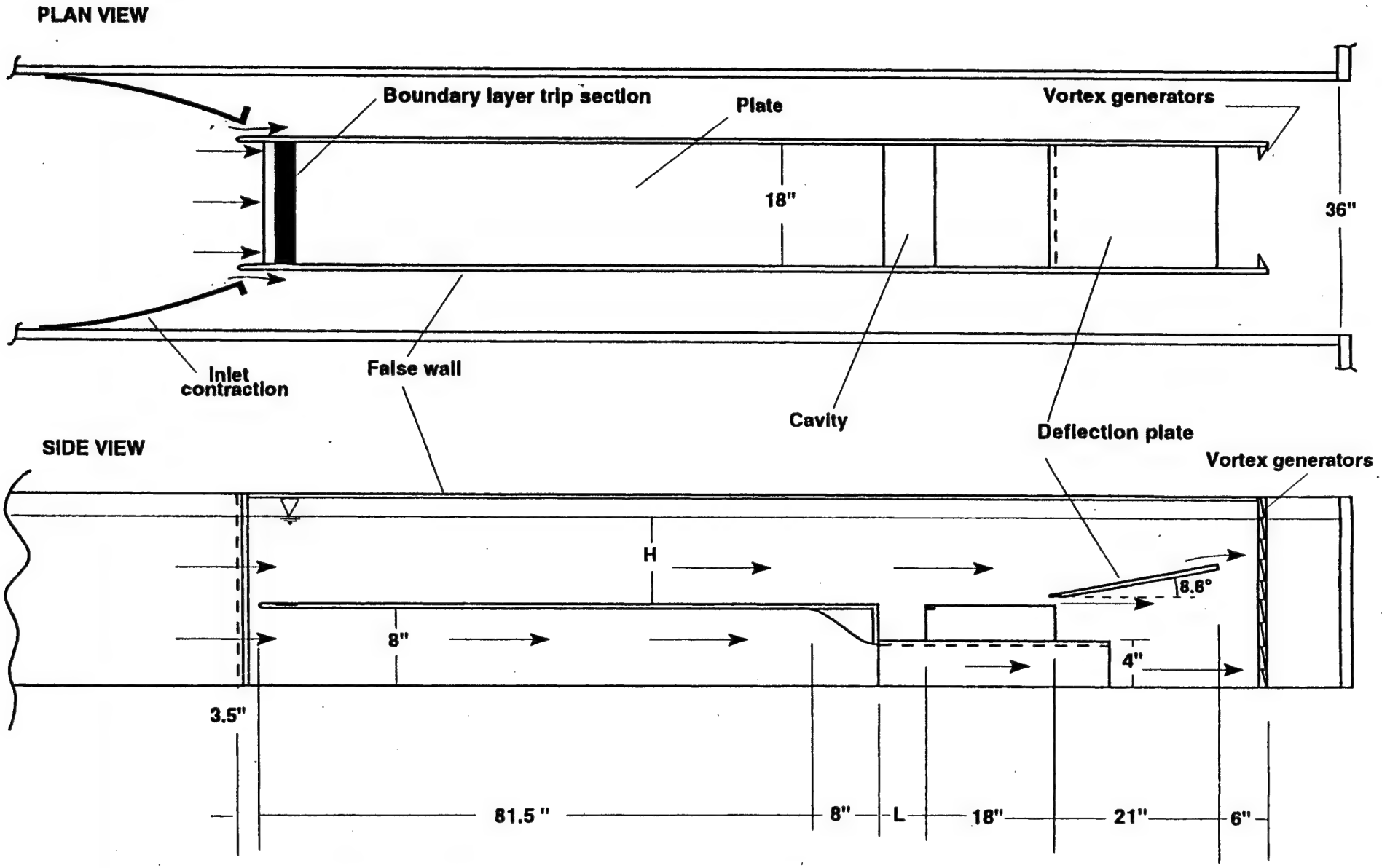

Figure 2: Overview of cavity test section located within main test section of water channel.

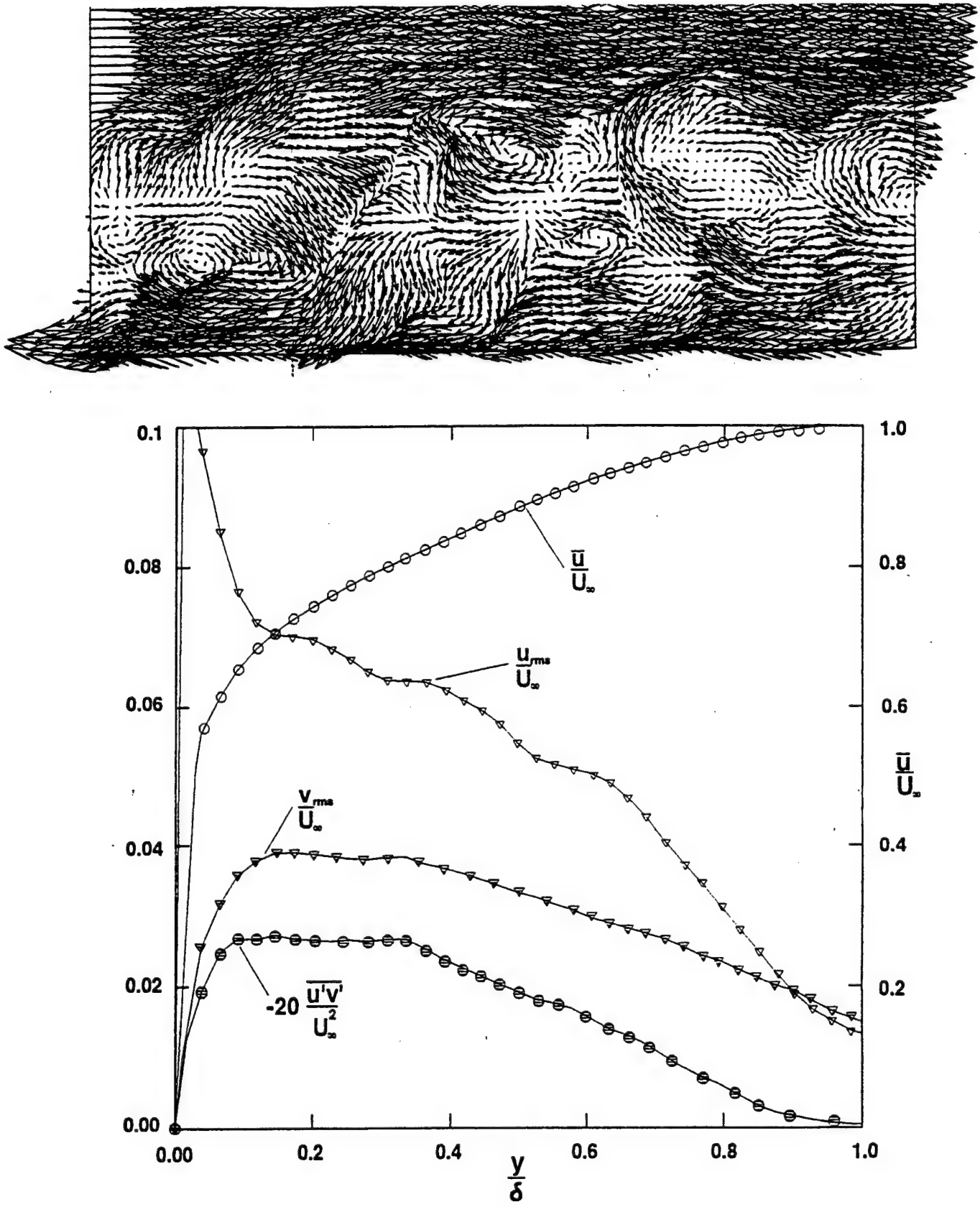

Figure 3: Representative image of instantaneous velocity field of turbulent boundary layer viewed in a reference frame moving at 0.8 U_∞; and variation of the mean $\bar{u}$ and fluctuating u_{rms} and v_{rms} velocities and the velocity correlation $-\overline{u'v'}$ across the boundary layer, all normalized by the freestream velocity U_∞.

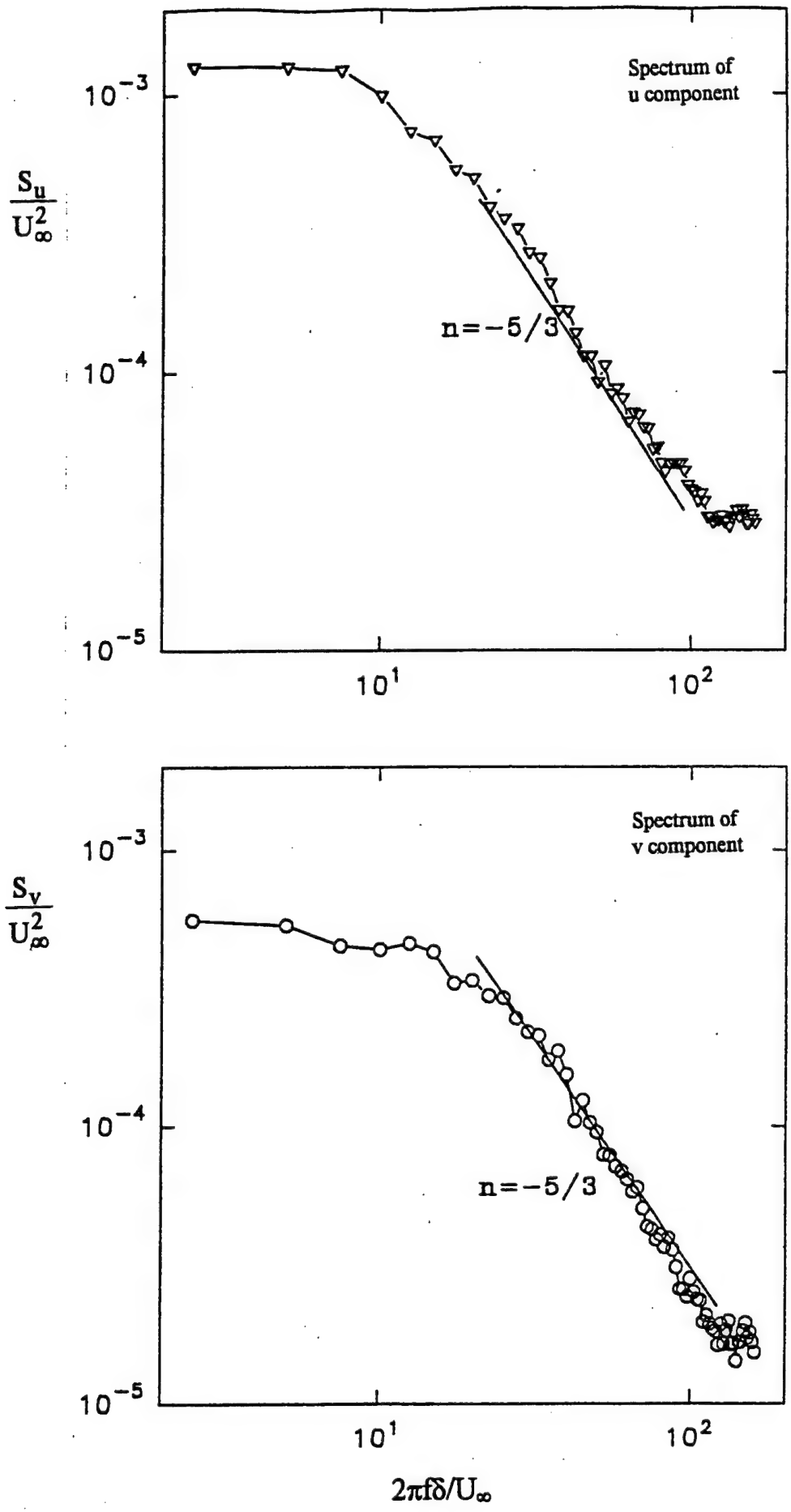

Figure 4: Spectra of velocity fluctuations in the turbulent boundary layer, as obtained from PIV data. The spectra were evaluated at a distance of 0.91 inches from the wall corresponding to 0.5δ, where $\delta = \delta_{995}$ is the boundary layer thickness.

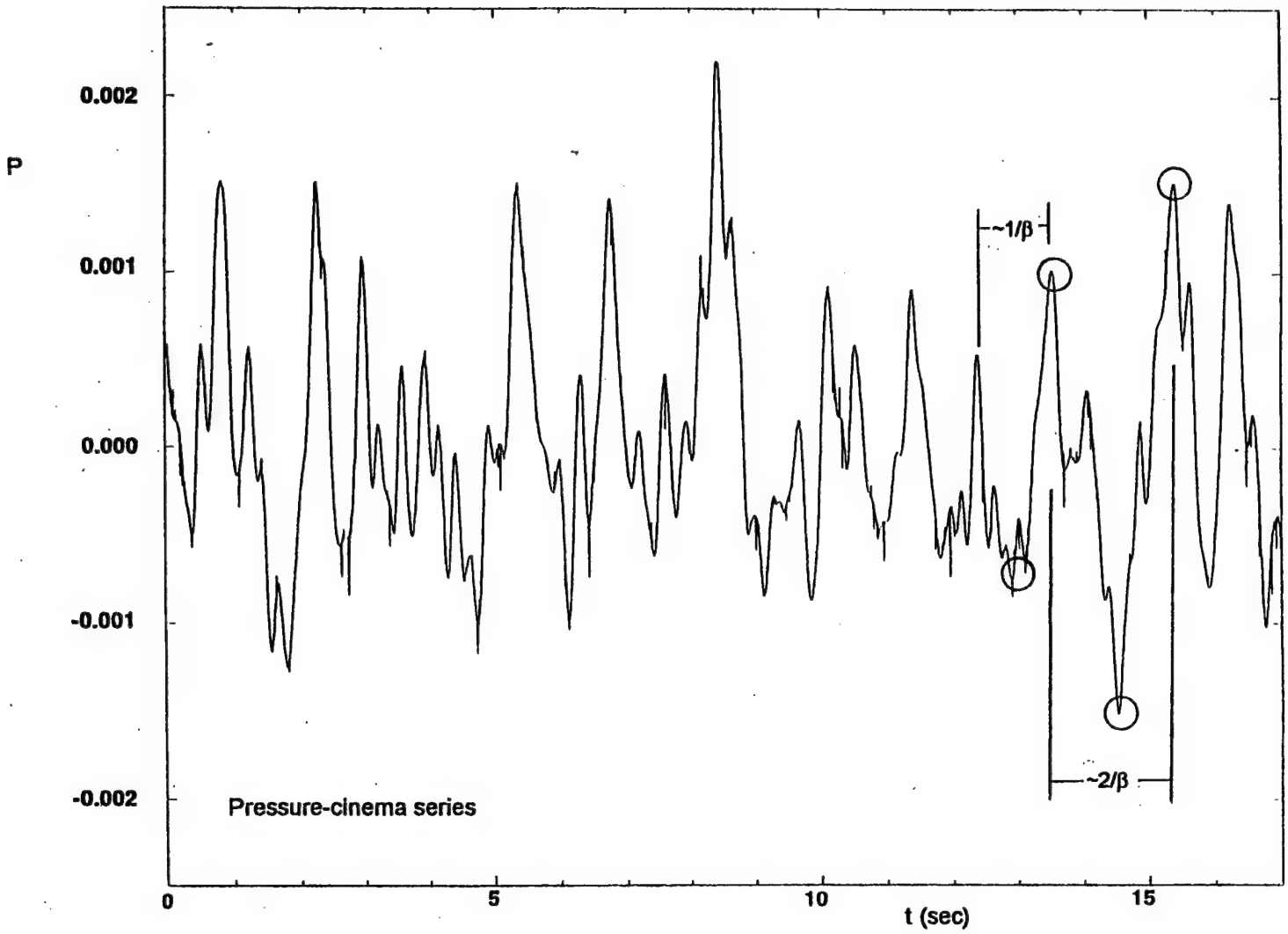

Figure 5: Time trace of pressure at impingement corner acquired simultaneously with the cinema PIV series. The framing rate of the cinema sequence is ten frames/sec and the first image of cinema sequence corresponds to t = 0.1 sec in the trace of pressure. Subsequent images correspond to t = 0.2, 0.3 sec and so on in pressure trace.

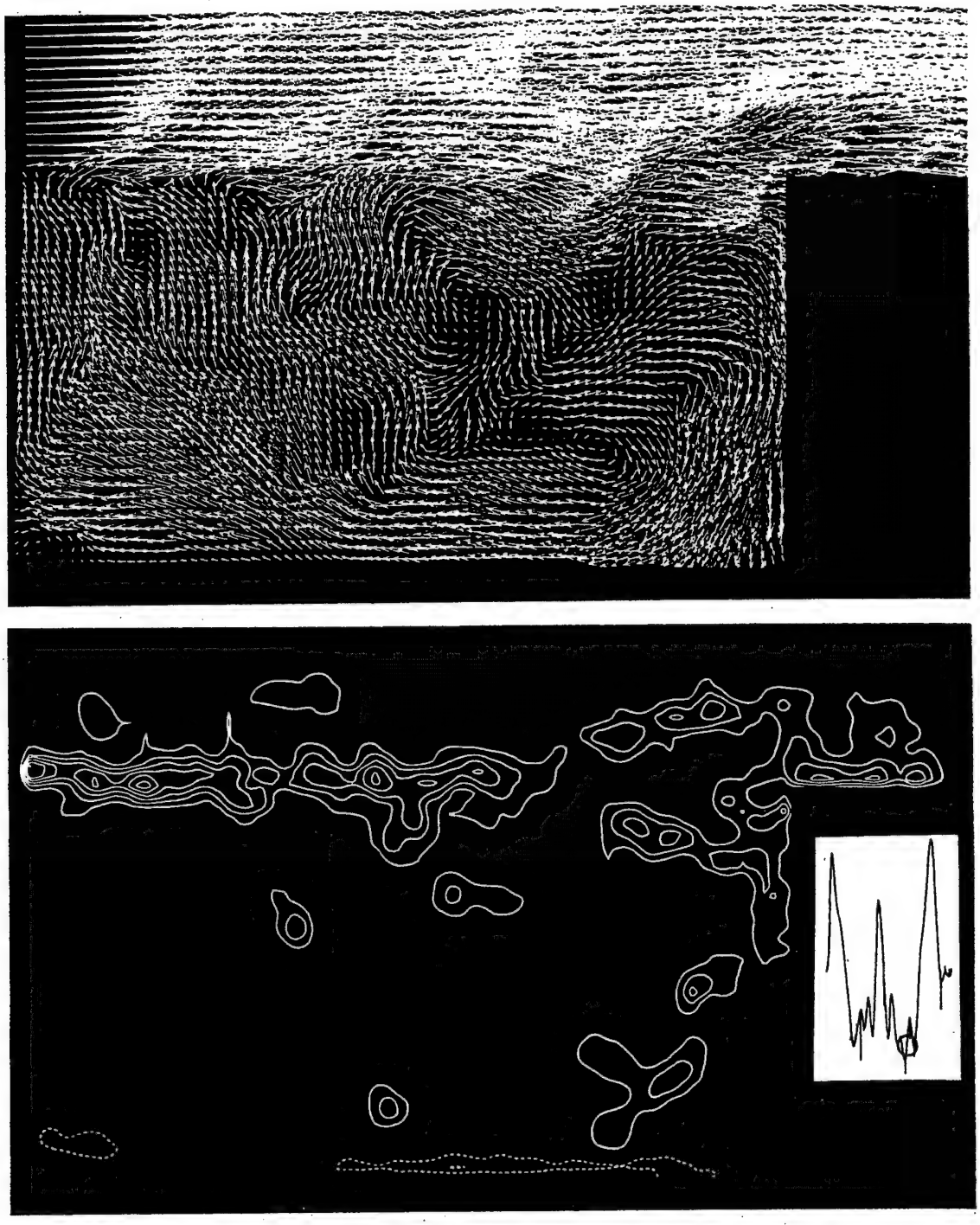

Figure 6a: Instantaneous distributions of velocity and vorticity during cavity oscillation in a mode corresponding approximately to the fundamental frequency β of the cavity shear layer. At the instant shown, the pressure at the corner has its maximum negative value.

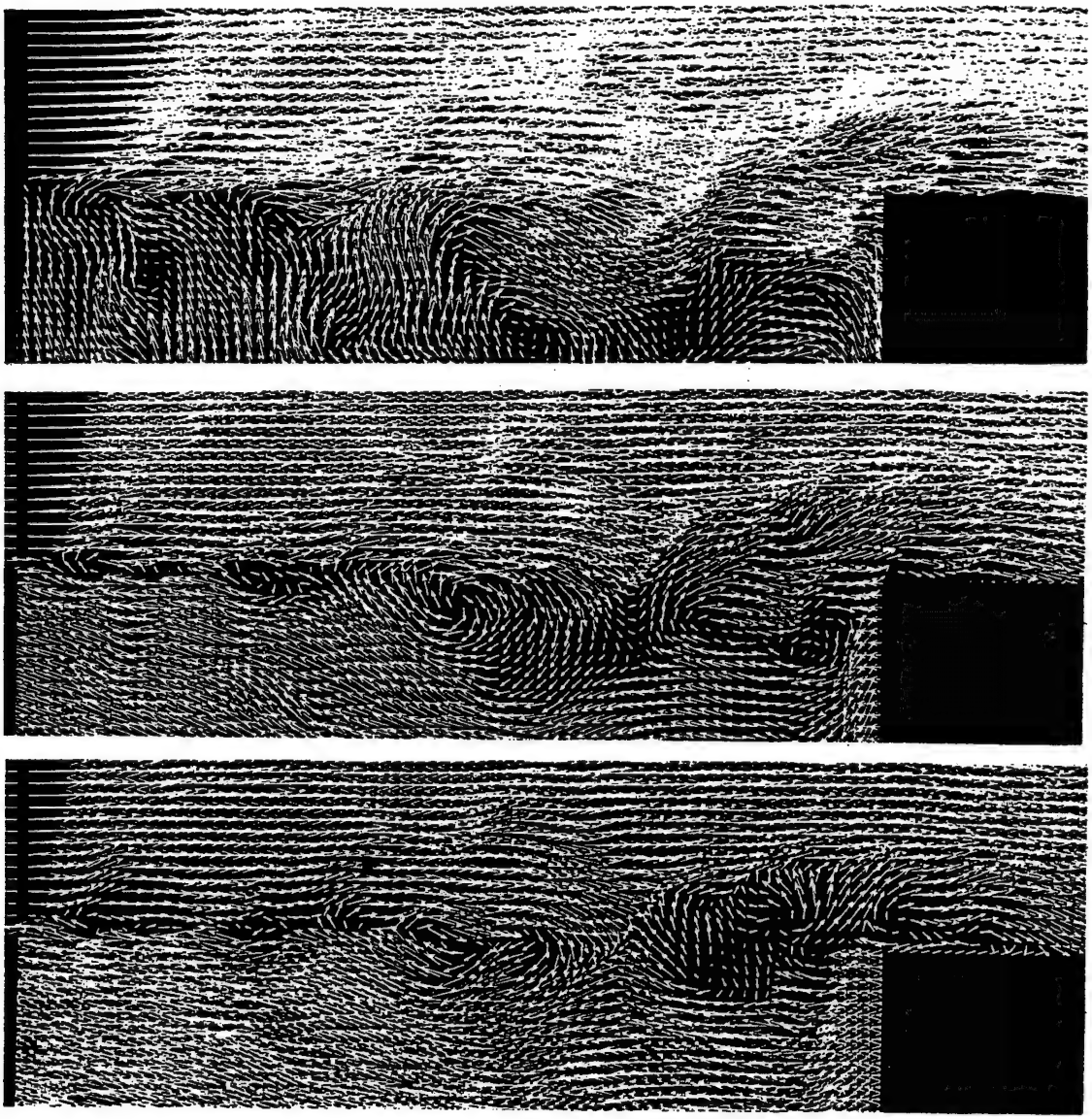

Figure 6b: Instantaneous distributions of velocity and vorticity during cavity oscillation in a mode corresponding approximately to the fundamental frequency β of the cavity shear layer. At the instant shown, the pressure at the corner has its maximum negative value. The velocity field is shown in reference frames moving at 0.25 and 0.50 U_∞, in which U_∞ is the freestream velocity.

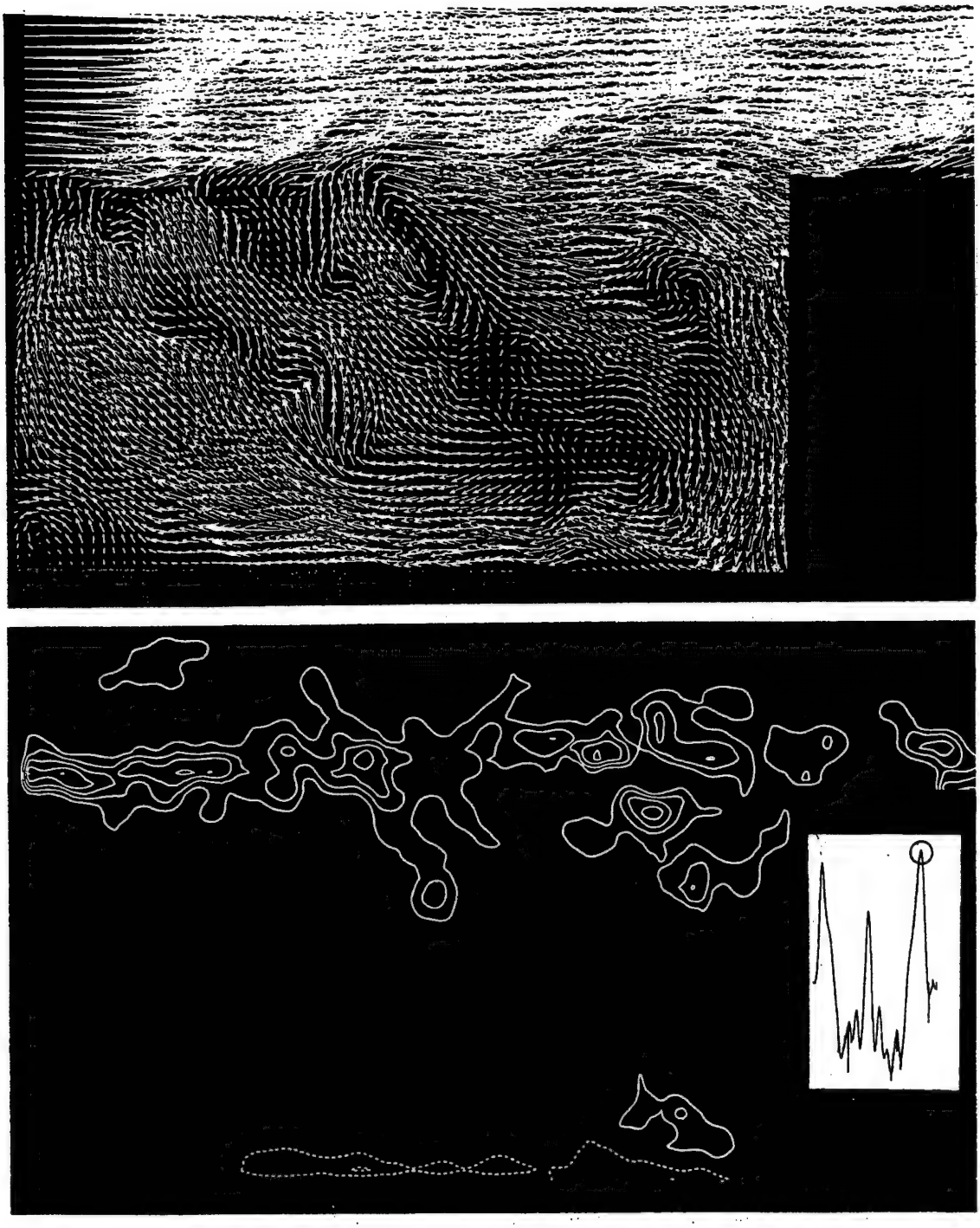

Figure 7: Instantaneous distributions of velocity and vorticity during cavity oscillation in a mode corresponding approximately to the fundamental frequency β of the cavity shear layer. At the instant shown, the pressure at the corner has its maximum positive value.

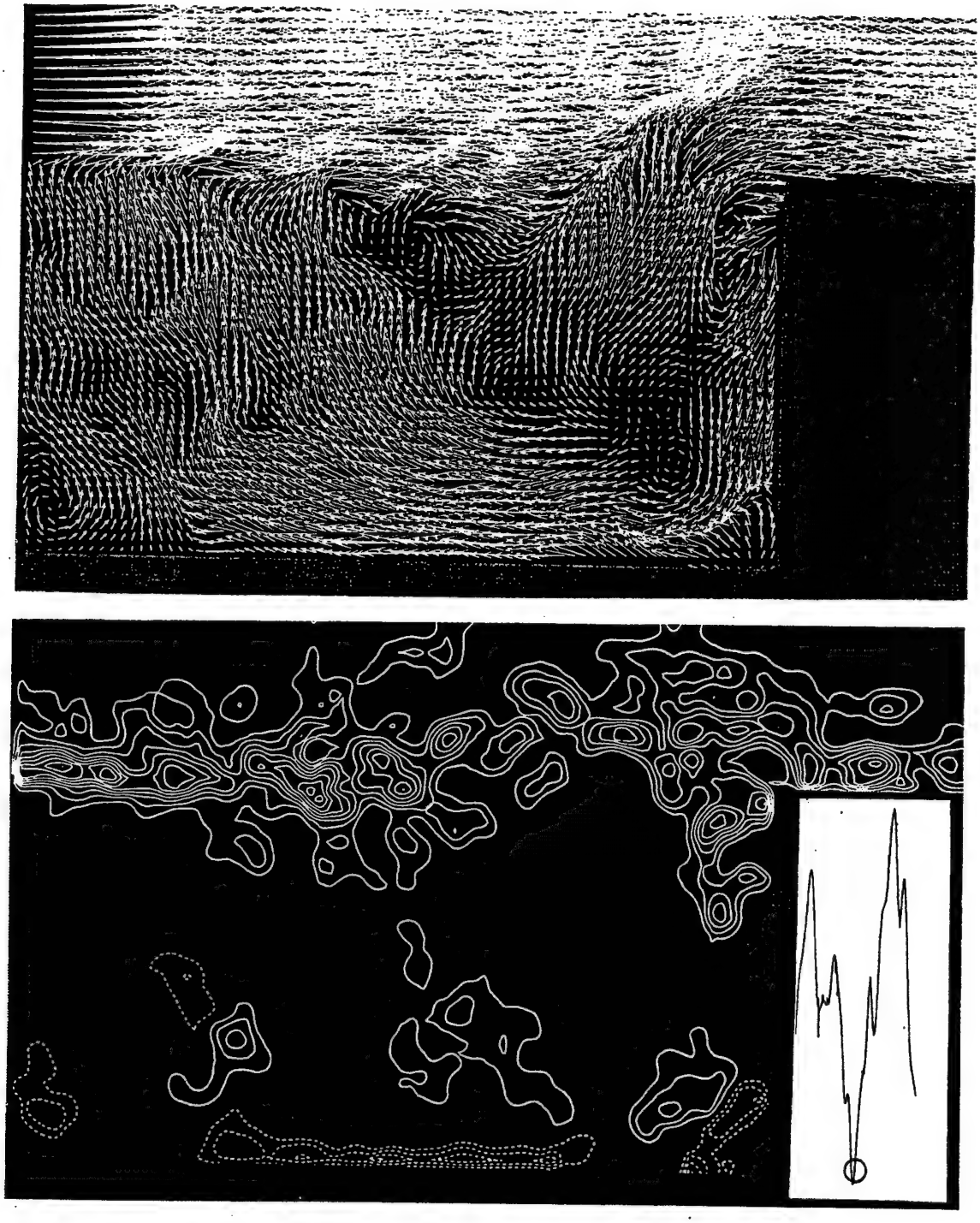

Figure 8: Instantaneous distributions of velocity and vorticity during cavity oscillation in a mode corresponding approximately to the subharmonic frequency $\beta/2$ of the most amplified component β of the cavity shear layer. At the instant shown, the pressure at the corner has its maximum negative value. (Images represent transformed version of those of Lin and Rockwell[27].)

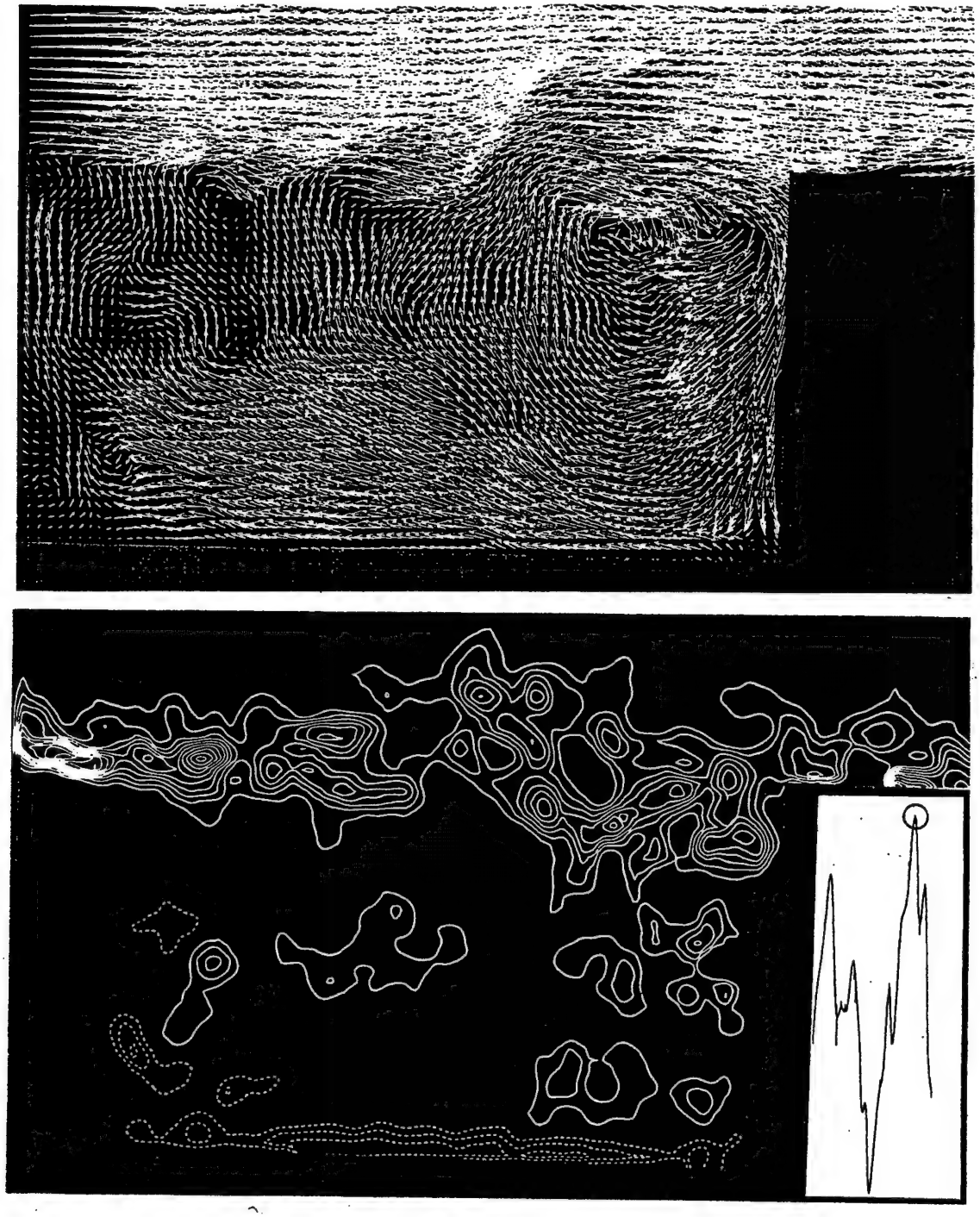

Figure 9: Instantaneous distributions of velocity and vorticity during cavity oscillation in a mode corresponding approximately to the subharmonic frequency $\beta/2$ of the most amplified, fundamental component β of the cavity shear layer. At the instant shown, the pressure at the corner has its maximum positive value.

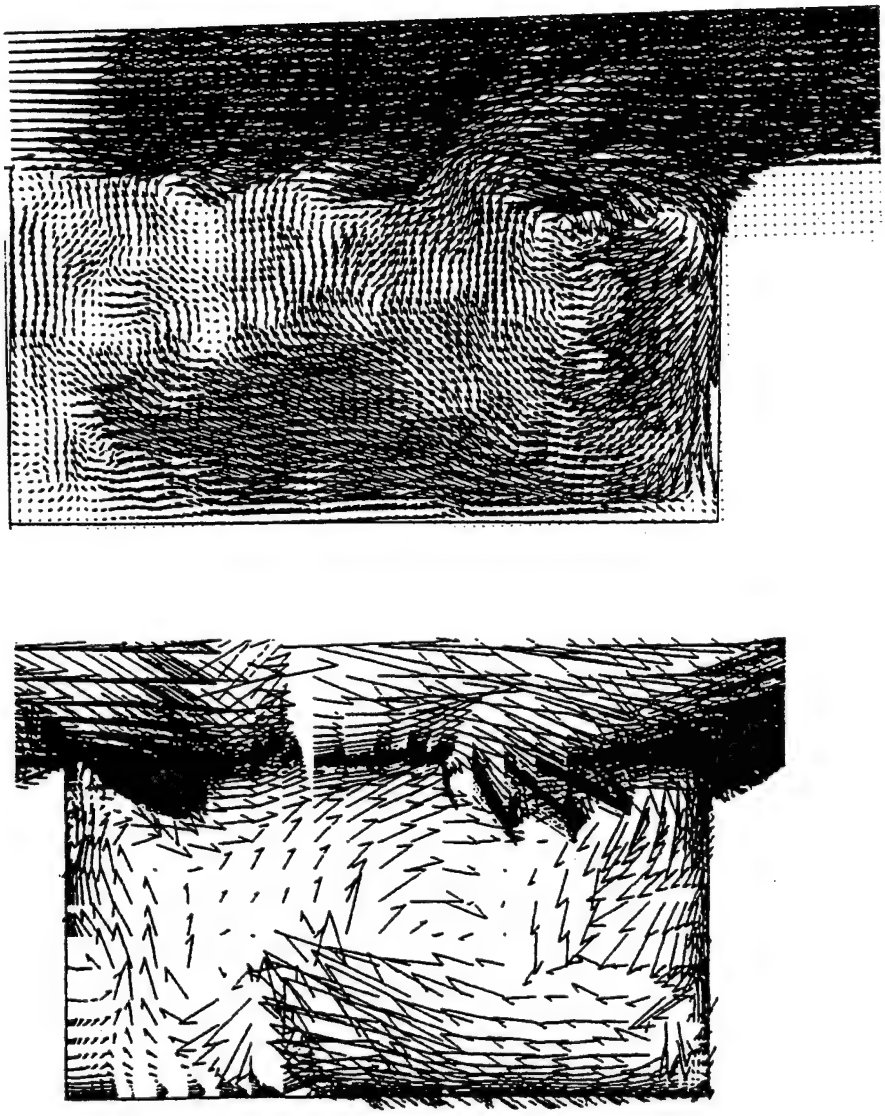

Figure 10: Comparison of representative instantaneous velocity field in cavity [top image] with instantaneous velocity field calculated using a large-eddy simulation technique by Takakura et al. (1996) [bottom image]. For the calculated flow, the flow region exterior to the cavity is supersonic.

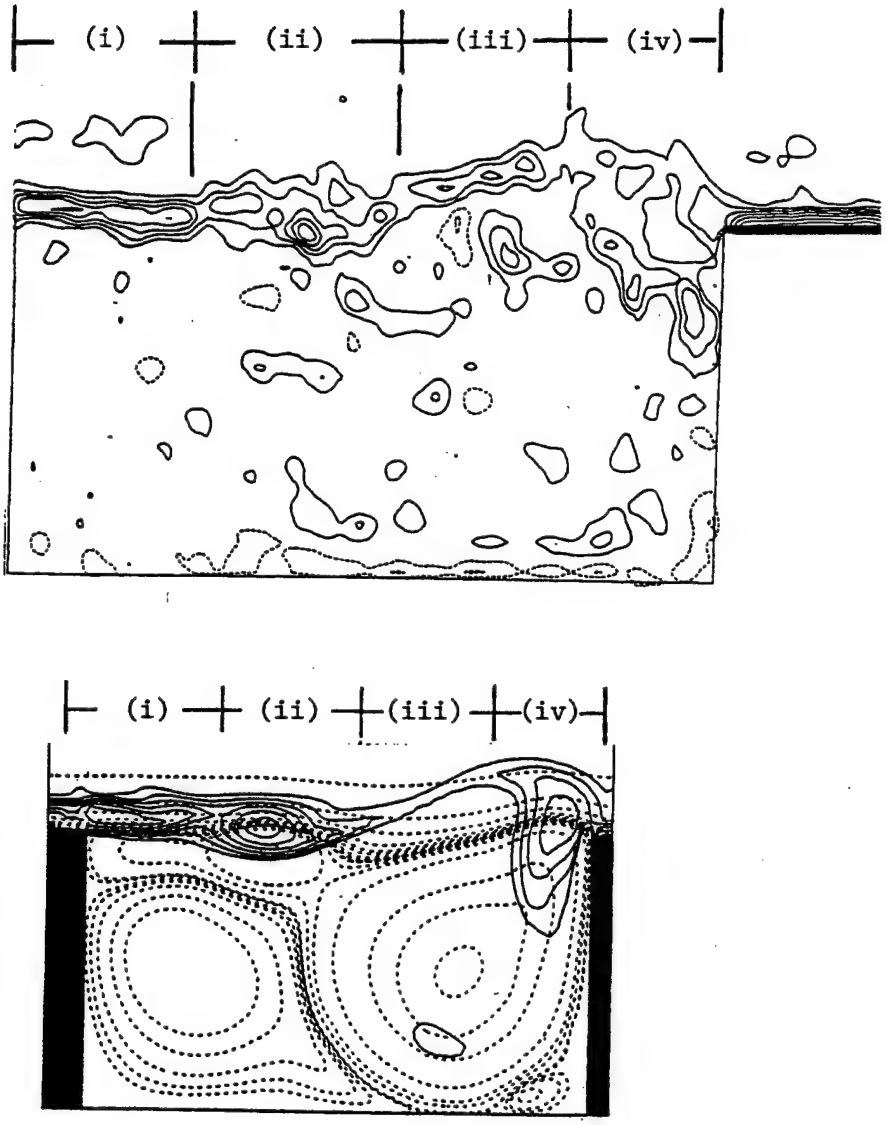

Figure 11: Comparison of representative instantaneous vorticity distribution in the oscillating shear layer [top image] with the instantaneous vorticity distribution numerically calculated by Pereira and Sousa (1995) [bottom image]. For numerically-calculated images, solid lines are vorticity contours and dashed lines are instantaneous streamlines.

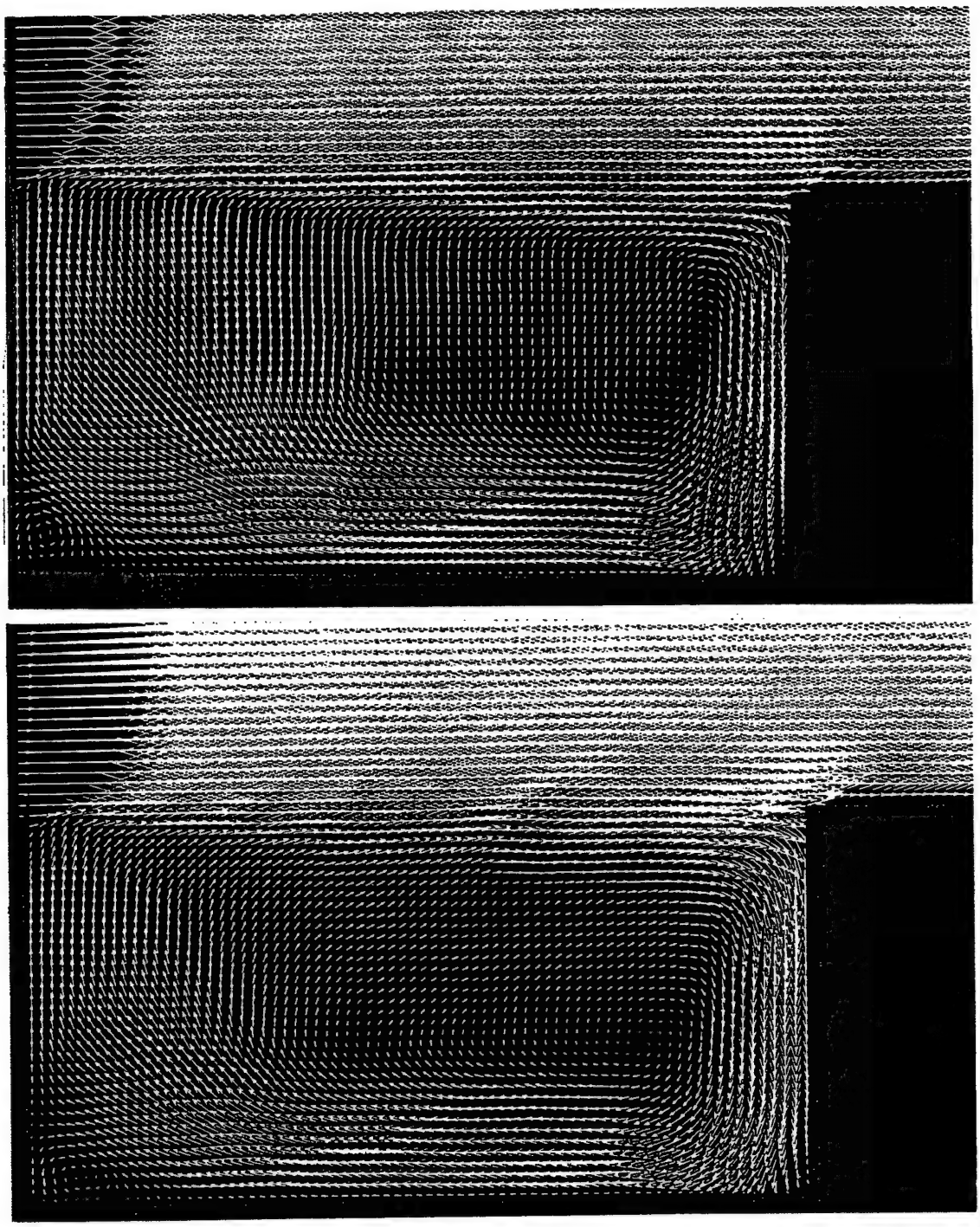

Figure 12: Distributions of averaged velocity $< V >$ based on cinema sequence [top image] and randomly-acquired sequence [bottom image].

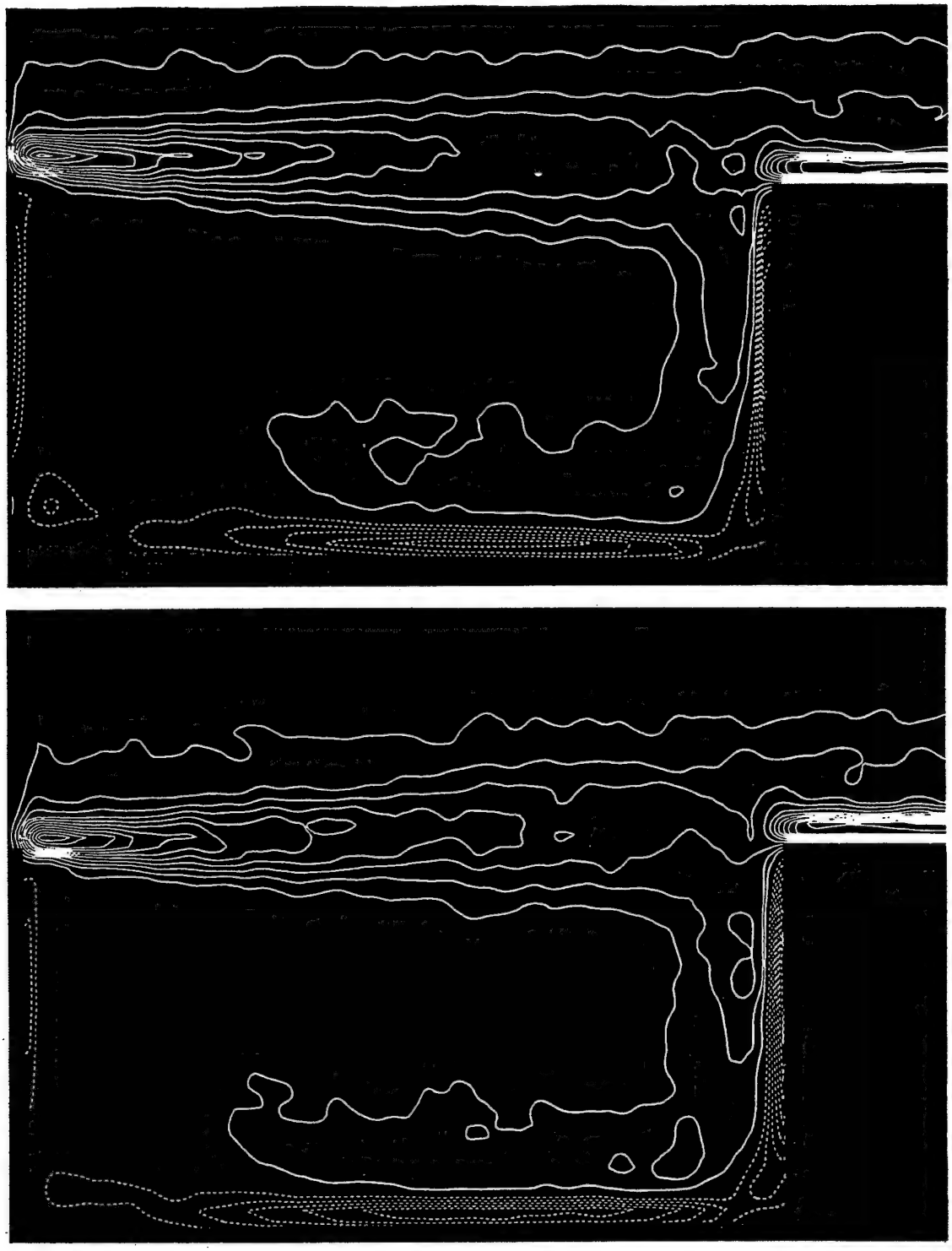

Figure 13: Contours of constant averaged vorticity $<\omega>$ corresponding to cinema sequence [top image] and randomly-acquired sequence [bottom image] of PIV images. Minimum positive and negative contour levels correspond to ± 2 sec^{-1} and incremental level to 2 sec^{-1}.

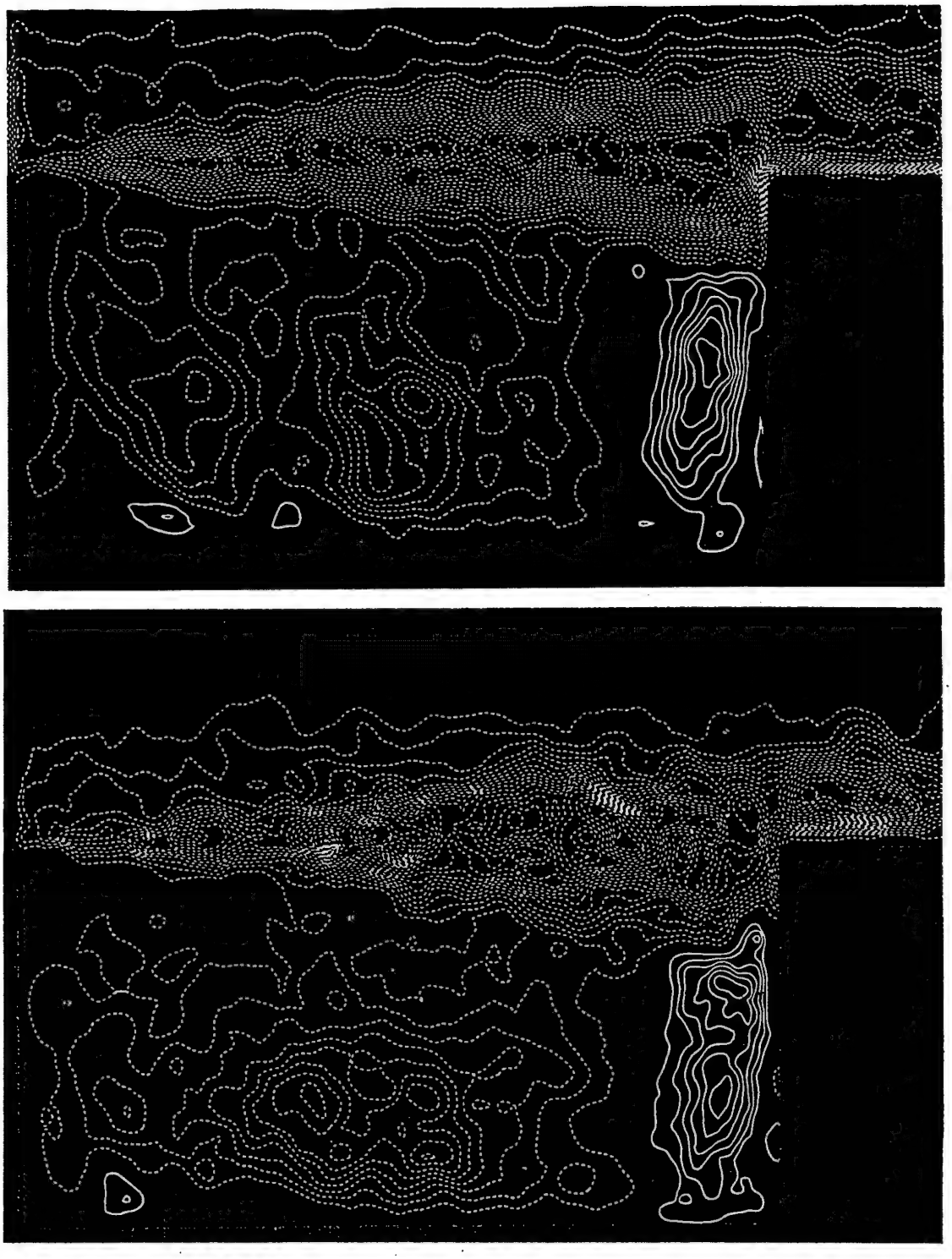

Figure 14: Contours of constant Reynolds stress normalized by the free-stream velocity $<u'v'>/U_\infty^2$ for cinema sequence [top image] and randomly-acquired sequence [bottom image] of PIV images. Minimum contour level corresponds to 0.0005 and incremental level is 0.0005.

APPENDIX J

Lin Two Cylr FIN 102301

FLOW PAST TWO CYLINDERS IN TANDEM:

INSTANTANEOUS AND AVERAGED FLOW STRUCTURE*

by

J.-C. LIN, Y. YANG† AND D. ROCKWELL

Department of Mechanical Engineering and Mechanics, 354 Packard Laboratory,

19 Memorial Drive West, Lehigh University, Bethlehem, PA 18015, U.S.A.

***Lin, J.-C., Yang, Y. and Rockwell, D. "Flow Past Two Cylinders in Tandem: Instantaneous and Averaged Flow Structure, *Journal of Fluids and Structures* in press.**

Number of pages: 35
Number of figures: 7
Number of manuscript copies submitted: 3

---

† On leave from Beijing Institute of Aerodynamics (BIA).

Running Headline: Cylinders in Tandem

Corresponding author:

Professor Donald Rockwell
Department of Mechanical Engineering and Mechanics
354 Packard Laboratory
19 Memorial Drive West
Lehigh University
Bethlehem, PA 18015 U.S.A.
Telephone: 610-758-4107
Fax: 610-758-4041
Email: dor0@lehigh.edu

ABSTRACT

A technique of high-image-density particle image velocimetry is employed to characterize the instantaneous and averaged patterns of velocity, vorticity and Reynolds stress due to flow past two cylinders in tandem. These features of the flow patterns are characterized in the gap region as a function of the distance between the cylinders. In turn, they are related to the patterns in the near-wake of the two-cylinder system.

Along the gap between the cylinders, small-scale concentrations of vorticity are formed in the separated shear layers. These concentrations buffet the surface boundary layer on the downstream cylinder, and thereby influence the eventual shedding of large-scale vortices. Within the gap, the instantaneous structure of the recirculation zones can exhibit both symmetrical and asymmetrical patterns.

In the near-wake of the downstream cylinder, the form of the vortex shedding, as well as the averaged patterns of the flow structure, are substantially altered, relative to the case of a single cylinder. The width of the near-wake, as represented by averaged patterns of vorticity, is substantially narrower and the magnitudes of the peak Reynolds stress are significantly attenuated. On the other hand, if the gap region is sufficiently large such that Kármán-like vortices form between the cylinders, the near-wake of the downstream cylinder shows distinctive patterns, and both the wake width and the magnitude of the Reynolds stresses become larger, relative to those at smaller gap width.

1. INTRODUCTION

Flow past two cylinders in tandem, whereby one cylinder is located downstream of the other, represents an important and remarkably complex flow configuration. In essence, the wake from the downstream cylinder is a strong function of both the steady and unsteady vorticity field incident upon it. The nature of this vorticity field is, of course, directly related to the gap between the tandem cylinders. From an experimental standpoint, the primary emphasis has been on determination of the time-averaged forces and surface pressures, most notably the base pressure, occasionally in conjunction with qualitative flow visualization. Using these approaches, it has been possible to gain insight into the cylinder loading and the overall flow characteristics. Zdravkovich (1977, 1982, 1987) provided an overview of loading characteristics and flow patterns. Zdravkovich & Pridden (1977) emphasized the discontinuous jump in base pressure at a critical spacing of the cylinders $L/D = 3.5$, in which L is the distance between centers of the cylinders and D is the cylinder diameter. Classifications of the qualitative flow regimes of the tandem cylinder arrangement are provided by Igarashi (1981, 1984) and Zdravkovich (1982). In essence, below a threshold value of L/D, referred to in the literature as the critical spacing, no vortex shedding occurs in the gap region between the cylinders, whereas above it, vortex shedding occurs from both cylinders. This threshold appears to be a function of Reynolds number. Qualitative flow visualization of the gap and near-wake region of the two-cylinder system is provided by Ishigai & Nishikawa (1972), Ljungkrona *et al.* (1991), Ljungkrona & Sunden (1993), and Wu *et al.* (1994). Ljungkrona *et al.* (1991, 1993) clearly show the important influence of Reynolds number. Furthermore, Ljungkrona *et al.* (1991) addressed the influence of the free-stream turbulence, and found that the critical spacing of the cylinders decreased as turbulence

intensity increased. Ishigai & Nishikawa (1972) showed qualitative portraits of change in the gap and near-wake flow patterns as the gap spacing was varied. Wu *et al.* (1994) show hydrogen bubble images of both the quasi-two-dimensional and spanwise patterns of the flow structure and, furthermore, provide spanwise coherence distributions (via hot wire measurements) as a function of gap width.

Igarashi (1981, 1984) considered a wide parameter range of Reynolds number versus gap spacing and defined a number of flow regimes in addition to those described in the foregoing. Unstable and bistable states, as well as jumps between states, are representative of the complex phenomena that can occur in a tandem cylinder arrangement.

Distributions of root-mean-square (rms) pressure about the surface of the downstream cylinder have been measured by Arie *et al.* (1983), Igarashi (1984), Ljungkrona *et al.* (1991) and Ljungkrona & Sundén (1993). The common feature of all of these distributions of fluctuating pressure is the occurrence of a well-defined peak(s) on the forebody region of the downstream cylinder at smaller values of cylinder gap, presumably a result of the unsteadiness of the impinging shear layer. At larger values of gap spacing L/D, these peaks can become particularly large, perhaps due to the impingement of Kármán-like vortices formed in the gap region.

Other types of characterizations of the gap region have involved surface oil-flow patterns, fluctuating pressure, surface film sensor, and surface heat transfer measurements. Igarashi (1984) employed surface oil patterns to show the relationship between the reattachment line and the pressure distribution on the downstream cylinder. Arie *et al.* (1983) also determined the root-mean-square lift and drag on the downstream cylinder, which exhibited much larger values than on the upstream cylinder. Lee &

Panagakos (1997) employed surface-mounted hot film sensors to provide simultaneous records of fluctuations about the periphery of the cylinder; a number of harmonics were evident in the unsteady signals in the base region. Hiwada *et al.* (1982) pursued the relation between local heat transfer and fluctuation velocity (via a hot wire probe), and found that the overall Nusselt number was 20% to 30% higher than for a single cylinder.

Numerical simulation of the vortex patterns and steady and unsteady loading at low Reynolds number was undertaken by Stansby *et al.* (1987) and Slaouti & Stansby (1992) using a vortex method. Recent efforts, employing different types of numerical simulation, include those of Mittal *et al.* (1997) and Farrant *et al.* (2000), also at relatively low values of Reynolds number.

In the event that one or both cylinders in a tandem arrangement are elastically-mounted, the mechanisms giving rise to self-excited oscillations are particularly challenging. Chen (1985) addressed the overall response characteristics of the cylinder system and defined mechanisms of the fluid-elastic instability. Zdravkovich (1985) focused on the manner in which the instability of the two-cylinder system arose and classified the nature of the fluid-elastic response. King & Johns (1976) showed that oscillations in both the cross-flow and in-flow directions may occur. Mahir & Rockwell (1996) subjected two tandem cylinders to controlled oscillation, with a prescribed phase angle between them and classified the modulated and locked-on response of the near-wake, in conjunction with the spectra of the wake velocity fluctuations. When considering elastic oscillations of the tandem cylinder system, it is important to distinguish between vibrations associated with vortex shedding and those due to a mechanism of interference galloping. Knisely & Nakagawa (1988), Knisely & Kawagoe (1990), and Knisely *et al.* (1995) addressed a central feature, namely the phase lag, or

delay time, between the cylinder motion and the unsteady lift force acting on the downstream cylinder that underwent oscillations.

The tandem cylinder arrangement may be viewed as an idealization of an array of a large number of cylinders and, no doubt, certain of the features generic to the tandem configuration may be present, at least to a degree, in an array. Païdoussis (1982), Chen (1984, 1987), Païdoussis & Price (1988) and Weaver & Fitzpatrick (1988) determined design guidelines and undertook quasi-analytical descriptions of this intriguing class of cylinder systems. Hetz *et al.* (1991) focused on the special configuration of five in-line cylinders and observed alternate vortex shedding in the gaps for a range of gap spacing. Ziada & Oengören (1993) defined regimes of vortex shedding involving either coupled or uncoupled interaction between adjacent wakes in an entire array. Price & Serdula (1995) used qualitative visualization to characterize the vortex shedding in an array of risers. Most recently, Sumner *et al.* (2000) employed a technique of particle image velocimetry to classify the flow patterns occurring in staggered configurations of two cylinders. Important features include shear layer reattachment, induced separation, vortex pairing and synchronization and vortex impingement.

The foregoing investigations have provided important insight into various features of the tandem cylinder system. Relatively little is understood, however, of the detailed flow structure, in both an instantaneous and time-averaged sense. In particular, for the range of higher Reynolds numbers of interest in the present investigation, where small-scale Kelvin-Helmholtz instabilities form in the separated shear layers, their existence is expected to alter substantially the patterns of instantaneous vorticity and averaged Reynolds stress in the gap region, as well as in the near-wake of the cylinder system. Such features are evident for the case of a single cylinder, as shown by Chyu & Rockwell

(1996). Moreover, within the gap region between the two cylinders, the possibility of instantaneous and averaged asymmetries of the flow patterns, and their consequence on the near-wake of the downstream cylinder, is of interest. All of these features are expected to be a function of the magnitude of the gap between the cylinders.

Regarding the near-wake of the downstream cylinder, the nature of possible formation of Kármán-like vortices, in relation to those formed from a single cylinder, is unclarified. Furthermore, the relationship between averaged patterns of vorticity, Reynolds stress and streamline topology has not been addressed. The aim of this investigation is to address these issues using a technique of quantitative imaging.

2. EXPERIMENTAL SYSTEM AND TECHNIQUES

An overview of the two-cylinder system is shown in Figure 1a. Each cylinder had a diameter D = 50.8 mm and a length L_c = 420 mm. The two-cylinder system was supported by false walls. The leading-edge of the false wall, which was beveled to a sharp edge along its exterior surface, extended a distance of 50.8 mm upstream of the centerline of the upstream cylinder. Moreover, the trailing-edge of each wall extended a distance 356 mm downstream of the centerline of the upstream cylinder. The height of each false wall was 660 mm. The magnitude of the spacing L between the cylinders could be adjusted by translating the downstream cylinder, while the upstream cylinder remained fixed. The entire cylinder-end plate system was suspended in the test section of the large-scale water channel, which had a width of 927 mm, a depth of 610 mm and a length of 4,880 mm. The water height was maintained at an elevation of 508 mm. Throughout the experiments, an inflow velocity U = 192 mm/sec was employed, yielding a Reynolds number, based on cylinder diameter, of Re = 10,000.

A digital technique of high-image-density particle image velocimetry was employed to determine the quantitative flow patterns generated by the two-cylinder system. A dual-pulsed Yag laser system was employed to generate a laser sheet. The output of the laser was transmitted through a cylindrical lens, which generated the planar laser sheet located a distance of 55 mm from the interior of the false wall. This laser sheet illuminated small particles with a diameter of 12 microns, which were seeded in the flow. The particles were metallic coated, hollow plastic spheres. Images were recorded using a digital camera having a resolution of 999 × 960 pixels. A frame-to-frame correlation technique was employed to determine the velocity vector for each interrogation area. The dimensions of the interrogation area employed throughout were 32 × 32 pixels square, and an overlap of 50% was employed. The high-image-density criterion was satisfied by ensuring that a minimum of fifty particle images was contained within the interrogation area. The effective grid size in the plane of the laser sheet was 2.1 mm, yielding a total of approximately 3,720 velocity vectors. For the images shown herein, regions of the freestream above and below the two-cylinder system, which are not of interest, have been cropped, in order to yield the fields of view shown in Figure 1b.

Images of instantaneous velocity fields were employed to attain instantaneous vorticity. In addition, an average of fifty instantaneous images led to averaged values of velocity $< V >$, vorticity $< \omega >$, normalized Reynolds stress $< uv > / U^2$, and averaged streamline topology. In addition, phase-averaged representations of the flow were employed to provide a guide for interpretation of instantaneous images. Four instantaneous images were employed for each average.

3. FLOW PATTERNS IN GAP REGION

Figures 2 and 3 focus on the major features of the flow patterns in the gap region as a function of dimensionless cylinder spacing *L/D*. A number of images show both the gap and the near-wake region; the latter will be considered in a subsequent section.

Figure 2a shows instantaneous patterns of velocity and vorticity for two values of dimensionless cylinder spacing *L/D* = 1.5 and 2.0. For each value of *L/D*, two instantaneous images are shown. They represent the basic types of instantaneous states, which involve symmetrical and asymmetrical patterns in the gap region. Velocity image (i) corresponds to the case *L/D* = 1.5. It exhibits a symmetrical pattern of jet-like flows from its upstream surface. As shown in the corresponding vorticity image (ii), these jet-like regions are associated with adjacent positive and negative contours of vorticity along the upstream surface of the cylinder. Small, low-level concentrations of vorticity are identifiable in the shear layers along the upper and lower sides of the gap. Moreover, the velocity image (iii) for the case *L/D* = 1.5 shows two recirculation zones of different character within the gap. The recirculation in the lower portion of the gap exhibits a well-defined swirl pattern of velocity vectors, in contrast to that in the upper portion. As shown in the corresponding vorticity image (iv), the lower recirculation region is associated with a concentration of positive (thick white line) vorticity. On the other hand, in the upper portion of the gap, there is no significant concentration of vorticity. Again, as in image (ii), the shear layers along the upper and lower sides of the gap indicate definable, small-scale concentrations of vorticity.

The images of instantaneous velocity and vorticity in images (v) through (viii) of Figure 2a correspond to *L/D* = 2.0. It is evident that image (v) corresponds to a nearly symmetrical pattern of velocity. A jet flow of substantial magnitude, which is oriented in

the upstream direction, exists along the centerline of the gap. Swirl patterns of velocity vectors occur on the lower and upper sides of this jet-like flow. The corresponding pattern of instantaneous vorticity of image (vi) shows that broadly distributed regions of vorticity exist in the recirculation zones on the upper and lower sides of the jet. In the separated shear layers bounding the upper and lower sides of the gap region, however, pronounced concentrations of vorticity are evident. In fact, the coalescence of adjacent concentrations occurs in the upper shear layer as it impinges upon the surface of the cylinder. Concerning images (vii) and (viii) at L/D = 2.0, a particularly well-defined swirl pattern of velocity vectors occurs in the lower region of impingement upon the cylinder. This region is associated with a larger-scale cluster of vorticity. On the other hand, only a weakly defined pattern of swirl occurs at the location of impingement of the upper shear layer, and it is located further upstream of the surface of the cylinder.

Considering the images of Figure 2a as a whole, it is evident that the instantaneous flow pattern exhibits intermittency between nearly symmetrical and asymmetrical patterns of velocity and vorticity.

Instantaneous patterns of velocity and vorticity are shown in Figure 2b for the limiting case L/D = 5.1. The gap between the cylinders is sufficiently large that Kármán-like vortices form in the gap region. Such a large-scale vortex is represented by the vertical, elongated cluster of positive vorticity E in the image at the top right of Figure 2b. The consequence of such incident vorticity is the rapid appearance of large-scale vortices in the wake of the cylinder, which are represented by the concentration of negative vorticity B from the upper side of the cylinder, and the positive layer of vorticity C from the lower side of the cylinder. This pattern of vortices E, B and C suggests a phase relationship between the arrival of a large-scale region of vorticity at the upstream

face of the cylinder and the timing of vortices B and C shed in the near-wake. In fact, this phase relationship is the same as that observed in the related investigation of Gaydon & Rockwell (1999), in which both the upstream and downstream cylinder were subjected to controlled oscillation in the transverse direction. As is evident in the image of the lower right of Figure 2b, the relative scale and position of vortices E, B and C is generally similar to that in the image at the upper right.

Figure 3 shows patterns of averaged velocity $< V >$, vorticity $< \omega >$, and Reynolds stress $< uv > / U^2$. Consider, first of all, the velocity and vorticity images. For the cases L/D = 1.5 and 2.0, swirl patterns of velocity vectors exist in the gap region. It is evident that these patterns are not symmetrical with respect to the centerline of the gap. That is, an asymmetrical bias is present, despite the geometrical symmetry. This is especially so at L/D = 1.5, for which patterns of concentrated vorticity are evident in the lower region of the gap, but not in the upper region. On the other hand, the broadly-distributed regions of vorticity for L/D = 1.5 tend toward a symmetrical pattern. Comparison of the images at L/D = 1.15, with those at L/D = 1.5 and 2.0, shows that no well-defined swirl patterns, i.e. recirculation zones, are evident in the gap region. At the other extreme, corresponding to L/D = 5.1, the cylinders are widely spaced and recirculation eddies do not exist in this case as well. Layers of positive and negative vorticity are confined to the region immediately adjacent to the upstream surface of the cylinder, and are associated with the unsteady impingement of the large-scale Kármán vortices upon the upstream surface of the cylinder. In contrast, for the case L/D = 2.0, the distinctive patterns are associated with the quasi-stationary recirculation vortices occurring in the gap region. Patterns of Reynolds stress are shown in the right column of Figure 3. They indicate that, as the cylinder spacing L/D increases, higher levels of Reynolds stress exist further

upstream of the cylinder. At L/D = 1.15, contours of Reynolds stress are barely detectable upstream of the center of the cylinder; at L/D = 1.5, they are more clearly defined; and at L/D = 2.0, substantial levels of Reynolds stress are evident at a distance of nearly one cylinder diameter upstream. This trend occurs in conjunction with the enhanced development of the small-scale vortical structures with increasing size of the gap, which is evident in the instantaneous images of Figure 2a. On the other hand, the Reynolds stress patterns for L/D = 5.1 are completely different. Thick layers of high $< uv >/U^2$ exist along the upstream face of the cylinder and, upstream of these layers, lower level regions of opposite-signed $< uv >/U^2$ occur. This fundamentally different pattern of Reynolds stress is apparently due to the rapid distortion of the large-scale Kármán structures, which are formed in the gap region and impinge upon the leading-surface of the cylinder.

4. FLOW PATTERNS IN THE NEAR-WAKE

Patterns of velocity and vorticity in the near-wake region are shown in Figure 4. Images are illustrated for the reference case of a single cylinder, as well as cylinders having various spacing L/D = 1.15, 1.5, 2.0 and 5.1. The left column of images shows a phase-averaged representation of the velocity field $< V >_p$ for each case. The phase reference corresponds to the instant at which formation of the large-scale vortex is completed from the upper surface of the cylinder. Four of these images were averaged in order to obtain the phase-averaged representation $< V >_p$. The middle column shows a representative pattern of instantaneous velocity V at the same phase. Finally, the corresponding patterns of instantaneous vorticity are given in the right column. Relative to the case of the single cylinder, patterns corresponding to cylinder spacing L/D = 1.15, 1.5 and 2.0 show a substantially narrower wake and formation of elongated vortices from the surface of the

cylinder. At L/D = 2.0, the patterns of velocity and vorticity along the upper and lower sides of the wake tend to become symmetrical. In contrast, at L/D = 5.1, the near-wake pattern is markedly asymmetrical, and the initial, large-scale vortex is formed very close to the base of the cylinder.

These features are further evident in the patterns of velocity and vorticity shown in Figure 5. The left column again shows, as a reference, the same patterns of phase-averaged velocity vectors $< V >_p$ as in Figure 4. The images of the middle and right columns compare the patterns of phase-averaged vorticity $< \omega >_p$ at values of phase separated by π. The near-wake patterns therefore tend to be mirror images of each other.

The consequence of these patterns of vortex formation on the time-averaged structure of the near-wake is shown in Figure 6. The patterns of averaged velocity $< V >$ exhibited in the left column show a narrowing of the near-wake for L/D = 1.15, 1.5 and 2.0, relative to the case of the single cylinder. At L/D = 5.1, this wake width is ill-defined, and exhibits a degree of asymmetry.

Patterns of time-averaged vorticity $< \omega >$ given in the middle column of Figure 6 show further features of the narrowed near-wake at L/D = 1.15 through 2.0. It is evident that both the positive and negative shear layers from the cylinder are deflected inwards toward the plane of symmetry of the near-wake, relative to the case of a single cylinder, where they tend to remain essentially parallel to the plane of symmetry, then degenerate to low levels of vorticity in the central portion of the wake. For the case L/D = 5.1, for which Kármán vortex formation occurs upstream of the cylinder, the region of high vorticity of each of the shear layers tends to remain close to the surface of the cylinder in the base region. Considering the overall pattern of averaged vorticity $< \omega >$ at L/D = 5.1, however, it degenerates to relatively low levels immediately downstream of the base

region and, furthermore, the overall patterns of low-level vorticity $< \omega >$ appear to be slightly deflected away from the plane of symmetry.

The values of time-averaged Reynolds stress $< uv >/U^2$ are represented in the right column of Figure 6. For the case of the single cylinder, the separated shear layers from the cylinder show a very high level of Reynolds stress at a distance of approximately $0.75D$ downstream of the base of the cylinder. This Reynolds stress has a peak value $< uv >/U^2 = 0.23$, in which U is the freestream velocity. Embedded within these layers of high Reynolds stress are two concentrated regions of $< uv >$, each of which is located adjacent to the base of the cylinder, and has an opposite sign relative to the concentrations in each of the respective separated layers from the cylinder. In these concentrations, the peak value of $< uv >/U^2 = 0.08$. Such concentrations are apparently associated with the relatively strong regions of recirculation near the base of the cylinder, which are evident in the corresponding pattern of averaged velocity $< V >$. The pattern of Reynolds stress distributions is very similar to that calculated by Mittal & Balachandar (1995) at a much lower value of Reynolds number. Their peak values of normalized Reynolds stress are $< uv >/U^2 = 0.19$ in the shear layer and 0.11 in the region immediately adjacent to the base of the cylinder.

The patterns of Reynolds stress for the two-cylinder system and, in particular, for $L/D = 1.15$, 1.5 and 2.0, are fundamentally different from the pattern for the single cylinder. First of all, their overall form involves layers of $< uv >/U^2$ that are closely spaced. Second, the peak values of Reynolds stress in these layers are significantly lower. For the values of $L/D = 1.15$, 1.5, 2.0, these peak values are $< uv >/U^2 = 0.081$, 0.078 and 0.047 respectively. Third, in the base region of the cylinder, very low levels of Reynolds stress occur, in contrast to the case of a single cylinder, which exhibit the

two concentrations of $< uv >$ in that region. At the extreme case of L/D = 5.1, which corresponds to the case where vortex formation occurs upstream of the cylinder, the region near the base of the cylinder shows high levels of Reynolds stress, in contrast to the smaller spacing L/D = 1.15 through 2.0. Moreover, for L/D = 5.1, the peak value of $< uv >/U^2$ = 0.097, compared with that at L/D = 2.0, for which $< uv >/U^2$ = 0.030.

Figure 7 shows patterns of averaged streamlines $< \psi >$in the near-wake. For the case of the single cylinder, the pattern of $< \psi >$ shows the well-known recirculation vortices. A similar pattern occurs for values of spacing from L/D = 1.15 through 2.0; however, it is narrower than the pattern for the single cylinder. In fact, this narrowing of the pattern of recirculation vortices is associated with inclined streamlines exterior to this region. They rapidly converge towards the plane of symmetry of the near-wake.

All of these features are related to the variation of the averaged streamwise velocity $< u >$ normalized by the incident free-stream velocity U, i.e. $< u >/U$ as shown in the right column of Figure 7. The largest magnitude of negative $< u >/U$ occurs for the single cylinder. This relatively large value of reverse flow in the region near the base of the cylinder is associated with the formation of particularly well-defined, large-scale vortices in the near wake, as shown in the images of Figures 4 and 5. For all cases of the two-cylinder system, i.e., all values of L/D, this magnitude is substantially reduced by about 40 percent. Moreover, the region of negative $< u >/U$ occurs in the range $0 \leq x/D \leq 0.6$ to 0.8 for all cases, including the single cylinder. This means that the substantial narrowing of the wake occurs with relatively little change in the movement of the zero velocity crossing at the plane of symmetry. This point can be interpreted as a saddle or half-saddle point in the corresponding images of the streamline patterns.

5. CONCLUDING REMARKS

The instantaneous and averaged flow structure past two circular cylinders in tandem has been interpreted relative to the corresponding structure of flow past a single cylinder. A number of distinguishing features have been identified, as summarized in the following.

(1) ***Unstable structure of shear layers along the gap between the cylinders.*** The gap region between the cylinders is characterized by two unstable shear layers along its outer boundaries. These shear layers exhibit small-scale Kelvin-Helmholtz vortices, which have a structure similar to that shown in the images of Chyu & Rockwell (1996) for the case of a single cylinder. It is well known that the development of these Kelvin-Helmholtz vortices is a function of Reynolds number. One therefore expects that the critical spacing, i.e., the cylinder spacing at which vortices are shed in the gap region, will be a function of Reynolds number. This sensitivity to Reynolds number is indicated in the visualization of Ljungkrona *et al.* (1991). For a large gap spacing ($L/D = 4$), variation of the Reynolds number was varied over the range $3.3 \times 10^3 \leq \mathrm{Re} \leq 12 \times 10^3$, and dramatic changes of the gap and near-wake flow patterns were observed; most remarkably, no vortex formation occurs in the gap at the lowest Re, while pronounced vortices occur in the gap at the largest Re. Further features of the Reynolds number dependence at different values of gap spacing are shown in the visualization of Ljungkrona & Sunden (1993). Due to the nature of their visualization technique, Kelvin-Helmholtz vortices were not observed in the shear layer, whereas they are visible in the visualization of Ishigari *et al.* (1972) at an equivalent spacing ($L/D = 4$) and Reynolds number ($\mathrm{Re} = 3.4 \times 10^3$) using a different visualization approach. For the case of a single cylinder, significant changes in the pattern of Kelvin-Helmholtz vortices are known to occur when the

Reynolds number is varied. Taken together with the present observations of well-defined Kelvin-Helmholtz vortices in the shear-layers in the gap region, it is anticipated that enhanced development of the Kelvin-Helmholtz vortices, at higher Reynolds number, will increase both the Reynolds stresses and the entrainment demands of the shear layers, thereby promoting a decrease in the value of the critical gap spacing at higher Reynolds number. Furthermore, at a constant value of Reynolds number, an increase in the level of free-stream turbulence is expected to also enhance the development of Kelvin-Helmholtz vortices. In fact, Ljungkrona *et al.* (1991) found that, as the level of the free-stream turbulence increased, the critical gap spacing decreased.

(2) ***Shear-layer buffeting of downstream cylinder.*** In. the present configuration, the small-scale Kelvin-Helmholtz vortices formed in the shear-layers along the gap eventually buffet the surface of the downstream cylinder. The level of Reynolds stress in these shear layers and the degree to which regions of significant Reynolds stress extend upstream of the impingement cylinder both increase with increasing values of cylinder spacing *L/D*. These effects are associated with different patterns of Kelvin-Helmholtz vortices in the shear layers. Their scale, as well as the interactions between them, increases with increasing values of dimensionless cylinder spacing *L/D*. In fact, at sufficiently large *L/D*, larger clusters of vorticity are evident near the impingement surface of the downstream cylinder. This means that the magnitude of the buffet loading of the downstream cylinder will increase with *L/D*. In fact, the unsteady pressure measurements of Ljungkrona *et al.* (1991), along the surface of the downstream cylinder, showed elevated values of rms pressure amplitude as the gap spacing was increased, prior to the critical spacing at which

large-scale vortex roll-up occurs in the gap. Furthermore, the rms pressure distributions of Igarashi (1984) show a pronounced peak at $\theta \cong 60°$, corresponding to the location of impingement of the shear layer. The amplitude of this peak increased with the value of Reynolds number. Similar peaks of the rms pressure distribution were measured by Ljungkrona & Sunden (1993) at $\theta \cong 75°$ for a lower range of Reynolds number.

A further consequence of this buffet loading is an upstream influence. That is, the unsteadiness in the impingement region will yield velocity and pressure perturbations in the upstream domain of the flow, including the sensitive region of the shear layer at the location of separation from the upstream cylinder. In turn, such perturbations can induce enhanced excitation of the shear layer at this location. These concepts are described by Rockwell (1983) for several classes of impinging shear layers.

(3) ***Recirculation eddies in gap region.*** The region between the shear layers along the gap can exhibit patterns of recirculation zones, i.e. eddies. Their strength, as well as their possible asymmetry with respect to the plane of symmetry of the gap, can show substantial intermittency, i.e., variations of instantaneous states. At a sufficiently large gap, a jet-like flow of relatively large magnitude is oriented in the upstream direction along the centerline of the gap region. This effect occurs for a dimensionless cylinder spacing $L/D = 2.0$, is mildly evident at $L/D = 1.5$, and does not exist at all for $L/D = 1.15$.

(4) ***Onset of Kármán vortex shedding and distinctive patterns of Reynolds stress in gap region.*** The features of the shear layers bounding the gap, as well as the flow patterns between them, which are defined in items (1) and (3), are radically altered

when the spacing L/D is sufficiently large. In this case, the separating shear layers from the upstream cylinder feed into the Kármán-like vortices, rather than impinging upon the downstream cylinder. Due to the eventual impingement of the Kármán vortices on the forward face of the downstream cylinder, a remarkably ordered pattern of Reynolds stress $< uv > / U^2$ occurs in this region.

(5) ***Vortex shedding in near-wake of downstream cylinder.*** All of the aforementioned observations have important consequences for the near-wake from the downstream cylinder. For values of cylinder spacing L/D up to L/D = 2.0, the Kármán-like vortices have a fundamentally different shape and orientation than those formed from a single cylinder. They become elongated with a tendency not to cut the opposing shear layer during the formation process. On the other hand, when the value of L/D is sufficiently large, Kármán shedding occurs in the gap region, and large-scale, Kármán-like vortices are formed very close to the base of the downstream cylinder.

The smoke visualization of Ljungkrona & Sunden (1993) also indicate rapid onset of the Kármán vortex from the downstream cylinder at a large value of gap spacing (L/D = 4). The present results indicate that vortical structures incident upon the downstream cylinder are severely distorted as they are swept about the cylinder and, in turn, predispose shedding from the cylinder. This process is accompanied by high values of Reynolds stress on both the upstream and downstream surfaces of the cylinder. Furthermore, all of the foregoing processes result in a Kármán-like vortex street that is wider than the street from a single cylinder.

(6) ***Time-averaged patterns of near-wake of downstream cylinder.*** Changes of the time-averaged features of the near-wake from the downstream cylinder are related to the aforementioned changes in Kármán-like shedding. Patterns of averaged vorticity

$< \omega >$ indicate that, at least up to $L/D = 2.0$, the separating layers from the cylinder are remarkably deflected towards the plane of symmetry of the cylinder. That is, the wake appears to narrow significantly. Associated with this process is a decrease in the peak value of Reynolds stress of the near-wake shear layers, relative to the case of a single cylinder. In fact, at $L/D = 2.0$, this peak Reynolds stress is approximately a factor of five smaller than the peak value for the case of the single cylinder.

At sufficiently large L/D, such that Kármán shedding occurs in the gap region, the separating shear layers are substantially deflected towards the base of the cylinder. For regions immediately downstream of this initial deflection, the patterns of vorticity are substantially broadened and diverge from the plane of the symmetry of the wake. This alteration of the vorticity field is associated with the highest value of Reynolds stress of the two-cylinder system.

(7) ***Classification of flow regimes.*** Igarashi (1981) has provided a classification of possible states of the flow in the gap and near-wake region of the two-cylinder system, as a function of both Reynolds number and gap spacing L/D. It was not the intention of the present investigation to provide quantitative images over a wide range of Reynolds number versus L/D space, but certain of the observations herein may elucidate some of the regimes described by Igarashi (1981). He describes a synchronized flow regime, whereby the vortex formation due to rollup of the shear layer in the gap region and the vortex shedding in the near-wake of the downstream cylinder are synchronized with the attachment of the gap shear layer to the other side of the downstream cylinder. Images presented herein suggest a degree of communication between vortex roll-up in the gap region and in the near-wake of the downstream cylinder. For example, in Figure 2a, the patterns of velocity

corresponding to images (iii) and (v) both show a well-defined swirl pattern in the lower region of the gap and a corresponding swirl pattern in the lower region of the near-wake of the downstream cylinder. Although this mechanism may not be equivalent to that of Igarashi (1981), it does suggest an interrelationship between the gap and near-wake regions. Another regime, which occurs at larger values of gap *L/D*, is termed a quasi-stationary vortex regime by Igarashi. Although these types of vortices in the gap region are certainly not due to Kármán-like shedding, the present imaging shows that they exhibit time-dependent states, involving instantaneous asymmetries of the flow pattern in the gap region. These features are evident in the images of Figure 2a. Further details of the intricate flow structure in the gap region are summarized at the beginning of Section 3.

ACKNOWLEDGEMENTS

The authors are grateful for the support of the NASA-Langley Research Center under Grant No. NAG-1-1885. Supplemental support was provided by the Air Force Office of Scientific Research, Grant No. F49620-00-1-0009 (533052), the Office of Naval Research, Grants No. N00014-1-0815 (533679) and N00014-98-1-0817 (533699), and the National Science Foundation under Grant No. CTS-9803734 (539442).

References

ARIE, M., KIYA, M., MORIYA, M. & MORI, H. 1983 Pressure fluctuations on the surface of two circular cylinders in tandem arrangement. *ASME Journal of Fluids Engineering* **105**, 161-167.

CHEN, S. S. 1984 Guidelines for instability flow velocity of tube arrays in crossflow. *Journal of Sound and Vibration* **93**, 439-455.

CHEN, S. S. 1987 *Flow Induced Vibration of Circular Cylinders*. Berlin: Springer-Verlag.

CHEN, Y. N. 1985 Flow-induced vibrations of in-line heat exchangers. In Proceedings of ASME Symposium on Flow-Induced Vibrations, **3** (eds. M. P. Païdoussis, J. Chenoweth and J. M. Bernstein), 163-170, New York: ASME.

CHYU, C.-K. & ROCKWELL, D. 1996 Near-wake structure of an oscillating cylinder: effect of controlled kelvin-helmholtz vortices. *Journal of Fluid Mechanics* **322**, 21-49.

FARRANT, T., TAN, M. & PRICE, W. G. 2000 A cell boundary element method applied to laminar vortex-shedding from arrays of cylinders in various arrangements. *Journal of Fluids and Structures* **14**, 375-402.

GAYDON, M. & ROCKWELL, D. 1999 Vortices incident upon an oscillating cylinder: flow structure and loading. *Journal of Fluids and Structures* **13**, 709-722.

HETZ, A. A., DHAUBHADEL, M. N. & TELIONIS, D. P. 1991 Vortex shedding over five in-line cylinders. *Journal of Fluids and Structures* **5**, 243-257.

HIWADA, MUNEHIKO, MABUCHI, IKUO, & YANAGIHARA, HIDEAKI 1982 Fluid flow and heat transfer around two circular cylinders. *Bulletin of the JSME*, **25**, 1737-1745.

IGARASHI, T. 1981 Characteristics of the flow around two circular cylinders arranged in tandem (part 1). *Bulletin of JSME* **24**, 323-331.

IGARASHI, T. 1984 Characteristics of the flow around two circular cylinders arranged in tandem (page 2). *Bulletin of JSME* **27**, 2380-2387.

ISHIGAI, SEIKAN, NISHIKAWA, EIICHI, NISHIMURA, KEIYA & CHO, KATSUZO 1972 Experimental study on structure of gas flow in tube banks with tube axes normal to flow. (Part 1, Karman vortex flow from two tubes at various spacings). *Bulletin of the JSME* **15**, 949-956.

KING, R. & JOHNS, J. 1976 Wake interaction experiments with two flexible circular cylinders in flowing water. *Journal of Sound and Vibration* **45**, 259-283.

KNISELY, C. W. & KAWAGOE, M. 1990 Force-displacement measurements on closely spaced tandem cylinders. *Journal of Wind Engineering and Industrial Aerodynamics* **33**, 81-90.

KNISELY, C. W. & NAKAGAWA, H. 1988 Delay time model for tandem cylinder vibration. *Journal of Hydroscience and Hydraulic Engineering* **6**, 1-15.

KNISELY, C. W., GAYDON, M. A., & ANDERSON, R. W. 1995 Effect of upstream separation geometry on the vibrations of the downstream cylinder of a staggered cylinder pair. In Flow-Induced Vibration (ed. P. W. Bearman), Balkema Press, Rotterdam.

LEE, T. & PANAGAKOS, A. 1997 Investigation of boundary layer behavior on single and tandem cylinders. *Fluid-Structure Interaction, Aeroelasticity, Flow-Induced Vibration and Noise.*, *1*, Ad-Vol. 53-1, 103-112.

LJUNGKRONA, L., NORBERG, CH. & SUNDÉN, B. 1991 Free-stream turbulence and tube spacing effects on surface pressure fluctuations for two tubes in an in-line arrangement. *Journal of Fluids and Structures* **5**, 701-727.

LJUNGKRONA, LARS & SUNDÉN, BENGT 1993 Flow visualization and surface pressure measurement on two tubes in an inline arrangement. *Experimental Thermal and Fluid Science* **6**, 15-27.

MAHIR, N. & ROCKWELL, D. 1996 Vortex formation from a forced system of two cylinders. Part I: Tandem arrangement. *Journal of Fluids and Structures* **10**, 473-489.

MITTAL, R. & BALACHANDAR, S. 1995 Effect of three-dimensionality on the lift and drag of the nominally two-dimensional cylinders. *Physics of Fluids* **7**, 1841-1865.

MITTAL, S., KUMAR, V. & RAGHUVANSHI, A. 1997 Unsteady incompressible flows past two cylinders in tandem and staggered arrangements. *International Journal for Numerical Methods in Fluids* **25**, 1315-1344.

PAÏDOUSSIS, M. P. 1982 A review of flow-induced vibrations in reactors and reactor components. *Nuclear Engineering and Design* **74**, 31-60.

PAÏDOUSSIS, M. P. & PRICE, S. J. 1988 The mechanisms underlying flow-induced instabilities of cylinder arrays in crossflow. *Journal of Fluid Mechanics* **187**, 45-59.

PRICE, S. J. & SERDULA, C. D. 1995 Flow visualization of vortex shedding around multi-tube marine risers in a steady current. In Flow-Induced Vibration (ed. P. W. Bearman), Proceedings of Sixth International Conference on Flow-Induced Vibration, London, United Kingdom, 10-12 April; 483-493. Rotterdam/Brookfield: A. A. Balkema Press.

ROCKWELL, D. 1983 Oscillations of impinging shear layers. *AIAA Journal* **21**, 645-664.

SLAOUTI, A. & STANSBY, P. K. 1992 Flow around two circular cylinders by the random-vortex method. *Journal of Fluids and Structures* **6**, 641-670.

STANSBY, P. K., SMITH, P. A. & PENOYRE, R. 1987 Flow around multiple cylinders by the vortex method. In Proceedings International Conference on Flow Induced Vibration, 41-50, Bowness-on-Windermere, England, Cranfield, U.K.: BHRS.

SUMNER, D., PRICE, S. J. & PAÏDOUSSIS, M. P. 2000 Flow-pattern identification for two staggered circular cylinders in cross-flow. *Journal of Fluid Mechanics* **411**, 263-303.

WEAVER, D. S. & FITZPATRICK, J. A. 1988 A review of cross-flow induced vibrations in heat exchanger tube arrays. *Journal of Fluids and Structures* **2**, 73-93.

WU, J., WELCH, L. W., WELSH, M. C., SHERIDAN, J. & WALKER, G. J. 1994 Spanwise wake structures of a circular cylinder and two circular cylinders in tandem". *Experimental Thermal and Fluid Science* **9**, 299-308.

ZDRAVKOVICH, M. M. 1977 Review of flow interference between two circular cylinders in various arrangements. *ASME Journal of Fluids Engineering* **99**, 618-633.

ZDRAVKOVICH, M. M. 1982 Flow induced oscillations of two interfering circular cylinders. In Proceedings International Conference on Flow Induced Vibration, 141-154, Bowness-on-Windermere, England, Cranfield, U.K.: BHRS.

ZDRAVKOVICH, M. M. 1985 Flow induced oscillations of two interfering circular cylinders. *Journal of Sound and Vibration* **101**, 511-521.

ZDRAVKOVICH, M. M. 1987 The effects of interference between circular cylinders in cross flow. *Journal of Fluids and Structures* **1**, 239-261.

ZDRAVKOVICH, M. M. & PRIDDEN, D. L. 1977 Interference between two circular cylinders: series of unexpected discontinuities. *Journal of Wind Engineering and Industrial Aerodynamics* **2**, 255-270.

ZIADA, S. & OENGÖREN, A. 1993 Vortex shedding in an in-line tube bundle with large tube spacings. *Journal of Fluids and Structures* **7**, 661-687.

LIST OF FIGURES

Figure 1a: Schematic of the two-cylinder system mounted between false walls.

Figure 1b: Schematic of two cylinders in tandem showing two principal fields of view for quantitative imaging. The first field of view concentrates on the gap region and the second on the near-wake region.

Figure 2a: Comparison of instantaneous states of the flow at a cylinder spacing L normalized with respect to cylinder diameter D of L/D = 1.5 and 2.0. For vorticity patterns, minimum ω_{min} and incremental $\Delta\omega$ are both 5 sec^{-1}.

Figure 2b: Instantaneous states of the flow at a large cylinder spacing L, normalized with respect to the cylinder diameter D, of L/D = 5.1 (top row of images). For patterns of vorticity, the minimum ω_{min} and incremental $\Delta\omega$ are both 5 sec^{-1}. The image at the lower right is from Gaydon and Rockwell (1999).

Figure 3: Averaged flow structure in gap and very near-wake region of downstream cylinder as a function of dimensionless cylinder spacing L/D. Patterns of averaged velocity $<V>$, vorticity $<\omega>$ and Reynolds stress $<uv>/U^2$ are shown. For vorticity patterns, minimum $<\omega_{min}>$ and incremental $<\Delta\omega>$ are both 2 sec^{-1}. For contours of constant Reynolds stress normalized by the free-stream velocity, $<uv>/U^2$, minimum and incremental levels are both 0.005.

Figure 4: Images of phase-averaged $<V>_p$ and instantaneous V velocity patterns in comparison with patterns of instantaneous vorticity ω at various values of dimensionless cylinder spacing L/D in comparison with the case of a single cylinder. For vorticity patterns, minimum ω_{min} and incremental $\Delta\omega$ are both 5 sec^{-1}.

Figure 5: Phase-averaged patterns of velocity $< V >_p$ and vorticity $< \omega >_p$ as a function of dimensionless cylinder spacing *L/D* relative to the case of a single cylinder. The middle column of images shows phase-referenced case corresponding to formation of a large-scale vortex from the upper surface of the cylinder and right column of images for vortex formation from the lower surface of the cylinder. For vorticity patterns, minimum $< \omega_{min} >$ and incremental $< \Delta\omega >$ are both 5 sec^{-1}.

Figure 6: Averaged structure of the near-wake from the downstream cylinder as a function of dimensionless cylinder spacing *L/D*. Patterns of velocity $< V >$, vorticity $< \omega >$ and Reynolds stress $< uv > / U^2$ are illustrated. All averages correspond to a time average, i.e., no phase reference was employed. For vorticity patterns, minimum $< \omega_{min} >$ and incremental $< \Delta\omega >$ are both 2 sec^{-1}. For constant Reynolds stress normalized by the free-stream velocity, $< uv > / U^2$, minimum and incremental levels are both 0.005.

Figure 7: Patterns of averaged streamlines $< \psi >$ in the near-wake region of the downstream cylinder. Also illustrated are variations of averaged streamwise velocity $< u > / U$ as a function of distance x downstream of the cylinder normalized by the cylinder diameter *D*.

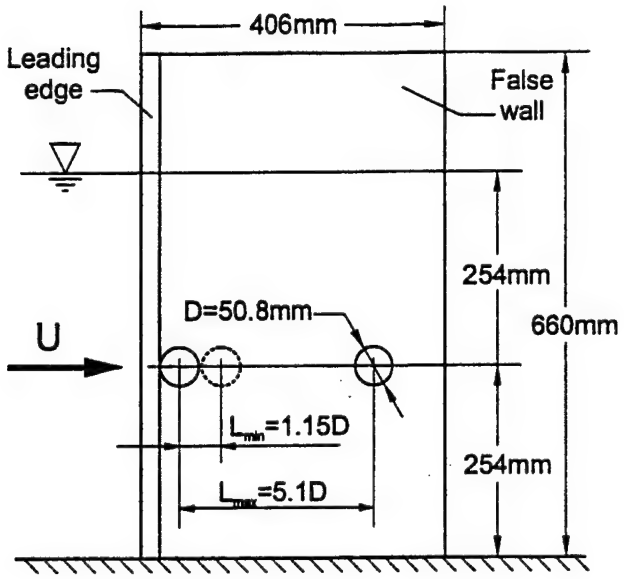

Figure 1a: Schematic of the two-cylinder system mounted between false walls.

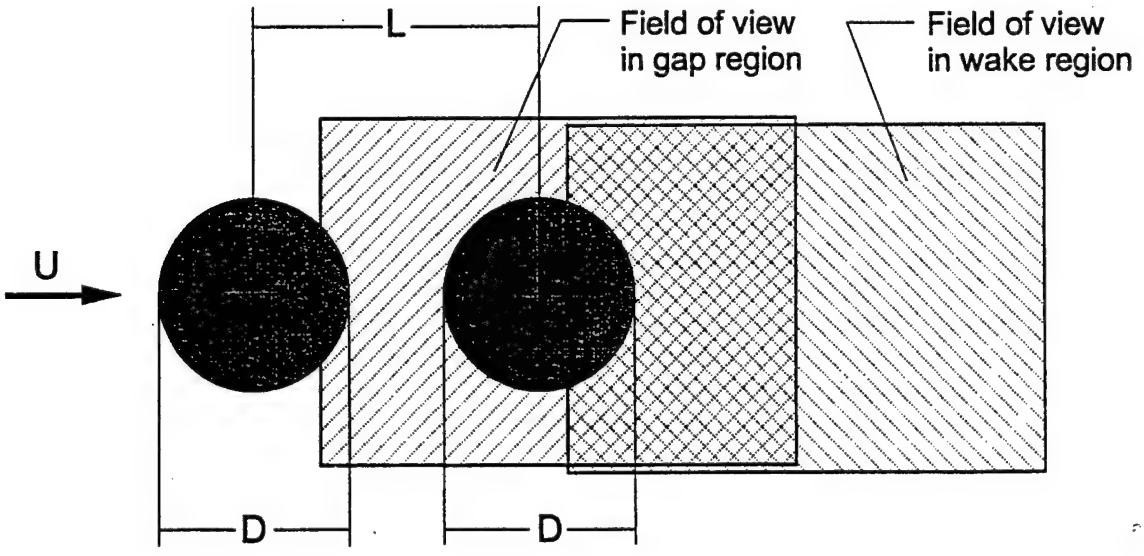

Figure 1b: Schematic of two cylinders in tandem showing two principal fields of view for quantitative imaging. The first field of view concentrates on the gap region and the second on the near-wake region.

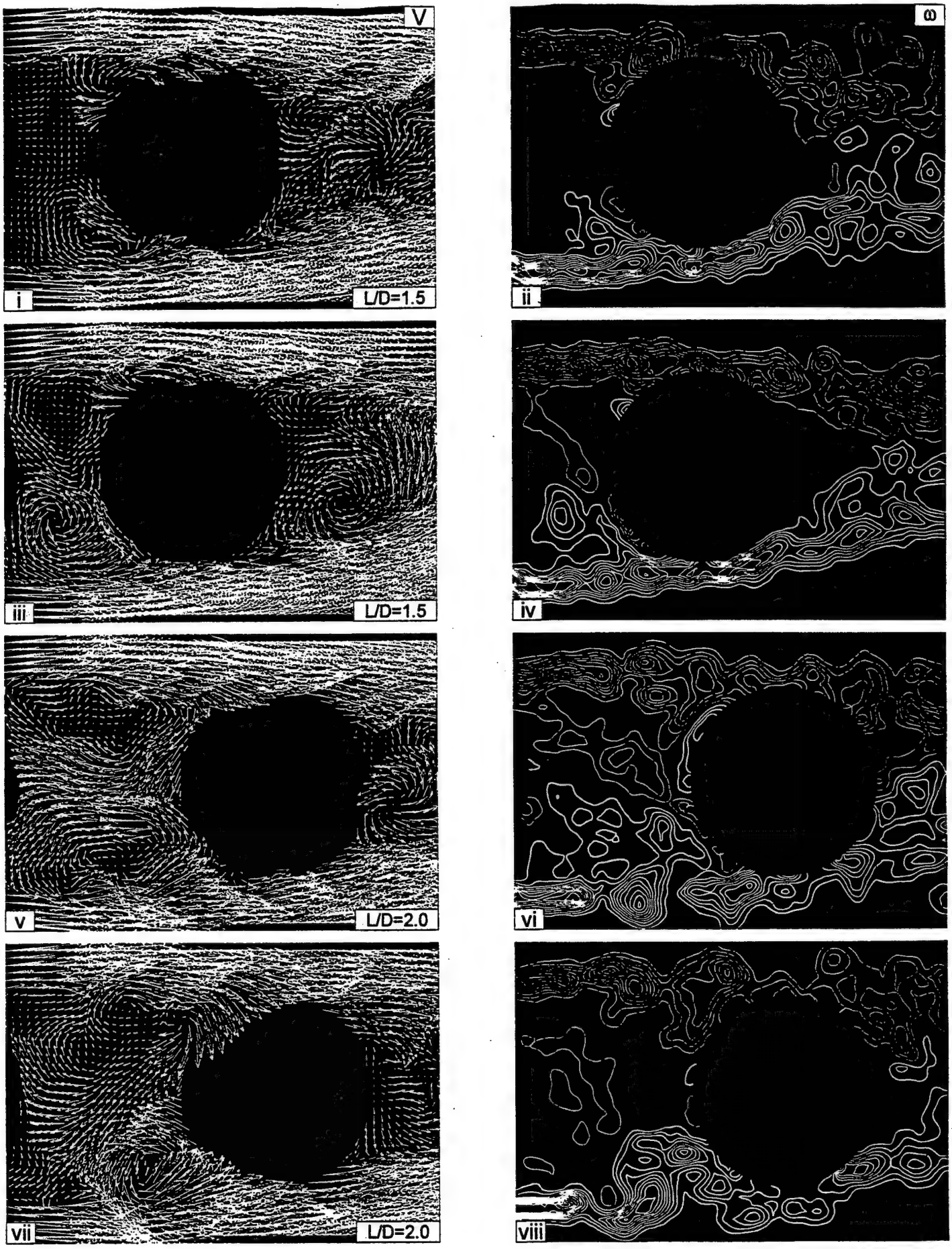

Figure 2a: Comparison of instantaneous states of the flow at a cylinder spacing L normalized with respect to cylinder diameter D of $L/D = 1.5$ and 2.0. For vorticity patterns, minimum ω_{min} and incremental $\Delta\omega$ are both 5 sec^{-1}.

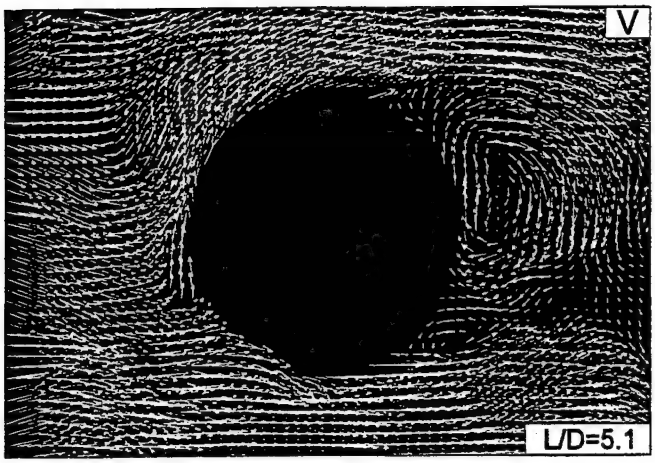

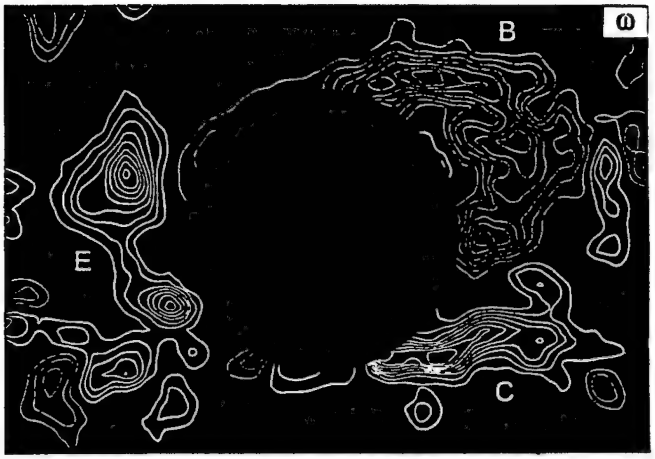

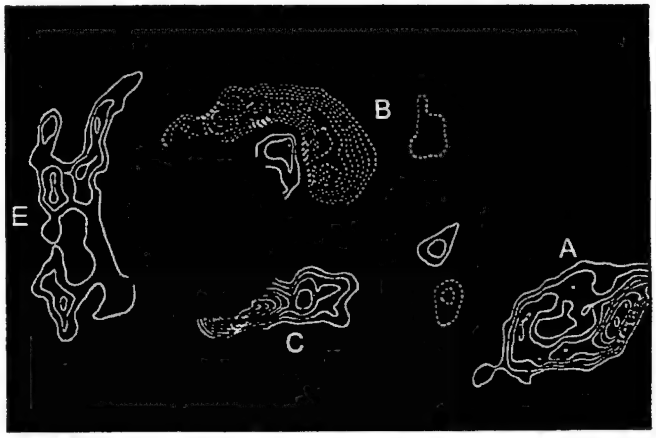

Figure 2b: Instantaneous states of the flow at a large cylinder spacing L, normalized with respect to the cylinder diameter D, of $L/D = 5.1$ (top row of images). For patterns of vorticity, the minimum ω_{min} and incremental $\Delta\omega$ are both 5 sec^{-1}. The image at the lower right is from Gaydon and Rockwell (1999).

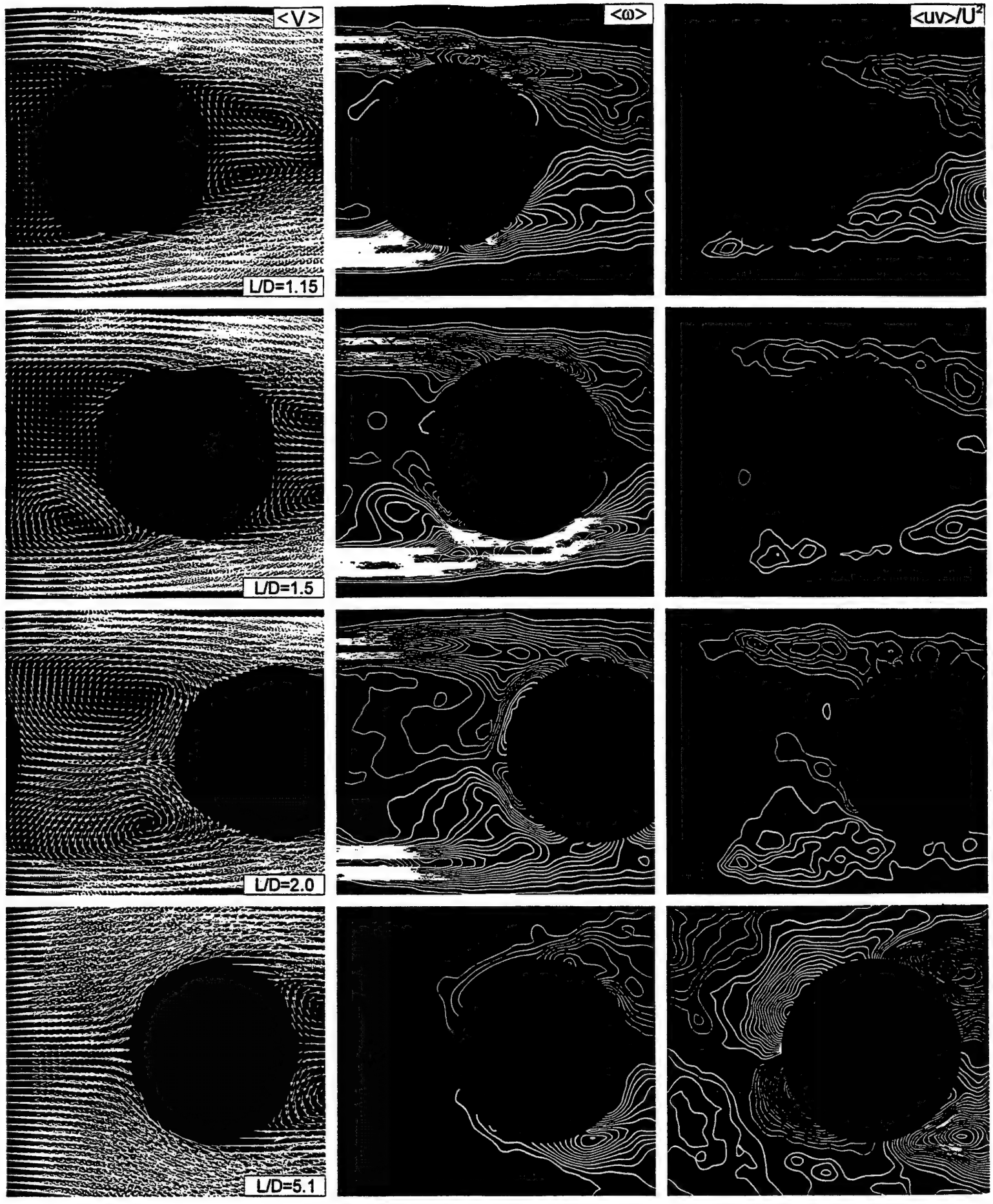

Figure 3: Averaged flow structure in gap and very near-wake region of downstream cylinder as a function of dimensionless cylinder spacing *L/D*. Patterns of averaged velocity $\langle V \rangle$, vorticity $\langle \omega \rangle$ and Reynolds stress $\langle uv \rangle / U^2$ are shown. For vorticity patterns, minimum $\langle \omega_{min} \rangle$ and incremental $\langle \Delta\omega \rangle$ are both 2 sec^{-1}. For contours of constant Reynolds stress normalized by the free-stream velocity, $\langle uv \rangle / U^2$, minimum and incremental levels are both 0.005.

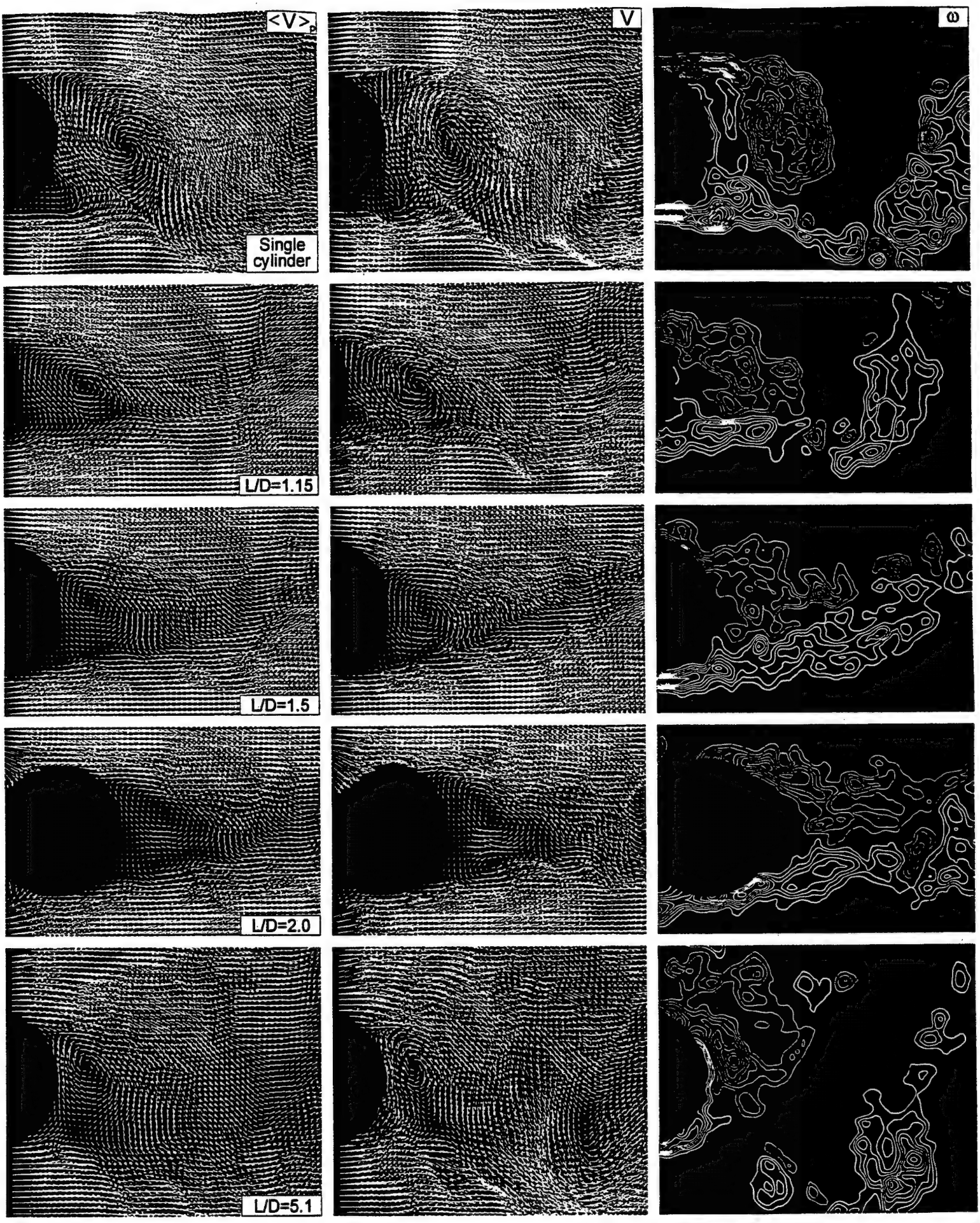

Figure 4: Images of Phase-averaged $\langle V \rangle_p$ and instantaneous V velocity patterns in comparison with patterns of instantaneous vorticity ω at various values of dimensionless cylinder spacing L/D in comparison with the case of a single cylinder. For vorticity patterns, minimum ω_{min} and incremental $\Delta\omega$ are both 5 sec^{-1}.

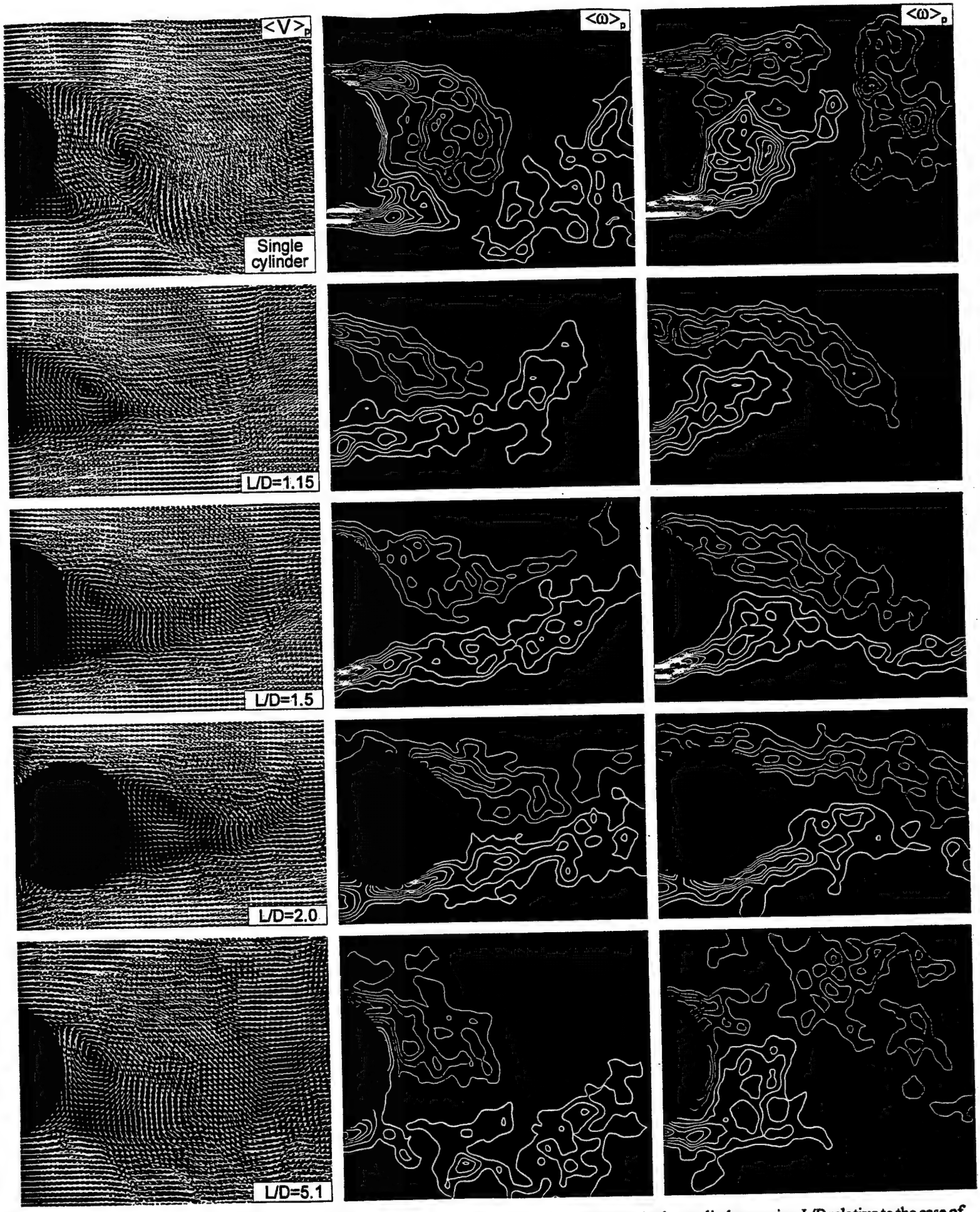

Figure 5: Phase-averaged patterns of velocity $\langle V \rangle_p$ and vorticity $\langle \omega \rangle_p$ as a function of dimensionless cylinder spacing L/D relative to the case of a single cylinder. The middle column of images shows phase-referenced case corresponding to formation of a large-scale vortex from the upper surface of the cylinder and right column of images for vortex formation from the lower surface of the cylinder. For vorticity patterns, minimum

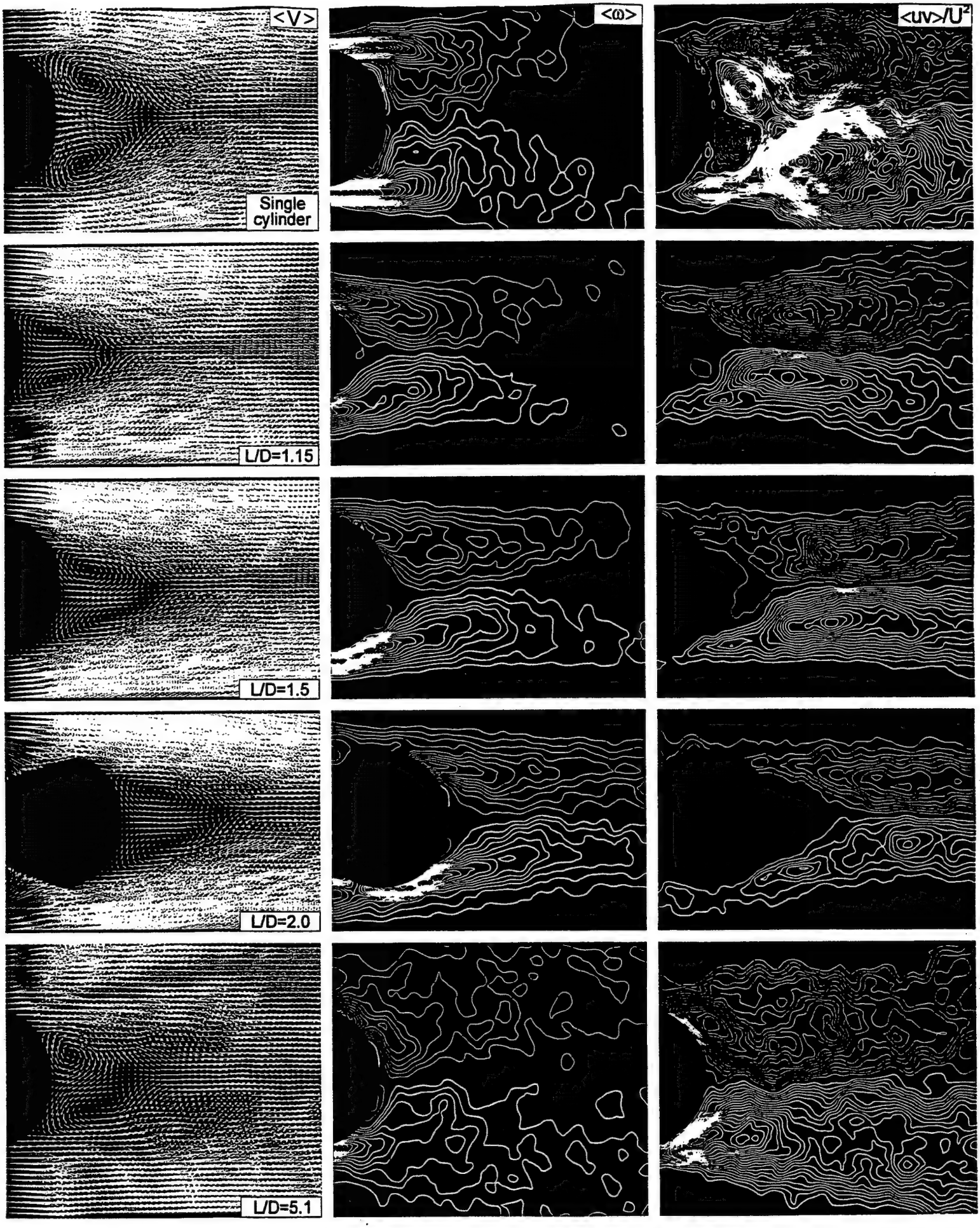

Figure 6: Averaged structure of the near-wake from the downstream cylinder as a function of dimensionless cylinder spacing *L/D*. Patterns of velocity $\langle V \rangle$, vorticity $\langle \omega \rangle$ and Reynolds Stress $\langle uv \rangle / U^2$ are illustrated. All averages correspond to a time average, i.e., no phase reference was employed. For vorticity patterns, minimum $\langle \omega \rangle$ and incremental $\langle \Delta\omega \rangle$ are both 2 sec^{-1}. For constant Reynolds stress normalized by the free-

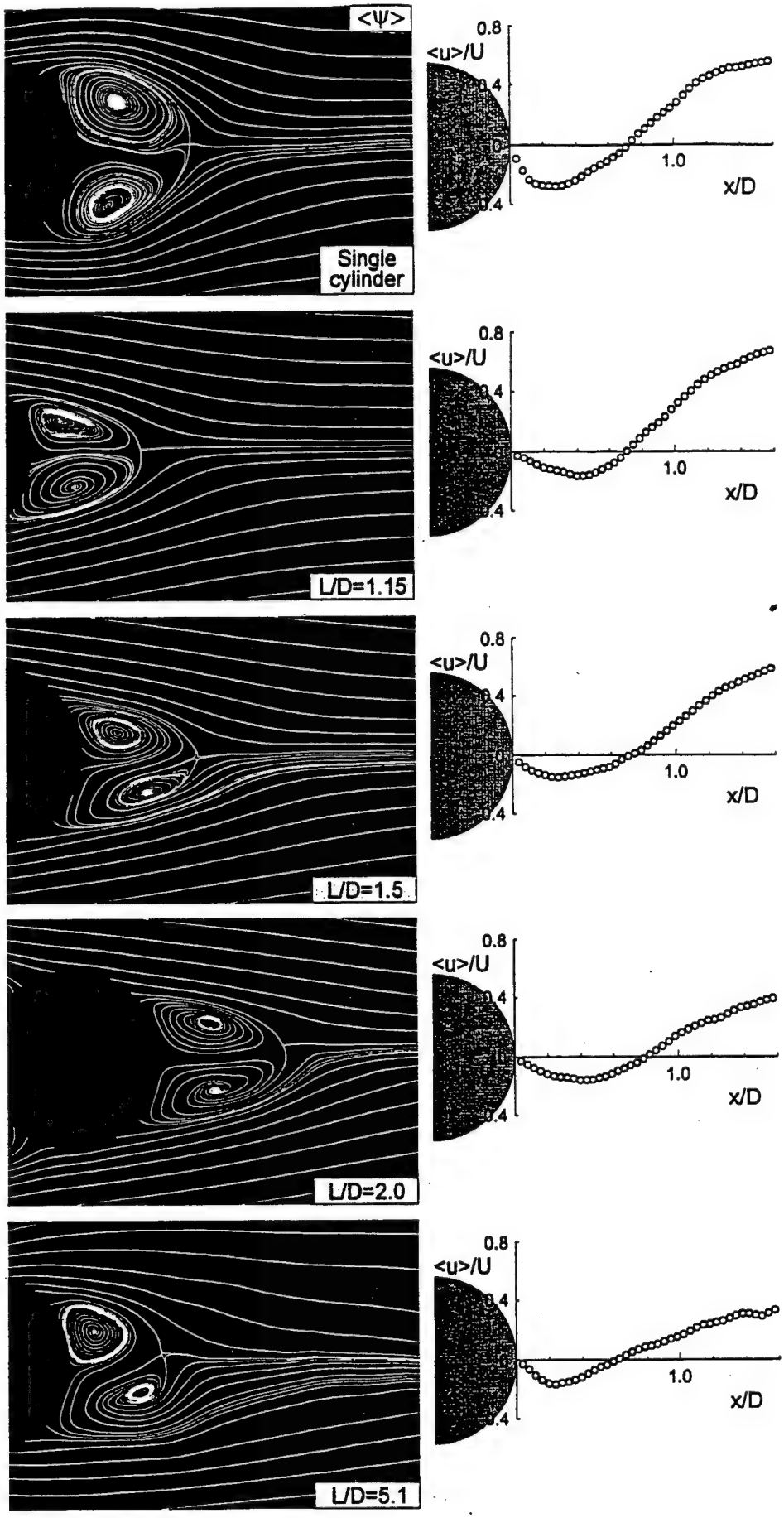

Figure 7: Patterns of averaged streamlines <ψ> in the near-wake region of the downstream cylinder. Also illustrated are variations of averaged streamwise velocity $\langle u \rangle / U$ as a function of distance x downstream of the cylinder normalized by the cylinder diameter D.

Frameworks for identification and assessment of coherent vortical structures in complex flows have been established in recent decades through experiments employing pointwise measurement techniques and numerical simulations. To date, these frameworks have seen relatively little use in experimental studies employing PIV which, for example, can overcome the assumption of "frozen" flow structure when employing a limited number of pointwise measurement stations. Formulation of new approaches for rapid identification and assessment of coherent flow structures can take advantage of recent and forthcoming advances in high spatial and temporal resolution using two- and three-dimensional PIV techniques.

Direct links to established theories are alternate paths for fully exploiting the capabilities of PIV. Most theoretical concepts can be expressed conveniently in terms of vorticity. Yet, the historical development of experimental techniques has, for the most part, involved interpretation of theoretical concepts on the basis of velocity. Experimentalists can now think in terms of global patterns of vorticity, which serve as a foundation for a more expeditious and, unambiguous, interpretation of complex flows. Of course, vorticity-based experiments and links to corresponding theories must address the challenges and uncertainties of measurements near solid surfaces, limited temporal resolution, and a finite field of view, which does not account for the entire previous history of the flow. These concerns will no doubt be addressed by emerging technologies and, hopefully, further theoretical developments. Despite present limitations, it has been demonstrated that even single, instantaneous images of vorticity can provide preliminary, but physically important, links to theoretical concepts. With anticipated advances in PIV techniques in the coming years, it is expected that vorticity-based approaches and interpretations will become even more fruitful.

Even in absence of the foregoing frameworks and links to theories, a substantial number of investigations, not addressed herein, have provided important quantitative guidance. For example, calculation of classical turbulence statistics is now a common feature of most investigations. Moreover, determination of phase-averaged representations of complex flows has been undertaken in a variety of scenarios. While a number of these investigations have incorporated the interpretation of instantaneous

images, continuing efforts would benefit from new approaches to exploiting the instantaneous, global characterizations of PIV, and the manner in which they can provide unique insight.

Parallel PIV and numerical experiments, with cross-comparison of results, have proved to be very worthwhile and, no doubt, will continue to be important in the years to come. Although these types of comparisons are not considered herein, it can generally be stated that most of them have been on the basis of instantaneous and averaged distributions of velocity-based parameters and vorticity. More effective and direct routes for experimental-numerical experiments may be attainable by employing an appropriate framework for identification and assessment of the organized features of the flow, or by invoking an appropriate theoretical model, as described in the foregoing. These types of approaches can, of course, also provide new insight strictly on the basis of laboratory experiments.

Acknowledgements

This manuscript is based on a Keynote Lecture given at the Third International Workshop on Particle Image Velocimetry, University of California, Santa Barbara, September 16-18, 1999. The author is grateful to the Workshop organizers for the opportunity to undertake this endeavor.

Financial support from the Office of Naval Research under Grant N00014-1-0815 (533679), monitored by Dr. Thomas Swean, the National Science Foundation with Grants CTS-9422432 and CTS-9803734, monitored by Drs. Roger Arndt and John Foss, the Air Force Office of Scientific Research, Grant F49620-99-1-0011, monitored by Dr. Steven Walker, and NASA Grant NAG-1-1885, monitored by Dr. Michael Walsh, is greatly appreciated. In addition, the author expresses his appreciation to Dr. Jung-Chang Lin for continuous and close collaboration.

LIST OF REFERENCES

Adrian RJ (1975) On the role of conditional averages in turbulence theory. In Proc. 4th Biennial Symposium on Turbulence in Liquids

Adrian R; Bonnet JP; Delville J; Hussain F; Lumley J; Métais O; Vassilicos C (1996) Eddy structure identification. CISM courses and lectures No. 353 (Bonnnet JP, Editor) Springer, Berlin

Antonia RA (1981) Conditional sampling in turbulence measurement. Ann. Rev. Fluid Mech 13: 131-156

Berkooz G; Holmes P; Lumley J L (1993) The proper orthogonal decomposition in the analysis of turbulent flows. Ann. Rev. Fluid Mech 25: 539-575

Blake WK (1986) Mechanics of Flow-Induced Sound and Vibration, Vols. 1 and 2. Academic Press, Inc., NY

Blevins RD (1990) Flow-Induced Vibration, 2nd Edition. Van Nostrand Reinhold, NY

Bonnet JP; Delville J; Glauser MN; Antonia RA; Bisset DK; Cole DR; Fiedler HE; Garem JH; Hilberg D; Jeong J; Kevlahan NKR; Ukeiley LS; Vincendeau E (1998) Collaborative testing of eddy structure identification methods in free-turbulent shear flows. Exp Fl 25: 197-225

Brown GL; Lopez JM (1990) Axisymmetric vortex breakdown. Part 2. Physical mechanisms. J Fluid Mech 221: 553-576

Bruecker C (1992) Study of vortex breakdown by particle tracking velocimetry (PTV). Part 2: Spiral-type vortex breakdown. Exp Fl 14: 133-138

Bruecker C; Althaus W (1992) Study of vortex breakdown by particle tracking velocimetry (PTV). Part 1: Bubble-type vortex breakdown. Exp Fl 13: 339-349

Bruggeman JC; Hirchberg A; van Dongen MEH; Wijnands APJ (1991) Self-sustained aeroacoustic pulsations in gas transport systems: Experimental study of the influence of closed side branches. J Sound Vib 150: 371-393

Chong M; Perry A; Cantwell B (1990) General classification of three-dimensional flow fields. Phys Fluids A 2: 765-777

Chyu CK; Rockwell D (1996) Near-wake structure of an oscillating cylinder: Effect of controlled shear-layer vortices. J Fluid Mech 322: 21-49

Cimbala JM (1984) Large structure in the far wakes of two-dimensional bluff bodies. Ph.D. Thesis, California Institute of Technology

Cimbala JM; Nagib HM; Roshko A (1988) Large structure in the far wakes of two-dimensional bluff bodies. J Fluid Mech 190: 265-298

Cipolla KM; Liakapoulos A; Rockwell D (1998) quantitative imaging in proper orthogonal decomposition of flow past a delta wing. AIAA J 36: 1247-1255

Dallmann U; Herberg Th; Gebing H; Su WH; Zhang HQ (1995) Flowfield diagnostics: Topological flow changes and spatio-temporal flow structure. AIAA Paper 95-0791, 33rd Aerospace Sciences Meeting and Exhibit, Jan 9-12, Reno, NV

Dallmann U; Schulte-Werning B (1990) Topological changes of axisymmetric and non-axisymmetric vortex flows. In Topological Fluid Mechanics (eds. H. Moffett; A. Tsinober), Proc IUTAM Symposium, Cambridge, Aug 13-18, 1989, 372-383

Escudier M (1988) Vortex breakdown: Observations and explanations. Prog Aero Sci 125: 189-229

Glauser MN; George WK (1992) Application of multipoint measurements for flow characterization. Exp Thermal Fluid Sci 5: 617-632

Graham JMR (1988) Computation of viscous separated flow using a particle method. In Numerical Methods in Fluid Mechanics, 3 (ed. K. W. Morton), Oxford: Oxford University Press 310-317

Gursul I; Lusseyran D; Rockwell D (1990) On interpretation of flow visualization of unsteady shear flows. Exp Fl 9: 257-266

Gursul I; Rockwell D (1991) Effect of concentration of vortices on streakline patterns. Exp Fl 10: 294-296.

Hall MG (1972) Vortex breakdown. Ann Rev Fluid Mech 4: 195-218

Hama FR (1962) Streaklines in a perturbed shear flow. Phys Fluids 5: 644-650

Ho C-M; Huerre P (1984) Perturbed free-shear layers. Ann Rev Fluid Mech 6: 365-424

Hourigan K; Welsh MC; Thompson MC; Stokes AN (1990) Aerodynamic sources of acoustic resonance in a duct with baffles. J Fluids Struc 4: 345-370

Howe MS (1975) Contributions to the theory of aerodynamic sound with application to excess jet noise and the theory of the flute. J Fluid Mech 71: 625-673

Howe MS (1980) The dissipation of sound at an edge. J Sound Vib 70: 407-411

Howe MS (1984) On the absorption of sound by turbulence and other highly dynamic flows. J Appl Math 32: 187-209

Howe MS (1998) Acoustics of Fluid-Structure Interactions. Cambridge University Press, NY

Huang H (1994) Limitations of and Improvement to PIV and Its Application to a Backward-Facing Step Flow. Doctoral dissertation, Technical University of Berlin, Wissenschaftliche Schriftenreihe Stroemungstechnik Band 1, D83, ISBN3-929937-74-3

Huerre P; Monkewitz PA (1990) Local and global instabilities and spatially developing flows. Ann Rev Fluid Mech 22: 473-537

Hunt JCR; Abell CJ; Peterka JA; Woo H (1978) Kinematical studies of the flows around free or surface-mounted obstacles; applying topology to flow visualization. J Fluid Mech 86: 179-200

Hussain F (1993) Understanding coherent structures through vortex dynamics. In: Eddy structure identification in free turbulent shear flows. Proc IUTAM Symp – Poitiers October 1992 (Bonnet JP; Glauser MN, editors) Kluwer Academic Publishers, Dordrecht, 13-26

Ikeda S; Yamamoto Y (1981) Lift forces on cylinders in oscillatory flows. Rep. Dept. Foundation Eng. and Coastal Eng., Saitama University, Japan, 10: 1-16

Kevlahan NKR; Hung JRC; Vassilicos JC (1993) A comparison of different analtyical techniques for identifying structures in turbulence. In: Eddy structure identification in free turbulent shear flows. Proc IUTAM Symp – Poitiers October 1992 (Bonnet JP; Glauser MN, editors) Kluwer Academic Publishers, Dordrecht, 311-324

Koumoutsakos P; Leonard A (1995) High-resolution simulations of the flow around an impulsively started cylinder using vortex methods. J Fluid Mech 296: 1-38

Kriesels PC; Peters MACM; Hirschberg A; Wijnands APJ (1995) High amplitude vortex-induced pulsations in a gas transport system. J Sound Vib 184: 343-368

Kurosaka M; Sundaram P (1986) Illustrative examples of streaklines in unsteady vortices: Interpretational difficulties revisited. Phys Fluids 29: 3474-3477

Leibovich S (1978) The structure of vortex breakdown. Ann Rev Fluid Mech 10: 221-246

Leibovich S (1984) Vortex stability and breakdown: Survey and extension. AIAA J 22: 1192-1206

Lesieur M (1993) Understanding coherent vortices through computational fluid dynamics. Theoretical and Comput. Fluid Dyn. 5: 177-193

Liakopoulos A; Blythe PA; Gunes H (1997) A reduced dynamical model of convective flows in tall heated cavities. Proc Royal Soc Lond A 453: 663-672

Lighthill J (1986) Fundamentals concerning wave loading on offshore structures. J Fluid Mech 173: 667-681

Lin J-C; Rockwell D (1994) Cinematographic system for high-image-density particle image velocimetry. Exp Fluids 17: 110-118

Lin J-C; Rockwell D (1995) Transient structure of vortex breakdown on a delta wing. AIAA J 33: 6-12

Lin J-C; Rockwell D (1996) Force identification by vorticity fields: Techniques based on flow imaging. J Fluids Struc 10: 663-668

Lin J-C; Rockwell D (1997) Quantitative interpretation of vortices from a cylinder oscillating in quiescent fluids. Exp Fl 23: 99-104

Lin J-C; Rockwell D (1999) Cinema PIV and its application to impinging vortex systems. J Fluids Eng 121: 720-724

Lugt HJ (1979) A dilemma of defining a vortex. In: Recent Developments in Theoretical and Experimental Fluid Mechanics, Springer-Verlag, NY 309

Lumley JL (1967) The structure of inhomogeneous turbulence. In: Atmospheric Turbulence and Wave Propagation (eds. AM Yaglom; VI Tatarski), Mauka, Moscow 166-178

Magness C; Robinson O; Rockwell D (1993) Instantaneous topology of the unsteady leading-edge vortex at high angle of attack. AIAA J 31: 1384-1391

Maskell EC (1955) Flow separation in three dimensions. RAE Report 2565

Moffatt HK; Tsinober A (1990) Topological Fluid Mechanics. Proc IUTAM Symposium, Cambridge, UK, Aug 13-18 1989, Cambridge University Press, Cambridge

Maull DJ; Milliner MC (1978) Sinusoidal flow past a circular cylinder. Coastal Eng 2: 149-168

Meneghini JR; Bearman PW (1995) Numerical simulation of high amplitude oscillatory flow about a circular cylinder. J Fluids Struc 9: 435-455

Milne-Thomson LM (1960) Theoretical Hydrodynamics, NY: Macmillan and Company

Naudascher E; Rockwell D (1994) Flow-Induced Vibrations: An Engineering Guide, Balkema Press, Rotterdam, April.

Noca F (1996) On the evaluation of instantaneous fluid-dynamic forces on a bluff body. GALCIT Report FM96-5, California Institute of Technology, Pasadena, CA

Noca F (1997) On the evaluation of time-dependent fluid dynamic forces on bluff bodies. Ph.D. Dissertation, California Institute of Technology, Pasadena, CA

Noca F; Shiels D; Jeon D (1997) Measuring instantaneous fluid dynamic forces on bodies using only velocity field and their derivatives. J Fluids Struc 11: 345-350

Noca F; Shiels D; Jeon D (1999) A comparison of methods for evaluating time-dependent fluid dynamic forces on bodies, using only velocity fields and their derivatives. J Fluids Struc (in press)

Oertel H Jr (1990) Wakes behind bluff bodies. Ann Rev Fluid Mech 22: 539-564

Oswatitsch K (1958) Die Abloesungsbedingung von Grenzschichten. In Grenzschichtforschung (ed. H. Goertler), 357-367, Springer-Verlag, Berlin

Ozgoren M; Sahin B; Rockwell D (2000) Structure of leading-edge vortices on a delta wing at high angle-of-attack. Submitted for publication

Perry A; Chong M (1987) A description of eddying motions and flow patterns using critical-point concepts. Ann Rev Fluid Mech 19: 125-155

Powell A (1961) On the edgetone. *J Acous Soc Amer* 33: 395-409

Rockwell D (1983) Oscillations of impinging shear layers. AIAA J 21: 645-664

Rockwell D (1998a) Vortex-body interactions. Ann Rev Fluid Mech 30: 199-299

Rockwell D (1998b) Quantitative imaging of flow-structure interactions. Proc 13th Australasian Fluid Mechanics Conference (eds. MC Thompson; K Hourigan), Vol. I (Session 1-5), Dept Mech Eng, Monash Univ, Melbourne, Australia, 13-18 Dec

Rockwell D; Naudascher E (1979) Self-sustained oscillations of impinging free shear layers. Ann Rev Fluid Mech 11: 67-97

Sarpkaya T (1963) Lift, drag, and added-mass coefficients for a circular cylinder immersed in a time-dependent flow. J Appl Mech 30: 13-15

Sarpkaya T (1968) An analytical study of separated flow about circular cylinders. J Basic Eng 90: 511-520

Schachenmann A; Rockwell D (1980) A quasi-standing wave phenomenon due to oscillating internal flow, J Fluids Eng 102: 70-77

Schachenmann A; Rockwell D (1982) Self-generation of organized waves in an impinging turbulent jet at low mach numbers. J Fluid Mech 117: 425-441

Shih C; Ding Z (1996) Trailing-edge jet control of the leading-edge vortices of a delta wing. AIAA J 34: 2642-2644

Sirovich L (1987) Turbulence and the dynamics of coherent structures, parts I – II. Quart Appl Math 45: 561-590

Stuart JT (1967) On finite amplitude oscillations in laminar mixing layers. J Fluid Mech 29: 417-440

Tobak M; Peake DJ (1982) Topology of three-dimensional separated flows. Ann Rev Fluid Mech 14: 61-85

Towfighi J; Rockwell D (1993) Instantaneous structure of vortex breakdown on a delta wing via particle image velocimetry. AIAA J 31: 1160-1163

Unal MF; Lin J-C; Rockwell D (1997) Force prediction by PIV imaging: A momentum-based approach. J Fluids Struc 11: 965-971

Visbal M; Gordnier RE (1994) Crossflow topology of vortical flows. AIAA J 32: 1085-1087

Vogel A; Lauterborn W (1988) Time-resolved particle image velocimetry used in the investigation of cavitation bubble dynamics. Appl Optics 27: 1869-1876

Williams DR; Hama F (1980) Streaklines in a shear layer perturbed by two waves. Phys Fluids 23: 442-447

Wu JC (1981) Theory of aerodynamic force and moment in viscous flows. AIAA J 19: 432-441

Zhong J; Huang TS; Adrian RJ (1998) Extracting 3D vortices in turbulent fluid flow. *IEEE Trans Pattern Analysis and Machine Intelligence* 20: 193-199

Zhu Q; Lin J-C; Unal MF; Rockwell D (2000) Motion of a cylinder adjacent to a free-surface: Flow patterns and loading. Submitted to Exp Fluids

LIST OF FIGURES

Figure 1: Topological concepts based on critical point theory applied to the leading-edge vortices on a delta wing subjected to pitch-up motion. Instantaneous pattern of velocity vectors (only a portion of image is shown), instantaneous sectional streamlines, and definition of key topological features, represented by saddle points S and nodes N. (Magness, Robinson and Rockwell, 1993)

Figure 2: Topological concepts based on critical point applied to a fully-turbulent boundary layer. Pattern of velocity vectors with superposed, darkened regions represent values of a two-dimensional discriminate that lie below a threshold value, and thereby indicate focus-type regions. (Zhong, Huang and Adrian, 1998)

Figure 3: Snapshot proper orthogonal decomposition (POD) applied to the leading-edge vortices on a delta wing. Patterns of velocity vectors (left column) and contours of constant vorticity (right column) are shown for original PIV data (top row of images), a reconstruction from three eigenmodes (middle row of images), and a reconstruction from six eigenmodes (bottom row of images). (Cipolla, Liakopoulos and Rockwell, 1998)

Figure 4: Schematic showing a simplified representation of small-scale shear-layer vortices and a Kármán vortex from a circular cylinder; the latter is due to a global (absolute) instability. L_f represents the formation length of the Kármán vortex, and D and L are the drag and lift on the cylinder.

Figure 5a: Patterns of instantaneous vorticity showing agglomeration of small-scale shear-layer vortices into a large-scale Kármán vortex. Re = 10,000. (Chyu and Rockwell, 1996)

Figure 5b: Zoomed-in view of bottom shear layer of Figure 5a, showing comparison of contours of constant vorticity (top image) and patterns of instantaneous streamlines in a reference frame moving at one-half of the free-stream velocity (middle image) and in the laboratory frame (bottom images). (Chyu and Rockwell, 1996)

Figure 5c: Comparison of contours of constant vorticity in the near-wake of a cylinder subjected to very small amplitude perturbations at the inherent frequency of formation of shear-layer vortices (left image), spatially-filtered pattern of instantaneous velocity vectors (middle image) and superposition of streamline pattern corresponding to spatially-averaged pattern of velocity vectors on contours of constant instantaneous vorticity (right image). (Chyu and Rockwell, 1996)

Figure 6: Schematic illustrating induced force $\underline{F}(t)$ and its drag D and lift L components, in relation to the distributed vorticity $\underline{\omega}(x,y,t)$ and the moment arm $\underline{x}$.

Figure 7: Identification of vortex contributions to lift L and drag D via cinematic imaging for a cylinder in transient motion beneath a free-surface. Vorticity ω and spatial

distributions of moments of vorticity $(M_\omega)_L$ and $(M_\omega)_D$ are shown for two widely separated frames N = 15 and 18 of a cinema PIV sequence. Differences of distributions of moments of vorticity $(\Delta M_\omega)_L$ and $(\Delta M_\omega)_D$ are also illustrated. (Zhu, Lin, Unal and Rockwell, 1999)

Figure 8: Representative PIV image corresponding to transient motion of a cylinder and typical control volumes CV1, CV2 and CV3 and coordinate origins O_a, O_b, and O_c employed for comparative assessment of force calculations. (Noca, Shiels and Jeon, 1999)

Figure 9: Schematic of self-sustaining oscillations due to impingement of a vortex system upon a stationary edge.

Figure 10: Patterns of instantaneous velocity (top image), vorticity (middle image) and vectors of the quantity $\underline{\omega} \wedge \underline{V}$ of the acoustic power integral for the case of a jet formed from a fully-turbulent channel flow, as illustrated in the schematic of Figure 9. Patterns of velocity and vorticity are excerpts from a highly time resolved cinema PIV sequence. (Lin and Rockwell, 1999, 2000)

Figure 11: Patterns of instantaneous velocity vectors due to flow past a cavity (top image). The boundary layer of the inflow is fully turbulent. Also shown is the structure of the instantaneous shear layer along the mouth of the cavity in various reference frames corresponding to: the laboratory frame (top image); a frame moving at 0.25 U_∞ (middle image) and at 0.5 U_∞ (bottom image), in which U_∞ is the freestream velocity. (Lin and Rockwell, 2000)

Figure 12: Schematic illustrating onset of vortex breakdown due to flow past a delta wing at high angle of attack.

Figure 13: Contours of constant averaged velocity $< V >$ (top image) and averaged vorticity $< \omega >$ (bottom image) for the case of vortex breakdown on a delta wing at high angle of attack. (Ozgoren, Sahin and Rockwell, 2000)

Figure 14: Superposition of contours of averaged velocity $< V >$ on contours of averaged vorticity $< \omega >$, taken from the images of Figure 13, in order to allow comparison of criteria for the onset of vortex breakdown. Upstream dot corresponds to criterion based on switch in sign of azimuthal vorticity; downstream dot represents the criterion based on occurrence of the stagnation point along the axis of the vortex. (Ozgoren, Sahin and Rockwell, 2000)

Figure 15: Contours of instantaneous azimuthal vorticity in the vicinity of vortex breakdown; image is one from a series used to construct the averaged contours of vorticity depicted in Figure 13. (Ozgoren, Sahin and Rockwell, 2000)

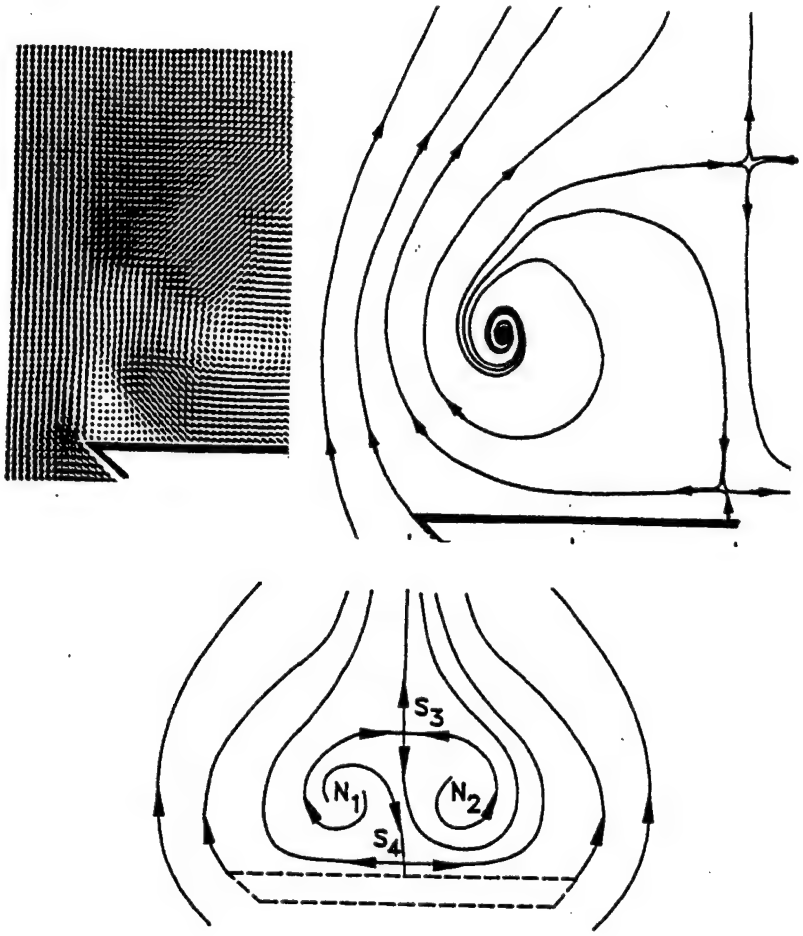

Figure 1: Topological concepts based on critical point theory applied to the leading-edge vortices on a delta wing subjected to pitch-up motion. Instantaneous pattern of velocity vectors (only a portion of image is shown), instantaneous sectional streamlines, and definition of key topological features, represented by saddle points S and nodes N. (Magness, Robinson and Rockwell, 1993)

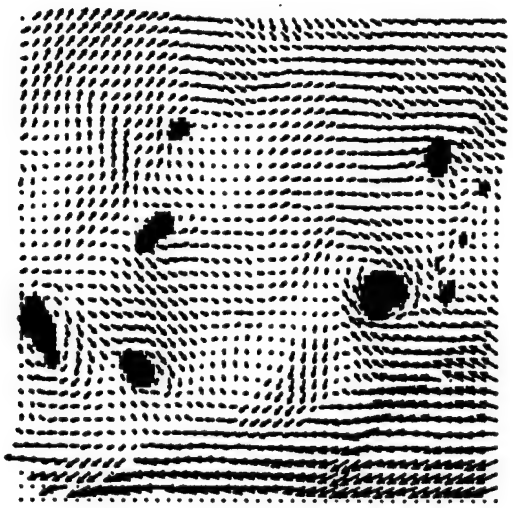

Figure 2: Topological concepts based on critical point applied to a fully-turbulent boundary layer. Pattern of velocity vectors with superposed, darkened regions represent values of a two-dimensional discriminate that lie below a threshold value, and thereby indicate focus-type regions. (Zhong, Huang and Adrian, 1998)

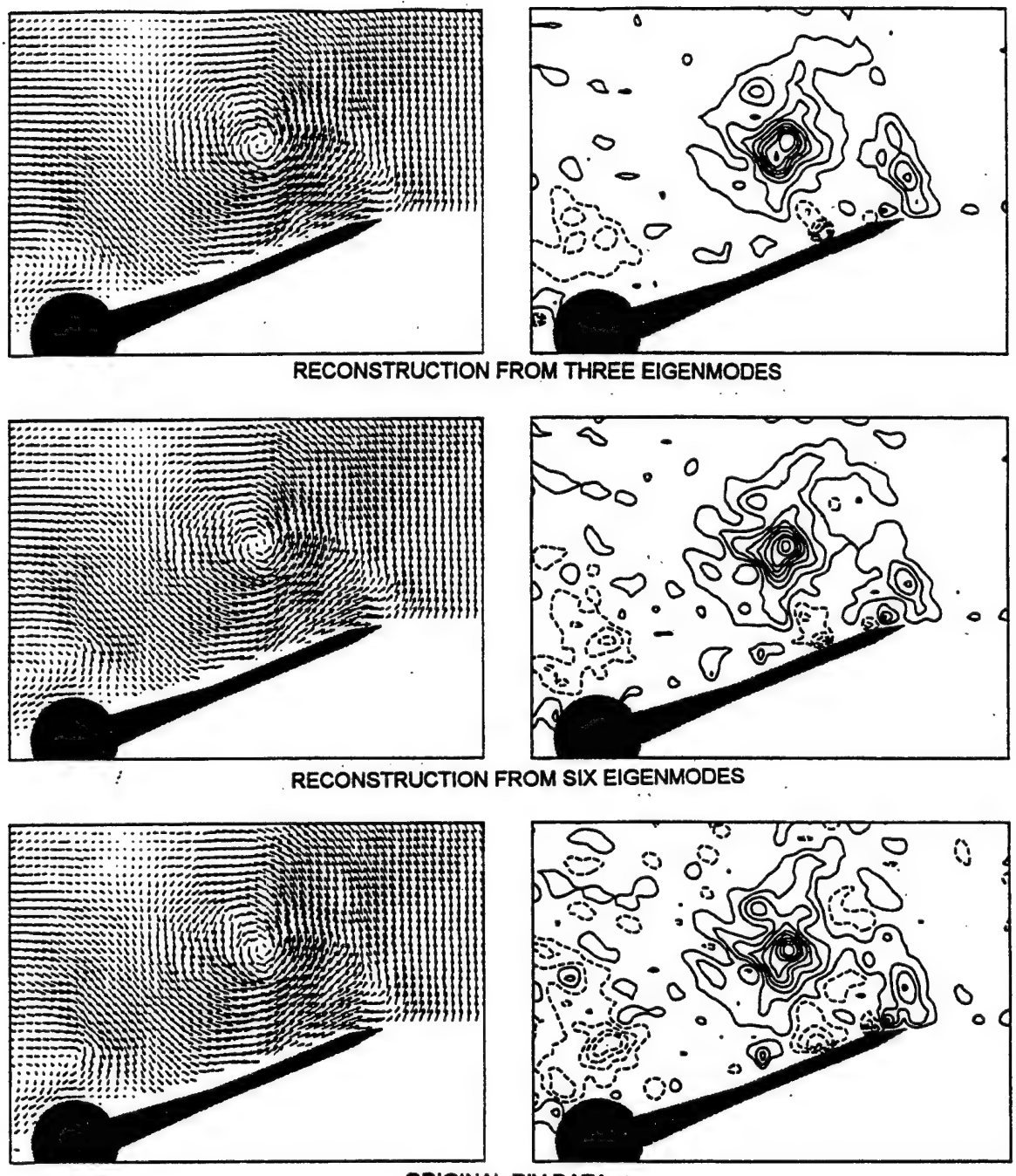

Figure 3: Snapshot proper orthogonal decomposition (POD) applied to the leading-edge vortices on a delta wing. Patterns of velocity vectors (left column) and contours of constant vorticity (right column) are shown for original PIV data (top row of images), a reconstruction from three eigenmodes (middle row of images), and a reconstruction from six eigenmodes (bottom row of images). (Cipolla, Liakopoulos and Rockwell, 1998)

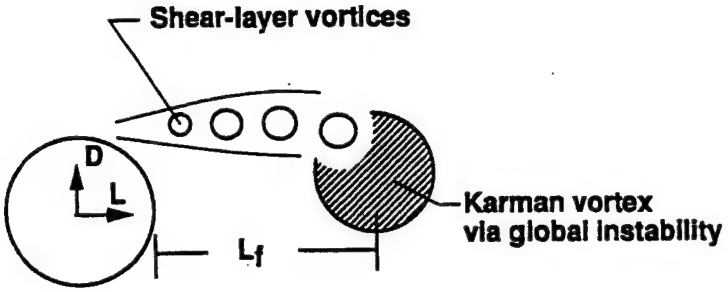

Figure 4: Schematic showing a simplified representation of small-scale shear-layer vortices and a Kármán vortex from a circular cylinder; the latter is due to a global (absolute) instability. L_f represents the formation length of the Kármán vortex, and D and L are the drag and lift on the cylinder.

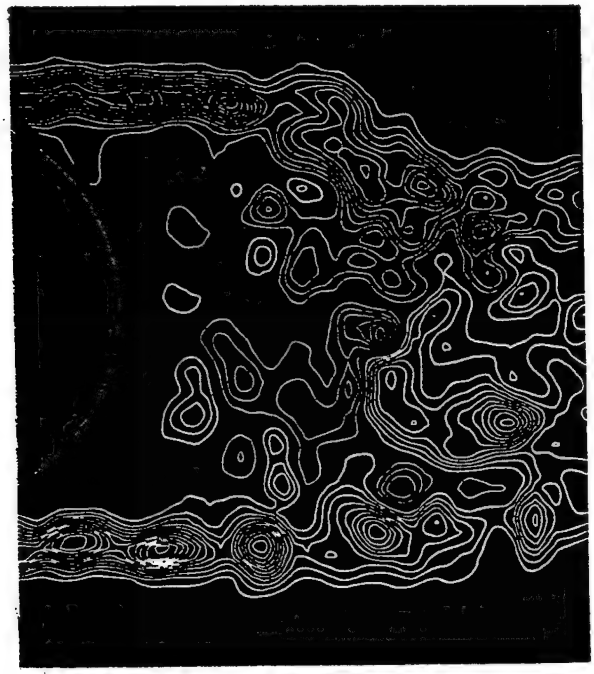

Figure 5a: Patterns of instantaneous vorticity showing agglomeration of small-scale shear-layer vortices into a large-scale Kármán vortex. Re = 10,000. (Chyu and Rockwell, 1996)

Figure 5b: Zoomed-in view of bottom shear layer of Figure 5a, showing comparison of contours of constant vorticity (top image) and patterns of instantaneous streamlines in a reference frame moving at one-half of the free-stream velocity (middle image) and in the laboratory frame (bottom images). (Chyu and Rockwell, 1996)

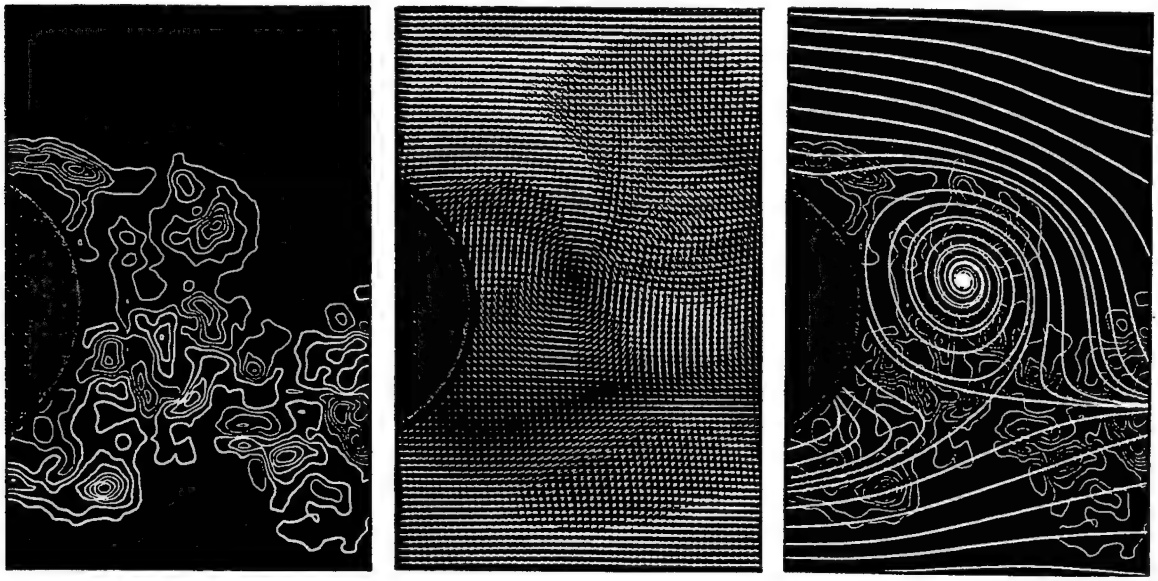

Figure 5c: Comparison of contours of constant vorticity in the near-wake of a cylinder subjected to very small amplitude perturbations at the inherent frequency of formation of shear-layer vortices (left image), spatially-filtered pattern of instantaneous velocity vectors (middle image) and superposition of streamline pattern corresponding to spatially-averaged pattern of velocity vectors on contours of constant instantaneous vorticity (right image). (Chyu and Rockwell, 1996)

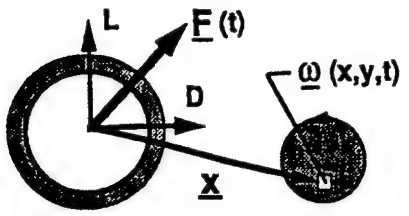

Figure 6: Schematic illustrating induced force $\underline{F}(t)$ and its drag D and lift L components, in relation to the distributed vorticity $\underline{\omega}(x,y,t)$ and the moment arm $\underline{x}$.

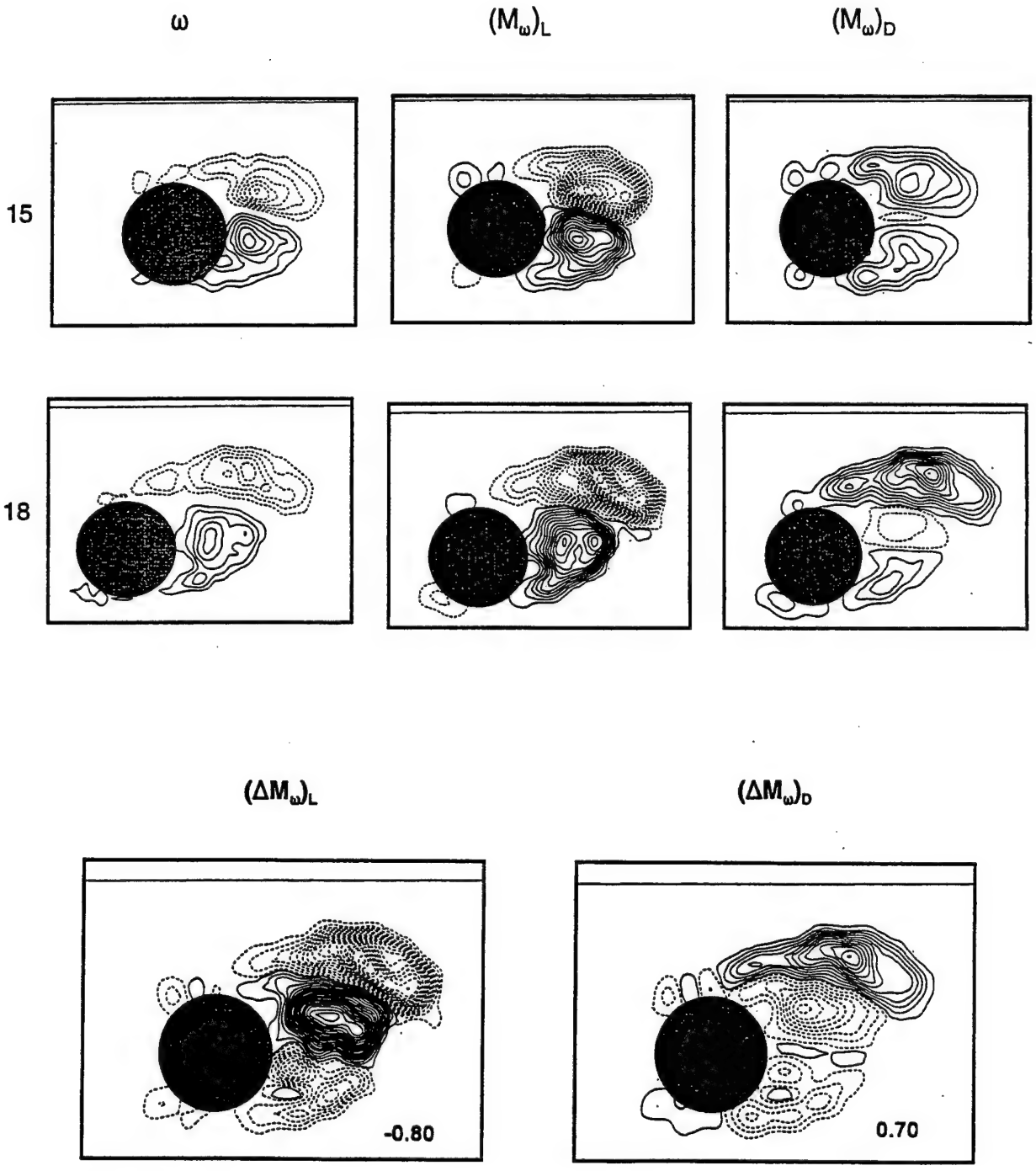

Figure 7: Identification of vortex contributions to lift L and drag D via cinematic imaging for a cylinder in transient motion beneath a free-surface. Vorticity ω and spatial distributions of moments of vorticity $(M_\omega)_L$ and $(M_\omega)_D$ are shown for two widely separated frames N = 15 and 18 of a cinema PIV sequence. Differences of distributions of

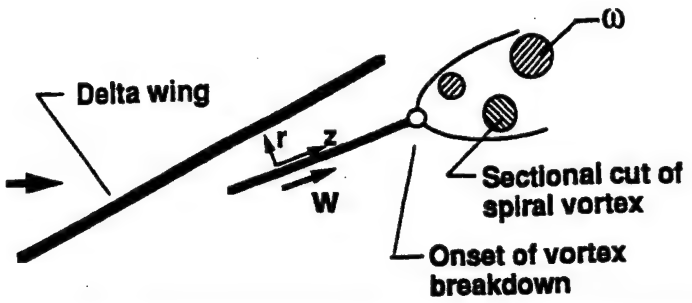

Figure 12: Schematic illustrating onset of vortex breakdown due to flow past a delta wing at high angle of attack.

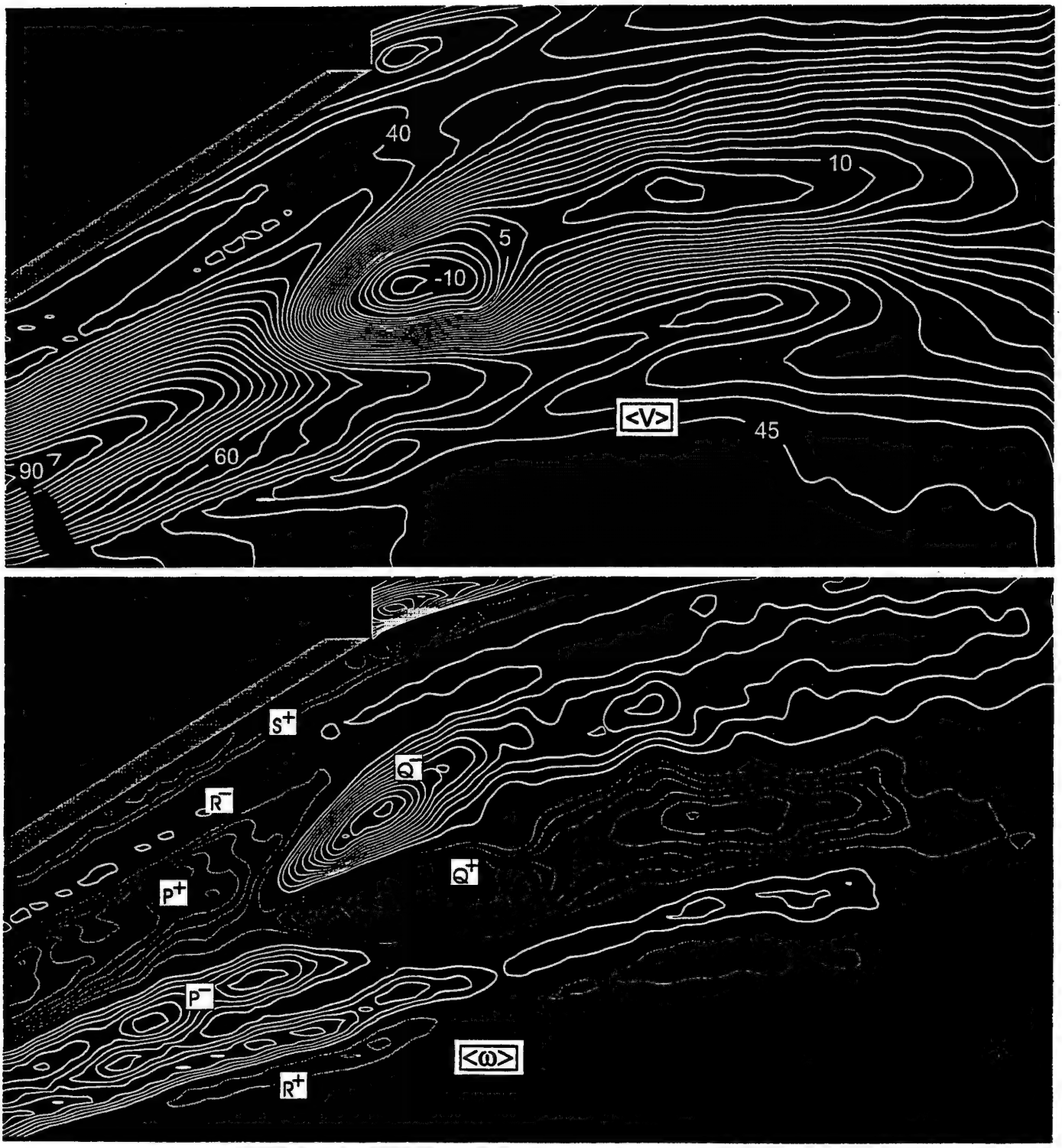

Figure 13: Contours of constant averaged velocity < V > (top image) and averaged vorticity < ω > (bottom image) for the case of vortex breakdown on a delta wing at high angle of attack. (Ozgoren, Sahin and Rockwell, 2000)

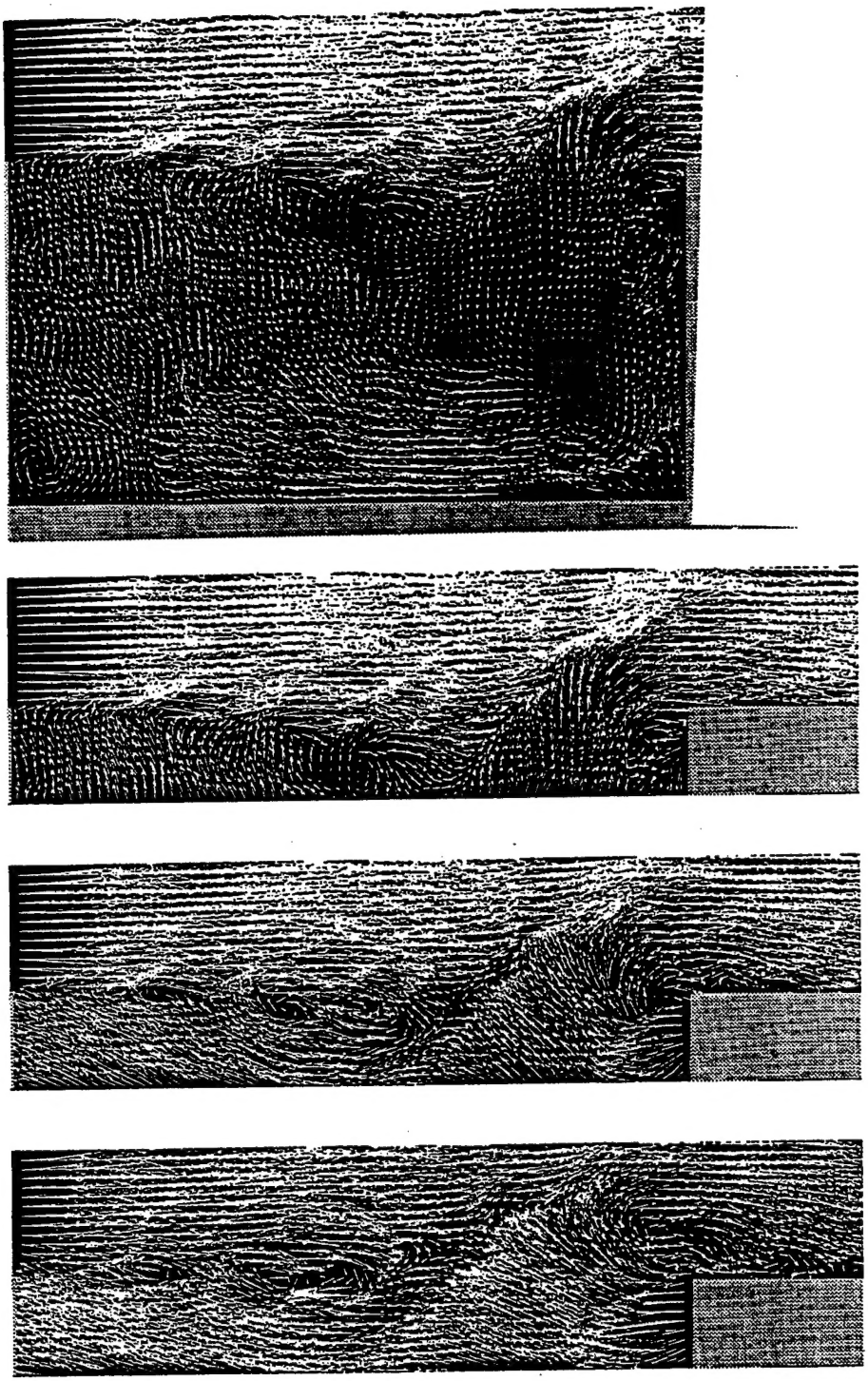

Figure 11: Patterns of instantaneous velocity vectors due to flow past a cavity (top image). The boundary layer of the inflow is fully turbulent. Also shown is the structure of the instantaneous shear layer along the mouth of the cavity in various reference frames corresponding to: the laboratory frame (top image); a frame moving at 0.25 U_∞ (middle image) and at 0.5 U_∞ (bottom image), in which U_∞ is the freestream velocity. (Lin and Rockwell, 2000)

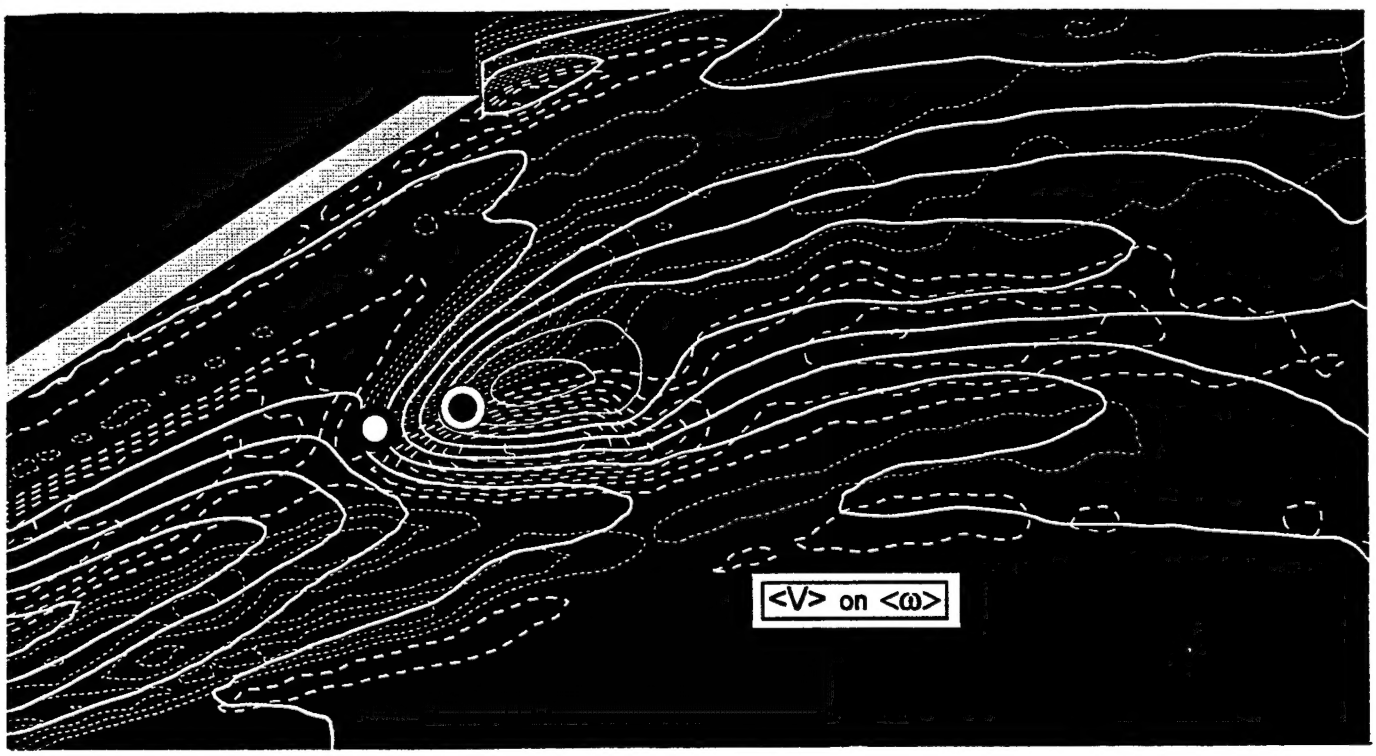

Figure 14: Superposition of contours of averaged velocity < V > on contours of averaged vorticity < ω >, taken from the images of Figure 13, in order to allow comparison of criteria for the onset of vortex breakdown. Upstream dot corresponds to criterion based on switch in sign of azimuthal vorticity; downstream dot represents the criterion based on occurrence of the stagnation point along the axis of the vortex. (Ozgoren, Sahin and Rockwell, 2000)

Figure 15: Contours of instantaneous azimuthal vorticity in the vicinity of vortex breakdown; image is one from a series used to construct the averaged contours of vorticity depicted in Figure 13. (Ozgoren, Sahin and Rockwell, 2000)

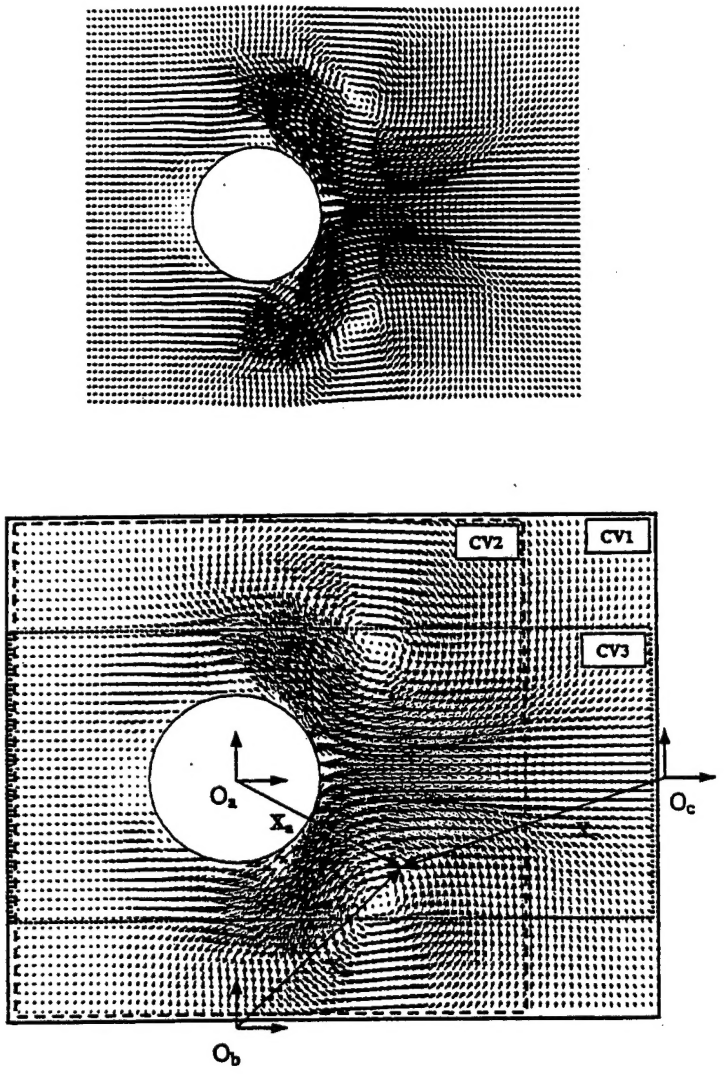

Figure 8: Representative PIV image corresponding to transient motion of a cylinder and typical control volumes CV1, CV2 and CV3 and coordinate origins O_a, O_b, and O_c employed for comparative assessment of force calculations. (Noca, Shiels and Jeon, 1999)

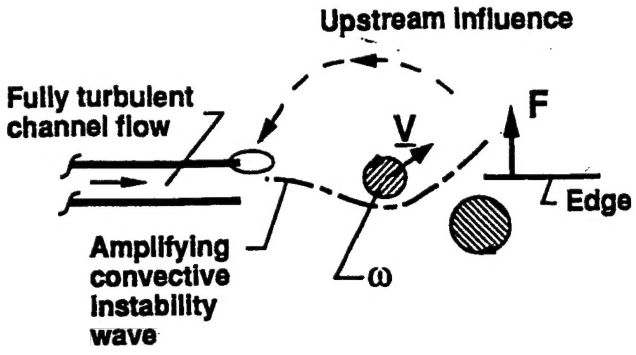

Figure 9: Schematic of self-sustaining oscillations due to impingement of a vortex system upon a stationary edge.

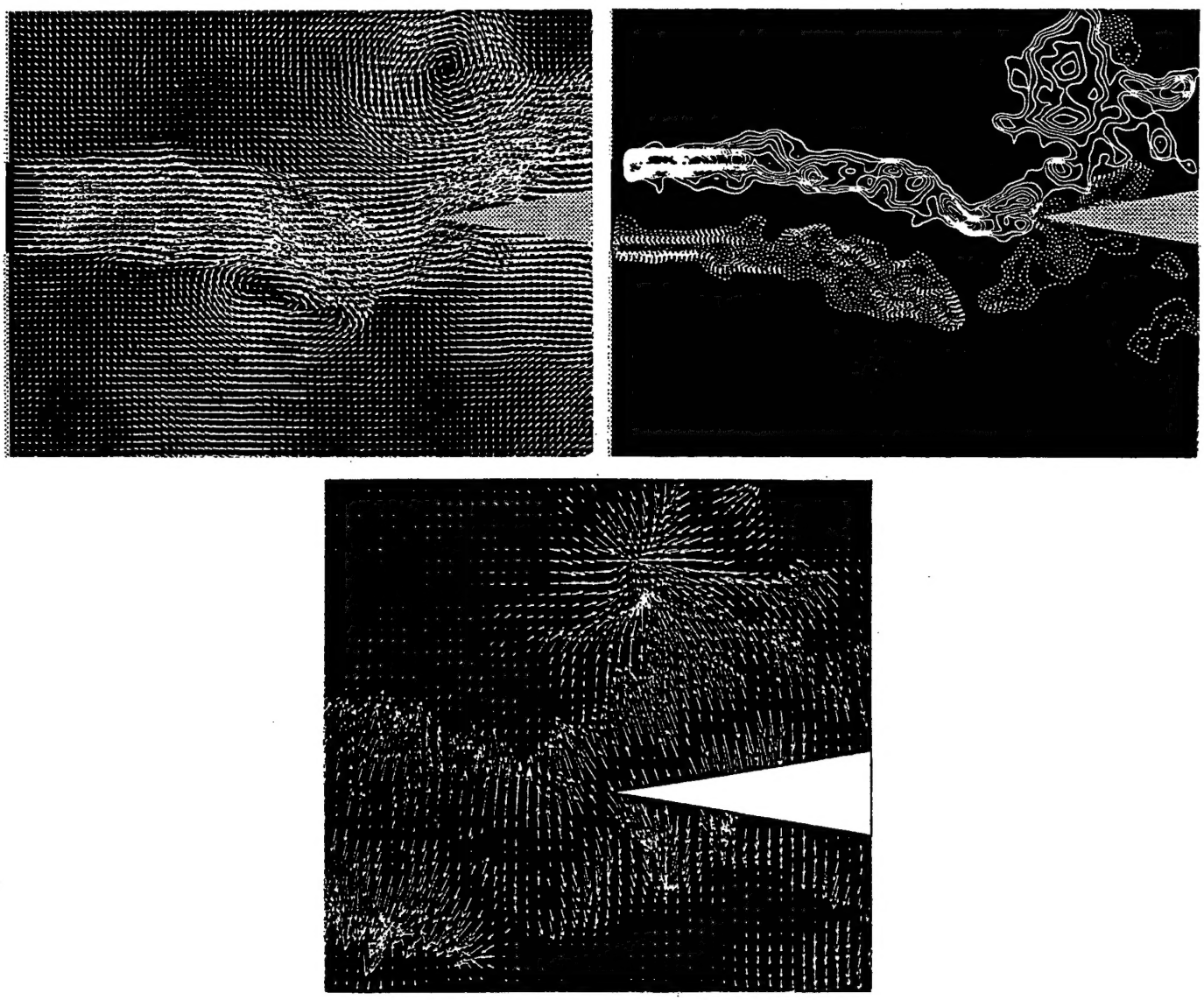

Figure 10: Patterns of instantaneous velocity (top image), vorticity (middle image) and vectors of the quantity $\underline{\omega} \wedge \underline{V}$ of the acoustic power integral for the case of a jet formed from a fully-turbulent channel flow, as illustrated in the schematic of Figure 9. Patterns of velocity and vorticity are excerpts from a highly time resolved cinema PIV sequence. (Lin and Rockwell,